Sorbonne Université

mémoire d'Habilitation à Diriger des Recherches

Couplage entre écoulements moyens et modes rapides en milieu stratifié

MICHEL Guillaume

Soutenue publiquement le 6 mai 2026 devant un jury composé de :

BOTTON Valéry	Rapporteur
DAUXOIS Thierry	Excusé
GALLAIRE François	Rapporteur
GALLET Basile	Rapporteur
LAGRÉE Pierre-Yves	Examinateur
WUNENBURGER Régis	Examinateur

Table des matières

Avant-propos **1**

1 Modes rapides instables : cas de la turbulence stratifiée **3**
1.1 Généralités sur la turbulence stratifiée . . . 3
1.1.1 Mouvement lagrangien dans un fluide stratifié au repos . . . 4
1.1.2 Approximation de Boussinesq . . . 5
1.1.3 Régime de paramètres de la turbulence stratifiée . . . 7
1.1.4 Une approche “à la Kolmogorov” . . . 9
1.1.5 Éléments de comparaison . . . 12
1.1.6 Qu'en est-il des ondes internes de gravité ? . . . 13
1.2 Couplage direct entre grandes échelles et modes rapides . . . 14
1.2.1 Instabilités non visqueuses des écoulements parallèles stratifiés . . . 14
1.2.2 Développement d'un modèle en échelles multiples . . . 16
1.2.3 Un premier modèle jouet . . . 17
1.3 Présentation synthétique du travail effectué . . . 20
1.3.1 Systèmes quasi-linéaires avec fluctuations potentiellement instables . . . 20
1.3.2 Couplage entre grandes échelles et modes rapides en turbulence stratifiée . . . 22
1.4 Perspectives . . . 23
1.4.1 Description cohérente de la couche critique . . . 24
1.4.2 Détermination de l'amplitude des fluctuations dans un cadre plus général . . . 25
1.4.3 Comparaison à des simulations numériques directes . . . 26

2 Modes rapides oscillants : streaming acoustique barocline **27**
2.1 Modélisation quasi-linéaire de la QBO . . . 27
2.1.1 Onde interne linéaire, non amortie, en l'absence d'écoulement moyen . . . 27
2.1.2 Onde interne linéaire, amortie, en présence d'un écoulement moyen constant . . . 29
2.1.3 Dynamique de l'écoulement moyen . . . 31
2.2 Streaming de Rayleigh dans un fluide homogène . . . 33
2.2.1 Mise en équation . . . 33
2.2.2 Résolution en échelles multiples . . . 35
2.3 Streaming acoustique dans un fluide inhomogène . . . 39
2.3.1 Mise en équation du streaming barocline . . . 40
2.3.2 Précisions et propriétés du système couplé . . . 42
2.4 Présentation synthétique du travail effectué . . . 44
2.4.1 Transferts thermiques dans un canal de rapport d'aspect $\delta \ll 1$ . . . 44
2.4.2 Transferts thermiques dans un canal de rapport d'aspect $\delta = O(1)$ . . . 46
2.4.3 Transition entre streaming de Rayleigh et streaming barocline . . . 49
2.4.4 Mise en évidence expérimentale . . . 51
2.5 Perspectives . . . 53
2.5.1 Amélioration de la méthode numérique . . . 53
2.5.2 Instabilité hydrodynamique dans le cas d'une onde acoustique verticale . . . 55
2.5.3 Effet de la gravité et convection thermo-vibrationnelle . . . 56
2.5.4 Réalisation d'une nouvelle expérience de streaming barocline . . . 57
2.5.5 Streaming barocline et ondes de surface . . . 57

3 Documents annexes **63**
3.1 Multiple scales analysis of slow–fast quasi-linear systems (présenté §1.3.1) . . . 65
3.2 Exploiting self-organized criticality in strongly stratified turbulence (présenté §1.3.2) . . . 83
3.3 Strong wave–mean-flow coupling in baroclinic acoustic streaming (présenté §2.4.1) . . . 115
3.4 Aspect-ratio-dependent heat transport by baroclinic acoustic streaming (présenté §2.4.2) . . . 143
3.5 Baroclinic transition in acoustic streaming : beyond Rayleigh's paradigm (présenté §2.4.3) . . . 161
3.6 Cooling by Baroclinic Acoustic Streaming (présenté §2.4.4) . . . 183
3.7 CV détaillé . . . 189

Bibliographie **193**

Avant-propos

Ce manuscrit présente des travaux effectués depuis ma soutenance de thèse (2017). Ils ont été principalement réalisés avec Greg Chini, professeur à l'université du New Hampshire, que j'ai rencontré au cours d'un programme de mécanique des fluides géophysiques à l'institut océanique de Woods Hole (États-Unis). Il m'a initié à ces sujets pendant mon post-doctorat et j'ai plaisir à poursuivre notre collaboration, notamment en co-encadrant la thèse de Remil Mushthaq (soutenue le 11 novembre 2025). Restreindre ce document à ces résultats constitue un ensemble cohérent, mais exclut mes autres centres d'intérêt : je ne parlerai donc ni d'ondes de surface, ni de couplage entre ondes et paroi mobile, ni de turbulence homogène ou diphasique. De cette manière, je me limite à mes thématiques de recherches indépendantes de celles entamées en master et doctorat. Je renvoie le lecteur souhaitant plus de détails sur l'ensemble de mon parcours à mon CV à la fin du chapitre 3.

Nous nous concentrons ici sur les milieux fluides stratifiés. Omniprésents en géophysique (atmosphère, océan), en astrophysique et dans l'industrie, ils sont principalement étudiés afin de prédire – voire maîtriser – leurs propriétés de transport. Nous détaillons deux cas où la stratification fait émerger un couplage fort entre des modes rapides et un écoulement lentement variable. Ce couplage est essentiel pour rendre compte des échanges de masse et de chaleur.

Le premier cas concerne la turbulence stratifiée. Dans ce système, la gravité agit comme une force de rappel efficace suivant une direction que nous désignerons comme verticale. Cette contrainte engendre la formation de structures anisotropes à grande échelle : l'écoulement s'organise en un empilement de couches verticalement minces et horizontalement étendues. Ces couches peuvent interagir entre elles pour transférer de l'énergie vers les petites échelles, de façon analogue à la cascade directe en turbulence 3D homogène isotrope. Par ailleurs, au sein de ces couches minces, le cisaillement peut déclencher des instabilités de type Kelvin-Helmholtz, transférant de l'énergie de façon non locale vers des modes d'extension horizontale beaucoup plus petite. En pratique, ces deux mécanismes coexistent, enrichissant la phénoménologie de la turbulence stratifiée par rapport à son homologue homogène. Notre travail a consisté à appliquer la méthode des échelles multiples, spatiales et temporelles, aux équations constitutives de la mécanique des fluides stratifiés, afin d'obtenir deux systèmes d'équations couplés : l'un décrivant l'évolution lente (en temps et en espace) des larges couches anisotropes, l'autre caractérisant l'évolution rapide des modes hydrodynamiques issus des instabilités. La structure mathématique de ce système couplé est originale ; le mécanisme de saturation de ces instabilités reposant intégralement sur une rétroaction sur les grandes structures. Une étude numérique nous a ensuite permis d'extraire des coefficients de mélange dans des configurations simplifiées.

Le second cas porte sur le streaming acoustique en présence d'inhomogénéités de densité. Dans un milieu au repos, il est établi depuis les années 1850 qu'une onde acoustique stationnaire engendre, via les termes non linéaires de l'équation de Navier-Stokes, un écoulement moyen appelé "écoulement rectifié" (ou "*streaming flow*"). Rayleigh calcula cet écoulement pour une onde stationnaire dans un canal d'épaisseur H telle que $\delta \ll H \ll \lambda$, avec δ l'épaisseur de la couche limite oscillante et λ la longueur d'onde acoustique. Ce phénomène est aujourd'hui exploité en microfluidique pour induire un mélange efficace dans la direction transversale. Dans les années 2000, une série d'expériences et de simulations numériques a montré que les prédictions de Rayleigh échouent à décrire le streaming dans les fluides inhomogènes : les profils spatiaux ne correspondent pas et les vitesses observées sont plusieurs ordres de grandeur supérieures à celles attendues. Nous présentons ici une étude théorique et expérimentale de ce phénomène. Une analyse en échelles multiples couple l'écoulement de streaming aux oscillations acoustiques : les ondes acoustiques forcent un écoulement moyen qui advecte les inhomogénéités de densité et, par ce biais, rétroagit sur les ondes. Le changement de régime induit par la stratification du fluide s'explique naturellement dans ce cadre. Nous avons détaillé cet effet avec pour perspective l'augmentation des transferts thermiques dans des milieux où ils sont limités, par exemple dans un gaz stablement stratifié au repos.

Ces deux exemples illustrent des couplages réciproques entre écoulements lentement variables et modes rapides qui disparaissent dans la limite d'un fluide homogène. Bien que ces problèmes soient fondamentalement différents, la structure mathématique du système couplé présente des similarités. En particulier, la dynamique des modes rapides, dite *quasi-linéaire*, ne comporte aucun terme non linéaire : sur l'échelle de temps rapide, les solutions sont des modes de taux de croissance réel (turbulence stratifiée) ou purement imaginaire (streaming acoustique). L'obtention des équations gouvernant l'évolution lente de l'amplitude de ces modes nécessite de prendre en compte la rétroaction sur l'écoulement lentement variable et demeure, à ma connaissance, peu documentée.

Ce document introduit successivement ces deux sujets en rappelant les notions essentielles nécessaires à leur compréhension. Les résultats sont ensuite résumés puis complétés par des perspectives envisagées à court et moyen terme. Les articles associés, reportés en toute fin de manuscrit, fournissent si besoin des détails supplémentaires.

Chapitre 1

Modes rapides instables : cas de la turbulence stratifiée

La première partie de ce manuscrit décrit le couplage entre les grandes structures de la turbulence stratifiée et des modes rapides, potentiellement instables et d'extension horizontale bien plus faible. Pour contextualiser ces résultats, une brève présentation de la turbulence en milieu stratifiée est proposée ici, abordant successivement l'approximation de Boussinesq, les nombres sans dimension (et en particulier le nombre de Froude) gouvernant le rapport d'aspect des structures anisotropes émergentes, ainsi que l'approche "à la Kolmogorov" pour décrire la cascade locale d'énergie. Cette introduction est loin d'être exhaustive et n'a pas pour ambition de se substituer aux nombreuses revues existantes. En particulier, les références [1–3] introduisent et discutent les différentes mesures du mélange, non détaillées ici.

Une des limites de l'hypothèse de cascade locale d'énergie réside dans l'existence avérées d'instabilités de type Kelvin-Helmholtz en turbulence stratifiée, causées par la structure de l'écoulement en couches minces frottement cisaillées. Après quelques rappels sur l'analyse de stabilité linéaire des écoulements parallèles stratifiés, le modèle en échelles multiples que nous avons développé sera présenté, puis son comportement générique illustré dans un cas plus simple. Enfin, une synthèse de nos résultats ainsi que quelques perspectives futures seront détaillées.

1.1 Généralités sur la turbulence stratifiée

Le problème étudié est schématisé Figure 1.1. À la manière d'une expérience de turbulence 3D homogène isotrope, il s'agit d'un fluide mis en mouvement par un ensemble de pièces mobiles dont on contrôle l'espacement et la vitesse de rotation. Toutefois, le fluide est ici initialement stratifié suivant la direction verticale : sa masse volumique est $\rho(\mathbf{r}, t = 0) = \rho_0(z)$. Cette dépendance est habituellement modélisée comme linéaire, d'une part pour simplifier l'analyse, d'autre part car cela est réalisable expérimentalement avec la méthode des deux bacs. Les pales sont invariantes dans la direction verticale, de longueur "infinie", et génèrent un écoulement horizontal. Par la suite, des instabilités font apparaître des composantes verticales qui favorisent le mélange. En fonction des différents paramètres (échelle intégrale L, vitesse imposée de l'écoulement à cette échelle U, stratification initiale $\mathrm{d}\rho_0/\mathrm{d}z$), nous souhaitons répondre aux questions suivantes :

1. Quelle est la structure spatio-temporelle de l'écoulement ?
2. Comment l'énergie est-elle répartie et transférée entre les différentes échelles ?
3. Si la stratification n'est pas maintenue aux extrémités du dispositif, quelle durée de forçage est nécessaire pour rendre le fluide homogène ?
4. Si une différence de température (pour un gaz) ou de salinité (pour de l'eau) est imposée entre les parois supérieure et inférieure, quelle durée faut-il pour atteindre le régime stationnaire ? Quel est alors le flux vertical moyen de chaleur ou de salinité ?
5. Existe-t-il une paramétrisation de ce régime turbulent capable de fournir des estimations fiables du comportement à grande échelle tout en évitant la simulation numérique des plus petites échelles ?

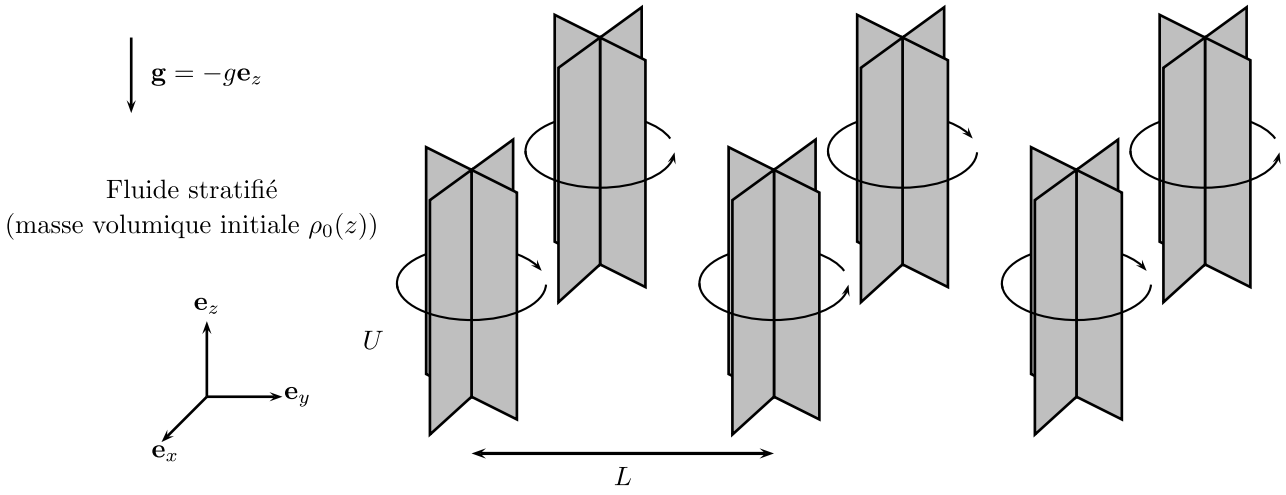

FIGURE 1.1 – Configuration canonique de turbulence stratifiée : un fluide initialement au repos et stratifié selon la coordonnée verticale est mis en mouvement à une vitesse U par un ensemble de pales espacées de L.

1.1.1 Mouvement lagrangien dans un fluide stratifié au repos

Une approche lagrangienne saisit simplement deux conséquences de la stratification dans un fluide au repos, de masse volumique $\rho_0(z)$. Considérons le bilan des forces exercées sur une particule de fluide de masse m et volume initial V_0, déplacée de sa position d'équilibre $\mathbf{r}_0$ d'une quantité infinitésimale $\delta\mathbf{r} = \delta x(t)\mathbf{e}_x + \delta y(t)\mathbf{e}_y + \delta z(t)\mathbf{e}_z$. En négligeant les phénomènes diffusifs, l'évolution est isentropique et la variation de volume s'exprime en fonction du coefficient de compressibilité isentropique χ_S,

$$\chi_S = -\frac{1}{V}\left(\frac{\partial V}{\partial P}\right)_S \Longrightarrow \delta V(t) = -V_0\chi_S\delta P(t). \tag{1.1}$$

Le fluide étant proche de son état d'équilibre, le champ de pression est hydrostatique et s'équilibre avec la pression de la particule de fluide (on néglige les modes acoustiques),

$$\delta P(t) = -\rho_0(z_0)g\delta z(t) \Longrightarrow \delta V = V_0\chi_S\rho_0(z_0)g\delta z(t). \tag{1.2}$$

La résultante des forces est la somme du poids et de la poussée d'Archimède,

$$\mathbf{F} = m\mathbf{g} + \mathbf{\Pi} = \{m - \rho_0\left[z_0 + \delta z(t)\right] \times \left[V_0 + \delta V(t)\right]\}\mathbf{g} \tag{1.3}$$

$$= \{m - \left[\rho_0(z_0) + \delta z(t)\frac{\mathrm{d}\rho_0}{\mathrm{d}z}(z_0)\right] \times V_0\left[1 + \chi_S\rho_0(z_0)g\delta z(t)\right]\}\mathbf{g} \tag{1.4}$$

$$= m\{1 - \left[1 + \delta z(t)\frac{1}{\rho_0(z_0)}\frac{\mathrm{d}\rho_0}{\mathrm{d}z}(z_0)\right] \times \left[1 + \chi_S\rho_0(z_0)g\delta z(t)\right]\}\mathbf{g} \tag{1.5}$$

$$= -m\delta z(t)N^2\mathbf{e}_z, \tag{1.6}$$

en restant au premier ordre en δz et en définissant le carré de la fréquence de Brunt-Väisälä

$$\boxed{N^2 = -g\left(\rho_0 g\chi_S + \frac{1}{\rho_0}\frac{\mathrm{d}\rho_0}{\mathrm{d}z}\right)} \tag{1.7}$$

Le mouvement vertical de la particule de fluide est alors solution de $\delta\ddot{z} + N^2\delta z = 0$. Ainsi :

1. Si $N^2 < 0$, $\delta z(t)$ diverge : la convection se déclenche de manière inconditionnelle.
2. Si $N^2 = 0$, l'équilibre est marginalement stable. On retrouve le gradient adiabatique $(\frac{\mathrm{d}\rho_0}{\mathrm{d}z})_{\mathrm{ad}} = -\rho_0^2 g\chi_S$ qui, pour l'air sec, équivaut à une variation de température d'environ $-10\ \mathrm{K}\cdot\mathrm{km}^{-1}$.
3. Si $N^2 > 0$, la particule de fluide effectue des oscillations verticales : il s'agit d'ondes internes de gravité. Leur période minimale, pour l'océan comme pour l'atmosphère, est de l'ordre de l'heure.

Approximation de la fréquence de Brunt-Väisälä

La fréquence de Brunt-Väisälä regroupe deux contributions : la première est liée à la compressibilité ($\rho_0 g \chi_S$), tandis que la seconde persiste pour une particule de fluide incompressible ($\rho_0^{-1} \mathrm{d}\rho_0/\mathrm{d}z$). Lorsque la stratification dépasse largement le gradient adiabatique, on peut approximer N^2 par le seul terme

$$N^2 \simeq -\frac{g}{\rho_0}\frac{\mathrm{d}\rho_0}{\mathrm{d}z}. \tag{1.8}$$

C'est par exemple le cas pour les expériences de laboratoire réalisées avec de l'eau de salinité variable ($|\mathrm{d}\rho_0/\mathrm{d}z| \sim 10^2$ kg $\cdot$ m^{-4}), ce qui se vérifie en calculant le gradient adiabatique $|\mathrm{d}\rho_0/\mathrm{d}z|_{\mathrm{adiab}} \simeq 5\ 10^{-3}$ kg $\cdot$ m^{-4} à partir de la vitesse du son $c_s = 1/\sqrt{\rho_0 \chi_S}$. En revanche, cela ne se justifie plus pour la modélisation de l'océan ou de l'atmosphère, où l'écart au gradient adiabatique reste modéré.

Aspects énergétiques

Si N^2 est positif et uniforme, cette force de rappel est associée à une énergie potentielle :

$$\mathbf{F} = -m\delta z N^2 \mathbf{e}_z = -\nabla\left(\frac{m\delta z^2 N^2}{2}\right) \equiv -\nabla \tilde{E}_p. \tag{1.9}$$

Les ondes internes de gravité réalisent, en moyenne, une équipartition entre cette énergie potentielle et l'énergie cinétique. Par la suite, on considérera des quantités volumiques, d'où la densité volumique d'énergie potentielle

$$\boxed{E_p = \frac{\rho_0}{2}(\delta z N)^2} \tag{1.10}$$

avec δz l'écart par rapport à la position initiale de la particule de fluide.

1.1.2 Approximation de Boussinesq

Revenons à une approche eulérienne. Pour les fluides stratifiés, il ne s'agit plus simplement de résoudre les équations de Navier-Stokes incompressibles : la thermodynamique doit aussi être prise en compte, comme le montre la présence de χ_S dans l'expression de N^2. Le système d'équations se complique alors considérablement, souvent inutilement. En effet, on peut démontrer que, sous certaines hypothèses, il se réduit à l'ordre dominant au jeu d'équations suivant : il s'agit de l'approximation de Boussinesq. En notant $\rho(\mathbf{r},t) = \rho_0 + \rho'(\mathbf{r},t)$ la masse volumique, $\tilde{b}(\mathbf{r},t) = -g\rho'(\mathbf{r},t)/\rho_0$ la flottabilité, $\mathbf{f}_{\mathrm{ext}}$ la densité volumique de force extérieure (hors gravité) et D le coefficient de diffusion approprié [1], on a :

$$\partial_t \mathbf{u} + (\mathbf{u}\cdot\nabla)\mathbf{u} = \mathbf{f}_{\mathrm{ext}} - \nabla\tilde{P} + \tilde{b}\mathbf{e}_z + \nu\triangle\mathbf{u}, \tag{1.11}$$

$$\nabla\cdot\mathbf{u} = 0, \tag{1.12}$$

$$\partial_t \tilde{b} + (\mathbf{u}\cdot\nabla)\tilde{b} = D\triangle\tilde{b}. \tag{1.13}$$

Par la suite, on s'intéressera à des stratifications initiales verticales, et posera donc $\tilde{b}(\mathbf{r},t) = b_{\mathrm{bg}}(z) + b(\mathbf{r},t)$. En absorbant dans une nouvelle pression P la contribution hydrostatique liée à $b_{\mathrm{bg}}(z)$, le système devient :

$$\partial_t \mathbf{u} + (\mathbf{u}\cdot\nabla)\mathbf{u} = \mathbf{f}_{\mathrm{ext}} - \nabla P + b\mathbf{e}_z + \nu\triangle\mathbf{u}, \tag{1.14}$$

$$\nabla\cdot\mathbf{u} = 0, \tag{1.15}$$

$$\partial_t b + (\mathbf{u}\cdot\nabla)b = -N^2 u_z + D\triangle b. \tag{1.16}$$

avec $N^2 = -\mathrm{d}b_{\mathrm{bg}}(z)/\mathrm{d}z$ déjà introduit par l'équation (1.7). On remarque en particulier que :

- les fluctuations de masse volumique ne persistent que dans le terme de pesanteur de (1.14)
- l'écoulement est incompressible
- ce jeu d'équations rend acceptable une périodicité suivant la direction verticale

1. Ce faisant, on s'interdit de décrire les effets de double diffusion pourtant pertinents en océanographie [4].

Cette approximation est tellement répandue qu'on en oublie parfois les hypothèses. Comme le montre la référence [5], elle résulte d'un développement à l'ordre dominant dans la limite $(\epsilon, Bo) \to 0$, avec $Bo = O(\epsilon)$ le "nombre de Boussinesq". Ces paramètres sont définis comme

$$\epsilon = \frac{U}{\sqrt{c_p T_0}}, \qquad Bo = \frac{H}{H_0}, \qquad H_0 = \frac{c_p T_0}{g}, \tag{1.17}$$

avec H, U, c_p et T_0 des valeurs caractéristiques de taille verticale des structures hydrodynamiques étudiées, vitesse horizontale, capacité thermique massique à pression constante et température. Pour un gaz, ϵ s'interprète comme le nombre de Mach ($\sqrt{c_p T}$ équivaut à la vitesse du son). H_0 désigne la hauteur caractéristique sur laquelle les propriétés du fluide évoluent à l'équilibre ($H_0 = 30$ km pour l'air - l'épaisseur de l'atmosphère isotherme à un facteur 7/2 près - et $H_0 = 120$ km pour l'eau). La condition $Bo \ll 1$ est donc facilement vérifiable hors du contexte de l'astrophysique.

Nous reviendrons sur la seconde hypothèse $Bo = O(\epsilon)$ plus tard dans ce chapitre. Elle peut s'énoncer ainsi : si la vitesse caractéristique horizontale U n'est pas émergente (comme dans le cas de la convection) mais imposée par un opérateur (par exemple, via une paroi mobile), alors elle doit satisfaire :

$$U \sim H\sqrt{\frac{g}{H_0}}. \tag{1.18}$$

Énergie dans l'approximation de Boussinesq

Le système (1.14 - 1.16) conserve l'énergie massique totale en l'absence de forçage et de dissipation,

$$E = \iiint \left(\frac{\mathbf{u}\cdot\mathbf{u}}{2} + \frac{b^2}{2N^2} \right) \mathrm{d}^3V. \tag{1.19}$$

L'énergie cinétique est complétée par la composante potentielle déjà rencontrée en (1.10) sous la forme $(\delta z N)^2/2$. En l'absence de diffusion, l'évolution de la flottabilité b par (1.16) a pour solution $\delta b(t) = -N^2 \delta z(t)$, qui établit le lien entre ces deux expressions.

En présence de forçage et dissipation, les contributions cinétique E_k et potentielle E_p évoluent selon

$$\dot{E}_\mathrm{k} = \iiint \mathbf{f}_\mathrm{ext}\cdot\mathbf{u}\ \mathrm{d}^3V + \iiint b u_z\ \mathrm{d}^3V + \iiint \nu\mathbf{u}\cdot\triangle\mathbf{u}\ \mathrm{d}^3V \tag{1.20}$$

$$= \iiint \mathbf{f}_\mathrm{ext}\cdot\mathbf{u}\ \mathrm{d}^3V + \iiint b u_z\ \mathrm{d}^3V - \underbrace{\frac{\nu}{2}\iiint \left(\partial_i u_j + \partial_j u_i\right)^2\ \mathrm{d}^3V}_{\epsilon_k} \tag{1.21}$$

et

$$\dot{E}_\mathrm{p} = -\iiint b u_z\ \mathrm{d}^3V + \iiint D b \triangle b\ \mathrm{d}^3V \tag{1.22}$$

$$= -\iiint b u_z\ \mathrm{d}^3V - \underbrace{D\iiint (\nabla b)^2\ \mathrm{d}^3V}_{\epsilon_p} \tag{1.23}$$

avec ϵ_p et ϵ_k les taux de dissipation d'énergie potentielle et cinétique et u_z la composante verticale de la vitesse. Ces expressions illustrent le transfert entre les composantes potentielle et cinétique lors de l'advection verticale d'inhomogénéités de densité. Elles sont également très utiles pour quantifier l'efficacité du mélange. Parmi les nombreux indicateurs proposés dans la littérature, on trouve (voir [6])

$$\eta = \frac{\epsilon_p}{\epsilon_k + \epsilon_p}, \tag{1.24}$$

dont une justification s'obtient en considérant un état stationnaire et en réalisant une moyenne temporelle, notée $\langle\cdot\rangle$, des équations d'évolution des différentes formes d'énergie :

$$\langle\epsilon_p\rangle = \langle \iiint b u_z\ \mathrm{d}^3V\rangle, \quad \langle\epsilon_k + \epsilon_p\rangle = \langle \iiint \mathbf{f}_\mathrm{ext}\cdot\mathbf{u}\ \mathrm{d}^3V\rangle. \tag{1.25}$$

Le coefficient η, défini à partir de ϵ_p et ϵ_k qui sont des sorties courantes des simulations numériques directes, compare le flux advectif à la puissance injectée. En d'autres termes, il s'agit du rapport entre le résultat souhaité (flux moyen de chaleur ou de salinité) et le coût énergétique nécessaire pour maintenir ce mélange accéléré.

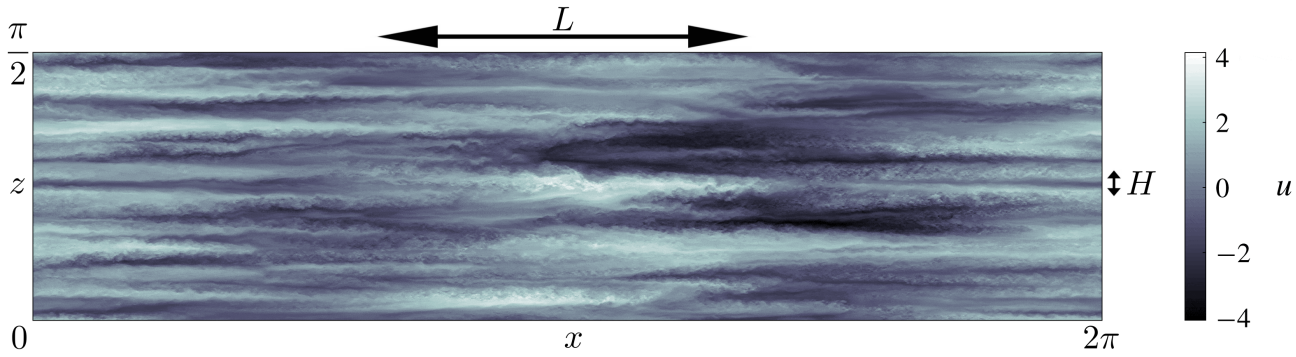

FIGURE 1.2 – Champ de vitesse horizontale en régime statistiquement stationnaire dans une simulation numérique directe tridimensionnelle de turbulence forcée et stratifiée. Les conditions aux limites sont périodiques dans les trois dimensions, le forçage injecte de l'énergie à l'échelle intégrale $L = 2\pi/3$. On observe l'émergence de couches minces d'épaisseur $H = L \times Fr$. Les paramètres sont $Pr = 1$, $Fr = 0.017$ et $Re = 7.78 \times 10^4$. Issue de [7].

1.1.3 Régime de paramètres de la turbulence stratifiée

Notre analyse de la turbulence stratifiée se fera dans le cadre de l'approximation de Boussinesq, qui offre une simplification substantielle du problème tout en restant pertinente pour modéliser les systèmes géophysiques.

Dispositif considéré et nombres sans dimension

Formellement, nous considérons un système stablement stratifié, infini, de fréquence de Brunt-Väisälä N, de viscosité cinématique ν et de coefficient de diffusion D uniformes. Le régime turbulent est obtenu grâce à un ensemble de pièces mobiles invariantes suivant la verticale, séparées d'une distance L et imposant une vitesse horizontale U, comme schématisé à la figure 1.1. Ainsi, seuls deux paramètres s'ajoutent par rapport à la turbulence 3D homogène isotrope : N et D. Outre le nombre de Reynolds Re, nous introduisons les nombres de Froude Fr et de Prandlt Pr,

$$\boxed{Re = \frac{UL}{\nu} \qquad Fr = \frac{U}{LN} \qquad Pr = \frac{\nu}{D}} \tag{1.26}$$

Le nombre de Prandlt dépend uniquement du fluide considéré, avec $Pr \sim 10^{-2}$ pour les métaux liquides, $Pr \simeq 1$ pour les gaz, $Pr \simeq 10$ pour l'eau et $Pr \sim 10^3$ pour des polymères. Pour l'atmosphère et l'océan, une approche asymptotique avec $Pr = O(1)$ convient donc.

Le nombre de Froude correspond au rapport entre la période d'oscillation minimale des ondes internes de gravité $2\pi/N$ et le temps de retournement de la circulation à l'échelle intégrale L/U. C'est le seul nombre sans dimension qui dépend de la stratification N : en maintenant (Re, Pr) constants, la limite homogène s'obtient pour $Fr \to \infty$ ($N \to 0$) tandis que $Fr \to 0$ décrit un régime fortement stratifié.

L'étude de la turbulence 3D homogène isotrope indique qu'une séparation d'échelle apparaît lorsque $Re \to \infty$. Nous nous plaçons donc dans la limite conjointe $\{Re \to \infty\ ,\ Fr \to 0,\ Pr = O(1)\}$. Il reste toutefois à préciser comment Re et Fr sont liés dans ce régime.

Observation de structures fortement anisotropes

Une simulation numérique directe fournit un premier aperçu du régime recherché, reporté à la figure 1.2. Bien que le champ de vitesse soit complexe, il met clairement en évidence l'émergence de structures anisotropes. Leur rapport d'aspect a fait l'objet de nombreuses études théoriques et numériques, aboutissant au consensus suivant : une structure de taille horizontale L acquiert spontanément une épaisseur

$$\boxed{H \sim L \times Fr} \tag{1.27}$$

Ce résultat est crucial pour la suite de l'analyse ; trois arguments le justifient, que je détaille ci-après.

Argument énergétique. Par hypothèse, les pales verticales en rotation imposent une vitesse horizontale U à l'écoulement. Une conversion intégrale de cette énergie cinétique par unité de volume $(\rho_0/2)U^2$ en énergie potentielle $(\rho_0/2) \times (HN)^2$ (cf. équation (1.10)) donne directement $H = U/N = L \times Fr$.

Argument de cohérence. À ma connaissance, cet argument n'a jamais été exposé dans la littérature, bien qu'il me semble pertinent. Comme indiqué §1.1.2, étant donné que la vitesse à l'échelle intégrale L est imposée par un opérateur externe, l'approximation de Boussinesq n'est justifiée que si

$$U \sim H\sqrt{\frac{g}{H_0}}. \tag{1.28}$$

Avec $H_0 \sim \rho_0/(\mathrm{d}\rho_0/\mathrm{d}z)$ et $N^2 \sim (g/\rho_0) \times (\mathrm{d}\rho_0/\mathrm{d}z)$, cette relation s'écrit également $H \sim L \times Fr$. Cette égalité est indispensable pour garantir la cohérence d'une description de la turbulence stratifiée dans l'approximation de Boussinesq. Ce n'est pas une preuve, mais si elle n'est pas vérifiée il ne sert à rien d'aller plus loin.

Argument d'auto-similarité. Cet argument, adapté de la référence [8], exploite l'idée que les structures à grande échelle que l'on souhaite décrire sont attendues indépendantes des coefficients de diffusion ν et D. Simplifions les équations dimensionnées (1.14 - 1.16) en éliminant (i) les termes qui disparaissent dans la limite $Fr \to 0$ quelle que soit la relation entre Fr, H/L et Re et (ii) les termes diffusifs liés à ν et D. L'étape (i), qui ne conserve que les effets dominants dans les milieux fortement stratifiés, sera plus claire une fois les équations adimensionnées explicitées (se référer à (1.34)). Il vient alors, en notant $\mathbf{u}_h$ et u_z les composantes horizontale et verticale de la vitesse,

$$\partial_t \mathbf{u}_h + (\mathbf{u}_h \cdot \nabla_h)\mathbf{u_h} + u_z \partial_z \mathbf{u}_h = -\nabla_h P, \quad 0 = -\partial_z P + b, \quad \nabla \cdot \mathbf{u} = 0, \quad \partial_t b + (\mathbf{u} \cdot \nabla) b = -N^2 u_z. \tag{1.29}$$

Par analyse dimensionnelle, suite à la disparition de Re et Pr, l'échelle émergente H vérifie

$$H = L \times \alpha(Fr), \tag{1.30}$$

où α est une fonction inconnue. Imposer l'invariance d'échelle de (1.29), sous-tendue par une image de gamme inertielle "à la Kolmogorov", mène à $\alpha(Fr) \propto Fr$. Il existe de nombreuses manières de formaliser cette démarche, et je mentionne ci-dessous les étapes que l'on enseigne aux mécaniciens de Sorbonne Université sur des cas plus simples :

1. Imposer des changements d'échelle aux huit grandeurs du problème $\{t, x, z, \mathbf{u}_h, u_z, P, b, N\}$, de la forme $t = t^* t'$ avec t^* un facteur d'échelle sans dimension.
2. Obtenir des contraintes sur les facteurs d'échelle pour que le système d'équations sur les nouvelles grandeurs $\{t', x', \ldots\}$ soit similaire au système d'équations initial. On en trouve cinq, permettant d'exprimer $\{z^*, b^*, P^*, u_z^*, t^*\}$ en fonction de trois facteurs d'échelle libres $\{x^*, u_h^*, N^*\}$, et en particulier $z^* = u_h^*/N^*$.
3. La relation (1.30) s'écrit après changement d'échelle

$$H' z^* = (L' x^*) \times \alpha\left(\frac{(U' u_h^*)}{(L' x^*)(N' N^*)}\right), \tag{1.31}$$

   or, d'après l'étape précédente, $z^* = u_h^*/N^*$, d'où

$$H' = L' \times \left(\frac{x^* N^*}{u_h^*}\right) \times \alpha\left[\frac{U'}{L' N'} \frac{u_h^*}{x^* N^*}\right]. \tag{1.32}$$

   L'invariance d'échelle est atteinte si cette relation ne fait plus intervenir les trois facteurs d'échelle libres $\{x^*, u_h^*, N^*\}$, c'est-à-dire si $\alpha(Fr) \propto Fr$, ce qui démontre le résultat annoncé.

Régime de paramètres de la turbulence stratifiée

Le rapport d'aspect des structures émergentes étant établi, nous introduisons des variables sans dimension. Cette étape permet de constater que l'anisotropie amplifie les phénomènes diffusifs suivant la petit dimension (ici la verticale), ce qui nous donnera un critère d'atteinte du régime turbulent. Dans les équations (1.14 - 1.16), on pose :

- $(x, y) = L\ (\tilde{x}, \tilde{y})$ (L dimension horizontale du forçage)
- $z = L\ Fr\ \tilde{z}$ ($H = L\ Fr$ épaisseur émergente des structures)
- $\mathbf{u}_h = U\ \tilde{\mathbf{u}}_h$ (U vitesse horizontale imposée par le forçage)
- $t = (L/U)\ \tilde{t}$ (L/U durée de retournement horizontal d'une structure)
- $P = U^2\ \tilde{P}$ pour conserver un terme de pression dans la dynamique horizontale
- $b = U^2/H\ \tilde{b}$ pour équilibrer le gradient de pression vertical
- $u_z = U\ Fr\ \tilde{u}_z$ pour conserver un équilibre entre $\partial_t b$ et $N^2 u_z$.

Il vient alors, en oubliant les tildes pour les variables sans dimension,

$$\partial_t \mathbf{u}_h + (\mathbf{u}_h \cdot \nabla_h)\mathbf{u}_h + u_z \partial_z \mathbf{u}_h = \mathbf{f}_{\text{ext}} - \nabla_h P + \frac{1}{Re}\left(\nabla_h^2 \mathbf{u}_h + \frac{1}{Fr^2}\partial_{zz}\mathbf{u}_h\right), \tag{1.33}$$

$$Fr^2\left[\partial_t u_z + (\mathbf{u}_h \cdot \nabla_h)u_z + u_z \partial_z u_z\right] = -\partial_z P + b + \frac{Fr^2}{Re}\left(\nabla_h^2 u_z + \frac{1}{Fr^2}\partial_{zz} u_z\right), \tag{1.34}$$

$$\nabla_h \cdot \mathbf{u}_h + \partial_z u_z = 0, \tag{1.35}$$

$$\partial_t b + (\mathbf{u}_h \cdot \nabla_h)b + u_z \partial_z b = -u_z + \frac{1}{PrRe}\left(\nabla_h^2 b + \frac{1}{Fr^2}\partial_{zz} b\right). \tag{1.36}$$

Des simplifications immédiates s'opèrent dans la limite ($Re \to \infty, Fr \to 0$) des milieux stratifiés turbulents :

$$\partial_t \mathbf{u}_h + (\mathbf{u}_h \cdot \nabla_h)\mathbf{u}_h + u_z \partial_z \mathbf{u}_h = \mathbf{f}_{\text{ext}} - \nabla_h P + \frac{1}{ReFr^2}\partial_{zz}\mathbf{u}_h, \tag{1.37}$$

$$0 = -\partial_z P + b, \tag{1.38}$$

$$\nabla_h \cdot \mathbf{u}_h + \partial_z u_z = 0, \tag{1.39}$$

$$\partial_t b + (\mathbf{u}_h \cdot \nabla_h)b + u_z \partial_z b = -u_z + \frac{1}{PrReFr^2}\partial_{zz} b. \tag{1.40}$$

Les nombres de Reynolds et Froude n'apparaissent plus qu'au travers d'un "nombre de Reynolds de flottabilité" $Re_b = Re\ Fr^2$ qui doit être grand pour que l'inertie domine les phénomènes dissipatifs. Pour les fluides usuels tels que $Pr = O(1)$, le passage de la turbulence homogène isotrope à la turbulence fortement stratifiée correspond à

$$\boxed{Fr \to 0 \qquad Re_b = Re\ Fr^2 \gg 1} \tag{1.41}$$

1.1.4 Une approche "à la Kolmogorov"

Par analogie avec la turbulence 3D homogène isotrope, pour laquelle l'approche de Kolmogorov décrit avec précision la répartition de l'énergie entre les différentes échelles spatiales, il est possible d'obtenir des spectres d'énergie autosimilaires en turbulence stratifiée [8–10]. Bien que la portée de ces résultats soit nettement plus restreinte, ils constituent néanmoins un point de comparaison incontournable.

Cascade d'énergie en turbulence 3D homogène isotrope

Rappelons les caractéristiques principales de la cascade d'énergie en turbulence 3D homogène isotrope. Un opérateur extérieur met en mouvement un objet de taille intégrale L à une vitesse U dans un fluide de masse volumique homogène ρ. Lorsque U est suffisamment élevée, la puissance injectée $\mathcal{P}$, d'origine inertielle, s'écrit

$$\mathcal{P} \sim \rho L^2 U^3. \tag{1.42}$$

La puissance moyenne dissipée par viscosité dynamique $\rho\nu$ à cette échelle L où le fluide se meut à la vitesse U,

$$\mathcal{P}'_L \sim \int_{L^3} \left(\rho\nu \frac{U}{L^2}\right) U\ \mathrm{d}^3\tau \sim \rho\nu L U^2, \tag{1.43}$$

ne l'équilibre pas. Plus précisément, le rapport de ces deux termes

$$\frac{\mathcal{P}'_L}{\mathcal{P}} \sim \frac{\rho\nu L U^2}{\rho L^2 U^3} \sim \frac{1}{Re} \ll 1, \tag{1.44}$$

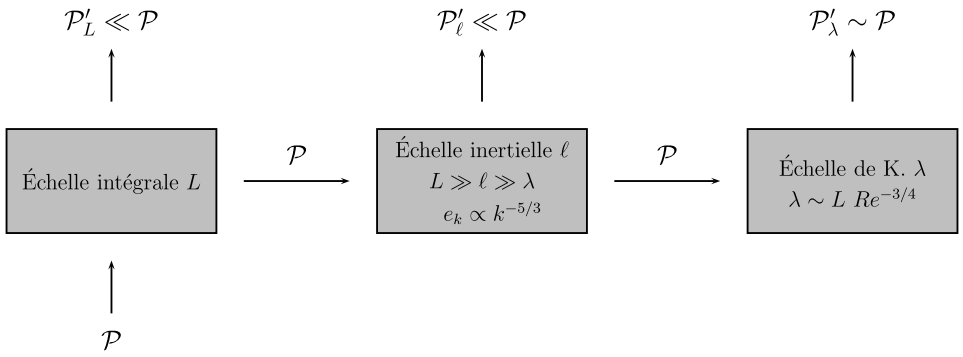

FIGURE 1.3 – Approche de Kolmogorov de la cascade d'énergie en turbulence 3D homogène isotrope. L'énergie injectée à l'échelle intégrale L est essentiellement dissipée autour de l'échelle de Kolmogorov $\lambda = L\ Re^{-3/4}$.

avec Re le nombre de Reynolds, supposé grand. Pour atteindre un régime permanent, une forme plus efficace de dissipation doit émerger. Seule la viscosité pouvant jouer ce rôle, elle doit œuvrer efficacement à une autre échelle, appelée échelle de Kolmogorov $\lambda \ll L$: la turbulence s'associe donc à une cascade d'énergie.

Si λ et L sont suffisamment séparés, on introduit l'échelle inertielle ℓ intermédiaire. L'hypothèse de Kolmogorov suppose un comportement intensif, correspondant à des interactions non linéaires locales ne transférant efficacement de l'énergie qu'entre structures de même taille. L'écoulement à une échelle ℓ est caractérisé par :

- La taille des structures impliquées ℓ
- La puissance par unité de volume devant être transférée aux échelles inférieures $\mathcal{P}/L^3$
- La vitesse caractéristique u_ℓ
- La masse volumique ρ

Nous avons "oublié" la viscosité (qui n'est efficace qu'à l'échelle de Kolmogorov) ainsi que les détails de l'échelle intégrale (L et U n'apparaissant qu'au travers de $\mathcal{P}/L^3$). Par analyse dimensionnelle,

$$u_\ell \sim (\varepsilon \ell)^{1/3}, \tag{1.45}$$

avec $\varepsilon = \mathcal{P}/(\rho L^3) \sim U^3/L$ le flux d'énergie par unité de masse. Pour tester ces prédictions, on trace la densité spectrale d'énergie cinétique par unité de masse e_k ($[e_k] = \mathrm{L}^3 \cdot \mathrm{T}^{-2}$) en fonction du nombre d'onde $k = 2\pi/\ell$,

$$e_k \sim \ell u_\ell^2 \sim \varepsilon^{2/3} k^{-5/3}. \tag{1.46}$$

La dépendance en $k^{-5/3}$, résultat fondamental de l'approche de Kolmogorov, est bien vérifiée expérimentalement. Il reste à déterminer l'échelle de Kolmogorov. Pour cela, comparons la puissance moyenne dissipée par viscosité à une échelle ℓ à celle injectée par l'opérateur extérieur,

$$\frac{\mathcal{P}'_\ell}{\mathcal{P}} \sim \frac{\rho \nu L^3 (u_\ell^2 \ell^{-2})}{\rho L^2 U^3} \sim \frac{1}{Re}\left(\frac{L}{\ell}\right)^{4/3} \underset{\mathcal{P}'_\lambda \sim \mathcal{P}}{\Longrightarrow} \lambda \sim \frac{L}{Re^{3/4}}. \tag{1.47}$$

Un schéma récapitulatif est reporté à la figure 1.3.

Stratification et longueur d'Ozmidov

Comment adapter ces résultats à la turbulence stratifiée ? Le point de départ est identique : les pales, schématisées à la figure 1.1, imposent une vitesse U horizontale à l'échelle L. Cette direction étant orthogonale à la stratification, la puissance injectée demeure $P \sim \rho_0 L^2 U^3$ et le flux d'énergie par unité de masse $\varepsilon \sim U^3/L$.

Cette puissance est dissipée par des structures très petites, peu affectées par la stratification. Supposons donc qu'à partir d'une échelle appelée longueur d'Ozmidov ℓ_O, la turbulence redevient 3D homogène isotrope avec des structures de vitesse $u_\ell \sim (\varepsilon \ell)^{1/3}$ qui transfèrent l'énergie jusqu'à l'échelle de Kolmogorov λ. Le domaine de validité de cette hypothèse s'obtient en évaluant, dans cette gamme inertielle 3D homogène isotrope, le rapport entre l'énergie cinétique et l'énergie potentielle associée à la stratification (1.10),

$$\frac{E_c}{E_p} \sim \frac{\rho_0 u_\ell^2}{\rho_0 (\ell N)^2} \sim \left(\frac{\varepsilon N^{-3}}{\ell^2}\right)^{2/3} \equiv \left(\frac{\ell_O}{\ell}\right)^{4/3}, \tag{1.48}$$

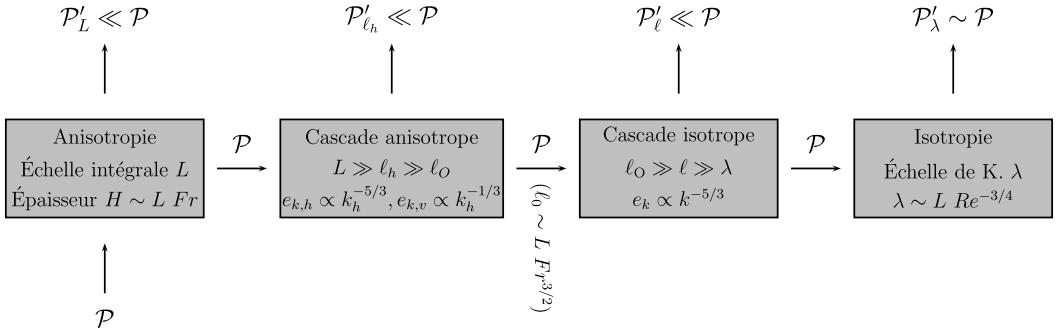

FIGURE 1.4 – Approche "à la Kolmogorov" de la turbulence stratifiée. Les étendues des cascades sont contrôlées par le nombre de Froude ($L/\ell_O = Fr^{-3/2}$) et le nombre de Reynolds de flottabilité ($\ell_O/\lambda = Re_b^{3/4}$), tandis que le rapport entre les échelles d'injection et de dissipation de l'énergie est toujours $\lambda/L = Re^{-3/4}$.

avec $\ell_O = \sqrt{\varepsilon/N^3}$. On trouve que, pour $\ell \ll \ell_O$, l'énergie cinétique domine et la stratification peut être oubliée : la turbulence est bien homogène. En exprimant ℓ_O et λ avec $Re = UL/\nu$, $Fr = U/(LN)$ et $Re_b = Re\ Fr^2$,

$$\boxed{\ell_O \equiv \sqrt{\frac{\varepsilon}{N^3}} \sim L\ Fr^{3/2} \qquad \lambda \equiv \frac{L}{Re^{3/4}} \sim \ell_O Re_b^{-3/4}} \tag{1.49}$$

Dans la limite de turbulence stratifiée (1.41), on obtient la hiérarchie de longueurs caractéristiques

$$\boxed{L \gg H \gg \ell_O \gg \lambda} \tag{1.50}$$

Gamme inertielle affectée par la stratification

Pour déterminer les spectres dans la gamme inertielle affectée par la stratification, on suppose que l'écoulement à une échelle horizontale ℓ_h ($L \gg \ell_h \gg \ell_O$) cascade localement une énergie par unité de masse $\epsilon \sim U^3/L$. D'après l'étude §1.1.3, les hypothèses suivantes sont posées pour les structures à cette échelle :

H1 taille verticale $\ell_z \sim u_h/N$ [d'après (1.27) et $Fr = U/(LN)$]
H2 vitesse verticale $u_z \sim u_h \ell_z/\ell_h$ [par incompressibilité, cf. (1.39)]
H3 énergie cinétique horizontale comparable à l'énergie potentielle [cf. argument énergétique pour (1.27)]
H4 transfert vers les petites échelles d'une énergie par unité de masse $\varepsilon \sim u_h^3/\ell_h$

Sous ces hypothèses, on peut exprimer les spectres d'énergie par unité de masse en fonction du nombre d'onde horizontal k_h ou vertical k_z :

- spectre d'énergie cinétique horizontale par unité de masse

$$e_{k,h}(k_h) \sim \ell_h u_h^2 \sim \varepsilon^{2/3} k_h^{-5/3}, \qquad \text{(H4)} \tag{1.51}$$
$$e_{k,h}(k_z) \sim \ell_z u_h^2 \sim \ell_z (N\ell_z)^2 \sim N^2 k_z^{-3}. \qquad \text{(H1)} \tag{1.52}$$

- spectre d'énergie cinétique verticale par unité de masse

$$e_{k,v}(k_h) \sim \ell_h u_z^2 \sim \frac{\varepsilon^{4/3}}{N^2} k_h^{-1/3}, \qquad \text{(H1+H2+H4)} \tag{1.53}$$
$$e_{k,v}(k_z) \sim \ell_z u_z^2 \sim \frac{\varepsilon^2}{N^4} k_z. \qquad \text{(H1+H2+H4)} \tag{1.54}$$

- spectre d'énergie potentielle par unité de masse

$$e_p(k_h) \sim e_{k,h}(k_h) \sim \varepsilon^{2/3} k_h^{-5/3}, \qquad \text{(H3)} \tag{1.55}$$
$$e_p(k_z) \sim e_{k,h}(k_z) \sim N^2 k_z^{-3}. \qquad \text{(H3)} \tag{1.56}$$

Ces spectres prédisent que les fluctuations de vitesse verticale u_z, d'ordre $U \times Fr$ à l'échelle intégrale, *augmentent* au cours de la cascade affectée par la stratification pour atteindre $U \times \sqrt{Fr}$ pour les structures de taille ℓ_O, puis diminuent aux plus petites échelles. La turbulence stratifiée, vue comme une succession de régimes auto-similaires, est représentée schématiquement à la figure 1.4.

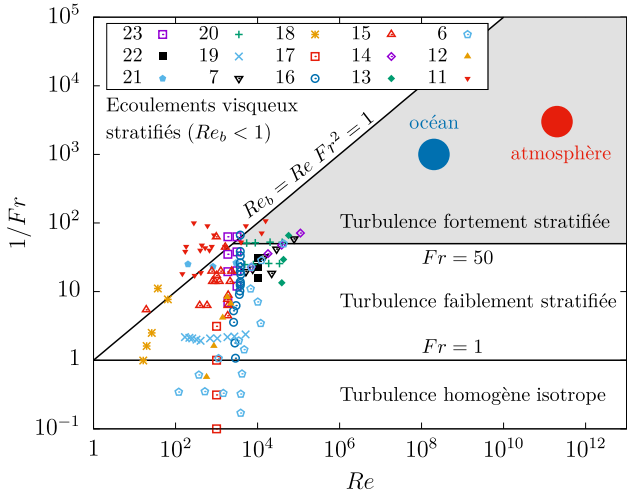

FIGURE 1.5 – Régimes de paramètres atteints par des simulations numériques directes récentes n'utilisant ni hyperviscosité ni modélisation des petites échelles. La légence précise la référence des études citées [6, 7, 11–23].

1.1.5 Éléments de comparaison

Ordres de grandeur pour les milieux naturels

Plusieurs écoulements géophysiques sont turbulents et fortement stratifiés. Des ordres de grandeur typiques sont présentés ci-dessous, en gardant à l'esprit que la variabilité spatiale et temporelle peut être très importante. Dans ces deux cas, on constate que le régime de turbulence stratifiée $\{Fr \ll 1, Re_b \gg 1\}$ est largement atteint.

L'océan : la couche supérieure de l'océan, de plusieurs centaines de mètres d'épaisseur, est stratifiée sous l'effet des variations verticales de température et salinité. On y mesure

- une fréquence de Brünt-Vaisala $N \sim 5\ 10^{-3}$ rad $\cdot$ s^{-1}
- un taux de dissipation d'énergie de $\varepsilon = O(10^{-10})$ à $O(10^{-7})$ m$^2 \cdot$ s^{-3}
- des vitesses horizontales $U \sim 10$ cm $\cdot$ s^{-1}

On en déduit [2] $L \simeq 10$ km, $Fr \simeq 10^{-3}$, $Re \simeq 10^9$, $Re_b \simeq 10^3$, $H \simeq 10$ m, $\ell_O \simeq 1$ m et $\lambda \simeq 1$ mm.

L'atmosphère : à partir de deux kilomètres d'altitude, la troposphère est stablement stratifiée. Ce phénomène est encore plus prononcé dans la stratosphère (entre 10 et 50 kilomètres d'altitude) à cause des rayonnements ultraviolets. On mesure dans la partie supérieure de la troposphère

- une fréquence de Brünt-Vaisala $N \sim 0.01$ rad $\cdot$ s^{-1}
- un taux de dissipation d'énergie de $\varepsilon = O(10^{-4})$ à $O(10^{-2})$ m$^2 \cdot$ s^{-3}
- des vitesses horizontales $U \sim 10$ m $\cdot$ s^{-1}

On en déduit $L \simeq 1000$ km, $Fr \simeq 10^{-3}$, $Re \simeq 10^{12}$, $Re_b \simeq 10^6$, $H \sim 1$ km, $\ell_O \sim 10$ m et $\lambda \simeq 1$ mm.

Simulations numériques directes

Pour vérifier ces relations, de nombreuses simulations numériques directes ont été réalisées. Sous l'approximation de Boussinesq, les équations impliquées ne présentent pas plus de difficultés que celles relatives à la turbulence homogène. Cependant, la séparation d'échelles spatiales nécessaire pour différentier les deux cascades (anisotrope puis isotrope) est considérable. La figure 1.5, qui présente les résultats numériques récents [6, 7, 11–24], montre que le régime $\{Fr \ll 1, Re_b \gg 1\}$ n'est atteint que marginalement.

De manière synthétique, les études numériques confirment la formation de structures élancées de rapport d'aspect Fr. Le profil vertical de densité est en escalier, avec de large portions de fluide quasi-homogènes séparées par de minces zones très fortement stratifiées (on parle de "couches" séparées par des "interfaces") [7]. Une très forte intermittence apparaît sur les statistiques de vitesse verticale [16, 24].

2. On rappelle $L = U^3/\varepsilon$, $Fr = U/(LN)$, $Re = UL/\nu$, $Re_b = Re\ Fr^2$, $H = L\ Fr$, $\ell_O = L\ Fr^{3/2}$ et $\lambda = L\ Re^{-3/4}$.

Les spectres d'énergie cinétique horizontale décroissent conformément aux prédictions en $k_h^{-5/3}$ attendues pour les turbulences homogène et stratifiée [11, 12, 20, 22]. En revanche, les variations verticales de cette énergie cinétique horizontale ne suivent la loi k_z^{-3}, prévue par l'équation (1.52), qu'après un filtrage spectral préalable du champ de vitesse. Cette étape consiste à isoler les composantes $k_h < 2\pi/\ell_O$ afin de séparer la cascade anisotrope et les modes isotropes étudiés ultérieurement [14]. Les spectres d'énergie cinétique verticales ont été beaucoup moins étudiés : les fluctuations de vitesse verticale maximale sont bien d'ordre $U \times \sqrt{Fr}$, mais ce maximum semble être atteint pour $k_h \sim L^{-1} \times Fr^{-1}$ plutôt que pour $k_h \sim (2\pi/\ell_O) \sim L^{-1}Fr^{-3/2}$ [23].

Enfin, l'existence de transferts d'énergie non locaux est régulièrement mentionnée. La référence [11] propose de séparer la cascade anisotrope en deux parties, la première pour $2\pi/k_h \in [L, L \times Fr]$ où ne sont observées que des structures fortement anisotropes, et la seconde entre $2\pi/k_h \in [L \times Fr, L \times Fr^{3/2}]$ où ces couches minces anisotropes coexistent avec des structures isotropes. Ces structures isotropes ont été qualitativement étudiées dans la référence [13] : fortement intermittentes, elles concentrent l'essentiel de la dissipation et du mélange dans le domaine, même si elles n'en occupent qu'une petite fraction (5% dans le jeu de paramètres étudié).

Expériences

Si le dispositif schématisé à la figure 1.1 est aisé à mettre en place au laboratoire, atteindre le régime de turbulence fortement stratifiée l'est bien moins. En effet, qu'il s'agisse d'eau dans laquelle on ajuste la concentration de sels (NaCl ou $MgCl_2$, par exemple) ou bien d'air chauffé par le haut, les fréquences de Brunt-Väisälä raisonnablement atteignables sont $N = O(1)$ rad $\cdot$ s^{-1}. Dans un dispositif de laboratoire de taille $L = O(1)$ m, atteindre la limite fortement stratifiée $Fr = U/(LN) \to 0$ implique donc de se limiter à des vitesses $U = O(10^{-2})$ m$\cdot$s^{-1}. Cela fixe le nombre de Reynolds $Re = UL/\nu = O(10^3)$ à $O(10^4)$, d'où un nombre de Reynolds de flottabilité $Re_b = Re\ Fr^2 = O(1)$ au maximum. On reste loin du régime turbulent $Re_b \gg 1$.

Il y a donc un compromis à réaliser entre forte stratification ($Fr \ll 1$) et turbulence développée ($Re_b \gg 1$) : atteindre des valeurs élevées de $Re_b = O(10^2)$ revient à se limiter à des stratifications $Fr = O(1)$ modestes [25, 26]. Un régime avec $Re_b = O(10)$ et $Fr = O(0.1)$ est atteint dans les expériences de conduit incliné stratifié [27], où deux réservoirs remplis de fluides de densités différentes sont reliés par un conduit légèrement incliné. Des spectres en $k^{-5/3}$ sont identifiables dans le régime de cascade isotrope ; en revanche, les prédictions relatives à la cascade locale anisotrope sont mises en défaut. Il faut modérer les implications de cette observation : les étendues des cascades anisotrope et isotrope, respectivement $Fr^{-3/2}$ et $Re_b^{3/4}$ (cf. Fig 1.4), restent ici limitées.

1.1.6 Qu'en est-il des ondes internes de gravité ?

Nous avons débuté ce chapitre en introduisant la fréquence N maximale des ondes internes de gravité, sans les mentionner par la suite, N étant simplement vu comme une mesure de la force de rappel verticale. Les caractéristiques de ces ondes s'obtiennent via le système de Boussinesq (1.14 - 1.16) linéarisé et non dissipatif,

$$\partial_t \mathbf{u} = -\nabla P + b\mathbf{e}_z, \quad \nabla \cdot \mathbf{u} = 0, \quad \partial_t b = -N^2 u_z, \tag{1.57}$$

en cherchant des solutions harmoniques $(\mathbf{u}, P, b) = (\mathbf{U}, \Pi, B)e^{i(\omega t - \mathbf{k}\cdot\mathbf{r})}$. En séparant les composantes horizontale et verticale du nombre d'onde $\mathbf{k} = \mathbf{k}_h + k_z\mathbf{e}_z$, la relation de dispersion $\omega = Nk_h/\sqrt{k_h^2 + k_z^2}$ s'obtient immédiatement, d'où l'on déduit $\omega \leqslant N$: ces ondes ont comme pulsation maximale N. Celles dont la structure spatiale correspond aux structures élancées identifiées précédemment en turbulence stratifiée sont telles que $k_z \gg |\mathbf{k}_h|$. À l'échelle intégrale, $k_z \sim |\mathbf{k}_\perp|/Fr$ mène à une période $2\pi\omega^{-1} \sim (N\ Fr)^{-1} \sim L/U$ déjà rencontrée pour caractériser les échanges d'énergie non linéaires [3] : les "structures élancées" décrites par le système réduit (1.37 - 1.40) sont un mélange d'ondes internes de gravité fortement non linéaires et de tourbillons.

Mentionnons l'existence de tout un pan de recherche sur la turbulence faible d'ondes internes. Cela correspond à des ondes internes forcées à grande échelle avec $k_\perp \sim L^{-1}$ et $k_z \sim H^{-1} \gg k_\perp$, mais avec des vitesses $U \ll NH$ (alors que $U \sim NH$ pour la turbulence fortement stratifiée). Une cascade d'énergie se développe grâce aux interactions non linéaires résonnantes entre ondes. Ces effets non linéaires restant limités, les périodes deviennent très rapides devant les durées d'interactions non linéaires, rendant possible une approche en échelles multiples. Ce régime ne sera pas abordé ici [4].

3. H1 ($\ell_z \sim u_z/N$) et H4 ($\epsilon \sim U^3/L \sim u_h^3/\ell_h$) impliquent que cette égalité persiste dans toute la cascade anisotrope.

4. Une introduction en français à la turbulence d'ondes dans le cas des ondes de surface peut être trouvée dans mon manuscrit de thèse [28], mais je recommande le livre de Nazarenko [29] pour les aspects théoriques ainsi que la revue expérimentale [30].

1.2 Couplage direct entre grandes échelles et modes rapides

1.2.1 Instabilités non visqueuses des écoulements parallèles stratifiés

En turbulence stratifiée, le poids devient une force de rappel selon la direction verticale entraînant l'émergence de structures fortement anisotropes (vitesse et taille verticales très faibles devant leurs équivalents horizontaux). De tels écoulements sont propices à l'apparition d'instabilités, la plus connue étant celle de Kelvin-Helmoltz. Elles sont ici caractérisées dans la limite d'un écoulement de base parallèle $\mathbf{U}(\mathbf{r},t) = U_0(z)\mathbf{e}_x$ et d'une dynamique non diffusive. Cette section est partiellement issue du livre de François Charru [31].

Équation de Taylor-Goldstein

Pour étudier la stabilité de l'état de base $\{U_0(z)\mathbf{e}_x,\ b_0 = 0\}$, on suit l'évolution temporelle de perturbations bidimensionnelles $\{\mathbf{u}(\mathbf{r},t) = u_h(x,z,t)\mathbf{e}_x + u_z(x,z,t)\mathbf{e}_z,\ b(x,z,t)\}$. Pour un fluide homogène, ce choix est dicté par le théorème de Squire, selon lequel une instabilité non visqueuse d'un écoulement parallèle est associée, à son seuil d'instabilité, à la croissance d'une perturbation 2D. Ce théorème reste valable dans un fluide stratifié soumis à un cisaillement vertical $U_0(z)\mathbf{e}_x$ [32] [5]. En reportant ce développement dans le système de Boussinesq (1.14 - 1.16), puis en linéarisant et en supprimant les termes diffusifs, on obtient :

$$\partial_t u_h + U_0(z)\partial_x u_h + u_z \partial_z U_0 = -\partial_x P, \tag{1.58}$$
$$\partial_t u_z + U_0(z)\partial_x u_z = -\partial_z P + b, \tag{1.59}$$
$$\partial_x u_h + \partial_z u_z = 0, \tag{1.60}$$
$$\partial_t b + U_0(z)\partial_x b = -N^2 u_z. \tag{1.61}$$

La perturbation étant bidimensionnelle et incompressible, on introduit une fonction de courant Ψ telle que $\{u_h = \partial_z\Psi, u_z = -\partial_x\Psi\}$, ce qui réduit ce jeu d'équations à

$$(\partial_t + U_0(z)\partial_x)\triangle\Psi = U_0''(z)\partial_x\Psi - \partial_x b, \qquad \partial_t b + U_0\partial_x b = N^2\partial_x\Psi. \tag{1.62}$$

Les coefficients de ces équations différentielles linéaires étant indépendants de x et de t, on cherche des solutions de la forme

$$\Psi(x,z,t) = \frac{1}{2}\left(\hat{\Psi}(z)e^{ik(x-ct)} + \text{c.c.}\right), \qquad b(x,z,t) = \frac{1}{2}\left(\hat{b}(z)e^{ik(x-ct)} + \text{c.c.}\right), \tag{1.63}$$

où c.c. désigne le complexe conjugué, k le nombre d'onde et c la vitesse de phase (potentiellement complexe). En injectant (1.63) dans (1.62), on obtient l'équation de Taylor-Goldstein :

$$\boxed{\left(\frac{\mathrm{d}^2}{\mathrm{d}z^2} - k^2\right)\hat{\Psi} = \frac{U_0''}{U_0 - c}\hat{\Psi} - \frac{N^2}{(U_0-c)^2}\hat{\Psi}} \tag{1.64}$$

Cette équation généralise l'équation de Rayleigh en milieu homogène ($N = 0$). L'étude de stabilité d'un profil de vitesse $U_0(z)$ donné consiste à déterminer, pour chaque nombre d'onde k réel, les valeurs de c autorisant des solutions non uniformément nulles de (1.64) qui vérifient les conditions aux limites [6].

Couches critiques

Dans les cas les plus simples, chaque valeur de k correspond à une unique vitesse de phase c qui n'égale jamais $U_0(z)$. L'analyse de stabilité est alors terminée : s'il existe un nombre d'onde k tel que $\mathrm{Im}(c) \neq 0$, alors ce mode croît (les valeurs de c admissibles sont complexes conjuguées) et son profil vertical $\hat{\Psi}(z)$ est connu.

Des complications arrivent lorsque $U_0(z) - c$ s'annule en une altitude z_c appelée "couche critique". D'après (1.64), $\hat{\Psi}''$ diverge, ce qui correspond à un saut de $\hat{\Psi}'$, c'est-à-dire de la vitesse horizontale $u_h = \partial_z\Psi$. Les solutions $\hat{\Psi}(z)$ restent calculables en résolvant (1.64) dans les zones où $U_0 - c \neq 0$ puis en les raccordant par continuité de la vitesse verticale $u_z = -\partial_x\Psi$, c'est-à-dire par continuité de $\hat{\Psi}$.

5. Il pourrait être mis en défaut pour un cisaillement horizontal $U_0(x)\mathbf{e}_y$ [33].
6. Typiquement $\hat{\Psi}(z = \pm\infty) = 0$ ou $\hat{\Psi}(z = \pm h) = 0$ pour annuler la vitesse verticale en ces endroits.

Dans les fluides homogènes, les couches critiques correspondent à des discontinuités de vitesses qui seraient régularisées par une viscosité finie. Dans les fluides stratifiés, il faut remarquer que (1.62) donne

$$\hat{b} = \frac{N^2}{U_0 - c}\hat{\Psi}. \tag{1.65}$$

La continuité de $\hat{\Psi}$, par continuité de vitesse verticale, implique donc qu'une couche limite est non seulement associée à une discontinuité de vitesse horizontale, mais aussi de masse volumique.

Conditions nécessaires pour l'existence d'instabilités

Il est possible de démontrer des conditions nécessaires sur $U_0(z)$ pour l'existence de modes instables :

- Pour un écoulement homogène ($N^2 = 0$), U_0 doit présenter un point d'inflexion [7] ; si U_0 est monotone, ce point doit en outre correspondre à un maximum de vorticité (critère de Fjortoft).
- Pour un écoulement inhomogène, le critère de Miles-Howard montre qu'il doit exister un point où le nombre de Richardson local satisfait $R_i < 1/4$, avec

$$R_i(z) = \frac{N^2}{U_0'(z)^2}. \tag{1.66}$$

Cela permet de prouver rapidement que certains écoulements sont stables en l'absence de viscosité, comme ceux de Couette et Poiseuille plans. Notons qu'une viscosité finie peut modifier cette conclusion : l'écoulement de Couette plan reste linéairement stable quelque soit le nombre de Reynolds, tandis que l'écoulement de Poiseuille plan devient linéairement instable pour $Re > 5\,772$. De plus, les conditions énoncées ici sont nécessaires mais pas suffisantes ; il est donc possible que l'écoulement reste linéairement stable même si ces conditions sont vérifiées.

Pertinence en turbulence stratifiée

Le régime de turbulence stratifiée s'accompagne de la formation de couches anisotropes : à l'échelle intégrale L de vitesse horizontale U, elles sont d'épaisseur $H \sim L\,Fr$ avec $Fr = U/(LN)$. Le nombre de Richardson local s'écrit alors

$$R_i = \frac{N^2}{U_0'(z)^2} \sim \frac{N^2H^2}{U^2} \sim \frac{N^2L^2}{U^2} \times Fr^2 \sim 1. \tag{1.67}$$

Ainsi, il n'y a aucune raison de supposer la stabilité de ces structures via le critère de Miles-Howard ; ce résultat reste valide pour toutes les échelles de la cascade anisotrope. Des mesures en océanographie montrent qu'en pratique ce paramètre reste proche de $1/4$ [34–36].

Le critère sur R_i n'est qu'une condition nécessaire d'instabilité pour des écoulements stationnaires non visqueux dont les champs de vitesse et de flottabilité ne dépendent que de la coordonnée verticale. Il faut donc se garder d'interpréter trop rapidement les conséquences de $R_i < 0.25$ en turbulence stratifiée (écoulements instationnaires avec des champs tridimensionnels). Un scénario possible, sur lequel repose les spectres obtenus §1.1.4, est que de telles instabilités, si jamais elles ont lieu, ont un effet négligeable sur la dynamique du système : $R_i \sim 1$ serait une conséquence fortuite de l'invariance d'échelle [37].

Il existe une interprétation complètement opposée à cette observation de $R_i = O(1)$. Dans ce second scénario [38–40], les grandes échelles voient leur vitesse croître progressivement sous l'effet des forces extérieures jusqu'à ce qu'une instabilité se déclenche à $R_i \sim 0.25$. Le mode émergent puise rapidement de l'énergie aux grandes échelles, son taux de croissance redevient négatif, il disparaît, puis le processus recommence. Le système s'éloigne alors peu de son état de stabilité marginale $R_i = O(1)$ uniquement à cause des échanges d'énergie non locaux. Ce raisonnement s'applique à toute la gamme de longueur comprise entre les échelles intégrale et la longueur d'Ozmidov. Ce scénario, où des échelles de temps très différentes (évolution lente des champs entre deux "avalanches" successives) conduisent à de l'intermittence et forme aux temps longs un régime auto-similaire où la stabilité marginale est approchée à chaque échelle, se place dans le cadre plus général de la criticité auto-organisée (*self-organized criticality*). De tels régimes sont observés en géophysique, en astrophysique et plus généralement dans un large éventail de systèmes dynamiques [41, 42].

7. Il s'agit du théorème de Rayleigh, dont la démonstration est triviale à partir de (1.64) : poser $N^2 = 0$, supposer l'existence d'un mode instable ($\mathrm{Im}(c) \neq 0$) multiplier par $\hat{\Psi}^*$ puis intégrer entre les hauteurs z_0 et z_1 telles que $\hat{\Psi}(z_0) = \hat{\Psi}(z_1) = 0$. La partie imaginaire de cette relation montre que U_0'' doit nécessairement changer de signe.

1.2.2 Développement d'un modèle en échelles multiples

Notre travail de recherche a consisté à développer un modèle qui capture le couplage entre une structure anisotrope (taille horizontale L, vitesse horizontale U, épaisseur $H \sim L\ Fr$, échelle de temps $T \sim L/U$) et des modes :

- d'échelle verticale H, fixée par la taille de la couche anisotrope
- d'échelle horizontale H, car les modes les plus instables dans l'équation de Taylor-Goldstein sont généralement isotropes
- évoluant sur une échelle de temps $\tau = T\ Fr$, car le taux de croissance $\sigma = (k \times \mathrm{Im}(c))^{-1}$ s'approxime, avec $k \sim H^{-1}$ et $\mathrm{Im}(c) \sim U$ pour une couche critique, à $\sigma \sim H/U \sim FrL/U \sim Fr\ T$
- de vitesse caractéristique $\sqrt{Fr}U$, déterminée a posteriori pour rétroagir sur les grandes échelles

Ces objets partagent une même dimension verticale, mais, dans la limite $Fr \to 0$ de la turbulence stratifiée, ils évoluent sur des échelles de longueur horizontale, de vitesse et de temps très différentes. Nous passons les étapes techniques, détaillées dans la publication associée, pour discuter du système obtenu. En notant avec des barres les grandeurs relatives aux grandes échelles et avec des apostrophes celles relatives aux petites structures :

Équations pour la dynamique lente des grandes échelles anisotropes

$$\left(\partial_t + \overline{\mathbf{u}}_h \cdot \overline{\nabla} + \overline{u}_z \partial_z\right) \overline{\mathbf{u}}_h = \overline{\mathbf{f}}_{\mathrm{ext}} - \overline{\nabla}\overline{p} - \partial_z \left(\overline{u'_z \mathbf{u}'_h}\right) + \frac{1}{Re_b}\partial_z^2 \overline{\mathbf{u}}_h, \tag{1.68}$$

$$0 = -\partial_z \overline{p} + \overline{b}, \tag{1.69}$$

$$\overline{\nabla} \cdot \overline{\mathbf{u}}_h + \partial_z \overline{u}_z = 0, \tag{1.70}$$

$$\left(\partial_t + \overline{\mathbf{u}}_h \cdot \overline{\nabla} + \overline{u}_z \partial_z\right) \overline{b} = -\overline{u}_z - \partial_z \left(\overline{u'_z b'}\right) + \frac{1}{PrRe_b}\partial_z^2 \overline{b}. \tag{1.71}$$

Équations pour la dynamique rapide des petites échelles isotropes

$$\left(\partial_\tau + \overline{\mathbf{u}}_h \cdot \nabla'\right) \mathbf{u}'_h + u'_z \partial_z \overline{\mathbf{u}}_h = -\nabla' p' + \frac{Fr}{Re_b}\left(\nabla'^2 + \partial_z^2\right) \mathbf{u}'_h, \tag{1.72}$$

$$\left(\partial_\tau + \overline{\mathbf{u}}_h \cdot \nabla'\right) u'_z = -\partial_z p' + b' + \frac{Fr}{Re_b}\left(\nabla'^2 + \partial_z^2\right) u'_z, \tag{1.73}$$

$$\nabla' \cdot \mathbf{u}'_h + \partial_z u'_z = 0, \tag{1.74}$$

$$\left(\partial_\tau + \overline{\mathbf{u}}_h \cdot \nabla'\right) b' + u'_z \partial_z \overline{b} = -u'_z + \frac{Fr}{PrRe_b}\left(\nabla'^2 + \partial_z^2\right) b'. \tag{1.75}$$

La dynamique des grandes échelles est très proche de celle obtenue précédemment, équations (1.37 - 1.40). La seule différence réside dans l'apparition d'une rétroaction des petites échelles. Ainsi, le transfert d'énergie local de la cascade anisotrope, associé aux termes inertiels non linéaires, coexiste avec des échanges non locaux via la divergence du tenseur de Reynolds ($\partial_z(\overline{u'_z \mathbf{u}'_h})$ et $\partial_z(\overline{u'_z b'})$). Des termes diffusifs $O(1/Re_b)$ apparaissent car ce système a été rigoureusement obtenu pour $Re_b = O(1)$, afin de caractériser également la transition vers la turbulence. La dynamique des petites échelles, très distincte, présente les caractéristiques suivantes :

1. les effets diffusifs sont bien plus faibles (ils sont conservés uniquement pour régulariser les couches critiques, mais ne devraient, à l'ordre dominant, pas être présents)
2. la dynamique verticale n'est plus hydrostatique
3. les non-linéarités impliquant deux termes rapides sont absents ; la saturation d'une éventuelle instabilité s'effectue donc par rétroaction sur les grandes échelles (on parle de dynamique quasi-linéaire).

Formellement, sur l'échelle de temps rapide, il s'agit donc d'un problème aux valeurs propres dont certains coefficients, traduisant le couplage avec les grandes échelles, évoluent sur le temps lent. Cette situation peut prêter à confusion : sur les échelles de temps rapides, des modes instables peuvent croître exponentiellement, ce qui semble contredire la possibilité d'un développement cohérent en échelles multiples et remettre en cause l'omission des termes non linéaires du type $(\mathbf{u}' \cdot \nabla)\mathbf{u}'$. La suite de ce chapitre présente des cas plus simples de systèmes quasi-linéaires afin de montrer qu'ils possèdent bien un sens physique, puis décrit une méthode d'analyse de ces systèmes.

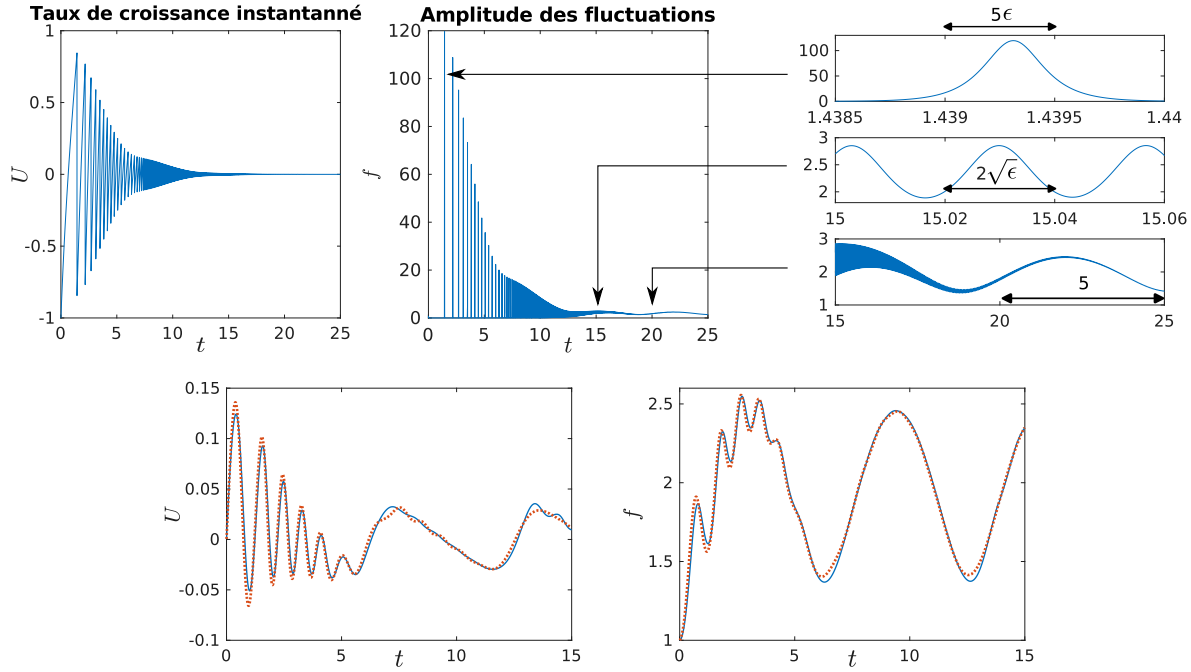

FIGURE 1.6 – Simulations numériques de (1.76 - 1.78). (haut) $\epsilon = 10^{-4}$ et $U(0) = -1$ (fluctuations initialement stables). La colonne de droite illustre les trois échelles de temps émergentes, rapide $O(\epsilon)$, intermédiaire $O(\sqrt{\epsilon})$ et lente $O(1)$. (bas) $\epsilon = 0.1$ et $U(0) = 0$ (fluctuations initialement marginalement stables). Les prédictions du modèle en échelles multiples, en pointillés, sont explicitées (1.100 - 1.103).

1.2.3 Un premier modèle jouet

Le système suivant, étudié pour le cadre de ce manuscrit, simplifie au maximum la dynamique précédente :

$$\frac{\mathrm{d}U}{\mathrm{d}t} = F_{\mathrm{ext}}(t) - \nu U - \frac{f^2}{2}, \tag{1.76}$$

$$\epsilon \frac{\mathrm{d}f}{\mathrm{d}t} = fU, \tag{1.77}$$

$$F_{\mathrm{ext}}(t) = 2 - \cos(t), \quad \nu = 1, \quad U(0) = \{-1, 0\}, \quad f(0) = 1. \tag{1.78}$$

Ici, U représente la vitesse des grandes structures anisotropes, soumises à un forçage extérieur, à la dissipation et à une rétroaction des petites échelles. La grandeur f modélise l'amplitude du mode isotrope, dont le taux de croissance dépend linéairement de l'écart au seuil $U = 0$. Les conditions initiales décrivent des fluctuations développées ($f > 0$) et marginalement ou totalement stables ($U(0) = 0$ ou $U(0) = -1$), qui vont stabiliser les grandes échelles via la rétroaction $-f^2/2$, tandis qu'une force extérieure $F_{\mathrm{ext}} > 0$ les amplifie. Ce système est conservatif en l'absence de forçage et de dissipation, avec

$$E = \frac{U^2}{2} + \epsilon \frac{f^2}{2}, \qquad \dot{E} = F_{\mathrm{ext}}\, U - \nu\, U^2. \tag{1.79}$$

La figure 1.6 (haut) reporte les résultats d'une simulation numérique de (1.76 - 1.78) pour $\epsilon = 10^{-4}$ et des fluctuations initialement stables $U(0) = -1$. Trois échelles de temps distinctes apparaissent :

- des variations rapides sur une échelle de temps $O(\epsilon)$, associées à de grandes excursions des fluctuations (*burst*), qui inversent le signe de $U = O(1)$
- des oscillations de période intermédiaire $O(\sqrt{\epsilon})$
- une évolution sur le temps lent $O(1)$, liée à modulation de la force extérieure

Après quelques unités de temps, le taux de croissance instantané U s'annule et la dynamique ne subsiste plus que sur l'échelle de temps lente. Les évolutions sur les temps rapide puis intermédiaire disparaissent successivement. Cet exemple est une première illustration du modèle quasi-linéaire §1.2.2 : même en l'absence de terme non linéaire "fluctuations-fluctuations", une instabilité peut être stabilisée par rétroaction sur son taux de croissance.

Développement en échelles multiples et remarques générales

Analysons maintenant, à l'aide de la méthode des échelles multiples, la disparition de l'échelle de temps intermédiaire $t/\sqrt{\epsilon}$ dans un cas où l'échelle de temps rapide n'apparaît pas ($U(0) = 0$) [8]. La figure 1.6 (bas) compare les résultats d'une simulation numérique avec ceux de l'approximation en échelles multiples ; l'accord est satisfaisant même pour une valeur modérée de $\epsilon = 0.1$.

Commençons par formaliser la séparation d'échelles entre un temps lent T et une phase intermédiaire ϕ,

$$T = t, \qquad \frac{\mathrm{d}\phi}{\mathrm{d}t} = \frac{\omega(T)}{\sqrt{\epsilon}}, \tag{1.80}$$

qui seront par la suite supposés indépendants. La pulsation $\omega(T)$ est un paramètre libre spécifié par la suite pour simplifier les expressions. Nous développons les fonctions en série d'un petit paramètre $\sqrt{\epsilon}$,

$$U(t) = \sqrt{\epsilon}U_1(T,\phi) + \epsilon U_2(T,\phi) + O(\epsilon^{3/2}), \tag{1.81}$$

$$f(t) = f_0(T,\phi) + \sqrt{\epsilon}f_1(T,\phi) + O(\epsilon). \tag{1.82}$$

Pour toute variable $X(T,\tau)$, on définit une moyenne sur le temps intermédiaire via

$$\overline{X}(T) = \lim_{n\to\infty} \frac{1}{2n\pi} \int_{-n\pi}^{n\pi} X(T,\phi)\mathrm{d}\phi. \tag{1.83}$$

Cette opération permet de séparer les variations sur les temps lents $\overline{X}(T)$ des fluctuations $X'(T,\tau)$,

$$X(T,\tau) = \overline{X}(T) + X'(T,\phi), \qquad \overline{X'} = 0. \tag{1.84}$$

D'après (1.77), quelque soit la valeur de U, la variable f ne peut pas changer de signe et reste donc strictement positive. Il est donc commode d'écrire

$$U = \epsilon \frac{\mathrm{d}\ln(f)}{\mathrm{d}t} = \epsilon^{3/2}\omega\frac{\partial \ln(f)}{\partial\phi} + \epsilon\frac{\partial\ln(f)}{\partial T}. \tag{1.85}$$

En comparant les moyennes sur le temps intermédiaire de (1.81) et (1.85), on obtient

$$\overline{U}_1 = 0, \qquad \overline{U}_2 = \frac{\mathrm{d}}{\mathrm{d}T}\,\overline{\ln\left(\overline{f}_0 + f_0'\right)}. \tag{1.86}$$

Dynamique à l'ordre dominant

La dynamique à l'ordre dominant est

$$\omega\frac{\partial U_1}{\partial\phi} = F_{\mathrm{ext}}(T) - \frac{f_0^2}{2}, \qquad \omega\frac{\partial f_0}{\partial\phi} = U_1\ f_0. \tag{1.87}$$

Une moyenne sur les temps intermédiaires mène à

$$0 = F_{\mathrm{ext}}(T) - \left[\frac{(\overline{f}_0)^2 + \overline{f_0'^2}}{2}\right], \qquad 0 = \overline{U_1'\ f_0'}, \tag{1.88}$$

et, en retranchant (1.88) à (1.87),

$$\omega\frac{\partial U_1'}{\partial\phi} = -\overline{f}_0 f_0' + \frac{(\overline{f_0'^2} - f_0'^2)}{2}, \qquad \omega\frac{\partial f_0'}{\partial\phi} = U_1'\ (f_0' + \overline{f}_0). \tag{1.89}$$

En combinant ces équations et fixant pour la suite $\omega(T) = \overline{f}_0(T)$, la dynamique de f_0' suit

$$\frac{\partial^2 f_0'}{\partial\phi^2}\left(\frac{\overline{f}_0}{\overline{f}_0 + f_0'}\right) - \left(\frac{\partial f_0'}{\partial\phi}\right)^2 \frac{\overline{f}_0}{(\overline{f}_0 + f_0')^2} + f_0' = \frac{\overline{f_0'^2} - f_0'^2}{2\overline{f}_0}, \tag{1.90}$$

8. L'exemple entier avec trois échelles de temps se traite aussi, mais son analyse est trop longue pour le propos développé ici.

dont il n'existe pas de solution explicite. Nous nous contentons d'une solution approchée dans la limite $|f_0'| \ll \overline{f}_0$,

$$f_0'(T,\phi) = A(T)e^{i\phi} + \frac{5A(T)^2}{6\overline{f}_0}e^{2i\phi} + \text{c.c.}, \qquad U_1'(T,\phi) = iA(T)e^{i\phi} + \frac{2iA(T)^2}{3\overline{f}_0}e^{2i\phi} + \text{c.c.} \tag{1.91}$$

L'équation (1.88) permet d'en déduire $\overline{f}_0$ [9] et la solution du problème s'écrit à l'ordre dominant

$$U_1(T,\phi) = iA(T)e^{i\phi} + \frac{2iA(T)^2}{3\overline{f}_0}e^{2i\phi} + \text{c.c.}, \tag{1.92}$$

$$f_0(T,\phi) = \sqrt{2F_{\text{ext}}(T) - 2|A(T)|^2} + \left[A(T)e^{i\phi} + \frac{5A(T)^2}{6\overline{f}_0}e^{2i\phi} + \text{c.c.}\right]. \tag{1.93}$$

Les conditions initiales fixent $A(0) \simeq -0.22$ et il reste à déterminer l'évolution temporelle de A.

Condition de solvabilité

Le formalisme général pour la démonstration de la condition de solvabilité n'est pas introduit ici : ce système est suffisamment simple pour une approche "directe". Le point de départ est la dynamique à l'ordre $O(\sqrt{\epsilon})$,

$$\omega\frac{\partial U_2}{\partial\phi} + \frac{\partial U_1}{\partial T} = -\nu\ U_1 - f_0\ f_1, \qquad \omega\frac{\partial f_1}{\partial\phi} + \frac{\partial f_0}{\partial T} = U_1\ f_1 + U_2\ f_0, \tag{1.94}$$

que l'on décompose entre composante lentement variable et fluctuations intermédiaires,

$$0 = \overline{f}_0\overline{f}_1 + \overline{f_0'f_1'}, \qquad \omega\frac{\partial U_2'}{\partial\phi} + \frac{\partial U_1'}{\partial T} = -\nu U_1' - f_0'\overline{f}_1 - f_1'\overline{f}_0 - f_0'f_1' + \overline{f_0'f_1'}, \tag{1.95}$$

$$\frac{\partial\overline{f}_0}{\partial T} = \overline{U_1'f_1'} + \overline{U}_2\overline{f}_0 + \overline{U_2'f_0'}, \quad \omega\frac{\partial f_1'}{\partial\phi} + \frac{\partial f_0'}{\partial T} = U_1'\overline{f}_1 + U_2'\overline{f}_0 + f_0'\overline{U}_2 + U_1'f_1' - \overline{U_1'f_1'} + U_2'f_0' - \overline{U_2'f_0'}. \tag{1.96}$$

En combinant ces équations avec $|A| \ll \overline{f}_0$, on forme une EDO pour U_2' n'impliquant plus f_1',

$$(\overline{f}_0)\left(\frac{\partial^2 U_2'}{\partial\phi^2} + U_2'\right) = -\frac{\partial^2 U_1'}{\partial T\partial\phi} - \nu\frac{\partial U_1'}{\partial\phi} - \overline{f}_1\frac{\partial f_0'}{\partial\phi} - \overline{f}_1 U_1' - \overline{U}_2 f_0' + \frac{\partial f_0'}{\partial T}, \tag{1.97}$$

dont on souhaite, pour conserver $U_2' = O(1)$, éliminer les termes résonnants. Cela revient à annuler les termes en pré-facteur de $e^{i\phi}$ et mène à

$$2i\frac{\mathrm{d}A}{\mathrm{d}t} = (-i\nu - 2\bar{f}_1 + i\bar{U}_2)A \underset{A=|A|e^{i\theta}}{\Longrightarrow} \frac{\mathrm{d}|A|}{\mathrm{d}T} = \left(\frac{\overline{U}_2 - \nu}{2}\right)|A|, \quad \frac{\mathrm{d}\theta}{\mathrm{d}T} = \overline{f}_1. \tag{1.98}$$

Connaissant $\overline{U}_2$ en fonction de $F_{\text{ext}}(T)$ et $A(T)$ et de leurs dérivées à partir de (1.86), une résolution numérique est possible sur l'échelle de temps lente pour obtenir la décroissance de $A(T)$. Si $|A(T)| \ll \overline{f}_0$,

$$\overline{U}_2 = \frac{\sin(T)}{4 - 2\cos(T)} \Longrightarrow A(T) = A(0)\left[2 - \cos(T)\right]^{1/4} e^{-\nu T/2}. \tag{1.99}$$

Synthèse

Les résultats obtenus sont, en revenant à une unique échelle de temps t,

$$U(t) = \sqrt{\epsilon}\left\{-2A(t)\sin\left[\phi(t)\right] - \frac{4A(t)^2}{3\omega(t)}\sin\left[2\phi(t)\right]\right\} + \epsilon\frac{\sin(t)}{4 - 2\cos(t)}, \tag{1.100}$$

$$f(t) = \omega(t) + 2A(t)\cos\left[\phi(t)\right] + \frac{5A(t)^2}{3\omega(t)}\cos\left[2\phi(t)\right], \tag{1.101}$$

$$A(t) = A(0)\left[2 - \cos(t)\right]^{1/4} e^{-\nu t/2}, \qquad A(0) = -0.22, \tag{1.102}$$

$$\omega(t) = \sqrt{2\left[2 - \cos(t)\right] - 2A(t)^2}, \qquad \phi(t) = \int_0^t \frac{\omega(s)}{\sqrt{\epsilon}}\mathrm{d}s. \tag{1.103}$$

9. Encore en supposant $|A| \ll \overline{f}_0$ pour avoir des expressions explicites. Le caractère positif de f fixe le signe de $\overline{f}_0 = +\sqrt{\ldots}$.

1.3 Présentation synthétique du travail effectué

1.3.1 Systèmes quasi-linéaires avec fluctuations potentiellement instables

L'exemple précédent de deux équations différentielles ordinaires couplées met en évidence une dynamique qui évolue spontanément vers des modes marginalement stables d'amplitude lentement variable en temps. Nous souhaitons appliquer la même analyse au modèle réduit obtenu pour la turbulence stratifiée et décrit par les équations (1.68 - 1.75). Cela est bien plus difficile, car il s'agit de huit équations aux dérivées partielles couplées dont la dynamique aux ordres supérieures s'avère très complexe.

Nous avons introduit une étape intermédiaire pour détailler les aspects techniques de l'étude en échelles multiples de ces systèmes quasi-linéaires. Le système étudié consiste en deux équations différentielles,

$$\frac{\partial \Theta}{\partial t} = P(x,t) - \nu\Theta - \eta^2, \qquad \Theta(x,0) = -1, \tag{1.104}$$

$$\epsilon\frac{\partial \eta}{\partial t} = \Theta\eta + \frac{\partial^2 \eta}{\partial x^2} - \epsilon\eta^3, \qquad \eta(x,0) = \cos\left(\frac{2\pi x}{L}\right), \tag{1.105}$$

avec $\Theta(x,t)$ le champ lentement variable qui va rendre instable des fluctuations $\eta(x,t)$. On peut le voir comme un modèle reliant l'écart de température d'une plaque horizontale $\Theta(x,t)$ au seuil d'instabilité de Rayleigh-Bénard. Cette plaque est chauffée par une puissance inhomogène spatialement et temporellement $P(x,t)$, subit des échanges thermiques linéaires avec un thermostat à $\Theta = 0$ et perd de l'énergie proportionnellement au carré de l'amplitude $\eta(x,t)$ du mode de convection lentement variable en x. Le champ $\eta(x,t)$, rendu localement instable lorsque $\Theta(x,t) > 0$, peut être équilibré par des non-linéarités et est également sensible aux lentes inhomogénéités spatiales via un terme diffusif. Les conditions initiales décrivent un système où des fluctuations d'amplitude finie sont exponentiellement amorties ($\Theta(x,0) < 0$ partout). Nous prenons un coefficient d'amortissement $\nu = 1$ ainsi qu'un choix arbitraire de chauffage inhomogène en temps et en espace, toujours positif :

$$P(x,t) = 1 + \frac{1}{2}\left[\cos(t)\cos(x) + \sin(0.6t)\cos(2x)\right]. \tag{1.106}$$

Les deux premières colonnes de la figure 1.7 montrent les résultats de simulations numériques directes pour $\epsilon = \{10^{-1}, 10^{-2}\}$. La même phénoménologie que pour le système d'EDO est observée, avec un transitoire d'excursions rapides et d'oscillations non linéaires intermédiaires, suivi d'un régime établi où les deux champs évoluent lentement dans le temps et l'espace. C'est ce dernier état que nous souhaitons capturer.

Nous réalisons un développement en échelles multiples pour séparer le temps lent T et la phase rapide ϕ (l'échelle de temps intermédiaire $t/\sqrt{\epsilon}$ n'est pas introduite, ce qui simplifie l'étude au prix d'un modèle ne capturant pas les oscillations non linéaires amorties). Sur l'échelle de temps rapide ϕ, à l'ordre dominant, le champ $\eta_0(x,T,\phi)$ est solution d'un problème aux valeurs propres dont les coefficients sont fixes (c'est-à-dire qu'ils ne dépendent que de T). La solution s'écrit donc formellement

$$\eta_0(x,T,\phi) = A(T)\hat{\eta}_0(x,T)e^{\phi}, \qquad \{T = t, \frac{\mathrm{d}\phi}{\mathrm{d}t} = \frac{\sigma(T)}{\epsilon}\}, \tag{1.107}$$

où $\hat{\eta}_0(x,T)$ est le vecteur propre décrivant la structure spatiale du mode d'amplitude lentement variable $A(T)$. Le taux de croissance $\sigma(T)$, nécessairement réel, dépend uniquement du champ lentement variable $\Theta_0(x,T)$. Trois situations peuvent alors émerger :

1. si $\sigma(T) < 0$, les fluctuations sont exponentiellement amorties sur le temps rapide, et leur amplitude moyenne sur le temps lent ne peut donc être que $A(T) = 0$. C'est notamment le cas à l'instant initial.
2. si $\sigma(T) = 0$, les fluctuations sont marginalement stables et autorisent une amplitude $A(T) \neq 0$. C'est le régime observé numériquement aux temps longs que nous souhaitons décrire.
3. si $\sigma(T) > 0$, une amplification exponentielle des fluctuations a lieu sur le temps court, ce qui invalide la séparation d'échelle supposée (en l'occurrence, que $\eta_0 = O(1)$). Ce régime, s'il est atteint, nécessite de reprendre toute l'analyse.

La prochaine étape consiste à déterminer l'évolution temporelle de $A(T)$. En suivant la démarche habituelle et en écrivant une condition de solvabilité à l'ordre suivant, nous obtenons une contrainte liant $\mathrm{d}A/\mathrm{d}T$ à des

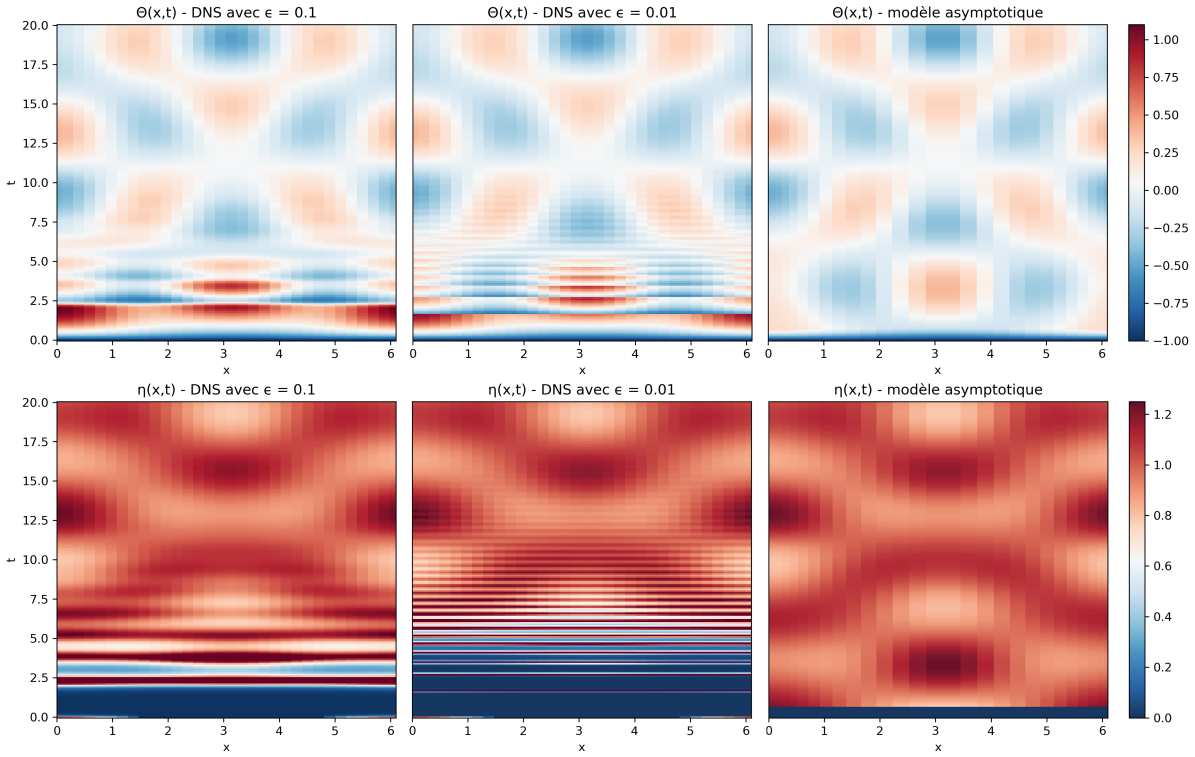

FIGURE 1.7 – (gauche et centre) Résolution numérique directe des équations (1.104 - 1.105) pour deux valeurs de ϵ. (droite) Modèle asymptotique où les fluctuations forcent le système à rester marginalement stable lorsque, en leur absence, le taux de croissance deviendrait strictement positif. J'ai effectué ces simulations dans l'environnement de calcul spectral Dedalus.

champs d'ordres supérieurs inconnus (faire le lien avec (1.98), qui implique $\overline{U}_2$ et $\overline{f}_1$ à déterminer par ailleurs). Une autre approche est nécessaire. Elle consiste à différentier le problème aux valeurs propres à l'ordre dominant par rapport au temps lent pour obtenir une équation régissant l'évolution temporelle du taux de croissance,

$$\frac{\mathrm{d}\sigma}{\mathrm{d}T} = \alpha - \beta A(T)^2, \tag{1.108}$$

avec

$$\alpha = \int_0^L (P - \nu\Theta_0)\hat{\eta}_0^2 \,\mathrm{d}x, \qquad \beta = \int_0^L \hat{\eta}_0^4 \,\mathrm{d}x. \tag{1.109}$$

Le coefficient α représente la variation du taux de croissance en l'absence de fluctuation. Il comprend une contribution strictement positive liée au chauffage $P(x,t) > 0$ et un terme de signe indéfini. Le coefficient $\beta > 0$ dépend uniquement de la structure du mode propre ; le terme $-\beta A(T)^2$ traduit la rétroaction stabilisante de η sur Θ. Le système est fermé de la manière suivante :

1. si $\sigma < 0$ ou $\{\sigma = 0,\ \alpha \leqslant 0\}$, le taux de croissance reste négatif ou nul même en l'absence de fluctuation, donc $A(T) = 0$.
2. si $\{\sigma = 0,\ \alpha > 0\}$, le taux de croissance deviendrait strictement positif sans les fluctuations. Les fluctuations marginalement stables acquièrent alors une amplitude finie prévenant leur instabilité, $A(T) = \sqrt{\alpha/\beta}$.

Cette dynamique est implémentée numériquement, une résolution d'un problème aux valeurs propres étant effectuée à chaque pas de temps. En contrepartie, l'échelle de temps rapide étant supprimée, le pas de temps peut être bien plus grand que dans une simulation numérique directe. Le résultat est visible dans la colonne de droite de la figure 1.7 : le régime établi est bien capturé, contrairement aux bursts et oscillations fortement non linéaires observés pour $t \in [2, 10]$. Il serait possible de capturer ces dernières en ajoutant une échelle de temps intermédiaire $O(t/\sqrt{\epsilon})$, mais l'étude deviendrait alors plus complexe (voir le modèle jouet précédent).

Pour plus de détails, se référer à la publication [43] reportée au chapitre 3.

1.3.2 Couplage entre grandes échelles et modes rapides en turbulence stratifiée

L'étude précédente ayant clarifié les étapes du traitement en échelles multiples, nous revenons au système décrivant les grandes échelles anisotropes couplées aux modes rapides isotropes, équations (1.68 - 1.75). Pour une première approche, nous le simplifions en supposant la dynamique bidimensionnelle et en négligeant les variations vis-à-vis des grandes échelles spatiales horizontales. Ainsi, il se réduit à :

$$\partial_t \overline{u} = \partial_z \left(\overline{\partial_z \psi' \partial_x \psi'} \right) + \frac{1}{Re_b} \partial_z^2 \overline{u} + \overline{f}, \tag{1.110}$$

$$\partial_t \overline{b} = \partial_z \left(\overline{b' \partial_x \psi'} \right) + \frac{1}{PrRe_b} \partial_z^2 \overline{b}, \tag{1.111}$$

$$(\partial_\tau + \overline{u}\partial_x) \triangle \psi' = \partial_x \psi' \partial_z^2 \overline{u} - \partial_x b' + \frac{Fr}{Re_b} \triangle^2 \psi', \tag{1.112}$$

$$(\partial_\tau + \overline{u}\partial_x) b' = (1 + \partial_z \overline{b}) \partial_x \psi' + \frac{Fr}{PrRe_b} \triangle b', \tag{1.113}$$

avec $\overline{u}(z,t)$ la vitesse horizontale des grandes échelles de flottabilité $\overline{b}(z,t)$. Les petites échelles, incompressibles et évoluant sur l'échelle de temps rapide τ, sont caractérisées par la fonction de courant $\psi'(x,z,t,\tau)$ ($u'_x = \partial_z \psi'$, $u'_z = -\partial_x \psi'$) et la flottabilité $b'(x,z,t,\tau)$. La phénoménologie suivante est attendue :

1. Au départ, le système est au repos ($\overline{u} = \overline{b} = 0$). Le mode le plus instable du problème aux valeurs propres (1.112 - 1.113) s'écrit

$$\psi'(x,z,\tau,t) = A(t)\hat{\psi}(z,t) e^{\sigma\tau + ik(t)x} + \text{c.c.}, \tag{1.114}$$

$$b'(x,z,\tau,t) = A(t)\hat{b}(z,t) e^{\sigma\tau + ik(t)x} + \text{c.c.}, \tag{1.115}$$

   avec $\text{Re}(\sigma) < 0$. Les fluctuations sont exponentiellement amorties sur le temps rapide.
2. Un opérateur exerce une densité volumique de force $\overline{f}$ sur les grandes échelles. Le champ de vitesse $\overline{u}$ croît, le cisaillement devient de plus en plus intense. Le taux de croissance du mode le plus instable, $\text{Re}(\sigma)$, s'approche de zéro tout en restant négatif.
3. Lorsque la stabilité marginale est atteinte, les modes rapides rétroagissent sur l'écoulement moyen. Après un transitoire, on obtient un état stationnaire où $\text{Re}(\sigma) = 0$ et $A(t) \neq 0$.

Pour formaliser cela, on insère les expressions (1.114-1.115) dans les équations (1.112 - 1.113) afin d'obtenir un problème aux valeurs propres sur l'échelle de temps rapide,

$$\mathcal{L} X = 0, \qquad X = \begin{pmatrix} \hat{\psi} \\ \hat{b} \end{pmatrix}, \tag{1.116}$$

avec $\mathcal{L}$ un opérateur linéaire (non auto-adjoint). Conformément à l'approche §1.3.1, on ne cherche pas les corrections d'ordre supérieur, car la condition de solvabilité ne fermerait pas le problème. Il faut dériver ce problème aux valeurs propres par rapport au temps lent :

$$\frac{\mathrm{d}\mathcal{L}}{\mathrm{d}t} X = -\mathcal{L} \frac{\mathrm{d}X}{\mathrm{d}t}. \tag{1.117}$$

Ensuite, on procède à l'élimination des termes résonnants (analogue à (1.97) sur le modèle jouet). Pour cela, on définit un produit vectoriel $(X_1|X_2)$ entre deux vecteurs X quelconques, calcule l'opérateur adjoint $\mathcal{L}^\dagger$, et explicite le produit scalaire de (1.117) avec un vecteur du noyau de $\mathcal{L}^\dagger$. Après calculs, on obtient l'équation d'évolution du taux de croissance :

$$\left(\frac{\partial \sigma_r}{\partial t} \right)_k = \alpha_r - \beta_r |A(t)|^2, \tag{1.118}$$

avec des expressions explicites pour les coefficients α_r et β_r. Cette relation fixe la valeur de $|A(t)|$ de façon à empêcher l'émergence de valeurs strictement positives de $\sigma_r(k,t)$ pour toute la gamme de nombres d'onde k.

Cette démarche est implémentée numériquement pour un écoulement de Kolmogorov dans un gaz initialement au repos et fortement stratifié :

$$\overline{f} = (9/Re_b)\cos(3z), \qquad Fr = 0.01, \qquad Pr = 1, \qquad \overline{u}(z,0) = \overline{b}(z,0) = 0. \tag{1.119}$$

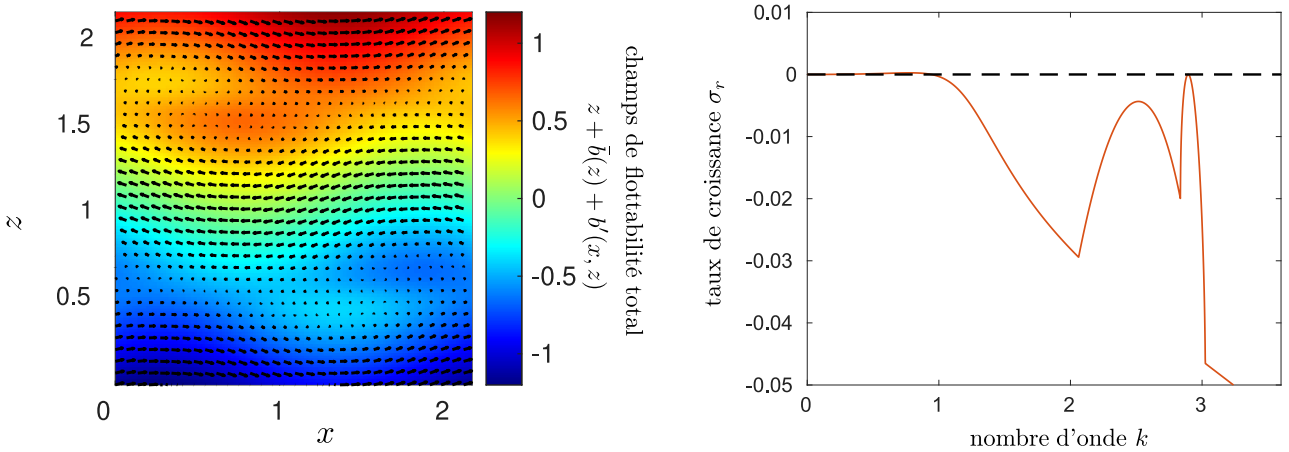

FIGURE 1.8 – (Gauche) état stationnaire obtenu pour $Fr = 0.01$ et $Re_b = 10$. Le champ de flottabilité est indiqué en couleur, les flèches représentent le champ de vitesse. (Droite) taux de croissance du mode le plus instable $\sigma_r(k)$, calculé dans l'état stationnaire. Le mode à $k \simeq 3$ est marginalement stable.

En l'absence d'instabilité, la densité de force $\overline{f}$ conduirait à un état laminaire stationnaire $\{\overline{u}_L = \cos(3z), \overline{b} = 0\}$, c'est-à-dire à un écoulement stratifié et cisaillé de période verticale proche de deux unités. Pour les valeurs de $Re_b \in [1, 10]$ étudiées, cette solution serait associée à un mode isotrope fortement instable pour un nombre d'onde $k \simeq 3$. On observe avec notre approche, pendant la croissance du cisaillement à grande échelle, l'apparition d'un mode d'une amplitude $A(t) \neq 0$ qui reste marginalement stable.

Sur de longues durées, le système converge vers des états stationnaires. Les champs ainsi que le spectre $\sigma_r(k)$ sont présentés à la figure 1.8. Ces états sont ensuite caractérisés, entre autres, par leur efficacité de mélange. Pour plus de détails, voir la publication [44] reportée au chapitre 3.

1.4 Perspectives

Ce chapitre revient sur l'image d'une cascade anisotrope locale en turbulence stratifiée. Une description plus fine, schématisée à la figure 1.9, inclut les modes isotropes résultant d'instabilités des écoulements stratifiés cisaillés. Cette extension permet, par exemple, de rendre compte de l'écart-type et du comportement fortement intermittent des vitesses verticales. Cette approche soulève de nombreuses questions :

- L'existence de ces modes isotropes modifie-t-elle notablement les lois d'échelle de la cascade anisotrope ?
- Une puissance moyenne traverse-t-elle le système de manière non locale via ces modes isotropes ? Si oui, quel est son sens et comment se compare-t-elle à la puissance transférée localement ?
- Ces modes sont-ils responsables du profil de densité en escalier ? Comment participent-ils au mélange ?

Ces interrogations sont d'autant plus centrales que, pour les écoulements atmosphériques et océaniques, la séparation des échelles de turbulence stratifiée est réellement atteinte ($Fr = O(10^{-3})$ et $Re_b = O(10^4 - 10^6)$). Ce régime de paramètres reste inaccessible aux simulations numériques directes ; une modélisation en échelles multiples apparaît donc comme une approche appropriée. Du point de vue de la modélisation, on se demande si un modèle en échelles multiples, tel que celui décrit ici, peut fournir une paramétrisation raisonnable des petites échelles pour les modèles climatiques [10]. Comment se compare-t-il aux modèles alternatifs capturant uniquement la cascade locale d'énergie ? Plus modestement, comment les résultats de ce modèle se confrontent-ils à des simulations numériques directes des équations de Boussinesq pour $Re \gg 1$? Des différences pourraient apparaître pour au moins deux raisons. D'une part, car le régime transitoire comporte des "bursts" (cf. §1.2.3) qui pourraient rendre cruciaux des termes non linéaires négligés dans le modèle. D'autre part, car le paramètre Fr est ici réintroduit comme une régularisation ad hoc.

Ces points méritent d'être approfondis afin d'évaluer la robustesse et la pertinence du formalisme en échelles multiples pour la description de la turbulence stratifiée à des paramètres géophysiques réalistes.

10. Obtenir une paramétrisation réaliste des grandes échelles, du mélange et du transport en turbulence stratifiée est l'un des "grands défis" de la mécanique des fluides géophysiques [45].

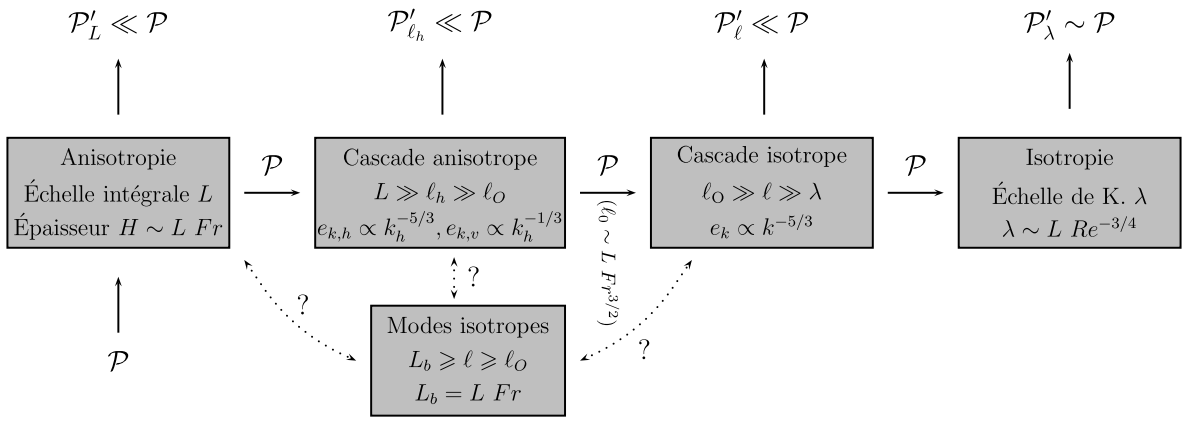

FIGURE 1.9 – Ajout de modes isotropes couplés à la cascade locale d'énergie. Les longueurs caractéristiques sont $L_b = L\ Fr$, $\ell_\mathrm{O} = L\ Fr^{3/2}$, $\lambda = \ell_\mathrm{O}\ Re_b^{-3/4} = L\ Re^{-3/4}$.

1.4.1 Description cohérente de la couche critique

Le modèle 2D décrit précédemment converge, dans le régime de paramètres étudié, vers un état stationnaire. Bien que la dynamique turbulente soit chaotique, de telles solutions non linéaires cohérentes exactes (*exact coherent state*) restent pertinentes et sont régulièrement approchées : cela a été particulièrement documenté dans le cadre des écoulements cisaillés homogènes [46–48] et s'est développé en turbulence stratifiée [15, 49].

Un premier point consiste à chercher une solution stationnaire du modèle réduit 2D dans la limite $Re_b \to \infty$ et $Fr \to 0$. Cela peut être réalisé à partir des équations (1.110 - 1.113), en posant

$$\partial_t = \partial_\tau = 0 \qquad \text{solution stationnaire} \tag{1.120}$$

$$Fr = \epsilon^2,\ Re_b = r\epsilon^{-1} \qquad \text{limite } Fr \to 0, Re_b \to \infty \tag{1.121}$$

$$\overline{f} = \epsilon f \sin(mz) \qquad \text{pour conserver l'état de base } \overline{u} = (fr/m^2)\sin(mz) = O(1) \tag{1.122}$$

$$(\psi', b') = (\hat{\psi}(z), \hat{b}(z))\exp(ikx) + \text{c.c.} \qquad \text{en supposant un unique nombre d'onde} \tag{1.123}$$

On obtient alors le système suivant

$$0 = ik\partial_z(\hat{\psi}\partial_z\hat{\psi}^* - \hat{\psi}^*\partial_z\hat{\psi}) + \epsilon r^{-1}\partial_z^2\overline{u} + \epsilon f\sin(mz), \tag{1.124}$$

$$0 = ik\partial_z(\hat{\psi}\hat{b}^* - \hat{\psi}^*\hat{b}) - \epsilon r^{-1}Pr^{-1}\partial_z^2\overline{b}, \tag{1.125}$$

$$\overline{u}(\partial_z^2 - k^2)\hat{\psi} = (\partial_z^2\overline{u})\hat{\psi} - \hat{b} + \frac{\epsilon^3}{ikr}(\partial_z^2 - k^2)^2\hat{\psi}, \tag{1.126}$$

$$\overline{u}\hat{b} = (1 + \partial_z\overline{b})\hat{\psi} + \frac{\epsilon^3}{ikrPr}(\partial_z^2 - k^2)\hat{b}. \tag{1.127}$$

Une solution analytique est potentiellement accessible dans la limite $\epsilon \to 0$. Elle correspondrait à une solution non linéaire exacte décrivant le couplage entre un écoulement stratifié cisaillé et un mode isotrope marginalement stable. Outre l'intérêt direct pour l'efficacité du mélange et le profil vertical de densité, la structure spatiale de cette solution impliquerait au moins deux échelles de longueur verticales différentes. En effet, la limite non diffusive $Fr \to 0$ associée à la formation d'une couche critique avec discontinuités de $\overline{u}$ et $\overline{b}$ serait régularisée sur une taille tendant vers zéro. Cette approche fournirait une expression de l'épaisseur de la couche critique, ainsi que des différents champs, en fonction des paramètres (Re_b, Fr).

Une fois cette nouvelle échelle de longueur (épaisseur de la couche critique) identifiée, il devient envisageable de revenir à la démonstration du modèle en échelles multiples (1.68 - 1.75) en introduisant explicitement cette échelle supplémentaire. L'objectif serait d'obtenir un système où tous les termes sont asymptotiquement justifiés : à ce jour, le terme diffusif en Fr/Re_b n'est pas rigoureusement justifié. Outre une description plus fine des phénomènes mis en jeu, cela retirerait le paramètre ad hoc Fr du jeu d'équations obtenu dans la limite $Fr \to 0$. Il resterait comme seuls paramètres Pr, d'ordre unité, et Re_b, contrôlant la transition vers la turbulence.

1.4.2 Détermination de l'amplitude des fluctuations dans un cadre plus général

L'analyse en échelles multiples fixe l'amplitude du mode instable de manière à conserver sa stabilité marginale. Plusieurs obstacles restent à surmonter pour généraliser cette approche :

1. Comment capturer efficacement l'évolution lente du nombre d'onde $k(t)$?
2. Comment fixer l'amplitude des fluctuations en présence de plusieurs modes marginalement stables ?
3. Comment conserver la grande échelle spatiale ?
4. Comment décrire des états avec $\beta < 0$ où la stabilité marginale est inatteignable ?

1 - Évolution lente du nombre d'onde. Le modèle décrit ici fixe l'amplitude du mode le plus instable de sorte que son taux de croissance $\sigma_r(k_{\max})$ ne devienne jamais strictement positif. Ce mode possède un nombre d'onde $k_{\max}$ qui évolue avec le temps ; il faut donc, à chaque pas de temps, résoudre une série de problèmes aux valeurs propres afin de déterminer le nombre d'onde $k_{\max}(t)$ qui maximise localement σ_r. Cette étape donne exactement l'extension spatiale des modes localisés et assure la stabilité sur toute une gamme de nombres d'onde, mais elle est coûteuse en temps de calcul. Dans un article récent [50], une méthode analytique a été développée pour obtenir

$$\frac{\mathrm{d}k_{\max}}{\mathrm{d}t} = \text{expression explicite en fonction des champs à un temps t.} \tag{1.128}$$

Adapter cette méthode à notre système réduit est délicat, car notre modèle est plus complexe que celui de la référence [50] ; néanmoins, une telle avancée serait très utile pour la simulation numérique de ces écoulements.

2 - Plusieurs modes marginalement stables. Comme le montre la figure 1.8 (droite), le taux de croissance $\sigma_r(k)$ peut présenter plusieurs maxima locaux. En augmentant le paramètre Re_b tout en maintenant le mode à $k \simeq 3$ marginalement stable, un nouveau mode instable apparaît autour de $k \simeq 2.5$ dont il faut également fixer l'amplitude. On peut alors écrire la superposition de deux modes :

$$\psi'(x,z,\tau,t) = A(t)\hat{\psi}_A(z,T)e^{\sigma_A\tau+ik_Ax} + B(t)\hat{\psi}_B(z,T)e^{\sigma_B\tau+ik_Bx} + \text{c.c.}, \tag{1.129}$$

ce qui mène aux équations d'évolution des taux de croissance

$$\frac{\mathrm{d}\sigma_A}{\mathrm{d}t} = \alpha_A - \beta_{AA}A(t)^2 - \beta_{AB}B(t)^2, \tag{1.130}$$

$$\frac{\mathrm{d}\sigma_B}{\mathrm{d}t} = \alpha_B - \beta_{BA}A(t)^2 - \beta_{BB}B(t)^2, \tag{1.131}$$

avec des expressions analytiques pour les coefficients α et β. Selon les signes de ces coefficients, il ne suffit plus d'annuler simplement les dérivées temporelles ; l'interaction entre les deux modes via l'écoulement moyen doit être prise en compte. Étudier cet effet sur un système plus simple permettrait de clarifier la procédure lorsque deux modes, puis un grand nombre, interviennent dans la dynamique.

3 - Fluctuations évoluant sur une grande échelle spatiale. Dans le modèle réduit, nous avons négligé la variation des champs sur la grande échelle spatiale horizontale $x_\perp$. Réintroduire cette dépendance est indispensable pour décrire des couches anisotropes réalistes où les caractéristiques des modes isotropes varient lentement en $x_\perp$. Si un seul mode est potentiellement instable, on peut généraliser la démarche présentée en écrivant une équation d'évolution sur $(\partial_t\sigma_r)_{x_h}$ qui spécifie, à chaque instant, le profil spatial d'amplitude $A(x_h)$ et de nombre d'onde $k(x_h)$. Le principal problème réside alors dans la discontinuité spatiale de ces profils, qui se répercute sur les champs à grande échelle $\overline{u}(x_h,z,t)$ et $\overline{b}(x_h,z,t)$. Aborder cette difficulté sur un exemple plus simple pourrait fournir des pistes de résolution.

4 - Paramètre $\beta < 0$. Lors de l'étude numérique du modèle réduit de turbulence stratifiée, des états avec $\beta_r < 0$ ont été rencontrés. Rappelons que β_r intervient dans l'évolution du taux de croissance,

$$\left(\frac{\partial \sigma_r}{\partial t}\right)_k = \alpha_r - \beta_r |A(t)|^2,$$

et capture la rétroaction des modes isotropes sur les grandes échelles. Lorsque $\beta_r < 0$, la rétroaction devient déstabilisante : une amplitude $|A|^2 > 0$ ne peut plus annuler le terme $\alpha_r > 0$, et le système devient exponentiellement instable sur l'échelle de temps rapide. Est-il possible de traiter ce transitoire de façon asymptotiquement justifiée, en raccordant la dynamique lente à un régime qui réintroduit l'échelle de temps rapide, puis, finalement, en revenant à une évolution lente après une certaine durée. Cette problématique pourrait être abordée en posant des conditions initiales appropriées pour les équations (1.110 - 1.113) et en comparant les résultats avec des simulations numériques directes du modèle réduit ainsi qu'avec les équations complètes de Boussinesq.

1.4.3 Comparaison à des simulations numériques directes

Il est indispensable d'attester la pertinence de cette démarche via des Simulations Numériques Directes (DNS) pour $Re_b \gg 1$. Cela permettrait d'identifier les variables de la dynamique chaotique turbulente qui sont bien décrites, en moyenne temporelle, par les états cohérents exacts calculés ici. Cette question n'est pas triviale, car le régime transitoire implique des "bursts" qui rendent cruciaux des termes non linéaires négligés jusqu'à présent. L'importance de ces fortes non-linéarités, comparables au déferlement des ondes internes de gravité, sur le régime obtenu à temps long demeure inconnue.

Même simplifié, le système réduit 2D étudié dans ce chapitre reste trop riche pour une comparaison directe : il autorise une lente évolution temporelle du nombre d'onde horizontal du mode marginalement stable, évolution qui ne pourrait être capturée dans une DNS que si la taille horizontale du domaine était extrêmement grande. Il conviendrait donc de :

1. Effectuer de nouvelles simulations numériques de ce modèle réduit pour une taille de domaine fixée (c'est-à-dire sans permettre à k à d'évoluer dans le temps).
2. Comparer ces résultats à des DNS des équations de Boussinesq dans un domaine 2D périodique en x.

Pour cela, j'envisage d'utiliser une nouvelle formulation en couches des équations de Navier-Stokes développée par Stéphane Popinet [51] [11]. Cette approche repose sur une discrétisation verticale lagrangienne, particulièrement adaptée aux structures fortement anisotropes rencontrées en turbulence stratifiée. La discrétisation verticale peut être adaptée en temps et en espace afin de résoudre finement les couches critiques émergentes tout en évitant un maillage excessif dans le reste du domaine. De plus, le code exploite les performances des cartes graphiques, accélérant notablement les calculs.

En réalisant des simulations numériques de l'ensemble du domaine et non plus d'une seule couche fine, il serait également possible de vérifier les différentes hypothèses sur les échelles mises en jeu dans l'analyse :

- les modes instables ont-ils la même épaisseur que la couche de cisaillement qui les crée ?
- sont-ils effectivement isotropes ?
- leur amplitude évolue-t-elle bien sur le temps long T associé à la couche de cisaillement ?
- leur vitesse caractéristique est-elle bien $\sqrt{Fr}U$?

Des procédures de détection automatique de ces modes instables ont déjà été développées pour les simulations numériques directes [13] ; ces questions sont abordables.

11. Nous encadrons de fait avec Stéphane Popinet, à l'heure où sont écrites ces lignes, un stagiaire sur ce sujet.

Chapitre 2

Modes rapides oscillants : streaming acoustique barocline

La deuxième partie de ce manuscrit s'intéresse au couplage réciproque entre des ondes acoustiques et un écoulement moyen dans un fluide stratifié. L'analyse en échelles multiples met en évidence une dynamique quasi-linéaire présentant de nombreuses similarités avec celle obtenue au chapitre précédent ainsi qu'avec l'explication de l'Oscillation Quasi Biennale (QBO) proposée par Plumb [52]. Avant de rentrer dans le cœur du sujet, nous commençons par une courte présentation de la QBO axée sur sa modélisation en échelles multiples.

2.1 Modélisation quasi-linéaire de la QBO

Depuis le milieu du XX$^{\text{e}}$ siècle, des mesures ont mis en évidence un vent moyen au sein de la stratosphère équatoriale, entre 20 et 40 km d'altitude. D'une vitesse de l'ordre de $O(10)$ m$\cdot$s^{-1}, ce courant est dirigé vers l'est ou l'ouest suivant l'altitude. Sa caractéristique la plus remarquable est sa dynamique temporelle : il change de sens tous les 28 mois. Cette durée de "quasiment" deux ans (d'où le nom) est décorrélée de la durée de rotation de la Terre autour du Soleil, l'existence et la dynamique de cet écoulement étant aujourd'hui comprises comme le résultat de la propagation d'ondes internes de gravité au sein de la stratosphère.

Nous décrivons successivement les propriétés de ces ondes internes, puis la dynamique de l'écoulement moyen. La présentation qui suit constitue une tentative de synthèse de la théorie de la QBO d'après les articles de Plumb [52, 53], malheureusement très élusifs quant aux approximations réalisées et comportant de nombreuses erreurs typographiques. Pour plus de détails sur ce phénomène, le lecteur pourra se référer à la revue [54]. Les questions toujours d'actualité concernent notamment sa prise en compte dans les modèles climatiques ainsi que l'origine des irrégularités des renversements observées durant la dernière décennie.

2.1.1 Onde interne linéaire, non amortie, en l'absence d'écoulement moyen

Pour commencer, détaillons les ondes forcées par des mouvements turbulents à la limite inférieure d'une stratosphère uniformément stratifiée. Dans un domaine cartésien à deux dimensions (x la longitude et z l'altitude), la forme linéaire et non dissipative des équations de Boussinesq s'écrit :

$$\partial_t \mathbf{u} = -\nabla P + b\mathbf{e}_z, \qquad \nabla \cdot \mathbf{u} = 0, \qquad \partial_t b = -N^2 u_z. \tag{2.1}$$

On cherche la réponse pour $z > 0$ à des fluctuations de vitesse verticale imposées par la condition aux limites

$$u_z(x, z = 0, t) = U_{\text{w}} e^{i(\omega t - k_x x)} + \text{c.c.}, \tag{2.2}$$

où $\{U_{\text{w}}, \omega, k_x\}$ sont des paramètres indépendantes. Une fonction de courant ψ telle que $\mathbf{u} = \partial_z \psi \mathbf{e}_x - \partial_x \psi \mathbf{e}_z$ réduit ce système à une seule équation différentielle scalaire,

$$\partial_{tt}(\partial_{xx} + \partial_{zz})\psi + N^2 \partial_{xx}\psi = 0, \qquad \partial_x \psi(x, z = 0, t) = -U_{\text{w}} e^{i(\omega t - k_x x)} + \text{c.c.} \tag{2.3}$$

Signes de $\{\omega, k_x, k_z\}$	$c_{\phi,x}$	$c_{\phi,z}$	$c_{g,x}$	$c_{g,z}$
$\omega > 0,\ k_x > 0,\ k_z > 0$	+	+	+	-
$\omega > 0,\ k_x > 0,\ k_z < 0$	+	-	+	+
$\omega > 0,\ k_x < 0,\ k_z > 0$	+	-	+	+
$\omega > 0,\ k_x < 0,\ k_z < 0$	+	+	+	-
$\omega < 0,\ k_x > 0,\ k_z > 0$	-	-	-	+
$\omega < 0,\ k_x > 0,\ k_z < 0$	-	+	-	-
$\omega < 0,\ k_x < 0,\ k_z > 0$	-	+	-	-
$\omega < 0,\ k_x < 0,\ k_z < 0$	-	-	-	+

TABLE 2.1 – Signes des vitesses de phase et de groupe suivant ceux de $\{\omega, k_x, k_z\}$ (pas d'écoulement moyen).

La solution est une onde plane,

$$\psi(x,z,t) = -i\frac{U_\mathrm{w}}{k_x}e^{i(\omega t - k_x - k_z z)} + \text{c.c.}, \qquad b = i\frac{N^2 U_\mathrm{w}}{\omega}e^{i(\omega t - k_x - k_z z)} + \text{c.c.}, \tag{2.4}$$

complétée par sa relation de dispersion,

$$\omega = \frac{\pm N k_x}{\sqrt{k_x^2 + k_z^2}}. \tag{2.5}$$

Cette relation conduit aux vitesses de phase et de groupe suivantes (les signes sont liés à celui de ω),

$$\mathbf{c}_\phi = \frac{\pm N k_x}{(k_x^2+k_z^2)^{3/2}}\left(k_x\mathbf{e}_x + k_z\mathbf{e}_z\right), \qquad \mathbf{c}_g = \frac{\pm N k_z}{(k_x^2+k_z^2)^{3/2}}\left(k_z\mathbf{e}_x - k_x\mathbf{e}_z\right). \tag{2.6}$$

Outre l'orthogonalité de ces vitesses, il faut remarquer que les combinaisons de signes possibles du triplet $\{\omega, k_x, k_z\}$ décrivent des situations physiques différentes ; les huit possibilités couvrent les quatre orientations admissibles distinctes de $\{\mathbf{c}_\phi, \mathbf{c}_g\}$, voir Table 2.1. En particulier, la direction de propagation horizontale (de l'énergie et de la phase) est uniquement déterminée par le signe de ω.

Aparté relié au chapitre précédent. Les mesures effectuées dans la haute atmosphère montrent que le spectre de puissance des ondes internes décroît rapidement avec le nombre d'onde vertical, typiquement comme k_z^{-3}. Une interprétation possible est qu'il s'agit d'un régime de stabilité marginale [55] : cette idée rappelle celle présentée au chapitre précédent, mais l'instabilité en question concerne exclusivement des ondes. Un seuil de "déferlement" des ondes internes de gravité est obtenu en cherchant l'amplitude U_w associée au gradient de densité qui équilibre le gradient adiabatique :

$$\left|\frac{\partial b}{\partial z}\right|_\mathrm{max} = N^2 \Longrightarrow U_\mathrm{w,max} = \frac{\omega}{k_z}. \tag{2.7}$$

$U_\mathrm{w} > U_\mathrm{w,max}$ déclencherait une instabilité convective, d'où un spectre d'énergie potentielle par unité de masse

$$e_p(k_z) \sim \frac{|b|^2_\mathrm{max}}{N^2}\frac{1}{k_z} \sim \left(\frac{N^2 U_\mathrm{w,max}}{\omega}\right)^2 \frac{1}{N^2 k_z} \sim \frac{N^2}{k_z^3}. \tag{2.8}$$

Ce seuil correspond à des vitesses maximales verticale $U_\mathrm{w,max} = \omega/k_z$ et horizontale $U_\mathrm{w,max}k_z/k_x = \omega/k_x$. Pour des fréquences $\omega \ll N$, la relation de dispersion indique d'une part que $k_z \gg k_x$ (l'énergie cinétique est alors essentiellement horizontale) et, d'autre part, que $\omega \sim N k_x/k_z$. Dans cette limite, le spectre d'énergie cinétique horizontale par unité de masse s'exprime ainsi :

$$e_{k,h}(k_z) \sim \frac{|\partial_z \psi|^2_\mathrm{max}}{k_z} \sim \frac{N^2}{k_z^3}. \tag{2.9}$$

Les spectres (2.8 - 2.9) coïncident avec ceux obtenus à partir d'un raisonnement différent basé sur la cascade d'énergie anisotrope, voir les équations (1.52) et (1.56). Les autres spectres dérivés dans ce cadre diffèrent.

2.1.2 Onde interne linéaire, amortie, en présence d'un écoulement moyen constant

Pour comprendre la QBO, il faut ajouter deux ingrédients :

1. Un mécanisme d'atténuation
2. Un écoulement horizontal lentement variable en temps et en espace

Par soucis de simplicité, cette étape incorpore uniquement la viscosité et un écoulement horizontal lentement variable en espace (mais indépendant du temps, supposé maintenu par un opérateur extérieur). En conservant la viscosité et les termes non linéaires, les équations de Boussinesq écrites pour le champ de vitesse

$$\mathbf{u}(\mathbf{r},t) = (\bar{u} + \partial_z\psi)\mathbf{e}_x - \partial_x\psi\mathbf{e}_z, \tag{2.10}$$

avec $\bar{u}(z)$ et $\psi(x,z,t)$ prennent la forme suivante :

$$\partial_{tz}\psi + [\bar{u} + (\partial_z\psi)]\,(\partial_{xz}\psi) - (\partial_x\psi)\,[\bar{u}' + (\partial_{zz}\psi)] = -\partial_x P + \nu\triangle\partial_z\psi + \nu\bar{u}'', \tag{2.11}$$

$$\partial_{tx}\psi + [\bar{u} + (\partial_z\psi)]\,(\partial_{xx}\psi) - (\partial_x\psi)(\partial_{xz}\psi) = \partial_z P - b + \nu\triangle\partial_x\psi, \tag{2.12}$$

$$\partial_t b + [\bar{u} + (\partial_z\psi)]\,(\partial_x b) - (\partial_x\psi)(\partial_z b) = N^2\partial_x\psi, \tag{2.13}$$

où $\triangle = \partial_{xx} + \partial_{zz}$. En éliminant la pression, on obtient :

$$\partial_t\triangle\psi + \partial_x b - \nu\triangle^2\psi = J(\psi,\triangle\psi) + \bar{u}''\partial_x\psi - \bar{u}\triangle\partial_x\psi, \tag{2.14}$$

$$\partial_t b - N^2\partial_x\psi = J(\psi,b) - \bar{u}\partial_x b, \tag{2.15}$$

avec $J(a,b) = (\partial_x a)(\partial_z b) - (\partial_z a)(\partial_x b)$. Il n'existe plus de solution analytique, et nous avançons en posant les hypothèses suivantes :

- Ondes internes de faibles amplitudes. Les effets non linéaires "ondes - ondes" (interactions entre ondes, "déferlement") sont négligeables.
- Ondes internes fortement anisotropes : $k_z \gg k_x$. La vitesse de phase est quasi-verticale, la vitesse de groupe quasi-horizontale et la pulsation satisfait $|\omega| \sim Nk_x/k_z \ll N$.
- Écoulement moyen comparable à la vitesse de groupe horizontale. Il réfracte ainsi fortement l'onde.
- Écoulement moyen et amortissement lentement variables verticalement, devant la longueur d'onde k_z^{-1}.

Cela se formalise en introduisant $\epsilon = \omega^2/N^2 \to 0$ et les variables sans dimension suivantes :

$$\tilde{t} = |\omega|t, \qquad \tilde{x} = |k_x|x, \qquad \tilde{Z} = \sqrt{\epsilon}|k_x|z, \qquad \frac{\nu k_x^2}{N} = \frac{\epsilon^{5/2}}{Re}, \qquad Re = O(1). \tag{2.16}$$

Concernant les échelles verticales, $k_z \simeq Nk_x/\omega \simeq k_x/\sqrt{\epsilon}$ dimensionne l'échelle rapide et $\tilde{Z}$ représente les variations verticales lentes de l'onde. Pour capturer les effets cumulatifs de la lente évolution du nombre d'onde [1], on utilise une approche WKBJ en définissant la phase spatiale rapide $\phi(z)$ telle que :

$$\frac{\mathrm{d}\phi}{\mathrm{d}z} = \frac{k_x}{\sqrt{\epsilon}}K_z(\tilde{Z}). \tag{2.17}$$

Les champs sont rendus sans dimension et développés en puissances de ϵ :

$$\bar{u}(z) = \frac{\sqrt{\epsilon}N}{|k_x|}\tilde{\bar{u}}(\tilde{Z}), \qquad \frac{\sqrt{\epsilon}N}{|k_x|} \text{ échelle de la vitesse de groupe horizontale} \tag{2.18}$$

$$\psi(x,z,t) = \frac{\epsilon^2 N}{k_x^2}\left[\tilde{\psi}_0 + \epsilon\tilde{\psi}_1 + O(\epsilon^2)\right] \qquad \text{correspond à } U_\mathrm{w} = \epsilon^2 U_{\mathrm{w,max}} \tag{2.19}$$

$$b(x,z,t) = \frac{\epsilon^{3/2}N^2}{|k_x|}\left[\tilde{b}_0 + \epsilon\tilde{b}_1 + O(\epsilon^2)\right] \qquad \text{correspond à } U_\mathrm{w} = \epsilon^2 U_{\mathrm{w,max}} \tag{2.20}$$

avec $\{\tilde{\psi}_0, \tilde{\psi}_1, \tilde{b}_0, \tilde{b}_1\}$ des fonctions de $\{\tilde{t}, \tilde{x}, \tilde{Z}, \phi\}$. Pour alléger les notations, les tildes seront omis ci-dessous.

1. Comme réalisé §1.2.3 sur le modèle jouet pour la lente évolution de la pulsation temporelle.

Ordre $O(1)$: À ce niveau, les équations et conditions aux limites deviennent

$$K_z^2(\partial_t + \bar{u}\partial_x)\partial_{\phi\phi}\psi_0 + \partial_x b_0 = 0, \tag{2.21}$$
$$(\partial_t + \bar{u}\partial_x)b_0 - \partial_x\psi_0 = 0, \tag{2.22}$$
$$\partial_x\psi(x,\phi,Z=0,t) = -e^{i(\Omega t - K_x x)} + \text{c.c.}, \tag{2.23}$$

avec $\Omega = \pm 1$ et $K_x = \pm 1$. En cherchant les solutions proportionnelles à $e^{i(\Omega t - K_x x - \phi)}$, la relation de dispersion

$$\Omega = K_x\bar{u} \pm \frac{K_x}{K_z} \tag{2.24}$$

implique $(\mathbf{c}_g - \bar{u}\mathbf{e}_x)\cdot\mathbf{c}_\phi = 0$. Le calcul de $\partial\Omega/\partial K_z$ montre qu'une propagation verticale ascendante de l'énergie intervient pour les quatre combinaisons suivantes :

$$\{K_x = -1, \Omega = \pm 1, K_z = \frac{-1}{\bar{u}+\Omega}\} \qquad \text{ou} \qquad \{K_x = 1, \Omega = \pm 1, K_z = \frac{1}{\bar{u}-\Omega}\}. \tag{2.25}$$

Par commodité, nous retenons $\{K_x = \Omega = 1\}$. Ainsi,

$$\psi_0 = \Psi_0(Z)e^{i(t-x-\phi)} + \text{c.c.}, \quad b_0 = K_z(Z)\Psi_0(Z)e^{i(t-x-\phi)} + \text{c.c.}, \quad \Psi_0(0) = -i, \quad K_z(Z) = \frac{1}{\bar{u}(Z)-1}. \tag{2.26}$$

Imposer $\bar{u} < 1$ évite toute réflexion totale sur une couche critique.

Ordre $O(\epsilon)$: Au rang suivant, le système s'écrit

$$K_z^2(\partial_t + \bar{u}\partial_x)\partial_\phi^2\psi_1 + \partial_x b_1 = -(\partial_t + \bar{u}\partial_x)\left[(2K_z\partial_Z + K_z')\,\partial_\phi\psi_0 + \partial_x^2\psi_0\right] + \frac{K_z^4}{Re}\partial_\phi^4\psi_0 + J(\psi_0, \triangle\psi_0), \tag{2.27}$$
$$(\partial_t + \bar{u}\partial_x)b_1 - \partial_x\psi_1 = J(\psi_0, b_0). \tag{2.28}$$

Éliminer les termes résonnants de (2.27) conduit à la condition de solvabilité

$$\frac{\Psi_0'}{\Psi_0} = -\frac{K_z^4}{2Re} - \frac{1}{2K_z}\left(\frac{\mathrm{d}K_z}{\mathrm{d}Z} + i\right) \Longrightarrow \Psi_0(Z) \propto \frac{1}{\sqrt{|K_z(Z)|}}\exp\left[\int_0^Z\left(-\frac{K_z^4(Z')}{2Re} - \frac{i}{2K_z(Z')}\right)\mathrm{d}Z'\right]. \tag{2.29}$$

On retrouve une modulation de l'amplitude en $|K_z|^{-1/2}$ assurant la conservation de l'action d'onde en l'absence d'amortissement [2], l'amortissement vertical visqueux ainsi que des corrections fines du nombre d'onde provenant de la réfraction par l'écoulement moyen.

$F(Z)$: le flux vertical de quantité de mouvement horizontale de l'onde, moyenné une période, vaut

$$F(Z) = \overline{u_x' u_z'} = -\overline{\partial_z\psi\partial_x\psi} = 2K_z|\Psi(Z)|^2 = F(0)\exp\left[-\int_0^Z \frac{K_z^4}{Re}\mathrm{d}Z\right]. \tag{2.30}$$

Ce flux $F(Z)$ s'annule en $Z \to \infty$ sous l'effet de la viscosité. La quantité de mouvement horizontale injectée dans les ondes en $z = 0$ devant être conservée, un transfert vers l'écoulement moyen a lieu.

2. Analogue à l'évolution d'un oscillateur harmonique dont on module lentement la pulsation propre : $\ddot{x} + \omega(t)^2 x = 0$ a pour solution approchée, lorsque $\omega(t)$ évolue sur une échelle de temps lente,

$$x(t) = \frac{c_0}{\sqrt{\omega(t)}}\cos\left(c_1 + \int_0^t \omega(s)\mathrm{d}s\right).$$

Cette solution est telle que l'énergie moyennée sur une période $E = \overline{\dot{x}^2/2 + \omega^2 x^2/2} \simeq c_0^2\omega(t)/2$ évolue dans le temps, contrairement à l'action d'onde $E/\omega(t)$.

2.1.3 Dynamique de l'écoulement moyen

Évolution de l'écoulement moyen sur un temps long

La solution précédente (2.26, 2.29) montre que, pour conserver la quantité de mouvement, une force est exercée sur l'écoulement moyen. On peut déterminer sa dynamique en séparant les variations temporelles rapides $\{\mathbf{u}', b'\}$ (ondes) et lentes $\{\bar{\mathbf{u}}, \bar{b}\}$ (écoulement moyen). Pour cela, n'importe quelle variable $X(\mathbf{r}, T, \tau)$ évoluant sur ces deux échelles de temps distinctes est écrite comme

$$X(T,\tau) = \bar{X}(T) + X'(T,\tau), \qquad \overline{X'} = 0, \tag{2.31}$$

où $\overline{(\cdot)}$ désigne la moyenne sur le temps rapide τ. En l'absence de force extérieure, le système de Boussinesq

$$\partial_t \mathbf{u} + (\mathbf{u}\cdot\nabla)\mathbf{u} = -\nabla P + b\mathbf{e}_z + \nu\triangle\mathbf{u}, \tag{2.32}$$

$$\nabla\cdot\mathbf{u} = 0, \tag{2.33}$$

$$\partial_t b + (\mathbf{u}\cdot\nabla)b = D\triangle b - N^2 u_z, \tag{2.34}$$

moyenné sur le temps rapide devient

$$\partial_T \bar{\mathbf{u}} + (\bar{\mathbf{u}}\cdot\nabla)\bar{\mathbf{u}} = -\overline{(\mathbf{u}'\cdot\nabla)\mathbf{u}'} - \nabla\bar{P} + \bar{b}\mathbf{e}_z + \nu\triangle\bar{\mathbf{u}}, \tag{2.35}$$

$$\nabla\cdot\bar{\mathbf{u}} = 0, \tag{2.36}$$

$$\partial_T \bar{b} + (\bar{\mathbf{u}}\cdot\nabla)\bar{b} = -\overline{(\mathbf{u}'\cdot\nabla)b'} + D\triangle\bar{b} - N^2\bar{u_z}. \tag{2.37}$$

Les deux termes $\overline{(\mathbf{u}'\cdot\nabla)\mathbf{u}'}$ et $\overline{(\mathbf{u}'\cdot\nabla)b'}$ affectent la dynamique de l'écoulement moyen : ils ont déjà été rencontrés au cours du chapitre précédent. Dans le cas présent, seul le premier terme nous intéresse,

$$\mathbf{f}_{\text{ondes}} = -\overline{(\mathbf{u}'\cdot\nabla)\mathbf{u}'} = \overline{\begin{pmatrix}\nabla(u'_x)\cdot\mathbf{u}'\\ \nabla(u'_y)\cdot\mathbf{u}'\\ \nabla(u'_z)\cdot\mathbf{u}'\end{pmatrix}} = -\overline{\begin{pmatrix}\nabla\cdot(u'_x\mathbf{u}') - u'_x(\nabla\cdot\mathbf{u}')\\ \nabla\cdot(u'_y\mathbf{u}') - u'_y(\nabla\cdot\mathbf{u}')\\ \nabla\cdot(u'_z\mathbf{u}') - u'_z(\nabla\cdot\mathbf{u}')\end{pmatrix}} = -\overline{\nabla\cdot\begin{pmatrix}u'^2_x & u'_xu'_y & u'_xu'_z\\ u'_xu'_y & u'^2_y & u'_yu'_z\\ u'_xu'_z & u'_yu'_z & u'^2_z\end{pmatrix}}. \tag{2.38}$$

Cette force volumique, l'opposée de la divergence du tenseur de Reynolds $\overline{u'_iu'_j}$, provient d'une variation du flux de quantité de mouvement : il s'agit ici d'une décroissance verticale du flux de quantité de mouvement horizontale de l'onde interne. Elle n'entraîne pas forcément l'apparition d'un écoulement moyen. En effet, d'après (2.35), si le terme $\mathbf{f}_{\text{ondes}}$ dérive d'un gradient, il peut être simplement équilibré par un gradient de pression moyenne $\bar{P}$ [3]. En suivant cette idée, on ré-écrit (2.38) sous la forme

$$\mathbf{f}_{\text{ondes}} = -\overline{(\mathbf{u}'\cdot\nabla)\mathbf{u}'} = -\nabla\left(\frac{\overline{\mathbf{u}'\cdot\mathbf{u}'}}{2}\right) + \overline{\mathbf{u}'\times(\nabla\times\mathbf{u}')}. \tag{2.39}$$

Cette expression montre clairement que, pour induire un écoulement moyen, une onde doit posséder une vorticité non nulle. Il s'agit d'une condition nécessaire mais non suffisante, le terme $\overline{\mathbf{u}'\times(\nabla\times\mathbf{u}')}$ pouvant potentiellement, lui aussi, dériver d'un gradient scalaire. Dans l'exemple présenté, les ondes internes sont effectivement de vorticité non nulle et l'on trouve

$$\mathbf{f}_{\text{ondes}} = \frac{\partial}{\partial Z}\left(-2K_z|\Psi(Z)|^2\mathbf{e}_x - 2|\Psi(Z)|^2\mathbf{e}_z\right). \tag{2.40}$$

La composante verticale génère une pression $\bar{P} = -2|\Psi|^2$, tandis que la composante horizontale force un écoulement moyen et revient exactement à $-F'(Z)$ introduit en (2.30). En toute rigueur, il serait nécessaire de reprendre l'étude précédente en ajoutant à $\{\tilde{u}, \tilde{\psi}, \tilde{b}\}$ une dépendance en un temps long $T = \epsilon^{7/2}Nt$. Les calculs précédents seraient identiques, et une moyenne sur le temps rapide fixerait l'évolution de l'écoulement moyen à

$$\frac{\partial\bar{u}}{\partial T} = -\frac{\partial F}{\partial Z} + \frac{1}{Re}\frac{\partial^2\bar{u}}{\partial Z^2}, \qquad F(Z,T) = F(0,T)\exp\left[-\int_0^Z \frac{\mathrm{d}Z'}{Re\times(1-\bar{u}(Z',T))^4}\right]. \tag{2.41}$$

Il s'agit de l'équation (2.2) de Plumb et McEwan [53] sans dissipation sur les parois solides.

3. Cela suppose l'absence de condition aux limites prescrivant des valeurs particulières pour la pression moyenne. Dans le cas présent, un gradient horizontale n'est pas admissible (car on impose un comportement périodique à grande échelle, la coordonnée x représentant la latitude), mais rien ne contraint sa structure verticale. De manière générale, à moins que le domaine soit entièrement limité par une paroi solide indéformable, il faut être attentif aux conditions aux limites avant d'invoquer cet argument.

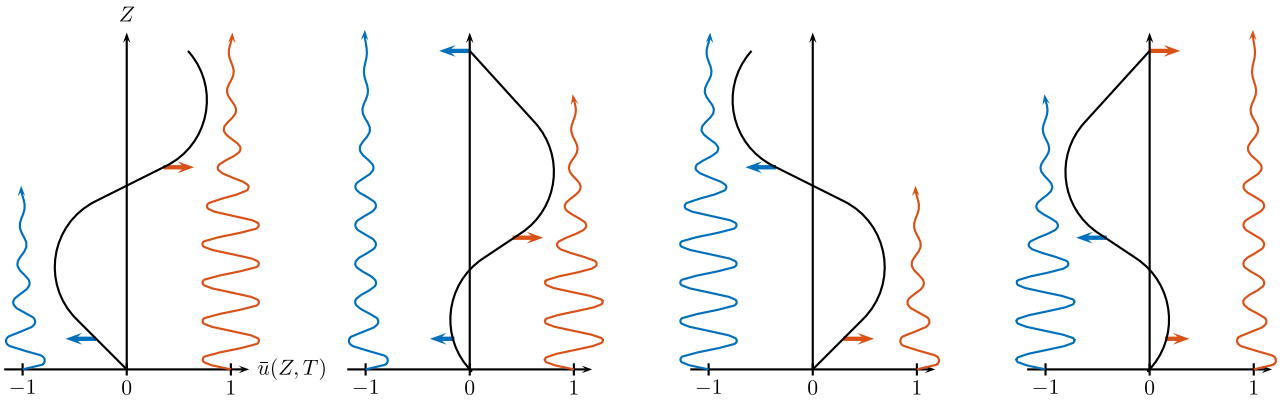

FIGURE 2.1 – Explication qualitative de la QBO comme le résultat de l'amortissement différentiel de deux ondes internes dirigées vers l'est (orange) ou l'ouest (bleu). Le trait plein noir représente l'écoulement moyen, tandis que les ondes et les forces qu'elles exercent sur l'écoulement moyen sont en couleur. Les différentes figures correspondent à des valeurs croissantes de temps "lent" et couvrent une période de la QBO. Adapté de [56].

Explication qualitative de la QBO

L'équation (2.41) montre que l'atténuation d'ondes internes telles que $F(0,T) > 0$ engendre un écoulement vers l'est (suivant $\mathbf{e}_x$). Dans la réalité, des ondes se propagent aussi bien suivant l'est que l'ouest. Le calcul s'adapte sans difficulté car les termes non linéaires n'apparaissent à l'ordre dominant ni dans la dynamique des ondes, ni dans la condition de solvabilité. En considérant deux ondes progressives de même amplitude, avec $\mathbf{c}_g \cdot \mathbf{e}_x$ positif ou négatif, il suffit de remplacer $F(Z,T)$ par la somme des contributions opposées :

$$F(Z,T) = \frac{F(0,T)}{2} \exp\left[-\int_0^Z \frac{\mathrm{d}Z'}{Re \times (1-\bar{u}(Z',T))^4}\right] - \frac{F(0,T)}{2} \exp\left[-\int_0^Z \frac{\mathrm{d}Z'}{Re \times (1+\bar{u}(Z',T))^4}\right]. \quad (2.42)$$

La force exercée sur l'écoulement moyen est ainsi maximale lorsque :

(i) la vitesse moyenne s'approche d'une des vitesses de groupe ($\bar{u} \simeq \pm 1$)

(ii) l'onde interne n'est pas encore totalement amortie (les exponentielles ne sont pas encore nulles)

Cela explique les oscillations spatio-temporelles du champ de vitesse moyen, donc la QBO, comme illustré dans la figure 2.1. Plus de détails sur la nature super-critique ou sous-critique de la bifurcation de Hopf menant à cet écoulement moyen ainsi que sur les expériences de laboratoire mimant la QBO sont reportés dans Ref. [57].

Les propriétés à retenir de cet exemple

La suite de ce manuscrit ne traitera plus d'ondes internes ni d'écoulements atmosphériques. La QBO a été présentée car elle illustre un couplage générique : (i) les ondes sont réfractées par l'écoulement moyen, (ii) leur atténuation affecte l'écoulement moyen puis (iii) cet écoulement évolue et réfracte différemment les ondes.

De plus, une dynamique quasi-linéaire émerge naturellement : les amplitudes des ondes n'étant pas suffisantes pour qu'elles "déferlent" ou interagissent entre elles, nous obtenons sur l'échelle de temps rapide un problème aux valeurs propres linéaire avec des coefficients lentement variables. Dans les travaux de Plumb, cette hypothèse est introduite de façon ad hoc par analogie avec le modèle de convection quasi-linéaire de Herring [58]. Ici, on montre qu'elle peut être asymptotiquement justifiée (ce n'est pas le cas pour le modèle de Herring).

Enfin, bien que cette structure quasi-linéaire soit très analogue à celle obtenue dans le chapitre précédent, sa résolution ne fait pas appel aux outils développés (fixer l'amplitude de la perturbation rapide pour rester dans le domaine de stabilité marginale). En effet, l'échelle de temps rapide décrit ici des ondes et non des écoulements instables : le taux de croissance réel est toujours nul et n'a pas à être contraint. Ce problème est également favorable parce qu'une expression explicite des ondes est disponible (équations 2.26 et 2.29), ce qui permet de réduire la dynamique à l'échelle de temps lente (équation 2.41). Ce n'est malheureusement pas courant.

Plus généralement, nous avons constaté que l'émergence d'un écoulement moyen nécessite des ondes de vorticité finie. Sinon, la divergence du tenseur de Reynolds se réduit à un simple un gradient de pression.

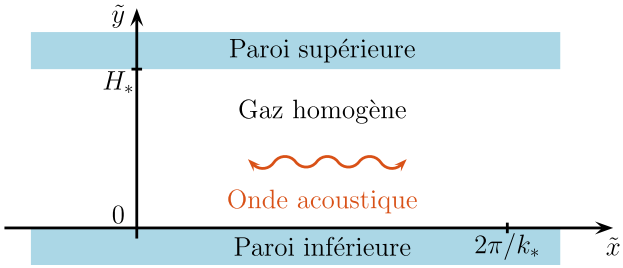

FIGURE 2.2 – Configuration pour l'étude du streaming de Rayleigh

2.2 Streaming de Rayleigh dans un fluide homogène

À l'image des ondes internes, les ondes acoustiques peuvent générer un écoulement moyen appelé "streaming acoustique". Ce phénomène a été observé dès le XVIII$^{\text{e}}$ siècle dans des tubes fermés : une onde stationnaire résonnante rassemble la poussière en amas situés aux nœuds de vitesse. L'invention des transducteurs piézoélectriques a permis de produire des ultrasons de grande amplitude tant dans l'air que dans l'eau, élargissant cet effet aux ondes progressives. Pour le mettre en évidence, il suffit de diriger une source ultrasonore vers un panache d'air chaud visualisé à l'aide d'un dispositif optique de type schlieren [59]. Les écoulements de streaming dus à ces deux types d'ondes sont aujourd'hui exploités pour améliorer le mélange dans des micro-canaux [60–62] et à plus grande échelle [63, 64]. L'analyse repose sur la séparation des échelles de temps des ondes acoustiques et de l'écoulement moyen, justifiant l'introduction de la divergence du tenseur de Reynolds. Pour une introduction au streaming acoustique, la revue de Lighthill [59] est incontournable. Celles de Riley [65, 66] et Nyborg [67] introduisent la vorticité des ondes ainsi que les calculs asymptotiques. Il n'y a cependant, à ma connaissance, aucune revue détaillant les nouvelles thématiques des vingt dernières années : outre l'application aux fluides inhomogènes abordée par la suite, mentionnons simplement ici le streaming autour de pointes acérées (rayon de courbure comparable ou inférieur à l'épaisseur de la couche limite oscillante) [68, 69], la caractérisation fine des jets forcés par des ondes progressives ainsi que les instabilités sous-jacentes [70–73], et enfin son rôle en association avec la pression de radiation pour le déplacement de particules [74, 75].

Les travaux présentés par la suite portent sur les écoulements de streaming causés par des ondes acoustiques stationnaires dans un gaz stratifié, nettement plus intenses que dans un gaz homogène. Pour les introduire, nous formalisons le calcul historique de Rayleigh en milieu homogène [76] avec la méthode des échelles multiples.

2.2.1 Mise en équation

Problème et équations constitutives

Nous souhaitons caractériser l'écoulement moyen engendré par une onde acoustique stationnaire horizontale dans un canal fin, comme représenté à la figure 2.2. L'onde, de pulsation ω_*, nombre d'onde k_* fixant la période spatiale $2\pi/k_*$, surpression maximale P_*, est soutenue par une force extérieure $\mathbf{F}_{\text{ext}*} = F_* \sin(k_*\tilde{x})\cos(\omega_*\tilde{t})\mathbf{e}_x$. Le gaz est supposé parfait, la viscosité de volume est négligée, tout comme la diffusion thermique, l'augmentation de température par dissipation visqueuse et la gravité. Les équations de conservation de la quantité de mouvement, de la masse, de l'énergie interne et l'équation d'état sont respectivement

$$\tilde{\rho}\left[\partial_{\tilde{t}}\tilde{\mathbf{u}} + (\tilde{\mathbf{u}}\cdot\tilde{\nabla})\tilde{\mathbf{u}}\right] = -\tilde{\nabla}\tilde{p} + \mu_*\left[\tilde{\nabla}^2\tilde{\mathbf{u}} + \frac{1}{3}\tilde{\nabla}(\tilde{\nabla}\cdot\tilde{\mathbf{u}})\right] + 2F_*\sin(k_*\tilde{x})\cos(\omega_*\tilde{t})\mathbf{e}_x, \tag{2.43}$$

$$\partial_{\tilde{t}}\tilde{\rho} + \tilde{\nabla}\cdot(\tilde{\rho}\tilde{\mathbf{u}}) = 0, \tag{2.44}$$

$$\tilde{\rho}c_v\left[\partial_{\tilde{t}}\tilde{T} + (\tilde{\mathbf{u}}\cdot\tilde{\nabla})\tilde{T}\right] = -\tilde{p}\left(\tilde{\nabla}\cdot\tilde{u}\right), \tag{2.45}$$

$$\tilde{p} = \tilde{\rho}R_*\tilde{T}. \tag{2.46}$$

Elles doivent être complétées par les conditions aux limites cinématiques et thermiques au niveau des parois

$$\tilde{\mathbf{u}}(\tilde{x},0,\tilde{t}) = \tilde{\mathbf{u}}(\tilde{x},H_*,\tilde{t}) = \mathbf{0}, \qquad \partial_{\tilde{z}}\tilde{T}(\tilde{x},0,\tilde{t}) = \partial_{\tilde{z}}\tilde{T}(\tilde{x},H_*,\tilde{t}) = 0. \tag{2.47}$$

Les tildes et les astérisques repèrent les grandeurs dimensionnées. Pour justifier (2.45), rappelons qu'en écrivant la conservation de la quantité de mouvement comme

$$\rho\left[\frac{\partial \mathbf{u}}{\partial t}+(\mathbf{u}\cdot\nabla)\mathbf{u}\right]=\nabla\cdot\overline{\overline{\sigma}}+\mathbf{f}, \tag{2.48}$$

avec $\overline{\overline{\sigma}}$ le tenseur des contraintes et $\mathbf{f}$ les forces volumiques extérieures, l'énergie interne volumique e vérifie [77]

$$\rho\left[\frac{\partial e}{\partial t}+(\mathbf{u}\cdot\nabla)e\right]=\sigma_{ij}\partial_j u_i-\nabla\cdot\mathbf{q}+q^*, \tag{2.49}$$

où le transfert thermique sur un système fermé $Q=-\int_{\mathcal{S}}\mathbf{q}\,\mathrm{d}^2S+\int_{\mathcal{V}}q^*\mathrm{d}^3V$ est la somme de transferts thermiques surfaciques et associés à des sources internes. Pour un fluide newtonien de viscosité dynamique de cisaillement μ et de viscosité dynamique de volume ξ constantes et uniformes,

$$\nabla\cdot\overline{\overline{\sigma}}=-\nabla P+\mu\triangle\mathbf{v}+\left(\frac{\mu}{3}+\xi\right)\nabla(\nabla\cdot\mathbf{u}), \tag{2.50}$$

$$\sigma_{ij}\partial_j u_i=-P(\nabla\cdot\mathbf{u})+D, \tag{2.51}$$

avec $D>0$ un terme caractérisant l'augmentation de température par dissipation visqueuse. Pour un gaz parfait, l'énergie interne e dépend uniquement de la température (première loi de Joule) et ses variations n'impliquent donc que la capacité thermique à volume constant c_v. La viscosité dynamique de volume ξ est quant à elle souvent négligée en réalisant l'hypothèse de Stokes, formellement valable uniquement pour un gaz monoatomique.

Équations adimensionnées

Passons maintenant à des grandeurs sans dimension. Les coordonnées de temps et d'espace sont par la suite comparées aux périodes temporelle et spatiale de l'onde, ainsi qu'à l'épaisseur du canal :

$$\tilde{x}=\frac{x}{k_*},\qquad \tilde{y}=H_*y,\qquad \tilde{t}=\frac{t}{a_*k_*}, \tag{2.52}$$

avec $a_*=\sqrt{\gamma R_*T_*}$ la vitesse du son dans le gaz parfait de température au repos T_* (R_* est le rapport de la constante des gaz parfaits sur la masse molaire, $\gamma=c_{p*}/c_{v*}$ est l'indice adiabatique). Les champs de vitesse $\tilde{\mathbf{u}}=\tilde{u}\mathbf{e}_x+\tilde{v}\mathbf{e}_y$, masse volumique, pression et température sont exprimés comme

$$\tilde{u}(\tilde{x},\tilde{y},\tilde{t})=a_*u(x,y,t), \tag{2.53}$$

$$\tilde{v}(\tilde{x},\tilde{y},\tilde{t})=a_*(H_*k_*)v(x,y,t), \tag{2.54}$$

$$\tilde{\rho}(\tilde{x},\tilde{y},\tilde{t})=\rho_*\rho(x,y,t),\qquad \rho_*=\frac{P_*}{R_*T_*} \tag{2.55}$$

$$\tilde{p}(\tilde{x},\tilde{y},\tilde{t})=P_*p(x,y,t), \tag{2.56}$$

$$\tilde{T}(\tilde{x},\tilde{y},\tilde{t})=T_*T(x,y,t), \tag{2.57}$$

avec (P_*,T_*) l'état thermodynamique du gaz au repos. Enfin, on pose pour simplifier les notations $F_*=\gamma P_*k_*F$, avec F un nombre sans dimension, $\delta=k_*H_*$ et $Re_w=\rho_*a_*/(k_*\mu_*)$. Les équations et conditions aux limites s'écrivent finalement [4],

$$\rho\left[\partial_t u+(u\partial_x+v\partial_y)\,u\right]=-\frac{1}{\gamma}\partial_x p+\frac{1}{\delta^2Re_w}\left[\left(\delta^2\partial_{xx}+\partial_{yy}\right)u+\frac{\delta^2}{3}\partial_x(\partial_x u+\partial_y v)\right]+2F\sin(x)\cos(t), \tag{2.58}$$

$$\rho\left[\partial_t v+(u\partial_x+v\partial_y)\,v\right]=-\frac{1}{\gamma\delta^2}\partial_y p+\frac{1}{\delta^2Re_w}\left[\left(\delta^2\partial_{xx}+\partial_{yy}\right)v+\frac{1}{3}\partial_y(\partial_x u+\partial_y v)\right], \tag{2.59}$$

$$\partial_t\rho+\partial_x(\rho u)+\partial_y(\rho v)=0, \tag{2.60}$$

$$\rho\left[\partial_t T+(u\partial_x+v\partial_y)T\right]=-(\gamma-1)p(\partial_x u+\partial_y v), \tag{2.61}$$

$$p=\rho T, \tag{2.62}$$

$$u(x,0,t)=u(x,1,t)=v(x,0,t)=v(x,1,t)=0, \tag{2.63}$$

$$\partial_z T(x,0,t)=\partial_y T(x,1,t)=0. \tag{2.64}$$

4. La relation de Mayer pour un gaz parfait, $c_{p*}-c_{v_*}=R_*$ ainsi que la définition de $\gamma=c_{p*}/c_{v*}$ mènent à $c_{v*}=R_*/(\gamma-1)$.

La solution est contrôlée par quatre nombres sans dimension :

1. L'indice adiabatique $\gamma = c_{p*}/c_{v*}$. Il reste proche de l'unité, avec $\gamma = 5/3$ pour un gaz monoatomique.
2. Le rapport d'aspect $\delta = k_* H_*$. Noter l'importance accrue des termes dissipatifs verticaux lorsque $\delta \ll 1$.
3. Le nombre de Reynolds basé sur la vitesse du son $Re_w = \rho_* a_*/(k_* \mu_*)$. Une onde libre est atténuée sur quelques périodes temporelles si $Re_w = O(1)$, et sur une durée bien plus longue si $Re_w \gg 1$.
4. La force extérieure F. Si $F \ll 1$, elle affecte seulement l'amplitude de l'onde et non son profil spatial.

Nous nous plaçons dorénavant dans un canal fin ($\delta \ll 1$) avec des ondes faiblement affectées par la dissipation et la force extérieure ($Re_w \gg 1,\ F \ll 1$). Pour formaliser ces hypothèses, on introduit un petit paramètre $\epsilon \to 0$ qui sera l'échelle de la vitesse acoustique ($\tilde{u} = O(\epsilon a_*)$) et on pose :

$$\gamma = O(1), \qquad \delta = \sqrt{\epsilon} h, \qquad Re_w = \frac{Re}{\epsilon^2}, \qquad F = \epsilon^{3/2} f, \tag{2.65}$$

où $\{h, Re, f\}$ sont des paramètres d'ordre $O(1)$. Le paramètre ϵ est en pratique très faible, typiquement 10^{-4}, d'où le choix d'introduire $\sqrt{\epsilon}$ pour dimensionner le rapport d'aspect.

2.2.2 Résolution en échelles multiples

Le paramètre ϵ sert à introduire de nouvelles échelles spatio-temporelles ; cela ne sera pas utile pour le temps, car nous supposons un régime établi où coexistent des ondes et un écoulement moyen stationnaire. Ainsi, toute variable $q(x, y, t)$ s'écrit

$$q(x, y, t) = q'(x, y, t) + \overline{q}(x, y), \qquad \overline{q'} = 0. \tag{2.66}$$

En revanche, l'apparition de couches limites oscillantes pour assurer le non-glissement se traduit par l'émergence d'une échelle de longueur $\delta_{\mathrm{BL}} = \sqrt{\mu_*/(\rho_* a_* k_*)}$ courte devant les dimensions géométriques du canal. En particulier, $\delta_{\mathrm{BL}}/H_* = \sqrt{\epsilon}/(h\sqrt{Re}) = O(\sqrt{\epsilon})$, ce qui est capturé par l'introduction de $\eta = \{y/\sqrt{\epsilon}, (1-y)/\sqrt{\epsilon}\}$ pour décrire les couches limites en $y = \{0, 1\}$. On passera, quand cela est simple, l'étape de séparation de la solution entre un domaine intérieur et les couches limites. Pour l'instant, contentons-nous de développer les champs,

$$(u, v) = \epsilon(u_1, v_1) + \epsilon^{3/2}(u_{3/2}, v_{3/2}) + \epsilon^2(u_2, v_2) + O(\epsilon^{5/2}), \tag{2.67}$$

$$P = 1 + \epsilon\pi_1 + \epsilon^{3/2}\pi_{3/2} + \epsilon^2\pi_2 + \epsilon^{5/2}\pi_{5/2} + \epsilon^3\pi^3 + O(\epsilon^{7/2}), \tag{2.68}$$

$$T = 1 + \epsilon\Theta_1 + \epsilon^{3/2}\Theta_{3/2} + \epsilon^2\Theta_2 + O(\epsilon^{5/2}), \tag{2.69}$$

$$\rho = 1 + \epsilon\rho_1 + \epsilon^{3/2}\rho_{3/2} + \epsilon^2\rho_2 + O(\epsilon^{5/2}). \tag{2.70}$$

L'absence de terme en $O(\epsilon^{1/2})$ résulte de l'échelle de la vitesse acoustique à l'ordre dominant $O(\epsilon a_*)$ (par définition de ϵ). Chaque terme est ensuite séparé entre une partie stationnaire et une partie oscillante, par exemple, $u_1(x, y, t) = u_1'(x, y, t) + \overline{u}_1(x, y)$. L'objectif principal est d'identifier le premier terme du développement de la vitesse dont la moyenne temporelle n'est pas nulle.

état stationnaire $O(1)$: les équations à l'ordre dominant, caractérisant un gaz parfait au repos, sont automatiquement vérifiées par la forme de la solution (2.67 - 2.70).

état stationnaire $O(\epsilon)$: moyenner les équations à cet ordre mène à $\overline{u}_1 = \overline{v}_1 = \overline{\pi}_1 = \overline{\Theta}_1 = \overline{\rho}_1 = 0$.

ondes $O(\epsilon)$: comme le forçage est purement horizontal, on cherche une onde dont la vitesse verticale dominante est nulle, $v_1' = 0$. On retrouve alors, à l'ordre $O(\epsilon)$, l'équation de d'Alembert :

$$\partial_{tt}\pi_1' - \partial_{xx}\pi_1' = 0, \quad \partial_t u_1' = -\gamma^{-1}\partial_x \pi_1', \quad \rho_1' = \gamma^{-1}\pi_1', \quad \Theta_1' = (1 - \gamma^{-1})\pi_1'. \tag{2.71}$$

L'onde plane $\pi_1' = (A/2)\cos(x)e^{it}$ + c.c. vérifie la condition aux limites thermique et de non-pénétration à la paroi, mais elle viole la condition de non-glissement. Une couche limite oscillante régularise ce comportement : près de $y = 0$, les équations à l'ordre dominant s'écrivent

$$\partial_t u_1' + \frac{\partial_x \pi_1'}{\gamma} = \frac{\partial_{\eta\eta} u_1'}{Reh}, \quad \partial_\eta \pi_1' = 0, \quad \partial_t \rho_1' + \partial_x u_1' + \partial_\eta v_{3/2}' = 0, \quad \partial_t \Theta_1' = (1-\gamma)(\partial_x u_1' + \partial_\eta v_{3/2}'), \quad \pi_1' = \rho_1' + \Theta_1'. \tag{2.72}$$

Après raccordement, la solution est, avec $\mathbb{R} = Reh^2/2$ un paramètre d'ordre l'unité,

$$\pi_1' = \frac{A}{2}\cos(x)\,e^{it} + \text{c.c.}, \qquad \Theta_1' = (1-\gamma^{-1})\pi_1', \qquad \rho_1' = \gamma^{-1}\pi_1', \qquad \text{(Intérieur et CL)} \tag{2.73}$$

$$u_1' = \begin{cases} -i\frac{A}{2\gamma}\sin(x)\,e^{it} + \text{c.c.} & \text{(Intérieur)} \\ -i\frac{A}{2\gamma}\left(1 - e^{-(1+i)\sqrt{\mathbb{R}}\eta}\right)\sin(x)e^{it} + \text{c.c.} & \text{(CL)} \end{cases} \tag{2.74}$$

$$v_{3/2}' = -\frac{A(1+i)\cos(x)e^{it}}{4\gamma\sqrt{\mathbb{R}}}\left(1 - e^{-(1+i)\sqrt{\mathbb{R}}\eta}\right) + \text{c.c.} \qquad \text{(CL)} \tag{2.75}$$

Les expressions dans la couche limite supérieure ne sont pas explicitées mais peuvent être obtenues par symétrie. Remarquons une propriété essentielle : $v_{3/2}'(x, \eta \to \infty, t) \neq 0$, c'est-à-dire qu'une faible vitesse verticale oscillante persiste à la sortie de la couche limite.

état stationnaire $O(\epsilon^{3/2})$: par moyenne temporelle des équations, $\overline{u}_{3/2} = \overline{v}_{3/2} = \overline{\pi}_{3/2} = \overline{\Theta}_{3/2} = \overline{\rho}_{3/2} = 0$. Il n'y a toujours pas d'écoulement moyen.

ondes $O(\epsilon^{3/2})$: les équations et conditions aux limites dans le cœur du fluide s'écrivent

$$\partial_t u_{3/2}' + \frac{\partial_x \pi_{3/2}'}{\gamma} = 2f\sin(x)\cos(t), \qquad \partial_y \pi_{3/2}' = 0, \tag{2.76}$$

$$\partial_t \rho_{3/2}' + \partial_x u_{3/2}' + \partial_y v_{3/2}' = 0, \qquad \partial_t \Theta_{3/2}' = (1-\gamma)(\partial_x u_{3/2}' + \partial_y v_{3/2}'), \tag{2.77}$$

$$\pi_{3/2}' = \rho_{3/2}' + \Theta_{3/2}', \qquad v_{3/2}'(x, y=0, t) = -\frac{A(1+i)\cos(x)e^{it}}{4\gamma\sqrt{\mathbb{R}}} + \text{c.c.} = -v_{3/2}'(x, y=1, t). \tag{2.78}$$

Il s'agit d'un système forcé traduisant l'équilibre entre la dissipation visqueuse, à l'origine de la condition aux limites en $y = \{0, 1\}$, et la force volumique. Précisons cette démarche en sommant les équations (2.77),

$$\partial_t \pi_{3/2}' = -\gamma(\partial_x u_{3/2}' + \partial_y v_{3/2}'), \tag{2.79}$$

que l'on intègre ensuite sur $y \in [0, 1]$, pour obtenir, en exploitant $\partial_y \pi_{3/2}' = 0$ et en posant $U_{3/2} = \int_0^1 u_{3/2}' \mathrm{d}y$,

$$\partial_x U_{3/2} + \frac{\partial_t \pi_{3/2}'}{\gamma} = -\int_0^1 (\partial_y v_{3/2}')\mathrm{d}y = 2v_{3/2}'(x, y=0, t) = -\frac{A(1+i)\cos(x)e^{it}}{2\gamma\sqrt{\mathbb{R}}} + \text{c.c.} \tag{2.80}$$

De même, (2.76) intégré suivant y donne

$$\partial_t U_{3/2} + \frac{\partial_x \pi_{3/2}'}{\gamma} = f\sin(x)e^{it} + \text{c.c.} \tag{2.81}$$

En combinant ces deux dernières équations, il vient

$$\partial_{tt} U_{3/2} - \partial_{xx} U_{3/2} = \left[if - \frac{A(1+i)}{2\gamma\sqrt{\mathbb{R}}}\right]\sin(x)e^{it} + \text{c.c.} = \left[f - \frac{A(1-i)}{2\gamma\sqrt{\mathbb{R}}}\right] i\sin(x)e^{it} + \text{c.c.} \tag{2.82}$$

L'existence d'une solution stationnaire nécessite l'annulation des termes résonnants. Cela fixe la valeur de la force externe qui compense les pertes visqueuses d'une onde acoustique d'amplitude A :

$$f = \frac{A(1-i)}{2\gamma\sqrt{\mathbb{R}}}. \tag{2.83}$$

En l'absence de la force extérieure f, nous obtiendrions à cet ordre une condition de solvabilité quantifiant la lente décroissance de l'amplitude de l'onde [5].

5. C'est par exemple comme cela que l'on calcule l'amortissement des ondes de surface près d'une paroi solide : la viscosité crée une couche limite oscillante, en sortie de laquelle persiste une petite vitesse normale à la paroi. Cette composante force en volume un écoulement qui atténue l'onde de surface.

état stationnaire $O(\epsilon^2)$: les équations (2.58) et (2.59) s'écrivent, à cet ordre et en moyenne temporelle,

$$\partial_y \overline{\pi}_2 = 0, \qquad \partial_x \overline{\pi}_2 = -\gamma \left(\overline{u_1' \partial_x u_1'} + \overline{\rho_1' \partial_t u_1'} \right). \tag{2.84}$$

On les simplifie en utilisant la conservation de la masse à l'ordre $O(\epsilon)$, $\partial_t \rho_1' + \partial_x u_1' = 0$, pour obtenir

$$\partial_y \overline{\pi}_2 = 0, \qquad \partial_x \overline{\pi}_2 = -\gamma \left(\overline{u_1' \partial_x u_1'} - \overline{u_1' \partial_t \rho_1'} \right) = -\gamma \partial_x \overline{(u_1'^2)} \qquad \Longrightarrow \overline{\pi}_2 = -\gamma \overline{(u_1'^2)} = -\frac{A^2}{2\gamma} \sin(x)^2. \tag{2.85}$$

On constate une première conséquence des non-linéarités acoustiques : le champ de pression moyen évolue. Cela peut être utilisé pour déplacer des particules solides, mais n'induit pas d'écoulement. L'équation de conservation de la masse mène à

$$\partial_x \overline{u}_2 + \partial_y \overline{v}_2 = 0, \tag{2.86}$$

traduisant l'incompressibilité de l'écoulement moyen. Cet écoulement est non nul à cet ordre. Pour le démontrer, on écrit l'équivalent de (2.84) dans la couche limite en $y = 0$,

$$\partial_\eta \overline{\pi}_2 = 0, \qquad \overline{\rho_1' \partial_t u_1'} + \overline{u_1' \partial_x u_1'} + \overline{v_{3/2}' \partial_\eta u_1'} = -\frac{\partial_x \overline{\pi}_2}{\gamma} + \frac{\partial_{\eta\eta} \overline{u}_2}{Reh^2}. \tag{2.87}$$

La variation de pression moyenne $\overline{\pi}_2(x, y)$, déjà calculée (2.85) dans l'intérieur du domaine, se propage donc dans la couche limite. En utilisant la conservation de la masse (2.72), on simplifie puis explicite

$$\partial_{\eta\eta} \overline{u}_2 = Reh^2 \left[\frac{\partial_x \overline{\pi}_2}{\gamma} + \partial_x \overline{(u_1'^2)} + \partial_\eta \overline{\left(u_1' v_{3/2}' \right)} \right] \tag{2.88}$$

$$= \frac{Reh^2 A^2 \sin(2x)}{4\gamma^2} \left\{ \left[\sin(\sqrt{\mathbb{R}}\eta) - 3\cos(\sqrt{\mathbb{R}}\eta) \right] e^{-\sqrt{\mathbb{R}}\eta} + e^{-2\sqrt{\mathbb{R}}\eta} \right\}, \tag{2.89}$$

que nous sommes en mesure d'intégrer avec les conditions aux limites $\overline{u}_2(x, \eta = 0) = \partial_\eta \overline{u}_2(x, \eta \to \infty) = 0$:

$$\overline{u}_2(x, \eta) = -\frac{A^2 \sin(2x)}{8\gamma^2} \left\{ 3 - \left[6\sin(\sqrt{\mathbb{R}}\eta) + 2\cos(\sqrt{\mathbb{R}}\eta) \right] e^{-\sqrt{\mathbb{R}}\eta} - e^{-2\sqrt{\mathbb{R}}\eta} \right\}. \tag{2.90}$$

Une vitesse moyenne persiste en sortie de couche limite : $\overline{u}_2(x, \eta \to \infty) \neq 0$. Il s'agit, dans le domaine intérieur, d'une vitesse de glissement effective $\overline{u}_{\text{slip}} = -3A^2 \sin(2x)/(8\gamma^2)$. Revenons aux variables dimensionnées : pour une onde de vitesse acoustique $\tilde{\mathbf{u}} = U_* \sin(k_* \tilde{x}) \sin(\omega_* \tilde{t}) \mathbf{e}_x$ (i.e., $U_* = A\epsilon a_*/\gamma$), cette vitesse de glissement s'écrit

$$\overline{u}_{\text{slip}*} = -\frac{3U_*^2}{8a_*} \sin(2k_* \tilde{x}). \tag{2.91}$$

En particulier, elle est dirigée vers les nœuds de vitesse acoustique et son échelle est $U_* \times (U_*/a_*)$, avec U_*/a_* le nombre de Mach acoustique en pratique très faible devant l'unité. Pour déterminer la structure spatiale de l'écoulement dans l'intérieur du domaine, il faut écrire les équations de conservation de la quantité de mouvement horizontale et verticale, (2.58) et (2.59), respectivement à l'ordre $O(\epsilon^3)$ et $O(\epsilon^2)$:

$$-\frac{\partial_x \pi_3}{\gamma} + \frac{1}{Reh^2} \left[h^2 \partial_{xx} u_1 + \partial_{yy} u_2 + \frac{h^2}{3} (\partial_{xx} u_1 + \partial_{xy} v_1) \right] = \partial_t u_3 + \rho_1 \partial_t u_2 + \rho_{3/2} \partial_t u_{3/2} + \rho_2 \partial_t u_1 \tag{2.92}$$

$$+ u_2 \partial_x u_1 + u_{3/2} \partial_x u_{3/2} + u_1 \partial_x u_2 + v_2 \partial_y u_1 + v_{3/2} \partial_y u_{3/2} + v_1 \partial_y u_2 + \rho_1 u_1 \partial_x u_1 + \rho_1 v_1 \partial_y u_1,$$

$$-\frac{\partial_y \pi_3}{\gamma h^2} + \frac{1}{Reh^2} \left[\partial_{yy} v_1 + \frac{1}{3} (\partial_{xy} u_1 + \partial_{yy} v_1) \right] = \partial_t v_2 + \rho_1 \partial_t v_1 + u_1 \partial_x v_1 + v_1 \partial_y v_1. \tag{2.93}$$

On supprime les termes nuls (v_1, $\partial_y u_1$ et $\partial_y u_{3/2}$) puis sépare les contributions oscillantes et stationnaires :

$$-\frac{\partial_x (\pi_3' + \overline{\pi}_3)}{\gamma} + \frac{1}{Reh^2} \left[h^2 \partial_{xx} u_1' + \partial_{yy} (u_2' + \overline{u}_2) + \frac{h^2}{3} \partial_{xx} u_1' \right] = \partial_t u_3' + \rho_1' \partial_t u_2' + \rho_{3/2}' \partial_t u_{3/2}' + (\rho_2' + \overline{\rho}_2) \partial_t u_1'$$

$$+ (u_2' + \overline{u}_2) \partial_x u_1' + u_{3/2}' \partial_x u_{3/2}' + u_1' \partial_x (u_2' + \overline{u}_2) + \rho_1' u_1' \partial_x u_1', \tag{2.94}$$

$$-\frac{\partial_y (\pi_3' + \overline{\pi}_3)}{\gamma h^2} + \frac{\partial_{xx} u_1'}{3Reh^2} = \partial_t v_2'. \tag{2.95}$$

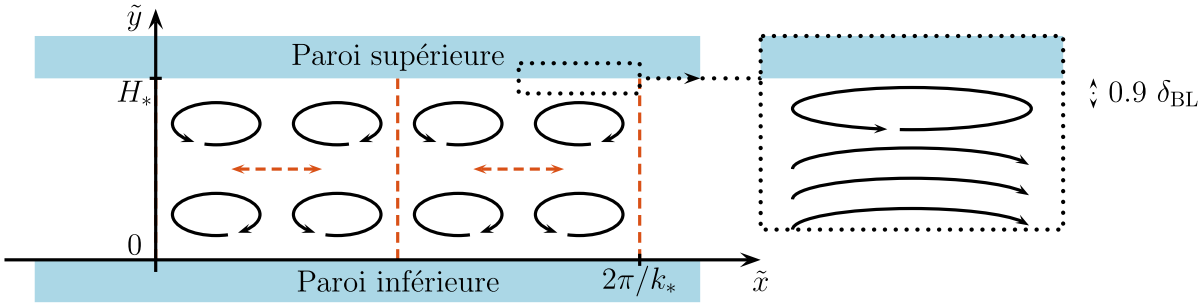

FIGURE 2.3 – Écoulement moyen créé par une onde acoustique stationnaire dans un canal horizontal fin. Le champ de vitesse de l'onde acoustique est schématisé en orange, les traits verticaux représentent ses nœuds. L'écoulement moyen dans l'intérieur du domaine (2.101) est représenté en noir, et son équivalent dans la couche limite oscillante est encadré à droite ((2.90) complété par $\partial_x \overline{u}_2 + \partial_\eta \overline{v}_{5/2} = 0$).

On effectue ensuite une moyenne temporelle,

$$-\frac{\partial_x \overline{\pi}_3}{\gamma} + \frac{\partial_{yy}\overline{u}_2}{Reh^2} = \overline{\rho_1' \partial_t u_2'} + \overline{\rho_{3/2}' \partial_t u_{3/2}'} + \overline{\rho_2' \partial_t u_1'} + \overline{u_2' \partial_x u_1'} + \overline{u_{3/2}' \partial_x u_{3/2}'} + \overline{u_1' \partial_x u_2'}, \tag{2.96}$$

$$-\frac{\partial_y \overline{\pi}_3}{\gamma h^2} = 0, \tag{2.97}$$

puis, par dérivation suivant y, en rappelant également que $\partial_y \rho_{3/2}' = \partial_y \pi_{3/2}' = 0$,

$$\frac{\partial_{yyy}\overline{u}_2}{Reh^2} = \overline{\rho_1' \partial_{ty} u_2'} + \overline{(\partial_y \rho_2')\partial_t u_1'} + \overline{(\partial_y u_2')\partial_x u_1'} + \overline{u_1' \partial_{xy} u_2'}. \tag{2.98}$$

Enfin, la dynamique non moyennée à l'ordre précédent s'écrit $\partial_y \pi_2' = 0$ (donc $\partial_y \rho_2' = 0$), ainsi que $\partial_t u_2' + \rho_1' \partial_t u_1' + u_1' \partial_x u_1' = -\gamma^{-1} \partial_x \pi_2'$, qui dérivé suivant y se réduit à $\partial_{ty} u_2' = 0$. Au final,

$$\frac{\partial_{yyy}\overline{u}_2}{Reh^2} = 0, \tag{2.99}$$

qu'il faut résoudre avec les conditions aux limites $\overline{u}_2(x, y=0) = \overline{u}_2(x, y=1) = \overline{u}_{\mathrm{slip}}$ ainsi que, par incompressibilité, $\int_0^1 \overline{u}_2 \mathrm{d}y = 0$. On trouve

$$\overline{u}_2(x,y) = u_{\mathrm{slip}}(1 - 6y + 6y^2) = \frac{3A^2}{8\gamma^2}(-1 + 6y - 6y^2)\sin(2x) \longrightarrow \overline{v}_2(x,y) = \frac{3A^2}{4\gamma^2}(y - 3y^2 + 2y^3)\cos(2x). \tag{2.100}$$

En revenant aux variables dimensionnées, l'écoulement moyen s'écrit

$$\tilde{\overline{u}} = \frac{3U_*^2}{16 a_*}\sin(2k_*\tilde{x})\left[1 - 3\left(\frac{\tilde{y} - (H_*/2)}{(H_*/2)}\right)^2\right], \quad \tilde{\overline{v}} = \frac{3U_*^2}{16 a_*} 2k_* \cos(2k_*\tilde{x})\left[\frac{H_*}{2} - \tilde{y} - \frac{(H_*/2 - \tilde{y})^3}{(H_*/2)^2}\right]. \tag{2.101}$$

Il s'agit des expressions démontrées par Rayleigh [6]. Ce champs de vitesse est représenté à la figure 2.3 et consiste en une superposition verticale de deux rouleaux dans le cœur du fluide, plus deux très fins confinés dans les couches limites inférieure et supérieure. Ce calcul a été effectué en supposant une épaisseur de canal H_* telle que $\delta_{BL} \ll H_* \ll 2\pi/k_*$ et il peut sans difficulté être généralisé en dehors de ces limites [78, 79] : on remarque alors que l'écoulement de streaming devient très faible lorsque $H_* < \delta_{BL}$, et reste confiné à une distance $2\pi/k_*$ des parois lorsque $H_* \gg 2\pi/k_*$.

6. cf. (93-94) dans [76], les signes étant opposés car nous considérons une onde de vitesse acoustique $\propto \sin(x)$ et non $\propto \cos(x)$.

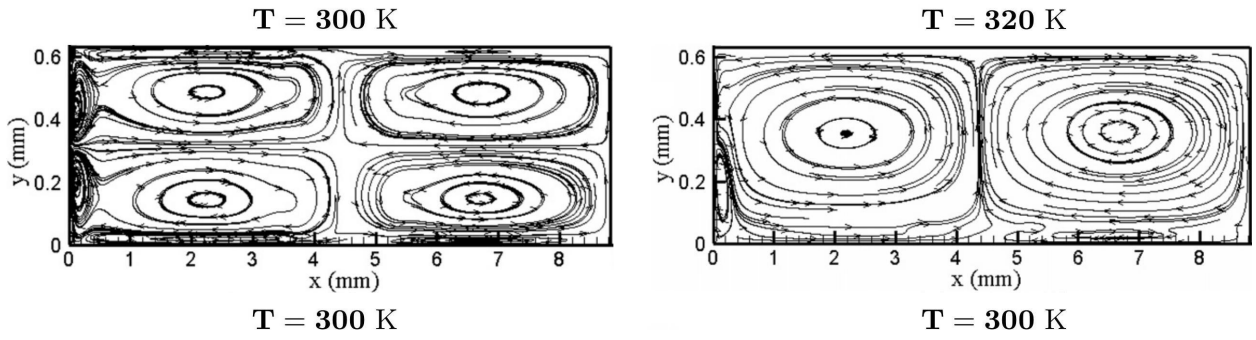

FIGURE 2.4 – Écoulement moyen créé par une onde acoustique stationnaire dans un canal horizontal et calculé numériquement via une simulation des équations de Navier-Stokes 2D compressibles (issue de [83]). Le domaine est rectangulaire (longueur 8.825 mm, épaisseur 0.633 mm), rempli de diazote à pression atmosphérique, et une onde acoustique est engendrée par la vibration horizontale de la paroi de gauche avec une amplitude de 10 μm et une fréquence de 20 kHz (fréquence du premier mode propre lorsque la température est uniforme à 300 K). La figure de gauche représente l'écoulement moyen observé après 120 périodes acoustiques avec des parois de même température et correspond aux prédictions de Rayleigh. La figure de droite lorsque la paroi supérieure est légèrement plus chaude que la paroi inférieure.

2.3 Streaming acoustique dans un fluide inhomogène

Mis à part une expérience effectuée en 1960 [80], ce n'est qu'au début des années 2000 qu'une série d'études expérimentales et numériques [81–87] a montré que le champ de vitesse calculé par Rayleigh (schématisé à la figure 2.3) évolue radicalement lorsque les parois solides sont à des températures différentes. L'illustration la plus parlante, présentée à la figure 2.4, provient des simulations numériques de Lin et Farouk [83] : en imposant une différence de température de 20°C entre les parois supérieure et inférieure, les deux cellules verticales fusionnent pour n'en former qu'une seule, dont la vitesse est nettement plus élevée. Ces résultats peuvent surprendre, étant donné que les propriétés des gaz varient peu avec la température (par exemple, la vitesse du son dans un gaz parfait $c_s \propto \sqrt{T}$).

Nous allons d'abord décrire comment capturer théoriquement ce nouvel écoulement moyen. Les travaux auxquels j'ai contribué seront présentés dans un second temps. L'origine de cette transition, élucidée en 2014 [88], peut être expliquée en quelques lignes après notre étude de la QBO. Dans cet exemple, la force par unité de masse

$$\mathbf{f}_{\text{ondes}} = -\overline{(\mathbf{u}' \cdot \nabla)\mathbf{u}'} = -\nabla\left(\frac{\overline{\mathbf{u}' \cdot \mathbf{u}'}}{2}\right) + \overline{\mathbf{u}' \times (\nabla \times \mathbf{u}')}, \tag{2.102}$$

nécessite $\nabla \times \mathbf{u}' \neq \mathbf{0}$ pour ne pas être trivialement équilibrée par un gradient de pression. Autrement dit, les ondes ne peuvent forcer un écoulement moyen que là où leur vorticité est non nulle. Dans un fluide homogène confiné, la vorticité apparaît sous l'effet de la viscosité et se localise au sein des couches limites oscillantes (c'est le mécanisme du streaming de Rayleigh). En revanche, lorsqu'un champ de densité $\rho_0(\mathbf{r})$ est inhomogène, de la vorticité est également générée par un mécanisme inviscide appelé "création de vorticité barocline" ou "baroclinicité". En prenant le rotationnel de l'équation d'Euler linéarisée, on obtient :

$$\nabla \times \left(\frac{\partial \mathbf{u}'}{\partial t} = -\frac{\nabla P'}{\rho_0}\right) \qquad \Longrightarrow \qquad \frac{\partial(\nabla \times \mathbf{u}')}{\partial t} = \frac{(\nabla \rho_0) \times (\nabla P')}{\rho_0^2}. \tag{2.103}$$

Ainsi, dans un fluide stratifié, les ondes acoustiques sont rotationnelles partout, même en dehors des couches limites. La force (2.102) ne se réduit donc plus trivialement à un gradient. Cet effet barocline n'est pas limité aux couches limites et agit dans l'ensemble du domaine : il devient dominant dès que la différence de température entre les parois dépasse une fraction de degré.

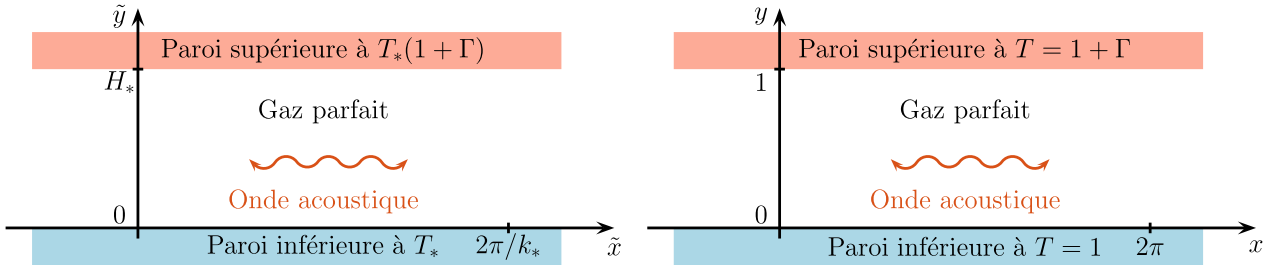

FIGURE 2.5 – Configuration pour l'étude du streaming barocline : avec des grandeurs dimensionnées à gauche, adimensionnées à droite. La gravité est absente de ce problème.

2.3.1 Mise en équation du streaming barocline

Pour calculer l'écoulement de streaming dans ces systèmes stratifiés, il est nécessaire de modifier l'approche de Rayleigh. Cela est ici détaillé pour un gaz parfait dans un canal fin, comme précédemment, mais avec des parois inférieure et supérieure de températures respectives T_* et $T_*(1+\Gamma)$, avec $\Gamma = O(1)$. Cette situation est schématisée à la figure 2.5. Le point crucial consiste à reconnaître que, dans ce cas, l'échelle de vitesse de l'écoulement de streaming n'est plus U_*^2/a_* (comme démontré (2.101)) mais U_*.

Échelle de vitesse de l'écoulement de streaming

Commençons par retrouver, via des arguments simples, l'échelle de vitesse horizontale U_*^2/a_* du streaming de Rayleigh. Celui-ci résulte de la force au sein des couches limites oscillantes d'épaisseur $\delta_{\rm BL} = \sqrt{\mu_*/(\rho_* a_* k_*)}$,

$$\mathbf{f}_{\rm ondes}\cdot\mathbf{e}_x \sim \overline{(\mathbf{u}'\cdot\nabla)\mathbf{u}'}\cdot\mathbf{e}_x \sim k_* U_*^2 + (\delta_{\rm BL} k_* U_*)\times\frac{U_*}{\delta_{\rm BL}} \sim k_* U_*^2. \tag{2.104}$$

Sur l'épaisseur de la couche limite $\delta_{\rm BL}$, cette force est partiellement équilibrée par la viscosité, d'où l'échelle de vitesse horizontale de l'écoulement moyen en sortie de couche limite $U_{\rm st}$

$$k_* U_*^2 \sim \nu_*\frac{U_{\rm st}}{\delta_{\rm BL}^2} \qquad\Longrightarrow\qquad U_{\rm st}\sim k_* U_*^2\frac{\delta_{\rm BL}^2}{\nu_*}\sim\frac{U_*^2}{a_*}. \tag{2.105}$$

Adaptons ce raisonnement au cas barocline. Pour un gaz parfait soumis à un gradient de température $T_*\Gamma/H_*\mathbf{e}_y$,

$$\frac{\nabla\rho_0}{\rho_0^2}\sim-\frac{\Gamma}{H_*\rho_0}\mathbf{e}_y. \tag{2.106}$$

Le gradient de pression acoustique horizontal s'évalue dans le cœur du fluide via l'équation d'Euler linéarisée,

$$\nabla P'\cdot\mathbf{e}_x = -\rho_0\partial_t\mathbf{u}\cdot\mathbf{e}_x\sim\rho_0\omega_* U_*. \tag{2.107}$$

L'équation (2.103) fixe donc l'échelle de la vorticité de l'onde acoustique :

$$|\nabla\times\mathbf{u}'|\sim\frac{1}{\omega_*}\left|\frac{(\nabla\rho_0)\times(\nabla P')}{\rho_0^2}\right|\sim\frac{1}{\omega_*}\times\frac{\Gamma}{H_*\rho_0}\times\rho_0 U_*\omega_*\sim\frac{\Gamma U_*}{H_*}. \tag{2.108}$$

D'après la décomposition (2.102), seule la composante $\overline{\mathbf{u}'\times(\nabla\times\mathbf{u}')}$ de $\mathbf{f}_{\rm ondes}$ est pertinente. Elle vaut ici

$$\mathbf{f}_{\rm ondes}\sim(U_*\mathbf{e}_x + k_* H_*\Gamma U_*\mathbf{e}_y)\times\frac{\Gamma U_*}{H_*}\mathbf{e}_z\sim\frac{\Gamma U_*}{H_*}\times(k_* H_*\Gamma U_*\mathbf{e}_x + U_*\mathbf{e}_y). \tag{2.109}$$

L'échelle de vitesse horizontale de l'écoulement de streaming $U_{\rm st}$ s'obtient en équilibrant cette force par unité de masse avec la viscosité (on rappelle $k_* H_* \ll 1$ ici),

$$\Gamma^2 U_*^2 k_*\sim\frac{\nu_* U_{\rm st}}{H_*^2}\Longrightarrow U_{\rm st}\sim\frac{\Gamma^2 U_*^2 k_* H_*^2}{\nu_*}\sim U_*\times\Gamma^2\times\delta^2\times\epsilon Re_w. \tag{2.110}$$

Étant donné $\Gamma = O(1)$, $\delta = O(\sqrt{\epsilon})$ et $Re_w = O(1/\epsilon^2)$, il vient $U_{\rm st} = O(U_*)$.

Résolution en échelles multiples

Les équations constitutives sont écrites ci-dessous :

$$\rho\left[\partial_t u + (u\partial_x + v\partial_y)\,u\right] = -\frac{1}{\gamma}\partial_x p + \frac{1}{\delta^2 Re_w}\left[\left(\delta^2\partial_{xx} + \partial_{yy}\right)u + \frac{\delta^2}{3}\partial_x(\partial_x u + \partial_y v)\right] + 2F\sin(x)\cos(t), \quad (2.111)$$

$$\rho\left[\partial_t v + (u\partial_x + v\partial_y)\,v\right] = -\frac{1}{\gamma\delta^2}\partial_y p + \frac{1}{\delta^2 Re_w}\left[\left(\delta^2\partial_{xx} + \partial_{yy}\right)v + \frac{1}{3}\partial_y(\partial_x u + \partial_y v)\right], \quad (2.112)$$

$$\partial_t\rho + \partial_x(\rho u) + \partial_y(\rho v) = 0, \quad (2.113)$$

$$\rho\left[\partial_t T + (u\partial_x + v\partial_y)T\right] = -(\gamma-1)p(\partial_x u + \partial_y v) + \frac{\gamma}{Pe_w\delta^2}\left(\delta^2\partial_{xx} + \partial_{yy}\right)T, \quad (2.114)$$

$$p = \rho T, \quad (2.115)$$

$$u(x,0,t) = u(x,1,t) = v(x,0,t) = v(x,1,t) = 0, \quad (2.116)$$

$$T(x,0,t) = 1, \quad T(x,1,t) = 1+\Gamma. \quad (2.117)$$

Deux différences les démarquent du streaming de Rayleigh : la première, fondamentale, vient des conditions aux limites thermiques (2.117), avec ici une condition isotherme qui remplace la limite adiabatique $\partial_y T = 0$. La seconde, plus anecdotique, est l'introduction de la diffusion thermique, qui doit nécessairement être conservée afin de reproduire l'état au repos d'un fluide entre deux parois à températures différentes. Cela se traduit par l'ajout d'un terme dimensionnel $\kappa_*\triangle\tilde{T}$ dans l'équation de conservation de l'énergie interne (2.45), avec κ_* la conductivité thermique. Après introduction des grandeurs sans dimension, ce terme s'écrit en fonction du nombre de Péclet $Pe_w = \rho_* c_{p*} a_*/(k_*\kappa_*)$, analogue au nombre de Reynolds $Re_w = \rho_* a_*/(k_*\mu_*)$. Les nombres sans dimension sont comme précédemment

$$\gamma = O(1), \qquad \delta = \sqrt{\epsilon}h, \qquad Re_w = \frac{Re}{\epsilon^2}, \qquad Pe_w = \frac{Pe}{\epsilon^2}, \qquad F = \epsilon^{3/2}f, \quad (2.118)$$

avec $\{h, Re, f, Pe, \Gamma\}$ des paramètres d'ordre $O(1)$. Les champs sont développés comme

$$(u,v) = \epsilon(u_1, v_1) + O(\epsilon^{3/2}), \quad (2.119)$$

$$P = 1 + \epsilon\pi_1 + \epsilon^{3/2}\pi_{3/2} + \epsilon^2\pi_2 + O(\epsilon^{5/2}), \quad (2.120)$$

$$T = T_B + \Theta_0 + \epsilon\Theta_1 + O(\epsilon^{3/2}), \qquad T_B = 1+\Gamma y \quad (2.121)$$

$$\rho = \rho_0 + \epsilon\rho_1 + O(\epsilon^{3/2}). \quad (2.122)$$

Contrairement au cas précédent, on autorise dès l'ordre dominant des variations de température Θ_0 et de densité ρ_0, car l'écoulement de streaming advecte les inhomogénéités de température du profil stratifié $T_B = 1+\Gamma y$. Le développement est de plus arrêté bien plus tôt : il n'est plus nécessaire de poursuivre à des ordres élevés pour capturer $U_{\rm st} = O(U_*) = O(\epsilon a_*)$. Enfin, la même séparation entre les composantes oscillante et stationnaire est posée, avec par exemple $\Theta_0(x,y,t) = \overline{\Theta}_0(x,y) + \Theta_0'(x,y,t)$.

état stationnaire $O(1)$ **:** On retrouve l'équation d'état $1 = \overline{\rho}_0(T_B + \overline{\Theta}_0)$. La première correction du champ de pression est de plus hydrostatique en conséquence du rapport d'aspect $\delta \ll 1$: (2.112) mène à $\partial_y\overline{\pi}_1 = 0$.

ondes $O(\epsilon)$ **:** les ondes acoustiques satisfont le système suivant :

$$\overline{\rho}_0\partial_t u_1' = -\gamma^{-1}\partial_x\pi_1', \qquad 0 = -\gamma^{-1}\partial_y\pi_1', \quad (2.123)$$

$$\partial_t\rho_1' + \partial_x(\overline{\rho}_0 u_1') + \partial_y(\overline{\rho}_0 v_1') = 0, \quad (2.124)$$

$$\overline{\rho}_0\left[\partial_t\Theta_1' + u_1'\partial_x\overline{\Theta}_0 + v_1'\partial_y(T_B + \overline{\Theta}_0)\right] = -(\gamma-1)(\partial_x u_1' + \partial_y v_1'), \quad (2.125)$$

$$\pi_1' = \overline{\rho}_0\Theta_1' + (T_B + \overline{\Theta}_0)\rho_1'. \quad (2.126)$$

Comme pour le problème de Rayleigh, les conditions aux limites de non-glissement et de température fixe à la paroi mènent à l'apparition de couches limites oscillantes. Elles sont ici passives et induisent un écoulement de streaming sous-dominant. Dans le cœur du fluide, ce problème doit simplement être résolu avec des conditions de non-pénétration ($v_1'(x,0,t) = v_1'(x,1,t) = 0$).

état stationnaire $O(\epsilon)$: l'écoulement de streaming stationnaire est quant à lui solution de :

$$\overline{\rho}_0 \left(\overline{u}_1 \partial_x \overline{u}_1 + \overline{v}_1 \partial_y \overline{u}_1\right) = -\frac{\partial_x \overline{\pi}_2}{\gamma} - \overline{\rho_1' \partial_t u_1'} - \overline{\rho}_0 \left(\overline{u_1' \partial_x u_1' + v_1' \partial_y u_1'}\right) + \frac{\partial_{yy} \overline{u}_1}{h^2 Re}, \tag{2.127}$$

$$0 = \partial_y \overline{\pi}_2, \tag{2.128}$$

$$\partial_x(\overline{\rho}_0 \overline{u}_1) + \partial_y(\overline{\rho}_0 \overline{v}_1) = 0, \tag{2.129}$$

$$\overline{\rho}_0 \left[\overline{u}_1 \partial_x \overline{\Theta}_0 + \overline{v}_1 \partial_y \left(T_B + \overline{\Theta}_0\right)\right] = (1-\gamma)(\partial_x \overline{u}_1 + \partial_y \overline{v}_1) + \frac{\gamma \partial_{yy} \overline{\Theta}_0}{Peh^2}. \tag{2.130}$$

L'analyse peut être poursuivie aux ordres supérieures pour, par exemple, relier la force oscillante à l'amplitude de l'onde acoustique. Cependant, si on la suppose fixée d'une manière ad hoc par un opérateur extérieur, nous avons déjà obtenu un système fermé. En effet :

- Connaissant les champs stationnaires ($\overline{\Theta}_0$, $\overline{\rho}_0$), (2.123-2.126) est un problème aux valeurs propres fournissant les pulsations et structures spatiales des modes acoustiques. Il comporte cinq équations pour cinq variables acoustiques $\{u_1', v_1', \rho_1', \Theta_1', \pi_1'\}$.
- Connaissant les vitesses acoustiques (u_1', v_1'), (2.127 - 2.130) complété par l'équation d'état $1 = \overline{\rho}_0(T_B + \overline{\Theta}_0)$ et les conditions aux limites est un problème aux limites caractérisant l'écoulement de streaming. Ses cinq équations donnent accès aux cinq champs $\{\overline{u}_1, \overline{v}_1, \overline{\rho}_0, \overline{\Theta}_0, \overline{\pi}_2\}$.

2.3.2 Précisions et propriétés du système couplé

Ondes acoustiques en milieu fortement inhomogène

Commençons par présenter une reformulation plus habituelle du jeu d'équations pour les ondes acoustiques. Avec l'équation d'état $1 = \overline{\rho}_0(T_B(y) + \overline{\Theta}_0)$ et (2.126), la combinaison (2.125) + $(T_B + \overline{\Theta}_0)$ (2.124) se réduit à

$$\partial_t \pi_1' + \gamma(\partial_x u_1' + \partial_y v_1') = 0. \tag{2.131}$$

Dans un domaine de rapport d'aspect $O(1)$, (2.123) devient

$$\overline{\rho}_0 \gamma \partial_t u_1' = -\partial_x \pi_1', \qquad \overline{\rho}_0 \gamma \partial_t v_1' = -\partial_y \pi_1'. \tag{2.132}$$

En éliminant les vitesses, on obtient une équation d'onde pour la pression acoustique :

$$\frac{\partial^2 \pi_1'}{\partial t^2} = \nabla \cdot \left(\frac{\nabla \pi_1'}{\overline{\rho}_0}\right). \tag{2.133}$$

En grandeurs dimensionnelles, cela correspond à l'équation habituelle des ondes acoustiques en milieu inhomogène

$$\frac{\partial^2 \tilde{p}'}{\partial \tilde{t}^2} = \tilde{\rho} c_s^2 \, \nabla \cdot \left(\frac{\nabla \tilde{p}'}{\tilde{\rho}}\right), \tag{2.134}$$

avec pour un gaz parfait $\tilde{\rho} c_s^2 = \tilde{P}\gamma$. Pour un canal fin, la dynamique verticale à l'ordre dominant est hydrostatique ($\partial_y \pi_1' = 0$) : nous travaillons effectivement dans une approximation d'épaisseur faible de (2.134).

Première reformulation du terme de forçage

Le terme $-\overline{\rho_1' \partial_t u_1'}$ peut être ré-écrit avec en faisant appel à la relation $\overline{\partial_t(\cdot)} = 0$ ainsi qu'à l'équation (2.124) :

$$-\overline{\rho_1' \partial_t u_1'} = -\overline{\left[\partial_t \left(\rho_1' u_1'\right) - u_1' \partial_t \rho_1'\right]} = 0 + \overline{u_1' \partial_t \rho_1'} = -\overline{u_1' \left[\partial_x(\overline{\rho}_0 u_1') + \partial_y(\overline{\rho}_0 v_1')\right]}. \tag{2.135}$$

La somme des termes de forçage acoustique de (2.127) devient alors :

$$-\overline{\rho_1' \partial_t u_1'} - \overline{\rho}_0 \left(\overline{u_1' \partial_x u_1' + v_1' \partial_y u_1'}\right) = -\overline{u_1' \left[\partial_x(\overline{\rho}_0 u_1') + \partial_y(\overline{\rho}_0 v_1')\right]} - \overline{\rho}_0 \left(\overline{u_1' \partial_x u_1' + v_1' \partial_y u_1'}\right) \tag{2.136}$$

$$= -\left[\overline{u_1' \partial_x(\overline{\rho}_0 u_1')} + \overline{(\overline{\rho}_0 u_1') \partial_x u_1'} + \overline{u_1' \partial_y(\overline{\rho}_0 v_1')} + \overline{(\overline{\rho}_0 v_1') \partial_y u_1'}\right] \tag{2.137}$$

$$= -\left[\partial_x(\overline{\rho}_0 \overline{u_1'^2}) + \partial_y(\overline{\rho}_0 \overline{u_1' v_1'})\right]. \tag{2.138}$$

Cette expression est l'opposé du premier élément de la divergence du tenseur de Reynolds [59]. En exploitant la forme générale de ce tenseur $\overline{\rho u_i' u_j'}$, la densité acoustique de force s'écrit

$$\mathbf{f}_{\text{ac}} = f_i \mathbf{e}_i, \qquad f_i = -\frac{\partial(\overline{\rho u_i' u_j'})}{\partial x_j}. \tag{2.139}$$

La contribution de Karlsen

En 2016, Karlsen et collaborateurs ont obtenu une expression simplifiée de la densité acoustique de force pour le streaming barocline [89]. La démonstration part de (2.139) et exploite une formule d'analyse vectorielle

$$\mathbf{f}_{\text{ac}} = -\text{div}(\overline{\rho u_i' u_j'}) = -\overline{(\mathbf{u}' \cdot \nabla)(\overline{\rho}\mathbf{u}')} + \overline{\rho}\overline{(\nabla \cdot \mathbf{u}')\mathbf{u}'}. \tag{2.140}$$

Commençons par analyser le second terme : (2.132) implique l'existence d'un potentiel scalaire ϕ tel que

$$\overline{\rho}\mathbf{u}' = -\nabla\phi, \qquad \partial_t \phi = -\gamma^{-1}\pi'. \tag{2.141}$$

L'équation d'ondes en milieu inhomogène pour un gaz parfait, (2.133), s'écrit alors

$$\frac{\partial^2 \phi}{\partial t^2} = \nabla \cdot \left(\frac{\nabla \phi}{\overline{\rho}} \right). \tag{2.142}$$

En utilisant ces relations, on montre que pour un mode propre ($\phi(\mathbf{r}, t) = e^{i\omega t}\hat{\phi}(\mathbf{r})$),

$$\overline{\rho}\overline{(\nabla \cdot \mathbf{u}')\mathbf{u}'} = -\overline{(\nabla \cdot \mathbf{u}')\nabla\phi} = \overline{\left[\nabla \cdot \left(\frac{\nabla\phi}{\overline{\rho}}\right)\right]\nabla\phi} = \overline{\left(\frac{\partial^2 \phi}{\partial t^2}\right)\nabla\phi} \propto \overline{\phi\nabla\phi} \propto \nabla\overline{\phi^2}. \tag{2.143}$$

Traitons ensuite le terme $\overline{(\mathbf{u}' \cdot \nabla)(\overline{\rho}\mathbf{u}')}$. En introduisant à nouveau ϕ et en appliquant l'identité de Bernoulli $[2(\mathbf{V} \cdot \nabla)\mathbf{V} = \nabla(\mathbf{V} \cdot \mathbf{V}) + (\nabla \times \mathbf{V}) \times \mathbf{V}]$:

$$(\mathbf{u}' \cdot \nabla)(\bar{\rho}\mathbf{u}') = \frac{1}{\bar{\rho}}\left[(\nabla\phi) \cdot \nabla\right](\nabla\phi) = \frac{1}{2\bar{\rho}}\{\nabla\left[(\nabla\phi)^2\right] + \left[\underbrace{(\nabla \times (\nabla\phi))}_{\mathbf{0}} \times (\nabla\phi)\right]\} = \frac{1}{2\bar{\rho}}\nabla\left[(\bar{\rho}\mathbf{u}') \cdot (\bar{\rho}\mathbf{u}')\right] \tag{2.144}$$

$$= \frac{1}{2\bar{\rho}}\nabla\left[\bar{\rho} \times (\bar{\rho}\mathbf{u}' \cdot \mathbf{u}')\right] = \frac{1}{2\bar{\rho}}\left[\bar{\rho}\nabla\left(\bar{\rho}\mathbf{u}' \cdot \mathbf{u}'\right) + (\bar{\rho}\mathbf{u}' \cdot \mathbf{u}')\nabla\bar{\rho}\right] = \frac{(\mathbf{u}' \cdot \mathbf{u}')}{2}\nabla\bar{\rho} + \nabla\left(\frac{\bar{\rho}\mathbf{u}' \cdot \mathbf{u}'}{2}\right). \tag{2.145}$$

En combinant les équations (2.140), (2.143) et (2.145), on retrouve le résultat de Karlsen :

$$\boxed{\text{À un terme dérivant d'un gradient près, } \mathbf{f}_{\text{ac}} = -\frac{\overline{(\mathbf{u}' \cdot \mathbf{u}')}}{2}\nabla\bar{\rho}} \tag{2.146}$$

Ondes stationnaires et progressives

L'expression de Karlsen, bien que concise, n'isole pas la composante rotationnelle de $\mathbf{f}_{\text{ac}}$: dans certain cas, le terme $\overline{(\mathbf{u}' \cdot \mathbf{u}')}\nabla\bar{\rho}$ dérive d'un potentiel scalaire. Cela s'observe dans la configuration étudiée, à savoir une onde acoustique horizontale dans une cavité verticalement stratifiée. Pour l'état initial $\nabla\bar{\rho} = f(y)\mathbf{e}_y$:

- La vitesse acoustique d'une onde stationnaire s'écrit $\mathbf{u}'(\mathbf{r}, t) = \cos(t + \varphi)\hat{\mathbf{u}}(x, y)$, et

$$-\frac{\overline{(\mathbf{u}' \cdot \mathbf{u}')}}{2}\nabla\bar{\rho} = -\frac{1}{4}\underbrace{(\hat{\mathbf{u}} \cdot \hat{\mathbf{u}})}_{f(x,y)}\underbrace{\nabla\bar{\rho}}_{g(y)\mathbf{e}_y}, \tag{2.147}$$

  se trouve pouvoir induire un écoulement.
- La vitesse acoustique d'une onde progressive en x s'écrit $\mathbf{u}'(\mathbf{r}, t) = \cos(t - x + \varphi)\hat{\mathbf{u}}(y)$, et

$$-\frac{\overline{(\mathbf{u}' \cdot \mathbf{u}')}}{2}\nabla\bar{\rho} = -\frac{1}{4}\underbrace{(\hat{\mathbf{u}} \cdot \hat{\mathbf{u}})}_{f(y)}\underbrace{\nabla\bar{\rho}}_{g(y)\mathbf{e}_y}, \tag{2.148}$$

  se réduit à un gradient, dont la seule conséquence est une modification de la pression moyenne.

On constate que les ondes stationnaires sont plus propices à l'émergence d'un écoulement de streaming barocline que les ondes progressives.

2.4 Présentation synthétique du travail effectué

2.4.1 Transferts thermiques dans un canal de rapport d'aspect $\delta \ll 1$

Notre première étude détaille les solutions du streaming barocline un canal fin ($\delta \ll 1$ avec $\delta = k_* H_*$) ([90], reportée au chapitre 3). Nous montrons d'abord que dans cette limite hydrostatique, l'équation d'onde rappelée ci-dessous,

$$\overline{\rho}_0 \partial_t u_1' = -\gamma^{-1}\partial_x \pi_1', \qquad 0 = -\gamma^{-1}\partial_y \pi_1', \tag{2.149}$$
$$\partial_t \rho_1' + \partial_x(\overline{\rho}_0 u_1') + \partial_y(\overline{\rho}_0 v_1') = 0, \tag{2.150}$$
$$\overline{\rho}_0 \left[\partial_t \Theta_1' + u_1'\partial_x \overline{\Theta}_0 + v_1'\partial_y(T_B + \overline{\Theta}_0)\right] = -(\gamma-1)(\partial_x u_1' + \partial_y v_1'), \tag{2.151}$$
$$\pi_1' = \overline{\rho}_0 \Theta_1' + (T_B + \overline{\Theta}_0)\rho_1', \tag{2.152}$$
$$\overline{\rho}_0 = \frac{1}{\overline{\Theta}_0 + T_B}, \tag{2.153}$$

se réduit à un problème aux valeurs propres à une unique dimension spatiale. Pour cela, nous cherchons des solutions sous forme de mode propre,

$$\pi_1'(x,y,t) = \frac{A}{2}\left[\hat{\pi}(x,y)e^{i\omega t} + \text{c.c.}\right], \quad u_1'(x,y,t) = \frac{A}{2}\left[\hat{u}(x,y)e^{i\omega t} + \text{c.c.}\right], \tag{2.154}$$

et de même pour v_1', ρ_1' et Θ_1'. En éliminant les variables auxiliaires, on montre que la solution s'écrit

$$\hat{u}(x,y) = \frac{i}{\gamma\omega\overline{\rho}_0(x,y)}\frac{\mathrm{d}\hat{\pi}}{\mathrm{d}x}, \qquad \hat{v}(x,y) = -\frac{\omega i y \hat{\pi}(x)}{\gamma} - \frac{i}{\gamma\omega}\frac{\mathrm{d}}{\mathrm{d}x}\left[\frac{\mathrm{d}\hat{\pi}}{\mathrm{d}x}\int_0^y \frac{\mathrm{d}y}{\overline{\rho}_0(x,y)}\right], \tag{2.155}$$

avec $\hat{\Theta}$ et $\hat{\rho}$ qui s'expriment également en fonction de $\hat{\pi}$, qui est solution de

$$\frac{\mathrm{d}}{\mathrm{d}x}\left(\alpha\frac{\mathrm{d}\hat{\pi}}{\mathrm{d}x}\right) + \omega^2\hat{\pi} = 0, \qquad \alpha(x) = \int_0^1 \frac{\mathrm{d}y}{\overline{\rho}_0(x,y)}, \qquad \frac{\mathrm{d}\hat{\pi}}{\mathrm{d}x}(x=0) = \frac{\mathrm{d}\hat{\pi}}{\mathrm{d}x}(x=2\pi) = 0. \tag{2.156}$$

Couplage à sens unique ($\overline{\Theta}_0 = 0$ pour les ondes acoustiques)

Grâce à cette simplification du problème aux valeurs propres, nous pouvons obtenir des solutions explicites dans le cas où $\overline{\Theta}_0 = 0$. Le champ de température sur lequel évolue les ondes se réduit alors au profil diffusif $T_B(y) = 1 + \Gamma y$, le coefficient $\alpha(x) = 1 + \Gamma/2$ devient indépendant de x et les modes propres s'écrivent

$$\hat{\pi}(x) = \cos(nx), \qquad \hat{u} = -\frac{i}{\gamma\sqrt{1+\Gamma/2}}(1+\Gamma y)\sin(nx), \qquad \hat{v} = -\frac{i\Gamma n}{2\gamma\sqrt{1+\Gamma/2}}y(1-y)\cos(nx), \tag{2.157}$$

avec n un entier naturel correspondant à l'indice du mode de pulsation

$$\omega = n\sqrt{1+\frac{\Gamma}{2}}. \tag{2.158}$$

Un instantané du champ de vitesse pour $n = \Gamma = 1$ est reporté Fig. 2.6 haut. Ces résultats montrent que :

- le champ de pression ne dépend que de x et a la même forme qu'en milieu homogène
- dans la limite d'un fluide homogène ($\Gamma \to 0$), on retrouve la solution en onde plane
- la stratification $\Gamma > 0$ augmente la valeur de la pulsation par rapport au cas homogène. Le facteur $\sqrt{1+\Gamma/2}$ s'appréhende mieux en revenant à la pulsation dimensionnelle, en radians par seconde,

$$\omega_* = a_* k_* \omega = \sqrt{\gamma R_* T_*}k_* n\sqrt{1+\Gamma/2} = n k_* \sqrt{\gamma R_* T_*(1+\Gamma/2)}. \tag{2.159}$$

  On retrouve l'expression de la pulsation dans un milieu homogène de température $T_B(y=1/2) = 1+\Gamma/2$.
- le champ de vitesse acoustique est maintenant de vorticité non nulle si $\Gamma \neq 0$:

$$\partial_x \hat{v} - \partial_y \hat{u} = \frac{i\Gamma\sin(nx)}{2\gamma\sqrt{1+\Gamma/2}}\left[n^2 y(1-y) - 1\right]. \tag{2.160}$$

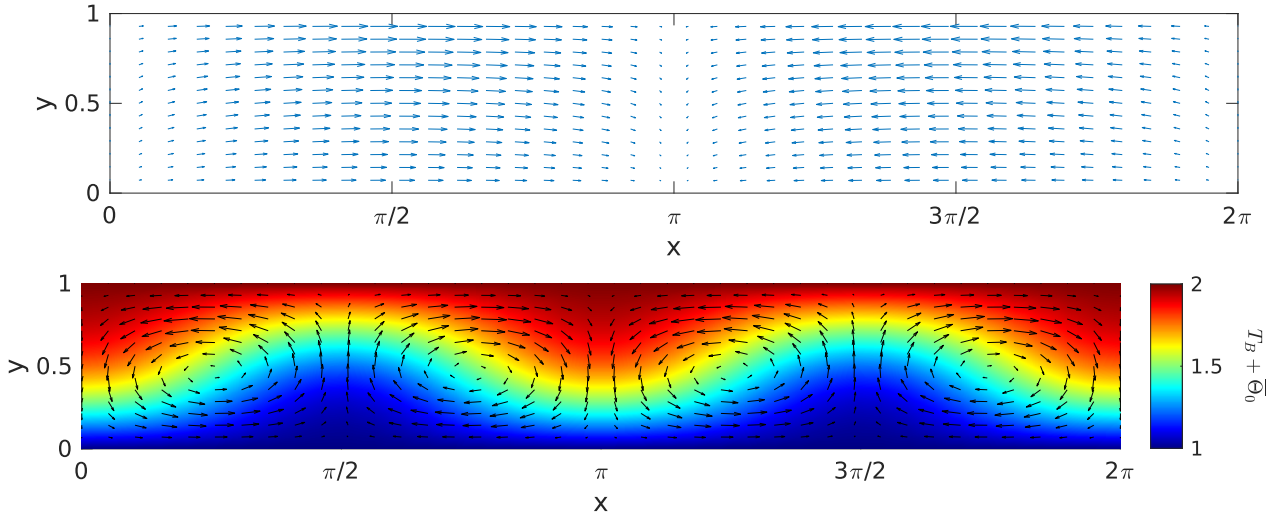

FIGURE 2.6 – (Haut) Représentation du champ de vitesse associé au mode propre fondamental ($n = 1$) dans un canal fin de température $T_B = 1 + y$ ($\Gamma = 1$). (Bas) Écoulement de streaming qui en résulte sous hypothèse de couplage à sens unique. Les paramètres correspondent à ceux de la figure 3 de la référence [90].

Cette onde acoustique, de vorticité finie, force un écoulement de streaming. Connaissant explicitement les champs acoustiques, nous calculons la densité de force acoustique, puis, en supposant les termes non linéaires négligeables, une solution analytique pour l'écoulement de streaming. Nous reportons le lecteur à l'article pour les détails analytiques [7]. Un aperçu de la forme de cet écoulement est reporté à la figure 2.6 bas : il s'agit de cellules de circulation qui advectent les inhomogénéités de température pour réaliser un mélange partiel. Cet écoulement s'accompagne d'une augmentation du flux de chaleur nécessaire à maintenir les températures des parois constantes. Cela est quantifié par le nombre de Nusselt, rapport entre le flux total et le flux diffusif, qui a été calculé pour $\Gamma = 1$ et vaut

$$Nu = 1 + 3.2 \times 10^{-10} (A^2 Re_s Pe_s h^4)^2. \tag{2.161}$$

Ce résultat est assez décourageant : bien que formellement d'ordre $O(1)$, le préfacteur numérique pour le calcul de $Nu - 1$ est ridiculement faible. La dépendance en h^8 ($h = k_* H_* / \sqrt{\epsilon}$) indique cependant une croissance rapide des transferts thermiques avec la hauteur du canal, ce qui motive une étude du régime $k_* H_* = O(1)$.

Couplage réciproque entre ondes acoustiques et écoulement de streaming

Les expressions analytiques présentées précédemment reposent sur deux approximations majeures :

1. les ondes acoustiques sont calculées en négligeant la perturbation de température induite par l'écoulement de streaming ($\overline{\Theta}_0 = 0$). c'est-à-dire à partir du profil de température purement diffusif $T_B(y) = 1 + \Gamma y$
2. l'écoulement de streaming est calculé en négligeant les termes non linéaires

Ces hypothèses sont valables tant que les amplitudes acoustiques restent faibles : le streaming est alors lent, il transporte peu les inhomogénéités de température et la rétroaction sur les ondes peut être ignorée. Pour des amplitudes plus importantes, il faut prendre en compte le couplage réciproque. Nous avons donc développé un algorithme numérique basé sur le code spectral Dedalus [91] qui introduit explicitement une échelle de temps lente (pour le streaming), formellement découplée de l'échelle de temps rapide (pour les ondes acoustiques). Cet algorithme suit les étapes reportées ci-dessous.

1. Initialisation du système dans son état diffusif au repos : $\overline{u}_1 = \overline{v}_1 = \overline{\Theta}_0 = 0$.
2. À partir du champ de température total $T_B + \overline{\Theta}_0$, on résout le problème aux valeurs propres 1D (2.156) afin de déterminer les caractéristiques du premier mode propre acoustique.

7. Par soucis de simplicité, cette sous-section utilise des conventions légèrement différentes pour la normalisation de $\hat{\pi}$.

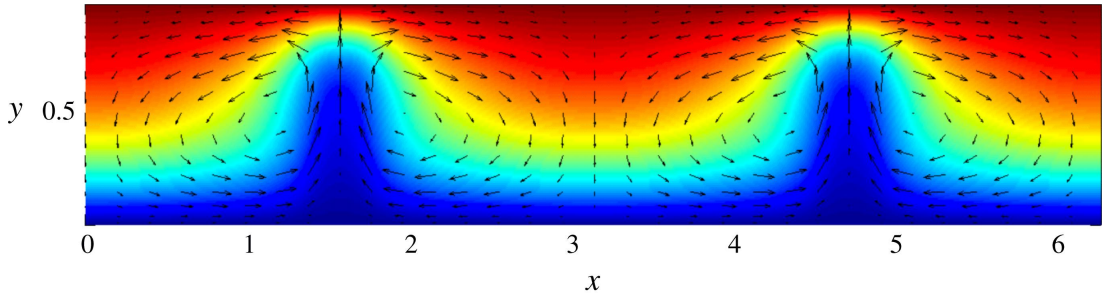

FIGURE 2.7 – Écoulement de streaming stationnaire (flèches) et champ de température associé (couleurs) pour $\Gamma = 1$ et $A = 2.8$. Les paramètres sont indiqués sur la figure 5 de la référence [90].

3. Avec le mode acoustique ainsi calculé, on évalue la densité de force acoustique $-\partial_x(\overline{\rho}_0\overline{u_1'^2}) - \partial_y(\overline{\rho}_0\overline{u_1'v_1'})$. Cette force est un terme source pour l'écoulement de streaming, cf. équation (2.127).
4. Un pas de temps, sur l'échelle de temps lente, est effectué pour l'écoulement de streaming. Cette mise à jour modifie, entre autres, le champ de température total $T_B + \overline{\Theta}_0$.
5. Retour à l'étape 2 : on recalcule le mode acoustique avec le nouveau profil de température.
6. Les étapes 2-5 sont répétées jusqu'à atteindre un état stationnaire.

Cette procédure est coûteuse numériquement car un problème aux valeurs propres est résolu à chaque pas de temps ; néanmoins, ce problème est 1D et l'ensemble reste largement plus abordable qu'une simulation numérique directe des équations de Navier-Stokes compressibles aux échelles de temps acoustiques. La figure 2.7 montre un écoulement de streaming obtenu avec la procédure ci-dessus. On observe une déformation importante du champ de température : la composante $\overline{\Theta}_0(x, y)$ n'est plus négligeable et modifie sensiblement le profil diffusif $T_B(y)$. La prise en compte du couplage réciproque est dans ce cas indispensable pour obtenir un résultat cohérent.

2.4.2 Transferts thermiques dans un canal de rapport d'aspect $\delta = O(1)$

L'étude précédente montre que le streaming barocline modifie peu les transferts thermiques dans un canal fin, mais cette légère modification augmente très rapidement avec le rapport d'aspect. Pour explorer les canaux de rapport d'aspect d'ordre unité, nous avons repris la même stratégie numérique : couplage itératif entre les ondes acoustiques et l'écoulement de streaming, implémenté dans le code spectral Dedalus (référence [92], reportée au chapitre 3, mis en avant dans un *Focus on Fluids* [93]).

Formellement, la seule différence réside dans le dimensionnement du rapport d'aspect $\delta = k_* H_*$, précédemment $\delta = h\sqrt{\epsilon}$ ($h = O(1)$) et maintenant $\delta = O(1)$. Cela affecte les équations. En particulier, les champs de pression $\overline{\pi}_2$ et π_1' ne sont plus uniformes en y : la dynamique devient totalement bidimensionnelle. Le problème aux valeurs propres acoustiques ne peut alors plus être réduit à une seule dimension spatiale, ce qui augmente le coût de calcul numérique.

À titre d'exemple, l'évolution temporelle des nombres de Nusselt (Nu_t et Nu_b, calculés respectivement à partir des transferts thermiques aux parois supérieure et inférieure) ainsi que la pulsation propre ω_0 est présentée à la figure 2.8. Le champ de température en régime stationnaire, où $Nu_t = Nu_b$, est également reporté. Pour toutes les simulations de cet article, les paramètres sont : $\Gamma = 0.3$, $\gamma = 1.4$, $Re = 2500$ et $Pe = 1775$.

Mise en évidence du couplage réciproque et du rôle de la vorticité acoustique

Ces simulations mettent en évidence la rétroaction de l'écoulement de streaming sur les ondes acoustiques. À cet effet, la figure 2.9 (haut) montre l'évolution, entre l'instant initial et le régime stationnaire, du rotationnel de la densité de force acoustique $\mathbf{f}_{\text{ac}}$, $(\nabla \times \mathbf{f}_{\text{ac}}) \cdot \mathbf{e}_z$. Cette grandeur, qui caractérise l'action des ondes acoustiques sur l'écoulement de streaming, n'est pas constante. Sa localisation progressive au niveau des parois peut être expliquée de deux manières équivalentes :

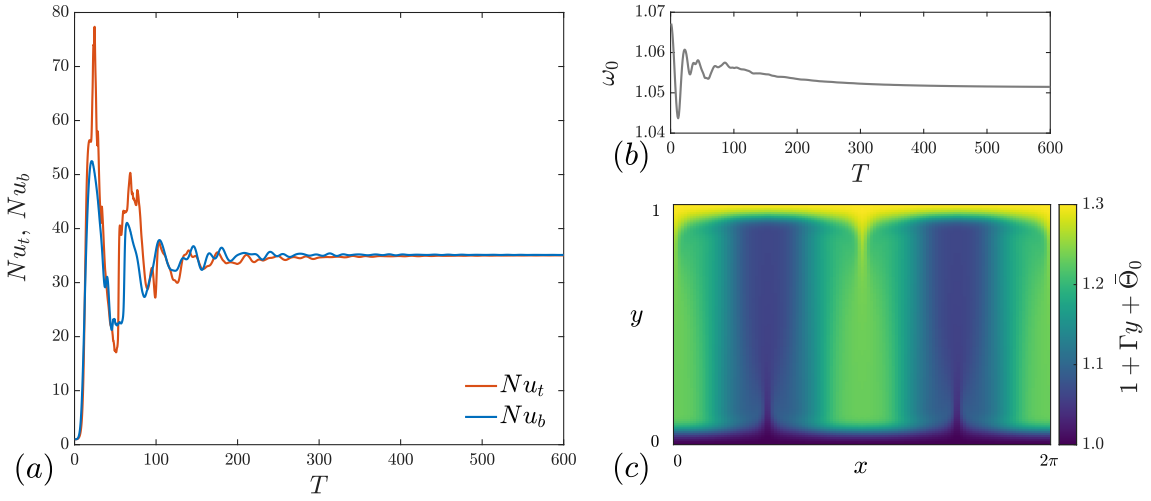

FIGURE 2.8 – Série temporelle pour $A = \delta = 4$ (a) des nombres de Nusselt (Nu_t, Nu_b) et (b) de la pulsation propre adimensionnée ω_0. Le champ de température en régime stationnaire $1 + \Gamma y + \overline{\Theta}_0$ est reporté en (c).

1. La vorticité acoustique, ingrédient crucial pour l'émergence d'un écoulement de streaming, évolue suivant

$$\frac{\partial(\nabla \times \mathbf{u}_1')}{\partial t} = \frac{(\nabla \overline{\rho}_0) \times (\nabla \pi_1')}{\overline{\rho}_0^2}. \tag{2.162}$$

   Pour le premier mode propre horizontal, $\nabla \pi_1'$ reste essentiellement aligné avec $\mathbf{e}_x$. Ainsi, la vorticité se concentre là où le gradient vertical de densité est fort, c'est-à-dire aux parois solides. Cette localisation est visible dans la partie centrale de la figure 2.9.

2. Dans la formulation de Karlsen, la force acoustique s'écrit, à un terme de gradient près, $-\overline{|\mathbf{u}_1'|^2}\nabla\overline{\rho}_0/2$. Le streaming modifie à la fois le champ de densité $\overline{\rho}_0$ et la répartition spatiale de l'énergie acoustique $\overline{|\mathbf{u}_1'|^2}$. Ce second point est illustré dans la partie inférieure de la figure 2.9.

Conséquences sur le transport thermique

La figure 2.8 montre qu'en régime (statistiquement) stationnaire, les nombres de Nusselt peuvent être nettement supérieurs à l'unité. Ces valeurs sont reportées sur la figure 2.10 à gauche, en fonction de l'amplitude de l'onde A (rapport d'aspect $\delta = 4$) et à droite, en fonction du rapport d'aspect δ (amplitudes $A = \{0.01, 4\}$). Afin de souligner le couplage réciproque entre l'écoulement et les ondes acoustiques, deux types de simulations ont été réalisés :

- "two-way coupling" : à chaque pas de temps lent, les propriétés des ondes acoustiques sont recalculées à partir du champ de densité actuel
- "one-way coupling" : la densité acoustique de force $\mathbf{f}_{\text{ac}}$ (et donc les propriétés des ondes acoustiques) est calculée uniquement à l'instant initial puis maintenue constante pendant toutes la simulation ; la rétroaction de l'écoulement sur les ondes est donc ignorée

Pour les faibles rapports d'aspect et en négligeant les non-linéarités de l'écoulement ainsi que sa rétroaction sur les ondes, l'expression (2.161) donne $Nu - 1 \propto A^4 h^8$. Cette loi est bien reproduite dans nos simulations pour $A \leqslant 0.01$. En revanche, pour des amplitudes plus importantes, des écarts significatifs sont observés tant par rapport à cette prédiction théorique qu'entre les simulations "one-way coupling" et "two-way coupling". Dans ce régime, il devient indispensable de résoudre le problème aux valeurs propres à chaque pas de temps afin de prédire correctement le transfert thermique.

Pour les faibles rapports d'aspect, $Nu - 1$ est petit mais croît rapidement avec le rapport d'aspect. Ici, avec $\delta = O(1)$, ces valeurs peuvent dépasser largement l'unité. Ce régime paraît le plus favorable pour obtenir des transferts thermiques importants, $Nu - 1$ diminuant progressivement lorsque δ augmente d'avantage.

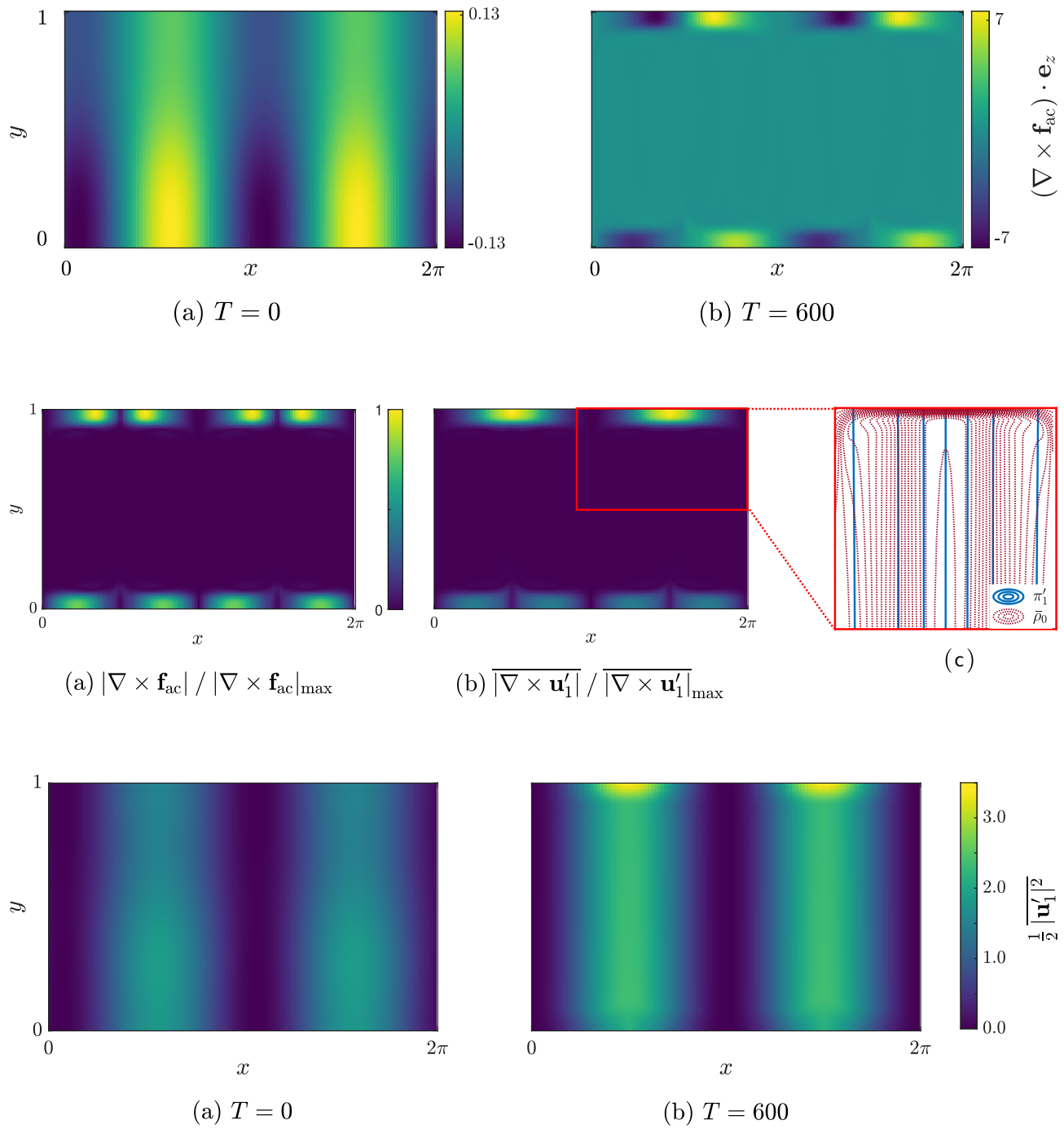

(a) $T = 0$ (b) $T = 600$

(a) $|\nabla \times \mathbf{f}_{\mathrm{ac}}| \,/\, |\nabla \times \mathbf{f}_{\mathrm{ac}}|_{\max}$ (b) $\overline{|\nabla \times \mathbf{u}_1'|} \,/\, \overline{|\nabla \times \mathbf{u}_1'|}_{\max}$ (c)

(a) $T = 0$ (b) $T = 600$

FIGURE 2.9 – Pour $A = \delta = 4$. (Haut) évolution du terme $(\nabla \times \mathbf{f}_{\mathrm{ac}}) \cdot \mathbf{e}_z$ forçant l'écoulement de streaming. (Milieu) comparaison en régime stationnaire (a) du rotationnel de la densité de force acoustique $|\nabla \times \mathbf{f}_{\mathrm{ac}}|/|\nabla \times \mathbf{f}_{\mathrm{ac}}|_{\max}$ et (b) de la vorticité acoustique $\overline{|\nabla \times \mathbf{u}_1'|}/\overline{|\nabla \times \mathbf{u}_1'|}_{\max}$. (c) montre l'origine de la vorticité acoustique en traçant les isobares acoustiques (π_1' constant) et les isopycnes moyennes ($\bar{\rho}_0$ constant).
(Bas) évolution de l'énergie cinétique acoustique moyenne entre l'instant initial (a) et l'état stationnaire (b).

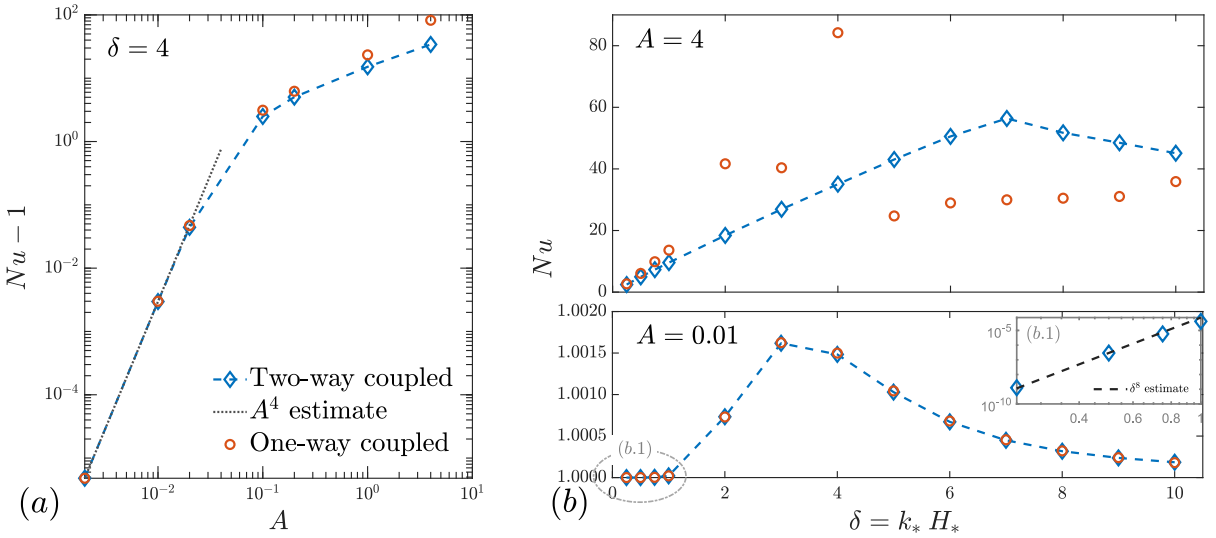

FIGURE 2.10 – (a) Nombre de Nusselt moins un atteint en régime stationnaire en fonction de l'amplitude de l'onde acoustique pour $\delta = 4$, avec la prédiction asymptotique $Nu - 1 \propto A^4$ attendue valide dans la limite $A \ll 1$. (b) Nombre de Nusselt atteint en régime stationnaire en fonction du rapport d'aspect pour $A = 4$ (haut) et $A = 0.01$ (bas). On observe que négliger la rétroaction de l'écoulement sur les ondes n'est raisonnable que dans ce second cas. L'encart montre $Nu - 1$ en fonction de δ avec la prédiction théorique $Nu - 1 \propto \delta^8$.

2.4.3 Transition entre streaming de Rayleigh et streaming barocline

En notant respectivement T_* et $T_*(1+\Gamma)$ les températures dimensionnées des parois inférieure et supérieure, nous avons jusqu'ici étudié séparément le streaming de Rayleigh pour les fluides homogènes ($\Gamma = 0$) et le streaming barocline pour des gaz fortement stratifiés ($\Gamma = O(1)$). Dans ce dernier cas, la stratification était si importante que l'écoulement de streaming barocline dominait largement la composante de Rayleigh issue de la dissipation dans les couches limites oscillantes.

Dans la référence [94], reportée au chapitre 3, nous nous sommes intéressés à la transition entre ces deux régimes, pour des différences de températures plus modestes ($\Gamma = O(\epsilon)$). Une solution explicite a été obtenue à l'aide de la méthode des échelles multiples. Ce travail a été mis en avant dans un *Focus on Fluids* [95].

Principales étapes de la résolution en échelles multiples

Dans un canal de rapport d'aspect $\delta = O(1)$ soumis à une faible stratification $\Gamma = O(\epsilon)$, les échelles des autres nombres sans dimension étant inchangées, la résolution en échelles multiples comporte les étapes suivantes.

Streaming à l'ordre $O(\epsilon)$. Contrairement au cas fortement stratifié, aucun écoulement moyen n'apparaît. Le champ de température uniforme est corrigé par la légère stratification pour mener au profil linéaire diffusif. Cette correction étant indépendante des ondes acoustiques, le streaming ne rétroagit pas sur les ondes.

Ondes à l'ordre $O(\epsilon)$. La légère stratification n'affecte pas les ondes acoustiques. On retrouve la solution d'onde plane dans le cœur du fluide, corrigée près des parois par des couches limites oscillantes.

Streaming à l'ordre $O(\epsilon^{3/2})$. Aucun écoulement moyen n'apparaît.

Ondes à l'ordre $O(\epsilon^{3/2})$. Dans la couche limite d'épaisseur $\delta_{BL} = k_*^{-1} O(\sqrt{\epsilon})$, qui assure le raccordement de la vitesse horizontale u_1' à la condition de non-glissement, une vitesse verticale $v_{3/2}'$ émerge. Cette vitesse ne s'annule pas à la sortie de couche limite et joue le rôle de condition aux limites effective pour le champ acoustique dans le cœur du fluide. On établit le lien entre l'amplitude de la force oscillante qui soutient l'onde, celle de l'onde et les phénomènes dissipatifs.

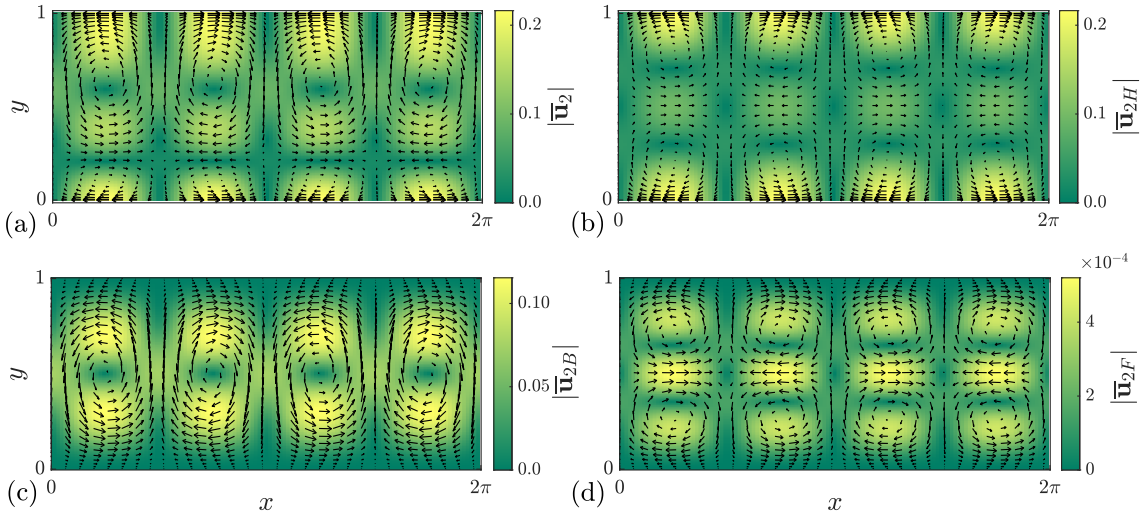

FIGURE 2.11 – Représentation de l'écoulement de streaming pour $A = 1$, $Re = 500$, $Pr = 0.71$, $\delta = 1$, $\gamma = 1.4$ et $\Gamma = 0.278\epsilon$. Le champ de vitesse total (a) s'écrit comme la somme des composantes de Rayleigh (b), barocline (c) et due au forçage (d).

Ondes à l'ordre $O(\epsilon^2)$. Les champs acoustiques calculés précédemment sont irrotationnels dans le cœur du fluide. Ce n'est pas le cas des corrections (u_2', v_2'), sensibles à la petite perturbation de température $\Gamma = O(\epsilon)$. On met notamment en évidence la génération de vorticité barocline, $\Omega_2' \neq 0$.

Streaming à l'ordre $O(\epsilon^2)$. Dans le cœur du fluide, un écoulement de streaming apparaît, résultant de trois mécanismes combinés : (i) la dissipation dans les couches limites, qui crée une vitesse de glissement effective, (ii) la création de vorticité barocline dans le cœur du fluide et (iii) les détails de la force oscillante qui soutient l'onde acoustique. En introduisant la fonction de courant $\overline{\Psi}_2$ de cet écoulement, on obtient l'équation :

$$\frac{\nabla^4 \overline{\Psi}_2}{Re} = B + F, \quad \partial_x \overline{\Psi}_2(x, y = 0) = \partial_x \overline{\Psi}_2(x, y = 1) = 0, \quad \partial_y \overline{\Psi}_2(x, y = 0) = \partial_y \overline{\Psi}_2(x, y = 1) = \delta \overline{u}_{\text{slip}}. \quad (2.163)$$

Par linéarité, on décompose $\overline{\Psi}_2 = \overline{\Psi}_{2H} + \overline{\Psi}_{2B} + \overline{\Psi}_{2F}$, avec :

- $\overline{\Psi}_{2H}$ solution de $\nabla^4 \overline{\Psi}_{2H} = 0$ avec les conditions aux limites incluant la vitesse de glissement. Cette composante correspond au streaming de Rayleigh et possède deux cellules de circulation superposées. Elle est représentée à la figure 2.11 (b).
- $\overline{\Psi}_{2B}$ solution de $\nabla^4 \overline{\Psi}_{2B} = B$ avec des conditions aux limites de non-pénétration et non-glissement. Le terme B, non explicité ici, est le seul qui implique Γ : il s'agit du forçage barocline. La structure spatiale de cette composante, visible à la figure 2.11 (c), comporte une unique cellule verticale.
- $\overline{\Psi}_{2F}$ solution de $\nabla^4 \overline{\Psi}_{2F} = F$ avec des conditions aux limites de non-pénétration et non-glissement. F provient de la moyenne du terme oscillant

$$\overline{\rho' \partial_t \mathbf{u}'} = \overline{\rho' \left(\frac{-\nabla \pi' + \mathbf{f}'}{\overline{\rho}} \right)}. \quad (2.164)$$

Pour un fluide homogène ou légèrement inhomogène, $(\overline{\rho})^{-1} \overline{\rho' \nabla \pi}$ s'écrit immédiatement sous la forme d'un gradient (car $\pi' \propto \rho'$ et $\overline{\rho}$ est alors uniforme). Ce n'est pas le cas, en général, du terme $\rho' \mathbf{f}'$; il engendre donc un écoulement de streaming. Dans le cas de faibles rapports d'aspect ($\delta \ll 1$), cet écoulement est formellement négligeable devant celui de Rayleigh : c'est également le cas en pratique dans le régime $\delta = O(1)$, comme observé à partir de l'échelle de la figure 2.11 (d).

Caractérisation de la solution

La solution obtenue rend compte d'expériences et simulations numériques antérieures (voir l'article complet). Le résultat principal de l'étude est la mesure de la différence de température associée à la transition du régime de Rayleigh au régime barocline. Pour cela, les énergies cinétiques moyennes sont calculées puis comparées :

$$K_H(\delta, Re, Pr, \gamma, A) = \frac{1}{\pi}\int_0^{2\pi}\int_0^1 |\nabla\overline{\Psi}_{2H}|^2 \mathrm{d}x\ \mathrm{d}y \tag{2.165}$$

et

$$K_B(\Gamma, \delta, Re, Pr, \gamma, A) = \frac{1}{\pi}\int_0^{2\pi}\int_0^1 |\nabla\overline{\Psi}_{2B}|^2 \mathrm{d}x\ \mathrm{d}y. \tag{2.166}$$

On définit la transition entre ces deux régimes par $K_H(\delta, Re, Pr, \gamma, A) = K_B(\Gamma = \Gamma_c, \delta, Re, Pr, \gamma, A)$. En résolvant cette équation, on obtient la différence de température dimensionnelle de la transition,

$$\Delta\Theta_{c_*} = \Gamma_c T_* = \frac{k_*\mu_*}{\rho_* a_*}\frac{\left[1 + \frac{\mu_* c_{p*}}{\kappa_*} + \frac{2}{3}\left(\frac{c_{p*}}{c_{v*}} - 1\right)\sqrt{\frac{\mu_* c_{p*}}{\kappa_*}}\right]}{1 + \frac{\mu_* c_{p*}}{\kappa_*}} F_c(k_* H_*)\, T_*. \tag{2.167}$$

Cette quantité dépend du nombre de Reynolds acoustique ($Re_w = \rho_* a_*/(k_*\mu_*)$, qui compare l'inertie à la dissipation dans le cœur du fluide, ici $Re_w \gg 1$), des propriétés du fluide ($c_{p*}/c_{v*} = \gamma$, $\mu_* c_{p*}/\kappa_* = Pr$) ainsi que d'une fonction explicite du rapport d'aspect $\delta = k_* H_*$.

À titre d'exemple, pour de l'air dans les conditions standards [8], un canal d'épaisseur $H_* = 1$ cm et une longueur d'onde $2\pi/k_* = 1.3$ cm (donc une fréquence $f_* = k_* a_*/(2\pi) = 25$ kHz), on évalue $\Delta\Theta_{c_*} = 0.15$ K. Les effets baroclines apparaissent rapidement : une différence d'une fraction de degré entre les parois suffit à rendre inadéquat le calcul de Rayleigh basé uniquement sur la dissipation dans les couches limites.

2.4.4 Mise en évidence expérimentale

Pour compléter ces approches théoriques et numériques, une mise en évidence expérimentale du refroidissement induit par streaming barocline a été réalisée (référence [96] et article au chapitre 3).

Le dispositif est schématisé à la figure 2.12 (gauche). Il s'agit d'une cavité de longueur $L = 10$ cm, hauteur $H = 5$ cm et profondeur $\ell = 3$ cm remplie d'air à pression atmosphérique. Une stratification stable est imposée via un élément chauffant (puissance $\mathcal{P}_{\mathrm{th}}$, en haut) et une circulation d'eau froide (en bas). Une puissance $\mathcal{P}_{\mathrm{ac}}$ est transférée à un haut-parleur qui force une onde acoustique stationnaire horizontale de fréquence f connue. En plus des puissances acoustique $\mathcal{P}_{\mathrm{ac}}$ et thermique $\mathcal{P}_{\mathrm{th}}$, des thermocouples mesurent les températures des parois supérieure et inférieure (T_h et T_c) et un capteur enregistre les oscillations de pression.

Dans un premier temps, on fixe $\{\mathcal{P}_{\mathrm{ac}} = 0.5\ \mathrm{W}, \mathcal{P}_{\mathrm{th}} = 8.8\ \mathrm{W}\}$ et on mesure la différence de température $T_h - T_c$ en fonction de la fréquence f du signal envoyé au haut-parleur. Comme le montre la figure 2.12 (droite), cette différence de température est constante aux basses fréquences ($T_h - T_c = \Delta T_0$) et chute de ΔT lorsqu'on s'approche de la première fréquence de résonance ($f \simeq 1.8$ kHz). La quantité $\Delta T/\Delta T_0$ représente donc la chute de température relative par streaming barocline.

Pour caractériser plus finement la dynamique du système, $\Delta T/\Delta T_0$ est mesuré en fonction de $\mathcal{P}_{\mathrm{ac}}$ et de la stratification au repos $\Gamma = \Delta T_0/T_c$. Ces résultats, publiés avant l'étude des systèmes de rapport d'aspect $\delta = O(1)$, sont comparés aux prédictions théoriques obtenues pour des cavités fines $\delta = O(\sqrt{\epsilon})$, même si dans l'expérience $\delta = 1.55$. En particulier, dans la limite $\delta \ll 1$, en négligeant le couplage réciproque du streaming sur les ondes et en linéarisant l'écoulement de streaming, l'équation (2.161) rappelée ci-dessous donne :

$$\frac{\Delta T}{\Delta T_0} \underset{\Gamma=1}{=} 3.2\times 10^{-10}(A^2 Re_s Pe_s h^4)^2. \tag{2.168}$$

Pour traiter les résultats expérimentaux, cette relation est généralisée à des valeurs arbitraires de Γ :

$$\frac{\Delta T}{\Delta T_0} = F(\Gamma)(A^2 Re_s Pe_s h^4)^2, \qquad F(1) = 3.2\times 10^{-10}. \tag{2.169}$$

8. $T_* = 273$ K, $\mu_* = 1.7\ 10^{-5}$ kg/(m s), $\rho_* = 1.3$ kg/m^3, $c_{p*} = 1.4 c_{v*} = 1.0\ 10^3$ J/(kg K), $\kappa_* = 0.024$ W/(m K), $a_* = 331$ m/s.

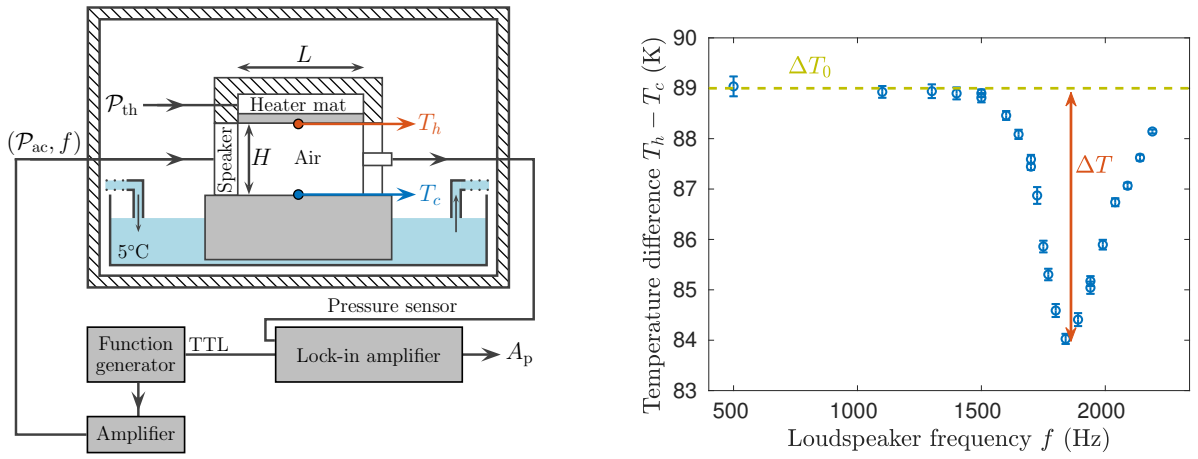

FIGURE 2.12 – (Gauche) Dispositif expérimental. Un haut-parleur, sollicité par un signal de fréquence f et de puissance $\mathcal{P}_{\rm ac}$, génère une onde acoustique d'amplitude locale A_p mesurée à l'extrémité opposée. La cavité acoustique, de hauteur H et de longueur L, est chauffée à son sommet (puissance $\mathcal{P}_{\rm th}$, température T_h) et refroidie à sa base (température T_c). Les zones grisées sont en Dural et celles hachurées sont des isolants thermiques. (Droite) Variation de la différence de température au sein de la cavité $T_h - T_c$ en fonction de la fréquence envoyée au haut-parleur f. Les puissances $\mathcal{P}_{\rm ac} = 0.5$ W et $\mathcal{P}_{\rm th} = 8.8$ W sont maintenues constantes. On définit alors la stratification au repos ΔT_0 et le refroidissement induit par le streaming ΔT.

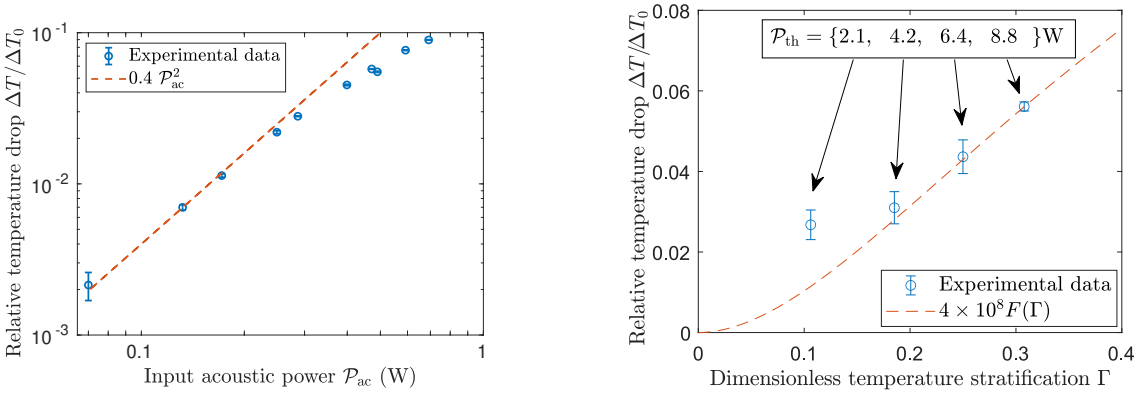

FIGURE 2.13 – (Gauche) Chute de température relative $\Delta T/\Delta T_0$ en fonction de la puissance fournie au haut-parleur $\mathcal{P}_{\rm ac}$, pour un chauffage constant $\mathcal{P}_{\rm th} = 8.8$ W. (Droite) Chute de température relative $\Delta T/\Delta T_0$ en fonction de la stratification adimensionnée $\Gamma = \Delta T_0/T_c$, pour une puissance fournie au haut-parleur $\mathcal{P}_{\rm ac} = 0.5$ W et différents chauffages $\mathcal{P}_{\rm th}$. $\Delta T/\Delta T_0$ serait constant si l'écoulement de streaming était indépendant de Γ. La courbe théorique repose sur les paramètres expérimentaux pour obtenir le pré-facteur 4×10^8, à l'exception de l'amplitude acoustique A qui est prise égale à 0.55 alors que la valeur mesurée est $A \simeq 1.8$.

La figure 2.13 (gauche) montre que l'on retrouve la dépendance en A^4 à basse puissance ($A \propto \sqrt{\mathcal{P}_{\rm ac}}$), c'est-à-dire tant que l'écoulement reste linéaire et sans rétroaction sur les ondes acoustiques. La figure 2.13 (droite) compare les résultats expérimentaux et la prédiction (2.169) : on observe la croissance attendue en fonction de Γ. Cette dépendance indique que l'écoulement de streaming est modifié par la stratification au repos, comme attendu pour le streaming barocline[9]. Toutefois, un accord quantitatif n'est observé que si le préfacteur $(A^2 Re_s Pe_s h^4)^2 \simeq 4 \times 10^8$, ce qui implique de choisir une amplitude acoustique $A \simeq 0.55$ au lieu de la valeur mesurée $A \simeq 1.8$. Cet écart s'explique probablement par deux facteurs : l'équation (2.169) (i) néglige l'effet de la gravité, qui agit ici comme une force de rappel efficace, et (ii) n'est valable que dans la limite $\delta \ll 1$, alors qu'ici $\delta = 1.55$.

9. Ça n'est pas le cas, par exemple, du streaming de Rayleigh ou la convection forcée.

2.5 Perspectives

2.5.1 Amélioration de la méthode numérique

Les simulations numériques pour des rapports d'aspect $\delta = O(1)$ ont montré que les nombres de Nusselt peuvent atteindre plusieurs dizaines. Cette amplification du transfert thermique croît rapidement avec l'amplitude de l'onde A, ce qui motive l'exploration de valeurs de A encore plus importantes. Dans ce régime, le streaming devient instationnaire et développe des structures spatiales fines, notamment des couches limites thermiques adjacentes aux parois, qui exigent une résolution spatiale accrue. Le coût de calcul augmente alors de façon significative. La lenteur du code provient principalement du fait qu'à chaque pas de temps il faut résoudre un problème aux valeurs propres afin d'obtenir la densité de force acoustique $\mathbf{f}_{\text{ac}}$ appropriée.

Pour accélérer le calcul, deux améliorations sont envisagées. Elles reposent sur l'équation des ondes dans un gaz parfait inhomogène (2.133), reproduite ci-dessous en ajoutant une dépendance du champ de densité moyen $\bar{\rho}$ en un temps lent T,

$$\frac{\partial^2 \pi'}{\partial t^2} = \nabla \cdot \left(\frac{\nabla \pi'}{\overline{\rho}(x, y, T)} \right). \tag{2.170}$$

En cherchant des solutions sous forme de modes propres lentement variables, on écrit $\pi' = \text{Re}\left[e^{i\omega(T)t}\hat{\pi}(x, y, T)\right]$, avec $\hat{\pi}$ périodique en x et associé à une vitesse verticale nulle aux parois :

$$\left[\omega^2 + \frac{\partial}{\partial x}\left(\frac{1}{\bar{\rho}}\frac{\partial}{\partial x}\right) + \frac{\partial}{\partial y}\left(\frac{1}{\bar{\rho}}\frac{\partial}{\partial y}\right)\right]\hat{\pi} = 0, \quad \hat{\pi}(0, y, T) = \hat{\pi}(2\pi, y, T), \quad \frac{\partial \hat{\pi}}{\partial y}(x, 0, T) = \frac{\partial \hat{\pi}}{\partial y}(x, 1, T) = 0. \tag{2.171}$$

Pour l'instant, nous résolvons numériquement (2.171) à chaque pas de temps comme un problème aux valeurs propres, c'est-à-dire en cherchant tous les couples $(\omega, \hat{\pi})$ solutions.

Passer d'un problème aux valeurs propres à un problème aux limites

En exploitant la connaissance, à l'instant T, de la pulsation propre $\omega(T)$ et de la structure spatiale $\hat{\pi}(T)$ du mode acoustique, on peut prévoir la valeur de $\omega(T + \mathrm{d}T)$ et ainsi transformer le problème aux valeurs propres en un problème aux limites. Formalisons cela en introduisant l'opérateur linéaire

$$\mathcal{L}(T) = \omega(T)^2 + \frac{\partial}{\partial x}\left(\frac{1}{\overline{\rho}(x, y, T)}\frac{\partial}{\partial x}\right) + \frac{\partial}{\partial y}\left(\frac{1}{\overline{\rho}(x, y, T)}\frac{\partial}{\partial y}\right), \tag{2.172}$$

et, pour deux solutions $\hat{f}$ et $\hat{g}$ de (2.171), un produit scalaire

$$(\hat{f}, \hat{g}) = \int_0^{2\pi}\int_0^1 \hat{f}(x, y, T)\hat{g}(x, y, T)\mathrm{d}x\mathrm{d}y. \tag{2.173}$$

Des intégrations par partie successives exploitant les conditions aux limites de (2.171) et la périodicité en x de $\overline{\rho}$ montrent que $\mathcal{L}$ est auto-adjoint, c'est-à-dire que, pour deux solutions $\hat{f}$ et $\hat{g}$, $(\hat{f}, \mathcal{L}\hat{g}) = (\mathcal{L}\hat{f}, \hat{g})$. En dérivant formellement $\mathcal{L}\hat{\pi} = 0$ par rapport au temps lent T,

$$\mathcal{L}\hat{\pi} = 0 \Longrightarrow \left(\frac{\partial \mathcal{L}}{\partial T}\right)\hat{\pi} + \mathcal{L}\frac{\partial \hat{\pi}}{\partial T} = 0. \tag{2.174}$$

En prenant le produit scalaire de ce résultat avec $\hat{\pi}$, on remarque d'une part

$$(\hat{\pi}, \mathcal{L}\frac{\partial \hat{\pi}}{\partial T}) = (\mathcal{L}\hat{\pi}, \frac{\partial \hat{\pi}}{\partial T}) = (0, \frac{\partial \hat{\pi}}{\partial T}) = 0, \tag{2.175}$$

et d'autre part

$$(\hat{\pi}, \mathcal{L}\frac{\partial \hat{\pi}}{\partial T}) = -(\hat{\pi}, \left(\frac{\partial \mathcal{L}}{\partial T}\right)\hat{\pi}) = -2\omega\frac{\mathrm{d}\omega}{\mathrm{d}T}(\hat{\pi}, \hat{\pi}) + \left(\hat{\pi}, \left[\frac{\partial}{\partial x}\left(\frac{\partial_T \overline{\rho}}{\overline{\rho}^2}\frac{\partial}{\partial x}\right) + \frac{\partial}{\partial y}\left(\frac{\partial_T \overline{\rho}}{\overline{\rho}^2}\frac{\partial}{\partial y}\right)\right]\hat{\pi}\right). \tag{2.176}$$

Combiner ces équations mène avec les conditions aux limites sur $\hat{\pi}$ à

$$\frac{\mathrm{d}\omega}{\mathrm{d}T} = \frac{1}{2\omega(T)(\hat{\pi},\hat{\pi})}\left(\hat{\pi}, \left[\frac{\partial}{\partial x}\left(\frac{\partial_T\overline{\rho}}{\overline{\rho}^2}\frac{\partial}{\partial x}\right) + \frac{\partial}{\partial y}\left(\frac{\partial_T\overline{\rho}}{\overline{\rho}^2}\frac{\partial}{\partial y}\right)\right]\hat{\pi}\right) \tag{2.177}$$

$$= \frac{1}{2\omega(T)(\hat{\pi},\hat{\pi})}\int_0^{2\pi}\int_0^1 \hat{\pi}\left[\frac{\partial}{\partial x}\left(\frac{\partial_T\overline{\rho}}{\overline{\rho}^2}\frac{\partial\hat{\pi}}{\partial x}\right) + \frac{\partial}{\partial y}\left(\frac{\partial_T\overline{\rho}}{\overline{\rho}^2}\frac{\partial\hat{\pi}}{\partial y}\right)\right]\mathrm{d}x\mathrm{d}y \tag{2.178}$$

$$= -\frac{1}{2\omega(T)(\hat{\pi},\hat{\pi})}\int_0^{2\pi}\int_0^1 \frac{\partial_T\overline{\rho}}{\overline{\rho}^2}\left[\left(\frac{\partial\hat{\pi}}{\partial x}\right)^2 + \left(\frac{\partial\hat{\pi}}{\partial y}\right)^2\right]\mathrm{d}x\mathrm{d}y. \tag{2.179}$$

Par ailleurs, la conservation de la masse permet de calculer $\partial_T\overline{\rho}$ à partir des champs à l'instant T. Ainsi, connaissant $\{\overline{\rho},\overline{u},\overline{v},\omega,\hat{\pi}\}$ au temps T, on peut prédire $\omega(T+\mathrm{d}T)$. Cela permet de transformer (2.171) d'un problème aux valeurs propres ($\{\omega,\hat{\pi}\}$ inconnus) à un problème aux limites ($\hat{\pi}$ inconnu). De plus, étant donné que la masse volumique évolue peu sur un pas de temps, le champ $\hat{\pi}(x,y,T)$ constitue une très bonne approximation de la solution recherchée $\hat{\pi}(x,y,T+\mathrm{d}T)$: une résolution itérative du problème aux limites avec cette estimation initiale devrait être significativement plus rapide.

Simplification du champ de pression et méthode de Rayleigh-Ritz

Si les temps de calculs restent trop lents, il faut chercher des solutions approchées. Le champs de pression affiché dans la figure 2.9 fournit une piste : π' est pratiquement indépendant de la coordonnées verticale, alors même que le champ de densité est fortement bidimensionnel (Fig. 2.8 (c)). Cela suggère que le champ de pression est bien approximé par la solution analytique obtenue dans la limite de faible rapport d'aspect (2.149-2.153),

$$\hat{u}(x,y) = \frac{i}{\gamma\omega\overline{\rho}_0(x,y)}\frac{\mathrm{d}\hat{\pi}}{\mathrm{d}x}, \qquad \hat{v}(x,y) = -\frac{\omega i y\hat{\pi}(x)}{\gamma} - \frac{i}{\gamma\omega}\frac{\mathrm{d}}{\mathrm{d}x}\left[\frac{\mathrm{d}\hat{\pi}}{\mathrm{d}x}\int_0^y \frac{\mathrm{d}y}{\overline{\rho}_0(x,y)}\right], \tag{2.180}$$

avec $\hat{\pi}$ indépendant de y et tel que

$$\frac{\mathrm{d}}{\mathrm{d}x}\left(\alpha\frac{\mathrm{d}\hat{\pi}}{\mathrm{d}x}\right) + \omega^2\hat{\pi} = 0, \qquad \alpha(x) = \int_0^1 \frac{\mathrm{d}y}{\overline{\rho}_0(x,y)}, \qquad \frac{\mathrm{d}\hat{\pi}}{\mathrm{d}x}(x=0) = \frac{\mathrm{d}\hat{\pi}}{\mathrm{d}x}(x=2\pi) = 0. \tag{2.181}$$

Dans cette limite hydrostatique, une vitesse verticale persiste et permet d'approximer finement la vorticité. Le problème aux valeurs propres est considérablement simplifié : outre la perte d'une dimension spatiale, (2.181) est sous la forme dite de Sturm Liouville. Cela assure qu'en définissant pour deux fonctions $\{\hat{f},\hat{g}\}$ périodiques

$$(\hat{f},\hat{g}) = \int_0^{2\pi}\hat{f}(x)\hat{g}(x)\mathrm{d}x, \tag{2.182}$$

1. les pulsations propres $\{\omega_i\}$ forment une suite strictement croissante
2. les vecteurs propres associés $\{\hat{\pi}_i\}$ sont orthogonaux et peuvent être utilisés comme base

Ces deux résultats permettent de chercher le mode propre fondamental grâce à la méthode de Rayleigh-Ritz. Le point de départ consiste à décomposer un champ quelconque sur la base orthonormée des modes propres :

$$\hat{\pi}(x) = \sum_i c_i\hat{\pi}_i, \qquad -\frac{\mathrm{d}}{\mathrm{d}x}\left(\alpha\frac{\mathrm{d}\hat{\pi}_i}{\mathrm{d}x}\right) = \omega_i^2\hat{\pi}_i, \qquad (\hat{\pi}_i,\hat{\pi}_j) = \delta_{i,j}, \qquad 0 < \omega_1 < \omega_2 < \dots \tag{2.183}$$

On introduit ensuite le "quotient de Rayleigh"

$$R = \frac{\left(\hat{\pi}, \left[-\frac{\mathrm{d}}{\mathrm{d}x}\left(\alpha\frac{\mathrm{d}}{\mathrm{d}x}\right)\right]\hat{\pi}\right)}{(\hat{\pi},\hat{\pi})} = \frac{\left(\sum_i c_i\hat{\pi}_i, \sum_j c_j\omega_j^2\hat{\pi}_j\right)}{\left(\sum_i c_i\hat{\pi}_i, \sum_j c_j\hat{\pi}_j\right)} = \frac{\sum_{i,j} c_ic_j\omega_j^2\left(\hat{\pi}_i,\hat{\pi}_j\right)}{\sum_{i,j} c_ic_j\left(\hat{\pi}_i,\hat{\pi}_j\right)} = \frac{\sum_i \omega_i^2c_i^2}{\sum_i c_i^2} \tag{2.184}$$

$$= \omega_1^2\left(\frac{\sum_i(\omega_i/\omega_1)^2c_i^2}{\sum_i c_i^2}\right). \tag{2.185}$$

Les pulsations propres étant croissantes, la fraction entre parenthèses est minimale si $\{c_1 \neq 0, c_{i>1} = 0\}$, autrement dit si le champ considéré $\hat{\pi}$ est proportionnel au mode propre fondamental $\hat{\pi}_1$. Minimiser R donne donc accès à la pulsation fondamentale ($R_{\min} = \omega_1^2$) ainsi qu'à la structure spatiale du mode fondamental $\hat{\pi}_1$. En supposant connue une approximation numérique de la structure du mode propre fondamental au temps t,

$$\hat{\pi}(x,t) = \sum_{n=1}^{N} c_n(t)\cos(nx), \tag{2.186}$$

le mode fondamental au temps $t + \mathrm{d}t$ s'obtient simplement en minimisant la fonctionnelle

$$R(\{c_n\}_{n=1..N}) = \frac{\left(\hat{\pi}, \left[-\frac{\mathrm{d}}{\mathrm{d}x}\left(\alpha(x,t+\mathrm{d}t)\frac{\mathrm{d}}{\mathrm{d}x}\right)\right]\hat{\pi}\right)}{(\hat{\pi},\hat{\pi})} \tag{2.187}$$

vis-à-vis de ses N variables, avec comme estimations initiales les valeurs de $\{c_n\}_{n=1..N}$ au temps t. Une fois le minimum atteint, les coefficients fournissent la structure du mode propre et la valeur de R sa pulsation propre. La minimisation devrait être rapide car l'estimation initiale est très proche du point cible. De plus, il est possible de limiter ce calcul aux premières harmoniques du champ de pression, en posant par exemple $N = 10$.

L'implémentation de ces méthodes nécessite des comparaisons fines avec le code déjà existant qui résout exactement le problème aux valeurs propres 2D, car la gamme de validité de cette approximation hydrostatique pour le champ de pression n'est pas connue. Cela permettra également de quantifier le gain en temps de calcul.

2.5.2 Instabilité hydrodynamique dans le cas d'une onde acoustique verticale

Un changement de comportement est attendu lorsque l'onde perturbant le gaz stratifié est *verticale* et non horizontale : l'écoulement de streaming apparaît via une instabilité dont l'étude, en prenant en compte le couplage réciproque de l'écoulement sur l'onde, serait originale théoriquement et proche d'applications concrètes.

Jusqu'à présent, nous avons considéré le mode acoustique stationnaire prolongeant en milieu stratifié l'onde plane $\hat{\pi}(x,y) = \cos(x)$. En pratique, nous avons constaté numériquement (cf. Fig. 2.9 milieu droit) et théoriquement (dans la limite des rapports d'aspect $\delta \ll 1$, cf. (2.149)) que le champ de pression acoustique reste largement indépendant de la coordonnée verticale y. Cela mène à une production de vorticité acoustique

$$\frac{\partial(\nabla\times\mathbf{u}')}{\partial t} = \frac{(\nabla\overline{\rho})\times(\nabla\pi')}{\overline{\rho}^2} \tag{2.188}$$

optimale dans l'état initial, les vecteurs $(\nabla\overline{\rho}) \propto \mathbf{e}_y$ et $(\nabla\pi') \propto \mathbf{e}_x$ étant orthogonaux. Expérimentalement, solliciter une telle onde se réalise grâce à un haut-parleur en $x = 0$, comme par exemple représenté Figure 2.12.

Supposons maintenant que l'onde acoustique est engendrée par une oscillation verticale de la paroi inférieure. Les modes propres sollicités sont alors des généralisations à des gaz stratifiés des solutions $\hat{\pi}(x,y) = \cos(n\pi y)$. Pour le profil diffusif de température $\bar{\rho} = 1/(1+\Gamma y)$, $\hat{\pi}(x,y)$ ne dépend effectivement que de y, annulant ainsi $(\nabla\overline{\rho})\times(\nabla\pi')$: le champ acoustique, irrotationnel, ne force plus d'écoulement moyen. Un gaz au repos fortement stratifié est donc à l'équilibre en présence d'une onde acoustique verticale, et ce quelle que soit son amplitude.

Cependant, il est très probable que cet équilibre deviennent linéairement instable pour des amplitudes acoustiques suffisantes (une petite perturbation du champ de densité créant localement de la vorticité acoustique, donc un écoulement de streaming barocline, pouvant l'amplifier). Cela permettrait de refroidir un gaz stratifié lorsque la différence de température entre les parois le contenant devient trop élevée.

Ce problème a récemment été considéré par Koulakis et Putterman [97]. D'après leurs calculs, une telle instabilité existe en effet, qu'ils caractérisent (i) en négligeant la rétroaction du streaming sur les ondes acoustiques et (ii) dans l'approximation de Boussinesq pour l'écoulement de streaming. Ces deux approximations, valides pour un gaz faiblement stratifié, sont mises en défaut lorsque $\Gamma = O(1)$. Plus gênant, l'approximation de Boussinesq n'est pas correctement réalisée, et des termes d'ordre dominant sont omis (la diffusion thermique est négligée mais pas la viscosité, pourtant du même ordre de grandeur dans un gaz).

Il serait intéressant de revenir sur l'étude théorique de cette configuration pour des gaz fortement stratifiés, quitte à extrapoler ensuite les résultats pour $\Gamma \to 0$. La linéarisation des équations gouvernant la dynamique de l'écoulement de streaming ne devrait pas poser de difficulté, mis à part que la petite perturbation de densité dont on souhaite caractériser le taux de croissance modifie également les champs acoustiques (solutions d'un problème aux valeurs propres), et donc $\mathbf{f}_{\mathrm{ac}}$. Cela rend l'étude de stabilité linéaire non standard. Nous pourrions également quantifier, a posteriori, l'influence de cette rétroaction sur les propriétés de la bifurcation.

2.5.3 Effet de la gravité et convection thermo-vibrationnelle

La configuration précédente est surprenamment proche de la convection naturelle :

- Un gaz stratifié en présence de gravité (mais sans onde acoustique) se déstabilise lorsque la différence de température dépasse une valeur seuil : c'est l'instabilité de Rayleigh-Bénard.
- Un gaz stratifié soumis à des ondes acoustiques verticales (mais sans gravité) se déstabilise lorsque la différence de température dépasse une valeur seuil : c'est l'instabilité discutée §2.5.2.

Ce parallèle peut être approfondi pour répondre aux questions suivantes :

1. Quelle différence de température maximale peut supporter un gaz stratifié au repos simultanément soumis à un champ de pesanteur et à des ondes acoustiques verticales ?
2. Comment la gravité modifie-t-elle les résultats relatifs au streaming causé par une onde horizontale discutés §2.4.2 ? Cela permet-il de rendre compte plus fidèlement des résultats expérimentaux §2.4.4 ?
3. En convection naturelle turbulente, quel est l'effet des ondes acoustiques sur le transfert thermique moyen ?

Ces questions nécessitent d'intégrer la pesanteur dans les équations de Navier-Stokes compressibles décrivant la dynamique du gaz fortement stratifié étudié §2.4.2, qui deviendraient alors

$$\bar{\rho}_0\left(\partial_T\bar{u}_1+\bar{u}_1\partial_x\bar{u}_1+\bar{v}_1\partial_y\bar{u}_1\right)=-\frac{\partial_x\bar{\pi}_2}{\gamma}-\left[\partial_x\left(\bar{\rho}_0\overline{u_1'^2}\right)+\partial_y\left(\bar{\rho}_0\overline{u_1'v_1'}\right)\right]+\frac{1}{Re}\left[\dots\right],$$

$$\bar{\rho}_0\left(\partial_T\bar{v}_1+\bar{u}_1\partial_x\bar{v}_1+\bar{v}_1\partial_y\bar{v}_1\right)=-\frac{\partial_y\bar{\pi}_2}{\gamma\delta^2}-\left[\partial_x\left(\bar{\rho}_0\overline{u_1'v_1'}\right)+\partial_y\left(\bar{\rho}_0\overline{v_1'^2}\right)\right]-\frac{Ri\bar{\rho}_0}{\epsilon\delta}+\frac{1}{Re}\left[\dots\right],$$

$$\partial_T\bar{\rho}_0+\partial_x\left(\bar{\rho}_0\bar{u}_1\right)+\partial_y\left(\bar{\rho}_0\bar{v}_1\right)=0, \tag{2.189}$$

$$\bar{\rho}_0\left[\partial_T\bar{\Theta}_0+\bar{u}_1\partial_x\bar{\Theta}_0+\bar{v}_1\left(\Gamma+\partial_y\bar{\Theta}_0\right)\right]=\left(1-\gamma\right)\left(\partial_x\bar{u}_1+\partial_y\bar{v}_1\right)+\frac{\gamma}{Pe}\left(\partial_{xx}\bar{\Theta}_0+\frac{1}{\delta^2}\partial_{yy}\bar{\Theta}_0\right), \tag{2.190}$$

$$\bar{\rho}_0=\left(1+\Gamma y+\bar{\Theta}_0\right)^{-1}, \tag{2.191}$$

en définissant le nombre de Richardson $Ri=g_*/(a_*^2k_*)$. Avec $g_*=10\ \mathrm{m\cdot s^{-2}}$, $a_*=333\ \mathrm{m\cdot s^{-1}}$ et $k_*=100\ \mathrm{m^{-1}}$ (longueur d'onde acoustique de 6 cm), il vient $Ri=10^{-6}$, qu'il est raisonnable de dimensionner comme ϵ : la gravité entre alors en compétition avec la densité de force acoustique et affecte la dynamique de l'écoulement à l'ordre dominant. Remarquons que ces équations, issues de l'analyse en échelles multiples, ne couplent pas les variations de pression et celles de densité, filtrant du même coup les ondes acoustiques. C'était une condition indispensable pour les traiter séparément et pouvoir évoluer le système numériquement avec un pas de temps très grand devant la période acoustique.

Ce système permet de répondre aux questions introduites précédemment. Il contraste fortement avec le jeu d'équations utilisé en convection thermo-vibrationnelle, à savoir un modèle de Boussinesq avec une densité de force additionnelle $\mathbf{f}_{TVC}=A\cos(\Omega_{TVC}t)\mathbf{e}_y$: l'oscillation repousse l'instabilité de Rayleigh-Bénard par stabilisation paramétrique [98, 99] et réduit les transferts thermiques en régime de convection naturelle turbulente [100]. Sous approximation de Boussinesq, l'écoulement incompressible ne peut pas soutenir d'onde acoustique, comme le montre l'échelle de la pulsation des oscillations verticales dans ces études,

$$\Omega_{TVC}=O\left(\frac{\mu_*}{\rho_*H_*^2}\right). \tag{2.192}$$

Par comparaison, les oscillations verticales que je souhaite étudier sont très rapides, générant des ondes acoustiques nécessitant la prise en compte de la compressibilité du milieu à l'échelle de temps acoustique,

$$\omega_*=O\left(\frac{a_*}{H_*}\right)\Longrightarrow O\left(\frac{\Omega_{TVC}}{\omega_*}\right)=\frac{1}{\delta Re_w}\ll 1, \tag{2.193}$$

en rappelant $\delta=k_*H_*=O(1)$ ici et $Re_w=\rho_*a_*/(k_*\mu_*)\gg 1$ si l'onde acoustique est atténuée sur une durée longue devant sa période (jusqu'à présent, $Re_w=Re/\epsilon^2$ avec $Re=O(1)$). La phénoménologie peut être radicalement différente, laissant par exemple espérer une augmentation des transferts thermiques turbulents [10].

Cette étude nécessite cependant d'avoir accompli les étapes précédentes, à savoir disposer d'un code rapide pour simuler des écoulements de streaming couplés avec des ondes acoustiques, et avoir caractérisé théoriquement l'instabilité d'une couche de gaz stratifié soumise à une onde verticale.

10. Car on s'attend déjà à ce qu'une onde acoustique verticale *diminue* le seuil d'apparition d'une instabilité de la couche de gaz.

2.5.4 Réalisation d'une nouvelle expérience de streaming barocline

Afin de dépasser les limitations du dispositif présenté à section 2.4.4, je propose une nouvelle expérience de streaming barocline, schématisée à la figure 2.14, qui repose sur quatre améliorations majeures :

Plus de chauffage latéral. Un haut-parleur chauffe l'air environnant en plus d'émettre des ondes acoustiques en raison de son rendement inférieur à l'unité. Dans l'expérience précédente, nous avons dû travailler à puissance constante fournie au haut-parleur pour séparer cet effet du streaming barocline. Ici, le haut-parleur sera remplacé par un plan oscillant entraîné par une tige reliée à un vibreur. L'échauffement sera ainsi déplacé au niveau du vibreur, éloigné de la cavité acoustique.

Des mesures variées. Au lieu de ne mesurer que les températures aux parois, des capteurs de flux thermique enregistrerons également les transferts thermiques. En comparant les flux supérieur et inférieur, les pertes thermiques latérales pourront être évaluées.

Nouveaux régimes de fonctionnement. Enfin, nous élargirons le champ d'étude au-delà de la configuration stablement stratifiée. Un chauffage par le bas sera possible, pour analyser le couplage entre convection naturelle et onde acoustique. Ce dispositif, réalisé avec l'aide de la plateforme expérimentale de Saint-Cyr habituée des expériences en vol parabolique, pourrait également être rendu compatible avec les exigences techniques associées, afin de tester la dynamique en microgravité.

Cadre d'étude théorique clarifié. Au niveau de l'analyse des résultats, de nombreux progrès ont également été réalisés depuis 2021. En particulier, ce système de rapport d'aspect $\delta = 1.05$ peut maintenant être comparé à des prédictions théoriques et numériques dans le régime $\delta = O(1)$ et pas seulement $\delta = O(\sqrt{\epsilon})$ (!)

2.5.5 Streaming barocline et ondes de surface

Le mécanisme du streaming barocline nécessite seulement des ondes dans un milieu de densité inhomogène. Nous avons jusqu'ici étudié les ondes acoustiques ; je souhaite étendre le même raisonnement aux ondes qui se développent la surface libre d'un fluide stratifié. Cela n'a, à ma connaissance, jamais été étudié, bien que cette situation se rencontre couramment dans les mélangeurs industriels où l'on agite un liquide de densité variable.

Ondes de surface dans un fluide stratifié

Commençons par aborder ce sujet dans le cas cartésien bidimensionnel, schématisé à la figure 2.15, avec :

- $\rho(z)$ et ρ_g les masses volumiques des phases liquide et gaz
- $\mathbf{g} = -g\mathbf{e}_z$ l'accélération de la pesanteur
- H la hauteur de fluide au repos
- $\eta(x,t)$ la perturbation de surface étudiée, de vecteur d'onde $\mathbf{k} = k\mathbf{e}_x$ et pulsation ω

Le profil de masse volumique $\rho(z)$ est pris linéaire, décroissant, faiblement variable $[\rho(0) - \rho(H) \ll \rho(0)]$ et grand devant ρ_g. De plus, la tension de surface est négligée [11], tout comme les effets diffusifs, et on se limite à des perturbations linéaires de l'état au repos. La dynamique s'inscrit alors dans l'approximation de Boussinesq [12],

$$\partial_t \mathbf{u} = -\nabla P + b\mathbf{e}_z, \tag{2.194}$$

$$\nabla \cdot \mathbf{u} = 0, \tag{2.195}$$

$$\partial_t b = -N^2 u_z, \qquad N^2 = \frac{g}{\rho}\frac{\mathrm{d}\rho}{\mathrm{d}z} = \frac{g}{H}\left(\frac{\rho(0)-\rho(H)}{\rho(0)}\right) \tag{2.196}$$

$$\partial_t \eta = u_z(x, z = H, t), \qquad P(x, z = H, t) = g\eta(x,t) \tag{2.197}$$

$$u_z(x, z = 0, t) = 0. \tag{2.198}$$

11. On considère une longueur d'onde grande devant l'échelle gravito-capillaire.

12. D'après §1.1.2, cela implique de dimensionner la vitesse oscillante $\omega\eta = O\left(\sqrt{gH(\rho(0)-\rho(H))/\rho(0)}\right)$.

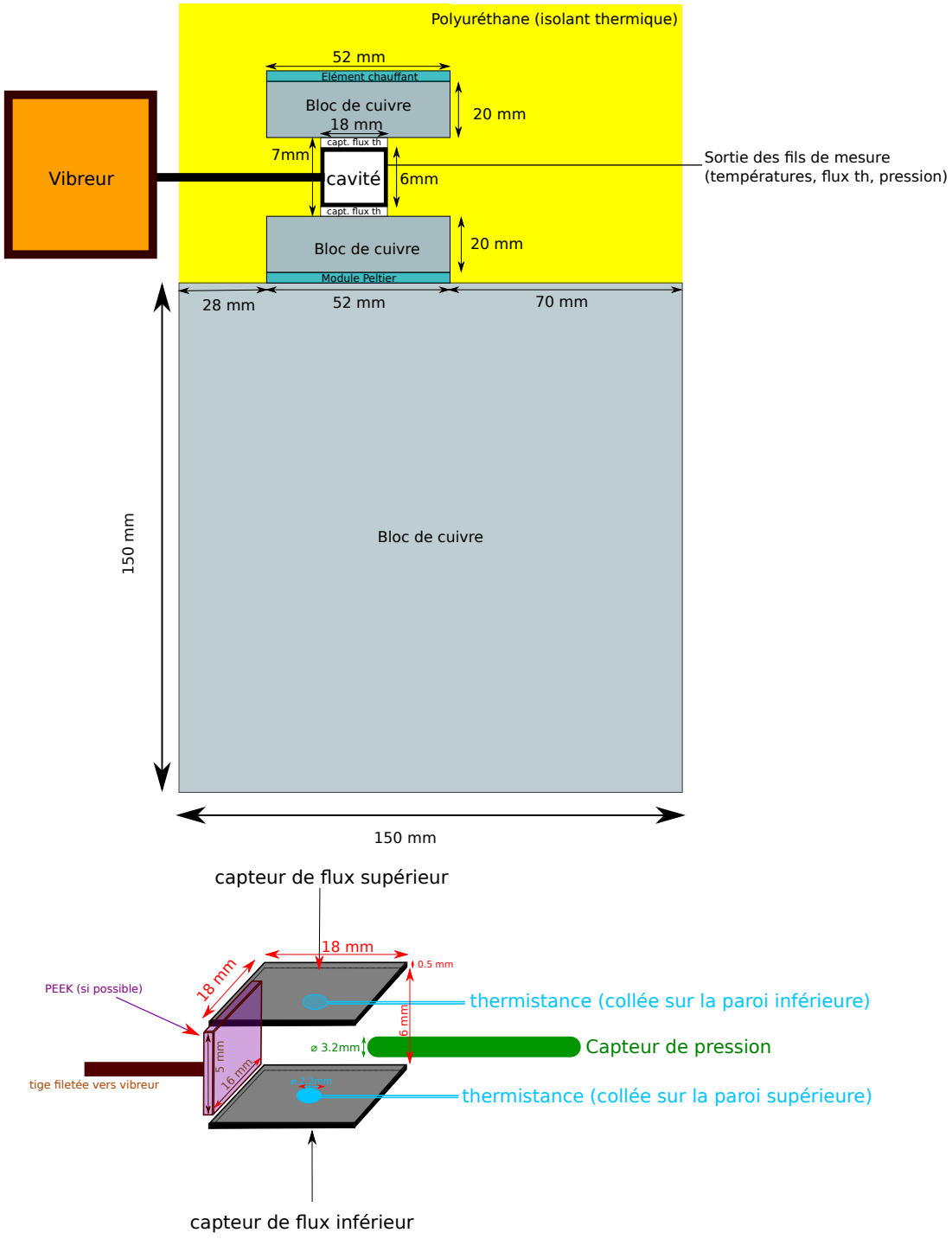

FIGURE 2.14 – Schéma du nouveau dispositif expérimental dédié à l'étude du streaming barocline. (Haut) Vue d'ensemble : la cavité acoustique, encastrée dans un isolant thermique, est reliée par ses faces supérieure et inférieure à des blocs de cuivre. La température de ces éléments est contrôlée par chauffage (bloc du haut) ou refroidissement (bloc du bas, connecté à un "thermostat" via un module Peltier). (Bas) Zoom sur la cavité acoustique : une onde acoustique horizontale, forcée par une plaque vibrante, est mesurée par un capteur de pression B&K 4138-A-015. Le transfert thermique causé par l'écoulement de streaming est caractérisé par deux capteurs de flux gSKIN XI 269C et de température Omega 44008.

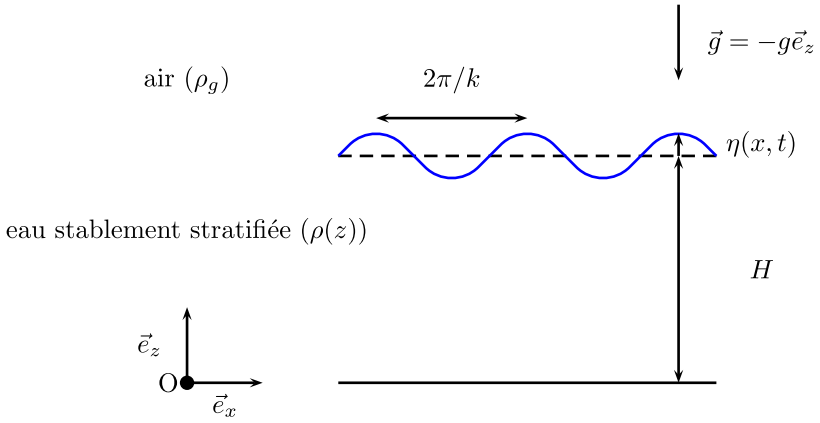

FIGURE 2.15 – Notations pour l'étude des vagues dans un fluide stratifié.

L'équation (2.197) décrit l'évolution temporelle linéarisée de la surface libre, et (2.198) la condition aux limites de non-pénétration au fond. En prenant le rotationnel de l'équation sur la quantité de mouvement (2.194), on remarque que le champ de vitesse ne dérive pas d'un potentiel scalaire. L'écoulement restant bidimensionnel et incompressible, on introduit une fonction de courant Ψ telle que $(u_x, u_z) = (\partial_z\Psi, -\partial_x\Psi)$. En éliminant le champ de pression, l'équation sur la quantité de mouvement

$$\partial_{tzz}\Psi + \partial_{txx}\Psi + \partial_x b = 0, \tag{2.199}$$

combinée à l'équation de flottabilité dérivée suivant x

$$\partial_{tx} b = N^2 \partial_{xx}\Psi, \tag{2.200}$$

mène à

$$\left(\partial_{ttxx} + \partial_{ttzz} + N^2\partial_{xx}\right)\Psi = 0. \tag{2.201}$$

Une onde stationnaire $\Psi(x,z,t) = f(z)\cos(\omega t)\cos(k_x x)$ doit alors vérifier (2.198) et (2.201), c'est-à-dire

$$\frac{\mathrm{d}^2 f}{\mathrm{d}z^2} = k_x^2\left(1 - \frac{N^2}{\omega^2}\right) f(z), \qquad f(0) = 0. \tag{2.202}$$

Supposons pour l'instant $\omega > N$ (vérifié a posteriori) et définissons $k_z = k_x\sqrt{1 - N^2/\omega^2}$ de manière à obtenir

$$f(z) = A\sinh(k_z z). \tag{2.203}$$

En dérivant par rapport à x la condition aux limites dynamique sur la pression à la surface libre puis en l'insérant dans l'équation sur la quantité de mouvement horizontale, on obtient

$$-g\partial_x\eta(x, z = H, t) = -\partial_x P(x, z = H, t) = \partial_{tz}\Psi(x, z = H, t). \tag{2.204}$$

Après dérivation temporelle et simplification avec la condition aux limites cinématique $\partial_t\eta = -\partial_x\Psi(x, z = H, t)$,

$$g(\partial_{xx}\Psi)(x, z = H, t) = (\partial_{ttz}\Psi)(x, z = H, t), \tag{2.205}$$

mène à la relation de dispersion

$$\boxed{\omega^2 = \frac{gk_x^2}{k_z}\ \tanh(k_z H)} \tag{2.206}$$

L'onde plane stationnaire dans un fluide uniformément stratifié s'écrit donc, avec $\eta_0 = Ak_x/[\omega \sinh(k_z H)]$ l'élévation de la surface libre,

$$\eta = \eta_0 \sin(k_x x)\sin(\omega t), \tag{2.207}$$

$$\Psi = \left(\frac{\eta_0 \omega}{k_x \sinh(k_z H)}\right)\cos(k_x x)\sinh(k_z z)\cos(\omega t), \tag{2.208}$$

$$u_x = \partial_z \Psi = \left(\frac{\eta_0 \omega k_z}{k_x \sinh(k_z H)}\right)\cos(k_x x)\cosh(k_z z)\cos(\omega t), \tag{2.209}$$

$$u_z = -\partial_x \Psi = \left(\frac{\eta_0 \omega}{\sinh(k_z H)}\right)\sin(k_x x)\sinh(k_z z)\cos(\omega t), \tag{2.210}$$

$$\Omega = \partial_z u_x - \partial_x u_z = -\left(\frac{\eta_0 k_x N^2}{\omega \sinh(k_z H)}\right)\cos(k_x x)\sinh(k_z z)\cos(\omega t), \tag{2.211}$$

$$k_z^2 + \frac{k_z N^2}{g\tanh(k_z H)} = k_x^2, \quad \omega^2 = \frac{g k_x^2}{k_z}\tanh(k_z H). \tag{2.212}$$

On remarque $k_z < k_x$, d'où $\omega > N$ qui vérifie notre hypothèse préalable. La stratification sépare les nombres d'onde horizontal et vertical, ce qui fait apparaître une vorticité oscillante.

Streaming dans un fluide stratifié

Comme pour les ondes acoustiques, la viscosité forme des couches limites oscillantes. Près des parois solides, un écoulement moyen apparaît en sortie de couche limite et s'interprète comme une vitesse de glissement effective (mécanisme de Rayleigh). Une couche limite existe aussi à la surface libre pour annuler la contrainte tangentielle : elle n'a pas d'effet sur le streaming pour les ondes planes stationnaires, mais résulte en un gradient d'écoulement moyen pour les ondes progressives [101].

L'inhomogénéité du champ de densité induisant la vorticité oscillante (2.211), on s'attend également à l'apparition d'un streaming barocline. Dans l'approximation de Boussinesq, il résulte de la densité de force

$$\mathbf{f}_{\text{ondes}} = -\overline{(\mathbf{u}\cdot\nabla)\mathbf{u}} = -\nabla\left(\frac{\overline{\mathbf{u}\cdot\mathbf{u}}}{2}\right) + \overline{\mathbf{u}\times(\nabla\times\mathbf{u})}. \tag{2.213}$$

En substituant les champs de vitesse obtenus pour une onde de surface plane (2.209 - 2.210), on trouve

$$\mathbf{f}_{\text{ondes}} = \frac{\eta_0^2\omega^2 k_z}{4\sinh(k_z H)^2}\left(\frac{k_z}{k_x}\sin(2k_x x)\mathbf{e}_x - \sinh(2k_z z)\mathbf{e}_z\right) \tag{2.214}$$

$$= -\left(\frac{\eta_0\omega}{2\sqrt{2}k_x\sinh(k_z H)}\right)^2 \nabla\left[k_z^2\cos(2k_x x) + k_x^2\cosh(2k_z z)\right]. \tag{2.215}$$

Bien l'écoulement oscillant soit rotationnel dans le cœur du fluide, cette force se réduit à un gradient : il n'y a pas de streaming barocline.

Pour comprendre ce résultat, on ré-exprime pour ce problème $\nabla\times\mathbf{f}_{\text{ondes}}$. Pour un mode propre de pulsation ω et de vorticité $\mathbf{\Omega} = \nabla\times\mathbf{u}$, (2.194) et (2.196) donnent

$$-\omega^2\mathbf{\Omega} = \partial_{tt}\mathbf{\Omega} = \nabla\times(\partial_t b\mathbf{e}_z) = \nabla\times(-N^2 u_z\mathbf{e}_z) \longrightarrow \mathbf{\Omega} = \frac{N^2}{\omega^2}\nabla\times(u_z\mathbf{e}_z) = \frac{N^2}{\omega^2}(\nabla u_z)\times\mathbf{e}_z. \tag{2.216}$$

D'après (2.213), la seule composante de $\mathbf{f}_{\text{ondes}}$ pouvant créer du streaming barocline devient

$$\mathbf{u}\times\mathbf{\Omega} = \frac{N^2}{\omega^2}\mathbf{u}\times[(\nabla u_z)\times\mathbf{e}_z] = \frac{N^2}{\omega^2}\left[u_z\nabla u_z - (\mathbf{u}\cdot\nabla u_z)\mathbf{e}_z\right] = \frac{N^2}{\omega^2}\left[\nabla\frac{u_z^2}{2} - (\mathbf{u}\cdot\nabla u_z)\mathbf{e}_z\right]. \tag{2.217}$$

On en déduit le rotationnel de la densité de force,

$$\nabla\times\mathbf{f}_{\text{ondes}} = -\frac{N^2}{\omega^2}\nabla\times\overline{[(\mathbf{u}\cdot\nabla u_z)\mathbf{e}_z]} = \frac{N^2}{\omega^2}\mathbf{e}_z\times\nabla\overline{(\mathbf{u}\cdot\nabla u_z)}. \tag{2.218}$$

Conclusion : dans l'approximation de Boussinesq, le streaming barocline apparaît si et seulement si le champ $(\mathbf{u}\cdot\nabla u_z)$ dépend d'une autre variable spatiale que z.

Effet de la géométrie

Pour l'onde de surface plane (2.207 - 2.212), on constate qu'en effet, $(\mathbf{u}\cdot\nabla u_z)$ ne dépend que de z :

$$\mathbf{u}\cdot\nabla u_z = u_x\partial_x u_z + u_z\partial_z u_z = \frac{(\eta_0\omega)^2 k_z}{2\sinh(k_z H)^2}\left[\cos(k_x x)^2\sinh(2k_z z) + \sin(k_x x)^2\sinh(2k_z z)\right] \tag{2.219}$$

$$= \frac{(\eta_0\omega)^2 k_z}{2\sinh(k_z H)^2}\sinh(2k_z z). \tag{2.220}$$

Les variations des différents termes de $\mathbf{u}\cdot\nabla u_z$ en x se compensent ici avec $\cos(k_x x)^2 + \sin(k_x x)^2 = 1$: cela n'a aucune généralité. Changeons de géométrie et intéressons-nous aux modes propres dans un réservoir cylindrique de hauteur H et de rayon R. Dans un fluide homogène, le champ de vitesse d'un mode propre axisymétrique (indice azimutal $m = 0$) s'écrit, avec J_0 la fonction de Bessel de première espèce d'ordre 0,

$$\mathbf{u} = U_0\left[J_0'(k_n r)\cosh(k_n z)\mathbf{e}_r + J_0(k_n r)\sinh(k_n z)\mathbf{e}_z\right], \qquad J_0'(k_n R) = 0. \tag{2.221}$$

On s'attend à ce que la stratification rende ce champ de vitesse rotationnel (probablement, comme dans le cas de l'onde plane, en dissociant les nombres d'onde radial et vertical), mais ne change pas le fait que

$$\mathbf{u}\cdot\nabla u_z = \frac{U_0^2}{2}\sinh(2kz)\left[J_m'(k_n r)^2 + J_m(k_n r)^2\right] \tag{2.222}$$

conserve une dépendance spatiale en la coordonnée radiale r. La stratification modifie donc nécessairement le streaming induit par une onde de surface dans un réservoir cylindrique. Parmi les questions ouvertes :

Comment le streaming barocline se compare-t-il au streaming de Rayleigh ? Pour les configurations habituelles, la stratification dans les liquides reste faible : l'analogue acoustique n'est donc pas le régime $\Delta T_* = O(T_*)$, mais plutôt la transition entre streaming de Rayleigh et barocline abordée §2.4.3. Est-il possible de mener un calcul similaire pour les ondes de surface ? Des difficultés techniques sont attendues : prise en compte de trois variables spatiales $\{r, \theta, z\}$ pour les ondes non-axisymétriques, modélisation de la ligne de contact mobile, plusieurs parois associées à des couches limites. Des simulations numériques directes avec le code Basilisk [102] permettraient de valider ces résultats. Nous travaillons actuellement avec Alice Marcotte à la réalisation d'un dispositif de PIV capable de mesurer l'écoulement de streaming dans un cylindre transparent oscillé verticalement, l'objectif à long terme étant l'étude des fluides stratifiés.

Comment le streaming barocline affecte-t-il le mélange ? Considérons un fluide stratifié contenu dans un réservoir cylindrique soumis à des oscillations (verticales ou horizontales). Ces mouvements forcent des ondes de surface, donc un écoulement de streaming barocline qui advecte les inhomogénéités de densité et accélère le mélange initialement diffusif. Cet effet est-il mesurable ? Peut-on prévoir la durée nécessaire à l'uniformisation quasi-complète du champ de densité ? Sur le temps long du mélange, nous retrouverons nécessairement le couplage réciproque entre l'onde de surface et l'écoulement moyen, qui peut être simulé numériquement avec un modèle quasi-linéaire. Là encore, les approches théoriques-numériques pourraient être abordées en parallèle de l'étude expérimentale.

Chapitre 3

Documents annexes

Je reporte ici les publications liées à ce manuscrit ainsi qu'un CV détaillé, à savoir successivement :

page 65 Article présenté section 1.3.1
"Multiple scales analysis of slow–fast quasi-linear systems"
Par Guillaume Michel et Gregory P. Chini
Publié dans *Proceedings of the Royal Society A*, volume 475, référence 20180630 (2019)

page 83 Article présenté section 1.3.2
"Exploiting self-organized criticality in strongly stratified turbulence"
Par Gregory P. Chini, Guillaume Michel, Keith Julien, Cesar B. Rocha et Colm-cille P. Caulfield
Publié dans *Journal of Fluid Mechanics*, volume 933, référence A22 (2022)

page 115 Article présenté section 2.4.1
"Strong wave–mean-flow coupling in baroclinic acoustic streaming"
Par Guillaume Michel et Gregory P. Chini
Publié dans *Journal of Fluid Mechanics*, volume 858, pages 536–564 (2019)

page 143 Article présenté section 2.4.2
"Aspect-ratio-dependent heat transport by baroclinic acoustic streaming"
Par Jacques Abdul Massih, Remil Mushthaq, Guillaume Michel et Gregory P. Chini
Publié dans *Journal of Fluid Mechanics*, volume 997, référence A7 (2024)

page 161 Article présenté section 2.4.3
"Baroclinic transition in acoustic streaming : beyond Rayleigh's paradigm"
Par Remil Mushthaq, Guillaume Michel et Gregory P. Chini
Publié dans *Journal of Fluid Mechanics*, volume 1017, référence A32 (2025)

page 183 Article présenté section 2.4.4
"Cooling by Baroclinic Acoustic Streaming"
Par Guillaume Michel et Christophe Gissinger
Publié dans *Physical Review Applied*, volume 16, référence L051003 (2021)

page 189 CV détaillé en date d'avril 2026

PROCEEDINGS A

rspa.royalsocietypublishing.org

Research

Check for updates

Article submitted to journal

Subject Areas:
mathematical physics, differential equations, fluid mechanics

Keywords:
multiple scale analysis, quasilinear systems, wave action, non-local energy transfers

Author for correspondence:
Guillaume Michel
e-mail: guillaume.michel@ens.fr

Multiple scales analysis of slow–fast quasilinear systems

G. Michel[1] and G. P. Chini[2]

[1]Laboratoire de Physique Statistique, École Normale Supérieure, CNRS, Université P. et M. Curie, Université Paris Diderot, Paris 75005, France
[2]Department of Mechanical Engineering and Program in Integrated Applied Mathematics, University of New Hampshire, Durham, NH 03824, USA

This article illustrates the application of multiple scales analysis to two archetypal quasilinear systems; i.e. to systems involving fast dynamical modes, called fluctuations, that are not directly influenced by fluctuation–fluctuation nonlinearities but nevertheless are strongly coupled to a slow variable whose evolution may be fully nonlinear. In the first case, fast waves drive a slow, spatially-inhomogeneous evolution of their celerity field. Multiple scales analysis confirms that, although the energy E, the angular frequency ω, and the modal structure of the waves evolve, the wave action E/ω is conserved in the absence of forcing and dissipation. In the second system, the fast modes undergo an instability that is saturated through a feedback on the slow variable. A new multiscale analysis is developed to treat this case. The key technical point, confirmed by the analysis, is that the fluctuation energy and mode structure evolve slowly to ensure that the slow field remains in a state of near marginal stability. These two model systems appear to be generic, being representative of many if not all quasilinear systems. In each case, numerical simulations of both the full and reduced dynamical systems are performed to highlight the accuracy and efficiency of the multiple scales approach. Python codes are provided as supplementary material.

THE ROYAL SOCIETY PUBLISHING

1. Introduction

Many physical, chemical, biological, and ecological systems evolve on disparate time scales. By explicitly accounting for this scale separation, multiple scales analysis enables reduced equations governing the slow evolution of the comparably fast processes to be derived. This flexible mathematical formalism has proven fruitful in a variety of contexts, not only enabling significant computational savings but also leading to the introduction of adiabatic invariants (e.g., wave action) and new governing equations (e.g., the nonlinear Schrödinger equation). In this article, we illustrate the derivation of reduced equations for *quasilinear* (QL) dynamical systems evolving on two distinct temporal scales. Slow–fast QL systems generically arise in the mathematical description of two broad classes of phenomena: (i) slowly-modulated waves, and (ii) instabilities that saturate through a feedback on the slow variable. A primary theme of the present work is that there are fundamental differences in the mathematical analysis of these multi-scale QL systems, with the latter requiring the introduction of a new asymptotic formalism.

QL systems have a characteristic mathematical structure comprising two sets of equations that govern the coupled evolution of slow variables, say $\bar{\mathbf{u}}$, and of fast fluctuations, say $\mathbf{u}'$. For instance, consider the Navier–Stokes equation for an incompressible and homogeneous fluid,

$$\frac{\partial \mathbf{u}}{\partial t} + (\mathbf{u}\cdot\nabla)\,\mathbf{u} = -\nabla\left(\frac{P}{\rho}\right) + \nu\triangle\mathbf{u}, \tag{1.1}$$

where $\mathbf{u}$ is the velocity field, P is the pressure, ρ is the (constant) density, ν is the kinematic viscosity, and $\triangle$ is the Laplacian operator, and assume that the dynamics is characterized by fast waves coupled with a mean velocity field that evolves comparably slowly in time. To account for this scale separation, we introduce a Reynolds-like decomposition $\mathbf{u} = \bar{\mathbf{u}} + \mathbf{u}'$, where $\overline{\mathbf{u}'} = 0$ and the bar refers to a (running) time average over many wave periods. With this expression, (1.1) becomes

$$\frac{\partial \bar{\mathbf{u}}}{\partial t} + (\bar{\mathbf{u}}\cdot\nabla)\,\bar{\mathbf{u}} + \overline{(\mathbf{u}'\cdot\nabla)\,\mathbf{u}'} = -\nabla\left(\frac{\overline{P}}{\rho}\right) + \nu\triangle\bar{\mathbf{u}}, \tag{1.2}$$

$$\frac{\partial \mathbf{u}'}{\partial t} + (\bar{\mathbf{u}}\cdot\nabla)\,\mathbf{u}' + (\mathbf{u}'\cdot\nabla)\,\bar{\mathbf{u}} + (\mathbf{u}'\cdot\nabla)\,\mathbf{u}' - \overline{(\mathbf{u}'\cdot\nabla)\,\mathbf{u}'} = -\nabla\left(\frac{P'}{\rho}\right) + \nu\triangle\mathbf{u}'. \tag{1.3}$$

The above set of equations is termed QL if the governing equations for the fluctuations $\mathbf{u}'$ do not include fluctuation–fluctuation nonlinearities; i.e., if the term $(\mathbf{u}'\cdot\nabla)\,\mathbf{u}'$ [and, hence, $\overline{(\mathbf{u}'\cdot\nabla)\,\mathbf{u}'}$] in (1.3) is negligible.

Frequently, wave systems satisfy the QL approximation: denoting the wavenumber of the waves by k, the angular frequency by ω, and the phase velocity (or "celerity") by c, then

$$\left|\frac{(\mathbf{u}'\cdot\nabla)\,\mathbf{u}'}{\partial_t\mathbf{u}'}\right| \sim \frac{u'k}{\omega} \sim \frac{u'}{c}, \tag{1.4}$$

which is a (generalized) Mach number. If this number is small compared to unity, then (1.3) reduces to QL form and the asymptotic methods introduced in this article can be applied. Since the nonlinear term $(\mathbf{u}'\cdot\nabla)\,\mathbf{u}'$ is neglected, quasilinearity also guarantees that the fluctuations cannot interact directly to generate new harmonics, thereby limiting the range of temporal scales that must be resolved in simulations. Nevertheless, the dynamics remains rich and the two-way nonlinear coupling between $\bar{\mathbf{u}}$ and $\mathbf{u}'$ is preserved: the cumulative effect of the fluctuation–fluctuation nonlinearities modifies the slow fields through the "Reynolds stress" divergence $\overline{(\mathbf{u}'\cdot\nabla)\,\mathbf{u}'}$ in (1.2), which in turn modifies the fluctuations through terms of the form $(\bar{\mathbf{u}}\cdot\nabla)\,\mathbf{u}'$ and $(\mathbf{u}'\cdot\nabla)\,\bar{\mathbf{u}}$. These attractive attributes account for the increasing prevalence of QL models in the atmospheric, oceanic, and astrophysical sciences (although in these models the averaging operation frequently is generalized to incorporate a spatial mean) and, more generally, in various branches of fluid mechanics, some examples of which are described below.

One well-documented QL phenomenon is the quasi-biennial oscillation of the winds in the lower equatorial stratosphere, which undergo reversals approximately every 14 months. This slowly-evolving flow results from a two-way coupling with internal gravity waves, which have a period of only a few tens of minutes [1]: the waves drive a shear flow through their Reynolds stress divergence, and the shear flow in return refracts the waves. Given the evident separation in temporal scales distinguishing the waves and the shear flow, along with the small Mach numbers characterizing the waves, these slow reversals can be captured in an idealized QL model [2,3]. As a second illustration, acoustic waves in a fluid exhibiting strong stable density inhomogeneities can nonlinearly interact to generate a mean Eulerian ("streaming") flow that advects the density inhomogeneities, thereby modifying the wave frequency, amplitude, and modal structure. This baroclinic acoustic streaming was first observed in high-intensity discharge lamps [4], with the wave period being $\sim 30\ \mu$s and the streaming flow evolving on a timescale ~ 0.1s, and subsequently shown to be described accurately by a QL dynamical system [5–7].

The application of multi-scale QL models is not restricted to dynamically-stable wave systems. Indeed, the QL reduction also has proved surprisingly effective for the investigation of spatiotemporally-chaotic and even turbulent dynamical systems dominated by spectrally non-local energy transfers. In this latter scenario, e.g., for turbulent fluid flows, the fluctuation term $\mathbf{u}'$ represents "eddies" and quasilinearity is realized when $\mathbf{u}' \ll \bar{\mathbf{u}}$, hence $(\mathbf{u}' \cdot \nabla)\,\mathbf{u}' \ll (\bar{\mathbf{u}} \cdot \nabla)\,\mathbf{u}'$. In the atmospheres of the Earth and gas giants, for example, turbulent small-scale eddies are known to drive slowly-evolving zonal jets that in turn undergo shear instabilities and spawn small-scale eddies. Both the QL character and the time-scale separation manifest in this coupled eddy/jet system can be derived in the limit of small forcing and dissipation [8], thus providing a consistent framework to explain the spontaneous generation of these jets [9]. Similarly, in strongly (stably) stratified turbulence, anisotropic layers of horizontally-moving fluid (oriented orthogonally to the direction of the imposed density gradient) spontaneously emerge that, owing to their relative motion, are susceptible to small-scale instabilities. A QL system has been derived in the asymptotic limit of strong stratification and shown to be capable of describing the dynamics of these anisotropic layers [10]. Other examples of turbulent yet approximately quasilinear dynamical systems include strongly rotating (but weakly stratified) flows, such as open-ocean deep convection and high-latitude abyssal ocean currents [11], and rotating astrophysical disks in which magnetic fields are generated [12].

In this work, we describe the multiple scales analysis of two systems that are intended to be representative of the two broad classes of QL dynamics, involving waves and instabilities, respectively. These examples are sufficiently simple that the derivations are reasonably concise, allowing us to highlight the differences: specifically, for QL systems exhibiting fast exponentially-growing instabilities rather than stable high-frequency wave motions, we show that the amplitudes of the "most dangerous" fluctuation modes are slaved to the slowly-evolving mean fields. The main novelty of our study is the new procedure we introduce to capture this slaving, which is not associated with the usual dissipative contraction to a slow manifold but rather with a marginal stability constraint. Furthermore, to illustrate the utility of the multiple scales approach in each case, direct numerical simulations of the master equations are compared to numerical simulations of the reduced models we derive. The simulations are coded in Python, using the open-source framework Dedalus, which allows for an easy and efficient implementation of initial-value, boundary-value, and eigenvalue problems [13]. Another attractive feature is that the user need only explicitly enter the equations, and the numerical scheme is then automatically generated. For completeness, all of the associated source files are commented and provided as supplementary material.

2. Modulated Waves

(a) Governing equations

The first system we analyze is a one-dimensional model of fast, linear waves that are coupled strongly to their celerity field. For simplicity, only a bounded spatial domain is considered, although the analysis can be generalized to wave propagation in spatially-extended domains. This system can be viewed as a generic model of wave/mean-flow interaction, crudely mimicking the phenomenology of, e.g., baroclinic acoustic streaming noted in the introduction. More generally, the analysis detailed in this section can be applied to any QL system in which the fluctuations are slowly-modulated waves that are *not susceptible to a rapidly-amplifying instability*. Here, the celerity field c and the wave field η are chosen to satisfy the following governing equations (and initial conditions):

$$\frac{\partial^2 c}{\partial t^2} = -(c-1) + \frac{\partial^3 c}{\partial x^2 \partial t} - c\left(\frac{\partial \eta}{\partial x}\right)^2, \qquad c(x,0) = 1, \ \frac{\partial c}{\partial t}(x,0) = 0, \tag{2.1}$$

$$\epsilon^2 \frac{\partial^2 \eta}{\partial t^2} = \frac{\partial}{\partial x}\left(c(x,t)^2 \frac{\partial \eta}{\partial x}\right), \qquad \eta(x,0) = \frac{2}{\sqrt{L}} \cos\left(\frac{2\pi x}{L}\right), \ \frac{\partial \eta}{\partial t}(x,0) = 0. \tag{2.2}$$

The spatial domain $x \in [0, L)$, and both c and η are L-periodic functions of x. Equation (2.2) is the one-dimensional (1D) wave equation with inhomogeneous celerity, where ϵ^2 is the square of a small parameter. (Note that all variables are dimensionless.) Equation (2.1) describes the evolution of an initially uniform celerity distorted by the wave-induced Reynolds stress and subject to both restoring and dissipative processes. This set of equations conserves, in the absence of dissipation, the total energy $E_{\rm tot} = E_{\rm c} + E_{\rm w}$, where $E_{\rm c}$ and $E_{\rm w}$ are, respectively, the "energy" of the celerity field and of the waves, defined by

$$E_{\rm c} = \frac{1}{2}\int_0^L \left[\left(\frac{\partial c}{\partial t}\right)^2 + (c-1)^2\right] {\rm d}x, \quad E_{\rm w} = \frac{1}{2}\int_0^L \left[\epsilon^2\left(\frac{\partial \eta}{\partial t}\right)^2 + c^2\left(\frac{\partial \eta}{\partial x}\right)^2\right] {\rm d}x. \tag{2.3}$$

For the given initial conditions, c and η are $O(1)$, implying the right-hand sides of (2.1) and (2.2) also are of order unity. Owing to the prefactor ϵ^2 on the left-hand side of (2.2), which can be interpreted as a measure of fluctuation inertia, we expect the wave field η to evolve on a much faster time scale than that characterizing the evolution of the celerity c.

(b) Leading-order equations

The dynamics thus evolves on both a fast, $O(\epsilon)$, and a slow, $O(1)$, time scale. To exploit this temporal scale separation, we introduce a fast phase ϕ and a slow time T, where

$$\frac{{\rm d}\phi}{{\rm d}t} = \frac{\omega(T)}{\epsilon}, \qquad T = t. \tag{2.4}$$

Crucially, ϕ and T are treated as *independent variables* in the subsequent analysis. The introduction of the phase ϕ through its non-constant time derivative captures the slow evolution of the wave angular frequency ω and is referred to as the WKBJ approximation [14]. Using the chain rule, $\partial_t \to (\omega(T)/\epsilon)\partial_\phi + \partial_T$, the governing equations become

$$\frac{\omega^2}{\epsilon^2}\frac{\partial^2 c}{\partial \phi^2} + \frac{1}{\epsilon}\left[2\omega \frac{\partial^2 c}{\partial \phi \partial T} + \frac{{\rm d}\omega}{{\rm d}T}\frac{\partial {\rm c}}{\partial \phi}\right] + \frac{\partial^2 c}{\partial T^2} = -(c-1) - c\left(\frac{\partial \eta}{\partial x}\right)^2 + \frac{\omega}{\epsilon}\frac{\partial^3 c}{\partial x^2 \partial \phi} + \frac{\partial^3 c}{\partial x^2 \partial T}, \tag{2.5}$$

$$\omega^2 \frac{\partial^2 \eta}{\partial \phi^2} + \epsilon\left[2\omega \frac{\partial^2 \eta}{\partial \phi \partial T} + \frac{{\rm d}\omega}{{\rm d}T}\frac{\partial \eta}{\partial \phi}\right] + \epsilon^2 \frac{\partial^2 \eta}{\partial T^2} = \frac{\partial}{\partial x}\left(c^2 \frac{\partial \eta}{\partial x}\right). \tag{2.6}$$

To proceed, c, η, and ω are expanded as asymptotic power series in ϵ,

$$\eta(x,\phi,T) = \eta_0(x,\phi,T) + \epsilon\eta_1(x,\phi,T) + O(\epsilon^2), \tag{2.7}$$

$$c(x,\phi,T) = c_0(x,\phi,T) + \epsilon c_1(x,\phi,T) + O(\epsilon^2), \tag{2.8}$$

$$\omega(T) = \omega_0(T) + \epsilon\omega_1(T) + O(\epsilon^2), \tag{2.9}$$

and substituted into (2.5)–(2.6). Since ϵ is small but variable, the resulting equations then can be solved order by order. At $O(1/\epsilon^2)$, (2.5) yields $\partial_\phi^2 c_0 = 0$, and since linear growth of c_0 with ϕ would result in unbounded growth of c_0, we conclude that c_0 is a function of x and T only. This result confirms that at leading order c is a field that evolves strictly on the slow time scale. With $\partial_\phi c_0 = 0$, (2.5) at order $O(1/\epsilon)$ requires $\partial_\phi c_1 = 0$; i.e., c_1 also is a function only of x and T. Finally, at $O(1)$, we obtain

$$\omega_0^2 \frac{\partial^2 c_2}{\partial\phi^2} + \frac{\partial^2 c_0}{\partial T^2} = -(c_0 - 1) - c_0\left(\frac{\partial\eta_0}{\partial x}\right)^2 + \frac{\partial^3 c_0}{\partial x^2 \partial T}. \tag{2.10}$$

We next introduce the fast average over ϕ (denoted with an overbar) of any function $f(x,\phi,T)$ bounded in ϕ :

$$\bar{f}(x,T) = \lim_{n\to\infty} \frac{1}{2n\pi}\int_{-n\pi}^{+n\pi} f(x,\phi,T)\mathrm{d}\phi, \quad \text{for integer } n. \tag{2.11}$$

This averaging operation provides a suitable definition of the overbar used to define the Reynolds decomposition $\mathbf{u} = \bar{\mathbf{u}} + \mathbf{u}'$ in the introduction. Applying this averaging procedure to (2.10), and recalling $\partial_\phi c_0 = 0$, yields a necessary condition for the sublinear growth of $\partial_\phi c_2$:

$$\frac{\partial^2 c_0}{\partial T^2} = -(c_0 - 1) - c_0\overline{\left(\frac{\partial\eta_0}{\partial x}\right)^2} + \frac{\partial^3 c_0}{\partial x^2 \partial T}. \tag{2.12}$$

In fact, it is readily confirmed using the resulting equation for c_2 [obtained by subtracting (2.12) from (2.10)] together with the expression for η_0 given below in (2.14) that (2.12) ensures the boundedness of c_2 on the slow time scale.

We now turn to the leading-order reduction of the fluctuation equation (2.6):

$$-\omega_0(T)^2\frac{\partial^2\eta_0}{\partial\phi^2} + \frac{\partial}{\partial x}\left(c_0(x,T)^2\frac{\partial\eta_0}{\partial x}\right) = 0. \tag{2.13}$$

Equations (2.12)–(2.13) comprise a two time-scale system, for which the fluctuation equation (2.13) does not involve nonlinear fluctuation–fluctuation terms (e.g., η_0^2) and thus is quasilinear. (Of course, for this system, no such nonlinearity was included in the master set of equations.) The key question that arises is how to accurately and efficiently integrate this two time-scale system? We proceed by observing that the solution of (2.13) is of the form

$$\eta_0(x,\phi,T) = A(T)\hat{\eta}_0(x,T)\cos\phi, \tag{2.14}$$

since c_0 does not depend on ϕ and noting that the solution component proportional to $\sin\phi$ vanishes as a result of the initial conditions (2.2) on η. Here, $A(T)$ is a slowly-evolving amplitude, and $\hat{\eta}_0$ is a function that characterizes the spatial structure of the wave mode. A normalization condition must be prescribed to make this decomposition unique; see (2.17). Crucially, at this stage of the analysis, the slow evolution of A is unknown. Indeed, the ansatz (2.14) converts the *initial-value* problem (2.13) into a *linear eigenvalue* problem that places no constraint on the modal amplitude. Consequently, the reduced system is not closed on the slow time scale. The objective of the remainder of the analysis is to derive an equation for $\mathrm{d}A/\mathrm{d}T$, which for this system is found by examining the equation for the correction field η_1.

(c) Inner product and adjoint operator

Multiple scales analysis, in its most general form, requires certain notions from linear algebra that we introduce here. Substituting (2.14) into (2.13), $\hat{\eta}_0$ is found to satisfy

$$\omega_0^2\hat{\eta}_0 + \frac{\partial}{\partial x}\left(c_0^2\frac{\partial\hat{\eta}_0}{\partial x}\right) = 0, \quad \hat{\eta}_0(0,T) = \hat{\eta}_0(L,T), \qquad \frac{\partial\hat{\eta}_0}{\partial x}(0,T) = \frac{\partial\hat{\eta}_0}{\partial x}(L,T). \tag{2.15}$$

This eigenvalue problem is linear, and can be expressed more compactly as $\mathcal{L}\hat{\eta}_0 = 0$, where the linear operator $\mathcal{L} = \omega_0^2 + \partial_x(c_0^2\partial_x)$, with periodic boundary conditions, acts on the function $\hat{\eta}_0$. For spatially-periodic and real-valued functions $f(x)$ and $g(x)$, we define the L^2 inner product

$$(f,g) = \int_0^L f(x)g(x)\,\mathrm{d}x. \tag{2.16}$$

An inner product defines a norm, and we choose to set $(\hat{\eta}_0,\hat{\eta}_0) = 1$; that is,

$$\int_0^L \hat{\eta}_0^2(x,T)\mathrm{d}x = 1. \tag{2.17}$$

This relation renders the decomposition (2.14) unique. Moreover, after integrating by parts and making use of the periodic boundary conditions, we obtain

$$(\mathcal{L}f,g) = \int_0^L g(x)\left(\omega_0^2 + \partial_x(c_0^2\partial_x)\right)f(x)\mathrm{d}x = \int_0^L f(x)\left(\omega_0^2 + \partial_x(c_0^2\partial_x)\right)g(x)\mathrm{d}x = (f,\mathcal{L}g). \tag{2.18}$$

This equality reveals that $\mathcal{L}$ is *self-adjoint*, a feature that, while not essential, simplifies the following analysis. For other boundary conditions (and/or other differential operators), the adjoint operator may not be equal to $\mathcal{L}$ but the following procedure can be appropriately modified [14]. As shown in the next subsection, computing the adjoint linear operator enables a *solvability condition* to be imposed on the equation for the correction field η_1, which, in turn, ensures that the asymptotic expansion (2.7) remains uniformly valid on the slow time scale T. This procedure generalizes the operation of "removing resonant or secular forcing terms" usually introduced in early lectures on multiple scales analysis [14].

(d) Conservation of wave action

The slow temporal evolution of A is obtained by collecting terms of order $O(\epsilon)$ in (2.6):

$$-\omega_0^2\frac{\partial^2\eta_1}{\partial\phi^2} + \frac{\partial}{\partial x}\left(c_0^2\frac{\partial\eta_1}{\partial x}\right) = 2\omega_0\frac{\partial^2\eta_0}{\partial T\partial\phi} + \frac{\mathrm{d}\omega_0}{\mathrm{d}T}\frac{\partial\eta_0}{\partial\phi} + 2\omega_0\omega_1\frac{\partial^2\eta_0}{\partial\phi^2} - 2\frac{\partial}{\partial x}\left(c_0c_1\frac{\partial\eta_0}{\partial x}\right). \tag{2.19}$$

Note that the left-hand sides of (2.19) and of (2.13) involve the same linear operator. By setting $\eta_1(x,\phi,T) = \hat{\eta}_{1,\mathrm{c}}(x,T)\cos\phi + \hat{\eta}_{1,\mathrm{s}}(x,T)\sin\phi$, (2.19) yields

$$\mathcal{L}\hat{\eta}_{1,\mathrm{c}} = F_{\mathrm{c}}, \qquad F_{\mathrm{c}} = -2\omega_0\omega_1 A\hat{\eta}_0 - 2A\frac{\partial}{\partial x}\left(c_0c_1\frac{\partial\hat{\eta}_0}{\partial x}\right), \tag{2.20}$$

$$\mathcal{L}\hat{\eta}_{1,\mathrm{s}} = F_{\mathrm{s}}, \qquad F_{\mathrm{s}} = -2\omega_0\left(\frac{\mathrm{d}A}{\mathrm{d}T}\hat{\eta}_0 + A\frac{\delta\hat{\eta}_0}{\delta T}\right) - A\frac{\mathrm{d}\omega_0}{\mathrm{d}T}\hat{\eta}_0. \tag{2.21}$$

The notation $\delta/\delta T$ is a short-hand for $(\partial_T c_0)\,\delta/\delta c_0$, where $\delta/\delta c_0$ denotes *functional differentiation* with respect to $c_0(x,T)$, as arises here because of the tight, two-way coupling between the waves and the slowly-evolving celerity field; specifically, the evolution of c_0 drives slow, $O(1)$ changes in the *leading-order* wave eigenfunction $\hat{\eta}_0$, rendering the analysis non-standard. Nevertheless, we demonstrate below that the required functional derivatives can be evaluated explicitly, obviating the need for costly sensitivity computations.

Taking the inner product of (2.20) with $\hat{\eta}_0$ and using the fact that $\mathcal{L}$ is self-adjoint, we obtain a solvability condition:

$$(F_{\rm c}, \hat{\eta}_0) = (\mathcal{L}\hat{\eta}_{1,{\rm c}}, \hat{\eta}_0) = (\hat{\eta}_{1,{\rm c}}, \mathcal{L}\hat{\eta}_0) = (\hat{\eta}_{1,{\rm c}}, 0) = 0; \tag{2.22}$$

i.e., the right-hand-side of (2.20) must be orthogonal to the null eigenvector of the (adjoint) linear operator. Consequently,

$$\omega_0\omega_1 \int_0^L \hat{\eta}_0^2 {\rm d}x = -\int_0^L \hat{\eta}_0 \frac{\partial}{\partial x}\left(c_0 c_1 \frac{\partial \hat{\eta}_0}{\partial x}\right) {\rm d}x = \int_0^L c_0 c_1 \left(\frac{\partial \hat{\eta}_0}{\partial x}\right)^2 {\rm d}x. \tag{2.23}$$

Using the normalization condition (2.17) then yields the following result:

$$\omega_1 = \frac{1}{\omega_0}\int_0^L c_0 c_1 \left(\frac{\partial \hat{\eta}_0}{\partial x}\right)^2 {\rm d}x. \tag{2.24}$$

This expression for the angular frequency correction ω_1, together with a relation for the evolution of the leading-order frequency ${\rm d}\omega_0/{\rm d}T$ (see Sec. (e)), is required only to close the system for the *correction* fields ω_1, c_1, η_1 arising at higher order, should they be desired. In contrast, the solvability condition $(F_{\rm s}, \hat{\eta}_0) = 0$ yields a slow evolution equation for $A(T)$. Specifically, we obtain

$$\left(2\omega_0 \frac{{\rm d}A}{{\rm d}T} + A\frac{{\rm d}\omega_0}{{\rm d}T}\right)\int_0^L \hat{\eta}_0^2 {\rm d}x = -A\omega_0 \frac{\rm d}{{\rm d}T}\left(\int_0^L \hat{\eta}_0^2 {\rm d}x\right) = 0; \tag{2.25}$$

the last equality is a consequence of the normalization (2.17), following an interchange of the order of functional differentiation and integration. Thus, we obtain the *amplitude equation*

$$2\omega_0 \frac{{\rm d}A}{{\rm d}T} + A\frac{{\rm d}\omega_0}{\partial T} = 0 \quad \Rightarrow \quad \frac{\rm d}{{\rm d}T}\left(A^2\omega_0\right) = 0. \tag{2.26}$$

The latter form of (2.26) reveals the existence of a conserved quantity in the limit of slow external processes (here, slow variation of the celerity c), termed an *adiabatic invariant*. Given that the leading-order energy of the waves $E_0 = (\omega_0 A)^2/2$, as computed from (2.3), the adiabatic invariant derived in (2.26) is the so-called *wave action* E_0/ω_0. Conservation of wave action is a generic property of all slowly-modulated, non-dissipative linear waves [15].

(e) Slow evolution of the angular frequency

With the formalism introduced in Sec. (c), it is possible to derive an additional equation that, although not necessary for this problem, is in fact crucial for predicting the slow dynamics of the system analyzed in Sec. 3. Accordingly, this additional condition is introduced here to facilitate comparison between the wave and instability problems and is derived by differentiating the leading-order eigenvalue equation (2.15) with respect to the slow time T:

$$\left[\omega_0^2 + \frac{\partial}{\partial x}\left(c_0^2 \frac{\partial}{\partial x}\right)\right]\frac{\delta\hat{\eta}_0}{\delta T} = -2\left[\omega_0 \frac{{\rm d}\omega_0}{{\rm d}T} + \frac{\partial}{\partial x}\left(c_0 \frac{\partial c_0}{\partial T}\frac{\partial}{\partial x}\right)\right]\hat{\eta}_0. \tag{2.27}$$

This system is of the form of $\mathcal{L}(\delta\hat{\eta}_0/\delta T) = G$, where G is the right-hand side of (2.27). Thus, a solvability condition is obtained by taking the inner product of (2.27) with $\hat{\eta}_0$, yielding

$$\frac{{\rm d}\omega_0}{{\rm d}T} = -\frac{1}{\omega_0}\int_0^L \hat{\eta}_0 \frac{\partial}{\partial x}\left(c_0 \frac{\partial c_0}{\partial T}\frac{\partial \hat{\eta}_0}{\partial x}\right){\rm d}x = \frac{1}{\omega_0}\int_0^L \left(\frac{\partial \hat{\eta}_0}{\partial x}\right)^2 c_0 \frac{\partial c_0}{\partial T}{\rm d}x. \tag{2.28}$$

This result provides an explicit evolution equation for the angular frequency of the waves.

(f) Numerical implementation

To assess the fidelity of the predicted slow dynamics to the actual system dynamics for small but finite values of ϵ, direct numerical simulations (DNS) of the governing equations (2.1)–(2.2) for various values of ϵ are compared to a numerical simulation of the reduced system (2.12), (2.15), and (2.26) obtained from the multiple scales analysis. All simulations are performed in a domain

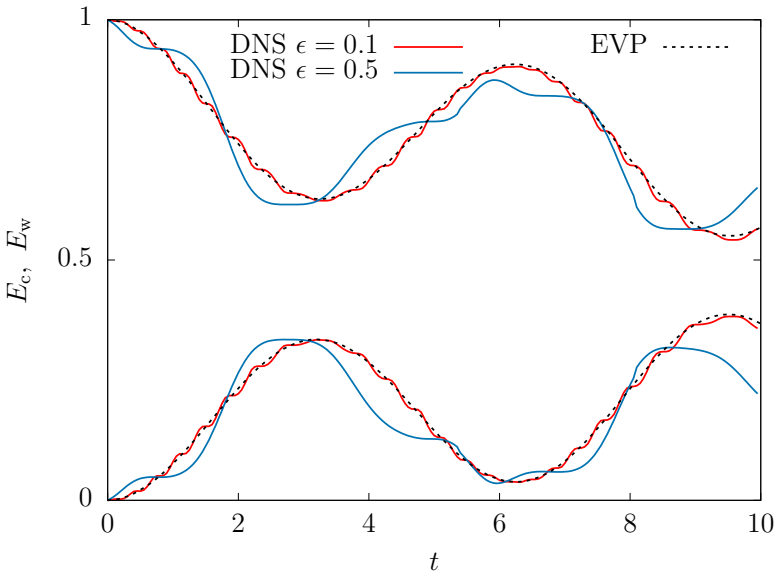

Figure 1. Energy of the waves E_w ($E_w(0) = 1$) and of the celerity field E_c ($E_c(0) = 0$) obtained from direct numerical simulations (DNS) for $\epsilon = \{0.1, 0.5\}$ and from the multiple scales model (derived in the limit $\epsilon \to 0$) in which the waves are computed via the solution of an eigenvalue problem (EVP) instead of being explicitly time-resolved.

of size $L = 2\pi$ with 32 grid points, use a second-order Runge-Kutta scheme, and output the time series of the energies E_c and E_w defined in (2.3). Although not documented here, the convergence of each simulation with increasing spatiotemporal resolution has been confirmed.

The DNS are performed by solving the system (2.1)–(2.2) using a Fourier pseudospectral method, the timestep being set in accord with a CFL condition (e.g., $dt \simeq 0.01$ for $\epsilon = 0.1$). The reduced model is discretized on a Chebyshev grid, a requirement of the Dedalus eigenvalue solver; note that only (2.12) is explicitly time-advanced. In this equation, the term involving the fluctuations can be expressed as

$$\overline{\left(\frac{\partial \eta_0}{\partial x}\right)^2} = \frac{E_0(T)}{\omega_0(T)^2}\left(\frac{\partial \hat{\eta}_0}{\partial x}\right)^2, \tag{2.29}$$

where $\omega_0(T)$ and $\hat{\eta}_0$ are obtained by numerically solving the eigenvalue problem (2.15) at each slow timestep rather than time-advancing (2.13) on the fast time scale, and the leading-order wave energy $E_0(T) = E_0(0)\omega_0(T)/\omega_0(0)$ owing to the conservation of wave action. For consistency with the initial conditions imposed in the DNS, we select $E_0(0) = \omega_0(0) = 1$. Since the waves are not explicitly time-resolved, the timestep can be increased by an order of magnitude ($dt = 0.1$) relative to that required for the DNS!

The time series of the energies are reported in Fig. 1. Excellent agreement is achieved even for modest values of ϵ, and, for $\epsilon = 0.1$, the simulations of the reduced equations provide a quantitatively accurate representation of the energy exchanges between the waves and the external medium. Of course, for this unforced and dissipative system, the total energy decays toward zero and a rest state is eventually reached. As noted in the introduction, the associated source files for these simulations are commented and provided as supplementary material. The files also can be used to generate space–time diagrams of the celerity field, should they be desired.

3. Unstable Fluctuations

(a) Governing equations

The second example provides an illustration of a QL system in which the fluctuations would grow (or decay) exponentially fast in the absence of feedback on the slow variable. Nevertheless, we confirm that scale separation can be preserved as a result of the two-way coupling. In this example, the slowly-evolving field $\Theta(x,t)$ and the fast fluctuation field $\eta(x,t)$ satisfy

$$\frac{\partial \Theta}{\partial t} = P - \nu\Theta - \eta^2, \qquad \Theta(x,0) = -1, \tag{3.1}$$

$$\epsilon\frac{\partial \eta}{\partial t} = \Theta\eta + \frac{\partial^2 \eta}{\partial x^2} - \epsilon\eta^3, \qquad \eta(x,0) = \cos\left(\frac{2\pi x}{L}\right), \tag{3.2}$$

respectively, subject to periodic boundary conditions in a domain of spatial period L. It may be noted that the fluctuations satisfy a Ginzburg–Landau (GL) equation, e.g., describing the evolution of a non-uniform pattern amplitude $\eta(x,t)$, although neither this specification nor interpretation is a requirement of the formalism. Moreover, unlike standard GL models, the "distance" to the instability threshold is controlled by the (slow) *field variable* Θ, which evolves according to (3.1), the terms on the right-hand side respectively representing an external forcing $P(x,t) > 0$, a linear damping ($\nu > 0$ is a damping coefficient), and a quadratic feedback from the fluctuations. The small parameter ϵ controls the temporal scale separation. The coupled system (3.1)–(3.2) crudely mimics, for instance, the QL reduction of the equations governing Rayleigh–Bénard convection first proposed by Herring [16].

The coupling between the two fields Θ and η is such that there exists an energy for this system, $E = E_\Theta + E_\eta$, where

$$E_\Theta = \frac{1}{2}\int_0^L \Theta^2 \,\mathrm{d}x, \qquad E_\eta = \frac{\epsilon}{2}\int_0^L \eta^2 \,\mathrm{d}x. \tag{3.3}$$

It transpires that at leading order in ϵ the nonlinear term in (3.2) is negligible and, thus, the total energy E is conserved in the absence of forcing ($P = 0$) and dissipation (requiring both $\nu = 0$ in (3.1) and zero diffusion in (3.2)). In the absence of the nonlinear term in (3.2), the system (3.1)–(3.2) becomes quasilinear.

(b) Leading-order equations

As for the slowly-modulated wave system considered in Sec. 2, the small parameter ϵ motivates the introduction of two scales ϕ and T, treated hereafter as independent variables and defined according to

$$\frac{\mathrm{d}\phi}{\mathrm{d}t} = \frac{\sigma(T)}{\epsilon}, \qquad T = t. \tag{3.4}$$

The notation σ rather than ω is used in this example to signify that the fluctuations may grow (or decay) exponentially rather than oscillate rapidly. Like ω, σ is defined to be an eigenvalue of a certain linear operator. A crucial distinction, however, is that while ω is the slowly-varying angular frequency of *any* one of a countable infinity of wave modes (see Sec. 2), σ is the slowly-evolving instantaneous growth rate of the *most unstable* (or least stable) fluctuation mode.

Using (3.4), the governing equations (3.1)–(3.2) become

$$\frac{\sigma}{\epsilon}\frac{\partial \Theta}{\partial \phi} + \frac{\partial \Theta}{\partial T} = P - \nu\Theta - \eta^2, \tag{3.5}$$

$$\frac{\sigma}{\epsilon}\frac{\partial \eta}{\partial \phi} + \frac{\partial \eta}{\partial T} = \frac{\Theta\eta}{\epsilon} + \frac{1}{\epsilon}\frac{\partial^2 \eta}{\partial x^2} - \eta^3. \tag{3.6}$$

This set of equations is solved order by order in ϵ after substituting the following asymptotic expansions for σ, Θ, and η:

$$\sigma(T) = \sigma_0(T) + \epsilon\sigma_1(T) + O(\epsilon^2), \tag{3.7}$$

$$\Theta(x,\phi,T) = \Theta_0(x,\phi,T) + \epsilon\Theta_1(x,\phi,T) + O(\epsilon^2), \tag{3.8}$$

$$\eta(x,\phi,T) = \eta_0(x,\phi,T) + \epsilon\eta_1(x,\phi,T) + O(\epsilon^2). \tag{3.9}$$

Equation (3.5) at $O(1/\epsilon)$ yields $\partial_\phi\Theta_0 = 0$; i.e., Θ_0 is a function strictly of x and T. At $O(1)$, the fast average introduced in (2.11) removes the term proportional to $\partial_\phi\Theta_1$, yielding

$$\frac{\partial\Theta_0}{\partial T} = P - \nu\Theta_0 - \overline{\eta_0^2}. \tag{3.10}$$

The leading-order fluctuation equation [i.e. Eq. (3.6) at $O(1/\epsilon)$] is

$$\sigma_0\frac{\partial\eta_0}{\partial\phi} = \Theta_0\eta_0 + \frac{\partial^2\eta_0}{\partial x^2}. \tag{3.11}$$

Equations (3.10)–(3.11) comprise a two time-scale system that (as for the modulated waves example) can be closed on the *fast* time scale upon making the non-asymptotic replacement $\partial_T \to (\sigma/\epsilon)\partial_\phi$. This system is also quasilinear: fluctuation–fluctuation nonlinearities are of higher order and have been consistently neglected in the fluctuation equation (3.11). Typically, the nonlinearity in (3.2), the equation from which (3.11) is derived, is crucial for the saturation of amplifying solutions that obey Ginzburg–Landau dynamics; its systematic omission in (3.11) implies that a distinct saturation mechanism is involved here.

Once again, the question that arises is how to accurately and efficiently integrate this slow–fast QL system when two formally independent time scales are retained? The combination of temporal scale separation and quasilinearity enables a modal solution of (3.11) to be expressed as

$$\eta_0(x,\phi,T) = A(T)\hat{\eta}_0(x,T)e^{\phi}, \tag{3.12}$$

where $A(T)$ is the slowly-varying modal amplitude, and $\hat{\eta}_0$ describes the spatial structure of the fluctuation mode. Note that A, $\hat{\eta}_0$, and ϕ are real-valued and that a suitable normalization condition on $\hat{\eta}_0$ is required to render the decomposition (3.12) unique; see (3.18). Upon substituting (3.12) into (3.11), σ_0 is identified as the maximum eigenvalue of the operator $(\Theta_0 + \partial_x^2)$. The leading-order fluctuation equation (3.11) seemingly places no constraint on the evolution of $A(T)$, confirming that the system (3.10)–(3.11) is *not* closed on the slow time scale.

Of course, the potential exponential growth (or decay) of the leading-order fluctuation field η_0 on the fast time scale would, if not properly addressed, break the posited scalings, as evidenced by the force acting on the slow field Θ_0:

$$\overline{\eta_0^2} = \lim_{n\to\infty}\frac{A^2\hat{\eta}_0^2}{2n\pi}\int_{-n\pi}^{+n\pi} e^{2\phi}\mathrm{d}\phi. \tag{3.13}$$

Note that, as for the fast temporal average introduced in (2.11), the fast time variable ranges from negative to positive infinity (rather than from, e.g., zero to positive infinity) while the slow time T is fixed. To ensure the convergence of this fast-time average for all x, one of the following two conditions must be satisfied: (i) $A(T) = 0$ or (ii) $\sigma(T) = \epsilon\mathrm{d}\phi/\mathrm{d}t = 0$ (implying the integrand in (3.13) is constant). These conditions thus require $A(T) = 0$ if the maximum instantaneous growth rate $\sigma(T)$ is non-zero, a natural consequence of exponentially-fast damping for $\sigma < 0$ and a requirement, were $\sigma > 0$, to preclude the blow-up of the fluctuations (and, hence, of the force (3.13)) on the fast time scale. With $A \equiv 0$, the leading-order dynamics reduces to (3.10) with $\overline{\eta_0^2} = 0$. Conversely, the fluctuations can have finite amplitude *only* if $\sigma = 0$; i.e, only if the fluctuations are *marginally stable*. Although σ initially need not equal zero, it continuously evolves under the forcing of the slow field and may eventually pass through zero. Heuristically, the persistence of one or more zero eigenvalues may be understood by recognizing that (i) Θ_0 is not an arbitrary function of x owing to the feedback from the fluctuations, and (ii) scale-separated

quasilinear systems with unstable fast fluctuations must self-tune to a state of near marginal stability. Indeed, as we demonstrate through this example, it is this regime that characterizes the long-term dynamics of the forced system.

Thus, if the largest eigenvalue σ_0 differs from zero, then the prescription is made that the modal amplitude $A = 0$. If, however, $\sigma_0 = 0$, then the coupled system (3.10)–(3.11) is not closed on the slow time scale: a slow evolution equation for $A(T)$ is required. In the next two subsections, we show how to derive such an equation. Although we enforce $\sigma = 0$ in the following analysis, we formally retain σ_0 explicitly in the derivation for clarity and generality of exposition. Since ϕ is constant for $\sigma = 0$, the amplitude A can be re-defined so that the leading-order fluctuation field

$$\eta_0(x, \phi, T) = A(T)\hat{\eta}_0(x, T) \tag{3.14}$$

and, accordingly, the fast-time average $\overline{\eta_0^2} = A^2\hat{\eta}_0^2$. The leading-order system therefore becomes

$$(-\sigma_0 + \Theta_0)\,\hat{\eta}_0 + \frac{\partial^2\hat{\eta}_0}{\partial x^2} = 0, \tag{3.15}$$

$$\frac{\partial\Theta_0}{\partial T} = P - \nu\Theta_0 - A(T)^2\hat{\eta}_0^2. \tag{3.16}$$

(c) Solvability condition

As in Sec. 2.(c), the eigenvalue problem (3.15) can be cast into the form $\mathcal{L}\hat{\eta}_0 = 0$, now with $\mathcal{L} = -\sigma_0 + \Theta_0 + \partial_x^2$. As a result of periodicity, the linear operator $\mathcal{L}$ is self-adjoint with the inner product defined in (2.16); i.e.,

$$(\mathcal{L}f, g) = \int_0^L g(x)(-\sigma_0 + \Theta_0 + \partial_x^2)f(x)\mathrm{d}x = \int_0^L f(x)(-\sigma_0 + \Theta_0 + \partial_{xx})g(x)\mathrm{d}x = (f, \mathcal{L}g). \tag{3.17}$$

This inner product is used to disentangle A and $\hat{\eta}_0$ by imposing $(\hat{\eta}_0, \hat{\eta}_0) = 1$; that is,

$$\int_0^L \hat{\eta}_0^2\mathrm{d}x = 1. \tag{3.18}$$

Guided by the analysis of the wave system, we first attempt to derive a slow-evolution equation for the amplitude A through the "usual procedure" introduced in Sec. 2 (d); namely, by ensuring that the higher-order fluctuation equations are solvable. Specifically, collecting terms at $O(1)$ in (3.6) leads to

$$\mathcal{L}\eta_1 = F, \qquad F = \frac{\partial\eta_0}{\partial T} - \Theta_1\eta_0 + \eta_0^3 = \left(\frac{\mathrm{d}A}{\mathrm{d}T} - A\Theta_1 + A^3\hat{\eta}_0^2\right)\hat{\eta}_0 + A\frac{\delta\hat{\eta}_0}{\delta T}, \tag{3.19}$$

where $\delta/\delta T = (\partial_T\Theta_0)\delta/\delta\Theta_0$. Forming the inner product of (3.19) with $\hat{\eta}_0$, we find that $(\mathcal{L}\eta_1, \hat{\eta}_0) = (\eta_1, \mathcal{L}\hat{\eta}_0) = 0$ and, hence, that $(F, \hat{\eta}_0) = 0$. Noting that the integral involving the functional derivative in $(F, \hat{\eta}_0)$ vanishes as a result of the normalization condition, we obtain

$$\frac{1}{A}\frac{\mathrm{d}A}{\mathrm{d}T} + A^2\int_0^L \hat{\eta}_0^4\mathrm{d}x = \int_0^L \Theta_1\hat{\eta}_0^2\mathrm{d}x. \tag{3.20}$$

In the wave problem, two solvability conditions emerge from the equation for η_1: a closure, (2.24), required to evolve the dynamics of the correction fields ω_1, η_1, and c_1 and an amplitude equation, (2.26), prescribing $\mathrm{d}A/\mathrm{d}T$ as a function of the leading-order variable ω_0. In contrast, in the present problem, only the single constraint (3.20), relating the time evolution of A to the *higher-order* field Θ_1, is obtained. To procure a closed set of equations, it is natural to attempt to include Θ_1 in the set of unknown fields. An equation for Θ_1 can be derived from (3.5) at $O(\epsilon)$, yielding $\partial_T\Theta_1$ as a function of η_0 and, disappointingly, of η_1, another unknown variable. Thus, similarly to (2.24), (3.20) is merely a constraint required to obtain the dynamics of the correction fields η_1 and Θ_1.

(d) Slow evolution of the growth rate

In this example, a suitable constraint on the amplitude A can be derived by employing an operation analogous to that performed (solely for illustrative purposes) in Sec. 2(e). Specifically, we differentiate the leading-order fluctuation equation (3.15) with respect to T, yielding

$$\mathcal{L}\frac{\delta\hat{\eta}_0}{\delta T} = \hat{\eta}_0\left(\frac{\mathrm{d}\sigma_0}{\mathrm{d}T} - \frac{\partial\Theta_0}{\partial T}\right). \tag{3.21}$$

A solvability condition is obtained by taking the inner product of (3.21) with $\hat{\eta}_0$, again utilizing the normalization condition on $\hat{\eta}_0$; *viz.*,

$$\frac{\mathrm{d}\sigma_0}{\mathrm{d}T} = \int_0^L \hat{\eta}_0^2\left(\frac{\partial\Theta_0}{\partial T}\right)\mathrm{d}x. \tag{3.22}$$

Upon substituting (3.16) into (3.22), this solvability condition reduces to

$$\frac{\mathrm{d}\sigma_0}{\mathrm{d}T} = \int_0^L \left(P - \nu\Theta_0 - A(T)^2\hat{\eta}_0^2\right)\hat{\eta}_0^2\,\mathrm{d}x \equiv \alpha - \beta A(T)^2, \tag{3.23}$$

where the real coefficients α and β are defined by

$$\alpha = \int_0^L (P - \nu\Theta_0)\hat{\eta}_0^2\,\mathrm{d}x, \qquad \beta = \int_0^L \hat{\eta}_0^4\,\mathrm{d}x. \tag{3.24}$$

Equation (3.23) prescribes the slow evolution of σ_0 as a function of the variables Θ_0 and $\hat{\eta}_0$ and, crucially, of the fluctuation amplitude A. Since, for non-zero A, σ_0 must be zero, the consistency of the multiple scales expansion excludes strictly positive values of $\mathrm{d}\sigma_0/\mathrm{d}T$, which would immediately lead to positive growth rates; i.e., to exponentially-growing fluctuations. This scenario arises only when $\alpha > 0$ and $\sigma_0 = 0$, in which case the amplitude $A(T)$ must be set to enforce $\mathrm{d}\sigma_0/\mathrm{d}T = 0$:

$$A(T) = \sqrt{\frac{\alpha}{\beta}} \quad \text{if } \sigma_0 = 0 \text{ and } \alpha > 0. \tag{3.25}$$

Equation (3.25) describes the effectively instantaneous (on the slow time scale) saturation of the instability via the feedback of the fluctuation field η_0 on the slow variable Θ_0.

(e) Numerical implementation

To demonstrate the efficacy of the proposed multi-scale algorithm, DNS of the governing equations (3.1)–(3.2) are compared to simulations of the multiple scales reduction given by (3.15), (3.16), and (3.25). All simulations are performed in a domain of size $L = 2\pi$ that is discretized with 32 grid points. The damping coefficient $\nu = 1$, and the external forcing

$$P = 1 + \frac{1}{2}\Big(\cos(t)\cos(x) + \sin(0.6t)\cos(2x)\Big). \tag{3.26}$$

A second-order Runge–Kutta time-stepping scheme is used with fixed time step $\mathrm{d}t = 0.01$ for the reduced model and $\mathrm{d}t = 0.005$ for the DNS. In the DNS, the governing equations (3.1)–(3.2) are solved using a Fourier pseudospectral method for $\epsilon = \{0.1, 0.01\}$, while the reduced equations (valid as $\epsilon \to 0$) are discretized using Chebyshev polynomials on a non-uniformly spaced grid. For simulations of the reduced system, only the mean equation (3.16) is explicitly evolved in time (recall that $T = t$). At every slow timestep, however, the eigenvalue problem (3.15) is solved to obtain σ_0 and $\hat{\eta}_0$. Finally, the amplitude of the fluctuations A is set according to

$$A(T) = \left\{ \begin{array}{ll} 0 & \text{if } \sigma_0 < 0 \text{ or } \alpha < 0, \\ \sqrt{\alpha/\beta} & \text{otherwise,} \end{array} \right\} \tag{3.27}$$

where the slowly-varying coefficients α and β have been defined in (3.24).

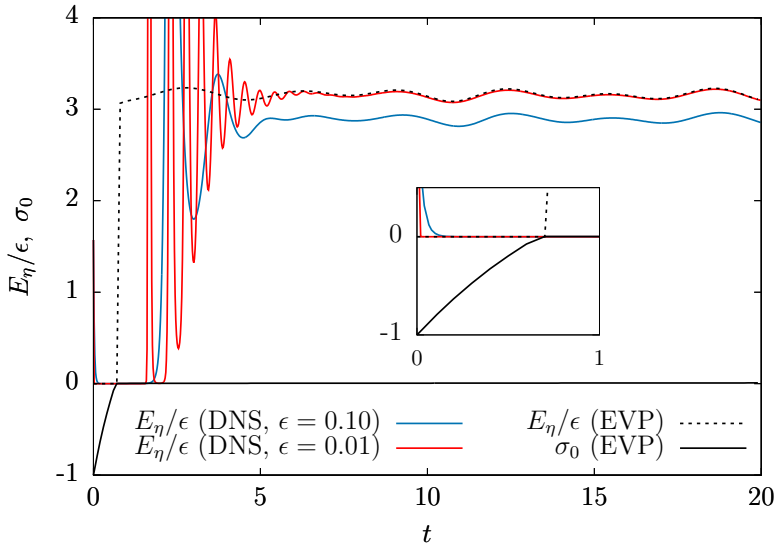

Figure 2. Normalized energy of the fluctuations E_η/ϵ computed from direct numerical simulations (DNS) for $\epsilon = \{0.1, 0.01\}$ and from a novel multiple scales algorithm in which the fluctuations are not time-evolved but computed from the solution to an eigenvalue problem (EVP). The maximum instantaneous growth rate, σ_0, obtained from the solution to the EVP is also reported.

As evident in Fig. 2, this procedure prevents σ_0 from becoming positive, thereby constraining the system to evolve along a marginal stability manifold. In practice, discretization and round-off errors preclude σ_0 from identically equalling zero. Accordingly, for the results reported here, a tolerance of 0.01 has been enforced: $0 \leq \sigma_0 \leq 0.01$. (Smaller tolerances can be achieved by decreasing the time step $\mathrm{d}t$). The time series of the normalized fluctuation energy (half the norm of η),

$$\frac{E_\eta}{\epsilon} = \int_0^L \frac{\eta^2}{2} \mathrm{d}x, \tag{3.28}$$

is also plotted in this figure. (Although not plotted here, space–time diagrams of both η and Θ can be generated using the source files provided as supplementary material.) Excellent agreement between the DNS and the reduced model is observed for $\epsilon \simeq 0.01$ *after* a transient that persists for a few slow time units. This "bursting" regime, evident in the DNS, is very sensitive to the initialization of the fluctuations, because the amplitude of the fluctuations is extremely small when positive growth rates are first attained. (Recall that, before this instant, the fluctuations experience approximately exponential decay.) This transient is absent from the reduced model, since the energy of the fluctuations is instantaneously adjusted to a finite value once a state with zero growth rate is reached.

(f) Additional comments

The multiple scales analysis described in this section applies to QL systems in which fluctuations have the potential to be amplified via a linear instability mechanism. These systems may have other attributes that warrant further discussion, as detailed below.

(i) Oscillatory instabilities

The key requirement of the algorithm – tuning the amplitude of the fluctuations to prevent their exponential growth – results from the possibility that the *real* part of the growth rate σ could become positive, regardless of the value and sign of the imaginary part. For the system analyzed

in this section, the imaginary part of the growth rate is strictly zero; i.e., the instability is stationary. Nevertheless, a similar procedure can be applied when a bifurcation gives rise to an oscillatory instability, as, for instance, can occur in the following modified system:

$$\frac{\partial \Theta}{\partial t} = P - \nu\Theta + \nu\frac{\partial^2 \Theta}{\partial x^2} - \epsilon^2 \left(\frac{\partial \eta}{\partial t}\right)^2, \qquad \Theta(x,0) = -1, \tag{3.29}$$

$$\epsilon^2 \frac{\partial^2 \eta}{\partial t^2} = \epsilon\Theta\frac{\partial \eta}{\partial t} + \frac{\partial^2 \eta}{\partial x^2}, \qquad \eta(x,0) = \cos\left(\frac{2\pi x}{L}\right), \ \frac{\partial \eta}{\partial t}(x,0) = 0. \tag{3.30}$$

In this example, (3.30) describes fast oscillatory motions (waves) of frequency $O(1/\epsilon)$ that are either damped or exponentially amplified by the slow field Θ. Generally, the growth rate σ is complex, but the amplitude of the fluctuations must be set, in the multiple scales analysis, by the requirement that the real part of σ should not increase once a state of marginal stability is reached.

(ii) Stabilizing nature of the fluctuation-induced feedback

Omitting the subscript '0', the time-derivative of the (real) growth rate σ obtained in (3.23) is given by

$$\frac{\mathrm{d}\sigma}{\mathrm{d}T} = \alpha - \beta A(T)^2, \tag{3.31}$$

where, again, T is the slow time variable, A is the amplitude of the fluctuations, and α and β are two real parameters. The multiple scales approach developed in this section only applies if $\beta > 0$, regardless of the value of α. (If $\alpha > 0$ and $\sigma = 0$, then $A = \sqrt{\alpha/\beta}$; otherwise $A = 0$). That is, the fluctuations must provide a *restoring* force, not drive the slow field toward an even more unstable state. Although $\beta > 0$ in the model analyzed here, see (3.24), this property is not generic; a slight modification of the set of equations (3.1)–(3.2) provides a counter-example:

$$\frac{\partial \Theta}{\partial t} = P - \nu\Theta - \eta^2 e^{-\Theta^2}, \tag{3.32}$$

$$\epsilon\frac{\partial \eta}{\partial t} = \Theta\eta e^{-\Theta^2} + \frac{\partial^2 \eta}{\partial x^2} - \epsilon\eta^3. \tag{3.33}$$

An analysis similar to that applied to (3.1)–(3.2) confirms that, for small values of ϵ, this system is of multi-scale QL form. The corresponding expression for β, however, is modified,

$$\beta = \int_0^L \hat{\eta}_0^4 \,\mathrm{d}x \Rightarrow \beta = \int_0^L \hat{\eta}_0^4 (1 - 2\Theta_0^2) e^{-2\Theta_0^2} \,\mathrm{d}x, \tag{3.34}$$

so that, crucially, β is no longer sign-definite. In the scenario $\sigma = 0$, $\alpha > 0$, and $\beta < 0$, the fluctuations cannot prevent positive values of the growth rate from being realized, thereby invalidating the posited asymptotic scalings. In fact, the resulting exponential growth would be saturated by the nonlinear term in (3.33) by a physical process not captured by the QL system. Nevertheless, asymptotic methods still can be applied to this regime via a suitable rescaling of the unknowns:

$$\sigma(T) = \sigma_0(T) + \epsilon\sigma_1(T) + O(\epsilon^2) \tag{3.35}$$

$$\Theta(x,\phi,T) = \Theta_0(x,\phi,T) + \epsilon\Theta_1(x,\phi,T) + O(\epsilon^2), \tag{3.36}$$

$$\eta(x,\phi,T) = \frac{\eta_0(x,\phi,T)}{\sqrt{\epsilon}} + \sqrt{\epsilon}\eta_1(x,\phi,T) + O(\epsilon\sqrt{\epsilon}). \tag{3.37}$$

With these expansions, the following set of equations is obtained at leading order in ϵ:

$$\sigma_0\frac{\partial \Theta_0}{\partial \phi} = -\eta_0^2 e^{-\Theta_0^2}, \tag{3.38}$$

$$\sigma_0\frac{\partial \eta_0}{\partial \phi} = \Theta_0\eta_0 e^{-\Theta_0^2} + \frac{\partial^2 \eta_0}{\partial x^2} - \eta_0^3, \tag{3.39}$$

where the leading-order growth rate σ_0 is still defined by the *linear* eigenvalue problem obtained from (3.39) without the nonlinear term. Thus, in this regime, the system evolves strictly on the fast time scale, with the dynamics taking the form of punctuated bursting. The asymptotic analysis also reveals that, in this regime, the slow external forcing P and damping $-\nu\Theta_0$ do not contribute to the leading-order dynamics. Numerically, both (3.38) and (3.39) must be co-evolved on the fast time scale until σ_0 reaches zero again, and the dynamics relaxes to a slow manifold describable by the asymptotic QL reduction.

(iii) Degeneracy of the marginal eigenvalue

Our last point concerns the assumption, implicitly made throughout this section, that the eigenvalue problem (3.15) has non-degenerate eigenvalues, at least for the eigenvalue having the largest growth rate (i.e., $\sigma = 0$ is a simple eigenvalue), in accord with the ansatz (3.12). In fact, the non-degeneracy of the leading eigenvalue can be demonstrated for this particular eigenvalue problem. Consider (3.15), and rewrite the variables as follows,

$$\hat{\eta}_0 \to \Psi, \qquad \sigma_0 \to -E, \qquad \Theta_0 \to -V. \tag{3.40}$$

Equation (3.15) then becomes

$$E\Psi = H\Psi, \qquad H = -\frac{\partial^2}{\partial x^2} + V, \tag{3.41}$$

subject to periodic boundary conditions. Thus, the eigenvector of largest growth rate σ_0 formally is equivalent to the ground state of the one-dimensional stationary Schrödinger equation, which is provably non-degenerate [17]. This property, however, clearly is very specific. More generally, it may be necessary to consider two (or more) independent marginal modes, each having its own amplitude. In this scenario, the corresponding number of equations describing the slow-time evolution of each associated growth rate can be derived, and the algorithm described in this section adapted accordingly.

4. Conclusion

Multiple scales analysis is usually introduced to capture the dynamics of a single variable or field evolving over disparate (spatio-)temporal scales. Canonical examples arise in the study of ordinary differential equations governing nonlinear oscillators (e.g., the van der Pol oscillator) and of partial differential equations governing nonlinear waves (e.g., the Korteveg-de-Vries equation). Quasilinear (QL) partial differential equations constitute an important class of dynamical systems that requires a generalization of this approach to treat two (or more) tightly coupled fields evolving on different time scales.

Most (if not all) multi-scale QL systems can be categorized into one of the two model systems analyzed in this article. For systems involving wave/mean-flow interactions, and more generally for any QL system in which the fluctuations are slowly modulated waves, an amplitude equation can be derived by imposing an appropriate solvability condition on the dynamics of the correction fields. As is well known [18,19], the amplitude equation reduces to the conservation of wave action if neither dissipation nor external forcing acts directly on the waves, in which case there exist complementary and, arguably, more elegant mathematical approaches – including the generalized Lagrangian mean formalism [15,20] and variational-based Hamiltonian methods [21,22] – to derive the appropriate conservation law(s) for the slow dynamics. Nevertheless, these alternative methods cannot readily incorporate forcing and dissipation, which are naturally and straightforwardly included in the methodology presented here. Moreover, the tight coupling between the wave and mean (e.g., celerity) fields renders our non-variational approach non-standard, as evidenced by the occurrence of *functional derivatives* in the coefficients arising in the amplitude equation that account for changes in the leading-order wave eigenfunction resulting from the slow evolution of the leading-order mean field; nevertheless, these functional derivatives can be explicitly evaluated, so that costly sensitivity analyses are not required.

For many QL systems, particularly those arising in the modeling of spatially anisotropic turbulent shear flows (e.g., in wall-bounded engineering flows and in geo- and astrophysical turbulence [8–12]), the fluctuations can exhibit various forms of dynamical instability. Generically, the QL reduction for such systems is only valid in the limit in which there is temporal scale separation and, in this limit ($\epsilon \to 0$ in our notation), the fluctuations can grow (or decay) exponentially on the fast time scale. Importantly, for these systems, any attempt to derive an amplitude equation for the slow evolution of the fluctuations by employing the "usual" multiple scales approach (i.e., seeking a solvability condition by examining the equations for the correction fields) *fails*, instead merely providing closures needed for evaluation of the corrections fields, should they be desired. A primary contribution of the present article is the introduction of a new multiple scales formalism that is applicable to QL systems that exhibit dynamically-unstable fluctuation fields. The essential point is that the slowly-evolving amplitude of the fluctuations must be instantaneously prescribed – i.e., slaved to the slow mean field(s) – to prevent positive growth rates from being realized once a state of marginal stability is attained. In ongoing work, we are applying this new formalism to strongly stratified turbulent shear flows.

We conclude by emphasizing that multiple scales analysis can yield a sizable improvement in computational efficiency, as the time step employed by the numerical time-integrator can be increased from a fraction of a fast-time unit to a fraction of a slow-time unit. Clearly, this reduction in computational expense is crucial for the study of several realistic physical systems exhibiting strong scale separation. (In the quasi-biennial oscillation, for instance, the slow and fast time scales are separated by five orders of magnitude!) Even for systems in which the scale separation is less extreme, QL models have proven useful in many applications [9,12,23–26]. We emphasize that when dynamical instabilities are possible these QL systems *must* self-tune toward a state of marginal stability, at least in a statistical (i.e., time-averaged) sense. Thus, the analysis and algorithm developed in Sec. 3 should prove valuable even for modest values of ϵ.

Data Accessibility. All data included in this article can be generated from the Python codes provided as supplementary material.

Authors' Contributions. GM and GPC conceived the mathematical models, interpreted the results, and wrote the paper. GM performed the numerical simulations. Both authors gave final approval for publication.

Competing Interests. We declare we have no competing interests.

Funding. This research was supported in part by the National Science Foundation under Grant No. NSF PHY-1748958.

Acknowledgements. The authors are grateful to S. Tobias, C. Doering, and K. Julien for fruitful discussions, and acknowledge the hospitality of the Kavli Institute for Theoretical Physics at the University of California, Santa Barbara, where much of this research was completed.

References

1. Lindzen RS, Holton JR. 1968 A theory of the quasi-biennial oscillation. *J. Atmos. Sci.* **25**, 1095–1107.
2. Plumb RA. 1977 The interaction of two internal waves with the mean flow: Implications for the theory of the quasi-biennial oscillation. *J. Atmos. Sci.* **34**, 1847–1858.
3. Plumb RA, McEwan AD. 1978 The instability of a forced standing wave in a viscous stratified fluid: A laboratory analogue of the quasi-biennial oscillation. *J. Atmos. Sci.* **35**, 1827–1839.
4. Dreeben TD, Chini GP. 2011 Two-dimensional streaming flows in high-intensity discharge lamps. *Phys. Fluids* **23**, 056101.
5. Chini GP, Malecha Z, Dreeben TD. 2014 Large-amplitude acoustic streaming. *J. Fluid Mech.* **744**, 329–351.
6. Michel G, Chini GP. 2018 Strong wave–mean-flow coupling in baroclinic acoustic streaming. *J. Fluid Mech.* **858**, 536–564.
7. Karlsen JT, Qui W, Augustsson P, Bruus H. 2018 Acoustic streaming and its suppression in inhomogeneous fluids. *Phys. Rev. Lett.* **120**, 054501.

8. Bouchet F, Nardini C, Tangarife T. 2013 Kinetic theory of jet dynamics in the stochastic barotropic and 2D Navier–Stokes equations. *J. Stat. Phys.* **153**, 572–625.
9. Tobias S, Marston JB. 2013 Direct statistical simulation of out-of-equilibrium jets. *Phys. Rev. Lett.* **110**, 104502.
10. Rocha C. 2015 Coupled reduced equations for strongly stratified flows. In Woods Hole Oceanographic Institution Technical Report, WHOI-2016-05
11. K. Julien 2018, private communication. See also: Nieves D, Grooms I, Julien K, Weiss JB. 2016 Investigations of non-hydrostatic, stably stratified and rapidly rotating flows. *J. Fluid Mech.* **801**, 430–458.
12. Squire J, Bhattacharjee A. 2015 Statistical simulation of the magnetorotational dynamo. *Phys. Rev. Lett.* **114**, 085002.
13. See the entry in the Astrophysical Source Code Library, http://ascl.net/1603.015, and the Dedalus project homepage http://dedalus-project.org.
14. See, e.g., Hinch EJ. 1991 *Perturbation methods*, Cambridge University Press; Bender CM, Orszag SA. 1999 *Advanded Mathematical Methods for Scientists and Engineers*, Springer–Verlag New-York; or Nayfeh AH. 2008 *Perturbation Methods*, John Wiley & Sons.
15. Andrews DG, Mcintyre ME. 1978 On wave–action and its relatives. *J. Fluid Mech.* **89** (4), 647–664.
16. Herring JR. 1963 Investigation of problems in thermal convection. *J. Atmos. Sci.* **20**, 325–338.
17. See, e.g., item 21 of Landau LD, Lifshitz EM. 1958 *Quantum Mechanics*, 2nd edition, Pergamon Press.
18. Kruskal M. 1962 Asymptotic theory of Hamiltonian and other systems with all solutions nearly periodic. *J. Math Phys.* **3**, 806–828 .
19. Kuzman GE. 1959 Asymptotic solutions of nonlinear second-order differential equations with variable coefficients. *J. Appl. Math. Mech.* **23**, 730–744.
20. Bühler O. 2009 *Waves and Mean Flows*, Cambridge University Press.
21. Whitham GB. 1974 *Linear and Nonlinear Waves*, John Wiley & Sons.
22. Salmon R. 1998 *Lectures on Geophysical Fluid Dynamics*, Oxford University Press.
23. Thomas VL, Lieu BK, Jovanović MR, Farrell BF, Ioannou PJ, Gayme DF. 2014 Self-sustaining turbulence in a restricted nonlinear model of plane Couette flow. *Phys. Fluids A* **26**, 105112.
24. Bretheim JU, Meneveau C, Gayme DF. 2015 Standard logarithmic mean velocity distribution in a band-limited restricted nonlinear model of turbulent flow in a half-channel. *Phys. Fluids* **27**, 011702.
25. Tobias SM, Marston JB. 2017 Three-dimensional rotating Couette flow via the generalised quasilinear approximation. *J. Fluid Mech.* **810**, 412–428.
26. Pausch M, Yang Q, Hwang Y, Eckhardt B. 2019 Quasilinear approximation for exact coherent states in parallel shear flows. *Fluid Dyn. Res.* **51**, 011402.

Exploiting self-organized criticality in strongly stratified turbulence

Gregory P. Chini[1,2]†, Guillaume Michel[3], Keith Julien[4], Cesar B. Rocha[5], and Colm-cille P. Caulfield[6]

[1]Program in Integrated Applied Mathematics, University of New Hampshire, Durham, NH 03824, USA

[2]Department of Mechanical Engineering, University of New Hampshire, Durham, NH 03824, USA

[3]Institut Jean Le Rond d'Alembert, Sorbonne Université, CNRS, UMR 7190 Paris, F-75005, France

[4]Department of Applied Mathematics, University of Colorado, Boulder, CO 80309, USA

[5]Department of Marine Sciences, University of Connecticut, Storrs, CT 06269, USA

[6]BP Institute and Department of Applied Mathematics & Theoretical Physics, Cambridge University, Cambridge, CB3 0WA UK

(Received xx; revised xx; accepted xx)

A multiscale reduced description of turbulent free shear flows in the presence of strong stabilizing density stratification is derived via asymptotic analysis of the Boussinesq equations in the simultaneous limits of small Froude and large Reynolds numbers. The analysis explicitly recognizes the occurrence of dynamics on disparate spatiotemporal scales, yielding simplified partial differential equations governing the coupled evolution of slow large-scale hydrostatic flows and fast small-scale isotropic instabilities and internal waves. The dynamics captured by the coupled reduced equations is illustrated in the context of two-dimensional strongly stratified Kolmogorov flow. A noteworthy feature of the reduced model is that the fluctuations are constrained to satisfy quasilinear (QL) dynamics about the comparably slowly-varying large-scale fields. Crucially, this QL reduction is not invoked as an *ad hoc* closure approximation, but rather is derived in a physically relevant and mathematically consistent distinguished limit. Further analysis of the resulting slow-fast QL system shows how the amplitude of the fast stratified-shear instabilities is slaved to the slowly-evolving mean fields to ensure the marginal stability of the latter. Physically, this marginal stability condition appears to be compatible with recent evidence of self-organized criticality in both observations and simulations of stratified turbulence. Algorithmically, the slaving of the fluctuation fields enables numerical simulations to be time-evolved strictly on the slow time scale of the hydrostatic flow. The reduced equations thus provide a solid mathematical foundation for future studies of three-dimensional strongly stratified turbulence in extreme parameter regimes of geophysical relevance and suggest avenues for new sub-grid-scale parameterizations.

1. Introduction

Strongly stratified turbulent flows occur routinely both in the natural and built environment. In many geoscientific and technological applications, these flows exert a controlling influence on the turbulent mixing of buoyancy, momentum and mass, yet numerous fundamental questions concerning the structure and mechanics of stratified

† Email address for correspondence: greg.chini@unh.edu

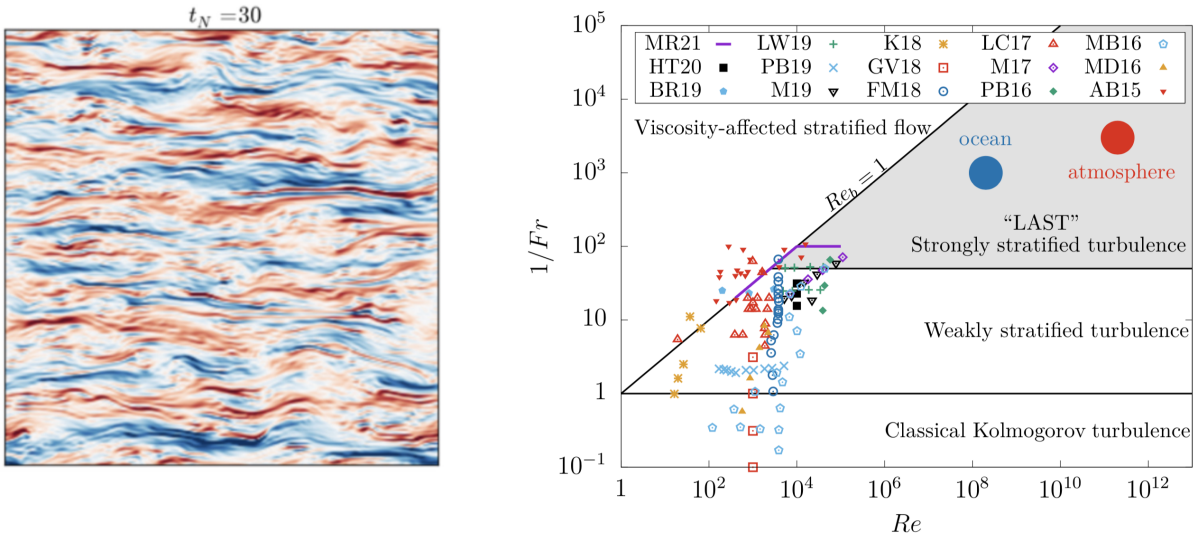

FIGURE 1. Physical attributes and parameter regime characterizing stratified turbulence. (a) Snapshot of the vorticity field in a freely-decaying two-dimensional (2D) DNS of the Boussinesq equations (in a doubly-periodic horizontal/vertical domain) for $Pr = 1$, $Fr = 0.02$ and $Re = 5 \times 10^5$ after 30 buoyancy time units $2\pi/N$ (i.e. $t_N = 30$), where N is the constant buoyancy frequency, initialized with a random vorticity field having a von-Karman-like spectrum. Note the emergence of highly anisotropic layers, with horizontal scales L much greater than their vertical thickness h, coexisting with small-scale, roughly isotropic variability suggestive of Kelvin–Helmholtz overturns. (b) Regime diagram adapted from Brethouwer et al. (2007). The 2D DNS and reduced multiscale simulations performed in the present work lie along the purple solid line, and typical values for the upper ocean and middle atmosphere are taken from Moum (1996) and Lindborg (2006). DNS published during the past six years are also reported: 'HT20' (Howland et al. 2020), 'BR19' (de Bruyn Kops and Riley 2019), 'LW19' (Lang and Waite 2019), 'PB19' (Portwood et al. 2019), 'M19' (Maffioli 2019), 'K18' (Khani 2018), 'GV18' (Garanaik and Venayagamoorthy 2018), 'FM18' (Feraco et al. 2018), 'LC17' (Lucas and Caulfield 2017), 'M17' (Maffioli 2017), 'PB16' (Portwood et al. 2016), 'MB16' (Maffioli et al. 2016), 'MD16' (Maffioli and Davidson 2016), 'AB15' (Augier et al. 2015). Note that there is slight variability in the precise definitions of both Fr and Re for certain data collected in this regime diagram and that there are not sharp transitions among the various regimes.

mixing in extreme parameter regimes remain open. Owing to the spontaneous emergence of both small-aspect-ratio hydrostatic flow structures having large horizontal scales and roughly isotropic, non-hydrostatic small-scale instabilities and waves (see figure 1*a*), an enormous range of spatiotemporal scales must be resolved. This scale disparity renders measurements and direct numerical simulations (DNS) of such strongly stratified turbulence, referred to as the *layered anisotropic stratified turbulence* (LAST) regime by Falder et al. (2016), especially challenging. In the oceans and atmosphere, for example, non-rotating stratified turbulence is considered to be the prevailing dynamics on horizontal length scales L smaller than that of the large-scale rotationally-constrained (quasi-geostrophic) flow and greater than the Ozmidov scale $L_O \equiv \sqrt{\epsilon_h/N^3}$, below which buoyancy forces are negligible. Here, ϵ_h and N are the turbulent kinetic energy dissipation rate and the buoyancy frequency, respectively. Presuming that $\epsilon_h \sim U^3/L$, where U is a horizontal velocity characterizing motions at horizontal scale L, it is straightforward to show that the ratio $L/L_O = O(Fr^{-3/2})$, where the (horizontal) Froude number $Fr \equiv U/(NL)$. Thus, in the limit of strong stratification, a large range of scales must be resolved. Indeed, when the Ozmidov scale is much larger than the Kolmogorov scale, two inertial ranges in principle must be captured. Collectively, these attributes render DNS of strongly stratified turbulence arduous even with state-of-the-art supercomputing power.

Away from boundaries and for fixed $O(1)$ Prandtl number Pr, stratified turbulence is governed by two external control parameters: the Froude number Fr and the Reynolds number $Re \equiv UL/\nu$, where ν is the kinematic viscosity. The challenges associated with accessing the LAST regime in the laboratory or via DNS of the governing Boussinesq equations are aptly described by Brethouwer et al. (2007). In particular, figure 1*b*, an adaptation of their regime diagram, confirms that recent DNS (i.e. simulations documented in the past six years employing algorithms devoid of hyperviscosity or any other *ad hoc* small-scale modeling) have been performed in a parameter regime orders of magnitude away from that characterizing the LAST regime of strongly stratified turbulence as it is believed to occur in the oceans and atmosphere, where $Re > 10^8$ and $Fr < 10^{-3}$ (based on 'outer' turbulence scales). Bartello and Tobias (2013) estimate that to employ DNS to settle a variety of fundamental scientific questions regarding the dynamics of strongly stratified turbulence would require the ratio of the maximum to minimum resolvable scale to be in the millions (i.e. in a single coordinate direction), yielding a formidable computational challenge. These questions include, for example, what is the mixing efficiency of strongly stratified turbulence in the LAST regime in the small-Fr, large-Re limit? Is this efficiency dependent upon the precise way in which these limits are taken? Does the resulting efficiency depend on the details of the initial stratification? Is the horizontal spectrum of horizontal kinetic energy independent of Fr as $Fr \to 0$ with $Re > 10/Fr^2$, as conjectured by some previous investigators (Lindborg 2006)? What is the physical origin of the tendency for strongly stratified turbulence to exhibit attributes of self-organized criticality (Smyth and Moum 2013; Holleman et al. 2016; Salehipour et al. 2018; Smyth et al. 2019)? To date, these and other important questions have not been conclusively answered.

In contrast to DNS, regional oceanic and atmospheric numerical circulation models do not attempt to resolve the small-scale dynamics of stratified mixing. Indeed, the fluid dynamical core of these computational models generally comprises the so-called *hydrostatic* primitive equations (Miller 2007; Klein 2010). Nevertheless, small-scale non-hydrostatic stratified mixing events—often although not exclusively associated with the breakdown of internal waves (Legg 2021; MacKinnon et al. 2017)—ultimately exert strong feedbacks on the resolved large-scale flow, particularly to close the global buoyancy budget (Ferrari and Wunsch 2004; Gregg et al. 2018); therefore, suitable parameterizations must be developed and implemented. Generally, these parameterizations are physically motivated but ultimately *ad hoc* and thus raise the attendant issues over robustness, accuracy and reliability. For ocean simulations, for example, Gregg et al. (2018) recently concluded that a constant mixing efficiency equal to 0.2 should continue to be used as a parametrization until a better understanding of stratified turbulence is achieved, despite significant discrepancies with *in situ* measurements of stratified mixing. (See Monismith et al. (2018) for an additional description of strongly stratified turbulence field data.) Even the sub-grid scale (SGS) models employed in large-eddy simulations (LES) are notoriously suspect in strongly stratified turbulence owing to the high degree of anisotropy of the dominant flow structures and the complex patterns of backscatter of energy from small to large scales. The recent numerical study by Khani (2018) has shown that, even for dimensionless parameters orders of magnitude different from those realised in nature, the mixing efficiency obtained from LES agrees with that computed from fully resolved DNS only when the spatial discretization used in the LES is comparable to or smaller than L_O. Consequently, LES must resolve a scale separation that is at least $O(Fr^{-3/2})$ to be reliable.

One intriguing aspect of strongly stratified turbulence is its tendency to exhibit aspects of *self-organized criticality*, particularly the condition of marginal stability. Indeed,

mounting evidence suggests an apparent connection between the gradient Richardson number observed in statistically-steady (or at least slowly-varying) stratified turbulence and the celebrated Miles–Howard criterion for linear instability of inviscid *laminar* stratified shear flows. For example, Smyth and Moum (2013) analyzed five years of data taken from the upper 150 meters of the eastern equatorial Pacific Ocean; their analysis clearly shows that in a depth range from 20 to 80 meters, in which diurnally-cycling stratified turbulence is evident, the probability density function (pdf) of the measured gradient Richardson number peaks at a value very close to 1/4. The authors argue that these measurements indicate deep-cycle stratified turbulence in the equatorial Pacific Ocean occurs about a mean state that is close to marginally stable and that the phenomenon is an example of self-organized critical behavior. Further discussion is provided by Smyth et al. (2019). Similarly, the field measurements of Holleman et al. (2016) in a salt-stratified estuary (the Connecticut River) show that, away from the river bottom, the tidally-driven, quasi-steady stratified turbulence is characterized by a median gradient Richardson number equal to 0.25. Perhaps the most compelling evidence to date of the potential for strongly-stratified turbulence to exhibit self-organized criticality is provided by Salehipour et al. (2018), who carried out DNS of stratified free shear layers in which there is a region of substantially enhanced density gradient embedded within the shear zone. Under these conditions, stratified turbulence is engendered by the breakdown of Holmboe instability waves. The authors show that this instability drives long-lived, quasi-stationary turbulent mixing events for which the pdf of the instantaneous, horizontally-averaged gradient Richardson number again has a maximum very close to 0.25. Although not of central relevance to the present investigation, Salehipour et al. (2018) also demonstrate that the resulting stratified turbulence exhibits other aspects of self-organized criticality, including scale-invariant 'avalanches' of small-scale turbulence. The authors argue that the emergence of a mean turbulence state with a gradient Richardson number approximately equal to one-quarter is not coincidental but instead is inherently connected to the intrinsic self-regulation of the strongly-stratified flow dynamics.

In this study, we develop a systematically simplified mathematical framework for theoretical and computational investigations of strongly stratified free shear flows that enables simulations in extreme parameter regimes of physical relevance while largely ameliorating the need for phenomenological modeling. Our approach is inspired by the work of Julien and Knobloch (2007), who demonstrate that multiple-scales asymptotic analysis can be used to derive reduced equations for turbulent flows subjected to external constraints such as rapid system rotation or a strong magnetic field. Heuristically, the strong constraint inhibits mode coupling in particular spatial directions and is associated with the emergence of highly anisotropic flow structures (e.g. turbulent Taylor columns in the rapid rotation scenario). Mathematically, particular dominant balances of terms in the governing equations (e.g. geostrophic balance) arise in extreme parameter regimes, and reduced equations can be derived by systematically perturbing about this balanced state.

In our work, the turbulence is strongly constrained by the imposed stabilizing stratification, but the Reynolds number is sufficiently large that the laminar state can be destabilized. We exploit this constraint to derive in the physically-relevant asymptotic limits of small Froude and large Reynolds numbers a closed reduced set of partial differential equations that captures the leading-order coupled dynamics of the large-scale anisotropic hydrostatic flow and small-scale non-hydrostatic instabilities and waves characterized by their commensurate horizontal and vertical length scales. The dynamics admitted by the coupled reduced equations is illustrated in the context of two-dimensional

(2D) strongly stratified Kolmogorov flow. A noteworthy feature of the reduced model is that the fluctuations are constrained to satisfy quasilinear (QL) dynamics about the comparably slowly-varying large-scale fields. Crucially, this QL reduction is not invoked as an *ad hoc* closure approximation, e.g. as in Fitzgerald and Farrell (2014, 2018), but rather is derived here in a physically relevant and mathematically consistent distinguished limit. The reduced equations thus provide a solid mathematical foundation for future studies of three-dimensional strongly stratified turbulence (i.e. of LAST) in extreme parameter regimes of geophysical relevance.

In subsequent sections, we first derive reduced equations for large Reynolds number strongly-stratified flow using multiple scales analysis (§ 2). We then introduce a novel scheme for integrating the resulting slow–fast QL system strictly on the slow time scale characterizing the mean-field evolution (§ 3). In § 4, we apply this new framework to the computation of exact coherent states (ECS) in strongly stratified Kolmogorov flow as an illustrative proof of concept of the utility of the reduced equation set. Finally, in § 5, we draw our conclusions and propose future avenues of research.

2. Multiple scales reduction of the Boussinesq equations

We consider a volume of stably stratified fluid far from any boundaries that is driven by an imposed body force. Density (or buoyancy) variations are incorporated through the Boussinesq approximation. In the LAST regime, it is well established that anisotropic flow structures emerge with horizontal scales $L \gg h$ (Riley and Lelong 2000; Riley and Lindborg 2013), where h is the typical vertical scale of variation of the dependent field variables (see figure 1*a*). Thus, we non-dimensionalize the governing Boussinesq equations anisotropically, scaling horizontal velocities with U, horizontal distance with L, time with L/U and pressure with $\rho_0 U^2$, where ρ_0 is a constant reference density, whereas vertical distance is scaled with h, vertical velocities with $Fr^2(L/h)U$ and buoyancy (more precisely, the negative reduced gravity) with U^2/h. The buoyancy scale is deduced by ensuring that hydrostatic balance can be attained on large horizontal scales, while, in the first instance, the scaling for the vertical velocity arises from balancing horizontal and vertical advection of buoyancy rather than from imposing three-dimensional (3D) incompressibility on those scales. The resulting dimensionless Boussinesq system can be expressed as

$$\partial_t \mathbf{u}_\perp + (\mathbf{u}_\perp \cdot \nabla_\perp)\,\mathbf{u}_\perp + \frac{Fr^2}{\alpha^2} W \partial_z \mathbf{u}_\perp = -\nabla_\perp p + \frac{1}{Re}\left[\nabla_\perp^2 + \frac{1}{\alpha^2}\partial_z^2\right]\mathbf{u}_\perp + \mathbf{f}_\perp, \tag{2.1}$$

$$Fr\left[\partial_t W + (\mathbf{u}_\perp \cdot \nabla_\perp)\,W + \frac{Fr^2}{\alpha^2} W \partial_z W\right] = \frac{1}{Fr}\left(-\partial_z p + b\right) + \frac{Fr}{Re}\left[\nabla_\perp^2 + \frac{1}{\alpha^2}\partial_z^2\right] W, \tag{2.2}$$

$$\nabla_\perp \cdot \mathbf{u}_\perp + \frac{Fr^2}{\alpha^2}\partial_z W = 0, \tag{2.3}$$

$$\partial_t b + (\mathbf{u}_\perp \cdot \nabla_\perp)\,b + \frac{Fr^2}{\alpha^2} W \partial_z b = -W + \frac{1}{PrRe}\left[\nabla_\perp^2 + \frac{1}{\alpha^2}\partial_z^2\right] b. \tag{2.4}$$

In (2.1)–(2.4), $\alpha \equiv h/L$ is the aspect ratio characterizing the anisotropy of typical large scale flow structures, and the subscript $\perp$ denotes the horizontal (x,y) plane, i.e. the plane perpendicular to gravity. The velocity vector $\mathbf{u}$=($\mathbf{u}_\perp$,W), where $\mathbf{u}_\perp$=(u,v) is the horizontal velocity vector and W is the vertical (z) velocity component; b is the buoyancy deviation from an imposed locally linearly-varying background profile (i.e. which varies on a much larger, dimensional scale height comparable to L) so that the total buoyancy

field is given by $z + b$; and p is the pressure. A body force $\mathbf{f}_\perp$ is incorporated into the horizontal momentum equations to drive the flow.

To obtain limiting equations governing the dynamics in the strongly stratified regime, a determination must be made regarding the behavior of the flow aspect-ratio α in the limit $Fr \to 0$. Lilly (1983) assumed that α remains fixed in that limit, in which case the reduced version of (2.1)–(2.4) governs layerwise – that is, essentially vertically decoupled – 2D dynamics. If, however, $\alpha = O(Fr)$ as $Fr \to 0$, as proposed later by Billant and Chomaz (2001), then (2.1)–(2.4) reduce to the so-called hydrostatic primitive equations (Riley and Lindborg 2013) governing strongly anisotropic but nevertheless 3D turbulence. [Interestingly, to the best of our knowledge, the compatibility of this scaling with the requirements for the self-consistency of the Boussinesq approximation, e.g. see Bois (1991), has never been analysed.] A spate of subsequent investigations has empirically confirmed the relevance of the Billant–Chomaz scaling (Waite and Bartello 2004; Lindborg 2006; Brethouwer et al. 2007; Augier et al. 2012, 2015; Maffioli and Davidson 2016; Lucas et al. 2017). Physically, the implication is that the as yet unspecified vertical length scale h of the large horizontal-scale flow structures dynamically self-adjusts to be $O(U/N)$, the so-called buoyancy scale; i.e. the *vertical* Froude number $U/(Nh) = O(1)$ as $Fr \to 0$. In the following analysis, we presume the Billant–Chomaz scaling is the relevant one for strongly stratified turbulence; i.e. we assume that the turbulence evolves to be in this inherently vertically layered and anisotropic state.

Although the hydrostatic primitive equations capture vertical mode coupling in the LAST regime, they necessarily fail to include small-scale, isotropic and non-hydrostatic dynamics, the effects of which usually must be phenomenologically modeled, as noted above. Here, we proceed more systematically by formally introducing 'fast' horizontal and temporal independent variables, $\boldsymbol{\chi}_\perp \equiv \mathbf{x}_\perp/Fr$ and $\tau \equiv t/Fr$, so that derivatives transform as

$$\nabla_\perp \to (1/Fr)\nabla_{\boldsymbol{\chi}_\perp} + \nabla_{\mathbf{x}_\perp} \text{ and } \partial_t \to (1/Fr)\partial_\tau + \partial_t \tag{2.5}$$

and by allowing each dependent field to depend on both $\boldsymbol{\chi}_\perp$ and $\mathbf{x}_\perp$ and on both τ and t, in accord with the multiple scales asymptotic formalism. By introducing these fast scales, we explicitly recognize the possibility for dynamics to occur on commensurate horizontal and vertical scales and on time scales of the order of the buoyancy period. Such motions can be readily observed in visualizations from DNS of strongly stratified turbulence (e.g. see Rorai et al. 2014; Waite 2014) and appear to be associated with various stratified shear instability mechanisms (e.g. Kelvin–Helmholtz billows and Holmboe waves). The fastest growing instability modes generally have streamwise wavelengths on the order of the shear layer thickness; i.e. in dimensional terms, $O(h)$. The DNS performed by Augier et al. (2012, 2015) provide further evidence of this scale separation and, in particular, of the importance of spectrally non-local energy transfers in stratified turbulence. Similarly, the recent DNS of Fritts et al. (2021) provides direct evidence of the coupling between disparate-scale motions, with small-scale stratified turbulence generated by the interaction between breaking mountain waves significantly modifying large (horizontal) scale zonal flows.

Next, we identify a physically relevant and (what proves to be a) mathematically consistent distinguished limit; namely, the limit $Fr \to 0$ with Pr fixed, $\alpha = Fr$ and the *buoyancy* Reynolds number $Re_b \equiv ReFr^2$ fixed. Numerous DNS studies and scaling arguments (Smyth and Moum 2000; Billant and Chomaz 2001; Brethouwer et al. 2007; Bartello and Tobias 2013; Maffioli and Davidson 2016) have isolated Re_b as a key control parameter in stratified turbulence; here, it arises naturally when considering vertical diffusion of the large-scale buoyancy and horizontal momentum fields. Note that Re_b is

directly proportional to the Gibson number or 'activity parameter' $Gn \equiv \varepsilon/(\nu N^2)$, often used in computational studies of stratified turbulence, when the turbulent scaling relation $\varepsilon = \tilde{c}U^3/L$ holds for some constant $\tilde{c}$. (See Portwood et al. (2016) for further discussion.) Unlike the emergent parameter Gn, however, Re_b is an external control parameter and thus more appropriate here. Once the reduced system has been derived, we are free to vary the numerical value of Re_b to investigate its impact on flow transitions and various other flow features.

Owing to the scaling of the Reynolds stress feedbacks onto the fast-horizontal/fast-time mean flow, the expansion proceeds in fractional powers of Fr. Accordingly, we introduce the asymptotic parameter $\epsilon \equiv \sqrt{Fr}$ and posit that

$$[\mathbf{u}_\perp, b, p] \sim [\mathbf{u}_{0\perp}, b_0, p_0] + \epsilon[\mathbf{u}_{1\perp}, b_1, p_1] + \epsilon^2[\mathbf{u}_{2\perp}, b_2, p_2] + \ldots, \tag{2.6}$$

$$W \sim \frac{1}{\epsilon}W_{-1} + W_0 + \epsilon W_1 + \ldots \tag{2.7}$$

The expansions for $\mathbf{u}_\perp$, b and p start at $O(1)$, reflecting our expectation that the dominant contribution to each of these fields arises on large horizontal scales, in accord with our non-dimensionalization. In contrast, in stratified turbulence, the vertical velocity is a *small-scale* quantity (Brethouwer et al. 2007; Maffioli and Davidson 2016). Thus, in our two-scale formalism, we anticipate that W will have a larger magnitude on the small horizontal scales ($\boldsymbol{\chi}_\perp$), where the flow will be shown to be non-hydrostatic, than on the large horizontal scales ($\mathbf{x}_\perp$). Recalling that $Fr = \alpha$, we note that the dimensional velocity scale for W simplifies to αU for the given distinguished limit, as expected on the basis of 3D incompressibility for flows with larger horizontal than vertical scales. Thus, the rescaling of the dimensionless vertical velocity by the factor $1/\epsilon$ in (2.7) corresponds to re-nondimensionalizing the vertical velocity with $\sqrt{Fr}U$. As shown subsequently, this rescaling simultaneously ensures that the fine scale dynamics occur on commensurate horizontal and vertical scales and, crucially, that the feedback of these ($\boldsymbol{\chi}_\perp$,τ)-varying fluctuations onto the ($\mathbf{x}_\perp$,t)-varying mean fields arises at the proper order. (Note that both the fluctuations and the mean fields vary on the same vertical coordinate z.) This rescaling is also broadly consistent with the results of DNS showing that the long-time or ensemble *mean-square* vertical velocity is $O(Fr)$, not $O(Fr^2)$, when normalized by U^2 (Maffioli and Davidson 2016).

We proceed by substituting expansions (2.6) and (2.7) into the Boussinesq equations (2.1)–(2.4) with multiscale derivatives and collecting terms at like order in ϵ. We also introduce the fast-averaging operation $\overline{(\cdot)}$ for multiscale functions $\phi(\boldsymbol{\chi}_\perp, \mathbf{x}_\perp, z, \tau, t; \epsilon)$ defined such that

$$\overline{\phi}(\mathbf{x}_\perp, z, t; \epsilon) \equiv \lim_{\tau_f, l_x, l_y \to \infty} \frac{1}{l_x l_y \tau_f} \int_0^{\tau_f} \int_{\mathbf{D}} \phi(\boldsymbol{\chi}_\perp, \mathbf{x}_\perp, z, \tau, t; \epsilon)\, \mathrm{d}\boldsymbol{\chi}_\perp \mathrm{d}\tau, \tag{2.8}$$

where $\mathbf{D}$ represents a horizontal $\boldsymbol{\chi}_\perp$-domain. In the definition (2.8), the limiting process is associated with length scales l_x and l_y that are large compared to the scale of $\boldsymbol{\chi}_\perp$-variation of the function ϕ but small compared to the scale of $\mathbf{x}_\perp$-variation; τ_f can be interpreted analogously for the time integration. In practice, we will take $\phi(\boldsymbol{\chi}_\perp, \mathbf{x}_\perp, z, \tau, t; \epsilon)$ to be doubly-periodic on $\mathbf{D}$, with 'fast' spatial periods l_x and l_y, so that the limits l_x, $l_y \to \infty$ need not be taken. As described § 3.2, our novel methodology for integrating the reduced equations obviates the apparent need to specify the fast spatial periods (l_x, l_y) and time-integration period τ_f arbitrarily. Finally, we note that the fast-averaging operation enables the multiscale fields to be decomposed into a slowly-varying mean component plus a fluctuation with zero fast-mean (denoted with a prime): $\phi = \overline{\phi} + \phi'$.

At $O(\epsilon^{-2})$, we obtain the following system of equations:

$$\begin{aligned} \partial_\tau \mathbf{u}_{0\perp} + (\mathbf{u}_{0\perp}\cdot\nabla_{\boldsymbol{\chi}_\perp})\,\mathbf{u}_{0\perp} &= -\nabla_{\boldsymbol{\chi}_\perp} p_0, \\ \partial_z p_0 &= b_0, \\ \partial_\tau b_0 + (\mathbf{u}_{0\perp}\cdot\nabla_{\boldsymbol{\chi}_\perp})\,b_0 &= 0, \\ \nabla_{\boldsymbol{\chi}_\perp}\cdot\mathbf{u}_{0\perp} &= 0. \end{aligned}$$

From the $O(\epsilon^{-2})$ continuity equation, the leading-order horizontal velocity can be decomposed into a fast-horizontal ($\boldsymbol{\chi}_\perp$) average plus a vortical contribution that is non-divergent on the fast horizontal scales; i.e.

$$\mathbf{u}_{0\perp} = \overline{\mathbf{u}}^{\chi}_{0\perp} + \nabla_{\boldsymbol{\chi}}\times\Psi_0\hat{e}_z$$

for scalar field Ψ_0, where $\overline{(\cdot)}^{\chi}$ indicates a fast-horizontal average, and $\hat{e}_z$ is a unit vector in the z direction. Applying this fast horizontal averaging operation to the $O(\epsilon^{-2})$ horizontal momentum equation, it is readily shown that $\overline{\mathbf{u}}^{\chi}_{0\perp} = \overline{\mathbf{u}}_{0\perp}$; that is, the leading-order fast-horizontally-averaged horizontal velocity also must be independent of the fast time variable τ. Substitution then yields

$$\partial_\tau \mathbf{u}^R_{0\perp} + \left(\overline{\mathbf{u}}_{0\perp} + \mathbf{u}^R_{0\perp}\right)\cdot\nabla_{\boldsymbol{\chi}_\perp}\mathbf{u}^R_{0\perp} = -\nabla_{\boldsymbol{\chi}_\perp} p_0,$$

where $\mathbf{u}^R_{0\perp} \equiv \nabla_{\boldsymbol{\chi}}\times\Psi_0\hat{e}_z$. Crucially, there is no energy source for the purely vortical, fast-$\boldsymbol{\chi}_\perp$ non-divergent velocity field $\mathbf{u}^R_{0\perp}$, which would be strained by the mean flow $\overline{\mathbf{u}}_{0\perp}$ and ultimately dissipated on a time scale intermediate to τ and t owing to shear-enhanced diffusion (Young and Jones 1991). Accordingly, we henceforth set $\mathbf{u}^R_{0\perp} = \mathbf{0}$, so that

$$\mathbf{u}_{0\perp} = \overline{\mathbf{u}}_{0\perp}, \tag{2.9}$$

an important simplification in the subsequent analysis. The $O(\epsilon^{-2})$ horizontal momentum equation then requires $\nabla_{\boldsymbol{\chi}_\perp} p_0 = 0$, further implying from the vertical momentum equation that $\nabla_{\boldsymbol{\chi}_\perp} b_0 = 0$. The $O(\epsilon^{-2})$ buoyancy equation then gives

$$b_0 = \overline{b}_0, \tag{2.10}$$

which also is a source of considerable subsequent simplification. Finally, note that the fast average of the $O(\epsilon^{-2})$ vertical momentum equation yields

$$\partial_z \overline{p}_0 = \overline{b}_0. \tag{2.11}$$

Thus, the large-scale flow is hydrostatically balanced at leading order.

Considering next the equations at $O(\epsilon^{-1})$, the fast-average of the continuity constraint

$$\nabla_{\boldsymbol{\chi}_\perp}\cdot\mathbf{u}_{1\perp} + \partial_z W_{-1} = 0$$

gives $\partial_z\overline{W}_{-1} = 0$, implying $\overline{W}_{-1} = 0$. This deduction confirms that the vertical velocity is larger on the small scales than it is on the coarse scales (presuming $W'_{-1} \neq 0$). Subtraction then gives the leading-order incompressibility condition for the fluctuating velocity field:

$$\nabla_{\boldsymbol{\chi}_\perp}\cdot\mathbf{u}'_{1\perp} + \partial_z W'_{-1} = 0. \tag{2.12}$$

At $O(\epsilon^{-1})$, an equation governing the leading-order dynamics of the fluctuating horizontal velocity field is obtained:

$$\partial_\tau \mathbf{u}'_{1\perp} + (\overline{\mathbf{u}}_{0\perp}\cdot\nabla_{\boldsymbol{\chi}_\perp})\,\mathbf{u}'_{1\perp} + W'_{-1}\partial_z\overline{\mathbf{u}}_{0\perp} + \nabla_{\boldsymbol{\chi}_\perp} p'_1 = 0. \tag{2.13}$$

In deriving this result we have tacitly assumed that the external forcing $\mathbf{f}_\perp$ is an $O(1)$ field. Similarly, after subtracting the fast-average result $\partial_z\overline{p}_1 = \overline{b}_1$, the $O(\epsilon^{-1})$ fluctuation

vertical momentum equation is

$$\partial_\tau W'_{-1} + (\overline{\mathbf{u}}_{0\perp} \cdot \nabla_{\boldsymbol{\chi}_\perp}) W'_{-1} + \partial_z p'_1 - b'_1 = 0, \tag{2.14}$$

while at $O(\epsilon^{-1})$ the buoyancy equation reduces to

$$\partial_\tau b'_1 + (\overline{\mathbf{u}}_{0\perp} \cdot \nabla_{\boldsymbol{\chi}_\perp}) b'_1 + W'_{-1} \partial_z \overline{b}_0 + W'_{-1} = 0. \tag{2.15}$$

To close the system, a set of constraints for the leading-order mean fields must be derived by fast-averaging the governing equations at $O(1)$. For example, the continuity equation for the slowly-varying mean fields is readily obtained:

$$\nabla_{\mathbf{x}_\perp} \cdot \overline{\mathbf{u}}_{0\perp} + \partial_z \overline{W}_0 = 0. \tag{2.16}$$

Next, the $O(1)$ horizontal momentum equation can be expressed as

$$\partial_\tau \mathbf{u}'_{2\perp} + (\overline{\mathbf{u}}_{0\perp} \cdot \nabla_{\boldsymbol{\chi}_\perp}) \mathbf{u}'_{2\perp} + W'_0 \partial_z \overline{\mathbf{u}}_{0\perp} + \nabla_{\boldsymbol{\chi}_\perp} p'_2 = -\Big[\partial_t \overline{\mathbf{u}}_{0\perp} + (\overline{\mathbf{u}}_{0\perp} \cdot \nabla_{\mathbf{x}_\perp}) \overline{\mathbf{u}}_{0\perp} + \overline{W}_0 \partial_z \overline{\mathbf{u}}_{0\perp} + (\mathbf{u}_{1\perp} \cdot \nabla_{\boldsymbol{\chi}_\perp}) \mathbf{u}'_{1\perp} + W'_{-1} \partial_z \mathbf{u}_{1\perp} + \nabla_{\mathbf{x}_\perp} p_0 - \frac{1}{Re_b} \partial_z^2 \overline{\mathbf{u}}_{0\perp} - \mathbf{f}_{0\perp}\Big].$$

For bounded behavior of the $O(\epsilon^2)$ fluctuation fields, a necessary condition is that the fast-average of the right-hand side of this equation must vanish. This solvability condition yields an equation for the slow evolution of the leading-order coarse-grained field $\overline{\mathbf{u}}_{0\perp}$:

$$\partial_t \overline{\mathbf{u}}_{0\perp} + (\overline{\mathbf{u}}_{0\perp} \cdot \nabla_{\mathbf{x}_\perp}) \overline{\mathbf{u}}_{0\perp} + \overline{W}_0 \partial_z \overline{\mathbf{u}}_{0\perp} = -\nabla_{\mathbf{x}_\perp} \overline{p}_0 - \partial_z \left(\overline{W'_{-1} \mathbf{u}'_{1\perp}}\right) + \frac{1}{Re_b} \partial_z^2 \overline{\mathbf{u}}_{0\perp} + \overline{\mathbf{f}}_{0\perp}, \tag{2.17}$$

where (2.12), the incompressibility of the leading-order fluctuation velocity field, has been used. The derivation of the equation governing the leading-order mean buoyancy field closely parallels that of the horizontal momentum equation. Specifically, at $O(1)$,

$$\partial_\tau b'_2 + (\overline{\mathbf{u}}_{0\perp} \cdot \nabla_{\boldsymbol{\chi}_\perp}) b'_2 + W'_0 \left(\partial_z \overline{b}_0 + 1\right) = -\Big[\partial_t \overline{b}_0 + (\overline{\mathbf{u}}_{0\perp} \cdot \nabla_{\mathbf{x}_\perp}) \overline{b}_0 + \overline{W}_0 \left(\partial_z \overline{b}_0 + 1\right) + (\mathbf{u}_{1\perp} \cdot \nabla_{\boldsymbol{\chi}_\perp}) b'_1 + W'_{-1} \partial_z b_1 - \frac{1}{PrRe_b} \partial_z^2 \overline{b}_0\Big].$$

Fast-averaging this equation yields the evolution equation for $\overline{b}_0$:

$$\partial_t \overline{b}_0 + (\overline{\mathbf{u}}_{0\perp} \cdot \nabla_{\mathbf{x}_\perp}) \overline{b}_0 + \overline{W}_0 \partial_z \overline{b}_0 + \overline{W}_0 = -\partial_z \left(\overline{W'_{-1} b'_1}\right) + \frac{1}{PrRe_b} \partial_z^2 \overline{b}_0. \tag{2.18}$$

Recalling (2.11), the derivation of the leading-order mean and fluctuation equations is complete. Nevertheless, one further point regarding this derivation should be made. Inspection of the left-hand sides of the fluctuation equations following (2.16) and (2.17) along with the corresponding forms of the $O(1)$ fluctuation continuity and vertical momentum equations reveals that, for boundedness of the $O(\epsilon^2)$ fluctuation fields over the fast space and time scales, a *second* solvability condition must be satisfied. Rather than yielding a slow evolution equation for the amplitude of the leading-order fluctuation fields, however, the required solvability condition simply constrains the evolution of the higher-order *corrections* to the leading-order mean fields; see Michel and Chini (2019) for further details regarding this subtle but important point. Since these mean-field corrections are not required to close the leading-order mean/fluctuation system, we do not pursue the required calculation here.

2.1. *Synopsis of the reduced system*

Equations (2.17), (2.11), (2.18) and (2.16) and (2.13), (2.14), (2.15) and (2.12) comprise a novel, multiscale reduced system. For ease of reference this system is reproduced here, where, for brevity of notation, the numeric subscripts have been omitted and $\overline{\nabla}$ and ∇' are used in lieu of $\nabla_{\mathbf{x}_\perp}$ and $\nabla_{\boldsymbol{\chi}_\perp}$, respectively.

Mean Dynamics

$$\left(\partial_t + \overline{\mathbf{u}}_\perp \cdot \overline{\nabla} + \overline{W}\partial_z\right)\overline{\mathbf{u}}_\perp = -\overline{\nabla}\overline{p} - \partial_z\left(\overline{W'\mathbf{u}'_\perp}\right) + \frac{1}{Re_b}\partial_z^2\overline{\mathbf{u}}_\perp + \overline{\mathbf{f}}_\perp, \tag{2.19}$$

$$0 = -\partial_z\overline{p} + \overline{b}, \tag{2.20}$$

$$\left(\partial_t + \overline{\mathbf{u}}_\perp \cdot \overline{\nabla} + \overline{W}\partial_z\right)\overline{b} = -\overline{W} - \partial_z\left(\overline{W'b'}\right) + \frac{1}{PrRe_b}\partial_z^2\overline{b}, \tag{2.21}$$

$$\overline{\nabla} \cdot \overline{\mathbf{u}}_\perp + \partial_z\overline{W} = 0. \tag{2.22}$$

Fluctuation Dynamics

$$\left(\partial_\tau + \overline{\mathbf{u}}_\perp \cdot \nabla'\right)\mathbf{u}'_\perp + W'\partial_z\overline{\mathbf{u}}_\perp = -\nabla' p' + \frac{Fr}{Re_b}\left(\nabla'^2 + \partial_z^2\right)\mathbf{u}'_\perp, \tag{2.23}$$

$$\left(\partial_\tau + \overline{\mathbf{u}}_\perp \cdot \nabla'\right)W' = -\partial_z p' + b' + \frac{Fr}{Re_b}\left(\nabla'^2 + \partial_z^2\right)W', \tag{2.24}$$

$$\left(\partial_\tau + \overline{\mathbf{u}}_\perp \cdot \nabla'\right)b' + W'\partial_z\overline{b} = -W' + \frac{Fr}{PrRe_b}\left(\nabla'^2 + \partial_z^2\right)b', \tag{2.25}$$

$$\nabla' \cdot \mathbf{u}'_\perp + \partial_z W' = 0. \tag{2.26}$$

2.2. *Generalized quasilinear (QL) structure of the reduced system*

Before attempting to integrate the multiscale reduced system numerically, it is instructive to examine the structure of these equations. In the absence of the Reynolds-stress and buoyancy-flux divergence terms, the mean equations (2.19)–(2.22) are readily seen to reduce to the hydrostatic primitive equations. Heuristically, this set of equations governs the comparably slowly-evolving, large-scale layer-like motions that are routinely observed in the LAST regime of strongly stratified turbulence. The correlations arising in these equations, which account for the collective effects of the small-scale flows on the strongly anisotropic large-scale motions, generally must be modeled phenomenologically. By exploiting the scale separation associated with the chosen distinguished limit, however, here we are able to avoid the usual closure difficulties via explicit derivation of the leading-order equations governing the evolution of the fluctuation fields [i.e. (2.23)–(2.26)]. Taken together, equations (2.19)–(2.26) comprise a *closed* reduced system. Direct calculation confirms that this system conserves energy in the absence of dissipation and forcing.

Inspection of (2.23)–(2.25) reveals that the fluctuations are advected horizontally by the mean flow and can interact with vertical gradients of the mean buoyancy and horizontal velocity fields. Equation (2.24) shows that the fluctuation dynamics are non-hydrostatic, as expected. Moreover, the fluctuation dynamics are 'quasilinear' with respect to the slowly-varying mean fields; that is, fluctuation/fluctuation nonlinearities are absent from the fluctuation equations, but their feedback on the coarse-grained fields is retained. Indeed, a central outcome of the present work is that the increasingly popular QL approximation for anisotropic turbulent flows (Fitzgerald and Farrell 2014; Constantinou, Lozano-Durán, Nikolaidis, Farrell, Ioannou and Jiménez 2014; Thomas et al. 2015; Kim et al. 2020; Fitzgerald and Farrell 2018) and the associated statistical formulations (variously referred to as CE2 and SSST: Tobias et al. (2011); Srinivasan and

Young (2012); Tobias and Marston (2013); Constantinou, Farrell and Ioannou (2014); Ait-Chaalal et al. (2016); Constantinou et al. (2016); Farrell et al. (2016, 2017)) can be formally justified for strongly stratified (and perhaps other) shear flows via multiscale asymptotic analysis. Since the mean fields are independent of the fast coordinates, the fluctuation equations are autonomous in $\boldsymbol{\chi}_\perp$ and there is no direct coupling among 'fast' Fourier modes; instead, these modes are coupled only through their contribution to the modification of the mean fields. By retaining slow spatiotemporal variability of the mean fields, our formulation in fact *extends* the usual QL reduction: precisely this sort of multiscale analysis provided inspiration for the so-called 'generalized quasilinear' or GQL approximation (Marston et al. 2016), which has been demonstrated to improve the accuracy of QL-based predictions significantly for only a modest increase in model complexity (Tobias and Marston 2017; Child et al. 2016). The reduced equations systematically derived here also can be compared to the 1D phenomenological model for fluctuating motions in stratified turbulence introduced in Rorai et al. (2014) and extended by Feraco et al. (2018). In particular, we find that while the linear coupling and damping of the temperature and vertical velocity are adequately captured by the phenomenological model, neither the instability nor the nonlinear saturation terms in the fluctuation dynamics, which are fundamental to interactions with the large scales, are properly characterized in the 1D model.

A final point concerns the role of diffusive effects in the multiscale reduced system. Owing to the anisotropic large-scale layering, vertical diffusion of momentum and buoyancy arises at leading-order in the mean equations. Although asymptotically, i.e. as a function of Fr as $Fr \to 0$, $Re_b = O(1)$ the effective diffusivity ($\propto 1/Re_b$) can be varied numerically to investigate different dynamical regimes captured by the reduced model. Indeed, many DNS studies have suggested that important regime transitions occur at $Re_b \gtrsim 10$ (Bartello and Tobias 2013; Maffioli and Davidson 2016; Lucas and Caulfield 2017; Lang and Waite 2019; Garanaik and Venayagamoorthy 2019). In contrast to the mean dynamics, the leading-order fluctuation equations are non-dissipative. Nevertheless, in writing (2.23)–(2.25), we have included formally higher-order Laplacian diffusion terms as a simple means of regularizing the fluctuation dynamics, should large z-gradients (e.g. possibly associated with critical layers) emerge. Although justifiable as a *composite* asymptotic approximation, this approach reintroduces the small parameter Fr into the limit system, and a more careful analysis would be required to ascertain whether other formally weak physical processes also may contribute to the dominant balance of terms in ultra-thin regions in which z-gradients become large. With this limitation understood, we proceed using the regularized reduced system (2.19)–(2.26). Nonetheless, as shown explicitly in § 4, the 2D non-dissipative fluctuation equations can be re-expressed as the Taylor–Goldstein (TG) equation (Craik 1985) since, formally, the mean fields are frozen during the fast evolution of the fluctuations. Thus, by inspection, it is clear that the reduced system captures all of the linear instabilities admitted by the TG equation, including the classical Kelvin–Helmholtz and Holmboe instabilities.

3. Integration of the reduced system

The structure of the reduced system (2.19)–(2.26) is suggestive of a heterogeneous multiscale algorithm (Engquist et al. 2007), in which fine-grained computations are performed on embedded domains in the local neighborhood of each coarse-scale grid point, thereby providing the fluxes that are needed to advance the coarse-scale fields. An alternative approach would be to interpret (2.19)–(2.26) as a physical space representation of the GQL formalism introduced by Marston et al. (2016). Regardless, a multiscale

implementation of some variety is required to exploit the full potential of the reduced model.

In the present study, however, we adopt the more modest goal of illustrating the dynamics that can be exhibited by the reduced system in small 2D domains with commensurate horizontal and vertical lengths (each of order h in dimensional terms). To this end we suppress the slow $\mathbf{x}_\perp$ derivatives, which immediately implies that $\overline{W} = 0$. The resulting (2D) reduced system can be expressed as

$$\partial_t \overline{u} = \partial_z \left(\overline{\partial_z \psi' \partial_\chi \psi'} \right) + \frac{1}{Re_b} \partial_z^2 \overline{u} + \overline{f}, \tag{3.1}$$

$$\partial_t \overline{b} = \partial_z \left(\overline{b' \partial_\chi \psi'} \right) + \frac{1}{PrRe_b} \partial_z^2 \overline{b}, \tag{3.2}$$

$$(\partial_\tau + \overline{u}\partial_\chi) \triangle \psi' = \partial_\chi \psi' \partial_z^2 \overline{u} - \partial_\chi b' + \frac{Fr}{Re_b} \triangle^2 \psi', \tag{3.3}$$

$$(\partial_\tau + \overline{u}\partial_\chi) b' = (1 + \partial_z \overline{b}) \partial_\chi \psi' + \frac{Fr}{PrRe_b} \triangle b' \tag{3.4}$$

where $u' \equiv \partial_z \psi'$, $W' \equiv -\partial_\chi \psi'$ and $\triangle = \partial_\chi^2 + \partial_z^2$. Although the dependence on the slow spatial coordinate(s) $\mathbf{x}_\perp$ has been suppressed, the reduced system (3.1)–(3.4) nevertheless still formally requires time advancement on *two* time scales (τ and t). Below, we employ two distinct strategies for integrating the reduced system. The first treats (3.1)–(3.4) as an initial-value problem on the fast time scale. The second is based on a new asymptotic analysis of slow-fast QL systems with fast instabilities and exploits the tendency of these systems to self-tune to a state of approximate marginal stability (Michel and Chini 2019).

3.1. *Single time-scale formulation*

One straightforward way to simulate the reduced equations (3.1)–(3.4) is to revert to a single time-scale formulation by making the non-asymptotic replacement $\partial_t = (1/Fr)\partial_\tau$ and by reinterpreting the fast ($\boldsymbol{\chi}_\perp$,τ) average as a strict horizontal average (only). This reformulation sacrifices certain advantages accrued via the multiples scales asymptotic analysis. In particular, the resulting system is numerically stiff owing to the reintroduction of Fr, and both the fast fluctuations and the slowly evolving mean fields have to be numerically co-evolved on the fast time scale τ. The advantage of this approach is that there is a clear protocol for discretizing this system in both space and time. In fact, the resulting equations are identical to those that would be obtained via an *ad hoc* QL approximation of the (2D) Boussinesq equations, in which flow fields are decomposed into a horizontal ('streamwise') average plus a fluctuation about that mean (Fitzgerald and Farrell 2018, 2019). Regarding the spatial discretization, owing to the QL structure *any* set of horizontal Fourier modes can be included. Nevertheless, since this set must be specified *a priori*, standard grids equispaced in physical or Fourier space generally are employed. As described in the following subsection, a chief virtue of the multiple time-scale formulation is that the intrinsic dynamics of the slow–fast QL system self-selects those wavenumbers and associated Fourier modes to be included. Consequently, in that formulation, the fast spatial domain is effectively infinite in extent; there is no *a priori* quantization of Fourier modes imposed by the seemingly arbitrary specification of l_x.

3.2. *Multiple time-scale formulation*

In our view, an algorithm that explicitly enforces the time scale separation between the mean and fluctuation fields in (3.1)–(3.4) is preferable. The method for integrating slow–fast QL systems with fast instabilities introduced by Michel and Chini (2019) leverages

the linearity and autonomy of the fluctuation dynamics on the fast time scale, which here implies that both ψ' and b' depend on the fast time τ only through a term of the form $e^{\sigma\tau}$, where σ is the (complex-valued, linear) growth rate. For the Reynolds stress divergence to remain finite in the mean field equations (3.1) and (3.2), either the real part of the growth rate or the amplitude of the fluctuations therefore must vanish. The crucial point, as we demonstrate below, is that for forced strongly stratified flows the fluctuation amplitude (if non-zero) is then slaved to the mean fields to ensure that the real part of the growth rate $\sigma_r = 0$; that is, to ensure that the Reynolds stress divergence modifies the evolution of $\bar{u}$ and $\bar{b}$ so that the mean fields always evolve (slowly) on a marginal-stability manifold. This constrained evolution is a mathematical manifestation of self-organized criticality, a physical attribute increasingly being associated with stratified turbulent shear flows (Salehipour et al. 2018; Smyth et al. 2019), although the argument that stratified flows adjust to a marginally stable 'pseudo-equilibrium' dates back at least to Turner (1973). The remainder of this section describes in detail the resulting multiscale algorithm.

First, note that fluctuation system (3.3)-(3.4) can be treated as a linear homogeneous eigenvalue problem by seeking modal solutions with real-valued wavenumber $k(t)$, (complex-valued) growth rate $\sigma(\overline{\mathbf{G}}, k)$, where $\overline{\mathbf{G}}$ denotes dependencies on the mean fields and their derivatives (i.e. $\bar{u}$, $\partial_z^2\bar{u}$ and $\partial_z\bar{b}$), and complex-valued amplitude A of slowly-varying magnitude $|A(t)|$:

$$\psi'(\chi, z, \tau; t) = A(t)\hat{\Psi}(z; t)e^{\sigma\tau + ik(t)\chi} + \text{c.c.}, \tag{3.5}$$

$$b'(\chi, z, \tau; t) = A(t)\hat{b}(z; t)e^{\sigma\tau + ik(t)\chi} + \text{c.c.}, \tag{3.6}$$

where $\sigma = \sigma_r + i\sigma_i$ for real σ_r and σ_i, c.c. denotes complex conjugate and we have indicated explicitly that the vertical eigenfunctions $\hat{\Psi}$ and $\hat{b}$ also may vary slowly with time. Recalling that the fluctuation horizontal velocity and buoyancy are $O(\epsilon)$ relative to the corresponding mean fields, it is clear from these expressions that the uniformity of the posited asymptotic expansions in (2.6) would be lost if $\sigma_r > 0$. Indeed, in that situation, the fluctuations would grow exponentially fast – on the fast time scale – while the mean fields remained locally frozen in time. Accordingly, as an asymptotic uniformity condition, we seek a solvability constraint that ensures $\sigma_r \leqslant 0$. In practice, there may be 'instants' during the slow evolution where this condition cannot be satisfied, in which case the fluctuations will attain large (but finite) amplitude and the $O(1)$ mean fields will respond rapidly; i.e. on the fast time scale. In these situations, temporal scale separation is *transiently* lost. Although the algorithm we develop can be modified to incorporate this intermittent bursting behavior properly (Ferraro 2019), this extension proves unnnecessary for the parameter regime explored in the present investigation and is not described here. In contrast, $\sigma_r < 0$ presents no conceptual or pragmatic difficulty, as disturbances are exponentially damped on the fast time scale and, therefore, the amplitude A is self-consistently set to zero. If $\sigma_r = 0$, then the averaging required for evaluation of the Reynolds stress divergence terms in the mean-field equations [e.g. $\partial_z\left(\overline{\partial_z\psi'\partial_\chi\psi'}\right)$ in (3.1)] is well-defined. Specifically,

$$\partial_z\left(\overline{\partial_z\psi'\partial_\chi\psi'}\right) = |A(t)|^2 ik\partial_z\left(\hat{\Psi}\partial_z\hat{\Psi}^* - \hat{\Psi}^*\partial_z\hat{\Psi}\right) \equiv |A(t)|^2\text{RS}_u, \tag{3.7}$$

$$\partial_z\left(\overline{b'\partial_\chi\psi'}\right) = |A(t)|^2 ik\partial_z\left(\hat{\Psi}\hat{b}^* - \hat{\Psi}^*\hat{b}\right) \equiv |A(t)|^2\text{RS}_b, \tag{3.8}$$

where RS_u and RS_b, defined above, have been introduced for brevity of notation, and an asterisk denotes complex conjugation. Thus, the QL system (3.1)-(3.4) reduces to the

hybrid slow-initial-value/fast-eigenvalue problem:

$$\partial_t \overline{u} = |A(t)|^2 \mathrm{RS}_u \; + \; \frac{1}{Re_b}\partial_z^2 \overline{u} + \overline{f}, \tag{3.9}$$

$$\partial_t \overline{b} = |A(t)|^2 \mathrm{RS}_b \; + \; \frac{1}{PrRe_b}\partial_z^2 \overline{b}, \tag{3.10}$$

$$(\sigma + ik\overline{u})(\partial_z^2 - k^2)\hat{\Psi} = ik(\partial_z^2 \overline{u})\hat{\Psi} - ik\hat{b} \; + \; \frac{Fr}{Re_b}(\partial_z^2 - k^2)^2 \hat{\Psi}, \tag{3.11}$$

$$(\sigma + ik\overline{u})\hat{b} = ik(1 + \partial_z \overline{b})\hat{\Psi} \; + \; \frac{Fr}{PrRe_b}(\partial_z^2 - k^2)\hat{b}, \tag{3.12}$$

where $|A(t)| = 0$ if $\sigma_r < 0$.

The central challenge is to determine self-consistently an equation for the *a priori* unknown amplitude function $|A(t)|$, which, of course, is not constrained via the solution of the linear homogeneous eigensystem (3.11)–(3.12). As demonstrated in Michel and Chini (2019), to derive this constraint on $|A(t)|$ in the case of marginal stability, i.e. when $\sigma_r = 0$, the linear eigensystem itself must be differentiated with respect to the slow time variable and an appropriate solvability condition enforced. This slow-time differentiation enables nonlinearity present in the coupled system (3.9)–(3.12) to be incorporated, as required for determination of the fluctuation amplitude.

To facilitate the required analysis, the linear subsystem (3.11)–(3.12) first is recast in the form $\mathcal{L}X = 0$, with $X = [\hat{\Psi}(z), \hat{b}(z)]^T$ and

$$\mathcal{L} = \begin{pmatrix} (\sigma + ik\overline{u})(\partial_z^2 - k^2) - ik\partial_z^2 \overline{u} - \frac{Fr}{Re_b}(\partial_z^2 - k^2)^2 & ik \\ -ik(1 + \partial_z \overline{b}) & \sigma + ik\overline{u} - \frac{Fr}{PrRe_b}(\partial_z - k^2) \end{pmatrix}, \tag{3.13}$$

complemented with periodic boundary conditions in z. With respect to the eigenproduct

$$(X_1 | X_2) \equiv \int_0^{l_z} X_1(z) X_2^*(z) \mathrm{d}z \qquad \forall \; (X_1, X_2), \tag{3.14}$$

the adjoint operator of $\mathcal{L}$, defined via $(\mathcal{L}X_1 | X_2) = (X_1 | \mathcal{L}^\dagger X_2)$, is given by

$$\mathcal{L}^\dagger = \begin{pmatrix} (\sigma^* - ik\overline{u})(\partial_z^2 - k^2) - 2ik\partial_z \overline{u}\partial_z - \frac{Fr}{Re_b}(\partial_z^2 - k^2)^2 & ik(1 + \partial_z \overline{b}) \\ -ik & \sigma^* - ik\overline{u} - \frac{Fr}{PrRe_b}(\partial_z - k^2) \end{pmatrix}. \tag{3.15}$$

Note that $\mathcal{L}$ is not self-adjoint ($\mathcal{L} \neq \mathcal{L}^\dagger$). The linear problem $\mathcal{L}X = 0$ is then differentiated with respect to the slow time t, yielding

$$\mathcal{L}\frac{\mathrm{d}X}{\mathrm{d}t} \; = \; -\frac{\mathrm{d}\mathcal{L}}{\mathrm{d}t}X, \tag{3.16}$$

where

$$\frac{\mathrm{d}\mathcal{L}}{\mathrm{d}t} = \begin{pmatrix} (\mathrm{d}\sigma/\mathrm{d}t + ik\partial_t \overline{u})(\partial_z^2 - k^2) - ik(\partial_z^2 \partial_t \overline{u}) & 0 \\ -ik\partial_z \partial_t \overline{b} & \mathrm{d}\sigma/\mathrm{d}t + ik\partial_t \overline{u} \end{pmatrix} + \frac{\mathrm{d}k}{\mathrm{d}t}M \tag{3.17}$$

and M is a matrix whose explicit computation turns out not to be necessary. Since $\mathcal{L}$ is singular, the linear system (3.16) is solvable if and only if the right-hand side is orthogonal to the corresponding null adjoint eigenvector $X^\dagger$ (the Fredholm alternative condition). This requirement can be readily confirmed by forming the inner product of left-hand side of (3.16) with respect to $X^\dagger$, i.e.

$$\left(\mathcal{L}\frac{\mathrm{d}X}{\mathrm{d}t}\middle| X^\dagger\right) = \left(\frac{\mathrm{d}X}{\mathrm{d}t}\middle| \mathcal{L}^\dagger X^\dagger\right) = \left(\frac{\mathrm{d}X}{\mathrm{d}t}\middle| 0\right) = 0. \tag{3.18}$$

Consequently, using (3.16), we obtain

$$\left(\frac{\mathrm{d}\mathcal{L}}{\mathrm{d}t}X\middle| X^\dagger\right) = 0. \tag{3.19}$$

Crucially, this constraint can be made explicit. Using the mean-field equations (3.9) and (3.10) and noting that $X^\dagger = [\hat{\Psi}^\dagger(z), \hat{b}^\dagger(z)]^T$, the solvability condition becomes

$$C_1\frac{\mathrm{d}\sigma}{\mathrm{d}t} = C_2|A(t)|^2 + C_3 + C_4\frac{\mathrm{d}k}{\mathrm{d}t}. \tag{3.20}$$

As for the matrix M, the computation of the coefficient C_4 proves unnecessary. The remaining coefficients are given by the following expressions:

$$C_1 = \frac{1}{ik}\int_0^{l_z}\left[\hat{\Psi}^{\dagger *}(\partial_z^2 - k^2)\hat{\Psi} + \hat{b}^{\dagger *}\hat{b}\right]\mathrm{d}z, \tag{3.21}$$

$$C_2 = \int_0^{l_z}\left\{\mathrm{RS}_u\left[\hat{\Psi}(\partial_z^2 + k^2)\hat{\Psi}^{\dagger *} + 2\partial_z\hat{\Psi}\partial_z\hat{\Psi}^{\dagger *} - \hat{b}\hat{b}^{\dagger *}\right] - \mathrm{RS}_b\left[\hat{b}^{\dagger *}\partial_z\hat{\Psi} + \hat{\Psi}\partial_z\hat{b}^{\dagger *}\right]\right\}\mathrm{d}z, \tag{3.22}$$

$$C_3 = \int_0^{l_z}\left\{\left(\overline{f} + \frac{\partial_z^2\overline{u}}{Re_b}\right)\left[\hat{\Psi}(\partial_z^2 + k^2)\hat{\Psi}^{\dagger *} + 2\partial_z\hat{\Psi}\partial_z\hat{\Psi}^{\dagger *} - \hat{b}\hat{b}^{\dagger *}\right] - \frac{\partial_z^2\overline{b}}{PrRe_b}\left(\hat{b}^{\dagger *}\partial_z\hat{\Psi} + \hat{\Psi}\partial_z\hat{b}^{\dagger *}\right)\right\}\mathrm{d}z. \tag{3.23}$$

Dividing both sides of (3.20) by C_1, the evolution of the linear growth rate σ_r therefore is given for *fixed* k by

$$\left(\frac{\partial\sigma_r}{\partial t}\right)_k = \alpha_r - \beta_r|A(t)|^2, \tag{3.24}$$

where both $\alpha_r = \mathrm{Re}\{C_3/C_1\}$ and $\beta_r = \mathrm{Re}\{-C_2/C_1\}$ are computable functionals of the slow fields $\overline{u}$ and $\overline{b}$, the forcing $\overline{f}$, the direct and adjoint eigenfunctions $[\hat{\Psi}, \hat{b}]^T$ and $[\hat{\Psi}^\dagger, \hat{b}^\dagger]^T$, respectively, the parameters Re_b and Pr and the wavenumber k. Note that the total temporal variation of the real part of the growth rate $\sigma(\overline{\mathbf{G}}, k)$,

$$\frac{\mathrm{d}\sigma_r}{\mathrm{d}t} = \left(\frac{\partial\sigma_r}{\partial t}\right)_k + \frac{\mathrm{d}k}{\mathrm{d}t}\left(\frac{\partial\sigma_r}{\partial k}\right)_{\overline{\mathbf{G}}}, \tag{3.25}$$

includes an additional contribution owing to the time variation of k. The second term on the right-hand side of this expression vanishes, however, provided that $k(t)$ is (locally) the most unstable mode, as required here. As discussed in detail in Michel and Chini (2019), temporal scale separation then requires (cf. (3.24)) that

$$|A(t)| = \begin{cases} \sqrt{\alpha_r/\beta_r} & \text{if } \sigma_r = 0,\ \alpha_r > 0 \text{ and } \beta_r > 0; \\ 0 & \text{otherwise.} \end{cases} \tag{3.26}$$

In contrast to its magnitude, the phase of $A(t)$ remains unconstrained in this formalism and, in fact, is not needed to evolve the reduced dynamics. Indeed, the reduced system (3.9)-(3.12) is invariant under any such phase change. In the fully nonlinear Boussinesq equations, this quantity would be fixed by the spatial phases of those fluctuation modes of generally small initial amplitude that become linearly unstable on the fast time scale; that is, this phase information ultimately depends on the details of the initial conditions, which are filtered in this framework. A primary virtue of this formalism is precisely that numerical time-integration need only be performed on the *slow* time scale t without the arbitrary reinitialization of the fluctuation fields at each slow time instant. Specifically, at each slow time step, the following algorithm is executed.

(i) The direct eigenvalue problem $\mathcal{L}X = 0$ is solved with periodic boundary conditions in z, and both the eigenvalue σ of largest real part and the corresponding eigenvector X are computed.

(ii) Step (i) is repeated over adjacent k (i.e. $k - \Delta k$ and $k + \Delta k$, for suitably small horizontal wavenumber increment Δk) to reach a wavenumber k corresponding to a local maximum of $\sigma_r(k)$.

(iii) If $\sigma_r(k) = 0$ (numerically, if $\sigma_r(k) \geqslant 0$), the adjoint eigenvalue problem $\mathcal{L}^\dagger X^\dagger = 0$ is solved with periodic boundary conditions in z, and a nonzero eigenvector $X^\dagger$ corresponding to the null eigenvalue is returned. The modal amplitude $|A(t)|$ is then computed through (3.26).

(iv) The mean fields $\overline{u}$ and $\overline{b}$ are then time-advanced using a suitable discretization of (3.9)–(3.10).

Finally, note that in the present formulation, k is determined by scanning over a range of wavenumbers at each slow time (step (ii) of the algorithm detailed above) to identify a local maximum of $\sigma_r(k)$. In companion work, we are seeking an extension of this algorithm that obviates the need to solve the eigenvalue problem repeatedly for different wavenumbers k by deriving a set of slow equations for both $|A(t)|$ *and* $\mathrm{d}k/\mathrm{d}t$; see Ferraro (2019). Regardless of the algorithmic details, the wavenumber k in the multiple time-scale formulation can smoothly vary on the slow time scale t. Crucially, this variation makes possible the accurate computation of the wavenumber that would be realized in the limit of an *infinite* horizontal domain, thereby ameliorating a recurring issue in the study of, e.g., the nonlinear dynamics of parallel shear flows and transition to turbulence (Tuckerman et al. 2020).

4. Illustrative application to strongly stratified Kolmogorov flow

In this section, we explore the dynamics of the reduced equations (3.1)–(3.4) when the flow is driven by an imposed (deterministic) mean body force that contains a single vertical wavenumber m: $\overline{f} = (m^2/Re_b)\cos(mz)$. The coefficient m^2/Re_b is chosen so that the resulting steady laminar velocity profile that would be driven in the absence of instabilities is simply $\overline{u}_L(z) = \cos(mz)$ (where a subscript 'L' is used to refer to the laminar or base state); i.e. we consider (2D) stratified Kolmogorov flow. For specificity, we fix the values of the parameters $m = 3$ and $Pr = 1$. Note that by choosing an order unity numerical value for the forcing wavenumber m, we are directly driving 'velocity layers,' each having a dimensional thickness of order $h = U/N$. To facilitate careful assessment of the performance of our multiple time-scale algorithm, we restrict the vertical extent of our computational domain to encompass only a single pair of shear layers, recognizing that in so doing we preclude the occurrence of potentially important long-wavelength instabilities in the vertical direction; in particular, see Balmforth and Young (2002), Balmforth and Young (2005) and Garaud et al. (2015).

As documented in § 4.1, linear stability analysis confirms that the base flow $\bar{u}_L$ is strongly unstable to small-amplitude perturbations. The resulting instabilities excite vertical motions that enhance mixing and sustain a buoyancy staircase. Consequently, the chosen stratified Kolmogorov flow configuration provides a framework to perform both (i) a quantitative comparison between DNS of the governing 2D Boussinesq equations and the reduced model derived for the LAST regime in the limit of small Froude and large Reynolds number, and (ii) an investigation of the mixing enhancement and mean buoyancy profile as Re_b is increased.

4.1. *Linear stability analysis*

We begin by considering the linear stability of $\overline{u}_L(z) = \cos(3z)$ in the presence of the imposed linear stratification (and zero mean perturbation, so that $\overline{b}_L(z) = 0$), as governed by the subsystem (3.3)–(3.4). Making a normal mode ansatz for a disturbance mode with χ-wavenumber k, $\psi'(\chi, z, \tau) = \hat{\psi}(z)\mathrm{e}^{ik(\chi - c\tau)} + \text{c.c.}$, where the complex phase speed $c \equiv \omega/k$ (for angular frequency ω), yields the TG equation in the non-dissipative limit $Fr/Re_b \to 0$:

$$\frac{d^2\hat{\psi}}{dz^2} + \left[\frac{\left(1 + \partial_z \overline{b}_L\right)}{\left(\overline{u}_L - c\right)^2} - \frac{\partial_z^2 \overline{u}_L}{\left(\overline{u}_L - c\right)} - k^2\right]\hat{\psi} = 0. \tag{4.1}$$

The local-in-time gradient Richardson number $Ri_g = (1 + \partial_z \overline{b})/|\partial_z \overline{u}|^2$. For the given basic-state profile, $\overline{u}_L(z) = \cos(3z)$ and $\overline{b}_L(z) = 0$, so the gradient Richardson number of the laminar state

$$Ri_{gL} = \frac{1}{m^2 \sin^2(mz)}, \tag{4.2}$$

which attains a minimum value $Ri_{gL_{\min}} = 1/m^2$ for $z = \pm\pi/(2m), \pm 3\pi/(2m) \ldots$ Thus, for the chosen parameter values $Ri_{gL_{\min}} = 1/9 < 1/4$, so the Miles–Howard necessary criterion for linear instability is satisfied. Of course, the incorporation of diffusion will modify this inviscid criterion, but the effective diffusivity Fr/Re_b is much less than unity in the subsequent numerical simulations and acts only as a regular perturbation to the non-dissipative problem in smooth regions of the flow.

4.2. *Nonlinear evolution*

To assess the performance of the reduced system quantitatively, a set of numerical simulations is performed for $Re_b = 1$ and decreasing values of Fr down to 10^{-2}. Three different numerical algorithms are compared, each implemented in the computing environment *Dedalus* (Burns et al. 2020). In each case, a pseudo-spectral method is used with a second-order Runge-Kutta time-stepping scheme. Python codes are provided as electronic supplementary material.

First, a set of direct numerical simulations (DNS) of the primitive 2D Boussinesq equations, that is (2.1)–(2.4) rendered two-dimensional, is performed. With $\alpha = Fr$, we note that the dimensionless total energy density is $(u^2 + Fr^2 w^2 + b^2)/2$. The domain, of vertical size $l_z = 2\pi/3$ and of horizontal size $L_x = (2\pi/k)Fr$, is discretized using a Fourier–Fourier pseudo-spectral method with 128 grid points in each direction. Note that k must be specified initially and remains fixed for the duration of the simulation.

The second algorithm is the single time-scale formulation of the QL system (STQL) introduced in § 3.1. These simulations also are set in a domain of size $l_z = 2\pi/3$ and $l_x = 2\pi/k$ using 128 grid points (cf. Fourier modes) in each direction. As for the DNS, k must be fixed *a priori*. Unlike the DNS, certain terms in the governing Boussinesq equations are consistently neglected in the STQL simulations, in accord with the multiple scales analysis performed in the limit $Fr \to 0$ with Re_b fixed.

The third numerical scheme integrates the multiple time-scale formulation of the QL system (MTQL). The equations governing the 1D evolution of the slowly-evolving mean fields $\bar{u}(z,t)$ and $\bar{b}(z,t)$, (3.1) and (3.2), respectively, are discretized using Chebyshev polynomials – rather than Fourier modes, for compatibility with the *Dedalus* eigenvalue solver – with 128 grid points. As detailed in § 3.2, the filtered dynamics of the fast fluctuations is obtained by solving at each slow time-step a 1D eigenvalue problem, yielding the instantaneous linear growth rate σ_r and vertical mode structure ($\hat{\Psi}(z;t)$ and

$\hat{b}(z;t)$) of the most unstable mode. Once the wavenumber k is updated and determined to correspond to a local maximum of $\sigma_r(k)$ within $\Delta k = 10^{-3}$, the amplitude of the fluctuation mode is set in accord with condition (3.26). Again, we emphasize that in the MTQL algorithm the wavenumber k is *not* fixed, but evolves so that the marginally stable wavenumber is tracked, with modes corresponding to adjacent values of k being linearly stable. In principle, the amplitude $A(t)$ of the fluctuation mode would be updated continually such that $\sigma_r = 0$ remains fixed; in practice, σ_r would remain very close to the first positive value computed, which depends on the specific value of the time step Δt but, in any case, will be very small compared to unity (e.g. $\sigma_r = 2 \times 10^{-4}$ for $Fr = 0.02$, $Re_b = 1$ and $\Delta t = 10^{-4}$). To achieve a steady state in which σ_r is independent of the time step, the modal amplitude $A(t)$ is artificially increased during the transient regime such that

$$\text{if } \sigma_r > 10^{-6} \text{ and } A > 0, \text{ then } A^2 = \frac{\alpha_r}{\beta_r} + \frac{\sigma_r}{1000\beta_r \Delta t}. \tag{4.3}$$

According to (3.24), σ_r will, if A is subject to this change, vary during the $(n+1)$-st time step according to $\Delta\sigma_r \equiv \sigma_r^{n+1} - \sigma_r^n = -\sigma_r^n/1000$, and therefore will relax exponentially to zero provided the stated conditions are satisfied. Note that this modification minimally affects the transient regime, and is no longer applied once a steady-state is reached, since then $\sigma_r < 10^{-6}$.

The same time step $\Delta t = 10^{-4}$ is used in all of the numerical simulations. It should be emphasized, however, that because the MTQL system is evolved on the slow time scale much larger values of Δt could be utilized for the MTQL simulation. Although a detailed study of the computational savings afforded by the MTQL algorithm is beyond the scope of this investigation, we note here that the steady state depicted subsequently for $Fr = 0.02$ and $Re_b = 1$ is also quantitatively reproduced with the MTQL algorithm using a time step $\Delta t = 0.01$ (i.e. 100 times larger) for which the DNS algorithm is numerically unstable.

We first discuss the MTQL dynamics for $Re_b = 1$ and $Fr = 0.02$. The simulation is forced from a rest state, i.e. with zero initial velocity and zero buoyancy deviation from the imposed background linear stratification. During the transient phase of the dynamics evident in figure 2a, the real part of the maximum growth rate over all horizontal wavenumbers greater than a minimum viscous threshold (see below) remains negative until $t \simeq 0.175$, when it reaches zero: the amplitude of the fluctuation fields A then jumps to a finite value to prevent further growth of σ_r. This behavior, which is clearly depicted in the movie included in the supplementary material, accounts for the discontinuity in the slow-time evolution of the total energy (see insert in figure 2*a*). A nonlinear steady state – one type of *exact coherent state* (ECS) arising in forced–dissipative nonlinear infinite-dimensional dynamical systems (Kawahara and Kida 2001; Lucas et al. 2017; Lucas and Caulfield 2017; Parker et al. 2019) – supported by a *single* horizontal mode with a wavenumber $k = 2.515$ eventually is attained. Note that this single-mode structure is emergent, not imposed.

Figure 2*b* shows the evolution of the growth-rate spectrum during the MTQL simulation. At $t = 1.5$, the earliest time depicted, all modes with wavenumbers greater than about unity are damped. We have confirmed that the linearly unstable oscillatory modes (with $\sigma_i \neq 0$) arising at small k disappear for vanishingly small stratification; in contrast, stratification is not a necessary condition for the instabilities evident at later times for $k \simeq 2.5$, a distinction recently made by Parker et al. (2019). For simplicity, we choose to avoid constraining the unstable modes arising at small k since σ_r remains very small – and is even smaller at larger values of Re_b (see the inset in figure 8) – for these modes when the mode with $O(1)$ k is saturated. Nevertheless, we emphasize that in principle the

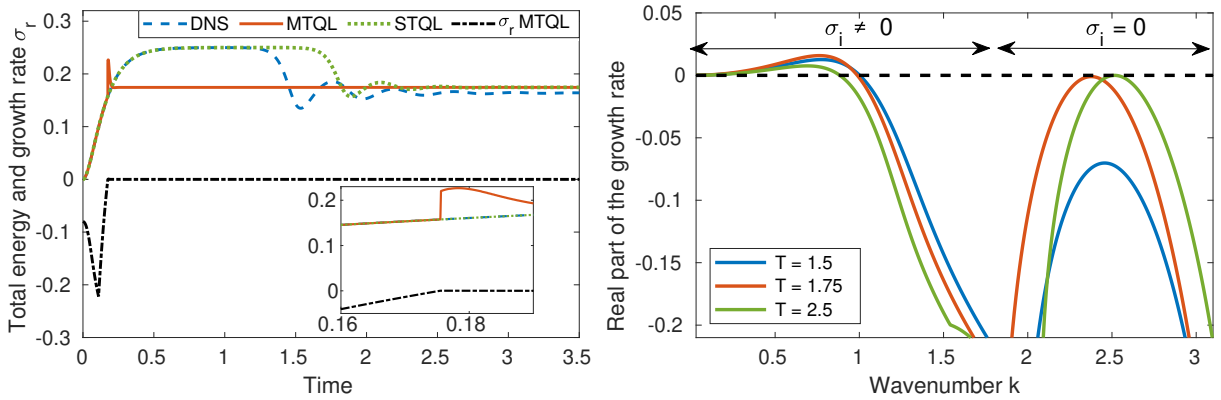

FIGURE 2. DNS, STQL and MTQL simulations of stratified Kolmogorov flow forced from a randomly perturbed rest state with $Re_b = 1$ and $Fr = 0.02$. (a) Total energy of the flow as a function of time. For the MTQL simulation, σ_r also is plotted. (b) Maximum fluctuation growth rate σ_r as a function of k shown for three different times during the MTQL simulation. Note the saturation of σ_r to zero at wavenumbers $k \simeq 2.5$ and the presence of weakly-amplified oscillatory modes (ignored in this study), with non-zero σ_i, at small k.

MTQL algorithm could be modified to marginalize these modes, too. At an intermediate time, $t = 1.75$, a marginal mode with wavenumber $k \simeq 2.25$ corresponds to the mode with locally maximum growth rate, but by $t = 2.5$ the wavenumber of this mode has evolved to $k \simeq 2.5$. For the given configuration, these modes with $O(1)$ k have zero phase speed (since $\sigma_i = 0$) and correspond to Kelvin–Helmholtz instabilities.

To perform a quantitative comparison of the three algorithms, both a DNS and STQL simulation also are run for the same parameters ($Re_b = 1$ and $Fr = 0.02$). For these simulations, the horizontal domain length, $L_x = (2\pi/k)Fr$ and $l_x = 2\pi/k$, respectively, is specified using $k = 2.515$, i.e. the emergent steady-state wavenumber obtained using the MTQL algorithm. Were it possible to perform the DNS and STQL simulation in the limit $L_x, l_x \to \infty$, we would expect an ECS with this horizontal wavenumber to be realized. The evolution of the total energy reported in figure 2 shows that, in all three simulations, there is an overshoot of the total energy density, corresponding to the "bursting regime" documented in Michel and Chini (2019) and observed in 3D DNS of the full Boussinesq equations (Rorai et al. 2014; Feraco et al. 2018). The MTQL and STQL simulations converge precisely to the same steady state, as can be confirmed by inspection of figures 2 and 3; of course, this convergence is not entirely surprising (although not guaranteed) given that the same equations are being solved in the *steady* limit [cf. (3.1)–(3.4)].

In figure 3, which shows the steady ECS computed using the DNS (left), MTQL (middle) and STQL (right) algorithms, color indicates the total buoyancy field, i.e. including the imposed background linear stratification, while arrows are used to depict the velocity field. To facilitate the comparison of the 2D structure, note that the DNS velocity field $(u, \epsilon^2 W)$ is plotted, while the corresponding fields $(\bar{u}_0 + \epsilon u_1', \epsilon W_{-1}')$ are shown for the STQL and MTQL simulations [cf. (2.6) and (2.7)]; that is, all velocity components are normalized by U. The agreement among the three steady-state ECS lends confidence to the asymptotically-reduced system (3.1)–(3.4) and thereby to the novel MTQL algorithm. The small quantitative discrepancy between the final energies of the ECS obtained from the DNS and via the STQL/MTQL algorithms (figure 2*a*) is partly attributable to the omission of the mean-field correction $\epsilon\overline{u}_1$ from the latter schemes. If desired, this correction could be self-consistently computed by carrying the

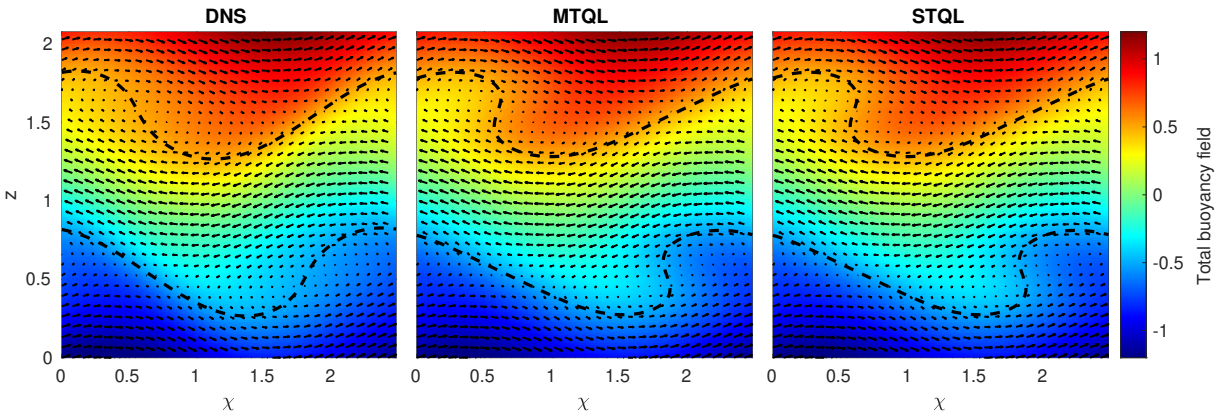

FIGURE 3. Comparison of the steady ECS computed in stratified Kolmogorov flow for $Re_b = 1$ and $Fr = 0.02$ using DNS (left), MTQL (center) and STQL (right) algorithms. The total buoyancy field (including the imposed linear profile) is shown in color, while arrows are used to depict the isotropically scaled velocity field in each case. To accentuate differences between the QL results and DNS, the total buoyancy contours $z + \bar{b} = \pm 0.5$ are highlighted (dashed curves).

analysis to higher-order, although we emphasize that the reduced system (3.1)–(3.4) is both asymptotically consistent (apart from the diffusive regularization) and closed.

The agreement between the DNS and MTQL/STQL simulations is expected to improve as Fr is decreased, since the reduced model is derived in the limit $Fr \to 0$. To assess the asymptotic convergence of the MTQL algorithm in that limit, a suite of DNS and MTQL simulations with $Re_b = 1$ is performed for a set of decreasing values of Fr. For the given parameter regime, the MTQL algorithm always converges to a steady state. The long-time dynamics exhibited by the DNS, however, becomes time-dependent for $Fr < 0.012$. Given that the fluctuation-induced mixing is of central importance (see § 4.3), we choose to compare, in figure 4, the energy of the fluctuation fields computed using DNS and the MTQL algorithm for $Fr \geqslant 0.012$. (In particular, the contribution of the fluctuations to the total energy is $O(Fr)$, hence the use of this proxy to examine quantitatively the limit $Fr \to 0$). Indeed, using Parseval's identity, the dimensionless total energy of the primitive 2D Boussinesq equations (with $\alpha = Fr$),

$$E_{\text{tot}} = \int \mathrm{d}\chi \mathrm{d}z \left(u^2 + Fr^2 w^2 + b^2\right)/2,$$

can be re-expressed as a sum of the energy contained in the various horizontal modes k; that is $E_{\text{tot}} = \sum_{k \geqslant 0} E_k$.

As evident in the figure, the relative error in the fluctuation energy is computed two different ways. The red circles show the relative error when the fluctuation energy is computed using the total DNS fluctuation energy summed across all horizontal Fourier modes with non-zero wavenumber. In addition, the blue squares show the relative error based on the DNS fluctuation energy contained only in the fundamental Fourier mode with wavenumber k. Clearly, both metrics confirm that solutions of the asymptotically-reduced equations converge to those of the full Boussinesq equations in the distinguished limit considered, namely, as $Fr \to 0$ with Re_b fixed, although only the data for the fundamental mode approximates the expected rate of decay in the relative error.

4.3. *Exact coherent states for larger Re_b*

Steady states can be reached in the MTQL simulations at $Re_b = 1$ even for $Fr < 0.012$, a regime in which the DNS exhibit persistent unsteady dynamics. Nevertheless, the long-

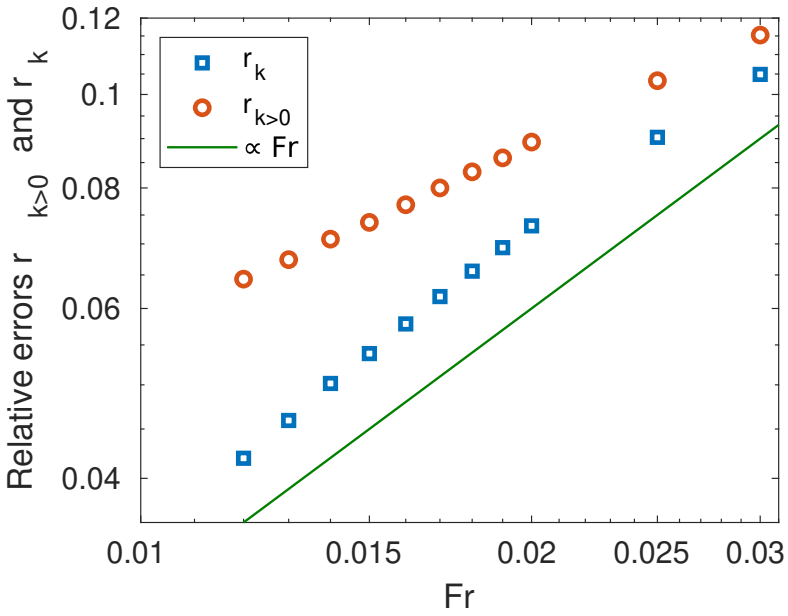

FIGURE 4. Convergence of the steady ECS computed at Re_b=1 using the asymptotically-reduced system (3.1)–(3.4) to the corresponding steady solution of the full 2D Boussinesq equations in the limit $Fr \to 0$. The red symbols show the relative error computed using the total fluctuation energy obtained from the DNS (the sum of the energy in each non-zero horizontal Fourier mode), i.e. $r_{k>0} = |E^{\rm DNS}_{k>0} - E^{\rm MTQL}_{k>0}|/E^{\rm DNS}_{k>0}$. The blue symbols show the relative error evaluated using the fluctuation energy only in the Fourier mode with the fundamental wavenumber k, again as obtained from the DNS, $r_k = |E^{\rm DNS}_k - E^{\rm MTQL}_k|/E^{\rm DNS}_k$. For reference, the solid green line has a slope equal to Fr^1.

time MTQL dynamics need not be steady or regular on the slow time scale, and for sufficiently large Re_b we anticipate that more complex dynamics would be exhibited within the two time-scale framework. For the parameter regime considered here, however, the MTQL algorithm – although ostensibly not specifically designed for this purpose – has the virtue of yielding *exact coherent states* (ECS) that would be linearly unstable within the full Boussinesq dynamics. For at least the last twenty years, such states have been known to be able to capture certain characteristic attributes of the turbulent regime; see e.g. Kawahara and Kida (2001). ECS have been of particular interest in the context of wall-bounded constant-density shear flows, where a general mechanism supporting such states has been identified (Hamilton et al. 1995). Numerical computation of ECS from the governing Navier–Stokes or Boussinesq equations typically requires recurrent flow analyses of expensive direct numerical simulations to provide suitable initial conditions for sophisticated Newton-hookstep solvers, although more efficient approaches have been proposed (Page and Kerswell 2020). In contrast, it is clear from the present investigation and related studies (Hall and Sherwin 2010; Beaume et al. 2015; Montemuro et al. 2020) that asymptotically-reduced systems, derived using multiple scales analysis, retain the dominant interactions that sustain such states while self-consistently filtering other dynamics, yielding more efficient algorithms for ECS computations and simultaneously exposing the underlying physical mechanisms.

Lucas et al. (2017) and Lucas and Caulfield (2017) computed ECS in 3D stratified Kolmogorov flow with a *horizontally-varying* forcing (in contrast to the present study). Of particular interest is the mixing efficiency associated with these ECS, which the authors were able to compute for $Re_b \leqslant 95$ and $Fr \geqslant 0.23$. With a similar aim, we compute by continuation steady-state ECS in 2D stratified Kolmogorov flow using the MTQL

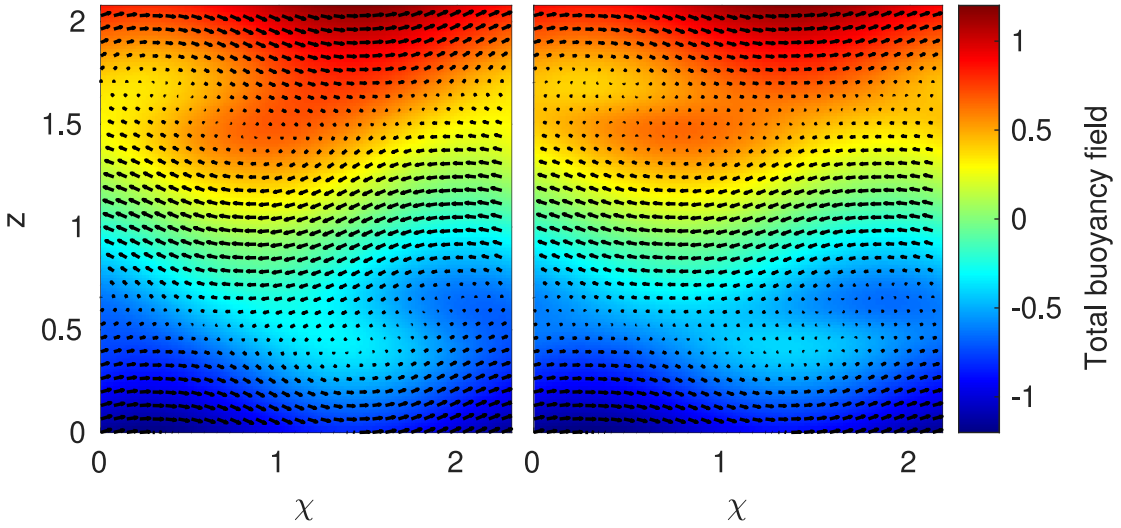

FIGURE 5. Comparison of steady ECS in stratified Kolmogorov flow for $Fr = 0.01$ and $Re_b = 1$ (left) and $Re_b = 10$ (right) computed using the MTQL algorithm. The total buoyancy field (including the imposed linear profile) is shown in color, while the arrows are used to depict the isotropically scaled velocity field in each case.

algorithm for $Fr = 0.01$ and $Re_b \in [1, 10]$; i.e. steady states obtained at given Re_b values are used as initial iterates in MTQL simulations performed at incrementally larger Re_b. We again emphasize that the horizontal domain size (or fundamental wavenumber) is not imposed *a priori* but rather is an emergent property of our computations.

The steady ECS fields for the two extreme values of Re_b are depicted in figure 5. Even these relatively simple (2D) steady states exhibit features that are commonly associated with stratified turbulence; in particular, the solutions indicate the spontaneous emergence of two layers of relatively well-mixed fluid centered on $z = \pi/6 \simeq 0.5$ and $z = \pi/2 \simeq 1.6$, separated by broader 'streams' flowing in opposite directions. This feature is even more clearly evident in the mean buoyancy and velocity profiles ($\bar{b}$ and $\bar{u}$) shown in figure 6 and can be interpreted in the light of the linear stability analysis described in § 4.1. The vertical locations of the mixed layers match those of the minima of the gradient Richardson number of the laminar flow; see (4.2). In the inviscid limit, these locations would correspond to critical layers in which $\bar{u}_L - c$ vanishes, leading to discontinuities in both the buoyancy and the vertical derivatives of the horizontal velocity. In practice, the small but finite viscosity smooths these abrupt variations and leads to layers of finite thickness. In the small Fr limit analyzed here, the system *self-adjusts* to an equilibrium state that is approximately marginally stable with respect to the emergent mean profiles – so the critical layer interpretation remains quantitatively valid provided that $\bar{u}_L$ is replaced with $\bar{u}$, and z (the background stratification) is replaced with $z + \bar{b}$.

The staircase-like profile of $z + b$ has been analyzed thoroughly in the recent 3D DNS study of Maffioli (2019), who measured the dimensionless third-order moment (i.e. the skewness)

$$S \equiv \frac{\left\langle (\partial_z b)^3 \right\rangle}{\left\langle (\partial_z b)^2 \right\rangle^{3/2}}, \tag{4.4}$$

where $\langle \cdot \rangle$ denotes a spatial average over the entire domain, and it should be recalled that $b(\chi, z) = \bar{b}(z) + b'(\chi, z)$ is the buoyancy deviation from the imposed linear profile (z). Interestingly, based on the DNS of Maffioli (2019), S does not appear to converge to a finite value in the strongly stratified turbulence regime. Instead, the author finds that

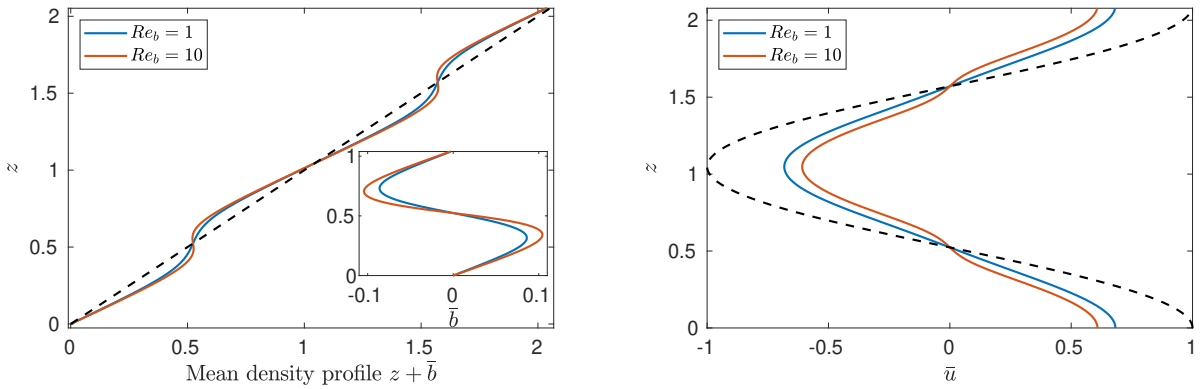

FIGURE 6. Steady-state mean vertical profiles of buoyancy (left) and horizontal velocity (right) computed using the MTQL algorithm for $Fr = 0.01$ and $Re_b = 1$ (blue) and $Re_b = 10$ (red). The dashed lines correspond to the unstable laminar state, with velocity profile $\bar{u}_L = \cos 3z$ and buoyancy perturbation $\bar{b} = 0$.

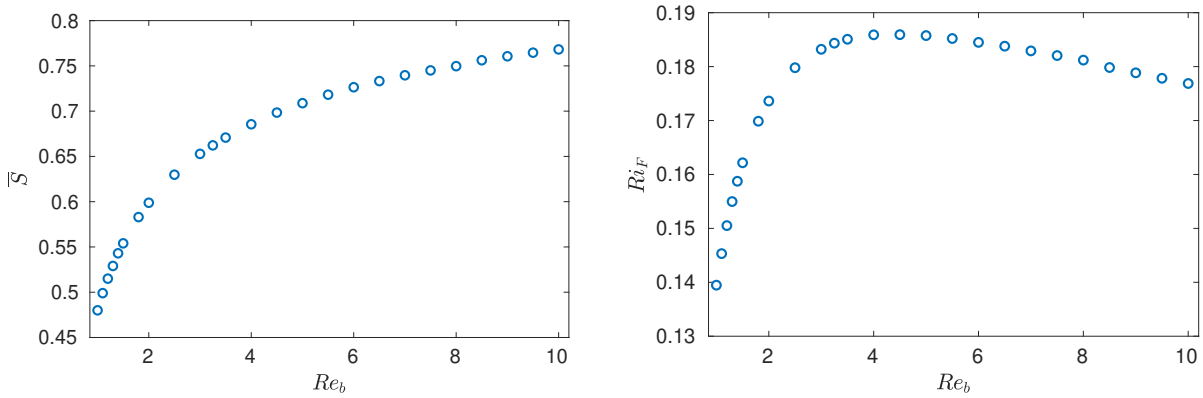

FIGURE 7. Mean quantities computed from the steady state ECS obtained at $Fr = 0.01$ as a function of Re_b. Left: skewnesses $\bar{S}$. Right: flux Richardson number Ri_F.

$S \sim cFr^{-0.41}$ (for some constant c), the dependence on Re_b not having been investigated. Noting that the layering evident in figure 6 is related directly to $\bar{b}$ rather than to b, we therefore also define the skewness of the horizontally-averaged buoyancy profile

$$\bar{S} = \frac{\left\langle \left(\partial_z \bar{b}\right)^3 \right\rangle}{\left\langle \left(\partial_z \bar{b}\right)^2 \right\rangle^{3/2}}. \tag{4.5}$$

Indeed, given the expansion (2.6), S reduces to $\bar{S}$ at leading order. The averaging over χ is, of course, straightforward in the present study owing to the multiple scales decomposition but would prove challenging in a DNS because of the spatial variation of the layer with χ. As shown in figure 7, $\bar{S}$ increases monotonically with Re_b with no sign of convergence to a finite value as Re_b is increased. A crude piecewise linear approximation of the buoyancy profiles yields an estimate of $\bar{S}$ as a function of the ratio of the height of the streams $h_{\rm st} \sim L \times Fr$ to that of the emergent mixed layer $h_{\rm ML}$ only (Maffioli 2019). This estimate suggests that $h_{\rm ML}/L$ does not become independent of Re_b in the strongly stratified limit; in particular, $h_{\rm ML}$ is not simply given by the Ozmidov scale $L_O \sim L \times Fr^{3/2}$.

Another quantity of interest is the mixing efficiency achieved by these steady ECS. Characterizing stratified mixing in the natural environment is a longstanding question, notably because stratified turbulence in the atmosphere and oceans occurs in a parameter regime in which both $Fr \ll 1$ and $Re_b \gg 1$. As discussed in detail by Gregg et al. (2018), an unfortunate additional source of complexity is that several different measures of

mixing have been proposed, which can differ significantly from each other in the turbulent regime; see e.g. Venayagamoorthy and Koseff (2016). Here, we choose to compute the flux Richardson number Ri_F, defined as the ratio of the volume-integrated buoyancy flux to the power injected by the external force:

$$Ri_F = \frac{\int \tilde{w}\,\tilde{b}\,\mathrm{d}V}{\int \tilde{\mathbf{f}}\cdot\tilde{\mathbf{u}}\,\mathrm{d}V}, \tag{4.6}$$

where tildes refer to dimensional variables. For steady ECS, this measure coincides with other quantities usually introduced to quantify the mixing, e.g. the mixing efficiency $\mathcal{E}$ based on the dissipation rates of kinetic and available potential energy; see Caulfield and Peltier (2000), Peltier and Caulfield (2003), Salehipour and Peltier (2015) and Maffioli et al. (2016). The DNS of Maffioli et al. (2016) and Portwood et al. (2019) suggest a constant flux coefficient $\Gamma = Ri_F/(1-Ri_F) \simeq 0.2$ in the strongly stratified turbulent limit, whereas the periodic-orbit ECS of Lucas and Caulfield (2017) indicate a progressive decrease toward zero as Re_b is increased. Note that the turbulent flux coefficient experiences strong variations as a function of Fr in the range $[0.05, 0.5]$ (Feraco et al. 2018) and that *in situ* measurements in the open ocean indicate a transition from a constant value to a decreasing one at $Re_b \gtrsim 100$ (Lozovatsky and Fernando 2013; Monismith et al. 2018) although there is still outstanding controversy; see Caulfield (2020, 2021). DNS in the regime $Fr \ll 1$ and $Re_b \gg 1$ clearly are needed to resolve this issue conclusively but are not feasible with current computing power (figure 1).

Given the scalings assumed here, the flux Richardson number defined in (4.6) is computed for the steady-state ECS via

$$Ri_F = -ik|A|^2 \frac{\int_0^{l_z} (\hat{\Psi}^*\hat{b} - \hat{\Psi}\hat{b}^*)\,\mathrm{d}z}{\int_0^{l_z} \bar{f}\,\bar{u}_0\,\mathrm{d}z}. \tag{4.7}$$

The variation of Ri_F with Re_b is shown in figure 7 (right). For the range of Re_b considered, Ri_F varies between 0.13 and 0.18. These values correspond to values of the flux coefficient Γ ranging from approximately 0.16 to 0.22, in reasonable accord with the upper bound on Ri_F of 0.15 proposed by Osborn (1980) and corresponding to $\Gamma \leqslant 0.2$. The overshoot of the mixing measure is reminiscent of that reported in both Maffioli et al. (2016) and Lucas and Caulfield (2017). Unfortunately, as in other investigations, larger values of Re_b would be required to establish the limiting behavior of Ri_F for these steady ECS. One virtue of the systematically-reduced formulation derived here is that it should facilitate such investigations. Although we leave this task for a future study, referring to figure 7 it is conceivable that Ri_F asymptotes to a value near 0.17 for large Re_b (again, for the given steady 2D ECS); intriguingly, this value corresponds to $\Gamma = 0.2$, as seen by Portwood et al. (2019).

Finally, we discuss the Re_b-dependence of the fluctuation growth-rate spectrum for the steady ECS. As evident in figure 8, the positive linear growth rate regime at small wavenumber is suppressed as Re_b is increased, partly justifying our choice to disregard these modes in this investigation since our reduced modeling efforts ultimately are aimed at accessing large values of Re_b. Interestingly, at $Re_b = 10$, there is a second local maxima in the growth rate (ignoring the low-wavenumber mode) around $k \simeq 2.5$ that plausibly could spawn the emergence of a second linearly unstable mode for which marginal stability also would have to be enforced. This eventuality could be treated by introducing a second non-zero modal amplitude $B(T)$ and vertical eigenfunctions $[\hat{\Psi}_B(z), \hat{b}_B(z)]$ corresponding to this wavenumber, labeled k_B, generalizing the procedure introduced in § 3.2: instead of the single equation $(\partial\sigma_{Ar}/\partial t)|_{k_A} = \alpha_{Ar} - \beta_{Ar}|A|^2$ for the growth rate

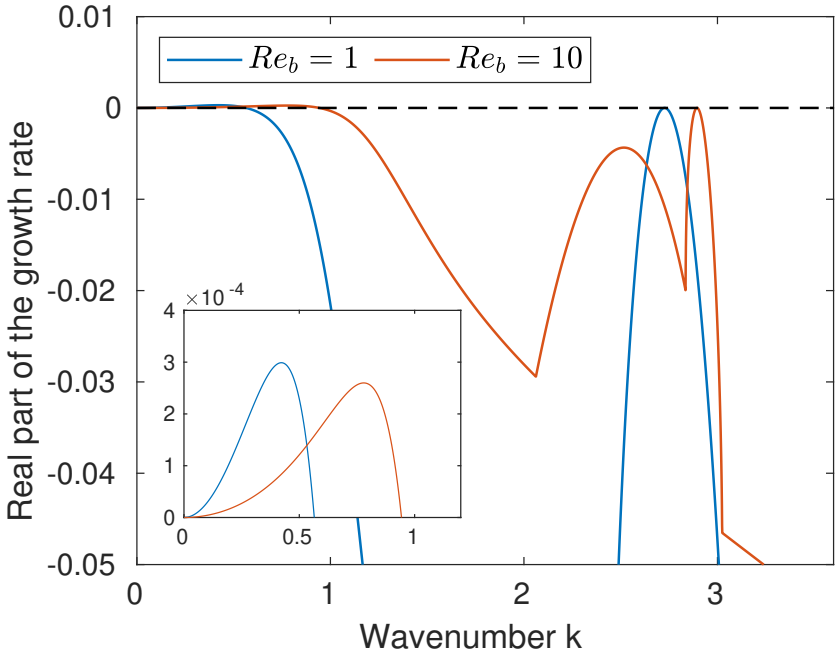

FIGURE 8. Maximum fluctuation-field growth rate as a function of k for the steady ECS computed at $Fr = 0.01$ and $Re_b = 1$ (blue) and $Re_b = 10$ (red). The inset shows the positive growth rates that arise for small k; comparing with figure 2*b* confirms that these low-wavenumber modes are viscous instabilities that vanish as $Re_b \to \infty$.

σ_{Ar} (with associated coefficients α_{Ar}, β_{Ar}) of the sole marginal mode with amplitude A, coupled equations for both σ_{Ar} and σ_{Br} would be derived and solved simultaneously. In this manner, the formalism enables *scale selective adaptivity*, in that modes representing newly emergent length scales are introduced only as needed rather than democratically. Again, this procedure can be implemented with no artificial quantization of wavenumbers imposed by the domain size.

In fact, the potential emergence of a second marginal mode is not the reason we limited this investigation of steady ECS to $Re_b \leqslant 10$. Rather, for $Re_b > 10$ with $Fr = 0.01$, the steady states become dynamically unstable even within the MTQL algorithm. Ultimately, at a certain time during the evolution, $\sigma_r = 0$, $\alpha_r > 0$ and $\beta_r < 0$. Physically, this situation corresponds to marginally stable fluctuations that would become linearly unstable (since $\alpha_r > 0$) and whose feedback on the mean field $\{\bar{u}, \bar{b}\}$ would render the mean field even more unstable (since $\beta_r < 0$). In practice, the fluctuation amplitude would reach such large values that the mean field would be forced to respond on the fast time scale, invalidating the *ansatz* of time scale separation (and possibly quasi-linearity). We emphasize, however, that preliminary studies confirm our expectation that this dynamic (a 'burst') persists only during a short transient, after which marginal stability is re-established and the MTQL algorithm can be restarted. This issue is described in Michel and Chini (2019), and some promising preliminary results involving modification of the MTQL algorithm to account for such bursting regimes are reported in Ferraro (2019). Notwithstanding this current limitation, we emphasize that the value $Re_b = 10$ is attained with the MTQL algorithm for a realistically small Froude number, *viz.* $Fr = 0.01$. In their 3D DNS, the smallest Froude number reached by Lucas and Caulfield (2017) is 0.008, for which $Re_b = 0.25$, and that by Maffioli and Davidson (2016) is 0.02, for which $Re_b = 17$. Although our study has been restricted to 2D stratified Kolmogorov flow, the ECS computations have been performed on a laptop computer, demonstrating the potential for asymptotically reduced modeling of strongly stratified flows with as yet inaccessibly

large Re_b and small Fr. In contrast, the recent DNS of the 2D Boussinesq equations carried out by Kumar et al. (2017) required high-performance computing resources to achieve $Re_b = 130$ (resp. $Re_b = 300$) for their smallest Froude numbers $Fr = 0.16$ (resp. $Fr = 0.31$), suggesting that only $O(1)$ values of Re_b could be attained for $Fr = 0.01$ with similar computational resources.

5. Conclusions

Direct numerical simulations consistently show that both local *and* non-local energy transfers occur in strongly stratified turbulence (Waite 2011; Khani and Waite 2013; Waite 2014; Augier et al. 2015; Khani and Waite 2016; Khani 2018). Heuristically, these transfers can be understood in terms of the dynamics of the characteristic layered and anisotropic flow structures – with much larger horizontal than vertical scales – that are formed owing to the strong stratification. These structures are weakly coupled along the vertical direction, facilitating the occurrence of strong shearing motions. Consequently, in addition to the local energy cascade driven by the self-interaction of these anisotropic structures, stratified shear instabilities can drive non-local energy transfers directly from the large-scale anisotropic flows to much smaller-scale, roughly isotropic motions. While the local energy cascade can be understood using a rescaled variant of Kolmogorov's approach to isotropic 3D turbulence, in particular to predict the energy spectra (Billant and Chomaz 2001; Lindborg 2006), this approach captures only a subset of the general dynamics. Not only are deviations from these energy spectra reported (Waite 2011, 2014; Augier et al. 2015) but also bursting events, manifested by the non-Gaussianity of the probability density functions of the temperature and vertical velocity (Rorai et al. 2014), that lead to a mixing enhancement (Feraco et al. 2018). Both effects may be ascribed to non-local energy transfers.

Guided by these results, we have used multiple scales asymptotic analysis to derive a reduced model of strongly stratified turbulence in the distinguished limit $Fr \to 0$ and $Re \to \infty$ with $Re_b = ReFr^2$ fixed, where the buoyancy Reynolds number Re_b emerges as a primary control parameter in the reduced equations that may be systematically increased (numerically) to explore the large Re_b regime. The analysis explicitly recognizes the occurrence of layered anisotropic stratified turbulence (LAST) with dynamics on disparate horizontal and temporal scales. The large scales are characterized by strongly anisotropic velocity layers, with horizontal scales $O(L)$ and vertical scales $O(FrL) = O(U/N)$ (i.e. the buoyancy scale) and corresponding horizontal velocity U and vertical velocity FrU, that evolve on a slow time scale L/U. The analysis confirms that in the small Fr limit, the large-scale dynamics is not only associated with nonlinear interactions with similar flow structures but also with small-scale structures. These latter structures are themselves isotropic, having spatial scales $O(FrL)$, velocity scales $O(\sqrt{Fr}U)$ and time scale $O(FrL/U) = O(1/N)$, i.e. comparable with the buoyancy period. A reduced set of equations is then obtained for the fields at both large and small scales. According to the reduced dynamics, the large scales can trigger small-scale (e.g. Kelvin-Helmoltz or Holmboe wave) instabilities and in return the small scales can exert feedbacks on the large scales through their Reynolds stress and buoyancy-flux divergences.

A central feature of the reduced dynamics is that the fluctuations satisfy equations that are linear with respect to the mean fields. Herein, this QL reduction is derived self-consistently in a well-defined asymptotic limit rather than being prescribed in an *ad hoc* fashion. Since the mean fields vary slowly in time, the potential exists for the fluctuation fields to grow exponentially while the mean fields remain essentially fixed. Instead, investigation of this and other slow-fast QL systems subject to fast instabilities

confirms that, over a wide parameter regime, the system *self-adjusts* to a state in which the mean fields are approximately marginally stable even though the laminar state that would be realized in the absence of instabilities is strongly unstable. Interestingly, this manifestation of self-organized criticality appears to be compatible with recent observations and DNS of stratified shear flows (Smyth and Moum 2013; Holleman et al. 2016; Salehipour et al. 2018; Smyth et al. 2019) and with the pioneering arguments of Turner (1973) and Sherman et al. (1978). Mathematically, the marginal stability constraint is required to ensure the uniformity of the asymptotic expansions posited in our analysis of strongly stratified shear flows. Following the approach introduced by Michel and Chini (2019), the fluctuation dynamics on the fast time scale can be replaced by a linear eigenvalue problem for the vertical structure of the marginal mode(s). The otherwise indeterminate fluctuation amplitude is set by a solvability condition *slaving* the amplitude to the mean fields to ensure that positive growth rates (on the fast time scale) will not be realized once a state of marginal stability is attained.

Computationally, three primary advantages of this approach accrue. Firstly, the time step for the coupled mean/fluctuation system can be chosen as a fraction of the time scale characterizing the *slow* evolution. By design, this time step is asymptotically much larger than the characteristic time of the fast dynamics. Secondly, the (small) characteristic horizontal length scale of the isotropic fluctuations evolves continuously to ensure that the wavenumber of the fastest-growing mode coincides with that of the marginal mode. Unlike DNS in finite domains, the fluctuation wavenumber is not quantized, effectively capturing the dynamics that would be realized in an arbitrarily large horizontal domain. Finally, our approach naturally enables scale-selective adaptivity, in that additional marginal modes with distinct horizontal wavenumbers can be identified and then introduced only when they are required by the evolving slow dynamics.

To confirm the accuracy and illustrate the merit of the asymptotically-reduced equations and novel multiscale algorithm, a suite of simulations has been performed in the simplified setting of strongly stratified 2D Kolmogorov flow in the absence of slow horizontal variability. Finite-amplitude ECS computed at fixed Re_b are shown to converge to the corresponding steady-state ECS of the full Boussinesq equations as Fr is systematically reduced, confirming the asymptotic validity of the reduced system. In addition, a parametric study of the ECS obtained with the multiscale algorithm for $Fr = 0.01$ and increasing values of Re_b ranging from one to ten reveals several interesting features. (Note that DNS in this regime yields persistent time-dependent dynamics.) Firstly, the ECS exhibit spontaneous layering, in which the background linear stratification develops a staircase-like profile with regions of increased stratification ('interfaces') separated by emergent well-mixed 'layers'. Although larger values of Re_b would be required to address the limiting behaviors of both the flux Richardson number and the skewness of the horizontally-averaged buoyancy profile, the former varies in a range corresponding to a turbulent flux coefficient Γ of approximately 0.2 while the latter suggests that the height of the emergent mixed layers does *not* reduce to the Ozmidov scale in strongly stratified turbulence.

We believe that extension of our multiscale reduced system to incorporate three-dimensional dynamics at higher Re_b ultimately will enable these and other outstanding questions regarding strongly stratified mixing to be addressed. Simultaneously, our approach opens new avenues for more accurate sub-grid-scale parameterizations, e.g. to be used in hydrostatic general circulation models, than currently can be achieved with variants of eddy-viscosity modeling. Several mathematical and algorithmic advances, however, are needed. Most importantly, the transient *fast* dynamics of the large scales must be properly captured: during these short periods, temporal scale separation is lost

at least intermittently. Reincorporation of slow horizontal spatial variability similarly is necessary, but raises attendant questions about the numerical treatment of the local downscale energy cascade that would be generated within the context of the multiscale system. A mathematical formalism for predicting the evolution of the wavenumber of the marginal mode not only would be more elegant but presumably more efficient than the rather brute-force approach implemented here. Finally, the reduced model itself could be improved by incorporating a second *vertical* scale to more properly account for the potentially complex dynamics that may be realized within the thin, emergent mixed layers. If feasible, this advance would obviate the need for reintroducing the Froude number Fr into the multiscale reduced system and may capture new dynamical phenomena associated with nonlinear critical layer dynamics. This extension also would be compatible with the emerging conceptual picture that the turbulent motions in apparently very strongly stratified turbulence, with small (global) values of Fr, occupy only a small fraction of the total stratified fluid volume – and in those regions, the stratification is locally very much eroded, as identified using a robust automatic algorithm by Portwood et al. (2016). All these challenges are the subject of ongoing research (e.g. see Ferraro 2019).

Funding. GPC and GM acknowledge the hospitality of the Kavli Institute for Theoretical Physics, where much of this research was completed and supported in part by the National Science Foundation under Grant No. NSF PHY-1748958. GPC also gratefully acknowledges support from the Office of Naval Research under Grant No. ONR-BRC N000141712307. All authors acknowledge support from the Woods Hole Summer Program in Geophysical Fluid Dynamics, where this work was initiated.
Declaration of Interests. The authors report no conflict of interest.

REFERENCES

Ait-Chaalal, F., Schneider, T., Meyer, B. and Marston, B. 2016. Cumulant expansions for atmospheric flows. *New Journal of Physics* 18(2): 1–24

Augier, P., Billant, P. and Chomaz, J.-M. 2015. Stratified turbulence forced with columnar dipoles: numerical study. *J. Fluid Mech.* 769: 403–443

Augier, P., Chomaz, J.-M. and Billant, P. 2012. Spectral analysis of the transition to turbulence from a dipole in stratified fluid. *J. Fluid Mech.* 713: 86–108

Balmforth, N. J. and Young, Y.-N. 2002. Stratified Kolmogorov flow. *J. Fluid Mech.* 450: 131–167

Balmforth, N. J. and Young, Y.-N. 2005. Stratified Kolmogorov flow. Part 2. *J. Fluid Mech.* 528: 23–42

Bartello, P. and Tobias, S. M. 2013. Sensitivity of stratified turbulence to the buoyancy Reynolds number. *J. Fluid Mech.* 725: 1–22

Beaume, C., Chini, G. P., Julien, K. and Knobloch, E. 2015. Reduced description of exact coherent states in parallel shear flows. *Phys. Rev. E* 91: 043010:1–18

Billant, P. and Chomaz, J.-M. 2001. Self-similarity of strongly stratified inviscid flows. *Physics of Fluids* 13(6): 1645

Bois, P. A. 1991. Asymptotic aspects of the Boussinesq approximation for gases and liquids. *Geophys. Astrophys. Fluid Dynamics* 58: 45

Brethouwer, G., Billant, P., Lindborg, E. and Chomaz, J.-M. 2007. Scaling analysis and simulation of strongly stratified turbulent flows. *J. Fluid Mech.* 585: 343–368

Burns, K. J., Vasil, G. M., Oishi, J. S., Lecoanet, D. and Brown, B. P. 2020. Dedalus: A flexible framework for numerical simulations with spectral methods. *Phys. Rev. Research* 2: 023068

Caulfield, C. P. 2020. Open questions in turbulent stratified mixing: Do we even know what we do not know? *Phys. Rev. Fluids* 5: 110518

Caulfield, C. P. 2021. Layering, instabilities, and mixing in turbulent stratified flows. *Ann. Rev. Fluid Mech.* 53: 113–145

Caulfield, C. P. and Peltier, W. R. 2000. The anatomy of the mixing transition in homogeneous and stratified free shear layers. *J. Fluid Mech.* 413: 1–47

Child, A., Hollerbach, R., Marston, B. and Tobias, S. 2016. Generalised quasilinear approximation of the helical magnetorotational instability. *Journal of Plasma Physics* 82(03): 905820302–18

Constantinou, N. C., Farrell, B. F. and Ioannou, P. J. 2014. Emergence and equilibration of jets in beta-plane turbulence: applications of stochastic structural stability theory. *Journal of the Atmospheric Sciences* 71: 1818–1842

Constantinou, N. C., Farrell, B. F. and Ioannou, P. J. 2016. Statistical state dynamics of jet–wave coexistence in barotropic beta-plane turbulence. *Journal of Atmospheric Sciences* 73(5): 2229–2253

Constantinou, N. C., Lozano-Durán, A., Nikolaidis, M.-A., Farrell, B. F., Ioannou, P. J. and Jiménez, J. 2014. Turbulence in the highly restricted dynamics of a closure at second order: comparison with DNS. *Journal of Physics: Conference Series* 506: 012004

Craik, A. D. D. 1985. *Wave Interactions and Fluid Flows*. Cambridge University Press, chapter Linear wave interactions

de Bruyn Kops, S. M. and Riley, J. J. 2019. The effects of stable stratification on the decay of initially isotropic homogeneous turbulence. *J. Fluid Mech.* 860: 787–821

Engquist, B., Li, X., Ren, W. and Vanden-Eijnden, E. 2007. Heterogeneous multiscale methods: a review. *Commun. Comput. Phys.* 2: 367–450

Falder, M., White, N. J. and Caulfield, C. P. 2016. Seismic imaging of rapid onset of stratified turbulence in the south Atlantic Ocean. *J. Phys. Oceanogr.* 46:4: 1023–1044

Farrell, B. F., Gayme, D. F. and Ioannou, P. J. 2017. A statistical state dynamics approach to wall turbulence. *Phil. Trans. R. Soc. A* 375: 20160081

Farrell, B. F., Ioannou, P. J., Jimenez, J., Constantinou, N., Lozano-Duran, A. and Nikolaidis, M.-A. 2016. A statistical state dynamics-based study of the structure and mechanism of large-scale motions in plane Poiseuille flow. *J. Fluid Mech.* 809: 290–315

Feraco, F., Marino, R., Pumir, A., Primavera, L., Mininni, P. D., Pouquet, A. and Rosenberg, D. 2018. Vertical drafts and mixing in stratified turbulence: Sharp transition with Froude number. *EPL* 123: 44002:1–7

Ferrari, R. and Wunsch, C. 2004. Vertical mixing, energy, and the general circulation of the oceans. *Ann. Rev. Fluid Mech.* 36: 281–314

Ferraro, A. 2019. Exploiting marginal stability in slow–fast quasilinear dynamical systems. *Proceedings of the Woods Hole Summer Program in Geophysical Fluid Dynamics*

Fitzgerald, J. G. and Farrell, B. F. 2014. Mechanisms of mean flow formation and suppression in two-dimensional Rayleigh-Bénard convection. *Phys. Fluids* 26: 054104

Fitzgerald, J. G. and Farrell, B. F. 2018. Statistical state dynamics of vertically sheared horizontal flows in two-dimensional stratified turbulence. *J. Fluid Mech.* 854: 544–590

Fitzgerald, J. G. and Farrell, B. F. 2019. Statistical state dynamics of buoyancy layer formation via the Phillips mechanism in two-dimensional stratified turbulence. *J. Fluid Mech.* 864: R3

Fritts, D. C., Lund, T. S., Wan, K. and Liu, H.-L. 2021. Numerical simulation of mountain waves over the southern Andes. Part II: Momentum fluxes and wave–mean-flow interactions. *J. Atmos. Sci.* 78: 3069–3088

Garanaik, A. and Venayagamoorthy, S. K. 2018. Assessment of small-scale anisotropy in stably stratified turbulent flow using direct numerical simulations. *Phys. Fluids* 30: 126602

Garanaik, A. and Venayagamoorthy, S. K. 2019. On the inference of the state of turbulence and mixing efficiency in stably stratified flows. *J. Fluid Mech.* 867: 323–333

Garaud, P., Gallet, B. and Bischoff, T. 2015. The stability of stratified spatially periodic shear flows at low Péclet number. *Phys. Fluids* 27: 084104

Gregg, M. C., D'Asaro, E. A., Riley, J. J. and Kunze, E. 2018. Mixing efficiency in the ocean. *Annu. Rev. Mar. Sci.* 10: 443–473

Hall, P. and Sherwin, S. 2010. Streamwise vortices in shear flows: harbingers of transition and the skeleton of coherent structures. *J. Fluid Mech.* 661: 178–205

Hamilton, J. M., Kim, J. and Waleffe, F. 1995. Regeneration mechanisms of near-wall turbulence structures. *J. Fluid Mech.* 287: 317–348

Holleman, R. C., Geyer, W. R. and Ralson, D. K. 2016. Stratified turbulence and mixing efficiency in a salt wedge estuary. *J. Phys. Oceanogr.* 46: 1769–1783

Howland, C. J., Taylor, J. R. and Caulfield, C. P. 2020. Mixing in forced stratified turbulence and its dependence on large-scale forcing. *J. Fluid Mech.* 898: A7

Julien, K. and Knobloch, E. 2007. Reduced models for fluid flows with strong constraints. *J. Math. Phys.* 48: 065405

Kawahara, G. and Kida, S. 2001. Periodic motion embedded in plane Couette turbulence: regeneration cycle and burst. *J. Fluid Mech.* 449: 291

Khani, S. 2018. Mixing efficiency in large-eddy simulations of stratified turbulence. *J. Fluid Mech.* 849: 373–394

Khani, S. and Waite, M. L. 2013. Effective eddy viscosity in stratified turbulence. *J. Turb.* 14: 49–70

Khani, S. and Waite, M. L. 2016. Backscatter in stratified turbulence. *Eur. J. Mech. B Fluids* 60: 1

Kim, E., Billant, P. and Gallaire, F. 2020. Nonlinear evolution of the centrifugal instability using a semilinear model. *J. Fluid Mech.* 897: A34

Klein, R. 2010. Scale-dependent models for atmospheric flows. *Annu. Rev. Fluid Mech.* 42: 249–274

Kumar, A., Verma, M. K. and Sukhatme, J. 2017. Phenomenology of two-dimensional stably stratified turbulence under large-scale forcing. *J. Turb.* 18: 219–239

Lang, C. J. and Waite, M. L. 2019. Scale-dependent anisotropy in forced stratified turbulence. *Phys. Rev. Fluids* 4: 044801

Legg, S. 2021. Mixing by oceanic lee waves. *Ann. Rev. Fluid Mech.* 53: 173–201

Lilly, D. K. 1983. Stratified turbulence and the mesoscale variability of the atmosphere. *J. Atmos. Sci.* 40(3): 749–761

Lindborg, E. 2006. The energy cascade in a strongly stratified fluid. *J. Fluid Mech.* 550: 207–242

Lozovatsky, I. D. and Fernando, H. J. S. 2013. Mixing efficiency in natural flows. *Phil. Trans. R. Soc. A* 371: 20120213

Lucas, D. and Caulfield, C. P. 2017. Irreversible mixing by unstable periodic orbits in buoyancy dominated stratified turbulence. *J. Fluid Mech.* 832: R1

Lucas, D., Caulfield, C. P. and Kerswell, R. R. 2017. Layer formation in horizontally forced stratified turbulence: connecting exact coherent structures to linear instabilities. *J. Fluid Mech.* 832: 409–437

MacKinnon, J. A., Zhao, Z., Whalen, C. B., Waterhouse, A. F., Trossman, D. S., Sun, O. M. and Laurent, L. C. S. 2017. Climate process team on internal wave-driven ocean mixing. *Bull. Amer. Met. Soc.* 98:11: 2429–2454

Maffioli, A. 2017. Vertical spectra of stratified turbulence at large horizontal scales. *Phys. Rev. Fluids* 2: 104802

Maffioli, A. 2019. Asymmetry of vertical buoyancy gradient in stratified turbulence. *J. Fluid Mech.* 870: 266–289

Maffioli, A., Brethouwer, G. and Lindborg, E. 2016. Mixing efficiency in stratified turbulence. *J. Fluid Mech.* 794: R3

Maffioli, A. and Davidson, P. A. 2016. Dynamics of stratified turbulence decaying from a high buoyancy Reynolds number. *J. Fluid Mech.* 786: 210–233

Marston, J. B., Chini, G. P. and Tobias, S. M. 2016. Generalized quasilinear approximation: application to zonal jets. *Physical Review Letters* 116(21): 214501

Michel, G. and Chini, G. 2019. Multiple scales analysis of slow-fast quasi-linear systems. *Proc. R. Soc. A* 475: 20180639

Miller, R. 2007. *Numerical Modeling of Ocean Circulation*. Cambridge University Press, chapter Primitive equation models

Monismith, S. G., Koseff, J. R. and White, B. L. 2018. Mixing efficiency in the presence of stratification: when is it constant? *Geophys. Res. Lett.* 45: 5627

Montemuro, B., White, C. M., Klewicki, J. C. and Chini, G. P. 2020. A self-sustaining process theory for uniform momentum zones and internal shear layers in high Reynolds number shear flows. *J. Fluid Mech.* 901: A28

Moum, J. N. 1996. Energy-containing scales of turbulence in the ocean thermocline. *J. Geophys. Res.* 101: 14095

Osborn, T. R. 1980. Estimates of the local rate of vertical diffusion from dissipation measurements. *J. Phys. Oceanogr.* 10: 83–89

Page, J. and Kerswell, R. R. 2020. Searching turbulence for periodic orbits with dynamic mode decomposition. *J. Fluid Mech.* 886: A28

Parker, J. P., Caulfield, C. P. and Kerswell, R. R. 2019. Kelvin-Helmoltz billows above Richardson number 1/4. *J. Fluid Mech.* 879: R1

Peltier, W. R. and Caulfield, C. P. 2003. Mixing efficiency in stratified shear flows. *Annu. Rev. Fluid Mech.* 35: 135–167

Portwood, G. D., de Bruyn Kops, S. M. and Caulfield, C. P. 2019. Asymptotic dynamics of high dynamic range stratified turbulence. *Phys. Rev. Lett.* 122: 194504

Portwood, G. D., de Bruyn Kops, S. M., Taylor, J. R., Salehipour, H. and Caulfield, C. P. 2016. Robust identification of dynamically distinct regions in stratified turbulence. *J. Fluid Mech.* 807: R2

Riley, J. J. and Lelong, M.-P. 2000. Fluid motions in the presence of strong stable stratification. *Annu. Rev. Fluid Mech.* 32: 613

Riley, J. J. and Lindborg, E. 2013. Recent progress in stratified turbulence. In *Ten chapters in Turbulence*, ed. P. A. Davidson, Cambridge University Press), p. 269

Rorai, C., Minini, P. D. and Pouquet, A. 2014. Turbulence comes in bursts in stably stratified flows. *Phys. Rev. E* 89: 043002

Salehipour, H. and Peltier, W. R. 2015. Diapycnal diffusivity, turbulent Prandtl number and mixing efficiency in Boussinesq stratified turbulence. *J. Fluid Mech.* 775: 464–500

Salehipour, H., Peltier, W. R. and Caulfield, C. P. 2018. Self-organized criticality of turbulence in strongly stratified mixing layers. *J. Fluid Mech.* 856: 228–256

Sherman, F. S., Imberger, J. and Corcos, G. M. 1978. Turbulence and mixing in stably stratified waters. *Ann. Rev. Fluid Mech.* 10: 267–288

Smyth, W. D. and Moum, J. N. 2000. Length scales of turbulence in stably stratified mixing layers. *Phys. Fluids* 12: 1327

Smyth, W. D. and Moum, J. N. 2013. Marginal instability and deep cycle turbulence in the eastern equatorial Pacific Ocean. *Geophys. Res. Lett.* 40: 1–5

Smyth, W. D., Nash, J. D. and Moum, J. M. 2019. Self-organized criticality in geophysical turbulence. *Nature Scientific Reports* 9:3747: 1–8

Srinivasan, K. and Young, W. R. 2012. Zonostrophic instability. *J. Atmos. Sci.* 69: 1633–1656

Thomas, V. L., Farrell, B. F., Ioannou, P. J. and Gayme, D. F. 2015. A minimal model of self-sustaining turbulence. *Physics of Fluids* 27(10): 105104

Tobias, S. M., Dagon, K. and Marston, J. B. 2011. Astrophysical fluid dynamics via direct statistical simulation. *Astrophys. J.* 727: 127–138

Tobias, S. M. and Marston, J. B. 2013. Direct statistical simulation of out-of-equilibrium jets. *Phys. Rev. Lett.* 110: 104502

Tobias, S. and Marston, B. 2017. Three-dimensional rotating Couette flow via the generalised quasilinear approximation. *J. Fluid Mech.* 810: 412–428

Tuckerman, L., Chantry, M. and Barkley, D. 2020. Patterns in wall-bounded shear flows. *Annu. Rev. Fluid Mech.* 52: 343

Turner, J. S. 1973. *Buoyancy Effects in Fluids*. Cambridge, U.K.: Cambridge University Press

Venayagamoorthy, S. K. and Koseff, J. R. 2016. On the flux Richardson number in stably stratified turbulence. *J. Fluid Mech.* 798: R1

Waite, M. L. 2011. Stratified turbulence at the buoyancy scale. *Phys. Fluids* 23: 066602

Waite, M. L. 2014. Direct numerical simulations of laboratory-scale stratified turbulence. In *Modelling Atmospheric and Oceanic Flows: Insights from Laboratory Experiments and Numerical Simulations*, ed. T. von Larcher and P. Williams, American Geophysical Union), pp. 159–175

Waite, M. L. and Bartello, P. 2004. Stratified turbulence dominated by vortical motion. *J. Fluid Mech.* 517: 281–308

Young, W. R. and Jones, S. 1991. Shear dispersion. *Phys. Fluids* A3: 1087–1101

This draft was prepared using the LaTeX style file belonging to the Journal of Fluid Mechanics 1

Strong wave–mean-flow coupling in baroclinic acoustic streaming

Guillaume Michel[1] and Gregory P. Chini[2]†

[1]Laboratoire de Physique Statistique, École Normale Supérieure, CNRS, Université P. et M. Curie, Université Paris Diderot, Paris 75005, France

[2]Department of Mechanical Engineering and Program in Integrated Applied Mathematics, University of New Hampshire, Durham, NH 03824, USA

(Received xx; revised xx; accepted xx)

The interaction of an acoustic wave with a stratified fluid can drive strong streaming flows owing to the baroclinic production of fluctuating vorticity, as recently demonstrated by Chini *et al.* (*J. Fluid Mech.*, **744**, 2014, pp. 329–351). In the present investigation, a set of wave/mean-flow interaction equations is derived that governs the coupled dynamics of a standing acoustic-wave mode of characteristic (small) amplitude ϵ and the streaming flow it drives in a thin channel with walls maintained at differing temperatures. Unlike classical Rayleigh streaming, the resulting mean flow arises at $O(\epsilon)$ rather than at $O(\epsilon^2)$. Consequently, fully two-way coupling between the waves and the mean flow is possible: the streaming is sufficiently strong to induce $O(1)$ rearrangements of the imposed background temperature and density fields, which modifies the spatial structure and frequency of the acoustic mode on the streaming time scale. A novel Wentzel–Kramers–Brillouin–Jeffreys analysis is developed to average over the fast wave dynamics, enabling the coupled system to be integrated strictly on the slow time scale of the streaming flow. Analytical solutions of the reduced system are derived for weak wave forcing and are shown to reproduce results from prior direct numerical simulations (DNS) of the compressible Navier–Stokes and heat equations with remarkable accuracy. Moreover, numerical simulations of the reduced system are performed in the regime of strong wave/mean-flow coupling for a fraction of the computational cost of the corresponding DNS. These simulations shed light on the potential for baroclinic acoustic streaming to be used as an effective means to enhance heat transfer.

Key words: acoustics, baroclinic flows, mixing enhancement

1. Introduction

Sound waves can drive Eulerian flows that evolve on a slow time scale compared to the period of the waves. The theoretical study of this phenomenon, called acoustic (or, in other contexts, steady) streaming, can be traced back to Rayleigh in the 19th century (Rayleigh 1884). Given that ultrasonic power sources are now routinely used in laboratory experiments, acoustic streaming has been widely observed, often as a source of unwanted flow. Nonetheless, streaming also has been recognized as a practical means to enhance transport and mixing and has, for instance, been used to improve the efficiency of chemical reactions occurring near a catalytic solid phase that otherwise would be

† Email address for correspondence: greg.chini@unh.edu

controlled by molecular diffusion (Bengtsson & Laurell 2004); to directly mix chemical species (Yaralioglu *et al.* 2004); and for activated irrigation in medical applications including root-canal procedures (Verhaagen *et al.* 2014). Heat also can be transported by streaming flows, and acoustic waves therefore can be used to accelerate the cooling of a hot object, as recently reviewed by Legay *et al.* (2011). Acoustic streaming technologies are of particular interest in the zero-gravity environment, where natural convective flows do not exist and acoustic thermal management systems may provide a reliable, efficient and lightweight alternative to fans.

In a characteristically lucid lecture, Lighthill identified the different regimes of acoustic streaming in a homogeneous medium (Lighthill 1978). Owing to attenuation mechanisms, acoustic waves generate a Reynolds stress divergence capable of driving a mean flow, which is balanced either by viscous forces (termed "Rayleigh streaming" if, in addition, the sound waves are damped in oscillatory boundary layers) or by inertia ("Stuart streaming"). The former regime occurs for small values of the streaming Reynolds number $Re_s = U_s L/\nu$, where U_s is a characteristic streaming speed, L is a typical dimension of the system and ν is the kinematic viscosity of the fluid. In Rayleigh streaming, the (laminar) cellular mean flow that is generated is localized within a few wavelengths of any solid boundary (Nyborg 1958); the streaming can be analytically computed for simple geometries, e.g. in a channel (Rayleigh 1884; Hamilton *et al.* 2003) or adjacent to a circular cylinder (Holtsmark *et al.* 1954). This regime has become important in microfluidics, where the vortices induced by acoustic streaming in microchannels can be used to mix chemicals (see references above). In contrast, for large Re_s, the streaming flow acquires a jet-like structure and can become turbulent (Stuart 1966; Lighthill 1978).

The presence of an inhomogeneous background temperature (or density) field strongly affects the fundamental mechanics and kinematics of acoustic streaming: streaming velocities are significantly enhanced and the flow patterns are substantially altered. These changes are evident in the early experiments of Fand & Kaye (1960) and in subsequent experiments and numerical simulations; see e.g. Loh *et al.* (2002), Hyun *et al.* (2005), Lin & Farouk (2008), Nabavi *et al.* (2008), Atkas & Ozgumus (2010), Dreeben & Chini (2011) and Karlsen *et al.* (2018). Consequently, the resulting flow and associated transport cannot be computed simply by coupling the corresponding isothermal (e.g. Rayleigh or Stuart) streaming with the heat or other appropriate transport equation. Instead, new physical phenomena occur, which renders this problem both complex and interesting. Experimental challenges arise because natural convection and acoustic streaming may be difficult to disentangle in the laboratory; numerical challenges result from the need to resolve compressible fluid dynamics on temporal scales ranging from the acoustic wave period to the slow time scale over which the streaming flow evolves; while the primary theoretical challenge is to elucidate the novel phenomenology resulting from fully two-way coupling between the sound waves and the mean flow.

This striking change in the character of the streaming has been observed in various contexts in which an agency *other* than viscosity generates vorticity in the oscillatory flow (e.g. the acoustic waves). Amin (1988) and Riley & Trinh (2001) noted fundamental changes in the steady streaming driven by a non-conservative body force in their study of fluid flow in the presence of g-jitter, i.e. a fluctuating gravitational field in an otherwise gravity-free environment. Motivated by the observation that streaming velocities in high-intensity discharge lamps are two orders of magnitude larger than those predicted by Rayleigh streaming theory (Dreeben & Chini 2011), Chini *et al.* (2014) derived a theory capable of accounting for both the observed streaming pattern and magnitude. As discussed more fully in § 2, the mechanism underlying this large-amplitude streaming is the baroclinic production of sound-wave vorticity arising from the misalignment of

fluctuating isobars and mean isopycnals. Similarly, non-classical streaming phenomena have been observed in microfluidic systems with gradients in density; in particular, Karlsen *et al.* (2016, 2018) recently obtained a local expression for the acoustic force density driving the streaming flow as a function of the acoustic-wave characteristics.

The primary objective of the present investigation is to systematically extend the recent theory of Chini *et al.* (2014) to efficiently capture the two-way coupling that can occur in baroclinic acoustic streaming and to quantify the concomitant heat transfer. Accordingly, a novel Wentzel–Kramers–Brillouin–Jeffreys (WKBJ) analysis is performed to enable prediction of the slow evolution of the acoustic wave amplitude, thereby obviating the need to explicitly simulate the fast oscillatory dynamics. We focus on perhaps the most well-documented acoustic streaming configuration: a thin two-dimensional channel with an imposed standing acoustic wave oscillating in the wall-parallel direction. For a homogeneous system, the resulting streaming flow was first described in the pioneering work of Rayleigh (1884) in the limits $Re_s \ll 1$ and $\delta_* \ll H_* \ll k_*^{-1}$, where $\delta_* = \sqrt{2\nu_*/\omega_*}$ is the thickness of the oscillatory (Stokes) boundary layers (ν_* is the kinematic viscosity, and ω_* is the wave angular frequency), H_* is the channel width and k_* is the wavenumber of the acoustic wave. The streaming flow comprises a wall-parallel array of counter-rotating vortices, stacked in the wall-normal direction and having a characteristic velocity $3U_*^2/(16a_*)$, where U_* is the maximum fluctuating velocity induced by the standing acoustic wave and a_* is the speed of sound. Experiments were first performed in a tube and showed quantitative agreement with the predictions of Rayleigh (Andrade 1931). Hamilton *et al.* (2003) extended this theoretical study to channels of arbitrary width H_*, the only restrictions being $Re_s \ll 1$ and $\delta_* \ll k_*^{-1}$. When the upper and lower walls of the channel are maintained at fixed but differing temperatures, both experiments and direct numerical simulations of the compressible Navier–Stokes and heat equations indicate a change in the streaming phenomenology: the stacked vortices merge and their characteristic velocity increases (Loh *et al.* 2002; Lin & Farouk 2008). To date, no theory has correctly predicted the resulting streaming-flow pattern and intensity; our study, which focuses on the regime $Re_s \gtrsim 1$, fills this gap in the literature.

The remainder of the paper is organized as follows. After formulating the problem for the instantaneous dynamics, we carry out a multiple scale analysis (§ 2) to obtain a reduced but two time-scale system. In § 3, we analyse the wave dynamics to show that this multiscale system can be integrated strictly on the slow time scale. We then consider, in § 4, the limit of weak wave forcing, in which the streaming flow does not produce appreciable feedback on the waves; in particular, we derive an approximate analytical solution and compare it to the streaming flow numerically computed by Lin & Farouk (2008), demonstrating excellent quantitative agreement. In § 5, we perform numerical simulations of our reduced model and characterize the resulting fully-coupled waves and mean flows. We summarize our key findings and suggest possible further extensions in § 6.

2. Two time-scale wave/mean-flow system

2.1. *Flow configuration*

The problem we consider is similar to that introduced in Chini *et al.* (2014). Specifically, we analyze the two-dimensional flow of an ideal gas, with specific gas constant R_* and constant dynamic viscosity μ_* and thermal conductivity κ_*, in a channel with walls separated by a distance H_* in the $\tilde{y}$ coordinate direction (see figure 1). Here and throughout, tildes refer to dimensional variables, while asterisks are used to denote dimensional parameters. Subsequently, overbars will be used to designate dimensionless

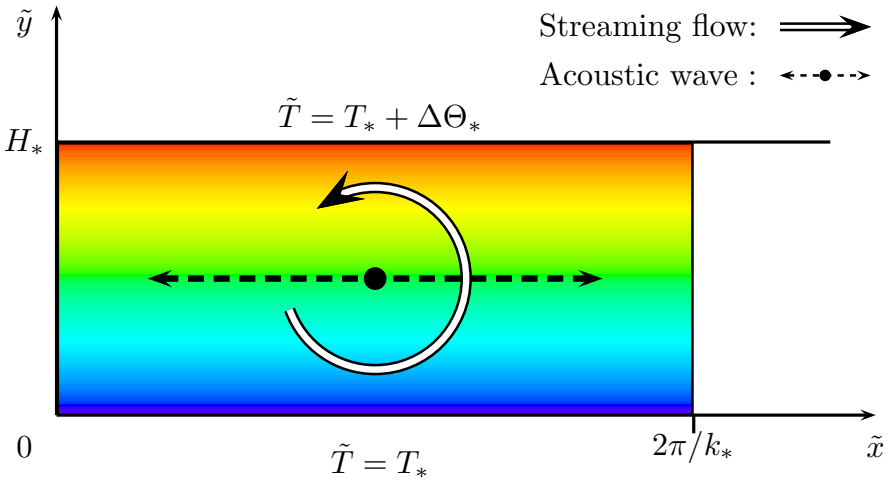

FIGURE 1. Schematic of the flow configuration. A thermally-stratified ideal gas is confined between the plane parallel walls of a long thin channel of height H_*. A standing acoustic wave of wavelength $2\pi/k_*$ interacts with the thermal stratification to drive a time-mean, or streaming, flow that is sufficiently strong to modify the wave dynamics. The thermal driving is imposed by fixing the temperature $\tilde{T}$ of the lower wall to be T_* and that of the upper wall to be $T_* + \Delta\Theta_*$.

time-averaged fields, while primes will be reserved for dimensionless oscillatory fields. The gas is presumed to be driven in an approximately time-periodic fashion, with frequency ω_*, yielding a standing sound wave with spatial wavenumber k_*. The velocity field is required to satisfy no-slip and zero normal-flow boundary conditions along the channel walls located at $\tilde{y} = 0$ and $\tilde{y} = H_*$. All dependent fields are required to satisfy a $2\pi/k_*$ periodicity condition in the horizontal ($\tilde{x}$) coordinate. In addition, to fix the spatial phase of the sound wave, we impose a symmetry condition along (or, equivalently, a zero mass-exchange condition across) $\tilde{x} = 0$; i.e. $\tilde{u}(0, \tilde{y}, \tilde{t})$=0, where $\tilde{u}$ is the $\tilde{x}$-velocity component and $\tilde{t}$ is the time variable. This additional boundary condition holds for any flow developing from initial conditions that are symmetric with respect to $\tilde{x} = 0$, e.g. for the quiescent diffusive state, since then both the initial conditions and the governing equations are invariant with respect to the transformation $\tilde{x} \to -\tilde{x}$, $\tilde{u} \to -\tilde{u}$ and $\tilde{v} \to \tilde{v}$.

In contrast to the study of Chini *et al.* (2014), the thermal driving is achieved by fixing the temperatures of the lower and upper walls to be T_* and $T_* + \Delta\Theta_*$, respectively, rather than by including a volumetric heat source. For convenience, we take the temperature differential $\Delta\Theta_* > 0$, but note that this restriction is not dynamically significant since we do not consider the influence of buoyancy (gravity) in this investigation. Denoting the density, pressure, temperature and velocity fields by $\tilde{\rho}$, $\tilde{p}$, $\tilde{T}$ and $\tilde{\mathbf{u}}$, respectively, where $\tilde{\mathbf{u}} = (\tilde{u}, \tilde{v})$ and $\tilde{v}$ is the $\tilde{y}$-velocity component, the governing (compressible) Navier–Stokes, continuity and energy equations and the ideal gas equation of state can be written as

$$\tilde{\rho}\left[\partial_{\tilde{t}}\tilde{\mathbf{u}} + (\tilde{\mathbf{u}}\cdot\tilde{\nabla})\tilde{\mathbf{u}}\right] = -\tilde{\nabla}\tilde{p} + \mu_*\left[\tilde{\nabla}^2\tilde{\mathbf{u}} + \frac{1}{3}\tilde{\nabla}(\tilde{\nabla}\cdot\tilde{\mathbf{u}})\right], \tag{2.1}$$

$$\partial_{\tilde{t}}\tilde{\rho} + \tilde{\nabla}\cdot(\tilde{\rho}\tilde{\mathbf{u}}) = 0, \tag{2.2}$$

$$\tilde{\rho}c_v\left[\partial_{\tilde{t}}\tilde{T} + (\tilde{\mathbf{u}}\cdot\tilde{\nabla})\tilde{T}\right] = -\tilde{p}\left(\tilde{\nabla}\cdot\tilde{u}\right) + \kappa_*\tilde{\nabla}^2\tilde{T}, \tag{2.3}$$

$$\tilde{p} = \tilde{\rho}R_*\tilde{T}, \tag{2.4}$$

where the two-dimensional gradient operator $\tilde{\nabla} = (\partial_{\tilde{x}}, \partial_{\tilde{y}})$. Note that dilatational (or 'bulk') viscosity has been neglected in (2.1), and viscous heating has been omitted in (2.3). In practice, the bulk viscosity vanishes for a monatomic gas and, according to early

Notation	Definition
$\tilde{\mathbf{u}} = (\tilde{u}, \tilde{v})$	Gas velocity
$\tilde{\rho}$	Gas density
$\tilde{p}$	Gas pressure
$\tilde{T}$	Gas temperature
$(\tilde{x}, \tilde{y})$	Horizontal, vertical (wall-normal) coordinate
$\tilde{t}$	Time variable
H_*	Channel height
k_*	Acoustic-wave horizontal wavenumber
μ_*	Dynamic viscosity
κ_*	Thermal conductivity
R_*	Specific gas constant
(c_{v_*}, c_{p_*})	Constant volume, pressure specific heat coefficient
$a_* = \sqrt{(c_{p_*}/c_{v_*})R_*T_*}$	Background sound speed
p_*	Background pressure field

TABLE 1. Dimensional variables and parameters

experiments, is smaller than the dynamic (or shear) viscosity for the specific diatomic ideal gas (i.e. nitrogen) studied here (Prangsma *et al.* 1973). More importantly, although significant variations in the dynamic viscosity may be expected owing to the temperature dependence of this coefficient, these variations are neglected to facilitate the analysis. The steady-state pressure and temperature fields in the absence of acoustic waves and streaming flow, that is for $\tilde{\mathbf{u}} = \mathbf{0}$, are referred to as the background fields (denoted with a subscript 'B') and are found to be

$$\tilde{T}_B = T_* \left(1 + \Gamma \frac{y_*}{H_*}\right), \qquad \tilde{p}_B = p_*, \tag{2.5}$$

where p_* is a constant and the dimensionless temperature differential $\Gamma \equiv \Delta\Theta_*/T_*$. Table 1 summarizes the dimensional fields and parameters used in the following analysis.

2.2. *Scaling and non-dimensionalisation*

To facilitate the asymptotic analysis, we non-dimensionalise the governing equations by scaling the dependent and independent variables as outlined in table 2. The $\tilde{x}$-velocity component is scaled with a_*, the sound speed at temperature T_*. This scaling introduces into the dimensionless governing equations the Strouhal number $S = a_*/U_*$, where U_* (rather than a_*) is a characteristic oscillatory velocity induced by the standing acoustic wave. The Strouhal number is large (10^3 or larger) in many applications, and therefore we introduce $\epsilon \equiv 1/S$ and consider the asymptotic limit $\epsilon \to 0$ with all other dimensionless parameters scaled as appropriate powers of ϵ. Since $\epsilon \ll 1$, the leading-order acoustic wave dynamics is linear. Nevertheless, weak wave–wave nonlinearities are crucial for acoustic streaming, as their cumulative effect can be significant over sufficiently many $[O(1/\epsilon)]$ acoustic wave periods (i.e. over the slow time scale). The implied temporal scale separation between the wave and streaming dynamics is readily achieved in both laboratory experiments and streaming-enabled technologies.

The $\tilde{x}$ and $\tilde{y}$ coordinates are scaled with k_*^{-1} and H_*, respectively, so that the gas lies in the domain defined by $x \in [0, 2\pi]$ and $y \in [0, 1]$. Time $\tilde{t}$ is non-dimensionalised using the inverse reference wave frequency $\omega_*^{-1} = (a_* k_*)^{-1}$. The vertical ($\tilde{y}$), or wall-normal, velocity component is scaled by $(k_* H_*)a_*$. The domain aspect ratio $\delta \equiv k_* H_*$ is assumed to be small and, more precisely, is chosen so that $\delta = \sqrt{\epsilon} h$, where h is a dimensionless

Variable	Scale	Parameter	Definition	Scaling
x	k_*^{-1}	Strouhal number S	a_*/U_*	$S = 1/\epsilon$
y	H_*	Aspect ratio δ	k_*H_*	$\delta = \sqrt{\epsilon}h$
t	$(a_*k_*)^{-1}$	Temperature gradient Γ	$\Delta\Theta_*/T_*$	$\Gamma = O(1)$
u	a_*	Reynolds number Re	$\rho_*U_*/(k_*\mu_*)$	$Re = Re_s/\epsilon$
v	$(k_*H_*)a_*$	Péclet number Pe	$\rho_*c_{p_*}U_*/(k_*\kappa_*)$	$Pe = Pe_s/\epsilon$
ρ	$\rho_* \equiv p_*/(R_*T_*)$	Specific heat ratio γ	c_{p_*}/c_{v_*}	$\gamma = O(1)$
T	T_*			
P	p_*			

TABLE 2. Dimensionless variables and parameters

parameter of order unity. Although the cross-channel heat flux is not expected to be maximized as $\delta \to 0$ (since the streaming flow will be largely horizontal), we follow Chini *et al.* (2014) and continue to focus on the small aspect-ratio regime for the following reasons. First, as noted in the introduction, most theoretical and computational studies have been performed in this regime, so meaningful comparisons to prior investigations can be made. Secondly, the analysis of the acoustic wave is simplified in a domain that is thin relative to the wavelength of the sound wave. Indeed, the acoustic wave then is dynamically constrained to maintain its first-mode wall-normal structure. Finally, in the small aspect-ratio regime, the leading-order fluctuating pressure gradient is orthogonal to the imposed background density gradient, resulting in a crucial baroclinic contribution to the production of fluctuating vorticity.

The temperature T_* of the lower wall is used to nondimensionalise the temperature field $\tilde{T}$. In the analysis that follows, Γ is fixed, i.e. $O(1)$, as $\epsilon \to 0$, although the smallness of ϵ in acoustic streaming ensures that our multiple scale analysis remains accurate even for $\Gamma \approx 0.1$, as will be evident in § 4, where we compare our theoretical predictions with the results of direct numerical simulations.

The Reynolds and Péclet numbers characterizing the acoustic waves are denoted Re and Pe, respectively. Since these parameters are very large compared to unity, both momentum and thermal diffusion can be neglected in the leading-order wave dynamics, at least in the domain interior. Note that in baroclinic acoustic streaming, typical streaming velocities also are of size U_* (in contrast to Rayleigh streaming, where streaming speeds are proportional to ϵU_*). Consequently, Re and Pe also would appear to characterize the streaming flow. Because we consider the limit of small aspect ratio, however, diffusion in the wall-normal (y) direction is enhanced by a factor $\delta^{-2} \propto \epsilon^{-1}$. We therefore define the streaming Reynolds and Péclet numbers $Re_s = \epsilon Re$ and $Pe_s = \epsilon Pe$ as in traditional Rayleigh streaming as the proper measure of mean inertia to the dominant mean diffusive effects.

2.3. *Asymptotic analysis*

Using the scalings described above (and summarized in table 2), the governing equations and boundary conditions can be recast in dimensionless form. The occurrence of the small parameter ϵ in the dimensionless system prompts a multiple scale asymptotic analysis in which the single time variable t characterizing the fast dynamics of the acoustic waves is augmented with a slow time variable $T \equiv \epsilon t$ to capture the cumulative effect of weakly nonlinear wave dynamics that ultimately drives streaming. Furthermore, we posit the following asymptotic expansions for the various fields:

$$(u, v) = \epsilon(u_1, v_1) + \epsilon^2(u_2, v_2) + O(\epsilon^3), \tag{2.6}$$

$$\pi = \epsilon\pi_1 + \epsilon^2\pi_2 + O(\epsilon^3), \tag{2.7}$$

$$\Theta = \Theta_0 + \epsilon\Theta_1 + O(\epsilon^2), \tag{2.8}$$

$$\rho = \rho_0 + \epsilon\rho_1 + O(\epsilon^2), \tag{2.9}$$

where $\pi = (\tilde{p} - \tilde{p}_B)/p_*$ and $\Theta = (\tilde{T} - \tilde{T}_B)/T_*$ are, respectively, the dimensionless perturbation pressure and temperature fields. Note that, at each order in these expansions, the field variables can have both fluctuating and mean components, which subsequently will be disentangled via the introduction of a fast-time averaging operation. Expansion (2.6) follows from the scaling of the Strouhal number ($S = 1/\epsilon$). The state equation constrains the temperature and density perturbations to be of the same order. In baroclinic acoustic streaming, the $O(\epsilon)$ streaming flow is sufficiently strong to induce $O(1)$ rearrangements of the background temperature and density fields over an $O(1/\epsilon)$ time period. Thus, in contrast to other studies of acoustic streaming in the presence of inhomogeneous temperature fields (e.g. Červenka & Bednarřik (2017)), it is crucial that the expansions for both Θ and ρ begin at $O(1)$, as first shown in Chini *et al.* (2014).

Owing to the large perturbations to the background density field, the natural frequency of an acoustic mode may evolve in time. Here, we extend the analysis of Chini *et al.* (2014) by employing a WKBJ approximation to properly capture this slow temporal evolution. Specifically, a generic dependent field $f(x, y, t)$ is re-expressed as $f(x, y, \phi, T)$, where ϕ and T are treated as independent variables. The rapidly-varying phase ϕ may be written as

$$\phi(t) = \frac{\Phi(T)}{\epsilon}, \tag{2.10}$$

where $\mathrm{d}\Phi/\mathrm{d}T$ is of order unity. We define the instantaneous angular frequency $\omega(T)$,

$$\omega(T) = \frac{\mathrm{d}\phi}{\mathrm{d}t} = \frac{\mathrm{d}\Phi}{\mathrm{d}T}, \tag{2.11}$$

and expand $\Phi = \Phi_0 + \epsilon\Phi_1 + O(\epsilon^2)$, so that

$$\omega = \omega_0 + \epsilon\omega_1 + O(\epsilon^2). \tag{2.12}$$

Finally, in order to distinguish the streaming flow from the acoustic wave, we introduce the fast-time average of a function $f(x, y, \phi, T)$,

$$\bar{f}(x, y, T) = \frac{1}{2n\pi}\int_{\phi}^{\phi+2n\pi} f(x, y, s, T)\mathrm{d}s \tag{2.13}$$

for sufficiently large positive integer n, so that any function can be decomposed such that

$$f(x, y, \phi, T) = \bar{f}(x, y, T) + f'(x, y, \phi, T), \tag{2.14}$$

where $\overline{f'} = 0$. Thus, f' represents the acoustic wave and $\bar{f}$ the streaming flow.

2.4. *Leading-order multiscale wave/mean-flow interaction equations*

The multiple time-scale governing equations for the coupled acoustic-wave/streaming-flow system were first derived in Chini *et al.* (2014) and are reproduced here for completeness. The evolution of the streaming fields is governed by the following equations:

$$\bar{\rho}_0\left(\partial_T\bar{u}_1 + \bar{u}_1\partial_x\bar{u}_1 + \bar{v}_1\partial_y\bar{u}_1\right) = -\frac{\partial_x\bar{\pi}_2}{\gamma} - \partial_x\left(\bar{\rho}_0\overline{u_1'^2}\right) - \partial_y\left(\bar{\rho}_0\overline{u_1'v_1'}\right) + \frac{\partial_{yy}\bar{u}_1}{Re_s h^2}, \tag{2.15}$$

$$\partial_y\bar{\pi}_2 = 0, \tag{2.16}$$

$$\partial_T\bar{\rho}_0 + \partial_x(\bar{\rho}_0\bar{u}_1) + \partial_y(\bar{\rho}_0\bar{v}_1) = 0, \tag{2.17}$$

$$\partial_T \bar{\Theta}_0 + \bar{u}_1 \partial_x \bar{\Theta}_0 + \bar{v}_1 \partial_y \left(\bar{\Theta}_0 + T_B\right) = (1-\gamma)(\bar{\Theta}_0 + T_B)(\partial_x \bar{u}_1 + \partial_y \bar{v}_1) + \frac{\gamma \partial_{yy} \bar{\Theta}_0}{Pe_s h^2 \bar{\rho}_0}, \quad (2.18)$$

$$\bar{\rho}_0 = \frac{1}{\bar{\Theta}_0 + T_B}. \quad (2.19)$$

In this slow-time system, the sole – but crucial – effect of the waves arises from the Reynolds stress divergence in the mean x-momentum equation (2.15) that drives the streaming flow. For a homogeneous fluid, this wave-induced force can be offset by a pressure gradient in the bulk: a Rayleigh streaming flow is driven at *next order* in ϵ by the Reynolds stress divergence acting in the oscillatory boundary layers that arise near the no-slip channel walls. In contrast, for baroclinic acoustic streaming, the mean temperature gradient causes this wave-induced forcing to be rotational even within the bulk interior of the domain. Consequently, the bulk force that is created cannot be balanced by a mere adjustment of the mean pressure gradient and instead induces a (strong) mean flow even in the absence of diffusive boundary layers. (Further discussion of this distinction is given in § 6.)

To evaluate this force, we employ the equations governing the leading-order acoustic wave dynamics, *viz.*

$$\omega_0 \bar{\rho_0} \partial_\phi u_1' + \frac{1}{\gamma} \partial_x \pi_1' = 0, \quad \partial_y \pi_1' = 0, \quad (2.20)$$

$$\omega_0 \partial_\phi \rho_1' + \partial_x (\bar{\rho}_0 u_1') + \partial_y (\bar{\rho}_0 v_1') = 0, \quad (2.21)$$

$$\omega_0 \partial_\phi \Theta_1' + u_1' \partial_x \bar{\Theta}_0 + v_1' \partial_y \left(\bar{\Theta}_0 + T_B\right) + (\gamma - 1)(\bar{\Theta}_0 + T_B)(\partial_x u_1' + \partial_y v_1') = 0, \quad (2.22)$$

$$\pi_1' - \rho_1' (\bar{\Theta}_0 + T_B) - \bar{\rho}_0 \Theta_1' = 0. \quad (2.23)$$

These equations describe the fast dynamics of approximately linear non-dissipative acoustic waves in a medium whose mean density field $\bar{\rho}_0$ evolves slowly in time. Conversely, the evolution of $\bar{\rho}_0(x, y, T)$ depends on the acoustic waves, as can be gleaned from inspection of (2.15)–(2.19). Note further that, here, unlike in Rayleigh streaming, the oscillatory Stokes layers are *dynamically passive* because the streaming induced by near-wall fluctuating viscous torques is $O(\epsilon^2)$ while the streaming flow governed by (2.15)–(2.19) is $O(\epsilon)$. Therefore, the leading-order wave field is required to satisfy only a zero normal-flow boundary condition at each wall, and the details of the oscillatory flow within the Stokes (boundary) layers do not have to be determined at this order (see § 6).

Taken together, these two sets of equations form a closed but *two time-scale* system. As emphasized in Chini *et al.* (2014), the fully two-way coupling between the waves and mean flow captured by this multiscale system renders it fundamentally distinct from classical Rayleigh streaming theory, in which the acoustic wave field can be computed first and then the response of the streaming flow to the acoustic wave forcing self-consistently determined (i.e. one-way coupling). Subsequently, Karlsen *et al.* (2016, 2018) also noted this two-way coupling in their computational studies of acoustic streaming in inhomogeneous fluids. Nevertheless, to make analytical progress, Chini *et al.* (2014) considered a small Prandtl-number limit in which the coupling is effectively one way. A primary contribution of the present investigation is to extend the analysis of Chini *et al.* (2014) to systematically treat fully two-way wave/mean-flow interactions. This extension requires the derivation of a novel amplitude equation governing the slow evolution of the acoustic waves, which can only be determined by carrying the asymptotic analysis to next order and imposing an appropriate solvability condition. Heuristically, the slow evolution of the waves is controlled by higher-order terms that, e.g., account for energy exchanges with the streaming flow or with the solid boundaries. In the next section, we show how these effects can be self-consistently incorporated.

3. Averaging over fast wave dynamics

We now characterize the dynamics of the acoustic waves on both the fast and slow time scales with the aim of eliminating the need to explicitly simulate the fast evolution. Inspection of (2.20)–(2.23) reveals that the wave dynamics directly depends on a single slowly-varying field: the leading-order mean density $\bar{\rho}_0 = (\bar{\Theta}_0 + T_B)^{-1}$. For purposes of the analysis described in this section, this field is presumed to be given. Consequently, the fluctuation equations (2.20)–(2.23) comprise a linear homogeneous system, and we henceforth consider a single eigenvector. A generic fluctuation field f_1' can be expressed as

$$f_1'(x, y, \phi, T) = \frac{A(T)}{2}\left(\hat{f}_1(x, y, T)e^{i\phi} + \text{c.c.}\right), \tag{3.1}$$

where f_1' stands for any fluctuation variable (u_1', v_1', ρ_1', π_1', Θ_1'); $A(T)$ is the slowly-evolving modal amplitude (here taken to be real without loss of generality); $\hat{f}$ is a complex function that describes the spatial structure of the mode; and c.c. denotes the complex conjugate. A normalization condition, specified subsequently, must be imposed on $\hat{f}$ to render this decomposition unique. We next describe the determination of the spatial structure of the mode (as defined by the functions $\hat{u}_1$, $\hat{v}_1$, etc.) and then derive a novel amplitude equation governing the slow evolution of the generally *a priori* unknown function $A(T)$.

3.1. *Mode structure*

Substituting the decomposition (3.1) into the fluctuation equations (2.20)–(2.23) yields a linear but non-separable two-dimensional (partial) differential eigenvalue problem for the spatial structure and frequency ω_0 of the leading-order fluctuation fields. By continuing to exploit the small aspect-ratio limit, we nevertheless are able to reduce the required computation to the solution of a one-dimensional eigenvalue problem – a crucial simplification.

To proceed, we note that, using (3.1), (2.21)–(2.23) can be combined to deduce

$$\hat{\pi}_1 = \frac{i\gamma}{\omega_0}\left(\partial_x \hat{u}_1 + \partial_y \hat{v}_1\right). \tag{3.2}$$

With this expression for the acoustic wave pressure $\hat{\pi}_1$, the momentum equations (2.20) become two coupled partial differential equations for $\hat{u}_1$ and $\hat{v}_1$:

$$\partial_x\left(\partial_x \hat{u}_1 + \partial_y \hat{v}_1\right) + \omega_0^2 \bar{\rho}_0 \hat{u}_1 = 0, \tag{3.3}$$

$$\partial_y\left(\partial_x \hat{u}_1 + \partial_y \hat{v}_1\right) = 0. \tag{3.4}$$

A further reduction to a single ordinary differential equation is possible by formally integrating a linear combination of these equations,

$$\partial_y(3.3) + \partial_x(3.4) \Rightarrow \partial_y\left(\bar{\rho}_0 \hat{u}_1\right) = 0 \Rightarrow \hat{u}_1 = \frac{q}{\bar{\rho}_0}, \tag{3.5}$$

where q is an unknown function of x and T only. Integration of (3.4) gives

$$\partial_x \hat{u}_1 + \partial_y \hat{v}_1 = g, \tag{3.6}$$

where g is a second unknown function of x and T only. Equations (3.3), (3.5) and (3.6) imply that $q = -g'/\omega_0^2$, where a prime is used to denote partial differentiation of the function g with respect to x, since the T dependence is parametric. The general solution of this system of equations can be obtained using the kinematic boundary condition

$\hat{v}_1(x, y = 0, T) = 0$, *viz.*

$$\hat{u}_1 = -\frac{g'}{\omega_0^2 \bar{\rho}_0}, \tag{3.7}$$

$$\hat{v}_1 = yg + \partial_x \left(\frac{g'}{\omega_0^2} \int_0^y \frac{\mathrm{d}y}{\bar{\rho}_0} \right). \tag{3.8}$$

Finally, the upper boundary condition $\hat{v}_1(x, y = 1, T) = 0$ provides a constraint on g and ω_0 in the form of the ordinary differential eigenvalue problem

$$\frac{\mathrm{d}}{\mathrm{d}x}(g'\alpha) + \omega_0^2 g = 0, \tag{3.9}$$

where

$$\alpha(x, T) = \int_0^1 \frac{\mathrm{d}y}{\bar{\rho}_0}. \tag{3.10}$$

To characterize the function $g(x, T)$, we first take, without loss of generality, $\hat{u}_1$ to be a real field: (3.3) and (3.4) then imply that $\hat{v}_1$ and, thence, g are also real-valued fields. Moreover, in order to ensure $\hat{u}_1(x = 0, y, T) = 0$, the ordinary differential equation (3.9) must be solved subject to the boundary conditions $g'(0) = g'(2\pi) = 0$. This requirement leads to an orthogonality condition: let (g_A, g_B) be two eigenvectors and (ω_A, ω_B) their angular eigenfrequencies; then

$$\int_0^{2\pi} g_A(x) g_B(x) \mathrm{d}x = \frac{1}{\omega_A^2 - \omega_B^2} \left[\alpha (g_A g_B' - g_B g_A') \right]_0^{2\pi} = 0. \tag{3.11}$$

Equation (3.11) provides a convenient scalar product on eigenvectors, and therefore we normalize them according to

$$\int_0^{2\pi} g(x)^2 \mathrm{d}x = 1. \tag{3.12}$$

This normalization condition resolves the ambiguity in the definition of $A(T)$ and $\hat{f}_1$ in (3.1).

3.2. *Wave amplitude*

As explained in the previous subsection, the acoustic mode shape $g(x, T)$ and frequency $\omega_0(T)$ can be computed at every time T for a given mean density profile $\bar{\rho}_0(x, y, T)$. The advection of hot or cold gas by the streaming flow will cause both g and ω_0 to evolve on the slow time scale and induce a two-way coupling between the waves and the streaming flow. The amplitude $A(T)$ of the acoustic mode is also expected to evolve on this slow time scale owing to dissipation by viscosity, energy exchanges with the streaming flow and walls and/or external forcing. To obtain an evolution equation for $A(T)$, we proceed as follows, relegating details to the appendices.

1. We collect terms in the dimensionless governing equations at $O(\epsilon^2)$. The resulting equations are reported in Appendix A.

2. We make the ansatz that generic $O(\epsilon^2)$ fluctuation field f_2' can be represented as

$$f_2'(x, y, T, \phi) = \frac{B(T)}{2} \left(\hat{f}_2(x, y, T) e^{i\phi} + \text{c.c.} \right) \tag{3.13}$$

and, in direct analogy with the manipulations performed in § 3.1, reduce the $O(\epsilon^2)$ fluctuation system for the five unknown fields $\hat{u}_2$, $\hat{v}_2$, $\hat{\pi}_2$, $\hat{\rho}_2$ and $\hat{\Theta}_2$ to a system of two

equations for the two fields $\hat{u}_2$ and $\hat{v}_2$. [Harmonics of the form $e^{i2\phi}$ also exist at this order, but are non-resonant and thus do not contribute to the slow-time dynamics; accordingly, these harmonics need not be explicitly computed.] The resulting system of equations has the form

$$\partial_x \left(\partial_x \hat{u}_2 + \partial_y \hat{v}_2\right) + \omega_0^2 \bar{\rho}_0 \hat{u}_2 = \mathcal{F}, \tag{3.14}$$

$$\partial_y \left(\partial_x \hat{u}_2 + \partial_y \hat{v}_2\right) = \mathcal{G}. \tag{3.15}$$

The linear operator acting on the left-hand side of this system is identical to that arising in the leading-order fluctuation equations (3.3)–(3.4). The right-hand side functions $\mathcal{F}$ and $\mathcal{G}$ include resonant forcing terms involving the leading-order fluctuations fields (f_1'). Analytical expressions for the imaginary parts of $\mathcal{F}$ and $\mathcal{G}$, which are needed for the derivation of the (real) amplitude equation, are given in Appendix B.

3. We derive a solvability condition for the $O(\epsilon^2)$ system, which requires determination of the adjoint linear operator, by invoking the Fredholm alternative theorem in the usual manner; see Appendix C.

4. We enforce the solvability condition to obtain an equation for $\mathrm{d}A/\mathrm{d}T$; cf. Appendix D.

Employing this procedure, we derive the following novel amplitude equation:

$$\frac{2}{A\omega_0^{-1}} \frac{\mathrm{d}(A\omega_0^{-1})}{\mathrm{d}T} = -\frac{i\omega_0}{Pe_s h^2} \int_D \mathrm{d}x\mathrm{d}y\, g\partial_{yy}\hat{\Theta}_1 - \frac{1}{2\omega_0^2} \int_D \mathrm{d}x\mathrm{d}y\, g'^2 \left(\bar{u}_1 \partial_x \bar{\rho}_0^{-1} + \bar{v}_1 \partial_y \bar{\rho}_0^{-1}\right) + \int_D \mathrm{d}x\mathrm{d}y \left(\partial_x \bar{u}_1 + \partial_y \bar{v}_1\right) \left[(1-\gamma)g^2 + \frac{g'^2}{\omega_0^2 \bar{\rho}_0} \left(\frac{Pe_s}{Re_s} - \frac{1}{2}\right)\right], \tag{3.16}$$

where $\int_D$ refers to definite integration over the spatial domain. (Note that, since the temperature and velocity fluctuations are out of phase, $\hat{\Theta}_1$ is strictly imaginary.) The lack of terms nonlinear in A in (3.16) confirms that phenomena such as shock-wave formation or harmonic generation are sub-dominant dynamical processes in the given parameter regime relative to, for example, heat exchange with the boundaries or energy exchange with the evolving stratified environment. In particular, the first term on the right-hand side of (3.16) accounts for the time-mean heat transfer between the waves and the boundaries. In § 4.5, we demonstrate that this term can be positive: in this scenario, the waves are driven by a process that is loosely akin to the classical thermoacoustic instability in which acoustic waves in a channel can be excited when a temperature gradient is imposed *along* the channel walls (Swift 1988). Owing to the occurrence of the mean fields $\bar{u}_1$, $\bar{v}_1$ and $\bar{\rho}_0$ in (3.16), the amplitude equation is, in fact, nonlinear. A distinguishing feature of (3.16) is that, unlike amplitude equations derived in numerous other contexts, determination of the coefficients requires evaluation of *functional derivatives* that capture the $O(1)$ variations in generic eigenfunction $\hat{f}_1$ caused by changes in the mean density field $\bar{\rho}_0$ that occur on the slow time T; see Appendices B and D for details.

The quantity $A\omega_0^{-1}$ on the left-hand side of (3.16) is proportional to the square-root of the dimensionless energy of the acoustic wave. Indeed, the leading-order dimensionless kinetic energy E_K of the acoustic wave averaged over the fast time scale is given by

$$\overline{E}_K \equiv \frac{1}{2} \int_0^{2\pi} \mathrm{d}x \int_0^1 \mathrm{d}y \bar{\rho}_0 \overline{u_1'^2} = \frac{A(T)^2}{4} \int_0^{2\pi} \mathrm{d}x \int_0^1 \mathrm{d}y \bar{\rho}_0 \hat{u}_1^2. \tag{3.17}$$

This expression can be evaluated using (3.7) to obtain

$$\overline{E}_K = \frac{A(T)^2}{4\omega_0^4}\int_0^{2\pi} \mathrm{d}x \int_0^1 \mathrm{d}y \frac{g'^2}{\bar{\rho}_0} = \frac{A(T)^2}{4\omega_0^4}\int_0^{2\pi} \mathrm{d}x g'^2 \alpha. \tag{3.18}$$

The last integral reduces to ω_0^2 following an integration by parts and ulitisation of the differential equation (3.9) and the normalization condition (3.12), yielding

$$\overline{E}_K = \left(\frac{A(T)}{2\omega_0}\right)^2. \tag{3.19}$$

The amplitude equation therefore can be interpreted as an energy balance for the acoustic wave, with the left-hand side of (3.16) equalling $(1/\overline{E}_K)\mathrm{d}\overline{E}_K/\mathrm{d}T$.

An important outcome of this study is that even allowing for two-way wave/mean-flow coupling, the WKBJ analysis enables the streaming flow to be computed *without* evolving the sound waves over the fast time scale. (Of course, in the absence of two-way coupling, as in classical Rayleigh streaming, this averaging is trivial.) Instead, the evolving spatial structure of the waves can be computed at every coarse time step (in a numerical simulation) by solving the one-dimensional eigenvalue problem (3.9), while the evolution of the amplitude can be determined by integrating (3.16) over the slow time scale. These computations are performed in conjunction with the numerical solution of the streaming equations (2.15)–(2.19).

4. One-way coupling

Although the asymptotically-reduced equations constitute a substantial simplification of the full compressible Navier–Stokes equations, they defy analytical solution owing to the occurrence of nonlinearities and two-way coupling between the waves and the streaming flow. For sufficiently weak streaming, however, an approximate steady-state solution can be derived: in this limit, mean advection is weak and the mean density perturbations are small, thereby ameliorating these two difficulties. Here, we derive this approximate analytical solution and demonstrate that it accurately describes results obtained from direct numerical simulations of the compressible Navier–Stokes and heat equations reported in the literature.

4.1. *Acoustic waves*

In this section, we assume that the mean density profile varies little and thus can be accurately approximated by the diffusive solution (2.5), i.e.

$$\bar{\rho}_0 = \frac{1}{T_B} = \frac{1}{1+\Gamma y}. \tag{4.1}$$

The coefficient α defined in (3.10) then does not depend on x and is simply equal to $1 + \Gamma/2$. The acoustic-wave eigenfunction g characterizing the shape of the acoustic mode follows from the solution of the second-order differential equation (3.9) and, with the prescribed boundary conditions $g'(0) = g'(2\pi) = 0$ and the normalization condition (3.12), is given by

$$g(x) = \frac{\cos(nx)}{\sqrt{\pi}}, \tag{4.2}$$

where the integer n is set to unity for this study. The angular frequency of this mode

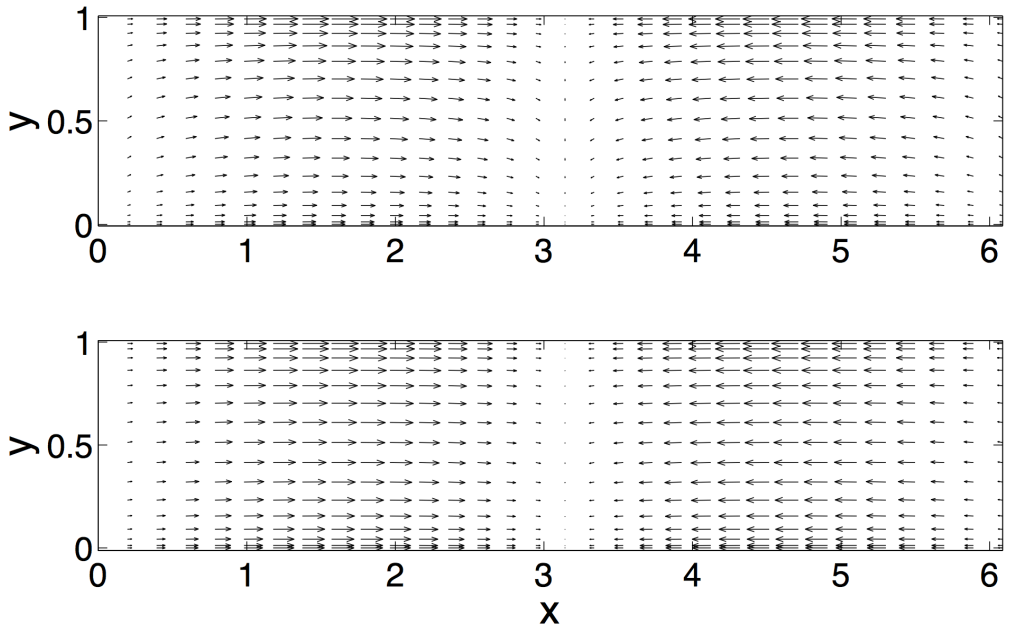

FIGURE 2. Standing acoustic-wave velocity field corresponding to the first (i.e. $n = 1$) eigenmode for $\Gamma = 1$ (upper) and $\Gamma = 0.2$ (lower), with $\gamma = 1.4$. Particularly in the upper plot, it is evident that the wall-normal (y) velocity component is non-zero owing to the background density stratification and, crucially, the wave is rotational. The lower plot is included to illustrate the dependence of the wave field on the stratification and because $\Gamma = 0.2$ is the value used in the direct numerical simulation performed by Lin & Farouk (2008) to which we compare our theoretical predictions.

$\omega_0 = \sqrt{1 + \Gamma/2}$, and the velocity field $(\hat{u}_1, \hat{v}_1)$ follows from (3.7)–(3.8) and reduces to

$$\hat{u}_1 = \frac{(1 + \Gamma y)\sin(x)}{(1 + \Gamma/2)\sqrt{\pi}}, \tag{4.3}$$

$$\hat{v}_1 = \frac{\Gamma y\,(1 - y)\cos(x)}{2(1 + \Gamma/2)\sqrt{\pi}}. \tag{4.4}$$

This velocity field is plotted in figure 2 for two different values of Γ. A rotational (vortical) component may be discerned, particularly for the $\Gamma = 1$ scenario, even though viscous torques are absent since the dynamics in oscillatory boundary layers has been self-consistently omitted. Crucially, the Reynolds stress divergence terms, here denoted $R(x, y)$, arising in (2.15) and responsible for driving the streaming flow can be explicitly evaluated:

$$R(x, y) = -\partial_x\left(\bar{\rho}_0\overline{u_1'^2}\right) - \partial_y\left(\bar{\rho}_0\overline{u_1'v_1'}\right) = -\frac{A^2}{2\pi(1 + \Gamma/2)^2}\left(1 + \frac{\Gamma}{4} + \frac{\Gamma y}{2}\right)\sin(2x). \tag{4.5}$$

If $\Gamma = 0$, i.e. for a homogeneous fluid, $R(x, y) = \partial_x[(A^2/4\pi)\cos(2x)]$. Clearly, in that case, the wave-induced Reynolds-stress divergence can be balanced by a mean pressure gradient, so that streaming is *not* directly driven; instead, the associated Rayleigh streaming flow arises at next order in ϵ owing to the action of viscous torques within oscillatory boundary layers. If, however, $\Gamma \neq 0$, then $R(x, y)$ can no longer be reduced to gradient form and, consequently, directly drives a streaming flow.

4.2. *Streaming flow*

We assume that the steady streaming driven by $R(x,y)$ given in (4.5) is sufficiently weak that the streaming equations (2.15)–(2.19) can be linearised. Note that, unlike Rayleigh streaming, the mean flow is compressible even though the streaming Mach number is negligible.

In a steady state, the pressure field can be eliminated from the linearised versions of equations (2.15)–(2.16), yielding

$$\partial_{xy}R = -\frac{\partial_{yyyx}\bar{u}_1}{Re_s h^2}, \tag{4.6}$$

while conservation of mass and internal energy (2.17)–(2.18) imply

$$\partial_x \bar{u}_1 = -\frac{(1+\Gamma y)}{\Gamma Pe_s h^2}\partial_{yyy}\bar{\Theta}_0. \tag{4.7}$$

Finally, we obtain from equations (4.5)–(4.7) a single differential equation for $\bar{\Theta}_0$:

$$(1+\Gamma y)\partial_{yyyyyy}\bar{\Theta}_0 + 3\Gamma\partial_{yyyyy}\bar{\Theta}_0 = -\frac{2A^2\Gamma^2 Re_s Pe_s h^4}{\pi(2+\Gamma)^2}\cos(2x). \tag{4.8}$$

This equation is supplemented with the boundary conditions:

(i) $\bar{\Theta}_0(x,y=0) = \bar{\Theta}_0(x,y=1) = 0$, since the wall temperatures are held constant;

(ii) $\partial_{yy}\bar{\Theta}_0(x,y=0) = \partial_{yy}\bar{\Theta}_0(x,y=1) = 0$, to enforce $\bar{v}_1 = 0$ at the walls [see (2.17)–(2.19)]; and

(iii) $\partial_{yyy}\bar{\Theta}_0(x,y=0) = \partial_{yyy}\bar{\Theta}_0(x,y=1) = 0$, to enforce the no-slip boundary condition at each wall, upon using (4.7).

With these boundary conditions, a unique solution can be found. For illustration, we focus on the case $\Gamma = 1$, for which

$$\bar{\Theta}_0(x,y) = -\frac{2A^2 Re_s Pe_s h^4}{9\pi}G(y)\cos(2x), \tag{4.9}$$

where

$$G(y) = \frac{1}{1080(-3+\log(16))}\Big[60(1+y)^2\log(1+y) \tag{4.10}$$
$$+ y(94 - 222\log(2) - 90y - 20y^2 - 5y^3(-5+\log(64)) + 3y^4(-3+\log(16)))\Big].$$

For the self-consistency of this approximation, the assumptions of one-way coupling and linear streaming dynamics require that the mean density change little during the evolution, i.e. $\bar{\Theta}_0 \ll 1$, and that the nonlinear terms be negligible, e.g. $\bar{u}_1^2 \ll 1$. From equations (2.15)–(2.19) and (4.9), these constraints imply (for $\Gamma = 1$) upper bounds on the dimensionless parameter combinations $A^2 Re_s h^2$ and $A^2 Re_s Pe_s h^4$.

4.3. *Comparison with previous work*

Using the analytical solution (4.9), various properties of the streaming flow can be deduced. First, the maximum dimensional baroclinic streaming velocity obtained here

$$\tilde{u}_B \propto (\max|G|)\, A^2 Re_s h^2 U_* \tag{4.11}$$

can be compared to the corresponding velocity $\tilde{u}_R$ in Rayleigh streaming resulting from dissipation in the Stokes boundary layers, i.e.

$$\tilde{u}_R \propto \epsilon A^2 U_*. \tag{4.12}$$

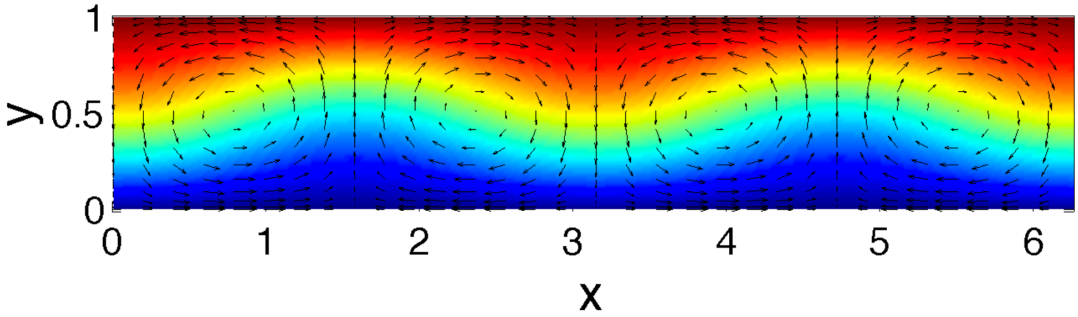

FIGURE 3. Analytically-predicted baroclinic streaming flow obtained in the limit of one-way coupling (i.e. for sufficiently weak sound waves, which implies upper bounds on $A^2 Re_s h^2$ and $A^2 Re_s Pe_s h^4$). Colour is used to indicate the total temperature (blue is cold). Recall that the lower boundary is colder than the upper boundary, and that gravitational forces have been neglected. The parameter values are the same as those used to compute the sound wave shown in figure 2 (lower plot); additionally, $A = 6$, $h = 2.3$, $Re_s = 5.7$ and $Pe_s = 4.1$. Collectively, these parameters correspond closely to the values employed by Lin & Farouk (2008) in their full numerical simulations of stratified acoustic streaming. In contrast to Rayleigh streaming, the cells span the channel.

Clearly, for small values of ϵ, the baroclinic streaming dominates any streaming driven by viscous torques acting in near-wall Stokes layers.

The streaming velocity field $(\bar{u}_1, \bar{v}_1)$ computed from (4.8) for $\Gamma = 0.2$ is plotted along with the total temperature $T_B + \bar{\Theta}_0$ in figure 3. Clearly, baroclinic streaming differs from Rayleigh streaming not only in intensity but also in spatial structure; specifically, here the streaming cells span the channel while in Rayleigh streaming the cells are stacked in the wall-normal direction. These various distinguishing properties accord with prior experiments and numerical simulations; e.g. see Loh *et al.* (2002); Hyun *et al.* (2005); Lin & Farouk (2008); Nabavi *et al.* (2008); Atkas & Ozgumus (2010); Dreeben & Chini (2011).

Quantitative comparisons can be made with the results of Lin & Farouk (2008), who performed direct numerical simulations of the compressible Navier–Stokes and heat equations specifically to investigate the impact of acoustic streaming in a thin channel on cross-channel heat transport. Thus, the system they considered is very similar to that studied here. In the absence of thermal driving, the streaming flow is accurately predicted by using Rayleigh's formulation and, accordingly, exhibits a pattern of counter-rotating cells *stacked* in the y direction. When a temperature difference is imposed, however, the stacked cells merge, resulting in counter-rotating cells that span the channel. In particular, for their case 1C, corresponding to the largest imposed temperature differential, the dimensionless parameters used by Lin & Farouk (2008) are approximately

$$\epsilon = 10^{-2}, \quad \gamma = 1.4, \quad \Gamma = 0.2, \quad h = 2.3, \quad Re_s = 5.7, \quad Pe_s = 4.1. \tag{4.13}$$

The amplitude A of the acoustic waves is not reported, but can reasonably be assumed to be similar to the value arising in the absence of thermal driving, for which $A \approx 6$. The authors report the values of the x (resp. y) component of the dimensional streaming velocity at $x = 3\pi/4$ (resp. $x = \pi/2$). We compute $\bar{u}_1$ and $\bar{v}_1$ for the same parameters in this one-way coupling limit, and then obtain the corresponding dimensional velocities by multiplying $\bar{u}_1$ by the sound speed $a_* = 353\ \mathrm{m \cdot s^{-1}}$ and $\bar{v}_1$ by $\sqrt{\epsilon} h a_*$. Figure 4 shows the resulting comparison. The evident quantitative agreement – with *no* adjustable parameters and despite the fact that the numerical simulations of Lin & Farouk (2008) include several physical effects (oscillatory boundary-layer dynamics, viscous heating, inertia and temperature-dependent viscosity and diffusivity coefficients) not incorporated in our

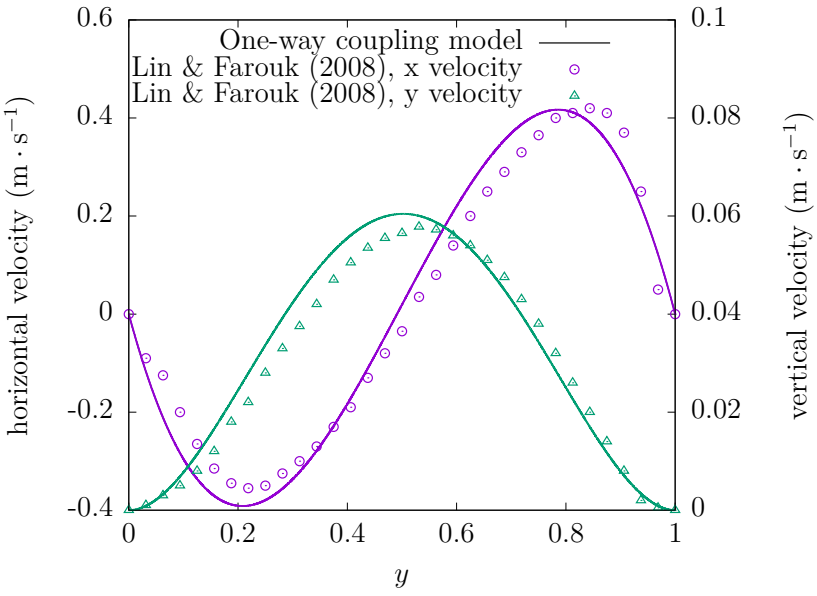

FIGURE 4. Comparison of the x and y components of the streaming velocity field extracted from the numerical simulations of the instantaneous (compressible) Navier–Stokes and heat equations performed by Lin & Farouk (2008) (their case 1C) with the corresponding streaming velocities predicted from the present theory in the limit of one-way wave/mean-flow coupling and linear streaming dynamics. The parameters correspond to: $A = 6$, $\Gamma = 0.2$, $\gamma = 1.4$, $h = 2.3$, $Re_s = 5.7$ and $Pe_s = 4.1$. Excellent quantitative agreement is observed *without* the use of any fitting parameters.

analysis – provides strong confirmation of the baroclinic streaming theory developed by Chini *et al.* (2014) and systematically extended in the present study.

4.4. *Heat flux enhancement*

The streaming flow enhances cross-channel heat transport, as we now demonstrate using the leading-order solutions derived in this section. For this purpose, we introduce the steady-state Nusselt number Nu as the ratio of the (dimensional) total heat flux $\dot{Q}_*$ to the diffusive flux,

$$Nu = \frac{\dot{Q}_*}{2\pi\kappa\Delta\Theta_*(k_*H_*)^{-1}}, \tag{4.14}$$

and compute $Nu - 1$. The total heat flux $\dot{Q}_*$ is evaluated at the top boundary,

$$\dot{Q}_* = \int_0^{2\pi k_*^{-1}} \kappa\partial_{\tilde{y}}\tilde{T}(\tilde{x}, \tilde{y} = H_*)\mathrm{d}\tilde{x} = \kappa(k_*H_*)^{-1}T_* \left[\int_0^{2\pi} \partial_y \left(T_B + \bar{\Theta}_0\right)(x, y = 1)\mathrm{d}x + O(\epsilon)\right], \tag{4.15}$$

so that the Nusselt number is given at leading order by

$$Nu = 1 + \frac{1}{2\pi\Gamma}\int_0^{2\pi} \partial_y\bar{\Theta}_0(x, y = 1)\mathrm{d}x + O(\epsilon). \tag{4.16}$$

Since viscous heating is neglected, the top and bottom heat fluxes are equal in a steady state; hence, the following result holds:

$$\int_0^{2\pi} [T\partial_y\Theta]_0^1 \,\mathrm{d}x = \int_0^{2\pi} \left[(1+\Gamma)\partial_y\Theta(x, y = 1) - \partial_y\Theta(x, y = 0)\right]\mathrm{d}x, \tag{4.17}$$

$$= \Gamma\int_0^{2\pi} \partial_y\bar{\Theta}_0(x, y = 1)\mathrm{d}x + O(\epsilon). \tag{4.18}$$

Moreover, from equations (2.17)–(2.19), the following equality can be derived,

$$\int_0^{2\pi} \mathrm{d}x \int_0^1 \mathrm{d}y\, T\partial_{yy}\bar{\Theta}_0 = 0 \Rightarrow \int_0^{2\pi} [T\partial_y\Theta]_0^1\, \mathrm{d}x = \int_0^{2\pi} \mathrm{d}x \int_0^1 \mathrm{d}y\, (\partial_y T)(\partial_y\bar{\Theta}_0) + O(\epsilon). \tag{4.19}$$

Finally, using the boundary condition $\bar{\Theta}_0 = 0$ at the top and bottom walls, we obtain

$$Nu - 1 = \frac{1}{2\pi\Gamma^2}\int_0^{2\pi} \mathrm{d}x \int_0^1 \mathrm{d}y (\partial_y T)(\partial_y\bar{\Theta}_0) + O(\epsilon) = \frac{1}{2\pi\Gamma^2}\int_0^{2\pi} \mathrm{d}x \int_0^1 \mathrm{d}y (\partial_y\bar{\Theta}_0)^2 + O(\epsilon). \tag{4.20}$$

In the limit of one-way coupling and for $\Gamma = 1$, we evaluate this quantity with the approximate expression (4.9) for $\bar{\Theta}_0$ derived in § 4.2,

$$Nu - 1 \simeq 3.2 \times 10^{-10}(A^2 Re_s Pe_s h^4)^2. \tag{4.21}$$

This expression should be contrasted with that obtained for Rayleigh streaming (i.e. for sufficiently small temperature differences) and computed by Vainshtein *et al.* (1995):

$$(Nu - 1)_{\mathrm{R}} = 6.2 \times 10^{-5}\left(\epsilon A^2 Pe_s h^2\right)^2. \tag{4.22}$$

This comparison indicates that, although the Nusselt number derived here is very small (as noted in § 4.2, for the validity of the one-way coupling assumption the dimensionless parameter combination $A^2 Re_s Pe_s h^4$ cannot be too large), it nevertheless is orders of magnitude larger than Nu resulting from boundary-layer-driven acoustic streaming provided that, numerically, $\epsilon \ll 10^{-2}$. Equation (4.21) also suggests that significant heat transport enhancement may be achieved in the limit $A^2 Re_s Pe_s h^4 \gg 1$, i.e. when there is strong two-way coupling between the acoustic waves and the streaming flow. This strong coupling scenario is investigated in § 5.

4.5. *Stability of the quiescent background state*

Intriguingly, the amplitude equation (3.16) suggests that an acoustic wave may be amplified via interaction with the solid boundaries. Indeed, the first term on the right-hand side of (3.16) does not depend on the streaming flow, and quantifies how the divergence of the acoustic-wave velocity field (i.e. $g(x)$) and the net heat flux to/from the solid boundaries [proportional to $\partial_y\hat{\Theta}_1(x, y = 1) - \partial_y\hat{\Theta}_1(x, y = 0)$] are coupled. In a certain parameter regime, this system may act as a thermoacoustic engine and spontaneously generate an acoustic wave that, in turn, would drive a streaming flow and increase the cross-channel heat transport.

To see this, note that $\hat{\Theta}_1$ can be determined from the acoustic wave solution derived in § 4.1 and then used to evaluate

$$-\frac{i\omega_0}{Pe_s h^2}\int_D \mathrm{d}x\mathrm{d}y\, g\partial_{yy}\hat{\Theta}_1 = \frac{-2\Gamma\left[1 + (2 - \Gamma)(\gamma - 1)\right]}{Pe_s h^2(1 + \Gamma/2)}. \tag{4.23}$$

Since $\gamma > 1$, this term is negative and damps the acoustic waves, *unless* the thermal forcing Γ is sufficiently strong. In that case, a proper discussion of the stability of the quiescent background state would require the evaluation of the acoustic-wave energy dissipation and temperature profile in the oscillatory boundary layers, which has been neglected here (see § 6). Nevertheless, this calculation suggests that such an instability, in which an acoustic wave spontaneously grows by a thermoacoustic effect even in the absence of an imposed wall-parallel (x) temperature gradient, is possible.

5. Two-way coupling

The analytical solution derived in § 4 and used to compute the heat flux enhancement is not valid when there is two-way coupling between the acoustic waves and the streaming flow, as occurs for sufficiently large values of the dimensionless parameter groups $A^2 Re_s h^2$ and $A^2 Re_s Pe_s h^4$. To investigate the dynamics in this regime, we perform numerical simulations of the reduced equations derived in § 2 and § 3 using the spectral computing environment Dedalus (Burns *et al.* 2018).

The spatial domain is discretized on a 512×128 ($x \times y$) grid using a Fourier–Chebyshev pseudospectral scheme. Temporal integration is performed strictly on the slow time scale T with a 2nd-order Runge–Kutta method. At each time step, the shape and angular frequency of the standing acoustic-wave mode are obtained by numerically solving the eigenvalue problem (3.9) derived in § 3.1 using a Chebyshev spectral method and global QZ algorithm. The amplitude of the acoustic mode A either is taken to be a prescribed time-independent value or evolved according to the amplitude equation with an additional constant input power P, resulting in a term $P/\overline{E}_K$ on the right-hand side of (3.16). In the first scenario, the forcing must be imagined to be tuned continuously to maintain the constancy of the wave amplitude, and the amplitude equation can then be utilised to self-consistently evaluate the power P required. In the second scenario, in which the input power P is held constant, (3.16) must be co-evolved numerically with the streaming equations.

Depending upon the parameter regime, numerical integration of (2.15)–(2.19) can result in a grid-scale instability manifesting as high-wavenumber variability in the x direction. To remedy this difficulty, we regularize the streaming dynamics simply by including the next-order terms in ϵ that, while formally small, introduce a viscous term of the form $\partial_{xx}\bar{u}_1$ in (2.15) and eliminate the numerical instability.

Here, we describe the the numerical simulations performed at constant amplitude A. The other parameters are chosen as follows:

$$\epsilon = 10^{-2}, \quad \gamma = 1.4, \quad \Gamma = 1, \quad h = 4, \quad Re_s = 4, \quad Pe_s = 4. \tag{5.1}$$

Although not depicted here, for small values of A the resulting steady-state velocity field agrees quantitatively with the one computed in § 4. As A is increased, however, the cellular streamline pattern evident in figure 3 changes into one dominated by narrow jet-like flow structures; see figure 5, which shows the steady-state fields obtained for $A = 2.8$. Unlike streaming at high Re_s in the absence of background density stratification (Vainshtein *et al.* 1995), symmetry with respect to the mid-plane $y = 1/2$ is broken. Moreover, for this simulation, the angular frequency of the acoustic waves changes by more than 3%, providing quantitative evidence of the two-way coupling between the waves and the streaming flow.

The heat-flux enhancement factors achieved by steady streaming states obtained for various values of A (and computed using (4.16)) are plotted in figure 6. For small values of A, the results follow the theoretical prediction derived in § 4, but ultimately deviate as the streaming flow develops localized jets. Even in the regime of strong coupling, the rapid growth of the Nusselt number ($Nu - 1 \propto A^4$) is qualitatively observed, strongly suggesting that significant increases in heat transport may be realized for sufficiently large values of A (see § 6).

6. Discussion

Both experiments and direct numerical simulations confirm that an imposed temperature difference or, more generally, any inhomogeneous background density field strongly

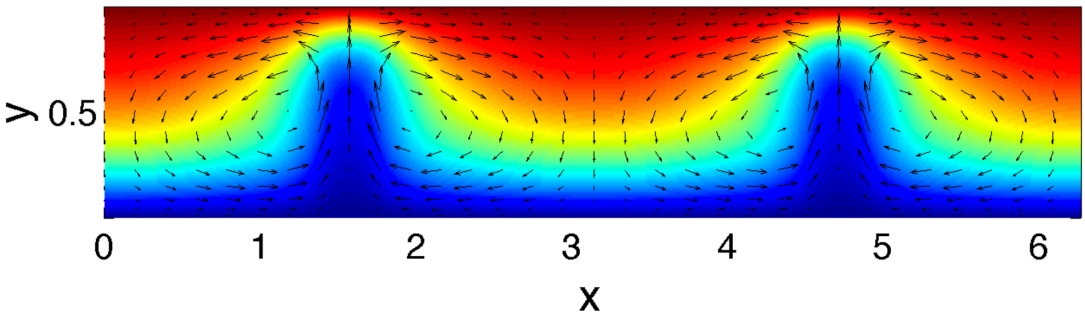

FIGURE 5. Steady-state streaming velocity (vector arrows) and total temperature (color) fields, $(\bar{u}_1,\bar{v}_1)$ and $T_B + \bar{\Theta}_0$, respectively, resulting from forcing at fixed acoustic-wave amplitude $A = 2.8$. The other parameters are chosen as follows: $\epsilon = 10^{-2}$, $\Gamma = 1$, $\gamma = 1.4$, $h = 4$, $Re_s = 4$ and $Pe_s = 4$. Observe the emergence of vertical jets.

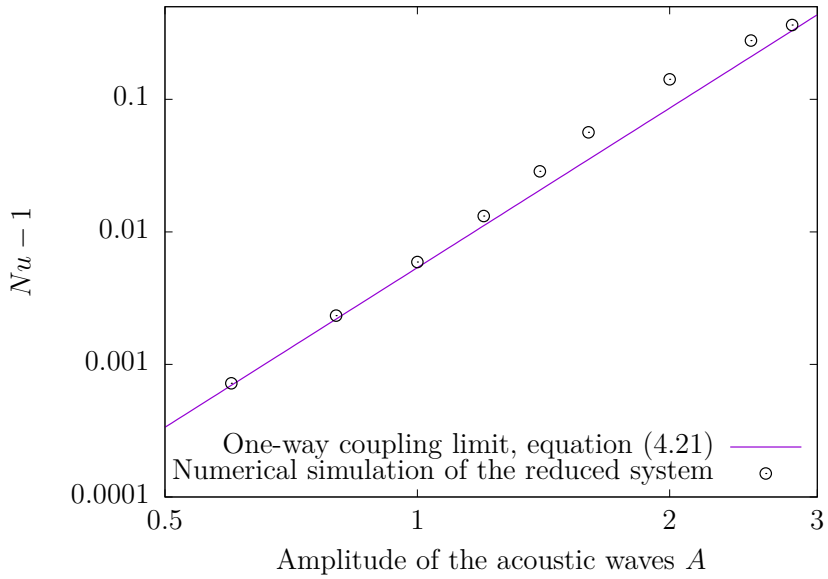

FIGURE 6. Nusselt number Nu versus forcing wave amplitude A for baroclinic acoustic streaming in the small aspect-ratio limit without and with two-way wave/mean-flow coupling.

affects both the pattern and intensity of acoustic streaming. To correctly predict the streaming dynamics, it is thus necessary to properly account for these density gradients, as in the work of Chini *et al.* (2014) and in the present study. The striking effect of the inhomogeneous density field on the streaming originates from the baroclinic generation of wave vorticity that occurs even in the absence of viscous torques. This vorticity generation mechanism is readily inferred by taking the curl of the linearised Euler equations describing the leading-order acoustic wave dynamics,

$$\tilde{\nabla} \times \left(\tilde{\rho} \partial_{\tilde{t}} \tilde{\mathbf{u}} = -\tilde{\nabla} \tilde{p} \right) \Rightarrow \partial_{\tilde{t}} \left(\tilde{\nabla} \times \tilde{\mathbf{u}} \right) = \frac{(\tilde{\nabla} \tilde{\rho}) \times (\tilde{\nabla} \tilde{p})}{\tilde{\rho}^2}, \tag{6.1}$$

and from the instantaneous acoustic-wave velocity field shown in figure 2. As already emphasized in Chini *et al.* (2014), this mechanism enhances the transfer of energy from the waves to the streaming flow; accordingly, this regime is appropriately termed *baroclinic acoustic streaming*.

A quantitative understanding of baroclinic acoustic streaming is necessary for ascertaining the extent to which acoustics can be used to improve the transport and mixing of heat or of any dense or light solute chemical species. The separation in time scales between the period of the waves and the dynamics of the streaming flow, typically $\gtrsim 10^3$,

renders multiple scale analysis very attractive if not essential. The analysis reported here has been shown to accurately describe acoustic streaming in a thin channel across which a temperature difference is imposed: the explicit solution derived in the limit of one-way coupling quantitatively fits the data of a previous direct numerical simulation of the instantaneous governing equations (cf. § 4.3). In the same limit, our analysis enables us to readily compute the heat flux enhancement engendered by the streaming and, in particular, to identify a very strong dependence of Nu on the dimensionless channel height h: $Nu-1 \propto h^8$ (see (4.21)). This result clearly indicates that, to enhance the heat flux in a channel, the frequency of the acoustic wave should be tuned so that the aspect ratio δ is of order unity.

The description of the $\delta = O(1)$ scaling regime also should be amenable to multiple scale analysis, an extension we are currently pursuing. In this regime, baroclinic streaming continues to dominate viscous streaming, yet it is possible to more naturally account for viscous losses in the oscillatory boundary layers. Indeed, whereas the *streaming flow* induced by viscous dissipation in the Stokes boundary layers can be shown to be of higher order in the reduced system (Chini *et al.* 2014), an order of magnitude estimate of the dimensional time scale $\tilde{\tau}_{BL}$ over which the energy dissipation in the boundary layers damps the waves is given by

$$\tilde{\tau}_{BL} \sim \frac{(k_*^{-1} H_*) \times \rho_* (a_* \epsilon)^2}{(k_*^{-1} \delta_{BL}) \times \mu_* (a_* \epsilon / \delta_{BL})^2} \sim \frac{h\sqrt{Re_s}}{\omega_* \sqrt{\epsilon}}, \tag{6.2}$$

where $\delta_{BL} \sim \sqrt{\mu_*/(\rho_* a_* k_*)}$ is the thickness of the Stokes layers. Therefore, viscous dissipation in the oscillatory boundary layers takes place on a time scale that falls intermediate to the slow and the fast scales, and thus cannot be easily introduced within the framework of the small aspect-ratio analysis. Here, these viscous losses are implicitly presumed to be offset by the wave forcing mechanism. (Note that in classical Rayleigh streaming, i.e. in a homogeneous medium, the dissipation time scale also lies between the wave period and the time required for steady streaming to be established.) Practically, this results in a difference between the heat flux at the upper and lower walls, and this difference is the input power necessary to sustain the out-of equilibrium state (Lin & Farouk 2008). With the scaling $\delta = O(1)$, however, viscous dissipation in the Stokes layers occurs on the streaming time scale ($\tilde{\tau}_{BL}\omega_* \propto 1/\epsilon$) and therefore can be readily incorporated into the analysis.

The present study extends the investigation of Chini *et al.* (2014), in which a similar multiple scale analysis is performed to predict acoustic streaming in a thin channel with cold top and bottom boundaries and an imposed volumetric heat source, in three significant ways. First, we have derived an analytical solution for baroclinic acoustic streaming in the limit of one-way coupling and $O(1)$ Prandtl number that quantitatively accords with prior direct numerical simulations. Secondly, we performed numerical simulations of the reduced system that captures the feedback from the streaming to the acoustic wave field, i.e. two-way wave/mean-flow coupling, as manifested by the deviation of the resulting heat flux enhancement from that predicted using the analytical solution. In this stronger streaming regime, there is a transition from a rather smoothly-varying cellular streaming flow for which the wave-induced Reynolds stress divergence is balanced by the mean viscous force to a flow exhibiting jet-like structures and thin (streaming) boundary layers, akin to the transition from the Rayleigh to Stuart streaming regimes. The detailed flow pattern, which exhibits only upward jets, differs from that realized at large Re_s in the absence of stratification. Finally, perhaps the primary advance of the present study is that the dynamics of a multiple time-scale quasilinear wave/mean-flow system has been

reduced to dynamical evolution strictly on the slow time scale: the spatial structure of the wave field is determined at each coarse time step from the solution of a 1D eigenvalue problem (§ 3.1), while the modal amplitude evolves according to (3.16).

This reduction yields immediate computational and theoretical advantages. Indeed, by numerically integrating the streaming equations (2.15)–(2.19) together with the wave amplitude equation (3.16) and eigenvalue problem (3.9), the instantaneous dynamics need not be simulated using supercomputing resources (e.g. as in Loh *et al.* (2002)) nor approximated by alternatively time-advancing the wave dynamics and the streaming flow (Karlsen *et al.* 2018). Our algorithm thereby enables accurate and inexpensive numerical simulations over several thousand acoustic-wave periods to be performed in a regime where the waves and streaming flow are strongly coupled. For example, in figure 7, we plot the evolution of the Nusselt number Nu and the wave amplitude A for baroclinic acoustic streaming with a small (dimensionless) constant input power $P = 10^{-3}$. Evidently, a steady state is not achieved until $T \approx 1000$, a time period corresponding to roughly $T/\epsilon = 10^5$ acoustic-wave cycles! Even using modern computational capabilities, direct numerical simulation of the instantaneous Navier–Stokes equations for this scenario would be prohibitively expensive. (For comparison, Lin & Farouk (2008) were able to run their case 1C simulations, discussed in § 4.3, for only a few hundered cycles.) This computational challenge highlights the value of the asymptotically-reduced model, including the amplitude equation (3.16), which obviates the need for directly simulating the fast dynamics. We note that the model of the quasi-biennial oscillation developed by Plumb (1977) has certain similarities with the one derived here for baroclinic acoustic streaming: in the former case, the internal gravity waves are explicitly determined using a WKBJ approximation, ultimately yielding a closed system for the mean (streaming) flow. The analog of the amplitude equation (3.16), however, has not been derived, with the waves instead being held at constant amplitude. From a theoretical perspective, the derivation of the amplitude equation directly reveals the potential for a thermoacoustic-like instability in which an acoustic wave spontaneously grows in a stably stratified background, thereby increasing the heat flux. It seems reasonable to assert that, without the amplitude equation, this instability would be difficult to anticipate and to mechanistically understand.

To conclude, we emphasize the importance of obtaining a quantitative understanding of the interaction of acoustic waves with a strongly stratified fluid. We are particularly interested in the potential heat-flux enhancement that can be achieved via baroclinic acoustic streaming in the absence of natural convection as a lightweight means of cooling electronics aboard spacecraft. For this purpose, the analysis performed here should be extended to allow for channel aspect ratios of order unity. For Earth-based applications, it also may be necessary to investigate the impact of buoyancy (gravitational) forces, which introduces into the analysis another dimensionless parameter, the Richardson number $Ri = g_*/(k_* a_*^2)$, where g_* is the acceleration of gravity. Using the values $g_* = 10\ \mathrm{m \cdot s^{-1}}$, $a_* = 333\ \mathrm{m \cdot s^{-1}}$ and $k_* = 100\ \mathrm{m^{-1}}$, we obtain $Ri = 10^{-6}$. Accordingly, if Ri were scaled in proportion to $\epsilon^{3/2}$, the mean-flow dynamics would be modified at leading-order in ϵ; i.e. incorporation of gravity would, indeed, modify the results reported here, implying that quantitative experimental validation of the present study would require micro-gravity or microscale (microfluidic) environments. Another important extension concerns the cooling of a hot object immersed in a fluid (e.g. again in the absence of natural convection) and subjected to acoustic-wave forcing. As for the internal flow configuration studied here, a streaming flow is expected to develop and thereby enhance heat transfer. To date, analysis of this fundamental problem, e.g. for a heated cylinder (first performed by Richardson (1967) and Davidson (1973); see Riley (2001) for additional references),

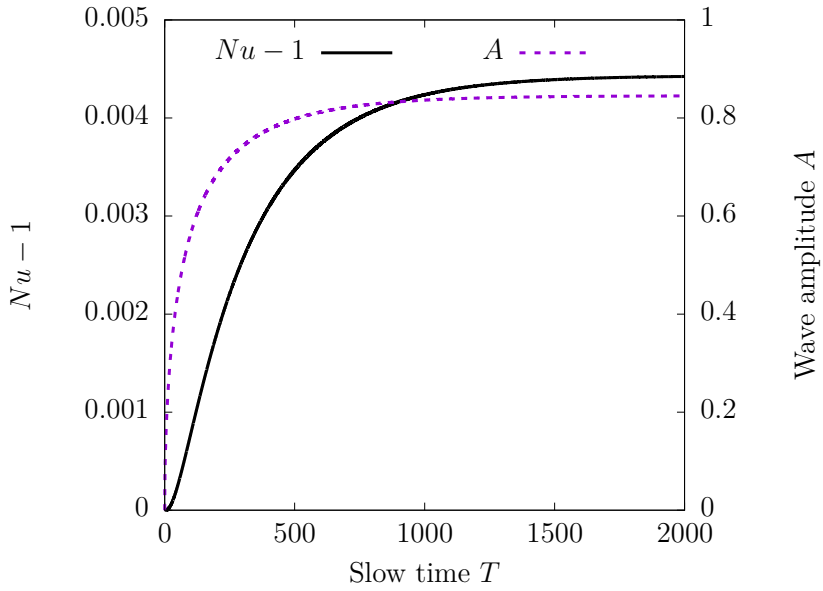

FIGURE 7. Evolution of the Nusselt number Nu and wave amplitude A with slow time T for baroclinic acoustic streaming with constant input power $P = 10^{-3}$. The remaining parameter values are specified in (5.1).

has been implicitly and, indeed, perhaps unknowingly restricted to small temperature anomalies. Again, if the temperature differential between the object and the ambient fluid is sufficiently large, fundamental changes in the streaming dynamics may be anticipated with important ramifications for mixing rates and heat transfer that have yet to be properly explored. Above all, very few experiments of the baroclinic acoustic streaming regime have been performed: well-controlled experiments in micro-gravity or stably stratified systems would be invaluable for quantitative assessment of the theory. Finally, a complementary perspective on acoustic streaming in stratified flows was recently offered by Beisner *et al.* (2015), who provided evidence that acoustically-induced mixing can suppress combustion in micro-gravity environments. This phenomenon, too, relies on the strong coupling between a density stratified fluid and an acoustic wave.

Acknowledgements

The authors are grateful to Keaton Burns for sharing his expertise on the Dedalus computing environment and for support from the 2017 Woods Hole Summer Program in Geophysical Fluid Dynamics (Woods Hole, MA), where much of this work was completed.

Appendix A.

In this appendix, we report the dimensionless set of equations for the waves at second order. (The leading order equations are given in (2.20)–(2.23); also see Chini *et al.* (2014).) In these equations, the linear operator acting on the $O(\epsilon^2)$ fluctuation fields is identified on the left-hand side and the inhomogeneous forcing arising from the leading-order terms is collected on the right-hand side.

(i) The x-component of the momentum equation is

$$\omega_0\bar{\rho}_0\partial_\phi u_2' + \frac{1}{\gamma}\partial_x\pi_2' = -\omega_0\left[\rho_1\partial_\phi u_1' - \overline{\rho_1'\partial_\phi u_1'}\right] - \omega_1\bar{\rho}_0\partial_\phi u_1'$$
$$-\bar{\rho}_0\left[\partial_T u_1' + u_1\partial_x u_1 - \overline{u_1\partial_x u_1} + v_1\partial_y u_1 - \overline{v_1\partial_y u_1}\right] + \frac{1}{Re_s h^2}\partial_{yy}u_1'. \qquad \text{(A 1)}$$

(ii) The y-component of the momentum equation is

$$\partial_y \pi_2' = -\gamma h^2 \bar{\rho}_0 \omega_0 \partial_\phi v_1'. \tag{A 2}$$

(iii) Conservation of mass requires

$$\omega_0 \partial_\phi \rho_2' + \partial_x(\bar{\rho}_0 u_2') + \partial_y(\bar{\rho}_0 v_2') = -\omega_1 \partial_\phi \rho_1' - \partial_T \rho_1' - \partial_x\left(\rho_1 u_1 - \overline{\rho_1 u_1}\right) - \partial_y\left(\rho_1 v_1 - \overline{\rho_1 v_1}\right). \tag{A 3}$$

(iv) The internal energy balance is

$$\begin{aligned} &\omega_0 \partial_\phi \Theta_2' + u_2' \partial_x \bar{\Theta}_0 + v_2' \partial_y\left(\bar{\Theta}_0 + T_B\right) + (\gamma - 1)\left[(T_B + \bar{\Theta}_0)(\partial_x u_2' + \partial_y v_2')\right] = \\ &-\omega_1 \partial_\phi \Theta_1' - \partial_T \Theta_1' - u_1 \partial_x \Theta_1 + \overline{u_1 \partial_x \Theta_1} - v_1 \partial_y \Theta_1 + \overline{v_1 \partial_y \Theta_1} \\ &+(1-\gamma)\left[\Theta_1(\partial_x u_1 + \partial_y v_1) - \overline{\Theta_1(\partial_x u_1 + \partial_y v_1)}\right] + \frac{\gamma}{\bar{\rho}_0 Pe_s h^2}\left(\partial_{yy}\Theta_1' - \frac{\rho_1' \partial_{yy}\bar{\Theta}_0}{\bar{\rho}_0}\right). \end{aligned} \tag{A 4}$$

(v) The equation of state is

$$\pi_2' - \rho_2'(T_B + \bar{\Theta}_0) - \bar{\rho}_0 \Theta_2' = \rho_1 \Theta_1 - \overline{\rho_1 \Theta_1}. \tag{A 5}$$

Appendix B.

We can reduce the set of equations given in Appendix A to (3.14)–(3.15). This procedure is strictly analogous to the corresponding manipulations performed at leading order. The imaginary parts of $\mathcal{F}$ and $\mathcal{G}$, respectively $\mathcal{F}_i$ and $\mathcal{G}_i$, are found to be

$$\begin{aligned} \mathcal{F}_i = &\frac{\omega_0}{\gamma}\partial_x \mathcal{H}_r - \frac{\omega_0 A(T)}{Re_s h^2}\partial_{yy}\hat{u}_1 + \omega_0 \bar{\rho}_0 \frac{\mathrm{d}A}{\mathrm{d}T}\hat{u}_1 \\ &+ \omega_0 \bar{\rho}_0 A(T)\left(\frac{\delta \hat{u}_1}{\delta T} + \hat{u}_1 \partial_x \bar{u}_1 + \bar{u}_1 \partial_x \hat{u}_1 + \hat{v}_1 \partial_y \bar{u}_1 + \bar{v}_1 \partial_y \hat{u}_1\right), \end{aligned} \tag{B 1}$$

and

$$\mathcal{G}_i = \left(\frac{\omega_0}{\gamma}\right)\partial_y \mathcal{H}_r, \tag{B 2}$$

where $\delta f/\delta T = (\partial \bar{\rho}_0/\partial T)(\delta f/\delta \bar{\rho}_0)$ is shorthand notation for a differentiation operation involving the functional derivative $\delta f/\delta \bar{\rho}_0$. (Strictly, $\delta f/\delta T$ should read $\mathrm{d}f/\mathrm{d}T$, but the δ-notation is used to emphasize that functional differentiation is involved.) $\mathcal{H}_r$ is defined by

$$\begin{aligned} \mathcal{H}_r = &\frac{i}{\omega_0 \bar{\rho}_0}\frac{\mathrm{d}A}{\mathrm{d}T}\hat{\rho}_1 + \frac{i}{\omega_0 \bar{\rho}_0}A(T)\left[\frac{\delta \hat{\rho}_1}{\delta T} + \partial_x(\hat{\rho}_1 \bar{u}_1) + \partial_y(\hat{\rho}_1 \bar{v}_1)\right] \\ &+\frac{iA(T)\bar{\rho}_0}{\omega_0}\left(\frac{1}{A(T)}\frac{\mathrm{d}A}{\mathrm{d}T}\hat{\Theta}_1 + \frac{\delta \hat{\Theta}_1}{\delta T} + \bar{u}_1 \partial_x \hat{\Theta}_1 + \bar{v}_1 \partial_y \hat{\Theta}_1\right) \\ &+\frac{iA(T)\bar{\rho}_0}{\omega_0}(\gamma - 1)\left[\hat{\Theta}_1(\partial_x \bar{u}_1 + \partial_y \bar{v}_1)\right] - \frac{iA(T)}{\omega_0}\frac{\gamma}{Pe_s h^2}\left(\partial_{yy}\hat{\Theta}_1 - \frac{\hat{\rho}_1}{\bar{\rho}_0}\partial_{yy}\bar{\Theta}_0\right). \end{aligned} \tag{B 3}$$

Appendix C.

In this appendix, we derive the solvability condition for the system (3.14)–(3.15). In the vector space $(\mathbb{R}^2 \to \mathbb{C})^2$, a vector

$$\mathbf{V} = \begin{pmatrix} \hat{u} \\ \hat{v} \end{pmatrix}. \tag{C 1}$$

The linear operator

$$\mathcal{L} = \begin{pmatrix} \partial_{xx} + \omega_0^2 \bar{\rho}_0 & \partial_{xy} \\ \partial_{xy} & \partial_{yy} \end{pmatrix}, \tag{C 2}$$

so the set of equations (3.14)–(3.15) is of the form $\mathcal{L}\mathbf{V} = \mathbf{F}$. Given two vectors $\mathbf{V}_A$ and $\mathbf{V}_B$, we define their scalar product

$$(\mathbf{V}_A|\mathbf{V}_B) \equiv \int_0^{2\pi} \mathrm{d}x \int_0^1 \mathrm{d}y \left(\mathbf{V}_A^{\mathrm{T}} \cdot \mathbf{V}_B^*\right) = \int_0^{2\pi} \mathrm{d}x \int_0^1 \mathrm{d}y \left(\hat{u}_A \hat{u}_B^* + \hat{v}_A \hat{v}_B^*\right), \tag{C 3}$$

where $\hat{f}^*$ stands for the complex conjugate of $\hat{f}$. Given the 2π-periodicity requirement in x and the kinematic boundary conditions in y, the operator $\mathcal{L}$ is self-adjoint ($\mathcal{L}^\dagger = \mathcal{L}$); i.e.

$$(\mathcal{L}\mathbf{V}_A|\mathbf{V}_B) = (\mathbf{V}_A|\mathcal{L}\mathbf{V}_B). \tag{C 4}$$

Therefore, the vectors in the kernel of $\mathcal{L}$ consist of the $O(\epsilon)$ acoustic-wave modes already described. Since one of these modes $\mathbf{V}_1 = (\hat{u}_1, \hat{v}_1)$, then

$$(\mathbf{F}|\mathbf{V}_1) = 0. \tag{C 5}$$

The imaginary part of (C 5) requires

$$\int \mathrm{d}x\mathrm{d}y \left(\mathcal{F}_i \hat{u}_1 + \mathcal{G}_i \hat{v}_1\right) = 0, \tag{C 6}$$

recalling that both $\hat{u}_1$ and $\hat{v}_1$ are real-valued (so $\hat{u}_1 = \hat{u}_1^*$ and $\hat{v}_1 = \hat{v}_1^*$).

Appendix D.

Evaluation of the solvability condition (C 6) requires functional forms for $\hat{u}_1$ and $\hat{v}_1$, as detailed in (3.7)–(3.9), and $\mathcal{F}_i$ and $\mathcal{G}_i$, whose explicit expressions are reported in (B 1)–(B 2). Obtaining (3.16) from (C 6) is a lengthy but straightforward calculation, except for the treatment of the functional derivatives. Certain functional derivatives can be simplified by exploiting the normalization condition; we illustrate this technical point through the computation of two integrals necessary to derive (3.16),

$$I_1 = 2\int_0^{2\pi} \mathrm{d}x g \frac{\delta g}{\delta T}, \tag{D 1}$$

and

$$I_2 = \int_0^{2\pi} \mathrm{d}x \int_0^1 \mathrm{d}y \hat{u}_1 \bar{\rho}_0 \frac{\delta \hat{u}_1}{\delta T}. \tag{D 2}$$

For a real-valued functional J of a function j, the functional derivative $\delta J/\delta j$ describes how $J(j)$ evolves when $j \to j + w$ with $|w| \to 0$:

$$\frac{\delta J}{\delta j}(w) = \lim_{\varepsilon \to 0} \left(\frac{J(j + \varepsilon w) - J(j)}{\varepsilon} \right). \tag{D 3}$$

In the present work, the functions we consider ($\hat{u}_1$, $\hat{v}_1$, etc.) have a functional dependence on $\bar{\rho}_0$ and also depend on the real parameters x and y. Specifically, we are interested in how the quantity $\hat{f}(x, y; \bar{\rho}_0)$ evolves at a fixed position x and y, while $\bar{\rho}_0$ evolves slowly in time. Formally, we therefore should define a functional $\hat{f}_{x,y}$ such that

$$\hat{f}_{x,y} \begin{cases} ([0, 2\pi] \times [0, 1] \to \mathbb{R}) \to \mathbb{C} \\ \bar{\rho}_0 \to \hat{f}(x, y; \bar{\rho}_0) \end{cases} \tag{D 4}$$

and the shorthand $\delta\hat{f}/\delta T$ should therefore be understood as

$$\frac{\delta\hat{f}}{\delta T} \to \frac{\delta\hat{f}_{x,y}}{\delta\bar{\rho}_0}(\partial_T\bar{\rho}_0). \tag{D 5}$$

The first integral I_1 is thus given by

$$I_1 = \int_0^{2\pi} \mathrm{d}x \frac{\delta g_x^2}{\delta\bar{\rho}_0}(\partial_T\bar{\rho}_0) = \lim_{\varepsilon\to 0}\left(\frac{\int_0^{2\pi}\mathrm{d}x g_x^2(\bar{\rho}_0+\varepsilon\partial_T\bar{\rho}_0) - \int_0^{2\pi}\mathrm{d}x g_x^2(\bar{\rho}_0)}{\varepsilon}\right). \tag{D 6}$$

According to the normalization condition (3.12), each of the integrals on the right-hand side of (D 6) is equal to unity so that $I_1 = 0$.

Similarly, the second integral is expressed as a function of g with (3.7),

$$I_2 = \frac{1}{\omega_0^2}\int_0^{2\pi}\mathrm{d}x\int_0^1 \mathrm{d}y g'\frac{\delta}{\delta T}\left(\frac{g'}{\omega_0^2\bar{\rho}_0}\right) \tag{D 7}$$

$$= \frac{1}{\omega_0^2}\int_0^{2\pi}\mathrm{d}x\int_0^1 \mathrm{d}y g'\left[\frac{1}{\omega_0^2\bar{\rho}_0}\frac{\delta g'}{\delta T} - \frac{2g'\partial_T\omega_0}{\bar{\rho}_0\omega_0^3} - \frac{g'\partial_T\bar{\rho}_0}{\omega_0^2\bar{\rho}_0^2}\right]. \tag{D 8}$$

The various contributions to (D 8) can be simplified using the function α introduced in (3.10) since only $\bar{\rho}_0$ depends on y:

$$I_2 = \frac{1}{\omega_0^4}\int_0^{2\pi}\mathrm{d}x g'\alpha\frac{\delta g'}{\delta T} - \frac{2\partial_T\omega_0}{\omega_0^5}\int_0^{2\pi}\mathrm{d}x\alpha g'^2 + \frac{1}{\omega_0^4}\int_0^{2\pi}\mathrm{d}x g'^2\partial_T\alpha. \tag{D 9}$$

The normalization condition (3.12) with the constitutive relation for g (3.9) yields

$$\int_0^{2\pi}\mathrm{d}x\alpha g'^2 = [\alpha g g']_0^{2\pi} + \int_0^{2\pi}\mathrm{d}x\omega_0^2 g^2 = \omega_0^2. \tag{D 10}$$

This result can be used to compute the first integral in (D 9),

$$\int_0^{2\pi}\mathrm{d}x\alpha\ g'\frac{\delta g'}{\delta T} = \frac{1}{2}\int_0^{2\pi}\mathrm{d}x\left(\frac{\delta(\alpha g'^2)}{\delta T} - g'^2\frac{\delta\alpha}{\delta T}\right) \tag{D 11}$$

$$= \frac{1}{2}\left[\lim_{\varepsilon\to 0}\left(\frac{\int_0^{2\pi}\mathrm{d}x(\alpha g'^2)(\bar{\rho}_0+\varepsilon\partial_T\bar{\rho}_0) - \int_0^{2\pi}\mathrm{d}x(\alpha g'^2)(\bar{\rho}_0)}{\varepsilon}\right) - \int_0^{2\pi}\mathrm{d}x g'^2\partial_T\alpha\right]$$

$$= \frac{1}{2}\left[2\omega_0\partial_T\omega_0 - \int_0^{2\pi}\mathrm{d}x g'^2\partial_T\alpha\right] = \omega_0\partial_T\omega_0 - \frac{1}{2}\int_0^{2\pi}\mathrm{d}x g'^2\partial_T\alpha.$$

Finally, we obtain

$$I_2 = -\frac{\partial_T\omega_0}{\omega_0^3} + \frac{1}{2\omega_0^4}\int_0^{2\pi}\mathrm{d}x g'^2\partial_T\alpha. \tag{D 12}$$

REFERENCES

Amin, N. 1988 The effect of g-jitter on heat transfer. *Proc. R. Soc. Lond. A* **419**, 151–172.

Andrade, E. N. 1931 On the circulation caused by the vibration of air in a tube. *Proc. R. Soc. Lond. A* **134**, 445–470.

Atkas, M. K. & Ozgumus, T. 2010 The effects of acoustic streaming on thermal convection in an enclosure with differentially heated horizontal walls. *Intl J. Heat Mass Transfer* **53**, 5289–5297.

Beisner, E., Wiggins, N. D., Yue, K-B, Rosales, M., Penny, J., Lockridge, J., Page, R., Smith, A. & Guerrero, L. 2015 Acoustic flame suppression mechanics in a microgravity environment. *Microgravity Sci. Technol.* **27**, 141–144.

Bengtsson, M. & Laurell, T. 2004 Ultrasonic agitation in microchannels. *Anal. Bioanal. Chem.* **378**, 1716–1721.

Burns, K. J., Vasil, G. M., Oishi, J. S., Lecoanet, D., Brown, B. P. & Quataert, E. 2018 See the dedalus entry in the astrophysical source code library, http://ascl.net/1603.015, and the dedalus project homepage, http://dedalus-project.org .

Červenka, M. & Bednarřik, M. 2017 Effect of inhomogeneous temperature fields on acoustic streaming structures in resonators. *J. Acoust. Soc. Am.* **141**, 4418–4426.

Chini, G. P., Malecha, Z. & Dreeben, T. D. 2014 Large-amplitude acoustic streaming. *J. Fluid Mech.* **744**, 329–351.

Davidson, B. J. 1973 Heat transfer from a vibrating circular cylinder. *Intl J. Heat Mass Transfer.* **16**, 1703–1727.

Dreeben, T. D. & Chini, G. P. 2011 Two-dimensional streaming flows in high-intensity dicharge lamps. *Phys. Fluids* **23**, 056101.

Fand, R.M. & Kaye, J. 1960 Acoustic streaming near a heated cylinder. *J. Acoust. Soc. Am.* **32**, 579–584.

Hamilton, M. F., Ilinskii, Y. A. & Zabolotskaya, E. A. 2003 Acoustic streaming generated by standing waves in two-dimensional channels of arbitrary with. *J. Acoust. Soc. Am.* **113**, 153–160.

Holtsmark, J., Johnsen, I., Sikkeland, T. & Skalvem, S. 1954 Boundary laer flow near a cylindrical obstacle in an oscillating, incompressible fluid. *J. Acoust. Soc. Am.* **26**, 26–39.

Hyun, S., Lee, D.-R. & Loh, B.-G. 2005 Investigation of convective heat transfer augmentation using acoustic streaming generated by ultrasonic vibrations. *Intl J. Heat Mass Transfer* **48**, 703–718.

Karlsen, J. T., Augustsson, P. & Bruus, H. 2016 Acoustic force density acting on inhomogeneous fluids in acoustic fields. *Phys. Rev. Lett.* **117**, 114504.

Karlsen, J. T., Qiu, W., Augustsson, P. & Bruus, H. 2018 Acoustic streaming and its suppression in inhomogeneous fluids. *Phys. Rev. Lett.* **120**, 054501.

Legay, M., Gondrexon, N., Person, S. Le, Boldo, P. & Bontemps, A. 2011 Enhancement of heat transfer by ultrasound: Review and recent advances. *Intl J. Chem. Engng* **2011**, 670108.

Lighthill, M. J. 1978 Acoustic streaming. *J. Sound Vib.* **61**, 391–418.

Lin, Y. & Farouk, B. 2008 Heat transfer in a rectangular chamber with differentially heated horizontal walls: Effects of a vibrating sidewall. *Intl J. Heat Mass Transfer* **51**, 3179–3189.

Loh, B.-G., Hyun, S., Ro, P. I. & Kleinstreuer, C. 2002 Acoustic streaming induced by ultrasonic flexural vibrations and associated enhancement of convective heat transfer. *J. Acoust. Soc. Am.* **111**, 875–883.

Nabavi, M., Siddiqui, K. & Dargahi, J. 2008 Influence of differentially heated horizontal walls on the streaming shape and velocity in a standing wave resonator. *Intl J. Heat Mass Transfer* **35**, 1061–1064.

Nyborg, W. L. 1958 Acoustic streaming near a boundary. *J. Acoust. Soc. Am.* **30**, 329–339.

Plumb, R. A. 1977 The interaction of two internal waves with the mean flow: implications for the theory of the quasi-biennial oscillation. *J. Atmos. Sci.* **34**, 12.

Prangsma, G. J., Alberga, A. H. & Beenakker, J. J. M. 1973 Ultrasonic determination of the volume viscosity of N_2, CO, CH and CD_4 between 77 and 300K. *Physica* **64**, 278–288.

Rayleigh, Lord 1884 On the circulation of air observed in Kundts tubes, and on some allied acoustical problems. *Philos. Trans. R. Soc. London* **175**, 1–21.

Richardson, P. D. 1967 Heat transfer from a circular cylinder by acoustic streaming. *J. Fluid Mech.* **30**, 337–355.

Riley, N. 2001 Steady streaming. *Annu. Rev. Fluid Mech.* **33**, 43–65.

Riley, N. & Trinh, E. H. 2001 Steady streaming in an oscillatory inviscid flow. *Phys. Fluids* **13**, 1956–1960.

Stuart, J. T. 1966 Double boundary layers in oscillatory viscous flow. *J. Fluid Mech.* **24**, 673–687.

Swift, G. W. 1988 Thermoacoustic engine. *J. Acoust. Soc. Am.* **84**, 1145–1180.

Vainshtein, P., Fichman, M. & Gutfinger, C. 1995 Acoustic enhancement of heat transfer between two parallel plates. *Intl J. Heat Mass Transfer* **38**, 1893–1899.

Verhaagen, B., Boutsioukis, C., van der Sluis, L. W. M. & Versluis, M. 2014 Acoustic streaming induced by an ultrasonically oscillating endodontic file. *J. Acoust. Soc. Am.* **135**, 1717–1730.

Yaralioglu, G. G., Wygant, I. O., Marentis, T. C. & Khuri-Yakub, B. T. 2004 Ultrasonic mixig in microfluidic channels using integrated transducers. *Anal. Chem.* **76**, 3694–3698.

J. Fluid Mech. (2024), *vol.* 997, A7, doi:10.1017/jfm.2024.744

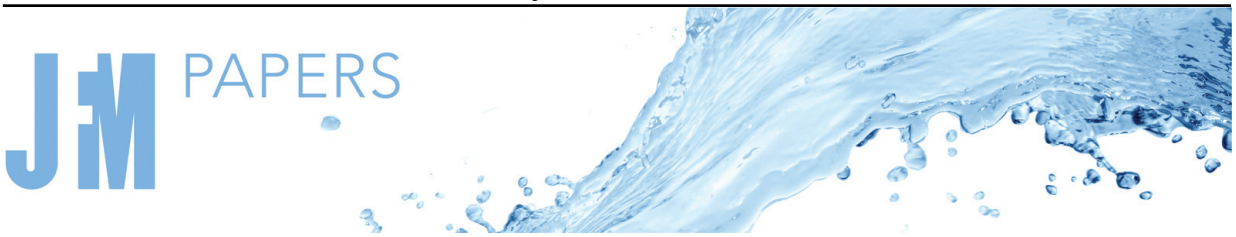

Aspect-ratio-dependent heat transport by baroclinic acoustic streaming

Jacques Abdul Massih[1], **Remil Mushthaq**[2], **Guillaume Michel**[3],† **and Gregory P. Chini**[1,2]

[1]Program in Integrated Applied Mathematics, University of New Hampshire, Durham, NH 03824, USA

[2]Department of Mechanical Engineering, University of New Hampshire, Durham, NH 03824, USA

[3]Sorbonne Université, CNRS, Institut Jean Le Rond d'Alembert, F-75005 Paris, France

(Received 11 April 2024; revised 30 June 2024; accepted 7 August 2024)

Standing acoustic waves have been known to generate Eulerian time-mean 'streaming' flows at least since the seminal investigation of Lord Rayleigh in the 1880s. Nevertheless, a recent body of numerical and experimental evidence has shown that inhomogeneities in the ambient density distribution lead to much faster flows than arise in classical Rayleigh streaming. The emergence of these unusually strong flows creates new opportunities to enhance heat transfer in systems in which convective cooling cannot otherwise be easily achieved. To assess this possibility, a theoretical study of acoustic streaming in an ideal gas confined in a rectangular channel with top and bottom walls maintained at fixed but differing temperatures is performed. A two time scale system of equations is utilized to efficiently capture the coupling between the fast acoustic waves and the slowly evolving streaming flow, enabling strongly nonlinear regimes to be accessed. A large suite of numerical simulations is carried out to probe the streaming dynamics, to highlight the critical role played by baroclinically generated wave vorticity and to quantify the additional heat flux induced by the standing acoustic wave. Proper treatment of the two-way coupling between the waves and mean flow is found to be essential for convergence to a self-consistent steady state, and the variation of the resulting acoustically enhanced steady-state heat flux with both the amplitude of the acoustic wave and the $O(1)$ aspect ratio of the channel is documented. For certain parameters, heat fluxes almost two orders of magnitude larger than those realizable by conduction alone can be attained.

Key words: gas dynamics

† Email address for correspondence: guillaume.michel@sorbonne-universite.fr

1. Introduction

Standing acoustic waves in homogeneous fluids have long been known to generate Eulerian mean flows. In the 19th century, the observation of air flows in a Kundt's tube by Dvorák (1876) was one of the three phenomena that led Rayleigh (1884) to develop his pioneering analysis of acoustic streaming. A general framework, reviewed by Riley (2001), has since been achieved: the Reynolds stress divergence induced by a standing acoustic wave generates a streaming flow provided this stress divergence cannot be balanced by a mean pressure gradient; that is, provided the acoustic wave has non-zero vorticity. If acoustic wave attenuation takes place over a much longer time scale than the acoustic period, fluctuating vorticity is localized in thin oscillatory boundary layers, and the characteristic streaming velocity scale $U_{s_*} = U_*^2/a_*$, with U_* the maximum acoustic-wave velocity and a_* the speed of sound. This streaming velocity remains modest and limits practical applications to microfluidics, where acoustic forcing is used to mix dilute chemicals along the direction transverse to the microchannel (Bengtsson & Laurell 2004). Recently, it has been shown that larger streaming velocities can be achieved if the solid boundaries include sharp edges having radii of curvature smaller than the thickness of the oscillating boundary layer, a promising finding albeit one that is difficult to realize experimentally (Huang *et al.* 2013; Zhang *et al.* 2019).

Standing acoustic waves in inhomogeneous fluids drive streaming flows with radically different features. This essential outcome of the last two decades stems from experimental evidence presented by Loh *et al.* (2002), Hyun, Lee & Loh (2005) and Stockwald, Kaestle & Ernst (2014), who reported streaming velocities in stratified gases two orders of magnitude larger than the estimate U_*^2/a_* and streaming patterns qualitatively different from that predicted by Rayleigh's theory (Dreeben & Chini 2011). This change of phenomenology is also apparent in direct numerical simulations (DNS) of the compressible Navier–Stokes equations (Lin & Farouk 2008; Aktas & Ozgumus 2010). Based on these results, Chini, Malecha & Dreeben (2014) derived a new set of wave–mean-flow interaction equations that are able to capture the dynamics of streaming flows in an inhomogeneous gas. These authors demonstrated that the physical origin of the enhanced streaming flows is the baroclinic production of fluctuating vorticity, as is evident by taking the curl of the linearized Euler equation, *viz.*

$$\boldsymbol{\nabla} \times \left(\rho_0 \frac{\partial \boldsymbol{u}'}{\partial t} = -\boldsymbol{\nabla} p' \right) \Rightarrow \frac{\partial (\boldsymbol{\nabla} \times \boldsymbol{u}')}{\partial t} = \frac{(\boldsymbol{\nabla} \rho_0) \times (\boldsymbol{\nabla} p')}{\rho_0^2}, \tag{1.1}$$

where ρ_0 is the non-uniform background density, $\boldsymbol{u}'$ is the acoustic wave velocity, p' is the acoustic wave pressure, $\boldsymbol{\nabla}$ is the spatial gradient operator and t is the time variable. Whereas the fluctuating vorticity required to drive streaming flows in homogeneous fluids results from viscous torques and is confined to thin Stokes boundary layers, in (stably) density stratified fluids wave vorticity can readily fill the entire domain owing to its generation via an inviscid process. Accounting for this fundamental change leads to a characteristic streaming velocity $U_{s_*} = U_*$ in strongly inhomogeneous fluids. Given that the acoustic Mach number U_*/a_* typically is very small compared with unity, this result provides a rationale for the large-amplitude streaming flows previously reported. Karlsen, Augustsson & Bruus (2016) extended this procedure to inhomogeneities in compressibility (negligible in gases) and demonstrated that, in an inhomogeneous gas, the wave-induced Reynolds stress divergence (i.e. the acoustic force density $\boldsymbol{f}_{ac}$) can be expressed as

$$\boldsymbol{f}_{ac} = -\tfrac{1}{2} \overline{|\boldsymbol{u}'|^2}\, \boldsymbol{\nabla} \rho_0, \tag{1.2}$$

where the overbar indicates a time average. This concise representation confirms that the forcing is inviscid and associated with baroclinicity (also proportional to $\nabla\rho_0$, as shown in (1.1)). Moreover, this expression correctly suggests that two-way coupling between the fast acoustic waves and the slowly evolving streaming flow can be realized. Specifically, in the framework of Chini *et al.* (2014) and Karlsen *et al.* (2016), the waves drive a streaming flow that advects inhomogeneities in density that, in turn, feed back on the wave velocity field $\boldsymbol{u}'$. Furthermore, given that the velocity field of the standing acoustic wave depends on the background density distribution over the entire domain, this two-way coupling is spatially non-local.

In addition to manifesting more complex dynamics, this new regime of streaming is practically important. In high-intensity discharge lamps, a temperature difference of several thousand degrees exists between the arc and the tube wall, enabling baroclinic acoustic streaming to be used to improve the efficiency of these lamps dramatically (Dreeben & Chini 2011; Chini *et al.* 2014). Similarly, streaming flows in thermoacoustic devices strongly depend on the inhomogeneous temperature distribution (Daru *et al.* 2021*a*, *b*). In microfluidics, properly accounting for inhomogeneities in both density and compressibility is crucial for obtaining accurate predictions of the acoustically driven mixing of different fluids (Karlsen *et al.* 2018; Pothuri, Azharudeen & Subramani 2019; Qiu *et al.* 2021). Acoustic wave forcing also has been proposed as an experimental means to mimic and tune gravity in regions where $\nabla(\overline{|\boldsymbol{u}'|^2})$ is spatially uniform, $\boldsymbol{f}_{ac}$ then being locally similar to gravity in the Boussinesq approximation up to a gradient term (Koulakis & Putterman 2021; Koulakis *et al.* 2023), although we stress that this connection no longer holds once two-way coupling sets in. Perhaps the most promising application involves the use of acoustics to enhance the rate of heat transfer from heated objects immersed in a cooler fluid medium, especially in scenarios in which forced convection is difficult to establish or natural convection does not occur (e.g. as for cooling electronic components aboard spacecraft).

Acoustic streaming in a straight channel with a temperature differential imposed between the top and bottom boundaries is a simple yet practical configuration in which to study the effects of inhomogeneity. Many prior studies have focused on the use of liquids as the working fluid, for which variations in compressibility also contribute to the acoustic force density (Karlsen *et al.* 2016). These studies include the large set of numerical simulations performed by Kumar *et al.* (2021) and Rajendran, Solomon & Subramani (2022) in which the effects of two-way coupling were neglected. Their results demonstrate that acoustics can either enhance or reduce the heat flux associated with natural convection depending on whether the acoustic wave displacements are, respectively, predominantly parallel or perpendicular to the channel walls. Here, we consider the second class of fluids, i.e. gases, typically air in experiments, approximated as an ideal gas in theoretical analyses. The experiments of Nabavi, Siddiqui & Dargahi (2008) clearly demonstrate that the streaming pattern derived in the homogeneous limit by Rayleigh (1884) is modified for temperature differences as low as a fraction of a degree. Results from DNS of the compressible Navier–Stokes equations for larger temperature differentials have been reported in Lin & Farouk (2008), Aktas & Ozgumus (2010) and Baran *et al.* (2022). The modest acoustic amplitudes considered in these simulations resulted in only minor modifications of the background density profile, allowing Michel & Chini (2019) to obtain an explicit expression for these baroclinic streaming flows by neglecting the two-way coupling. Larger acoustic amplitudes lead to two-way coupling, as analysed theoretically by Chini *et al.* (2014), Karlsen *et al.* (2018) and Michel & Chini (2019) and realized experimentally by Michel & Gissinger (2021).

Dimensional variable or parameter	Definition
$\tilde{\boldsymbol{u}} = (\tilde{u}, \tilde{v})$	Gas velocity
$\tilde{\rho}$	Gas density
$\tilde{p}$	Gas pressure
$\tilde{T}$	Gas temperature
$(\tilde{x}, \tilde{y})$	Horizontal, vertical (wall-normal) coordinate
$\tilde{t}$	Time variable
H_*	Channel height
$2\pi/k_*$	Horizontal wavelength of acoustic wave
μ_*	Dynamic viscosity
κ_*	Thermal conductivity
R_*	Specific gas constant
(c_{v_*}, c_{p_*})	Constant volume, pressure specific heat coefficient
$a_* = \sqrt{(c_{p_*}/c_{v_*})R_*T_*}$	Background sound speed
p_*	Background pressure

Table 1. Dimensional variables and parameters.

In the present study, the dynamics of an ideal gas undergoing standing acoustic-wave oscillations in a differentially heated channel is investigated using an extension of the wave–mean-flow interaction equations derived in Michel & Chini (2019). Our main objective is to characterize the strongly nonlinear regimes attained at large acoustic amplitudes that manifest two-way coupling. More specifically, we quantify the dependence of the acoustically enhanced heat flux on the geometry of the flow, i.e. on the aspect ratio $\delta = k_*H_*$, where k_* is the acoustic-wave wavenumber and H_* the height of the channel. Previous theoretical investigations have shown that the heat-transfer enhancement becomes negligible in the limit $\delta \to 0$ (Michel & Chini 2019), while recent DNS performed for modest acoustic amplitudes suggest that maximum enhancement is reached for $\delta = O(1)$, although these simulations did not achieve strong two-way coupling (Malecha 2023). Moreover, the scaling of the heat flux with the wave amplitude is largely undocumented in this regime. Presuming the background temperature field is homogenized in the interior of the domain as a result of the streaming-induced mixing, baroclinicity (and, hence, the acoustic force density) will localize near the walls. The consequence of this qualitative change in behaviour on the generation of steady mechanical and thermal boundary layers and on the overall heat transfer rate is also addressed in the present investigation.

The remainder of this article is organized as follows. The two time scale wave–mean-flow system governing the two-way coupled dynamics for arbitrary (but fixed) values of δ is introduced in § 2. The numerical algorithm for simulating the wave–mean-flow interaction equations is described in § 3, where detailed results are also presented. A summary of our key findings and their potential implications is given in § 4.

2. Problem formulation

2.1. *Flow configuration*

The flow configuration is similar to that investigated by Michel & Chini (2019). Dimensional variables are denoted with tildes and dimensional parameters with asterisks. These variables and parameters and their definitions are summarized in table 1.

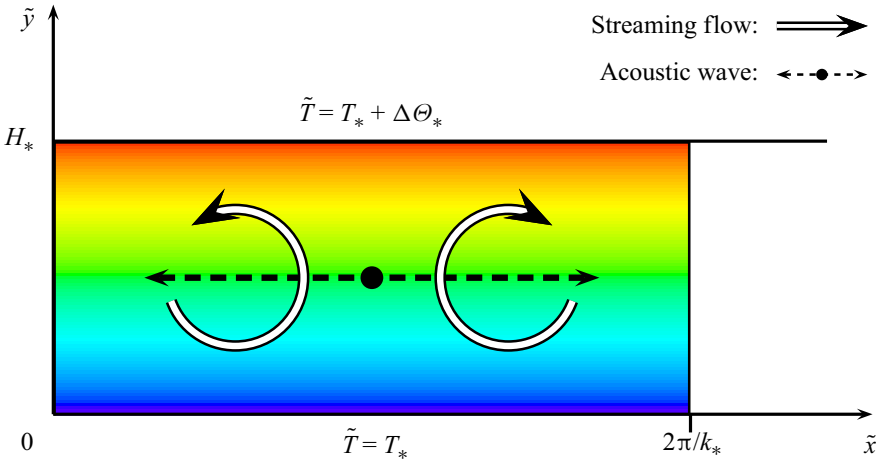

Figure 1. Schematic of the 2-D system configuration, similar to Michel & Chini (2019). An ideal gas is confined between two horizontal, no-slip and impermeable walls separated by a distance H_*. The temperatures of the lower and upper walls are fixed at T_* and $T_* + \Delta\Theta_*$, respectively (but note that gravity is not included). A standing acoustic wave of horizontal wavenumber k_* generates a counter-rotating cellular streaming flow spanning the channel that enhances the initially diffusive heat flux.

As illustrated in figure 1, we investigate the two-dimensional (2-D) dynamics of an ideal gas in an infinitely long channel of height H_*. No-slip and zero normal-flow boundary conditions on the velocity along with Dirichlet conditions on the temperature are imposed along each horizontal wall, with the temperature set to T_* at $\tilde{y} = 0$ and to $T_* + \Delta\Theta_*$ at $\tilde{y} = H_*$. This environment is assumed to be gravity-free and, thus, the imposed temperature differential $\Delta\Theta_* > 0$ neither generates natural convection nor restoring forces. In the absence of acoustic forcing, a linear temperature profile is established owing to the strictly diffusive heat flux across the channel. An unspecified external agency then drives a standing acoustic wave of angular frequency ω_* and wavenumber k_* along the horizontal ($\tilde{x}$) direction to generate a streaming flow that enhances this heat flux. The horizontal (spatial) periodicity $2\pi/k_*$ of the acoustic wave is presumed constant, being fixed in laboratory experiments, for example, by the finite horizontal length of the channel (or, more properly, cavity). Consequently, the angular frequency ω_* may vary with time as the temperature field slowly evolves. Moreover, the spatial phase of the acoustic wave is fixed by setting to zero the horizontal velocity component at $\tilde{x} = 0$, i.e. $\tilde{u}(\tilde{x} = 0, \tilde{y}, \tilde{t}) = 0$, where $(\tilde{x}, \tilde{y})$ are the horizontal and vertical coordinates and $\tilde{t}$ is the time variable.

The flow is governed by the compressible Navier–Stokes equations, supplemented by the energy equation and the ideal gas equation of state,

$$\tilde{\rho}\left[\partial_{\tilde{t}}\tilde{\boldsymbol{u}} + (\tilde{\boldsymbol{u}}\cdot\tilde{\boldsymbol{\nabla}})\tilde{\boldsymbol{u}}\right] = -\tilde{\boldsymbol{\nabla}}\tilde{p} + \mu_*\left[\tilde{\nabla}^2\tilde{\boldsymbol{u}} + \tfrac{1}{3}\tilde{\boldsymbol{\nabla}}(\tilde{\boldsymbol{\nabla}}\cdot\tilde{\boldsymbol{u}})\right], \tag{2.1}$$

$$\partial_{\tilde{t}}\tilde{\rho} + \tilde{\boldsymbol{\nabla}}\cdot(\tilde{\rho}\tilde{\boldsymbol{u}}) = 0, \tag{2.2}$$

$$\tilde{\rho}c_{v_*}\left[\partial_{\tilde{t}}\tilde{T} + (\tilde{\boldsymbol{u}}\cdot\tilde{\boldsymbol{\nabla}})\tilde{T}\right] = -\tilde{p}\left(\tilde{\boldsymbol{\nabla}}\cdot\tilde{u}\right) + \kappa_*\tilde{\nabla}^2\tilde{T}, \tag{2.3}$$

$$\tilde{p} = \tilde{\rho}R_*\tilde{T}, \tag{2.4}$$

where $\tilde{\rho}$, $\tilde{p}$, $\tilde{T}$ and $\tilde{\boldsymbol{u}} = (\tilde{u}, \tilde{v})$ denote the density, pressure, temperature and velocity fields, respectively, and $\tilde{\boldsymbol{\nabla}} = (\partial_{\tilde{x}}, \partial_{\tilde{y}})$. As discussed in Michel & Chini (2019), bulk viscosity and viscous heating are neglected and the variation of dynamic viscosity with temperature is ignored in (2.1)–(2.4).

Variable	Scale	Parameter	Definition	Scaling
x	k_*^{-1}	Acoustic Mach number ϵ	U_*/a_*	$\epsilon \ll 1$
y	H_*	Aspect ratio δ	k_*H_*	$\delta = O(1)$
t	$(a_*k_*)^{-1}$	Temperature gradient Γ	$\Delta\Theta_*/T_*$	$\Gamma = O(1)$
u	a_*	Reynolds number Re	$\rho_*U_*/(k_*\mu_*)$	$Re = O(1)$
v	$(k_*H_*)a_*$	Péclet number Pe	$\rho_*c_{p_*}U_*/(k_*\kappa_*)$	$Pe = O(1)$
ρ	$\rho_* \equiv p_*/(R_*T_*)$	Specific heat ratio γ	c_{p_*}/c_{v_*}	$\gamma = O(1)$
Θ	T_*	—	—	—
P	p_*	—	—	—

Table 2. Dimensionless variables and parameters, as in the previous analyses of Chini *et al.* (2014) and Michel & Chini (2019) except for the aspect ratio, the Reynolds number and the Péclet number, which in the present work are $O(1)$ quantities (asymptotically).

2.2. *Scaling and non-dimensionalization*

Dimensionless variables and parameters are introduced using the scalings given in table 2. The small parameter subsequently used in the asymptotic analysis is the acoustic Mach number $\epsilon = U_*/a_*$, also referred to as the inverse Strouhal number of the oscillating flow. The dimensionless temperature differential $\Gamma = \Delta\Theta_*/T_*$ is taken to be fixed and order unity as $\epsilon \to 0$ to characterize a stratified gas in which baroclinicity plays a crucial role. This distinguished limit is similar to that adopted in Chini *et al.* (2014) and Michel & Chini (2019). In contrast with these previous investigations, which focused on long thin channels for which $\delta = O(\sqrt{\epsilon})$, in this work we consider acoustic waves with horizontal wavelengths comparable to the height of the channel, i.e. $\delta = O(1)$. Note that the Reynolds and Péclet numbers based on the acoustic-wave oscillatory velocity and wavelength also characterize the streaming flow, which has typical velocities of order $U_{S_*} = U_*$ and develops structures having a spatial periodicity comparable to that of the waves. (In Chini *et al.* (2014) and Michel & Chini (2019), cross-channel, i.e. vertical, diffusion is enhanced owing to the thinness of the channel, resulting in a disparity between the acoustic and streaming Reynolds numbers.)

It is instructive to compare these scalings with typical experimental values. Using the definitions given in table 2, the acoustic cavity considered by Michel & Gissinger (2021), for instance, would be characterized by the following parameter values: $\epsilon = 1.8 \times 10^{-4}$, $\delta = 1.5$, $\Gamma \in [0.1, 0.3]$, $Re = 134$, $Pe = 86$ and $A \in [0.2, 2]$ (where the wave amplitude $A = O(1)$ is introduced in § 2.4). Thus, the scaling requirements $\epsilon \ll 1$, $\delta = O(1)$, $\Gamma = O(1)$, $Re = O(1)$ and $Pe = O(1)$ encompass this set-up.

2.3. *Asymptotic analysis*

A multiple time scale analysis of the governing equations is performed (i) to disentangle the dynamics of the fast acoustic waves from the comparatively slowly evolving streaming flow and (ii) to consistently suppress negligible terms to simplify the numerical implementation and facilitate appropriate physical interpretation. To this end, we expand the various fields in powers of the small dimensionless parameter ϵ:

$$(u, v) = \epsilon(u_1, v_1) + O(\epsilon^2), \tag{2.5}$$

$$P = 1 + \epsilon\pi_1 + \epsilon^2\pi_2 + O(\epsilon^3), \tag{2.6}$$

$$\Theta = 1 + \Gamma y + \Theta_0 + \epsilon\Theta_1 + O(\epsilon^2), \tag{2.7}$$

$$\rho = \rho_0 + \epsilon\rho_1 + O(\epsilon^2). \tag{2.8}$$

Note that the dimensionless temperature $\tilde{T}/T_*$ is denoted by Θ, cf. (2.7), rather than by T, the latter notation being reserved for the 'slow' time variable (see below).

In the absence of acoustic waves, $u = v = 0$ and, in steady state, the temperature profile reduces to the conduction profile, $\Theta = 1 + \Gamma y$, with the pressure being uniform since gravity is neglected. When excited, the leading-order acoustic velocity is $O(\epsilon)$, by definition since $U_* = \epsilon a_*$, and similarly small perturbations in the pressure and temperature fields are generated. The $O(1)$ temperature disturbance Θ_0 arises from the reorganization of temperature inhomogeneities by the strong streaming flow, as shall be made explicit in the wave–mean-flow interaction equations given subsequently.

The distinction between the waves and the streaming flow can be made based on a separation of time scales. While the acoustic wave fields exhibit fast oscillations with zero mean value, the streaming flow effectively remains constant over this time scale, evolving instead on a slow time $T \equiv \epsilon t$. The formal separation is captured via a Wentzel–Kramers–Brillouin–Jeffreys approximation through the introduction of a rapidly varying phase $\phi(t) = \Phi(T)/\epsilon$. In this framework, any field $f(x, y, t)$ is expressed as $f(x, y, \phi, T)$, where ϕ and T are taken to be independent variables, and thus can be decomposed as

$$f(x, y, \phi, T) = \bar{f}(x, y, T) + f'(x, y, \phi; T). \tag{2.9}$$

Here, the streaming flow component is represented by

$$\bar{f}(x, y, T) = \frac{1}{2\pi n}\int_{\phi}^{\phi+2n\pi} f(x, y, s, T)\,\mathrm{d}s \tag{2.10}$$

for sufficiently large positive integer n (and arbitrary ϕ). In contrast, $f'(x, y, \phi; T)$ describes the acoustic wave of zero mean value ($\overline{f'}(x, y, \phi; T) = 0$). Finally, the instantaneous angular frequency $\omega(T)$ satisfies

$$\omega(T) = \frac{\mathrm{d}\phi}{\mathrm{d}t} = \frac{\mathrm{d}\Phi}{\mathrm{d}T} = \omega_0(T) + O(\epsilon). \tag{2.11}$$

2.4. *Leading-order multiscale wave–mean-flow interaction equations*

This multiscale analytical approach has been used by Chini *et al.* (2014) to derive a closed set of equations describing the coupled dynamics of the acoustic wave and the streaming flow. The present formulation differs only in the scaling of the aspect ratio and diffusive terms, which can be easily traced in the derivation. Here, we simply state the resulting leading-order equations.

The dynamics of the streaming flow is governed by the following mean-flow system:

$$\bar{\rho}_0\left(\partial_T\bar{u}_1 + \bar{u}_1\partial_x\bar{u}_1 + \bar{v}_1\partial_y\bar{u}_1\right) = -\frac{\partial_x\bar{\pi}_2}{\gamma} - \left[\partial_x\left(\bar{\rho}_0\overline{u_1'^2}\right) + \partial_y\left(\bar{\rho}_0\overline{u_1'v_1'}\right)\right]$$
$$+\frac{1}{Re}\left[\partial_{xx}\bar{u}_1 + \frac{1}{\delta^2}\partial_{yy}\bar{u}_1 + \frac{1}{3}\left(\partial_{xx}\bar{u}_1 + \partial_{xy}\bar{v}_1\right)\right], \tag{2.12}$$

$$\bar{\rho}_0\left(\partial_T\bar{v}_1+\bar{u}_1\partial_x\bar{v}_1+\bar{v}_1\partial_y\bar{v}_1\right)=-\frac{\partial_y\bar{\pi}_2}{\gamma\delta^2}-\left[\partial_x\left(\bar{\rho}_0\overline{u_1'v_1'}\right)+\partial_y\left(\bar{\rho}_0\overline{v_1'^2}\right)\right]$$
$$+\frac{1}{Re}\left[\partial_{xx}\bar{v}_1+\frac{1}{\delta^2}\partial_{yy}\bar{v}_1+\frac{1}{3\delta^2}\left(\partial_{xy}\bar{u}_1+\partial_{yy}\bar{v}_1\right)\right], \tag{2.13}$$

$$\partial_T\bar{\rho}_0+\partial_x\left(\bar{\rho}_0\bar{u}_1\right)+\partial_y\left(\bar{\rho}_0\bar{v}_1\right)=0, \tag{2.14}$$

$$\bar{\rho}_0\left[\partial_T\bar{\Theta}_0+\bar{u}_1\partial_x\bar{\Theta}_0+\bar{v}_1\left(\Gamma+\partial_y\bar{\Theta}_0\right)\right]=(1-\gamma)\left(\partial_x\bar{u}_1+\partial_y\bar{v}_1\right)$$
$$+\frac{\gamma}{Pe}\left(\partial_{xx}\bar{\Theta}_0+\frac{1}{\delta^2}\partial_{yy}\bar{\Theta}_0\right), \tag{2.15}$$

$$\bar{\rho}_0=\frac{1}{1+\Gamma y+\bar{\Theta}_0}. \tag{2.16}$$

This system describes the wave-averaged motion of a compressible ideal gas driven by an acoustic force density $\boldsymbol{f}_{ac}=-\boldsymbol{\nabla}\cdot(\bar{\rho}_0\overline{\boldsymbol{u}_1'\boldsymbol{u}_1'})$ that, for an ideal gas, can be reduced to $-(1/2)\overline{|\boldsymbol{u}_1'|^2}\boldsymbol{\nabla}\bar{\rho}_0$ (up to a pressure gradient), as reported in (1.2) (Karlsen *et al.* 2016). If the acoustic force density is fixed, the problem reduces to that of forced convection.

In baroclinic acoustic streaming, however, the situation is considerably more subtle, as the slowly evolving temperature disturbance $\bar{\Theta}_0$, and hence the density field $\bar{\rho}_0$, feeds back on the acoustic wave. This coupling is clearly evident in the corresponding equations for the waves, *viz.*

$$\omega_0\bar{\rho}_0\partial_\phi u_1'+\frac{1}{\gamma}\partial_x\pi_1'=0, \tag{2.17}$$

$$\omega_0\bar{\rho}_0\partial_\phi v_1'+\frac{1}{\gamma\delta^2}\partial_y\pi_1'=0, \tag{2.18}$$

$$\omega_0\partial_\phi\rho_1'+\partial_x\left(\bar{\rho}_0u_1'\right)+\partial_y\left(\bar{\rho}_0v_1'\right)=0, \tag{2.19}$$

$$\omega_0\partial_\phi\Theta_1'+u_1'\partial_x\bar{\Theta}_0+v_1'\left(\Gamma+\partial_y\bar{\Theta}_0\right)+\frac{\gamma-1}{\bar{\rho}_0}\left(\partial_xu_1'+\partial_yv_1'\right)=0, \tag{2.20}$$

$$\pi_1'=\frac{\rho_1'}{\bar{\rho}_0}+\bar{\rho}_0\Theta_1'. \tag{2.21}$$

On the fast time scale, the dynamics of the acoustic waves is governed by a linear homogeneous system, the solution of which consists of a sum of modes of various amplitudes and angular frequencies. Here, however, we assume that only one acoustic mode is externally forced, i.e. only one wave has finite amplitude. This acoustic mode has dimensional horizontal wavenumber k_* and is the solution of the eigenvalue problem for the wave associated with the lowest eigenvalue (i.e. the smallest angular frequency) that also has a non-uniform horizontal structure. Thus, any oscillatory field f_1', representing $(u_1', v_1', \pi_1', \Theta_1', \rho_1')$, can be expressed as

$$f_1'(x,y,\phi;T)=\frac{A(T)}{2}\left[\hat{f}_1(x,y;T)\mathrm{e}^{\mathrm{i}\phi}+\text{c.c.}\right], \tag{2.22}$$

where c.c. denotes the complex conjugate, $A(T)$ is the amplitude of the mode and $\hat{f}_1$ is a complex function that characterizes its spatial structure. For $A(T)$ to be uniquely specified,

a normalization condition must be imposed; we opt to require the eigenmodes to satisfy

$$\max_{x\in[0,2\pi],y\in[0,1]} \left|\hat{\pi}_1(x, y, T)\right| = 1. \tag{2.23}$$

In practice, this amplitude A can be readily inferred experimentally from the (dimensional) steady-state amplitude of the pressure oscillations measured by a sensor at (x_s, y_s), which yields $\epsilon A|\hat{\pi}(x_s, y_s)|p_*$. In the limit of very narrow channels (Michel & Chini 2019), the eigenvalue problem for the lowest mode can be reduced to a one-dimensional problem (in x) that can be solved analytically for a linear temperature profile. Moreover, in that limit, the multiple scale analysis can be carried out to next order to obtain an equation governing the temporal evolution of the modal amplitude $A(T)$. Unfortunately, the corresponding higher-order analysis cannot be easily executed for the fully 2-D eigenvalue problem obtained here. The amplitude of the acoustic mode therefore will be assumed to be constant, i.e. an external control parameter, in this investigation for simplicity. Experimentally, this specification could be achieved via slowly varying acoustic forcing mechanisms controlled by the feedback of a pressure sensor.

3. Numerical simulations of the wave–mean-flow equations

3.1. *Methods*

The two time scale quasilinear wave–mean-flow interaction system obtained in § 2.4 is integrated numerically over the slow time variable T. Specifically, we solve the initial-value problem (2.12)–(2.16) governing the slow evolution of the streaming fields using a third-order four-stage Runge–Kutta scheme implemented in the spectral computational framework Dedalus (Burns *et al.* 2020). Equations (2.14) and (2.15) are reformulated to yield a divergence condition on the streaming velocity field and a modified energy equation, *viz.*

$$\partial_x \bar{u}_1 + \partial_y \bar{v}_1 = \frac{1}{Pe}\left(\partial_{xx}\bar{\Theta}_0 + \frac{1}{\delta^2}\partial_{yy}\bar{\Theta}_0\right), \tag{3.1}$$

$$\bar{\rho}_0\left[\partial_T\bar{\Theta}_0 + \bar{u}_1\partial_x\bar{\Theta}_0 + \bar{v}_1\left(\Gamma + \partial_y\bar{\Theta}_0\right)\right] = \frac{1}{Pe}\left(\partial_{xx}\bar{\Theta}_0 + \frac{1}{\delta^2}\partial_{yy}\bar{\Theta}_0\right). \tag{3.2}$$

At each (slow) time step, the acoustic fields $\hat{u}_1$ and $\hat{v}_1$ are required to evaluate the wave-induced Reynolds stress divergence. Accordingly, the set of equations (2.17)–(2.21) governing the fast wave dynamics is consolidated to form an eigenvalue problem for the fluctuating pressure field:

$$\partial_x\left[\frac{1}{\bar{\rho}_0}\partial_x\pi_1'\right] + \delta^{-2}\partial_y\left[\frac{1}{\bar{\rho}_0}\partial_y\pi_1'\right] = \omega_0^2\,\partial_{\phi\phi}\pi_1'. \tag{3.3}$$

We solve, at each time step, the 2-D eigenvalue problem (3.3) in MATLAB using a Fourier–Chebyshev collocation discretization (Trefethen 2000; Driscoll, Hale & Trefethen 2014). In both the Dedalus and MATLAB codes, Fourier series in the periodic x-direction and Chebyshev polynomials in the wall-normal y-direction are used to represent all field variables. The number of modes is chosen to correspond to a 122×122 spatial grid resolution, and the time step $\Delta T = 0.01$. Numerical convergence in space and time has been verified.

To model a physical experiment in which a specific acoustic mode is forced for time $T \geqslant 0$, the steady basic conduction state ($\bar{\Theta}_0 = \bar{v}_0 = \bar{u}_0 = 0$) is taken as the initial

condition. The solution of the eigenvalue problem targets the horizontal standing wave of smallest non-zero eigenvalue. For particular values of δ, standing waves along the vertical direction may share the same angular frequency as the horizontal mode of interest, but in practice the nature of the forcing (e.g. oscillating horizontal or vertical walls) would ensure that only one of these modes is excited. Both the resulting eigenfunction and eigenfrequency can vary with T. The results discussed in this section are obtained for various acoustic wave amplitudes A and aspect ratios δ, keeping the following parameters fixed:

$$\Gamma = 0.3, \quad \gamma = 1.4, \quad Re = 2500, \quad Pe = 1775. \tag{3.4a–d}$$

This set of parameters corresponds to using air as the working fluid, for which $\gamma = 1.4$ and the Prandtl number $Pe/Re = 0.71$, inside an acoustic cavity similar to the one employed by Michel & Gissinger (2021) but with larger Reynolds and Péclet numbers to clearly reveal strongly nonlinear dynamical behaviour. We monitor the top- and bottom-wall Nusselt numbers, defined as the ratio of the respective heat fluxes at the upper and lower channel walls to the strictly conductive heat flux and evaluated as

$$Nu_t(T) = 1 + \frac{1}{2\pi\Gamma}\int_0^{2\pi} \partial_y \bar{\Theta}_0(x, 1, T)\,\mathrm{d}x, \quad Nu_b(T) = 1 + \frac{1}{2\pi\Gamma}\int_0^{2\pi} \partial_y \bar{\Theta}_0(x, 0, T)\,\mathrm{d}x, \tag{3.5a,b}$$

where the subscripts 't' and 'b' denote 'top' and 'bottom'. In a steady state, integrating (3.1) over the entire domain yields the expected equality $Nu_t(\infty) = Nu_b(\infty) \equiv Nu$.

This numerical approach, in which an eigenvalue problem is solved at each time step to account for the slow evolution of the acoustic mode, has been introduced in Karlsen *et al.* (2018) and Michel & Chini (2019) and is necessary to consistently capture the acoustic force density $-(1/2)\overline{|\boldsymbol{u}_1'|^2}\boldsymbol{\nabla}\bar{\rho}_0$, since $\boldsymbol{u}_1'$ depends non-locally on the entire background density field $\bar{\rho}_0(x, y, T)$. Nevertheless, the relevance of regularly updating the acoustic wave fields remains insufficiently documented, leading to its arbitrary omission in most subsequent investigations. To quantitatively assess the importance of two-way coupling, we therefore also performed a set of numerical simulations, referred to as 'one-way coupled', in which the temporal integration is carried out without solving the eigenvalue problem at each time step. Instead, $\boldsymbol{f}_{ac}(x, y, T)$ is set to $-(1/2)\overline{|\boldsymbol{u}_1'|^2}\boldsymbol{\nabla}\bar{\rho}_0$ evaluated at the initial time $T = 0$. We acknowledge that several alternative 'one-way coupled' approximations can be proposed, such as (i) only fixing $\overline{|\boldsymbol{u}_1'|^2}$ in time and evaluating $\boldsymbol{f}_{ac}$ using the actual density gradient $\boldsymbol{\nabla}\bar{\rho}_0$ or (ii) setting the fluctuating pressure $\pi'(x, y, T, \phi) = A\cos(x)\cos(\phi)$ (i.e. a single Fourier mode in x that is independent of y) and evaluating the acoustic force density with the fluctuating acoustic velocity obtained from (2.17) and the current density gradient. The latter option may be appropriate for well-mixed steady states realized at large dimensionless amplitude A (see § 3.4).

3.2. *Convergence to a steady state*

For small and intermediate acoustic wave amplitudes A, our numerical simulations reveal that the system converges to parameter-dependent steady states. A typical run for $\delta = 4$ and $A = 4$ shows that a few hundred slow time units are required to reach this steady state; see figure 2 and the animation included in the supplemental material available at https://doi.org/10.1017/jfm.2024.744. This requirement highlights the importance of using a multiple-scale algorithm, since a single time unit corresponds in practice to hundreds or thousands of acoustic cycles (cf. $\epsilon \approx 10^{-4}$ for the set-up of Michel & Gissinger (2021) discussed in § 2.2). During the transient regime, the top and bottom heat fluxes evolve

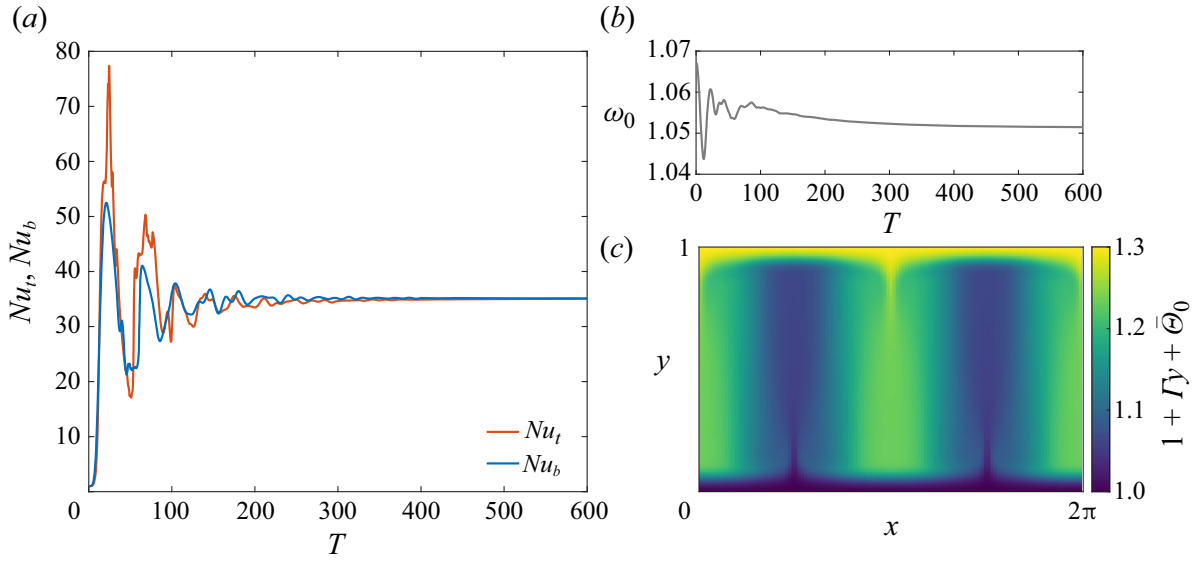

Figure 2. Time series for $A = 4$ and $\delta = 4$ of (a) the top and bottom Nusselt numbers (Nu_t, Nu_b) and (b) of the acoustic-wave angular frequency ω_0. The total steady-state temperature field $1 + \Gamma y + \bar{\Theta}_0$ shown in (c) exhibits strong variations in x associated with localized jets at $x = \{0, \pi/2, \pi, 3\pi/2, 2\pi\}$ and boundary layers in y close to both walls.

non-monotonically, ultimately converging to a common value significantly larger than the conductive heat flux. The variation of Nu with the amplitude of the wave A and with the aspect ratio δ will be discussed in § 3.4.

This steady state exhibits both thermal boundary layers and vertical jets. Low-amplitude waves ($A \ll 1$) generate smooth cellular structures (not shown here, for brevity), similar to the ones computed theoretically and numerically in Michel & Chini (2019) for $\delta \ll 1$ and in the DNS of Lin & Farouk (2008), Aktas & Ozgumus (2010), Baran *et al.* (2022) and Malecha (2023).

To gain a more detailed understanding of these steady states, we further analyse the Reynolds stress divergence, also referred to as the acoustic force density $\boldsymbol{f}_{ac}$, resulting from the acoustic wave. This force density, corresponding to the second terms on the right-hand sides of (2.12)–(2.13), is balanced by mean inertia, mean viscous forces and the mean pressure gradient. Crucially, the part of this wave forcing that actually sustains the streaming flow, i.e. the part that is not balanced by a mean pressure gradient, is given by the curl $\boldsymbol{\nabla} \times \boldsymbol{f}_{ac}$. In figure 3, we plot this (scalar) field at the initial time, when the mean temperature distribution corresponds to the linear conduction profile, and in the steady state. The striking difference confirms the two-way coupling between the waves and the streaming flow in this system, in contrast to the usual forced convection configuration. A streaming flow generated by the curl of the acoustic force modifies the mean density distribution and, hence, the properties of the acoustic waves and therefore also $\boldsymbol{\nabla} \times \boldsymbol{f}_{ac}$.

As noted in § 1, the generation of fluctuating vorticity in a gas is key to understanding streaming flows. In a homogeneous gas, a non-zero acoustic-wave vorticity implies that the acoustic force density

$$\boldsymbol{f}_{ac} \equiv -\boldsymbol{\nabla} \cdot \left(\bar{\rho}_0 \, \overline{\boldsymbol{u}_1' \boldsymbol{u}_1'} \right) = -\bar{\rho}_0 \, \boldsymbol{\nabla} \cdot \left(\overline{\boldsymbol{u}_1' \boldsymbol{u}_1'} \right) = \text{gradient term} - \bar{\rho}_0 \, \overline{\left(\boldsymbol{\nabla} \times \boldsymbol{u}_1' \right) \times \boldsymbol{u}_1'} \quad (3.6)$$

generically cannot be balanced by a gradient term and, thus, may drive a streaming flow. Acoustic-wave vorticity in that case is usually generated by viscous and/or thermal diffusion in thin oscillatory boundary layers. In an inhomogeneous and inviscid gas, the

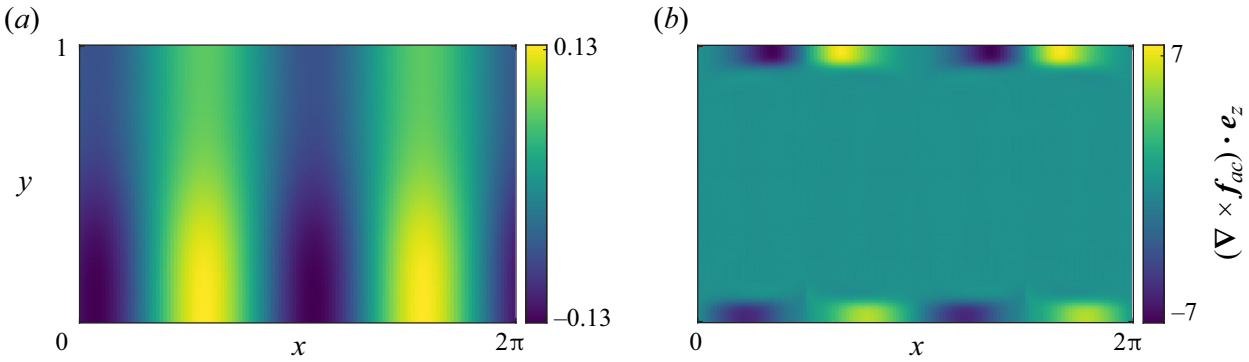

Figure 3. Evolution for $A = 4$ and $\delta = 4$ of the curl of the acoustic force density $\nabla \times \boldsymbol{f}_{ac}$: the initial condition (a) and the steady state (b). Here $\boldsymbol{e}_z \equiv \boldsymbol{e}_x \times \boldsymbol{e}_y$, where $\boldsymbol{e}_x$ and $\boldsymbol{e}_y$ are unit vectors in the x and y directions, respectively. The feedback from the evolving streaming density field $\overline{\rho}_0$ leads to the localization of $\nabla \times \boldsymbol{f}_{ac}$ near the upper and lower walls.

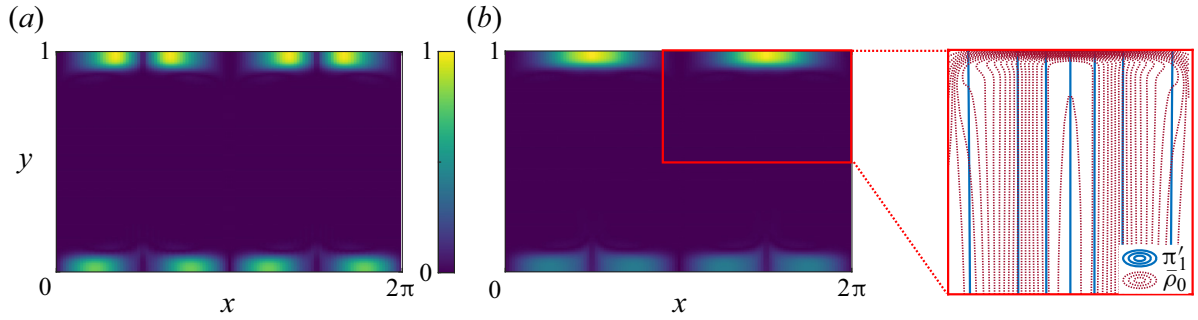

Figure 4. Comparison for $A = 4$ and $\delta = 4$ of the normalized steady-state amplitudes of (a) the curl of the Reynolds stress divergence $\nabla \times \boldsymbol{f}_{ac}$ and (b) the acoustic-wave vorticity $\nabla \times \boldsymbol{u}_1'$: ($a$) $|\nabla \times \boldsymbol{f}_{ac}|/|\nabla \times \boldsymbol{f}_{ac}|_{max}$; ($b$) $|\overline{\nabla \times \boldsymbol{u}_1'}|/|\overline{\nabla \times \boldsymbol{u}_1'}|_{max}$. Since a horizontal standing acoustic mode is considered, the fluctuating isobars (isovalues of p') are essentially vertical – see inset in (b) – and acoustic vorticity is therefore localized where vertical gradients of density exist (see (1.1)), i.e. in the top and bottom boundary layers.

acoustic force density instead reduces to (Karlsen *et al.* 2016)

$$\boldsymbol{f}_{ac} \equiv -\nabla \cdot \left(\bar{\rho}_0 \overline{\boldsymbol{u}_1' \boldsymbol{u}_1'}\right) = \text{gradient term} - \tfrac{1}{2} \overline{\left|\boldsymbol{u}_1'\right|^2} \nabla \bar{\rho}_0 \tag{3.7}$$

$$= \text{gradient term} - \tfrac{1}{2} \left(\bar{\rho}_0 \overline{\left(\nabla \times \boldsymbol{u}_1'\right) \times \boldsymbol{u}_1'} + \overline{(\boldsymbol{u}_1' \cdot \nabla \overline{\rho}_0) \boldsymbol{u}_1'}\right), \tag{3.8}$$

where (3.8) can be derived directly from (3.7) and the leading-order fluctuating equations. In the absence of acoustic-wave vorticity, i.e. in the absence of fluctuating baroclinicity $\nabla \overline{\rho}_0 \times \nabla \pi_1' = 0$, the steady-state contribution to $\nabla \times \boldsymbol{f}_{ac}$ from the term $\overline{(\boldsymbol{u}_1' \cdot \nabla \bar{\rho}_0) \boldsymbol{u}_1'}$ in (3.8) is negligible. Thus, even in inhomogeneous gases, acoustic-wave vorticity plays a crucial role in driving streaming flows. Physical insights follow from and qualitative predictions can be made based on this understanding. First, it accounts for the localization of $\nabla \times \boldsymbol{f}_{ac}$ close to the walls, as evident in figure 3. As shown in figure 4, $\nabla \times \boldsymbol{f}_{ac}$ is significant only in regions where acoustic-wave vorticity also is large in magnitude; and wave vorticity is confined to thermal boundary layers, since the fluctuating isobars and the mean isopycnals are almost orthogonal there (see (1.1)). Second, this understanding explains why the orientation of the standing acoustic wave is crucial in such systems. Consider, for example, a configuration in which the initial conduction state of the present set-up is perturbed with a standing wave oscillating along the vertical rather

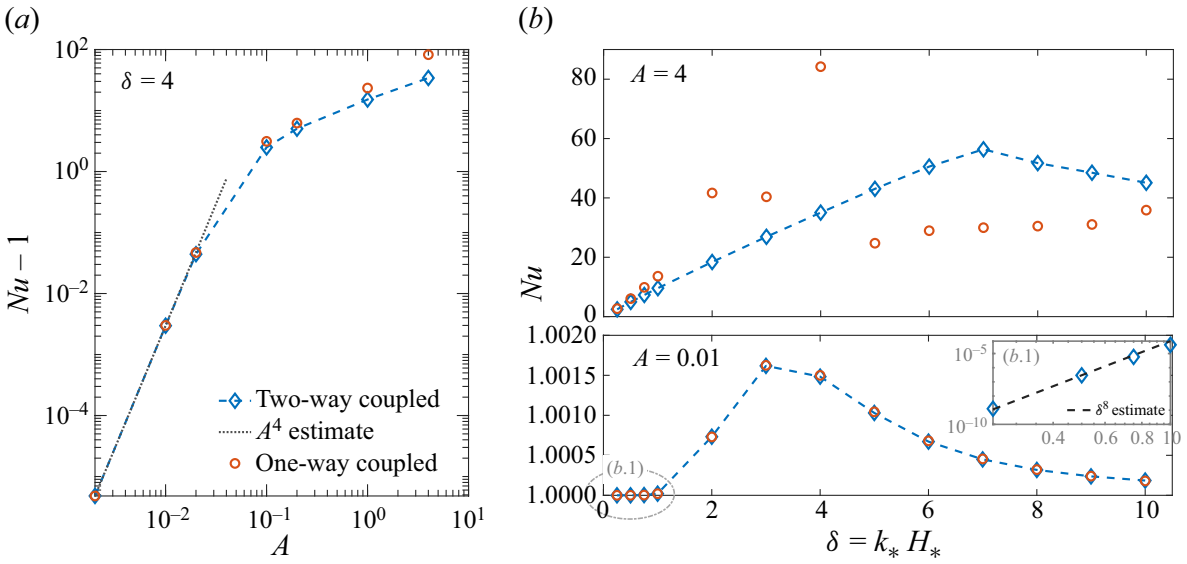

Figure 5. (*a*) Steady-state Nusselt number Nu (minus one) as a function of the acoustic wave amplitude A for $\delta = 4$, along with the asymptotic prediction $Nu - 1 \propto A^4$ that can be derived in the limit $A \ll 1$. (*b*) Steady-state Nusselt number Nu as a function of the aspect ratio δ for both $A = 4$ and $A = 0.01$. The one-way coupled simulations, in which the evolution of the acoustic waves is neglected, provide accurate results only in the small amplitude limit $A \ll 1$. The inset (*b*.1) shows $Nu - 1$ (rather than Nu) versus δ.

than horizontal direction: the fluctuating isobars and the mean isopycnals would then be approximately aligned, resulting in zero acoustic vorticity and, consequently, negligible baroclinic acoustic streaming (see also Kumar *et al.* (2021)).

3.3. *Dependence on wave amplitude*

The influence of the acoustic wave amplitude A is investigated through a suite of numerical simulations performed for the same fixed aspect ratio $\delta = 4$ but for various values of $A \in [2 \times 10^{-3}, 4]$. All simulations converge to steady states, with the Nusselt number Nu plotted in figure 5(*a*). The results are compared with one-way coupled simulations (defined in § 3.1) that also converge to steady states for $A \in [2 \times 10^{-3}, 0.2]$. In the range $A \in [1, 4]$, the one-way coupled dynamics evolves to statistically stationary states, and the corresponding Nusselt numbers are obtained by time-averaging over more than 10^3 slow time units.

In the limit of small acoustic-wave amplitude $A \ll 1$, the acoustic force density $\boldsymbol{f}_{ac} \propto A^2$ generates weak streaming flows and correspondingly small changes in the background temperature fields. Although of limited practical interest since the resulting Nusselt numbers are close to unity, this regime can be easily analysed theoretically by neglecting the evolution of the acoustic wave properties, i.e. by assuming that the one-way coupled dynamics provides an accurate approximation. Similarly to the analysis of Michel & Chini (2019), which assumes $\delta \ll 1$, we obtain for $\delta = O(1)$ that

$$Nu - 1 \underset{A \ll 1}{=} A^4 Re^2 Pe^2 \gamma^{-4} F(\delta, \Gamma), \tag{3.9}$$

with $F(\delta, \Gamma)$ a function that has to be computed numerically; in the limit $\delta \ll 1$, $F(\delta, \Gamma) = \delta^8 G(\Gamma)$ for some function $G(\Gamma)$, as predicted by Michel & Chini (2019). The results of the numerical simulations reported in figure 5 support the A^4 scaling

for $A \leqslant 0.02$, a range for which one-way and two-way coupled simulations yield nearly indistinguishable results.

Figure 5 also reveals that the one-way coupled numerical simulations and resulting theoretical prediction (3.9) fail to capture the two-way coupling that emerges for $A \geqslant 0.1$. In this regime, Nu is significantly larger than unity, and accurate results can be obtained only by using the full machinery of the multiple-scale numerical algorithm implemented in our numerical simulations.

3.4. *Dependence on aspect ratio*

The impact of varying the aspect ratio $\delta = k_* H_*$ is investigated with a set of numerical simulations performed for fixed $A = 0.01$ or 4 and varying $\delta \in [0.25, 10]$. This variation can be interpreted as being achieved, for example, by adjusting the channel height H_*, since δ is the only parameter involving H_* (see table 2).

The Nusselt numbers reported in figure 5(*b*) for small acoustic amplitude $A = 0.01$ reach a maximum for $\delta \simeq 3$. Since the acoustic amplitude $A \ll 1$, the evolution of the acoustic wave properties can be neglected, and the one-way coupled simulations accurately describe this regime. The Nusselt number is found to converge to unity as $\delta \to 0$, following the asymptotic scaling law $Nu - 1 \propto \delta^8$ derived in Michel & Chini (2019), which evidently here holds for $\delta \leqslant 1$ (see the inset in figure 5*b*). For $A = 4$, the feedback on the acoustic waves is essential, and two-way coupled simulations are required to reach a consistent steady state. In this case, the Nusselt number still exhibits significant variation with the aspect ratio, with a maximum value of $Nu = 56.4$ at $\delta = 7$. In this two-way coupled regime, the aspect ratio that maximizes the Nusselt number is expected to depend on all other parameters (Γ, Re, Pe, γ) in a complicated fashion. Given that, in practice, the height of the acoustic cavity is not easily modified once an experimental apparatus is built, these simulations are particularly valuable for identifying optimal parameters beforehand.

The evolution of the streaming fields with δ is depicted in figures 6 and 7. For the smallest value of δ (=0.25), diffusion in the wall-normal (y) direction prevails over inertia (see the factor $1/\delta^2$ in (2.12) and (2.13)) and smooth cellular structures are observed, similar to the ones reported in Lin & Farouk (2008), Aktas & Ozgumus (2010), Baran *et al.* (2022) and Malecha (2023). For larger values of δ, top and bottom boundary layers accompanied by vertical jet-like structures are generated. For such flows, the x-averaged temperature $1 + \Gamma y + \langle \bar{\Theta}_0(x, y) \rangle_x$, where $\langle (\cdot) \rangle_x$ denotes an x-average, does not monotonically vary from 1 at $y = 0$ to $1 + \Gamma$ at $y = 1$, but instead displays thin regions of reversed temperature gradient. The same feature is observed in quasilinear models of buoyancy-driven convection (Herring 1968; O'Connor, Lecoanet & Anders 2021). In these reduced models, convection is driven by the interaction between hydrodynamic modes, assumed to be linearized solutions that evolve on a fast time scale determined by an eigenvalue problem in which the more slowly evolving temperature arises as a non-constant coefficient, and the slowly evolving temperature field itself, which is forced by flux divergences analogous to a wave-induced Reynolds stress divergence. Note that these emerging viscous and thermal boundary layers have a thickness that remains large compared with that of the oscillatory Stokes layers, induced by the no-slip condition at each wall, exhibited by the acoustic velocity field. These Stokes layers, which are passive in our analysis – only generating a higher-order (i.e. weaker) streaming flow – and, thus, self-consistently not resolved in our model, are of dimensional thickness $\delta^*_{BL} = \sqrt{\mu_*/(\rho_* a_* k_*)}$. The corresponding dimensionless expression is $\delta^*_{BL}/H_* = \delta^{-1}\sqrt{\epsilon/Re}$.

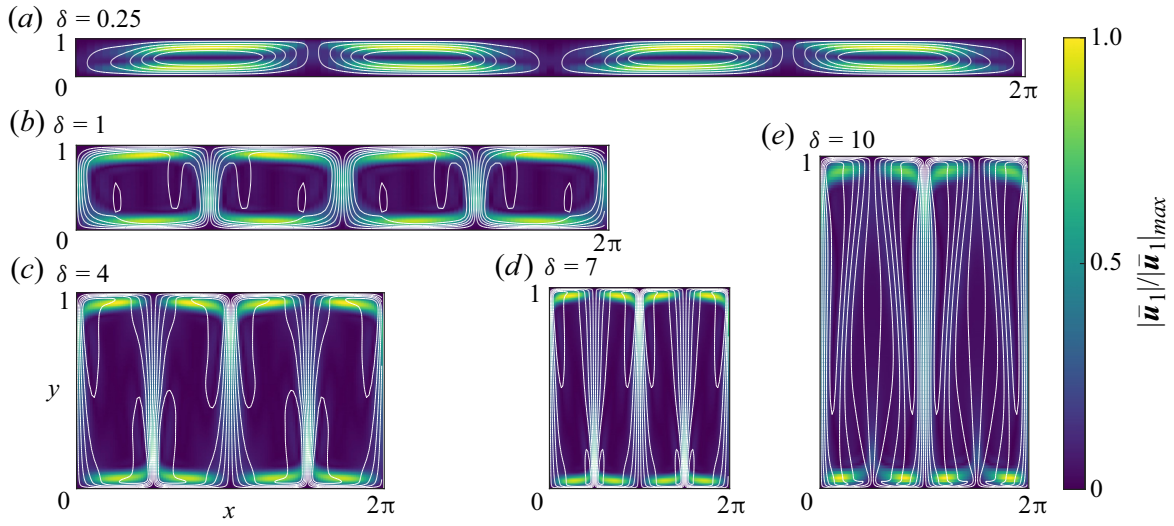

Figure 6. Steady-state streaming velocity fields for $A = 4$ and various aspect ratios δ. The white lines are isovalues of the mass current potential ϕ_ρ, defined such that $\bar{\rho}_0\bar{\boldsymbol{u}}_1 = \boldsymbol{\nabla}\phi_\rho$, and the colours correspond to the normalized velocity magnitude ($|\bar{\boldsymbol{u}}_1|/|\bar{\boldsymbol{u}}_1|_{max}$). The ratio of the height to width of each panel is set to the respective value of δ to facilitate qualitative comparison.

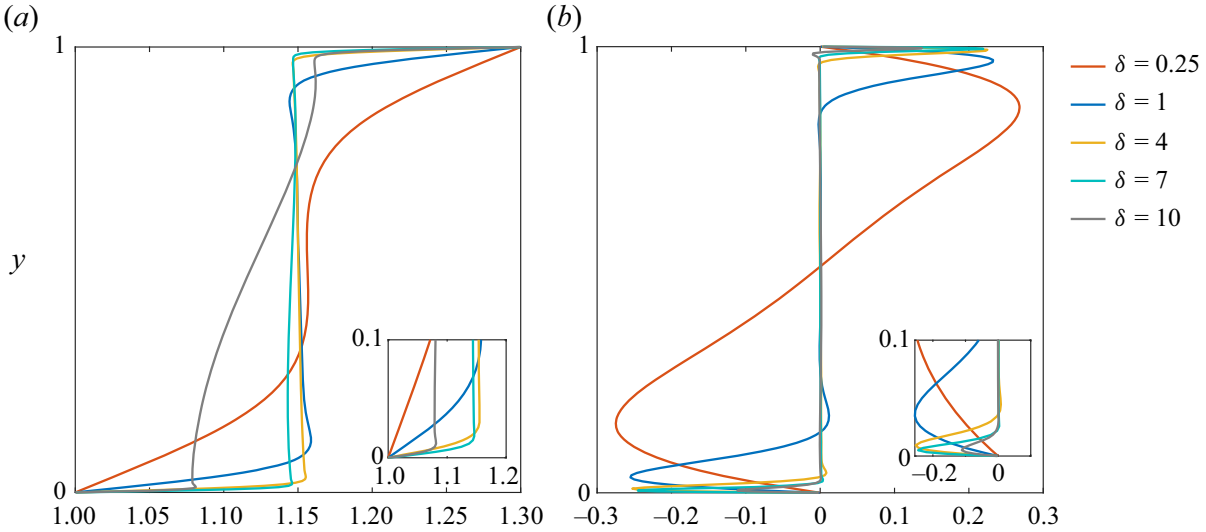

Figure 7. Wall-normal profiles of steady-state streaming temperature and horizontal velocity for $A = 4$ and various aspect ratios δ. (*a*) The total streaming temperature averaged over the horizontal x direction, $1 + \Gamma y + \langle\bar{\Theta}_0(x, y)\rangle_x$. (*b*) The streaming x-velocity component at a fixed location $x = \pi/4$, i.e. $\bar{u}_1(x = \pi/4, y)$. The smooth profiles observed for $\delta = 0.25$ develop viscous and thermal boundary layers as δ increases.

4. Conclusion

The interaction between a thermally stratified gas and a standing acoustic wave has been investigated in a channel with top and bottom walls of fixed but differing temperatures. As shown in Chini *et al.* (2014), Karlsen *et al.* (2016), Karlsen *et al.* (2018) and Michel & Chini (2019), a two-way coupling develops in such inhomogeneous systems between the streaming flow, which is forced by the standing acoustic wave, and the wave, whose properties are modified by the varying background temperature. The present study extends the work of Michel & Chini (2019) to characterize the resulting heat fluxes in channels having heights comparable to the acoustic-wave wavelength. Moreover, the numerical simulations reported here highlight several features of baroclinic streaming that are not clearly apparent in the literature.

For the given geometry, the evolution of the Nusselt number Nu, i.e. the heat flux normalized by that realized in the absence of the acoustic wave, is of primary interest. In contrast with scaling laws derived in the limit of small acoustic amplitudes, see (3.9), and with previous investigations in narrow channels (Michel & Chini 2019), we report values of Nu significantly larger than unity. This finding supports the practical potential of acoustics to enhance heat transfer in situations where forced convection is difficult to establish. The numerical algorithm that has been developed, coupling an initial value problem to an eigenvalue problem, can be used to determine the geometry that maximizes the Nusselt number for given acoustic amplitudes and gas properties, as shown for two specific sets of dimensionless parameters in figure 5(*b*). Moreover, the results reported here constitute a reference case for future investigations seeking to further increase Nu by tuning the boundary conditions (e.g. enforcing a constant heat flux instead of a constant temperature along the upper boundary to better model a heat source, or allowing for a non-zero wall-normal velocity to model a porous substrate).

We also document several features of baroclinic streaming that are expected to be generic and to apply, for instance, to the interaction of a standing acoustic wave with air surrounding a hot (or cold) cylinder or sphere or filling a half-plane above a warmer horizontal wall. In each scenario, these features can be traced to the baroclinic generation of acoustic-wave vorticity. In strongly stratified gases, streaming flows are forced where the curl of the acoustic force density is non-zero; this only occurs where the acoustic-wave vorticity does not vanish, i.e. where the fluctuating isobars and mean isopycnals are approximately orthogonal. The following sequence of events therefore can be anticipated for an inhomogeneous gas suddenly forced by a standing acoustic wave. (i) Given a smooth initial distribution of the thermal inhomogeneity, acoustic-wave vorticity will spread throughout the domain and drive a streaming flow (figure 3*a*). (ii) The streaming flow will mix the interior of the fluid, causing inhomogeneities in temperature to largely be confined to thin boundary layers (figures 2*c* and 7*a*). (iii) This evolution in the temperature field will modify the characteristics of the acoustic wave; in particular, acoustic vorticity, and hence the component of the acoustic force density effectively driving the streaming flow, also will localize in these boundary layers (figure 4). (iv) The streaming flow will develop viscous boundary layers close to the hot (or cold) solid boundary (figure 7*b*) that results in jets sustaining the mixing in the interior of the domain (figure 6*b–e*). We conjecture that a transition to turbulence also may be expected to occur as the acoustic amplitude or Reynolds number is further increased.

This dynamical picture highlights the two-way coupling between the acoustic wave and streaming flow. To stress this point, we carried out one-way coupled simulations in which the acoustic wave fields are not updated as the streaming temperature field evolves. The resulting statistically stationary state is no longer strictly steady and the associated heat flux is not accurately estimated; see figure 5. Holding the acoustic velocities fixed in the evaluation of the acoustic force density (1.2), either to simplify the numerical algorithm by not regularly solving an eigenvalue problem or to draw an analogy with an effective gravitational field (Koulakis & Putterman 2021; Koulakis *et al.* 2023), therefore restricts the validity of the approach to waves of vanishing amplitude that do not drive any significant streaming flow and for which the advection of temperature inhomogeneities can be neglected. Indeed, figure 8, which shows the acoustic wave kinetic energy for both one-way (figure 8*a*) and properly two-way (figure 8*b*) coupled simulations, confirms that merely updating the mean density distribution in the acoustic force density (1.2) is not sufficient for reliable and robust simulation of these flows. Multiple scale analysis is the appropriate approach to treat such disparate time scale coupling. Finally, this multiscale analysis can be extended to identify the scaling of the temperature differential across the

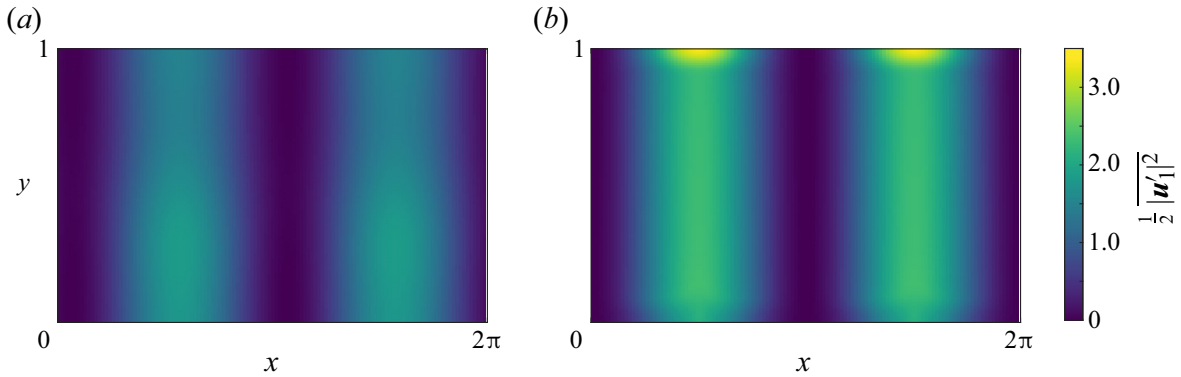

Figure 8. Evolution for $A = 4$ and $\delta = 4$ of the acoustic-wave kinetic energy $\frac{1}{2}\overline{|\boldsymbol{u}_1'|^2}$: the initial condition (*a*) and the steady state (*b*). The evolution of the acoustic-wave kinetic energy, in addition to the streaming density field, also results in significant modifications to the acoustic force density (1.2).

domain $\Gamma = \Delta\Theta_*/T_*$ for which the feedback of the streaming flow on the wave must be included, i.e. to identify the crossover between pure Rayleigh streaming ($\Gamma = 0$) and baroclinic streaming ($\Gamma = O(1)$).

Supplementary movie. Supplementary movie is available at https://doi.org/10.1017/jfm.2024.744.

Funding. This work is supported by Centre national d'études spatiales (CNES). We also acknowledge support from the Woods Hole Geophysical Fluid Dynamics Summer School (NSF 1829864), where this work was initiated.

Declaration of interests. The authors report no conflict of interest.

Author ORCIDs.
Remil Mushthaq https://orcid.org/0000-0002-8793-0299;
Guillaume Michel https://orcid.org/0000-0003-3982-5838;
Gregory P. Chini https://orcid.org/0000-0001-5539-3364.

References

Aktas, M.K. & Ozgumus, T. 2010 The effects of acoustic streaming on thermal convection in an enclosure with differentially heated horizontal walls. *Intl J. Heat Mass Transfer* **53** (23), 5289–5297.

Baran, B., Machaj, K., Malecha, Z. & Tomczuk, K. 2022 Numerical study of baroclinic acoustic streaming phenomenon for various flow parameters. *Energies* **15** (3), 854.

Bengtsson, M. & Laurell, T. 2004 Ultrasonic agitation in microchannels. *Anal. Bioanal. Chem.* **378** (7), 1716–1721.

Burns, K., Vasil, J., Geoffrey, M., Oishi, J.S., Lecoanet, D. & Brown, B.P. 2020 Dedalus: a flexible framework for numerical simulations with spectral methods. *Phys. Rev. Res.* **2** (2), 023068.

Chini, G.P., Malecha, Z. & Dreeben, T.D. 2014 Large-amplitude acoustic streaming. *J. Fluid Mech.* **744**, 329–351.

Daru, V., Weisman, C., Baltean-Carlès, D. & Bailliet, H. 2021*a* Acoustically induced thermal effects on Rayleigh streaming. *J. Fluid Mech.* **911**, A7.

Daru, V., Weisman, C., Baltean-Carlès, D. & Bailliet, H. 2021*b* A numerical study of the coupling between Rayleigh streaming and heat transfer at high acoustic level. *J. Acoust. Soc. Am.* **150** (6), 4501–4510.

Dreeben, T.D. & Chini, G.P. 2011 Two-dimensional streaming flows in high-intensity discharge lamps. *Phys. Fluids* **23** (5), 056101.

Driscoll, T.A, Hale, N. & Trefethen, L.N. 2014 *Chebfun Guide*. Pafnuty Publications.

Dvorák, V. 1876 Ueber die akustische anziehung und abstossung. *Ann. Phys.* **233** (1), 42–73.

Herring, J.R. 1968 Investigation of problems in thermal convection. *J. Atmos. Sci.* **20**, 325–338.

Huang, P.-H., Xie, Y., Ahmed, D., Rufo, J., Nama, N., Chen, Y., Chan, C.Y. & Huang, T.J. 2013 An acoustofluidic micromixer based on oscillating sidewall sharp-edges. *Lab on a Chip* **13**, 3847–3852.

Hyun, S., Lee, D.-R. & Loh, B.-G. 2005 Investigation of convective heat transfer augmentation using acoustic streaming generated by ultrasonic vibrations. *Intl J. Heat Mass Transfer* **48** (3), 703–718.

Karlsen, J.T., Augustsson, P. & Bruus, H. 2016 Acoustic force density acting on inhomogeneous fluids in acoustic fields. *Phys. Rev. Lett.* **117**, 114504.

Karlsen, J.T., Qiu, W., Augustsson, P. & Bruus, H. 2018 Acoustic streaming and its suppression in inhomogeneous fluids. *Phys. Rev. Lett.* **120**, 054501.

Koulakis, J.P., Ofek, Y., Pree, S. & Putterman, S. 2023 Thermal convection in a central force field mediated by sound. *Phys. Rev. Lett.* **130**, 034002.

Koulakis, J.P. & Putterman, S. 2021 Convective instability in a stratified ideal gas containing an acoustic field. *J. Fluid Mech.* **915**, A25.

Kumar, V., Azharudeen, M., Pothuri, C. & Subramani, K. 2021 Heat transfer mechanism driven by acoustic body force under acoustic fields. *Phys. Rev. Fluids* **6**, 073501.

Lin, Y. & Farouk, B. 2008 Heat transfer in a rectangular chamber with differentially heated horizontal walls: effects of a vibrating sidewall. *Intl J. Heat Mass Transfer* **51** (11), 3179–3189.

Loh, B.-G., Hyun, S., Ro, P.I. & Kleinstreuer, C. 2002 Acoustic streaming induced by ultrasonic flexural vibrations and associated enhancement of convective heat transfer. *J. Acoust. Soc. Am.* **111** (2), 875–883.

Malecha, Z. 2023 Three-dimensional numerical study of acoustic streaming phenomenon in rectangular resonator. *Fluid Dyn. Res.* **55** (1), 015504.

Michel, G. & Chini, G.P. 2019 Strong wave–mean-flow coupling in baroclinic acoustic streaming. *J. Fluid Mech.* **858**, 536–564.

Michel, G. & Gissinger, C. 2021 Cooling by baroclinic acoustic streaming. *Phys. Rev. Appl.* **16**, L051003.

Nabavi, M., Siddiqui, K. & Dargahi, J. 2008 Influence of differentially heated horizontal walls on the streaming shape and velocity in a standing wave resonator. *Intl Commun. Heat Mass Transfer* **35** (9), 1061–1064.

O'Connor, L., Lecoanet, D. & Anders, E.H. 2021 Marginally stable thermal equilibria of Rayleigh–Bénard convection. *Phys. Rev. Fluids* **6**, 093501.

Pothuri, C., Azharudeen, M. & Subramani, K. 2019 Rapid mixing in microchannel using standing bulk acoustic waves. *Phys. Fluids* **31** (12), 122001.

Qiu, W., Joergensen, J.H., Corato, E., Bruus, H. & Augustsson, P. 2021 Fast microscale acoustic streaming driven by a temperature-gradient-induced nondissipative acoustic body force. *Phys. Rev. Lett.* **127**, 064501.

Rajendran, V.K., Solomon, J. & Subramani, K. 2022 Heat transfer and flow patterns in a minichannel with various acoustic standing wave configurations and thermal boundary conditions. *Intl J. Heat Mass Transfer* **194**, 122923.

Rayleigh, Lord 1884 I. On the circulation of air observed in Kundt's tubes, and on some allied acoustical problems. *Phil. Trans. R. Soc. Lond.* **175**, 1–21.

Riley, N. 2001 Steady streaming. *Annu. Rev. Fluid Mech.* **33** (1), 43–65.

Stockwald, K., Kaestle, H.J. & Ernst, H. 2014 Highly efficient metal halide HID systems with acoustically stabilized convection. *IEEE Trans. Ind. Applics.* **50**, 94–103.

Trefethen, L.N. 2000 *Spectral Methods in MATLAB*. SIAM.

Zhang, C., Guo, X., Brunet, P., Costalonga, M. & Royon, L. 2019 Acoustic streaming near a sharp structure and its mixing performance characterization. *Microfluid Nanofluid* **23** (9), 104.

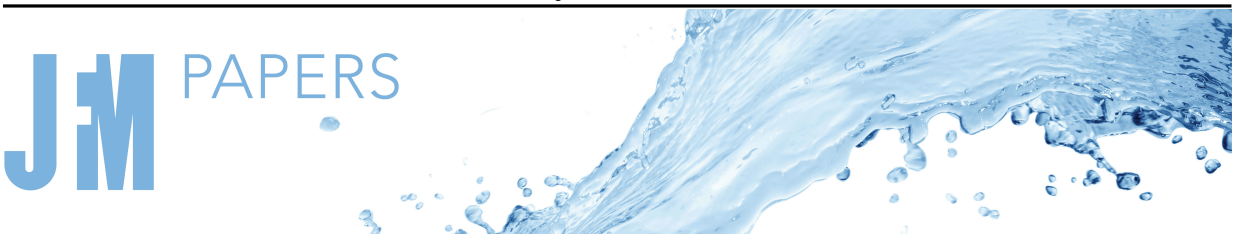

Baroclinic transition in acoustic streaming: beyond Rayleigh's paradigm

Remil Mushthaq[1], **Guillaume Michel**[2] and **Gregory P. Chini**[1,3]

[1]Department of Mechanical Engineering, University of New Hampshire, Durham, NH 03824, USA

[2]Sorbonne Université, CNRS, Institut Jean Le Rond d'Alembert, F-75005 Paris, France

[3]Program in Integrated Applied Mathematics, University of New Hampshire, Durham, NH 03824, USA

Corresponding author: Guillaume Michel, guillaume.michel@sorbonne-universite.fr

(Received 4 March 2025; revised 13 June 2025; accepted 6 July 2025)

Standing acoustic waves in a channel generate time-mean Eulerian flows. In homogeneous fluids, these streaming flows have been shown by Rayleigh to result from viscous attenuation of the waves in oscillatory boundary (i.e. Stokes) layers. However, the strength and structure of the mean flow significantly depart from the predictions of Rayleigh when inhomogeneities in fluid compressibility or density are present. This change in mean flow behaviour is of particular interest in thermal management, as streaming flows can be used to enhance cooling. In this work, we consider standing acoustic wave oscillations of an ideal gas in a differentially heated channel with hot- and cold-wall temperatures respectively set to $T_* + \Delta\Theta_*$ and T_*. An asymptotic analysis for a normalised temperature differential $\Delta\Theta_*/T_*$ comparable to the small acoustic Mach number is performed to capture the transition between the two documented regimes of Rayleigh streaming ($\Delta\Theta_* = 0$) and baroclinic streaming ($\Delta\Theta_* = O(T_*)$). Our analytical solution accounts for existing experimental and numerical results and elucidates the separate contributions of viscous torques in Stokes layers and baroclinic forcing in the interior to driving the streaming flow. The analysis yields a scaling estimate for the temperature difference $\Delta\Theta_{c_*}$ at which baroclinic driving is comparable to viscous forcing, signalling the smooth transition from Rayleigh to baroclinic acoustic streaming.

Key words: gas dynamics

1. Introduction

Since the seminal work of Rayleigh (1884, 1896), Eulerian time-mean flows generated by standing acoustic waves have garnered significant interest. As reviewed by Riley (1997,

2001), these streaming flows occur when the divergence of the wave-induced Reynolds stress cannot be fully balanced by a mean pressure gradient, i.e. when the waves have non-zero vorticity. In a channel filled with a homogeneous fluid, standing acoustic waves are irrotational in most of the domain, and streaming flows are driven by wave-induced viscous torques that arise in thin oscillatory boundary (i.e. Stokes) layers. The mean flows in this Rayleigh streaming regime have a characteristic speed $U_{s_*} = U_*^2/a_*$, where U_* is the typical value of the oscillating acoustic velocity and a_* the speed of sound, and are utilized predominantly in microfluidic applications (Bengtsson & Laurell 2004). The streaming flows driven by standing acoustic waves in an inhomogeneous fluid differ radically. Experiments conducted in thermally stratified gases reveal streaming patterns distinct from those predicted by Rayleigh and streaming velocities that are two orders of magnitude larger than U_*^2/a_* (Loh *et al.* 2002; Hyun, Lee & Loh 2005; Stockwald *et al.* 2014). These effects were also reported in direct numerical simulations (DNS) of the compressible Navier–Stokes equations (Lin & Farouk 2008; Aktas & Ozgumus 2010). To explain these features, a set of wave/mean-flow equations that captures the dynamics of streaming flows in strongly inhomogeneous gases was derived by Chini, Malecha & Dreeben (2014). In this framework, the temperature is assumed to vary significantly across the domain (specifically, the imposed temperature difference $\Delta\Theta_* = O(T_*)$, with T_* the cold-wall temperature), and the resulting streaming flows, of characteristic speed $U_{s_*} = U_*$, are found to be driven predominantly by the wave-induced Reynolds stress divergence in the bulk. Indeed, in inhomogeneous gases, acoustic waves acquire vorticity as a result of an inviscid process termed baroclinicity, and this regime is therefore referred to as 'baroclinic streaming'. Unlike Rayleigh streaming, baroclinic streaming is characterised by two-way coupling: the streaming flow driven by the waves modifies the temperature field, which in turn alters the structure of the waves. This approach can be extended to liquids, for which inhomogeneities in compressibility must also be included (Karlsen, Augustsson & Bruus 2016).

Acoustic streaming in straight channels with differentially heated walls has been extensively studied both numerically and experimentally to document this departure from Rayleigh streaming. Recent experiments of Qiu *et al.* (2021) demonstrate that inhomogeneities in liquid microchannels induced by thermal gradients can give rise to remarkably fast and distinctly patterned acoustic streaming. Their results underscore the critical role of baroclinic effects, even at modest temperature gradients. Here, we restrict our discussion to gases, for which significant density variations can be achieved. Large temperature differences have been treated experimentally (Hyun *et al.* 2005; Stockwald *et al.* 2014; Michel & Gissinger 2021) and numerically (Lin & Farouk 2008; Aktas & Ozgumus 2010), in which case the streaming flows can be analysed by assuming that $\Delta\Theta_* = O(T_*)$ (Michel & Chini 2019; Massih *et al.* 2024). However, experiments also demonstrate that Rayleigh streaming patterns are modified by temperature differences as small as a fraction of a degree (Nabavi, Siddiqui & Dargahi 2008). Although Rayleigh ($\Delta\Theta_* = 0$) and baroclinic ($\Delta\Theta_* = O(T_*)$) acoustic streaming have been separately studied extensively, an analytical solution bridging the transition between these regimes has not yet been reported in the more general setting when both processes are operative. Prior efforts to quantify the transition under the thin microchannel approximation ($k_* H_* \ll 1$) offer insight in a restricted regime (Daru *et al.* 2021).

In the present study, such a solution is derived for an ideal gas confined in a differentially heated straight channel and driven by a standing acoustic wave oscillating in the wall-parallel ('horizontal') direction. The aspect ratio of the set-up is $O(1)$, and buoyancy is neglected. A systematic asymptotic analysis enables the solution to be derived in the interior of the domain as well as in the oscillatory boundary layers (BLs).

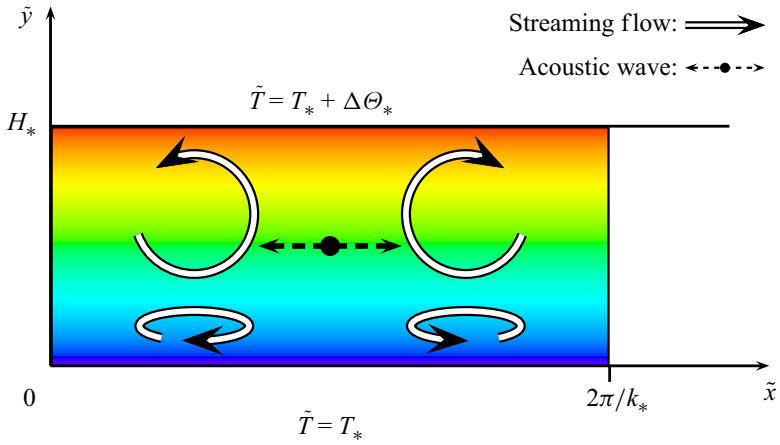

Figure 1. Schematic of the flow configuration. An ideal gas is confined between two horizontal, no-slip and impermeable walls separated by a distance H_*. The temperatures of the cold and hot walls are fixed at T_* and $T_* + \Delta\Theta_*$, respectively. Gravity is neglected. In the regime where the mean flow transitions from Rayleigh to baroclinic streaming, a standing acoustic wave of horizontal wavenumber k_* generates a counter-rotating stacked cellular streaming flow, where the cells closer to the hot wall span the majority of the channel height.

The contributions from viscous attenuation in the BLs and baroclinic forcing in the interior to driving the streaming flow are analysed in detail, and the critical temperature difference at which the flow transitions from Rayleigh to baroclinic streaming is determined as a function of the governing parameters. This result should provide useful guidance for future experimental and numerical studies by revealing whether one streaming mechanism dominates or both BL forcing and baroclinicity must be considered.

The remainder of this article is organised as follows. The two-time-scale wave/mean-flow system is introduced in § 2. The asymptotic analysis of and the explicit analytical solution to this system are presented in § 3. This solution is then validated against existing theoretical work, numerical results and experimental observations (§ 4). A summary of our key findings, which are contrasted with Rayleigh streaming and baroclinic acoustic streaming occurring in isolation, is given in § 5.

2. Problem formulation

2.1. *Flow configuration*

We investigate streaming of an ideal gas in a differentially heated horizontal channel subjected to standing horizontal acoustic-wave oscillations having a wavelength commensurate with the channel height, as illustrated in figure 1. Except for the temperature difference $\Delta\Theta_*$ that is assumed much smaller, this set-up is similar to that used to investigate baroclinic acoustic streaming in Massih *et al.* (2024). The dimensional variables and parameters, defined in table 1, are indicated using tildes and asterisks, respectively. Gravity is neglected and only two-dimensional dynamics is considered. Periodic boundary conditions are imposed along the horizontal ($\tilde{x}$) direction, setting the horizontal wavelength $2\pi/k_*$. The hot and cold walls are modelled as no-slip, no-penetration, isothermal boundaries maintained at constant but different temperatures, respectively $T_* + \Delta\Theta_*$ and T_*. In the absence of the acoustic wave, heat simply diffuses across the channel: there is no fluid motion, and the steady temperature profile is linear in the wall-normal ($\tilde{y}$) coordinate. A wall-parallel conservative acoustic body force of angular frequency ω_* excites and sustains the acoustic waves without directly driving a mean flow. The system is governed by the compressible Navier–Stokes equations,

Dimensional variable or parameter	Definition
$\tilde{\boldsymbol{u}} = (\tilde{u}, \tilde{v})$	Gas velocity
$\tilde{\rho}$	Gas density
$\tilde{p}$	Gas pressure
$\tilde{T}$	Gas temperature
$\tilde{\mathbb{F}}$	External force density
$(\tilde{x}, \tilde{y})$	Wall-parallel, wall-normal coordinates (referred to as horizontal and vertical, respectively)
$\tilde{t}$	Time variable
H_*	Channel height
$2\pi/k_*$	Horizontal wavelength of acoustic wave
μ_*	Dynamic viscosity
κ_*	Thermal conductivity
R_*	Specific gas constant
(c_{v_*}, c_{p_*})	Constant volume, pressure specific heat coefficient
$a_* = \sqrt{(c_{p_*}/c_{v_*})R_*T_*}$	Background sound speed
p_*	Background pressure
U_*	Typical acoustic wave velocity
u_{*max}	Maximum interior horizontal wave velocity

Table 1. Dimensional variables and parameters.

supplemented with conservation of mass and internal energy, and with the ideal gas equation of state:

$$\tilde{\rho}[\partial_{\tilde{t}}\tilde{\boldsymbol{u}} + (\tilde{\boldsymbol{u}} \cdot \tilde{\boldsymbol{\nabla}})\tilde{\boldsymbol{u}}] = -\tilde{\boldsymbol{\nabla}}\tilde{p} + \mu_* \left[\tilde{\boldsymbol{\nabla}}^2\tilde{\boldsymbol{u}} + \frac{1}{3}\tilde{\boldsymbol{\nabla}}(\tilde{\boldsymbol{\nabla}} \cdot \tilde{\boldsymbol{u}})\right] + \tilde{\mathbb{F}}(\tilde{x}, \tilde{t})\, \boldsymbol{e}_x, \tag{2.1}$$

$$\partial_{\tilde{t}}\tilde{\rho} + \tilde{\boldsymbol{\nabla}} \cdot (\tilde{\rho}\tilde{\boldsymbol{u}}) = 0, \tag{2.2}$$

$$\tilde{\rho} c_v[\partial_{\tilde{t}}\tilde{T} + (\tilde{\boldsymbol{u}} \cdot \tilde{\boldsymbol{\nabla}})\tilde{T}] = -\tilde{p}(\tilde{\boldsymbol{\nabla}} \cdot \tilde{u}) + \kappa_* \tilde{\nabla}^2 \tilde{T}, \tag{2.3}$$

$$\tilde{p} = \tilde{\rho} R_* \tilde{T}, \tag{2.4}$$

where $\tilde{\rho}$, $\tilde{p}$, $\tilde{T}$ and $\tilde{\boldsymbol{u}} = (\tilde{u}, \tilde{v})$ denote the density, pressure, temperature and velocity fields, respectively, and $\tilde{\boldsymbol{\nabla}} \equiv (\partial_{\tilde{x}}, \partial_{\tilde{y}})$. Bulk viscosity and viscous heating are neglected for convenience and analytical tractability, as is the temperature dependence of the viscosity and thermal conductivity (see the discussion in Michel & Chini (2019)).

2.2. *Scaling and non-dimensionalisation*

The scalings and the definition of dimensionless variables and parameters are reported in table 2. Except for the imposed temperature difference, these scalings are similar to those reported in Massih *et al.* (2024). The acoustic Mach number ϵ, which is also the inverse of the Strouhal number associated with the oscillatory flow, is assumed small and is used to order the subsequent asymptotic analysis. In this study, the dimensionless temperature differential is assumed to be finite but weak: $\hat{\Gamma} = O(\epsilon)$. As will become evident, this scaling enables the streaming flow generated by viscous torques in oscillatory BLs and that from baroclinic torques in the interior of the domain to arise at the same order in ϵ. The remaining parameters, including the aspect ratio δ, are taken to be $O(1)$.

Note that the Reynolds and Péclet numbers $Re = O(1)$ and $Pe = O(1)$ here compare the nonlinear terms with viscous and thermal diffusion in the body of the fluid. Note that other definitions of these coefficients can be found in the literature: a 'wave' Reynolds number (Re_w) based on the sound speed is sometimes introduced ($Re_w = \rho_* a_*/(k_*\mu_*) = Re/\epsilon$,

Variable	Scale	Parameter	Definition	Scaling
x	k_*^{-1}	Acoustic Mach number ϵ	U_*/a_*	$\epsilon \ll 1$
y	H_*	Aspect ratio δ	$k_* H_*$	$\delta = O(1)$
t	$(a_* k_*)^{-1}$	Temperature difference $\hat{\Gamma}$	$\Delta\Theta_*/T_*$	$\hat{\Gamma} = \epsilon\Gamma = O(\epsilon)$
u	a_*	Reynolds number Re	$\rho_* U_*/(k_*\mu_*)$	$Re = O(1)$
v	$(k_* H_*)a_*$	Péclet number Pe	$\rho_* c_{p_*} U_*/(k_*\kappa_*)$	$Pe = O(1)$
ρ	$\rho_* \equiv p_*/(R_* T_*)$	Prandtl number Pr	$\mu_* c_{p*}/\kappa_*$	$Pr = Pe/Re = O(1)$
Θ	T_*	Specific heat ratio γ	c_{p_*}/c_{v_*}	$\gamma = O(1)$
P	p_*	Acoustic wave amplitude $\mathbb{A}$	$\gamma\, u_{*_{max}}/U_*$	$\mathbb{A} = O(1)$
$\mathbb{F}$	$k_*\, p_*$			

Table 2. Dimensionless variables and parameters, similar to the previous analysis of Massih *et al.* (2024) except for the dimensionless temperature difference $\hat{\Gamma}$, which in the present work is asymptotically small.

here $Re_w \gg 1$), which compares unsteady inertia with net viscous forces and confirms that viscous terms do not affect the waves at leading order; or a streaming Reynolds number (Re_s) based on the appropriate velocity scale for the streaming flow $U_{s_*} = \epsilon^2 a_*$ ($Re_s = \rho_* \epsilon^2 a_*/(k_*\mu_*) = \epsilon\, Re$, here $Re_s \ll 1$), showing that nonlinear advection plays no part in the dynamics of the streaming flow in the regimes we investigate (Lighthill 1978). Using the scalings detailed in table 2, the dimensionless set of equations can be expressed as

$$\rho\,[\partial_t \boldsymbol{u} + (\boldsymbol{u}\cdot\boldsymbol{\nabla})\boldsymbol{u}] = -\frac{1}{\gamma}\boldsymbol{\nabla} p + \frac{\epsilon}{Re}\left[\boldsymbol{\nabla}^2\boldsymbol{u} + \frac{1}{3}\boldsymbol{\nabla}(\boldsymbol{\nabla}\cdot\boldsymbol{u})\right] + \mathbb{F}(x,t)\boldsymbol{e}_x, \tag{2.5}$$

$$\partial_t \rho + \boldsymbol{\nabla}\cdot(\rho\boldsymbol{u}) = 0, \tag{2.6}$$

$$\rho\,[\partial_t T + (\boldsymbol{u}\cdot\boldsymbol{\nabla})T] = (1-\gamma)p\,(\boldsymbol{\nabla}\cdot u) + \frac{\gamma\,\epsilon}{Pe}\nabla^2 T, \tag{2.7}$$

$$p = \rho T, \tag{2.8}$$

where dimensionless variables are not decorated with tildes, $\boldsymbol{\nabla} \equiv (\partial_x, \delta^{-1}\partial_y)$ and the velocity field $\boldsymbol{u} \equiv (u, \delta v)$. No-slip and no-penetration boundary conditions are complemented with the thermal boundary conditions $T(x, y=0, t) = 1$ and $T(x, y = 1, t) = 1 + \epsilon\Gamma$.

The scaling of the Reynolds number $Re = O(1)$, implying $Re_w = O(1/\epsilon)$, ensures that viscous forcing is negligible in the interior of the domain for the leading-order acoustic wave dynamics. However, these viscous forces drive oscillatory BLs of typical dimensional width $\delta_{s_*} = \sqrt{\mu_*/(\rho_*\omega_*)} = k_*^{-1}\sqrt{\epsilon/Re}$. The dynamics in these oscillatory BLs near the cold and hot walls, hereafter referred to as C-BL and H-BL, is captured by introducing rescaled wall-normal coordinates $\eta_c \equiv \epsilon^{-1/2} y$ and $\eta_h \equiv \epsilon^{-1/2}(1-y)$, respectively. In the analysis that follows, the rescaled wall-normal coordinates in both BLs are commonly represented using η without a subscript.

3. Asymptotic analysis

The steady streaming and oscillating fields are disentangled by introducing the time average $\overline{q}$ of any field $q(x, y, t)$ over an acoustic wave period. Fields therefore can be split into mean and fluctuation components:

$$q\,(x, y, t) = \overline{q}\,(x, y) + q'\,(x, y, t)\,, \tag{3.1}$$

where q' is the fluctuating component and $\overline{q'} = 0$. Further, each field is asymptotically expanded in one-half powers of ϵ as shown below:

$$(u, v) = \epsilon\,(u_1', 0) + \epsilon^{3/2}\big(u_{3/2}', v_{3/2}'\big) + \epsilon^2\left[\big(u_2', v_2'\big) + (\overline{u}_2, \overline{v}_2)\right] + O(\epsilon^{5/2}), \tag{3.2}$$

$$P = 1 + \epsilon\,\pi_1' + \epsilon^{3/2}\pi_{3/2}' + \epsilon^2\left[\pi_2' + \overline{\pi}_2\right] + \epsilon^{5/2}\left[\pi_{5/2}' + \overline{\pi}_{5/2}\right] + \epsilon^3\left[\pi_3' + \overline{\pi}_3\right] + O(\epsilon^{7/2}), \tag{3.3}$$

$$\Theta = 1 + \epsilon\,\left[\Gamma\, y + \Theta_1'\right] + \epsilon^{3/2}\Theta_{3/2}' + \epsilon^2\left[\overline{\Theta}_2 + \Theta_2'\right] + O(\epsilon^{5/2}), \tag{3.4}$$

$$\rho = 1 + \epsilon\,\left[\overline{\rho}_1 + \rho_1'\right] + \epsilon^{3/2}\rho_{3/2}' + \epsilon^2\left[\overline{\rho}_2 + \rho_2'\right] + O(\epsilon^{5/2}), \tag{3.5}$$

$$\mathbb{F} = \epsilon^{3/2}\mathbb{F}_{3/2}'(x, t) + O(\epsilon^2). \tag{3.6}$$

Here, we consider a plane horizontal standing acoustic wave of $O(\epsilon)$ amplitude. Note that expansion in fractional powers of ϵ results from the existence of thin BLs of dimensionless width $O(\sqrt{\epsilon})$. Since, by construction, the leading-order wave fields are $O(\epsilon)$, the corrections are even smaller (i.e. approach zero faster than $O(\epsilon)$), and no $O(\sqrt{\epsilon})$ corrections to the mean fields are forced. The external force that sustains waves of wavenumber k_* and inverse angular frequency $(a_* k_*)^{-1}$, respectively used as the scales for x and t, is chosen to be of the form

$$\mathbb{F}_{3/2}'(x, t) = \mathbb{F}_{3/2}\sin(x)\,\mathrm{e}^{\mathrm{i}t} + \text{c.c.}, \tag{3.7}$$

where c.c. denotes the complex conjugate. An explicit analytical expression for the coefficient $\mathbb{F}_{3/2}$ is derived in § 3.5. The expansions for the various fields are then substituted into the dimensionless governing equations, and the dynamics at sequential orders in the small parameter ϵ is independently analysed.

3.1. *Acoustic and steady dynamics at* $O(1)$

At this order the gas is steady (all fluctuating and mean flow speeds are smaller than the speed of sound) and homogeneous (the imposed temperature difference is assumed to be small compared with the cold-wall temperature).

3.2. *Steady dynamics at* $O(\epsilon)$

No streaming flow arises at this order. The imposed temperature difference between the boundaries maintains the linear temperature and density profiles $\epsilon\Gamma y$ and $\epsilon\overline{\rho}_1$, with $\overline{\rho}_1 = -\Gamma y$.

3.3. *Acoustic dynamics at* $O(\epsilon)$

The $O(\epsilon)$ dynamics in the interior satisfies

$$\partial_t u_1' + \gamma^{-1}\partial_x \pi_1' = 0, \tag{3.8}$$

$$\partial_y \pi_1' = 0, \tag{3.9}$$

$$\partial_t \rho_1' + \partial_x u_1' = 0, \tag{3.10}$$

$$\partial_t \Theta_1' + (\gamma - 1)\,\partial_x u_1' = 0, \tag{3.11}$$

$$\pi_1' - \rho_1' - \Theta_1' = 0, \tag{3.12}$$

which can be collapsed to the one-dimensional second-order wave equation:

$$\partial_{tt}\pi_1' = \partial_{xx}\pi_1', \quad \text{with} \quad \partial_t u_1' = -\gamma^{-1}\partial_x \pi_1', \quad \rho_1' = \gamma^{-1}\pi_1', \quad \Theta_1' = (1-\gamma^{-1})\pi_1'. \tag{3.13}$$

Since the oscillatory flow driven by the plane wave does not satisfy the no-slip and isothermal boundary conditions at the walls, Stokes layers are generated.

The $O(\epsilon)$ dynamics in the BLs is governed by

$$\partial_t u_1' + \gamma^{-1}\partial_x \pi_1' - (Re\delta^2)^{-1}\partial_{\eta\eta} u_1' = 0, \tag{3.14}$$

$$\partial_\eta \pi_1' = 0, \tag{3.15}$$

$$\partial_t \rho_1' + \partial_x u_1' \pm \partial_\eta v_{3/2}' = 0, \tag{3.16}$$

$$\partial_t \Theta_1' + (\gamma-1)\,(\partial_x u_1' \pm \partial_\eta v_{3/2}') - \gamma (Pe\delta^2)^{-1}\partial_{\eta\eta}\Theta_1' = 0, \tag{3.17}$$

$$\pi_1' - \rho_1' - \Theta_1' = 0, \tag{3.18}$$

where the first-order wall-normal partial derivatives in the C-BL are $+\partial_\eta$ and those in the H-BL are $-\partial_\eta$.

The complete acoustic wave solution at $O(\epsilon)$, which satisfies the isothermal, no-slip and no-penetration conditions at the boundaries and asymptotically matches with the horizontal standing-wave solution obtained in the interior, is found to be

$$\pi_1' = \frac{\mathbb{A}}{2}\cos(x)\,\mathrm{e}^{\mathrm{i}t} + \text{c.c.} \qquad \text{(interior and BLs)}, \tag{3.19}$$

$$u_1' = \begin{cases} -\mathrm{i}\dfrac{\mathbb{A}}{2\gamma}\sin(x)\,\mathrm{e}^{\mathrm{i}t} + \text{c.c.} & \text{(interior)} \\ -\mathrm{i}\dfrac{\mathbb{A}}{2\gamma}(1-\mathrm{e}^{-(1+\mathrm{i})\sqrt{\mathbb{R}}\eta})\sin(x)\mathrm{e}^{\mathrm{i}t} + \text{c.c.} & \text{(BLs)}, \end{cases} \tag{3.20}$$

$$v_{3/2}' = \begin{cases} -\dfrac{\mathbb{A}(1+\mathrm{i})\,\cos(x)\mathrm{e}^{\mathrm{i}t}}{4\gamma\sqrt{\mathbb{R}\mathbb{P}}}[(1-\mathrm{e}^{-(1+\mathrm{i})\sqrt{\mathbb{R}}\eta})\sqrt{\mathbb{P}} + (\gamma-1)(1-\mathrm{e}^{-(1+\mathrm{i})\sqrt{\mathbb{P}}\eta})\sqrt{\mathbb{R}}] \\ \quad +\text{c.c.} \quad \text{(C-BL)} \\ \dfrac{\mathbb{A}(1+\mathrm{i})\,\cos(x)\mathrm{e}^{\mathrm{i}t}}{4\gamma\sqrt{\mathbb{R}\mathbb{P}}}[(1-\mathrm{e}^{-(1+\mathrm{i})\sqrt{\mathbb{R}}\eta})\sqrt{\mathbb{P}} + (\gamma-1)(1-\mathrm{e}^{-(1+\mathrm{i})\sqrt{\mathbb{P}}\eta})\sqrt{\mathbb{R}}] \\ \quad +\text{c.c.} \quad \text{(H-BL)}, \end{cases} \tag{3.21}$$

$$\Theta_1' = \begin{cases} (1-\gamma^{-1})\pi_1' & \text{(interior)} \\ (1-\gamma^{-1})\dfrac{\mathbb{A}}{2}(1-\mathrm{e}^{-(1+\mathrm{i})\sqrt{\mathbb{P}}\eta})\cos(x)\mathrm{e}^{\mathrm{i}t} + \text{c.c.} & \text{(BLs)}, \end{cases} \tag{3.22}$$

$$\rho_1' = \begin{cases} \gamma^{-1}\pi_1' & \text{(interior)} \\ \gamma^{-1}\dfrac{\mathbb{A}}{2}(1+(\gamma-1)\mathrm{e}^{-(1+\mathrm{i})\sqrt{\mathbb{P}}\eta})\cos(x)\mathrm{e}^{\mathrm{i}t} + \text{c.c.} & \text{(BLs)}. \end{cases} \tag{3.23}$$

Here, $\mathbb{R} \equiv Re\delta^2/2$ and $\mathbb{P} \equiv Pe\delta^2/2$ are the aspect-ratio-dependent Reynolds and Péclet numbers and $\mathbb{A}$ is the $O(1)$ acoustic pressure wave amplitude. The expression for $v_{3/2}'$ in the interior is derived in the higher-order analysis that follows. At $O(\epsilon)$, the acoustic velocity field in the interior is irrotational, and acoustic wave vorticity is confined to the BLs.

3.4. *Steady dynamics at* $O(\epsilon^{3/2})$

No corrections to the streaming fields arise at this order.

3.5. *Acoustic dynamics at* $O(\epsilon^{3/2})$

The vertical velocity that emerges in the leading-order BLs does not vanish as $\eta \to \infty$; see (3.21). The oscillating field it generates would, in the absence of forcing, lead to a slow decay of the leading-order wave amplitude. Here, a stationary state is sustained by the weak external forcing $\mathbb{F}'_{3/2}$ in the interior.

The governing equations at $O(\epsilon^{3/2})$ in the interior are

$$\partial_t u'_{3/2} + \gamma^{-1}\partial_x \pi'_{3/2} = \mathbb{F}_{3/2} \sin(x)\, \mathrm{e}^{\mathrm{i}t} + \text{c.c.}, \tag{3.24}$$

$$\partial_t v'_{3/2} + (\gamma\delta^2)^{-1}\partial_y \pi'_{3/2} = 0, \tag{3.25}$$

$$\partial_t \rho'_{3/2} + \partial_x u'_{3/2} + \partial_y v'_{3/2} = 0, \tag{3.26}$$

$$\partial_t \Theta'_{3/2} + (\gamma - 1)(\partial_x u'_{3/2} + \partial_y v'_{3/2}) = 0, \tag{3.27}$$

$$\pi'_{3/2} - \rho'_{3/2} - \Theta'_{3/2} = 0. \tag{3.28}$$

In the BLs the waves must satisfy

$$\partial_t u'_{3/2} + \gamma^{-1}\partial_x \pi'_{3/2} - (Re\delta^2)^{-1}\partial_{\eta\eta} u'_{3/2} = \mathbb{F}_{3/2} \sin(x)\, \mathrm{e}^{\mathrm{i}t} + \text{c.c.}, \tag{3.29}$$

$$\partial_\eta \pi'_{3/2} = 0, \tag{3.30}$$

$$\partial_t \rho'_{3/2} + \partial_x u'_{3/2} \pm \partial_\eta v'_2 = 0, \tag{3.31}$$

$$\partial_t \Theta'_{3/2} + (\gamma - 1)(\partial_x u'_{3/2} \pm \partial_\eta v'_2) - \gamma (Pe\delta^2)^{-1}\partial_{\eta\eta}\Theta'_{3/2} = 0, \tag{3.32}$$

$$\pi'_{3/2} - \rho'_{3/2} - \Theta'_{3/2} = 0. \tag{3.33}$$

This set of equations can be solved analytically with appropriate boundary and matching conditions; see Appendix A. In particular, the balance between external forcing and diffusion is explicit:

$$\mathbb{F}_{3/2} = (1 - i)\,\frac{\mathbb{A}}{2\gamma}\left(\frac{(\gamma - 1)}{\sqrt{\mathbb{P}}} + \frac{1}{\sqrt{\mathbb{R}}}\right). \tag{3.34}$$

At $O(\epsilon^{3/2})$, acoustic wave vorticity remains localised in the BLs ($\boldsymbol{\Omega}'_{3/2} = \boldsymbol{\nabla} \times \boldsymbol{u}'_{3/2} = \boldsymbol{0}$ in the interior, as shown by taking the curl of the momentum equations (3.24)–(3.25)).

3.6. *Steady dynamics at* $O(\epsilon^2)$ *(part 1)*

The $O(\epsilon^2)$ equations characterising the steady pressure field $\overline{\pi}_2$ in the interior are

$$\gamma^{-1}\partial_x \overline{\pi}_2 = -\overline{\rho'_1 \partial_t u'_1} - \overline{u'_1 \partial_x u'_1} = \overline{(\partial_t \rho'_1) u'_1} - \overline{u'_1 \partial_x u'_1} = -\partial_x \overline{(u'_1)^2}, \tag{3.35}$$

$$\partial_y \overline{\pi}_2 = 0, \tag{3.36}$$

where (3.35) has been simplified using (3.10). Thus, to within an arbitrary constant, the mean pressure $\overline{\pi}_2 = -\gamma\overline{(u'_1)^2}$.

A streaming flow emerges as the consequence of nonlinearity. Specifically, in the BLs,

$$(\boldsymbol{u}' \cdot \boldsymbol{\nabla})\boldsymbol{u}' = \boldsymbol{\nabla}\left(\frac{1}{2}\,\boldsymbol{u}' \cdot \boldsymbol{u}'\right) + (\boldsymbol{\nabla} \times \boldsymbol{u}') \times \boldsymbol{u}' \tag{3.37}$$

includes an $O(\epsilon^2)$ component $(\boldsymbol{\nabla} \times \boldsymbol{u}') \times \boldsymbol{u}'$ that (i) is non-zero since the $O(\epsilon)$ acoustic vorticity is non-zero in the BL, (ii) cannot be completely balanced by a pressure gradient

and (iii) consists of both an oscillating term proportional to e^{2it} that generates harmonics and, crucially, a steady component. As first established by Rayleigh, this term drives a streaming flow in the BL that is viscously communicated to the interior and that can be computed through the momentum equations only. The inertial term in the x-momentum equation can be transformed using (3.16) and recast as

$$\rho_1'\partial_t u_1' + u_1'\partial_x u_1' \pm v_{3/2}'\partial_\eta u_1' = \partial_t(\rho_1' u_1') + \partial_x\left(u_1'^2\right) \pm \partial_\eta\left(u_1' v_{3/2}'\right), \tag{3.38}$$

and we therefore consider

$$-\gamma^{-1}\partial_x\overline{\pi}_2 + (Re\delta^2)^{-1}\partial_{\eta\eta}\overline{u}_2 = \partial_x(\overline{u_1' u_1'}) \pm \partial_\eta(\overline{u_1' v_{3/2}'}), \tag{3.39}$$

$$\partial_\eta\overline{\pi}_2 = 0. \tag{3.40}$$

This reduced set of equations is unaltered by the imposed temperature difference and can be solved explicitly for $\overline{u}_2$ given the acoustic fields already derived, the expression for $\overline{\pi}_2$ in the interior and the boundary and matching conditions $\overline{u}_2(x, 0) = 0$ and $\lim_{\eta\to\infty}\partial_\eta\overline{u}_2(x, \eta) = 0$. The full solution is reported in Appendix B and has a non-zero limit as $\eta \to \infty$ that corresponds to an effective slip velocity $\overline{u}_{slip}$ acting on the interior flow, which is independent of the aspect ratio δ and given by

$$\overline{u}_{slip} = -\frac{3\mathbb{A}^2}{8\gamma^2(Pe + Re)}\left(Pe + \frac{2(\gamma-1)}{3}\sqrt{PeRe} + Re\right)\sin(2x). \tag{3.41}$$

Since $\gamma > 1$, the slip velocity is directed towards the acoustic wave velocity nodes (located at $x = p\pi$, $p \in \mathbb{Z}$) (Lighthill 1978). Its dimensional expression in the absence of thermal diffusivity is more commonly reported: setting $Pe \to \infty$ results in a dimensional slip velocity $\overline{u}_{slip_*} = -[3U_0^2/(8a_*)]\sin(2k_*\tilde{x})$, with $U_0 = (\mathbb{A}/\gamma)\epsilon a_*$ the amplitude of the leading-order acoustic wave velocity in the interior.

The streaming velocity field $\overline{\boldsymbol{u}}_2$ in the interior is found by solving the time-averaged momentum equation at $O(\epsilon^3)$ and the continuity equation at $O(\epsilon^2)$:

$$-\frac{\boldsymbol{\nabla}\overline{\pi}_3}{\gamma} + \frac{\boldsymbol{\nabla}^2\overline{\boldsymbol{u}}_2}{Re} = \overline{(\boldsymbol{u}_1'\cdot\boldsymbol{\nabla})\boldsymbol{u}_2' + (\boldsymbol{u}_{3/2}'\cdot\boldsymbol{\nabla})\boldsymbol{u}_{3/2}' + (\boldsymbol{u}_2'\cdot\boldsymbol{\nabla})\boldsymbol{u}_1' + \overline{\rho}_1(\boldsymbol{u}_1'\cdot\boldsymbol{\nabla})\boldsymbol{u}_1'}$$
$$\overline{+\rho_1'\partial_t\boldsymbol{u}_2' + \rho_{3/2}'\partial_t\boldsymbol{u}_{3/2}' + \rho_2'\partial_t\boldsymbol{u}_1'}, \tag{3.42}$$

$$\boldsymbol{\nabla}\cdot\overline{\boldsymbol{u}}_2 = 0, \tag{3.43}$$

where the nonlinear term $\partial_x(\overline{\rho_1' u_1'})$ has not been included in (3.43) because $\overline{\rho_1' u_1'} = 0$. Most of the nonlinear terms in (3.42) can be balanced by a pressure gradient and those driving streaming flows are readily identified by taking the curl of this equation. Since acoustic vorticity vanishes in the interior at $O(\epsilon)$ and $O(\epsilon^{3/2})$, substantial simplifications occur, detailed in Appendix C.1. With $\overline{\boldsymbol{u}}_2 = -\boldsymbol{\nabla}\times(\overline{\psi}_2\boldsymbol{e}_z)$ (i.e. $(\overline{u}_2, \overline{v}_2) = \delta^{-1}(-\partial_y\overline{\psi}_2, \partial_x\overline{\psi}_2)$), where $\boldsymbol{e}_z \equiv \boldsymbol{e}_x \times \boldsymbol{e}_y$, the stream function $\overline{\psi}_2$ can be obtained by solving the following equation:

$$\frac{1}{Re}\boldsymbol{\nabla}^4\overline{\psi}_2\boldsymbol{e}_z = \overline{\boldsymbol{\nabla}\times\left(\boldsymbol{\Omega}_2'\times\boldsymbol{u}_1'\right) + (\boldsymbol{\nabla}\overline{\rho}_1/2)\times\left[\boldsymbol{\nabla}\left(\boldsymbol{u}_1'\cdot\boldsymbol{u}_1'\right)\right] + \boldsymbol{u}_{3/2}'\times(\partial_t\mathbb{F}_{3/2}'\boldsymbol{e}_x)}$$
$$\overline{+\boldsymbol{\nabla}\times\left[\rho_1'\partial_t\boldsymbol{u}_2' + \rho_2'\partial_t\boldsymbol{u}_1'\right]}. \tag{3.44}$$

The $O(\epsilon^2)$ acoustic fields are required to proceed.

3.7. *Acoustic dynamics at $O(\epsilon^2)$*

The momentum equations governing the $O(\epsilon^2)$ acoustic dynamics in the interior are

$$\partial_t u_2' + \gamma^{-1}\partial_x \pi_2' = \left(\Gamma y - \rho_1'\right)\partial_t u_1' + \overline{\rho_1'\partial_t u_1'} - u_1'\partial_x u_1' + \overline{u_1'\partial_x u_1'} + (3Re)^{-1}4\partial_{xx}u_1' + \mathbb{F}_2(x,t), \tag{3.45}$$

$$\partial_t v_2' + (\gamma\delta^2)^{-1}\partial_y \pi_2' = 0, \tag{3.46}$$

$$\partial_t \rho_2' + \partial_x u_2' + \partial_y v_2' = -\partial_x\left[\left(\rho_1' - \Gamma y\right)u_1'\right] + \overline{\partial_x\left(\rho_1' u_1'\right)}, \tag{3.47}$$

$$\partial_t \Theta_2' + (\gamma-1)\left(\partial_x u_2' + \partial_y v_2'\right) = \left(\Gamma y - \rho_1'\right)\partial_t\Theta_1' + \overline{\rho_1'\partial_t\Theta_1'} - u_1'\partial_x\Theta_1' + \overline{u_1'\partial_x\Theta_1'} + \gamma Pe^{-1}\partial_{xx}\Theta_1' + (1-\gamma)\left(\pi_1'\partial_x u_1' - \overline{\pi_1'\partial_x u_1'}\right), \tag{3.48}$$

$$\pi_2' - \rho_2' - \Theta_2' = \left(\Theta_1' + \Gamma y\right)\rho_1' - \overline{\Theta_1'\rho_1'} - \Gamma y\Theta_1'. \tag{3.49}$$

Since the leading-order acoustic fields in the interior do not depend on y, using (3.45) and (3.46) it can be seen that acoustic wave vorticity $\Omega_2' = \delta\partial_x v_2' - \delta^{-1}\partial_y u_2'$ is generated according to

$$\partial_t \Omega_2' = -\delta^{-1}\partial_y\left(\Gamma y\partial_t u_1'\right) = -\delta^{-1}\Gamma\partial_t u_1' \rightarrow \boldsymbol{\Omega}_2' = -\frac{\Gamma u_1'}{\delta}\boldsymbol{e}_z. \tag{3.50}$$

In contrast to corresponding results at $O(\epsilon)$ and $O(\epsilon^{3/2})$, at $O(\epsilon^2)$ the wave vorticity is non-zero as a result of the imposed temperature difference Γ. This solution can be used to evaluate certain nonlinear forcing terms already introduced, e.g.

$$\overline{(\nabla\overline{\rho}_1/2)\times\left[\nabla\left(\boldsymbol{u}_1'\cdot\boldsymbol{u}_1'\right)\right] + \nabla\times\left(\boldsymbol{\Omega}_2'\times\boldsymbol{u}_1'\right)} = -\overline{\left(\partial_x u_1'\right)\boldsymbol{\Omega}_2'} + \overline{\partial_x\left(u_1'\boldsymbol{\Omega}_2'\right)} = \overline{u_1'\partial_x\boldsymbol{\Omega}_2'}. \tag{3.51}$$

Moreover, as detailed in Appendix C.2, using these results we can show that

$$\overline{\nabla\times\left(\rho_1'\partial_t\boldsymbol{u}_2' + \rho_2'\partial_t\boldsymbol{u}_1'\right)} = \boldsymbol{0}. \tag{3.52}$$

3.8. *Steady streaming at $O(\epsilon^2)$ (part 2)*

Now that the forcing terms involving the $O(\epsilon^2)$ acoustic fields have been computed, the streaming flow can be evaluated. The equation for the stream function reduces to

$$\frac{1}{Re}\nabla^4\overline{\psi}_2 = \underbrace{\overline{u_1'\partial_x\Omega_2'}}_{B} - \underbrace{\overline{\delta\, v_{3/2}'\partial_t\mathbb{F}_{3/2}'}}_{F}, \tag{3.53}$$

with the baroclinic and external forcing terms respectively defined as

$$B \equiv \overline{u_1'\partial_x\Omega_2'} = -\frac{\mathbb{A}^2\Gamma}{4\delta\gamma^2}\sin(2x), \qquad F \equiv -\overline{\delta v_{3/2}'\partial_t\mathbb{F}_{3/2}'} = -\delta\left(y-\frac{1}{2}\right)\left|\mathbb{F}_{3/2}\right|^2\sin(2x). \tag{3.54}$$

This equation is supplemented with the following no-penetration and slip velocity conditions:

$$\partial_x\overline{\psi}_2(x,y=0) = \partial_x\overline{\psi}_2(x,y=1) = 0, \qquad \partial_y\overline{\psi}_2(x,y=0) = \partial_y\overline{\psi}_2(x,y=1) = \delta\overline{u}_{slip}, \tag{3.55}$$

with $\overline{u}_{slip}$ reported in (3.41). An explicit solution for $\overline{\psi}_2$ can be computed; a representative velocity field is shown in figure 2(*a*) for a specific set of dimensionless parameters.

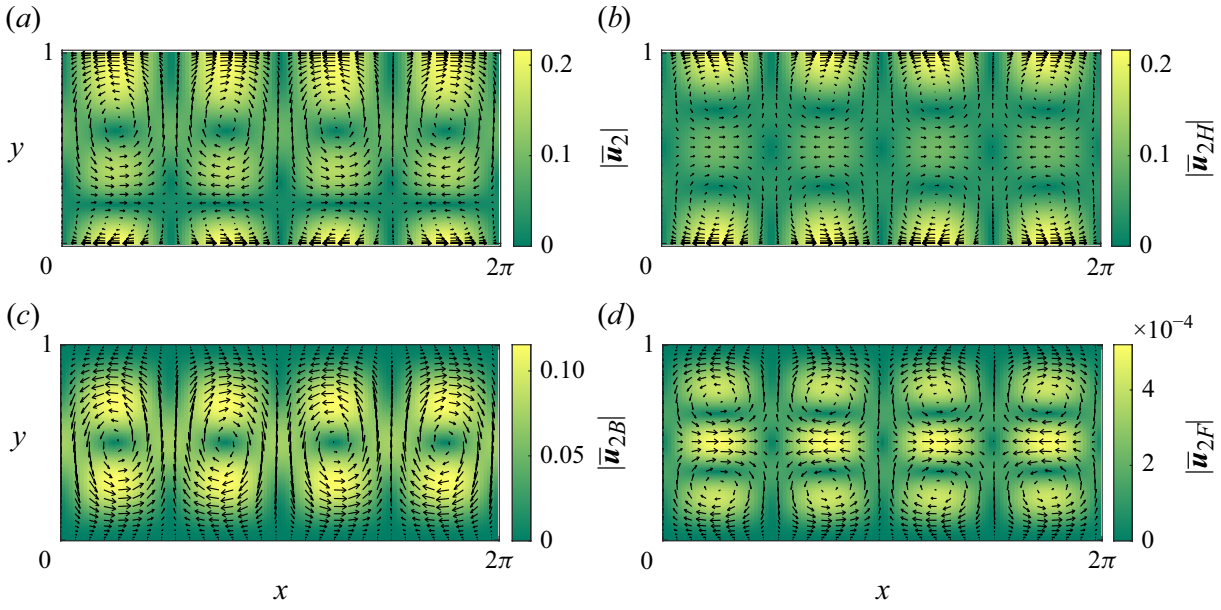

Figure 2. Visualisation of the strength and orientation of the streaming velocity field in the channel interior. (*a*) The total velocity field $\overline{\boldsymbol{u}}_2$, (*b*) the homogeneous Rayleigh streaming component $\overline{\boldsymbol{u}}_{2H}$, (*c*) the baroclinic contribution $\overline{\boldsymbol{u}}_{2B}$ and (*d*) the inhomogeneous component $\overline{\boldsymbol{u}}_{2F}$ resulting from the specified external body force. Components $\overline{\boldsymbol{u}}_{2H}$ and $\overline{\boldsymbol{u}}_{2F}$ have stacked multicellular structure while a single pair of cells that spans the channel interior is manifest in $\overline{\boldsymbol{u}}_{2B}$. The components $\overline{\boldsymbol{u}}_{2H}$, $\overline{\boldsymbol{u}}_{2F}$ and $\overline{\boldsymbol{u}}_{2B}$ possess wall-normal symmetry about the mid-plane, which is not reflected in the total velocity field $\overline{\boldsymbol{u}}_2$. The parameters correspond to $A = 1$, $Re = 500$, $Pr = 0.71$, $\delta = 1$, $\gamma = 1.4$ and $\Gamma = \Gamma_c = 0.278$ (Γ_c is defined in § 4.2).

To gain physical insight into the various contributions generating this streaming flow, it is instructive to split the stream function into three components:

$$\overline{\psi}_2 = \overline{\psi}_{2H} + \overline{\psi}_{2B} + \overline{\psi}_{2F}, \tag{3.56}$$

where these functions (explicitly reported in Appendix D) have the following properties.

(i) Component $\overline{\psi}_{2H}$ is the solution of the homogeneous partial differential equation $\boldsymbol{\nabla}^4\overline{\psi}_{2H} = 0$ with the full boundary conditions (3.55). This component corresponds to the extension to $O(1)$ aspect ratio of the solution obtained by Rayleigh for fluids of uniform (mean) temperature. As shown in figure 2(*b*), the velocity field consists of stacked counter-rotating cells and is symmetric with respect to $y = 1/2$. This contribution is independent of the imposed temperature difference Γ.

(ii) Component $\overline{\psi}_{2B}$ is the solution of the inhomogeneous partial differential equation $\boldsymbol{\nabla}^4\overline{\psi}_{2B} = Re\,\mathrm{B}$, with no-penetration and no-slip boundary conditions ($\partial_x\overline{\psi}_{2B}(x, y = 0) = \partial_x\overline{\psi}_{2B}(x, y = 1) = \partial_y\overline{\psi}_{2B}(x, y = 0) = \partial_y\overline{\psi}_{2B}(x, y = 1) = 0$). It is the only component $\overline{\psi}_{2B}$ that involves the temperature difference Γ and therefore describes the baroclinic component of the streaming flow. This component consists of a cellular flow that spans the entire height of the channel; see figure 2(*c*).

(iii) Component $\overline{\psi}_{2F}$ is the solution of the inhomogeneous partial differential equation $\boldsymbol{\nabla}^4\overline{\psi}_{2F} = Re\,\mathrm{F}$, subject to no-penetration and no-slip boundary conditions. This component of the flow depends on the details of the wave forcing mechanism, and would differ if the acoustic wave were generated by an oscillating wall rather than by an external body force. (A periodic motion of a solid boundary also generates streaming (Lighthill 1978).) However, this contribution is found to be negligible for the set of dimensionless parameters considered here, as for instance evident in figure 2(*d*).

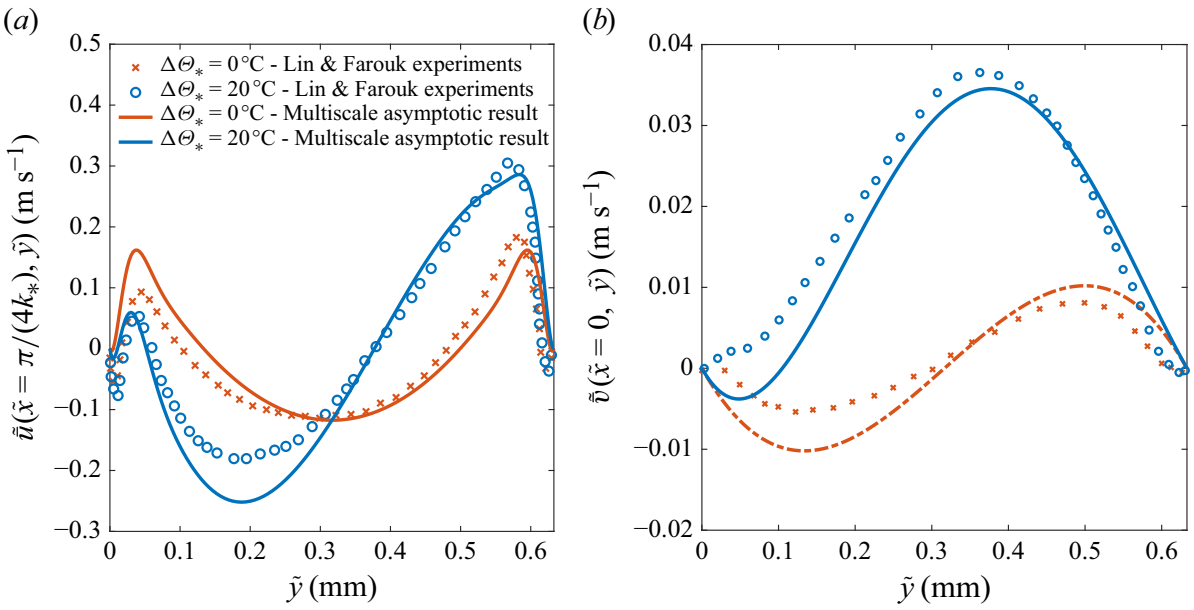

Figure 3. Comparison of the present analytical solution with the (*a*) x and (*b*) y components of the streaming velocity field (at $\tilde{x} = \pi/(4k_*)$ and $\tilde{x} = 0$ respectively) from the DNS performed by Lin & Farouk (2008) (their cases 1A and 1B). The full composite solution representing the dynamics in the BLs as well as the interior is shown by the solid curves. The parameters correspond to $A = 6.37$, $Re = 631$, $Pe = 448$, $\delta = 0.2252$, $\gamma = 5/3$, $\epsilon = 10^{-2}$ and $\Gamma = \{0, 6.67\}$. For these parameters, the critical temperature difference $\Gamma_c = 4.45$, i.e. $\Delta\Theta_{*_c} \approx 13.4\,°C$ (Γ_c is defined in § 4.2).

4. Validation, results and discussion

4.1. *Comparison with previous studies*

The streaming flow derived in § 3.8 is now compared with other theoretical and numerical solutions reported in the literature. In the absence of an external temperature difference and thermal diffusion, the solution converges to that derived by Rayleigh in the limit of narrow channels. Specifically, as discussed in § 3.6, the slip velocity in the absence of thermal diffusion reads $\overline{u}_{slip_*} = -[3U_0^2/(8a_*)]\sin(2k_*\tilde{x})$. Since, in the limit $\delta \to 0$, $\overline{\psi}_{2H} \to -\delta\,\overline{u}_{slip}\,y\,(2y^2 - 3y + 1)$, the corresponding leading-order dimensional streaming velocity becomes

$$\tilde{\bar{u}}_H \sim \frac{3U_0^2}{16a_*}\sin(2k_*\tilde{x})\left[1 - 3\left(\frac{(H_*/2) - \tilde{y}}{(H_*/2)}\right)^2\right], \tag{4.1}$$

$$\tilde{\bar{v}}_H \sim \frac{3U_0^2}{16a_*}2k_*\cos(2k_*\tilde{x})\left[\frac{H_*}{2} - \tilde{y} - \frac{(H_*/2 - \tilde{y})^3}{(H_*/2)^2}\right], \tag{4.2}$$

which are the same as (93)–(94) in Rayleigh (1884) (except for the signs since Rayleigh considered an acoustic velocity field $\propto \cos(k_*\tilde{x})$ whereas it is here $\propto \sin(k_*\tilde{x})$).

When a finite temperature difference is imposed ($\Gamma \neq 0$), the solution derived in the current work can be compared with DNS of the compressible Navier–Stokes equations performed by Lin & Farouk (2008); see figure 3. To account for the finite width of the oscillatory BLs of the DNS, a composite analytical solution (Van Dyke 1969) is obtained by adding the streaming velocity profile in the BLs (§ 3.6) with that in the interior (§ 3.8). Reasonable agreement is observed, some discrepancy being expected since the DNS employs a different forcing mechanism (an oscillating wall) and incorporates variations of viscosity and thermal conductivity with temperature. In this regime, a qualitative

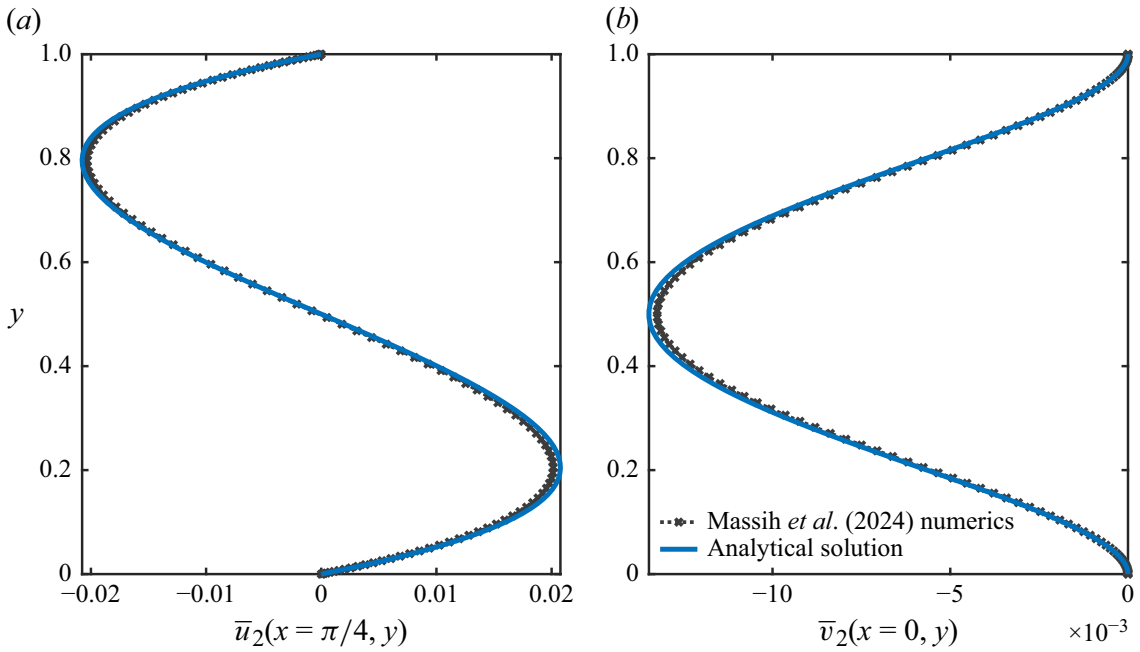

Figure 4. Comparison of the present analytical solution with the (*a*) x and (*b*) y components of the streaming velocity field (at $x = \pi/4$ and $x = 0$ respectively) obtained using the two-way coupled numerical algorithm of Massih *et al.* (2024) that assumes $\hat{\Gamma} = O(1)$ (instead of $\hat{\Gamma} = O(\epsilon)$ for the present analysis). The parameters correspond to $A = 0.01$, $Re = 2500$, $Pe = 1775$, $\delta = 1$, $\gamma = 1.4$, $\epsilon = 3 \times 10^{-4}$ and $\hat{\Gamma} = \epsilon\Gamma = 0.03 \gg \epsilon\Gamma_c$ (Γ_c, defined in § 4.2, is 0.056 for this set of parameters).

comparison also is subsequently made with the experimental observations of Nabavi *et al.* (2008).

For even larger imposed temperature differences $\hat{\Gamma} = \Delta\Theta_*/T_*$, we compare the solution derived in this work assuming $\hat{\Gamma} = \epsilon\Gamma$, with $\Gamma = O(1)$, with the numerical results obtained by Massih *et al.* (2024) in the asymptotic limit $\hat{\Gamma} = O(1)$. For this comparison, we consider a finite temperature difference of $\hat{\Gamma} = 0.03$, treated as $O(1)$ in the numerical algorithm of Massih *et al.* (2024) and as $\Gamma = 0.03/\epsilon$ in the current framework, all the other dimensionless parameters being identical ($A = 0.01$, $Re = 2500$, $Pe = 1775$, $\delta = 1$ and $\gamma = 1.4$). The small parameter ϵ is arbitrarily set to 3×10^{-4}. The wall-normal profiles of the x and y streaming velocity components in the interior of the domain are shown in figure 4. The new asymptotic model captures the numerical results, with the accuracy improving in the limit $\epsilon \to 0$, as expected. In this strongly stratified limit, the streaming velocity field is largely dominated by the baroclinic component $\overline{\boldsymbol{u}}_{2B}$, with the other components being orders of magnitude smaller for the chosen parameter values.

4.2. *Critical non-dimensional temperature difference* Γ_c

Figure 5 shows the interior streamlines of the streaming flow, with the magnitude of the streaming velocity $|\overline{\boldsymbol{u}}_2|$ shown in colour, for domains of aspect ratio $\delta = 1$ and $\delta = 10$. The analytical solution captures the evolution of the structure and intensity of the streaming flow as the temperature difference increases. A parametric threshold can be defined to quantify the transition from the stacked multicellular Rayleigh streaming to the unicellular baroclinic acoustic streaming, i.e. from $\overline{\boldsymbol{u}}_{2H} = \boldsymbol{\nabla} \times (\overline{\psi}_{2H}\boldsymbol{e}_z)$ to $\overline{\boldsymbol{u}}_{2B} = \boldsymbol{\nabla} \times (\overline{\psi}_{2B}\boldsymbol{e}_z)$. To that end, we define a kinetic energy parameter for each component of the streaming flow:

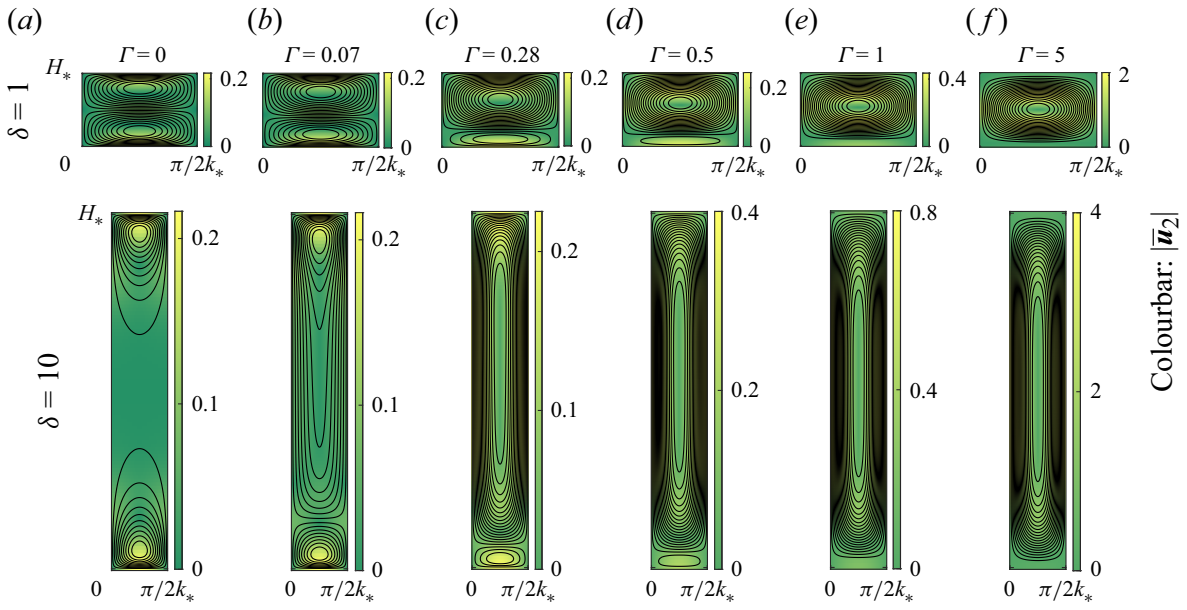

Figure 5. Streaming flow for $A = 1$, $Re = 500$, $Pr = 0.71$, $\gamma = 1.4$, $\delta = \{1, 10\}$ and (*a*) $\Gamma = 0$, (*b*) $\Gamma = 0.07$, (*c*) $\Gamma = 0.28$, (*d*) $\Gamma = 0.5$, (*e*) $\Gamma = 1$ and (*f*) $\Gamma = 5$. The streaming velocity increases with the imposed temperature difference, while the cells closer to the hot boundary expand vertically and those closer to the cold wall shrink. For this set of parameters, $\Gamma_c(\delta = 1) = 0.28$ and $\Gamma_c(\delta = 10) = 0.07$. The ($x$) width of the domain plotted corresponds to one half of an acoustic wave wavelength.

$$K_H \equiv \frac{1}{\pi}\int_0^{2\pi}\int_0^1 |\overline{\boldsymbol{u}}_{2H}|^2 \,\mathrm{d}x\,\mathrm{d}y = \frac{1}{\pi}\int_0^{2\pi}\int_0^1 \left|\boldsymbol{\nabla}\overline{\psi}_{2H}\right|^2 \mathrm{d}x\mathrm{d}y, \tag{4.3}$$

$$K_B \equiv \frac{1}{\pi}\int_0^{2\pi}\int_0^1 |\overline{\boldsymbol{u}}_{2B}|^2 \,\mathrm{d}x\,\mathrm{d}y = \frac{1}{\pi}\int_0^{2\pi}\int_0^1 \left|\boldsymbol{\nabla}\overline{\psi}_{2B}\right|^2 \mathrm{d}x\mathrm{d}y, \tag{4.4}$$

$$K_F \equiv \frac{1}{\pi}\int_0^{2\pi}\int_0^1 |\overline{\boldsymbol{u}}_{2F}|^2 \,\mathrm{d}x\,\mathrm{d}y = \frac{1}{\pi}\int_0^{2\pi}\int_0^1 \left|\boldsymbol{\nabla}\overline{\psi}_{2F}\right|^2 \mathrm{d}x\mathrm{d}y. \tag{4.5}$$

The analytical expressions for these coefficients are reported in Appendix E. Note that $|\overline{\boldsymbol{u}}_2|^2 \neq |\overline{\boldsymbol{u}}_{2H}|^2 + |\overline{\boldsymbol{u}}_{2B}|^2 + |\overline{\boldsymbol{u}}_{2F}|^2$. Since only K_B depends on Γ, a critical temperature difference Γ_c can be defined such that

$$K_H\,(\delta,\, Re,\, Pr,\, \gamma,\, A) = K_B\,(\Gamma = \Gamma_c,\, \delta,\, Re,\, Pr,\, \gamma,\, A)\,. \tag{4.6}$$

For the set of parameters reported in figure 5, $\Gamma_c = 0.28$ for $\delta = 1$ and $\Gamma_c = 0.07$ for $\delta = 10$, which qualitatively corresponds to a hot cell that spans around 80 % of the height of the channel. The dependence of Γ_c on other independent parameters can also be investigated. Using the expressions reported in Appendix E,

$$\begin{aligned} K_H &= \mathbb{A}^4\gamma^{-4}\left[1 + Pr + 2(\gamma-1)\sqrt{Pr}/3\right]^2 (1+Pr)^{-2} F_H(\delta), \\ K_B &= \mathbb{A}^4\Gamma^2 Re^2\gamma^{-4} F_B(\delta), \end{aligned} \tag{4.7}$$

and therefore

$$\hat{\Gamma}_c = \epsilon\,\Gamma_c = \frac{1}{Re_w}\left(1 + \frac{2(\gamma-1)\sqrt{Pr}}{3(1+Pr)}\right) F_c(\delta) \tag{4.8}$$

is notably independent of the wave amplitude $\mathbb{A}$ and inversely proportional to $Re_w = \rho_*\, a_*/(k_*\,\mu_*)$. The terms grouped in parentheses represent the dependence of Γ_c on the

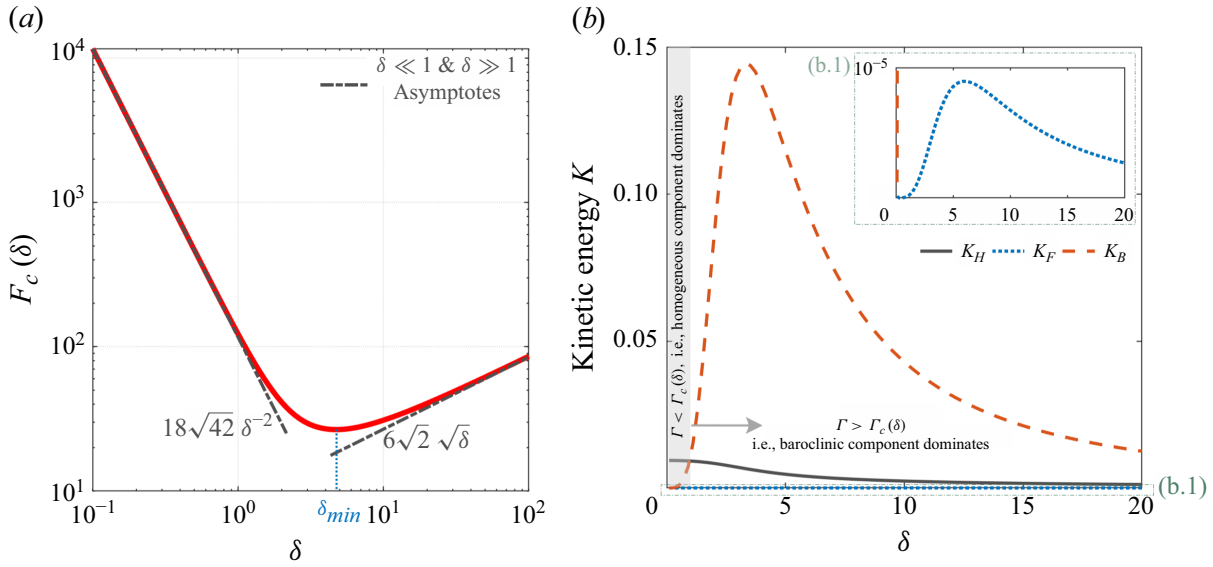

Figure 6. (*a*) Aspect-ratio dependence of the function F_c to which the critical temperature difference Γ_c is proportional (see (4.8)). As the imposed temperature difference increases, the transition from Rayleigh to baroclinic streaming first occurs at $\delta = \delta_{min} = 4.74$. In the narrow channel limit the critical temperature difference $\Gamma_c = O(\delta^{-2})$, while in the tall channel limit the critical temperature difference $\Gamma_c = O(\sqrt{\delta})$ (see (4.9)). (*b*) Kinetic energy parameters K_H, K_F and K_B as functions of the aspect ratio δ ($A = 1$, $\Gamma = 0.5$, $Re = 300$, $Pr = 0.71$ and $\gamma = 1.4$).

fluid properties. The dependence of Γ_c on the channel geometry (δ) is non-monotonic: F_c has a minimum for $\delta = \delta_{min} = 4.74$ and satisfies

$$F_c(\delta_{min}) = 26.68, \qquad F_c(\delta) \underset{\delta \ll 1}{\simeq} 18\sqrt{42}\,\delta^{-2}, \qquad F_c(\delta) \underset{\delta \gg 1}{\simeq} 6\sqrt{2}\,\sqrt{\delta}. \tag{4.9}$$

The dependence of F_c and each of the kinetic energy parameters on the aspect ratio δ is shown in figure 6. In particular, the kinetic energy parameter corresponding to the specific acoustic wave forcing mechanism, K_F, is found to be several orders of magnitude smaller than the others. The most consequential result is that Γ_c is minimum for $\delta_{min} = 4.74$ independently of all the other dimensionless parameters and significantly increases as δ departs from this value. This knowledge should prove valuable for the design of an experimental set-up aiming to show this transition near δ_{min}. In cases where streaming flows are undesirable, our result highlights the extreme sensitivity of channels of aspect ratios near this value to external temperature differences.

To further emphasise the role of Γ_c in dictating the flow morphology, we qualitatively analyse the observations of Nabavi *et al.* (2008), who report experimental measurements of the streaming flow in an acoustic resonator subject to external temperature differences. For the set of dimensionless parameters considered by those authors ($A = 7$, $Re = 1236.5$, $Pe = 953$, $\delta = 0.7$, $\gamma = 1.4$ and $\epsilon = 10^{-3}$), we compute $\Gamma_c = 0.214$, corresponding to a dimensional critical temperature difference $\Delta\Theta_{c_*} = 0.06\ ^\circ\mathrm{C}$ across the channel. Although the experimental regime (particularly $Re = 1236.5 \approx 1/\epsilon$ and $Pe = 953 \approx 1/\epsilon$) seemingly falls outside the range of asymptotic validity of the current analysis, the analytical results presented here nevertheless capture the transition that was found to occur between $\Delta\Theta_* = 0\ ^\circ\mathrm{C}$ and $\Delta\Theta_* = 0.3\ ^\circ\mathrm{C}$. In fact, knowledge of the critical temperature difference Γ_c could be used to inform future experiments aiming to precisely track the transition in flow morphology. Figure 7(*a*) compares the wall-normal structure of the interior horizontal streaming velocity $\overline{u}_2$ for different temperature differences $\Delta\Theta_* = \{0, 0.06, 0.3\}\ ^\circ\mathrm{C}$. The corresponding normalised velocity fields are also shown in figure 7(*b*). The fields obtained

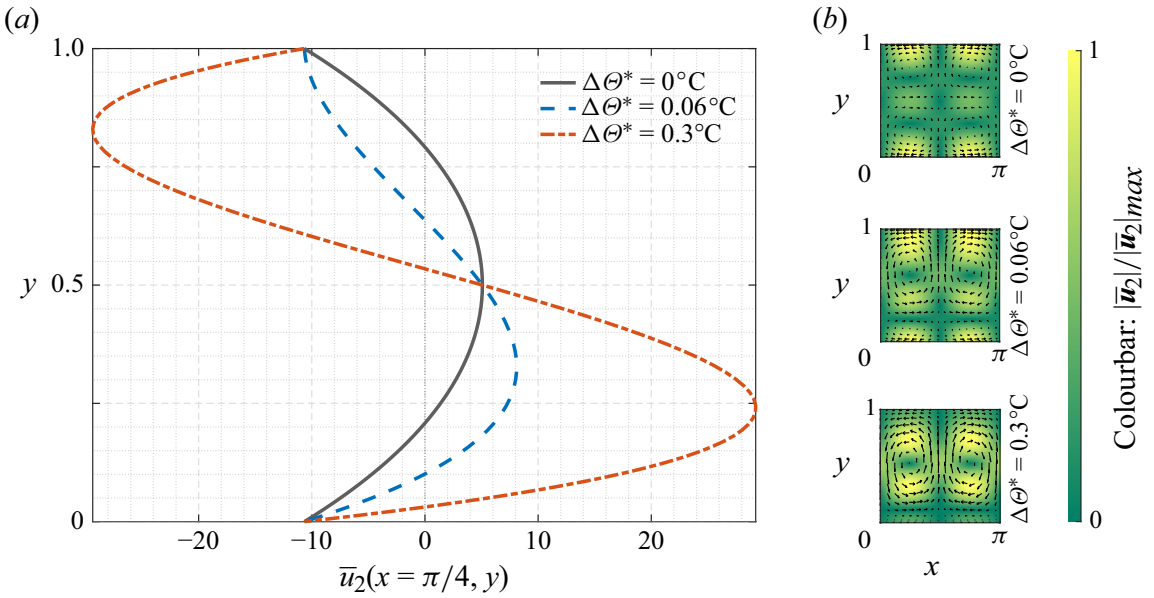

Figure 7. Streaming flow predicted for the dimensionless parameters reported in Nabavi *et al.* (2008): $A = 7$, $Re = 1236.5$, $Pe = 953$, $\delta = 0.7$, $\gamma = 1.4$ and $\epsilon = 10^{-3}$. (*a*) Vertical profile of the interior horizontal streaming velocity $\overline{u}_2(x = \pi/4,\ y)$ and (*b*) normalised streaming velocity field $|\overline{\boldsymbol{u}}_2|/|\overline{\boldsymbol{u}}_2|_{max}$ and velocity vectors for $\Gamma = 0$ ($\Delta\Theta_* = 0$ °C), $\Gamma = \Gamma_c = 0.214$ ($\Delta\Theta_{c_*} = 0.06$ °C) and $\Gamma = 1$ ($\Delta\Theta_* = 0.3$ °C). For this set of parameters, $\Gamma_c = 0.214$ ($\Delta\Theta_{c_*} = 0.06$ °C) lies in the transition range evident in figure 4 of Nabavi *et al.* (2008).

for $\Delta\Theta_* = 0$ °C and $\Delta\Theta_* = 0.3$ °C compare well with the experimental results reported in Nabavi *et al.* (2008).

5. Conclusion

In this investigation we analyse the streaming flows generated by a standing acoustic wave in a channel with hot and cold walls held at fixed but differing temperatures (respectively $T_* + \Delta\Theta_*$ and T_*). Using asymptotic approximations, an analytical solution is derived that characterises the smooth transition from Rayleigh streaming to baroclinic acoustic streaming. This solution accounts for prior experimental and numerical observations: as the temperature difference increases, the stacked cellular structure characteristic of Rayleigh streaming transforms to a unicellular structure, in which the cells span the height of the channel and streaming velocities are enhanced significantly. The present study enables the extensive exploration of this transition by providing an analytical expression for the associated acoustic wave and streaming fields.

In this intermediate regime, the streaming flow $\overline{\boldsymbol{u}}_2$ is expressed as the sum of three contributions. The first, $\overline{\boldsymbol{u}}_{2H}$, is driven by viscous torques in the oscillatory BLs and extends the solution derived by Rayleigh to $O(1)$ aspect ratios. The second, $\overline{\boldsymbol{u}}_{2B}$, is directly proportional to the imposed temperature difference and, in particular, is directly related to the acoustic wave vorticity generated baroclinically in the interior of the channel. The third contribution, $\overline{\boldsymbol{u}}_{2F}$, depends on the details of the wave forcing mechanism and in practice is found to be negligible. A critical temperature difference $\Delta\Theta_{c_*}$ can be defined based on equating the kinetic energies of the viscous and baroclinically driven streaming flows to quantify the transition from $\overline{\boldsymbol{u}}_{2H}$ to $\overline{\boldsymbol{u}}_{2B}$ as $\Delta\Theta_*$ is increased. We show that

$$\Delta\Theta_{c_*} = \epsilon\ \Gamma_c\ T_* = \frac{k_*\mu_*}{\rho_* a_*}\frac{\left[1 + \dfrac{\mu_* c_{p*}}{\kappa_*} + \dfrac{2}{3}\left(\dfrac{c_{p*}}{c_{v*}} - 1\right)\sqrt{\dfrac{\mu_* c_{p*}}{\kappa_*}}\right]}{1 + \dfrac{\mu_* c_{p*}}{\kappa_*}} F_c(k_* H_*)\ T_*, \qquad (5.1)$$

Attribute	Rayleigh streaming (RS)	Transition from RS to BAS	Baroclinic acoustic streaming (BAS)
Schematic	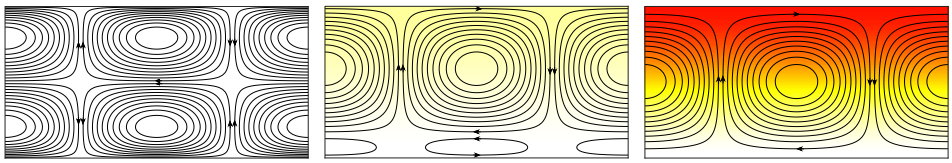		
Temperature difference	$\Delta\Theta_* \ll \Delta\Theta_{c_*}$	$\Delta\Theta_* = O(\Delta\Theta_{c_*})$	$\Delta\Theta_* \gg \Delta\Theta_{c_*}$
Streaming velocity scale	$U_{s_*} = U_*^2/a_*$	$U_{s_*} = U_*^2/a_*$	$U_{s_*} = U_*$
Driving mechanism	Attenuation (BLs) and wave forcing mechanism	Baroclinicity (interior), attenuation (BLs) and wave forcing mechanism	Baroclinicity (interior)
Features	Stacked cells and symmetry about $\tilde{y} = H_*/2$	Stacked cells and no symmetry about $\tilde{y} = H_*/2$	Single cell and no symmetry about $\tilde{y} = H_*/2$ (see Massih *et al.* 2024)
Solution	Asymptotic analytical approximations exist	Asymptotic analytical approximations exist	Numerical solution only
Dynamics	The waves drive a mean flow. No feedback from the mean flow	The waves drive a mean flow. No feedback from the mean flow	The waves drive a mean flow. The mean flow affects the waves

Table 3. Summary of acoustic streaming regimes in a differentially heated channel. Recall that U_* is the typical acoustic wave velocity, a_* the speed of sound, $\Delta\Theta_*$ the temperature difference across the channel of height H_* and $\Delta\Theta_{c_*}$ the critical temperature difference given in (5.1).

where F_c is an explicit function that has a minimum value of 27 for $k_*H_* = 4.74$. For air at standard temperature and pressure as a working fluid ($T_* = 273\,\mathrm{K}$, $\mu_* = 1.7 \times 10^{-5}\,\mathrm{kg\,(m\,s)^{-1}}$, $\rho_* = 1.3\,\mathrm{kg\,m^{-3}}$, $c_{p*} = 1.0 \times 10^3\,\mathrm{J\,(kg\,K)^{-1}}$, $c_{v*} = c_{p*}/1.4$, $\kappa_* = 0.024\,\mathrm{W\,(m\,K)^{-1}}$, $a_* = 331\,\mathrm{m\,s^{-1}}$), a channel of height $H_* = 1\,\mathrm{cm}$ and an acoustic wave of wavenumber $k_* = 4.74/H_* = 474\,\mathrm{m^{-1}}$ (and, thus, $f_* = k_*a_*/(2\pi) = 25\,\mathrm{kHz}$), we find $\Delta\Theta_{c_*} = 0.15\,\mathrm{K}$. Larger channel heights with the same aspect ratio would further reduce this critical temperature difference (for $H_* = 10\,\mathrm{cm}$ and $k_* = 4.74/H_*$, $\Delta\Theta_{c_*} = 15\,\mathrm{mK}$). This estimate demonstrates the extreme sensitivity of streaming flows in a gas to temperature inhomogeneities.

The estimation of this transitional temperature gradient also aids in the design of experiments. First, $\Delta\Theta_{c_*}$ should be computed and compared with the actual temperature difference $\Delta\Theta_*$. If $\Delta\Theta_* \ll \Delta\Theta_{c_*}$, baroclinicity can be neglected and Rayleigh's approach for homogeneous fluids used. For $\Delta\Theta_* = O(\Delta\Theta_{c_*})$, the present analytical solution should be employed, whereas a larger temperature difference $\Delta\Theta_* \gg \Delta\Theta_{c*}$ generates two-way coupling between the waves and the streaming flows that is captured in the framework developed in Chini *et al.* (2014), Michel & Chini (2019) and Massih *et al.* (2024). Table 3 compares these various regimes of acoustic streaming in a gas and highlights the transition from Rayleigh streaming to baroclinic acoustic streaming.

Declaration of interests. The authors report no conflict of interest.

Appendix A. Analytical solutions for the acoustic waves at $O(\epsilon^{3/2})$

The $O(\epsilon^{3/2})$ acoustic fields in the interior are

$$\pi'_{3/2} = [(\delta^2\gamma\mathbb{F}_{3/2}/2)y^2 + C_1 y + C_2]\cos(x)\,\mathrm{e}^{\mathrm{i}t} + \text{c.c.} \quad \text{(interior)}, \tag{A1}$$

$$u'_{3/2} = \mathrm{i}\gamma^{-1}[(\delta^2\gamma\mathbb{F}_{3/2}/2)y^2 + C_1 y + C_2 + \mathbb{F}_{3/2}\gamma]\sin(x)\,\mathrm{e}^{\mathrm{i}t} + \text{c.c.} \quad \text{(interior)}, \tag{A2}$$

$$v'_{3/2} = \mathrm{i}(\gamma\delta^2)^{-1}[(\delta^2\gamma\mathbb{F}_{3/2})y + C_1]\cos(x)\,\mathrm{e}^{\mathrm{i}t} + \text{c.c.} \quad \text{(interior)}, \tag{A3}$$

$$\Theta'_{3/2} = (1-\gamma^{-1})\pi'_{3/2} \quad \text{(interior)}, \tag{A4}$$

$$\rho'_{3/2} = \gamma^{-1}\pi'_{3/2} \quad \text{(interior)}. \tag{A5}$$

The vertical velocity field $v'_{3/2}$ evaluated at $y=0$ in the interior (A3) must match the value obtained in the cold-wall BL as $\eta\to\infty$ (3.21) and analogously at $y=1$. This matching is achieved by setting

$$C_1 = -\frac{\delta^2\gamma}{2}\mathbb{F}_{3/2}, \qquad \mathbb{F}_{3/2} = (1-i)\,\frac{\mathbb{A}}{2\gamma}\left(\frac{(\gamma-1)}{\sqrt{\mathbb{P}}} + \frac{1}{\sqrt{\mathbb{R}}}\right). \tag{A6}$$

The constant C_2 seemingly remains undetermined at this stage. We determine C_2 by noting that the corresponding acoustic field has exactly the same form as that obtained at $O(\epsilon)$, consisting of a plane horizontal wave with BLs to satisfy the no-slip and isothermal boundary conditions. Thus, the wave solution associated with the constant C_2 merely corresponds to an $O(\epsilon)$ modification of the leading-order acoustic wave amplitude $\mathbb{A}$ and does not encapsulate any new physical phenomena. Accordingly, we choose to set $C_2 = -\gamma\mathbb{F}_{3/2}$ to ensure a zero oscillatory horizontal velocity in the interior close to each boundary and thereby obviate the need for mechanical BLs at this order. The thermal boundary layer, however, remains and the following expression for the fields close to the walls is obtained:

$$\pi'_{3/2} = -\gamma\mathbb{F}_{3/2}\cos(x)\mathrm{e}^{\mathrm{i}t} + \text{c.c.} \quad \text{(BLs)}, \tag{A7}$$

$$u'_{3/2} = 0 \quad \text{(BLs)}, \tag{A8}$$

$$v'_2 = \begin{cases} \mathbb{F}_{3/2}\left[\mathrm{i}\eta + \dfrac{(1+\mathrm{i})}{2\sqrt{\mathbb{P}}}(\gamma-1)(1-\mathrm{e}^{-(1+\mathrm{i})\sqrt{\mathbb{P}}\eta})\right]\cos(x)\mathrm{e}^{\mathrm{i}t} + \text{c.c.} \quad \text{(C-BL)} \\ -\mathbb{F}_{3/2}\left[\mathrm{i}\eta + \dfrac{(1+\mathrm{i})}{2\sqrt{\mathbb{P}}}(\gamma-1)(1-\mathrm{e}^{-(1+\mathrm{i})\sqrt{\mathbb{P}}\eta})\right]\cos(x)\,\mathrm{e}^{\mathrm{i}t} + \text{c.c.} \quad \text{(H-BL)}, \end{cases} \tag{A9}$$

$$\Theta'_{3/2} = -\mathbb{F}_{3/2}(\gamma-1)\left[1-\mathrm{e}^{-(1+\mathrm{i})\sqrt{\mathbb{P}}\eta}\right]\cos(x)\,\mathrm{e}^{\mathrm{i}t} + \text{c.c.} \quad \text{(BLs)}, \tag{A10}$$

$$\rho'_{3/2} = -\mathbb{F}_{3/2}\left[1+(\gamma-1)\mathrm{e}^{-(1+\mathrm{i})\sqrt{\mathbb{P}}\eta}\right]\cos(x)\,\mathrm{e}^{\mathrm{i}t} + \text{c.c.} \quad \text{(BLs)}. \tag{A11}$$

Appendix B. Leading-order streaming flow in the BLs

The leading-order streaming flow in the BLs is explicitly given by

$$\begin{aligned}\overline{u}_2 = \frac{\mathbb{A}^2\sin(2x)\mathrm{e}^{-[(1+\mathrm{i})(\sqrt{\mathbb{P}}+\sqrt{\mathbb{R}})+\sqrt{\mathbb{R}}]\eta}}{8\gamma^2\mathbb{P}(\mathbb{P}+\mathbb{R})}\Big\{ &-\mathrm{i}(\gamma-1)\mathbb{R}(\mathbb{P}+\mathbb{R})\mathrm{e}^{(2+\mathrm{i})\sqrt{\mathbb{R}}\eta} \\ &+\mathbb{P}(\mathbb{P}+\mathbb{R})\mathrm{e}^{[(1+\mathrm{i})\sqrt{\mathbb{P}}+\mathrm{i}\sqrt{\mathbb{R}}]\eta} + \mathrm{i}(\gamma-1)\mathbb{R}(\mathbb{P}+\mathbb{R})\mathrm{e}^{[2\mathrm{i}\sqrt{\mathbb{P}}+(2+\mathrm{i})\sqrt{\mathbb{R}}]\eta} \\ &-(\gamma-1)\mathbb{R}[(\sqrt{\mathbb{P}\mathbb{R}}+\mathrm{i}\mathbb{P})\mathrm{e}^{(\sqrt{\mathbb{R}}+2\mathrm{i}\sqrt{\mathbb{P}})\eta} + (\sqrt{\mathbb{P}\mathbb{R}}-\mathrm{i}\mathbb{P})\mathrm{e}^{(1+2\mathrm{i})\sqrt{\mathbb{R}}\eta}] \\ &+\sqrt{\mathbb{P}}(\mathbb{P}+\mathbb{R})[(\gamma-1)\sqrt{\mathbb{R}}+(1+3\mathrm{i})\sqrt{\mathbb{P}}]\mathrm{e}^{[\sqrt{\mathbb{R}}+(1+\mathrm{i})\sqrt{\mathbb{P}}]\eta}\end{aligned}$$

$$- \mathbb{P}[2(\gamma-1)\sqrt{\mathbb{P}\mathbb{R}} + 3(\mathbb{P}+\mathbb{R})]\mathrm{e}^{[(1+\mathrm{i})(\sqrt{\mathbb{P}}+\sqrt{\mathbb{R}})+\sqrt{\mathbb{R}}]\eta}$$
$$+ \sqrt{\mathbb{P}}(\mathbb{P}+\mathbb{R})[(\gamma-1)\sqrt{\mathbb{R}} + (1-3\mathrm{i})\sqrt{\mathbb{P}}]\mathrm{e}^{[(1+\mathrm{i})\sqrt{\mathbb{P}}+(1+2\mathrm{i})\sqrt{\mathbb{R}}]\eta}\Big\}. \tag{B1}$$

Appendix C. Simplification of the torques driving the streaming flow

C.1. *Using vector identities and equations at lower order*

Various nonlinear terms in the expression for the stream function (obtained by taking the curl of (3.42)) can be simplified. In particular, since the acoustic vorticity in the interior vanishes at $O(\epsilon^{3/2})$,

$$\boldsymbol{\nabla}\times\left[(\boldsymbol{u}'_{3/2}\cdot\boldsymbol{\nabla})\boldsymbol{u}'_{3/2}\right] = \boldsymbol{\nabla}\times\left[\frac{1}{2}\boldsymbol{\nabla}(\boldsymbol{u}'_{3/2}\cdot\boldsymbol{u}'_{3/2}) + (\boldsymbol{\nabla}\times\boldsymbol{u}'_{3/2})\times\boldsymbol{u}'_{3/2}\right] = \boldsymbol{0}. \tag{C1}$$

Similarly, exploiting vector identities and that $\boldsymbol{\Omega}'_{\boldsymbol{1}} = \boldsymbol{0}$ in the interior yields both

$$\begin{aligned}\boldsymbol{\nabla}\times\left[(\boldsymbol{u}'_1\cdot\boldsymbol{\nabla})\boldsymbol{u}'_2 + (\boldsymbol{u}'_2\cdot\boldsymbol{\nabla})\boldsymbol{u}'_1\right] &= \boldsymbol{\nabla}\times\left[\boldsymbol{\nabla}(\boldsymbol{u}'_2\cdot\boldsymbol{u}'_1) + (\boldsymbol{\nabla}\times\boldsymbol{u}'_2)\times\boldsymbol{u}'_1 + (\boldsymbol{\nabla}\times\boldsymbol{u}'_1)\times\boldsymbol{u}'_2\right]\\ &= \boldsymbol{\nabla}\times(\boldsymbol{\Omega}'_2\times\boldsymbol{u}'_1)\end{aligned} \tag{C2}$$

and

$$\begin{aligned}2\boldsymbol{\nabla}\times\left[\overline{\rho}_1(\boldsymbol{u}'_1\cdot\boldsymbol{\nabla})\boldsymbol{u}'_1\right] &= \boldsymbol{\nabla}\times\left[\overline{\rho}_1\boldsymbol{\nabla}(\boldsymbol{u}'_1\cdot\boldsymbol{u}'_1) + 2\,\overline{\rho}_1(\boldsymbol{\nabla}\times\boldsymbol{u}'_1)\times\boldsymbol{u}'_1\right]\\ &= \boldsymbol{\nabla}\times\left[\overline{\rho}_1\boldsymbol{\nabla}(\boldsymbol{u}'_1\cdot\boldsymbol{u}'_1)\right] = (\boldsymbol{\nabla}\overline{\rho}_1)\times\left[\boldsymbol{\nabla}(\boldsymbol{u}'_1\cdot\boldsymbol{u}'_1)\right].\end{aligned} \tag{C3}$$

The nonlinear term involving the $O(\epsilon^{3/2})$ acoustic fields does not vanish and can be related to the external force density $\mathbb{F}'_{3/2}$ with the use of (3.24) and (A5):

$$\begin{aligned}\boldsymbol{\nabla}\times(\rho'_{3/2}\partial_t\boldsymbol{u}'_{3/2}) &= \boldsymbol{\nabla}\times\left(\gamma^{-1}\pi'_{3/2}\left[-\gamma^{-1}\boldsymbol{\nabla}\pi'_{3/2} + \mathbb{F}'_{3/2}\boldsymbol{e}_x\right]\right)\\ &= -\gamma^{-1}\delta^{-1}\partial_y(\pi'_{3/2}\mathbb{F}'_{3/2})\boldsymbol{e}_z = -(\gamma\delta)^{-1}(\partial_y\pi'_{3/2})\mathbb{F}'_{3/2}\boldsymbol{e}_z &\text{(C4)}\\ &= \mathbb{F}'_{3/2}\partial_t(\delta\, v'_{3/2})\boldsymbol{e}_z. &\text{(C5)}\end{aligned}$$

Hence, $\overline{\boldsymbol{\nabla}\times(\rho'_{3/2}\partial_t\boldsymbol{u}'_{3/2})} = -\overline{\delta\, v'_{3/2}\,\partial_t\mathbb{F}'_{3/2}}\,\boldsymbol{e}_z$.

C.2. *Using acoustic equations at $O(\epsilon^2)$*

The nonlinear terms $\overline{\boldsymbol{\nabla}\times(\rho'_2\partial_t\boldsymbol{u}'_1)}$ and $\overline{\boldsymbol{\nabla}\times(\rho'_1\partial_t\boldsymbol{u}'_2)}$ require a special analysis but their sum is found to vanish. First, note that $\gamma^{-1}\partial_y$((3.47) + (3.48)) leads, with (3.49), to

$$\partial_y\left(\partial_x u'_2 + \partial_y v'_2\right) = -\gamma^{-1}\partial_{ty}\pi'_2 = \delta^2\partial_{tt}v'_2, \tag{C6}$$

and, therefore, with the use of (3.47), (3.50) and (C6),

$$\begin{aligned}\overline{\boldsymbol{\nabla}\times(\rho'_2\partial_t\boldsymbol{u}'_1)} &= -\overline{\boldsymbol{\nabla}\times(\boldsymbol{u}'_1\partial_t\rho'_2)} = -\overline{\boldsymbol{\nabla}\times\left[u'_1(\Gamma y\partial_x u'_1 - \partial_x u'_2 - \partial_y v'_2)\boldsymbol{e}_x\right]}\\ &= -\delta^{-1}\partial_y\overline{\left[u'_1(\Gamma y\partial_x u'_1 - \partial_x u'_2 - \partial_y v'_2)\right]}\boldsymbol{e}_z &\text{(C7)}\\ &= -\delta^{-1}\overline{\left[u'_1\Gamma\partial_x u'_1 - u'_1\partial_y(\partial_x u'_2 + \partial_y v'_2)\right]}\boldsymbol{e}_z\\ &= \overline{\Omega'_2\partial_x u'_1}\boldsymbol{e}_z + \delta\overline{u'_1\partial_{tt}v'_2}\boldsymbol{e}_z = \overline{\Omega'_2\partial_x u'_1}\boldsymbol{e}_z - \delta\overline{u'_1 v'_2}\boldsymbol{e}_z. &\text{(C8)}\end{aligned}$$

The other nonlinear term can be simplified as well, using successively (3.10), (3.50) and (C8):

$$\begin{aligned}\overline{\boldsymbol{\nabla}\times\left(\rho_1'\partial_t\boldsymbol{u}_2'\right)} &= -\overline{\boldsymbol{\nabla}\times\left(\boldsymbol{u}_2'\partial_t\rho_1'\right)} = \overline{\boldsymbol{\nabla}\times\left(\boldsymbol{u}_2'\partial_x u_1'\right)} = \delta^{-1}\partial_y\overline{\left(u_2'\partial_x u_1'\right)}\boldsymbol{e}_z - \delta\partial_x\overline{\left(v_2'\partial_x u_1'\right)}\boldsymbol{e}_z \\ &= \overline{\left(\delta^{-1}\partial_y u_2' - \delta\partial_x v_2'\right)\partial_x u_1'}\boldsymbol{e}_z - \delta\overline{v_2'\partial_{xx}u_1'}\boldsymbol{e}_z = -\overline{\Omega_2'\partial_x u_1'}\boldsymbol{e}_z + \delta\overline{v_2'u_1'}\boldsymbol{e}_z \\ &= -\overline{\boldsymbol{\nabla}\times\left(\rho_2'\partial_t\boldsymbol{u}_1'\right)}. \end{aligned} \tag{C9}$$

Appendix D. Expression for the leading-order stream function

As detailed in § 3.8, the leading-order streaming flow can be expressed as ($\overline{u}_2 = -\delta^{-1}\partial_y\overline{\psi}_2$, $\overline{v}_2 = \delta^{-1}\partial_x\overline{\psi}_2$), where the stream function $\overline{\psi}_2 = \overline{\psi}_{2H} + \overline{\psi}_{2B} + \overline{\psi}_{2F}$ and

$$\overline{\psi}_{2H} = -\frac{\delta\overline{u}_{slip}}{\sinh(2\delta) - 2\delta}\{(y-1)\sinh(2\delta y) + y\sinh[2\delta(1-y)]\}, \tag{D1}$$

$$\begin{aligned}\overline{\psi}_{2B} = \frac{\mathbb{A}^2\Gamma\mathbb{R}\sin(2x)}{64\delta^3\gamma^2\left[\delta+\cosh(\delta)\sinh(\delta)\right]}&\{-\sinh(2\delta)+\cosh(2\delta y)[2\delta(1-y)+\sinh(2\delta)] \\ &+ 2\delta y\cosh[2\delta(y-1)] - 2[\delta+\sinh(\delta)^2\sinh(2\delta y)]\}, \end{aligned} \tag{D2}$$

$$\begin{aligned}\overline{\psi}_{2F} = \frac{\mathbb{R}\mathbb{F}_{3/2}\mathbb{F}^*_{3/2}\sin(2x)}{32\delta\left[\delta-\cosh(\delta)\sinh(\delta)\right]}&\{\cosh(2\delta y)[2\delta(y-1)+(1-2y)\sinh(2\delta)] \\ &+ 2\delta y\cosh[2\delta(y-1)] - (2y-1)[2\delta-\sinh(2\delta)-2\sinh(\delta)^2\sinh(2\delta y)]\}, \end{aligned} \tag{D3}$$

with $\overline{u}_{slip}$ and $\mathbb{F}_{3/2}$ given in (3.41) and (3.34).

Appendix E. Kinetic energy parameters (K_H, K_F, K_B)

The parameters (K_H, K_F, K_B) defined in (4.3)–(4.5) are given by

$$\begin{aligned}K_H = \frac{\mathbb{A}^4\sinh(\delta)(2(\gamma-1)\sqrt{\mathbb{P}}\sqrt{\mathbb{R}}+3\mathbb{P}+3\mathbb{R})^2}{512\delta\gamma^4(\mathbb{P}+\mathbb{R})^2(\delta-\sinh(\delta)\cosh(\delta))^2}& \\ \{-(8\delta^2+1)\cosh(\delta)+4\delta\sinh(\delta)+\cosh(3\delta)\},& \end{aligned} \tag{E1}$$

$$\begin{aligned}K_F = \frac{\mathbb{A}^4((\gamma-1)\sqrt{\mathbb{R}}+\sqrt{\mathbb{P}})^4}{12288\delta^5\gamma^4\mathbb{P}^2(\delta-\sinh(\delta)\cosh(\delta))^2}&\{108(\delta^3+\delta)\cosh(2\delta) \\ &- 3(5\delta^2+7)\sinh(4\delta) + 2\delta(\delta^2+18)\cosh(4\delta) + 2\delta(8\delta^4+29\delta^2-72) \\ &- 2(20\delta^4+111\delta^2-21)\sinh(2\delta)\}, \end{aligned} \tag{E2}$$

$$\begin{aligned}K_B = \frac{\mathbb{A}^4\Gamma^2\mathbb{R}^2}{1024\delta^7\gamma^4(2\delta+\sinh(2\delta))^2}&\{2\delta(8\delta^2+9)+2(12\delta^2+5)\sinh(2\delta) \\ &- 5\sinh(4\delta) - 20\delta\cosh(2\delta) + 2\delta\cosh(4\delta)\}. \end{aligned} \tag{E3}$$

References

Aktas, M.K. & Ozgumus, T. 2010 The effects of acoustic streaming on thermal convection in an enclosure with differentially heated horizontal walls. *Intl J. Heat Mass Transfer* **53** (23), 5289–5297.

Bengtsson, M. & Laurell, T. 2004 Ultrasonic agitation in microchannels. *Anal. Bioanal. Chem.* **378** (7), 1716–1721.

Chini, G.P., Malecha, Z. & Dreeben, T.D. 2014 Large-amplitude acoustic streaming. *J. Fluid Mech.* **744**, 329–351.

DARU, V., WEISMAN, C., BALTEAN-CARLÈS, D. & BAILLIET, H. 2021 Acoustically induced thermal effects on Rayleigh streaming. *J. Fluid Mech.* **911**, A7.

HYUN, S., LEE, D.-R. & LOH, B.-G. 2005 Investigation of convective heat transfer augmentation using acoustic streaming generated by ultrasonic vibrations. *Intl J. Heat Mass Transfer* **48** (3), 703–718.

KARLSEN, J.T., AUGUSTSSON, P. & BRUUS, H. 2016 Acoustic force density acting on inhomogeneous fluids in acoustic fields. *Phys. Rev. Lett.* **117**, 114504.

LIGHTHILL, M.J. 1978 Acoustic streaming. *J. Sound Vib.* **61**, 391–418.

LIN, Y. & FAROUK, B. 2008 Heat transfer in a rectangular chamber with differentially heated horizontal walls: effects of a vibrating sidewall. *Intl J. Heat Mass Transfer* **51** (11), 3179–3189.

LOH, B.-G., HYUN, S., RO, P.I. & KLEINSTREUER, C. 2002 Acoustic streaming induced by ultrasonic flexural vibrations and associated enhancement of convective heat transfer. *J. Acoust. Soc. Am.* **111** (2), 875–883.

MASSIH, J.A., MUSHTHAQ, R., MICHEL, G. & CHINI, G.P. 2024 Aspect-ratio-dependent heat transport by baroclinic acoustic streaming. *J. Fluid Mech.* **997**, A7.

MICHEL, G. & CHINI, G.P. 2019 Strong wave–mean-flow coupling in baroclinic acoustic streaming. *J. Fluid Mech.* **858**, 536–564.

MICHEL, G. & GISSINGER, C. 2021 Cooling by baroclinic acoustic streaming. *Phys. Rev. Appl.* **16**, L051003.

NABAVI, M., SIDDIQUI, K. & DARGAHI, J. 2008 Influence of differentially heated horizontal walls on the streaming shape and velocity in a standing wave resonator. *Intl Commun. Heat Mass Transfer* **35** (9), 1061–1064.

QIU, W., JOERGENSEN, J.H., CORATO, E., BRUUS, H. & AUGUSTSSON, P. 2021 Fast microscale acoustic streaming driven by a temperature-gradient-induced nondissipative acoustic body force. *Phys. Rev. Lett.* **127**, 064501.

RAYLEIGH, J.W.S.B. 1896 *The Theory of Sound*, vol. 2, Macmillan.

RAYLEIGH, LORD 1884 I. on the circulation of air observed in Kundt's tubes, and on some allied acoustical problems. *Phil. Trans. R. Soc. Lond.* **175**, 1–21.

RILEY, N. 1997 Acoustic streaming. In *Encyclopedia of Acoustics*, chap. 30, pp. 321–327. John Wiley & Sons. Ltd.

RILEY, N. 2001 Steady streaming. *Annu. Rev. Fluid Mech.* **33** (1), 43–65.

STOCKWALD, K., KAESTLE, H. & ERNST, H. 2014 Highly efficient metal halide HID systems with acoustically stabilized convection. *IEEE Trans. Ind. Applics.* **50**, 94–103,

VAN DYKE, M. 1969 Higher-order boundary-layer theory. *Annu. Rev. Fluid Mech.* **1** (1969), 265–292.

Cooling by Baroclinic Acoustic Streaming

Guillaume Michel, Christophe Gissinger

Cooling by baroclinic acoustic streaming

Guillaume Michel[1]* and Christophe Gissinger[2,3]
[1] *Sorbonne Université, CNRS, Institut Jean Le Rond d'Alembert, F-75005 Paris, France*
[2] *Laboratoire de Physique de l'Ecole normale supérieure, ENS, Université PSL, CNRS, Sorbonne Université, Université de Paris, Paris, France and*
[3] *Institut Universitaire de France (IUF)*
(Dated: November 15, 2021)

In the absence of natural convection, efficient heat transfers rely on externally forced flows. Generating such flows with acoustic waves rather than mechanical fans would enable remote locations to be cooled using virtually infinite lifetime transducers. This outlook is reinforced by the recent discovery that standing acoustic waves drive streaming flows of much higher velocities if the background medium is inhomogeneous. This regime of streaming is investigated experimentally in a cavity filled with stably-stratified air in which horizontal sound waves are found to significantly enhance heat transfers. The additional heat flux scales as the square of the input acoustic power for low amplitude waves and increases with the air stratification. These two features qualitatively match theoretical predictions, although corrections possibly ascribed to gravity are observed.

Introduction.— The generation of streaming flows by acoustic waves in homogeneous fluids requires a dissipation mechanism [1]. Close to solid boundaries, viscosity generates oscillating boundary layers that can locally force a mean flow: this so-called *Rayleigh streaming* is used in microfluidics to improve the efficiency of catalytic solid phases [2] or to mix chemicals [3]. In the bulk, the attenuation of acoustic beams forces jets, a phenomenon referred to as quartz wind. As reviewed in Ref. [4], most studies investigating the effect of acoustic waves on heat transfers typically involve generating such progressive ultrasonic beams with a few hundred watts in a liquid to trigger cavitation and/or drive forced convection.

Over the last few decades, a very different picture has emerged for acoustic streaming in *inhomogeneous* fluids. Experiments and numerical simulations with standing waves started investigating this regime and reported radically different streaming patterns, in some cases several orders of magnitude faster than the corresponding ones in homogeneous fluids [5–10]. This regime of streaming was rationalized theoretically for gases by Chini *et al.* [11] and termed *baroclinic acoustic streaming*. Its most noticeable feature is that the acoustic wave vorticity required to drive streaming no longer results from dissipation but is a consequence of baroclinicity, an inviscid process. This mechanism can be inferred from the curl of the linearized Euler equation describing the leading-order acoustic wave dynamics:

$$\nabla \times \left(\rho \frac{\partial \mathbf{u}}{\partial t} = -\nabla p \right) \Rightarrow \frac{\partial (\nabla \times \mathbf{u})}{\partial t} = \frac{(\nabla \rho) \times (\nabla p)}{\rho^2}, \quad (1)$$

where ρ is the time-averaged density, $\mathbf{u}$ is the acoustic wave velocity and p is the acoustic wave pressure. Whereas inviscid acoustic waves in homogeneous fluids have no vorticity, Eq. (1) demonstrates that this no longer holds in the presence of a background stratification as a result of baroclinic production of vorticity. The acoustic force density driving these streaming flows has then been derived in the general case of liquids, for both density and compressibility inhomogeneities [12]. Since the properties of the acoustic modes (frequency and eigenfunction) depend on these background fields, a subtle two-way coupling takes place: the fast acoustic waves generate a slowly varying mean flow that advects inhomogeneities and feeds back on the acoustic waves.

Several applications of this regime of streaming are already documented. It can significantly improve the efficiency of high-intensity discharge lamps, in which the mean temperature varies by thousands of degrees between the center and the walls [10]. In microfluidics, it affects the acoustically-induced mixing of different fluids [13]. According to an experiment with water in a microchannel, a local temperature fluctuation of ~ 0.2 K is sufficient to distort the streaming pattern observed in a homogeneous fluid [14]. The baroclinic streaming flow in a stratified gas enclosed between two horizontal walls is characterized in Ref. [15] and quantitatively fits previous numerical simulations (see also Ref. [16] in the limit of small temperature gradients). It suggests a new procedure based on *stationary* waves to acoustically enhance heat transfers in the absence of natural convection, e.g. for stably stratified or zero-gravity environments [15, 17]. However, several thermal properties of this system, crucial for assessing the potential of acoustic streaming for practical applications such as cooling electronics aboard spacecraft, are still missing.

In this letter, we show that baroclinic streaming can significantly enhance heat transfers and characterize this cooling effect as a function of both the acoustic wave properties and the gas stratification. The results are compared with theoretical predictions from dissipation-based streaming [18] and baroclinic streaming in Ref. [15].

* email: guillaume.michel@upmc.fr

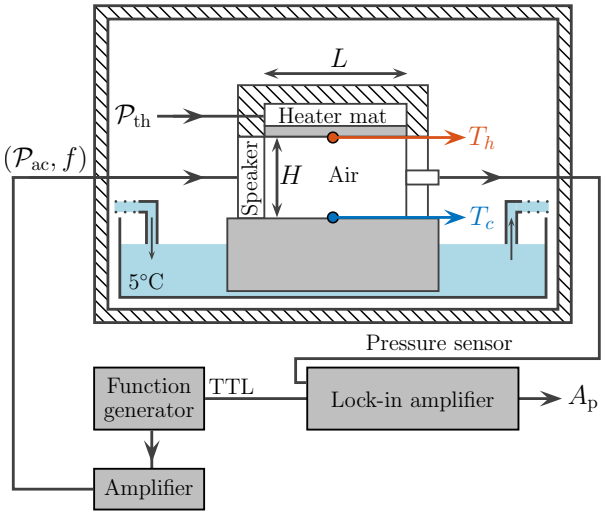

FIG. 1. Experimental setup. A speaker, driven by a harmonic signal of frequency f and power $\mathcal{P}_{\rm ac}$, generates an acoustic wave of local amplitude A_p measured at the opposite end. The cavity of height H and length L is heated at the top (power $\mathcal{P}_{\rm th}$, temperature T_h) and cooled at the bottom (temperature T_c). The width ℓ is not displayed. Gray areas represent dural samples and hatched areas represent thermal insulators.

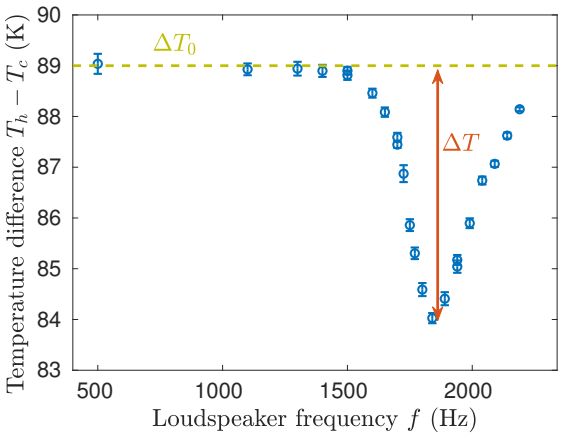

FIG. 2. Top to bottom temperature difference $T_h - T_c$ as a function of the forcing frequency f for $\mathcal{P}_{\rm ac} = 0.5$ W and $\mathcal{P}_{\rm th} = 8.8$ W. The corresponding temperature stratification ΔT_0 and streaming temperature drop ΔT are also reported.

Experiment.— The experiment sketched in Fig. 1 consists of a cavity of length $L = 10$ cm, height $H = 5.0$ cm and width $\ell = 3.0$ cm filled with air at atmospheric pressure. Heat is injected at the top wall at a rate $\mathcal{P}_{\rm th}$ through an RS Pro silicon heater mat fixed on a metallic plate. The bottom wall is a block of dural laterally cooled by means of water at 5°C provided by a Lauda Master thermostat. The top and bottom temperatures at the center of these boundaries, measured by type K thermocouples and Keithley 2700 multimeters, are denoted by T_h and T_c. A Visaton SC-5 tweeter subject to an input sinusoidal signal of frequency f and power $\mathcal{P}_{\rm ac}$ constitutes one lateral wall of this cavity, at the opposite end of which a PCB 103A02 sensor is fixed. The signal from this sensor, processed by a PCB 480E09 signal conditioner and a Standford Research Systems SR 830 lock-in amplifier synchronized on the frequency f, yields an accurate measurement of the local amplitude $A_{\rm p}$ of the oscillating pressure field. The remaining boundaries are 10 mm thick PEEK samples, this material being chosen for its thermal insulation properties and heat resistance. The entire setup is surrounded by thermal insulators, and the room itself is air conditioned to further reduce the daily temperature oscillations. Stationary states are reached after a transient of one hour corresponding to thermal diffusion in the lateral PEEK boundaries. Measurements of $(T_h, T_c, A_{\rm p})$ as a function of the input parameters $(\mathcal{P}_{\rm th}, \mathcal{P}_{\rm ac}, f)$ are performed during two hours once stationary states are achieved and repeated between 3 and 9 times for statistics, the data reported in this letter summarizing around 2000 hours of acquisition.

A first run is performed for various frequencies f, the injected heat $\mathcal{P}_{\rm th} = 8.8$ W and input power in the loudspeaker $\mathcal{P}_{\rm ac} = 0.5$ W being constant. The top to bottom temperature difference, reported in Fig. 2, reaches a minimum at around 1.84 kHz. This frequency corresponds to the first acoustic mode of the cavity, which would read $a/(2L)$ for a homogeneous gas, with a the speed of sound. Under the assumption of a linear temperature stratification and a thin cavity, this eigenvalue problem still allows a simple analytic solution [15]:

$$f_0 = \frac{a_{\rm c}}{2L}\sqrt{1 + \left(\frac{T_h - T_c}{2T_c}\right)}, \qquad (2)$$

where the sound speed, no longer uniform, is $a_{\rm c}$ at T_c. With $a_{\rm c} = 335$ m $\cdot$ s^{-1} and the mean values for this run $T_c = 16$°C and $T_h = 105$°C, eq. (2) yields $f_0 = 1.8$ kHz. From Fig. 2, we define the temperature stratification $\Delta T_0 = 89$ K as the low frequency limit of $T_h - T_c$ and the streaming temperature drop $\Delta T = 5$ K as the variation range of $T_h - T_c$. Note that ΔT_0 corresponds to the top to bottom temperature difference in the absence of acoustic waves, when the input power in the speaker is directly converted to heat. The remainder of this investigation details how ΔT_0 and ΔT depend on $\mathcal{P}_{\rm th}$ and $\mathcal{P}_{\rm ac}$.

The procedure leading to Fig. 2 is repeated for various input acoustic power $\mathcal{P}_{\rm ac}$ at fixed heating $\mathcal{P}_{\rm th} = 8.8$ W, the resulting relative temperature drop $\Delta T/\Delta T_0$ being reported in Fig. 3. A quadratic function $0.4\ \mathcal{P}_{\rm ac}^2$ fits the data in the limit $\Delta T/\Delta T_0 \to 0$, while overestimating those obtained at high acoustic power.

Similarly, the influence of the dimensionless temperature stratification $\Gamma = \Delta T_0/T_c$ is investigated with runs performed for varying $\mathcal{P}_{\rm th}$ at fixed $\mathcal{P}_{\rm ac} = 0.5$ W. The relative temperature drop, reported in Fig. 4, increases with Γ and can be approximated by $4\times10^8 F(\Gamma)$ with F a

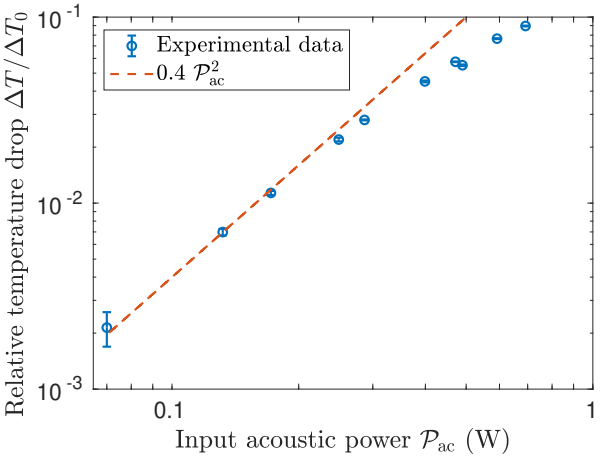

FIG. 3. Relative temperature drop $\Delta T/\Delta T_0$ as a function of the injected power in the loudspeaker $\mathcal{P}_{ac}$ for $\mathcal{P}_{th} = 8.8$ W.

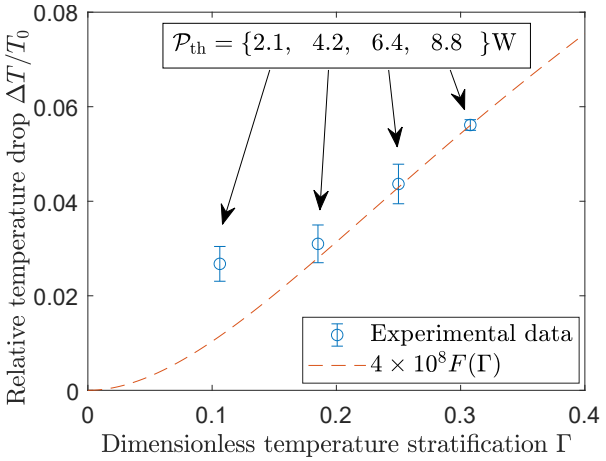

FIG. 4. Relative temperature drop $\Delta T/\Delta T_0$ as a function of the dimensionless temperature stratification $\Gamma = \Delta T_0/T_c$ for fixed power supplied to the loudspeaker $\mathcal{P}_{ac} = 0.5$ W and various heating $\mathcal{P}_{th}$. Note that $\Delta T/\Delta T_0$ would be constant if the streaming flow were independent of Γ.

theoretical function with no fit parameter detailed in the Appendix. The amplitude A_p of the oscillating pressure field is found to be (25 ± 2) Pa. It provides the typical acoustic velocity, $U \sim A_p/(\rho a_c) \sim 6\ \mathrm{cm \cdot s^{-1}}$, with ρ the air density.

Overall, these results demonstrate that, in a stratified gas, a significant temperature drop can be obtained by forcing a standing wave at resonance even for acoustic powers $\mathcal{P}_{ac} < 1$ W orders of magnitude below the ones typically used for cooling in liquids (a few hundred watts [4]). This cooling is found to increase with both the acoustic power and the thermal stratification.

Dimensional parameters	Assumed value
Sound speed a_c (at T_c)	$335\ \mathrm{m \cdot s^{-1}}$
Typical acoustic velocity U	$6\ \mathrm{cm \cdot s^{-1}}$
Horizontal wave number k	$\pi/L = 31\ \mathrm{m^{-1}}$
Height of the cavity H	50 mm
Air density ρ (at T_c)	$1.25\ \mathrm{kg \cdot m^{-1}}$
Dynamic viscosity μ (indep. of T)	$18\ \mu\mathrm{Pa \cdot s}$
Thermal conductivity κ (indep. of T)	$28\ \mathrm{mW \cdot K^{-1}}$
Isobaric specific heat c_p (indep. of T)	$1.0\ \mathrm{kJ \cdot kg^{-1} \cdot K^{-1}}$

TABLE I. Dimensional parameters used to model this experiment.

Dimensionless parameters	Definition	Value
Inverse Strouhal number ε	U/a_c	1.8×10^{-4}
Aspect ratio h	$kH/\sqrt{\varepsilon}$	1.2×10^2
Streaming Reynolds number Re_s	$\varepsilon\rho U/(k\mu)$	2.4×10^{-2}
Streaming Peclet number Pe_s	$\varepsilon\rho c_p U/(k\kappa)$	1.5×10^{-2}
Temperature gradient Γ	$\Delta T_0/T_c$	$0.1 \leqslant \Gamma \leqslant 0.3$

TABLE II. Dimensionless parameters describing the streaming flow.

Discussion.— These results are compared with theoretical predictions based on Rayleigh streaming [18] and baroclinic streaming [15]. Both models apply to an ideal gas enclosed in a thin cavity and subject to the following main assumptions: the dynamics is two-dimensional, the top and bottom walls are at fixed temperature, parameters such as μ, κ and c_p are assumed independent of temperature (see Tab. I) and, most importantly, gravity is neglected. Although this last assumption precludes any quantitative comparison with the present experiment in which gravity acts as a strong restoring force, it is of interest to investigate if the associated scaling laws hold.

From the dimensional parameters used to model this experiment and listed in Tab. I, several dimensionless numbers can be defined, see Tab. II. The multiple scales theory of baroclinic streaming expands the various fields as series of $\varepsilon \ll 1$ and scales h, Re_s, Pe_s and Γ as $O(1)$. The smallness of ε in this experiment supports such multiple scales analysis. In the limit $\Delta T \ll \Delta T_0$ where the background density field can be approximated by the one at rest, the constant power and constant temperature boundary conditions become equivalent and the following temperature drop is derived:

$$\frac{\Delta T}{\Delta T_0} = F(\Gamma)(A^2 Re_s Pe_s h^4)^2, \tag{3}$$

where A is the dimensionless amplitude of the wave, assumed of $O(1)$ in the analysis and related to A_p through

$$A_p = \frac{\varepsilon p_{atm} A \gamma}{\sqrt{\pi\left(1 + \frac{\Gamma}{2}\right)}}, \tag{4}$$

with $p_{\rm atm} = 10^5$ Pa the ambient pressure and $\gamma = 1.4$ the specific heat ratio.

It is instructive to compare eq. (3) with the temperature drop that would be achieved by forced convection with a fan of fixed rotation rate, $\Delta T \propto \Delta T_0$: baroclinic acoustic streaming is such that $\Delta T \propto F(\Gamma)\Delta T_0$ with $F(\Gamma)$ an increasing function in the range $\Gamma \in [0, 1.05]$, evidencing that increasing the temperature stratification ΔT_0 also affects the streaming flow. With the dimensionless parameters listed in Tab. II, an arbitrary constant amplitude $A = 0.55$ makes the right hand sides of eq. (3) become $4 \times 10^8 F(\Gamma)$, corresponding to the dashed line plotted in Fig. 4 that fits our data for $\Gamma \geqslant 0.2$. Inferring A from (4) with $\Gamma \simeq 0.2$ and $A_{\rm p} = 25$ Pa instead leads to $A \simeq 1.8$ that overestimates the temperature drop.

In comparison, the temperature drop resulting from Rayleigh streaming driven by dissipation in the boundary layers and dominant for homogeneous fluids is [18]

$$\frac{(\Delta T)_R}{\Delta T_0} = 6.2 \times 10^{-5} (\varepsilon A^2 Pe_s h^2)^2. \qquad (5)$$

With $A \sim 2$, the streaming temperature drop $(\Delta T)_R \sim 10^{-6}\Delta T_0$ is negligible. This confirms that dissipation-based streaming is irrelevant in the presence of large temperature inhomogeneities.

Note that the scaling $\Delta T/\Delta T_0 \propto \mathcal{P}_{\rm ac}^2$ observed in Fig. 3 as $\mathcal{P}_{\rm ac} \to 0$ is consistent with both Rayleigh and baroclinic streaming. In this limit, the two theories predict that both the relative temperature drop and the power transferred by the waves to the streaming flow scale as A^4. The injected acoustic power $\mathcal{P}_{\rm ac}$ is then mainly balanced by the dissipation of energy in the oscillating boundary layers (proportional to A^2), hence $A \propto \sqrt{\mathcal{P}_{\rm ac}}$ and $\Delta T/\Delta T_0 \propto A^4 \propto \mathcal{P}_{\rm ac}^2$.

Conclusion.— Acoustic streaming resulting from inhomogeneities in the mean density field rather than dissipation processes recently emerged as an efficient mechanism to drive mean flows. Such setups typically stem from the use of different liquids [12, 13] or from large temperature fluctuations in a gas [5–10, 19]. This affects not only the pattern of the streaming flow, but also its velocity. Indeed, whereas Rayleigh streaming is of velocity $O(U^2/a)$, with U the typical acoustic velocity and a the sound speed, baroclinic streaming in strongly stratified systems can be $O(U)$ [15]. Such strong streaming flow could enhance diffusive heat transfers observed in stably-stratified gas on earth or close to hot electronic devices aboard spacecraft. The present experiment confirms this potential, by decreasing the temperature difference across a stably-stratified gas by almost 10°C with low-power stationary acoustic waves ($\mathcal{P}_{\rm ac} < 1$ W), in qualitative agreement with theoretical predictions [15] in which gravity is neglected, and several orders of magnitude above estimates based on Rayleigh streaming. This outlook is even more promising since the temperature drop increases more than linearly with the temperature difference, as measured by the right hand side of eq. (3): since $F(1) \simeq 2.2\ F(0.32)$, a setup with $\{T_c = -62°\text{C}, T_h = 150°\text{C}\}$ should for instance be associated with a relative temperature drop $\Delta T/T_0$ 120 % higher than the one described Fig. 2 with $\{T_c = 16°\text{C}, T_h = 103°\text{C}\}$.

At least two perspectives emerge from this work. First, the experimental investigation of more intense acoustic waves, associated with streaming Reynolds numbers $Re_s \gg 1$ for which the streaming flow would presumably involve jets and/or turbulence [1]. The theoretical approach of such setups remains challenging and requires numerical simulations accounting for two-way coupling between the acoustic waves and the streaming flow [11, 15]. Second, similar large-amplitude streaming flows should be expected wherever stationary acoustic waves develop in inhomogeneous fluids, as for instance in thermoacoustic devices [20] and in acoustically-trapped spherical plasma bulbs [16, 21].

This work is supported by CNES. CG acknowledges financial support from the French program 'JCJC' managed by Agence Nationale de la Recherche (Grant ANR-19-CE30-0025-01).

Appendix In this appendix is derived the function $F(\Gamma)$ introduced in Eq. (3) from the multiple scales model of Ref. [15]. Following their notations, the dimensionless mean temperature field $\bar{\Theta}_0(x, y, \Gamma)$ is a solution of their equation (4.8),

$$(1+\Gamma y)\partial_{yyyyyy}\bar{\Theta}_0 + 3\Gamma\partial_{yyyyy}\bar{\Theta}_0 = -\frac{2A^2\Gamma^2 Re_s Pe_s h^4}{\pi(2+\Gamma)^2}\cos(2x), \qquad (6)$$

complemented with six boundary conditions, setting to zero $\bar{\Theta}_0$, $\partial_{yy}\bar{\Theta}_0$ and $\partial_{yyy}\bar{\Theta}_0$ at $y = 0$ and $y = 1$ (whatever x). The solution is found to be

$$\bar{\Theta}_0(x, y, \Gamma) = -\frac{2A^2\Gamma^2 Re_s Pe_s h^4}{\pi(2+\Gamma)^2} G_\Gamma(y)\cos(2x), \qquad (7)$$

where $G_\Gamma(y)$ is only reported in Ref. [15] for $\Gamma = 1$. Here, $G_\Gamma(y)$ is computed with Mathematica and reads

$$G_\Gamma(y) = \frac{A + B + C}{D}, \qquad (8)$$

where

$$A = \Gamma^2(y-1)y\{45 + \Gamma[46 + 3\Gamma + y + 3\Gamma y \qquad (9)$$
$$- (9+7\Gamma)y^2 + 3(2+\Gamma)y^3]\} - 30\Gamma\ln(1+\Gamma y), \qquad (10)$$
$$B = 3\Gamma^2(\Gamma+1)y\left(-7 + 10y - 5y^3 + 2y^4\right)\ln(\Gamma)$$
$$+ 30(1+\Gamma)(1+2\Gamma)y\ln(1+\Gamma) - 30\ln(1+\Gamma y), \qquad (11)$$
$$C = -3\Gamma^2(1+\Gamma)y[-7 + y^3(-5+2y)]\ln\left(\Gamma(1+\Gamma)\right)$$
$$+ 20\ln(1+\Gamma y) + 10\Gamma y\ln\left(\Gamma(1+\Gamma y)\right), \qquad (12)$$
$$D = 1080\Gamma^3\left[\Gamma(2+\Gamma) + 2(1+\Gamma)\ln(\Gamma) - 2(1+\Gamma)\ln\left(\Gamma(1+\Gamma)\right)\right]. \qquad (13)$$

Following (4.19) of Ref. [15], the function $F(\Gamma)$ is then

$$F(\Gamma) = \frac{\Gamma^2}{\pi^2(2+\Gamma)^4}\int_0^1 G'_\Gamma(y)^2 \mathrm{d}y. \qquad (14)$$

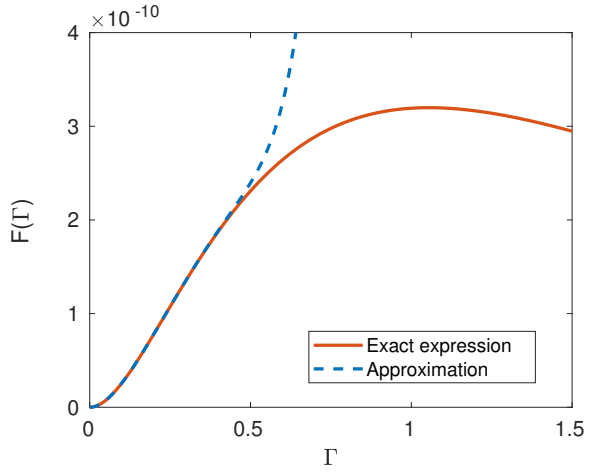

FIG. 5. Function $F(\Gamma)$ associated with cooling by baroclinic streaming and the approximation for $\Gamma < 0.4$ used in the present study.

It can be approximated in the range $\Gamma < 0.4$ by its 10-th Taylor polynomial

$$F(\Gamma) \simeq 10^{-8} \sum_{n=2}^{10} a_n \Gamma^n \tag{15}$$

with

$$a_2 = 0.3464,\ a_3 = -1.039,\ a_4 = 1.855,\ a_5 = -2.57,$$
$$a_6 = 3.06,\ a_7 = -3.3,\ a_8 = 3.3,\ a_9 = -3.2,\ a_{10} = 3. \tag{16}$$

Both the exact expression (14) and the approximation (15-16) are plotted in Fig 5.

[1] M. Lighthill, Acoustic Streaming, J. Sound Vib. **61**, 391 (1978).
[2] M. Bengtsson and T. Laurell, Ultrasonic Agitation in Microchannels, Anal Bioanal Chem **378**, 1716 (2004).
[3] G. G. Yaralioglu, I. O. Wygant, T. C. Marentis, and B. T. Khuri-Yakub, Ultrasonic mixing in microfluidic channels using integrated transducers, Anal. Chem. **76**, 3694 (2004).
[4] M. Legay, N. Gondrexon, S. L. Person, P. Boldo, and A. Bontemps, Enhancement of Heat Transfer by Ultrasound: Review and Recent Advances, Intl J. Chem. Engng **2011**, 670108 (2011).
[5] B.-G. Loh, S. Hyun, P. I. Ro, and C. Kleinstreuer, Acoustic streaming induced by ultrasonic flexural vibrations and associated enhancement of convective heat transfer, J. Acoust. Soc. Am. **111**, 875 (2002).
[6] S. Hyun, D.-R. Mee, and B.-G. Loh, Investigation of convective heat transfer augmentation using acoustic streaming generated by ultrasonic vibrations, Intl J. Heat Mass Transfer **48**, 703 (2005).
[7] Y. Lin and B. Farouk, Heat transfer in a rectangular chamber with differentially heated horizontal walls: Effects of a vibrating sidewall, Intl J. Heat Mass Transfer **51**, 3179 (2008).
[8] M. Nabavi, K. Siddiqui, and J. Dargahi, Influence of differentially heated horizontal walls on the streaming shape and velocity in a standing wave resonator, Intl J. Heat Mass Transfer **35**, 1061 (2008).
[9] M. K. Aktas and T. Ozgumus, The effects of acoustic streaming on thermal convection in an enclosure with differentially heated horizontal walls, Intl J. Heat Mass Transfer **53**, 5289 (2010).
[10] T. D. Dreeben and G. P. Chini, Two-dimensional streaming flows in high-intensity discharge lamps, Phys. Fluids **23**, 056101 (2011).
[11] G. P. Chini, Z. Malecha, and T. D. Dreeben, Large-amplitude acoustique streaming, J. Fluid Mech. **744**, 329 (2014).
[12] J. T. Karlsen, P. Augustsson, and H. Bruus, Acoustic Force Density Acting on Inhomogeneous Fluids in Acoustic Fields, Phys. Rev. Lett. **117**, 114504 (2016).
[13] J. T. Karlsen, W. Qiu, P. Augustsson, and H. Bruus, Acoustic Streaming and Its Suppression in Inhomogeneous Fluids, Phys. Rev. Lett. **120**, 054501 (2018).
[14] W. Qui, J.H. Joergensen, E. Corato, H. Bruus, and P. Augustsson, Fast Microscale Acoustic Streaming Driven by a Temperature-Gradient-Induced Nondissipative Acoustic Body Force, Phys. Rev. Lett. **127**, 064501 (2021).
[15] G. Michel and G. P. Chini, Strong wave–mean-flow coupling in baroclinic acoustic streaming, J. Fluid Mech. **858**, 536 (2018).
[16] J. P. Koulakis and S. Putterman, Convective instability in a stratified ideal gas containing an acoustic field, J. Fluid Mech. **915**, A25 (2021).
[17] V. Kumar, M. Azharudeen, C. Pothuri, and K. Subramani, Heat transfer mechanism driven by acoustic body force under acoustic fields, Phys. Rev. Fluids **6**, 073501 (2021).
[18] P. Vainshtein, M. Fichman, and C. Gutfinger, Acoustic enhancement of heat transfer between two parallel plates, Int. J. Heat Mass Transfer. **38**, 1893 (1995).
[19] R. M. Fand and J. Kaye, Acoustic Streaming near a Heated Cylinder, J. Acoust. Soc. Am. **32**, 579 (1960).
[20] V. Daru, C. Weisman, D. Baltean-Carlès, and H. Bailliet, Acoustically induced thermal effects on Rayleigh streaming, J. Fluid Mech. **911**, A7 (2021).
[21] J. P. Koulakis, S. Pree, A. L. F. Thornton, and S. Putterman, Trapping of plasma enabled by pycnoclinic acoustic force, Phys. Rev. E **98**, 043103 (2018).

Guillaume Michel

Français, né le [redacted]
Tél : [redacted]
Mél : guillaume.michel@sorbonne-universite.fr
Site internet : http://www.ida.upmc.fr/~michel
ORCID ID : 0000-0003-3982-5838
Researcher ID : B-3241-2017
Google Scholar : QXG2wxIAAAAJ
Mis à jour en avril 2026

Situation professionnelle

2019 – présent **Maître de conférences**, Institut Jean le Rond d'Alembert, Sorbonne Université

2017 – 2019 **Post-doctorat**, Woods Hole et Santa Barbara, USA
encadrant : Greg Chini

2013 – 2017 **Thèse**, École Normale Supérieure de Paris
directeurs de thèse : François Pétrélis et Stephan Fauve
intitulé : *Parois et ondes de surface : dissipation, effet Doppler et interactions non linéaires*

2009 – 2013 **Élève à l'École Normale Supérieure de Paris**
2013 : préparation de l'agrégation de physique, reçu 2e sur l'ensemble des candidats
2012 : master 2 de physique des liquides, mention Très Bien
stage de recherche de six mois à l'ENS Paris (encadré par Johann Herault)
2011 : stage de recherche de six mois à Brisbane, Australie (encadré par Debra Searles)

Prix, bourses d'études et financements

2024 Lauréat du Prix Jacques Herbrand (Physique) de l'Académie des Sciences

2019 – 2024 Financements reçus du CNES, du CNRS (« Peps ») et de Sorbonne Université pour l'étude du streaming acoustique

2018 Invité six mois au Kavli Institute for Theoretical Physics, Santa Barbara, USA

2017 Geophysical Fluid Dynamics Fellowship, Woods Hole Oceanographic Institution, USA

Enseignements

2019 – présent **Charge d'enseignement de 192 h/an à Sorbonne Université, dont**
Responsable des travaux pratiques de mécanique sur la plateforme expérimentale
Structures élastiques, *Base de la MMC* et *Équilibre, stabilité et vibrations* (TD et TP de L3)
Acoustique générale et *MMC Fluide* (TD de M1)
Calcul scientifique (CM et TP de M1)

2013 – 2019 **Charge d'enseignement de 192 h/an à l'École Normale Supérieure de Paris, dont**
Projets expérimentaux (TP de L3)
Physique expérimentale (CM et TP de M1)
Transformations d'énergie et *Équations aux dérivées partielles non linéaires* (TD de M1)
Optique géométrique et ondulatoire et *Thermodynamique* (CM aux candidats à l'agrégation)
TP et corrections de montages et de leçons (candidats à l'agrégation)

Campagnes de mesure

2015 – présent Dix campagnes dans le bassin de houle de l'École Centrale de Nantes

2018 – 2026 Deux campagnes de vol parabolique organisée par le CNES

Publications

[1] **Baroclinic transition in acoustic streaming: beyond Rayleigh's paradigm**
R. Mushthaq, G. Michel et G. P. Chini, *Journal of Fluid Mechanics* 1017, A32 (2025)

[2] **Rayleigh-Bénard Convection with Phase Change Close to the Critical Point**
V. Mouet, G. Michel, F. Pétrélis et S. Fauve, *Physical Review Letters* 134, 104001 (2025)

[3] **Coupled dynamics of a wave and moving boundary**
G. Michel, *Comptes Rendus. Physique* 26, 259-270 (2025)

[4] **Aspect-ratio-dependent heat transport by baroclinic acoustic streaming**
J. A. Massih et al., *Journal of Fluid Mechanics* 997, A7 (2024)

[5] **Fluctuation Relations at Large Scales in Three-Dimensional Hydrodynamic Turbulence**
A. Alexakis, S. Chibbaro et G. Michel, *EPL* 144, 43001 (2023)

[6] **Nonlinear dispersion relation in integrable turbulence**
A. Tikan et al., *Scientific Reports* 12, 10386 (2022)

[7] **Statistics of rogue waves in isotropic wave fields**
G. Michel, F. Bonnefoy, G. Ducrozet et E. Falcon, *Journal of Fluid Mechanics* 943, A26 (2022)

[8] **Prediction and manipulation of hydrodynamic rogue waves via nonlinear spectral engineering**
A. Tikan et al., *Physical Review Fluids* 7, 054401 (2022)

[9] **Exploiting self-organized criticality in strongly stratified turbulence**
G. Chini et al., *Journal of Fluid Mechanics* 933, A22 (2022)

[10] **Cooling by Baroclinic Acoustic Streaming**
G. Michel et C. Gissinger, *Physical Review Applied* 16, L051003 (2021)

[11] **Nonlinear Spectral Synthesis of Soliton Gas in Deep-Water Surface Gravity Waves**
P. Suret et al., *Physical Review Letters* 125, 264101 (2020)

[12] **Saturation of the inverse cascade in surface gravity wave turbulence**
E. Falcon et al., *Physical Review Letters* 125, 134501 (2020)

[13] **Emergence of Peregrine solitons in integrable turbulence of deep water gravity waves**
G. Michel et al., *Physical Review Fluids* 5, 082801 (2020)

[14] **From modulational instability to focusing dam breaks in water waves**
F. Bonnefoy et al., *Physical Review Fluids* 5, 034802 (2020)

[15] **Capillary wave turbulence experiments in microgravity**
M. Berhanu et al., *EPL* 128, 34001 (2019)

[16] **Multiple scales analysis of slow–fast quasi-linear systems**
G. Michel et G. Chini, *Proceedings of the Royal Society A* 475, 20180630 (2019)

[17] **Three-wave interactions among surface gravity waves in a cylindrical container**
G. Michel, *Physical Review Fluids* 4, 012801 (2019)

[18] **Strong wave – mean-flow coupling in baroclinic acoustic streaming**
G. Michel et G. Chini, *Journal of Fluid Mechanics* 858, 536 (2018)

[19] **Coexistence of solitons and extreme events in deep water surface waves**
A. Cazaubiel et al., *Physical Review Fluids* 3, 114802 (2018)

[20] **Self-similar gravity wave spectra resulting from the modulation of bound waves**
G. Michel et al., *Physical Review Fluids* 3, 054801 (2018)

[21] **Experimental observation of four-wave resonant interactions in a wave basin**
F. Bonnefoy et al., *La Houille Blanche (Revue internationale de l'eau)* 5, 56 (2017)

[22] **Observation of thermal equilibrium in capillary wave turbulence**
G. Michel, F. Pétrélis et S. Fauve, *Physical Review Letters* 118, 144502 (2017)

[23] **Instabilities on a turbulent background**
S. Fauve, J. Hérault, G. Michel et F. Pétrélis, *Journal of Statistical Mechanics*, 064001 (2017)

[24] **Observation of nonlinear sloshing induced by wetting dynamics**
G. Michel, F. Pétrélis et S. Fauve, *Physical Review Fluids* 2, 022801 (2017)

[25] **The generalized Doppler effect for surface waves**
G. Michel, *EPL* 116, 44002 (2016)

[26] **Observation of resonant interactions among surface gravity waves**
F. Bonnefoy et al., *Journal of Fluid Mechanics* 805, R3 (2016)

[27] **Bifurcations of a large-scale circulation in a quasi-bidimensional turbulent flow**
G. Michel, J. Herault, F. Pétrélis et S. Fauve, *EPL* 115, 64004 (2016)

[28] **Acoustic Measurement of Surface Wave Damping by a Meniscus**
G. Michel, F. Pétrélis et S. Fauve, *Physical Review Letters* 116, 174301 (2016)

[29] **Local fluctuation theorem for large systems**
G. Michel et D. J. Searles, *Physical Review Letters* 110, 260602 (2013)

[30] **Contribution of the stochastic forces to the fluctuation theorem**
G. Michel et D. J. Searles, *Physical Review E* 85, 0421202 (2012)

Travaux de vulgarisation

Comment naissent les vagues scélérates ?
Guillaume Michel, *The Conversation* (2020)

La physique d'un verre d'eau
Guillaume Michel, *Le Rayon – Revue de la SFP* (2018)

Livre

Physique PCSI
Guillaume Michel, Arnaud Raoux, Paul Tondelier et Emmanuel Van Brackel
De Boeck Université, 768 p. (2017)

Participation à la vie scientifique

Referee	*Physical Review Letters, Physical Review E, Physical Review Applied, Physics Letters A, Journal of the Acoustical Society of America, Fluids, Journal of Fluid Mechanics, Journal of Marine Science and Engineering* et *Fluids*
Encadrement	Co-encadrement avec Greg Chini de la thèse Remil Mushthaq (soutenue le 11/11/2025) Co-encadrement avec François Pétrélis et Stephan Fauve d'une partie de la thèse de Valentin Mouet (soutenue le 03/10/2024) Encadrement de deux étudiants en stage de Master (Thibaud Vernier et Arman Aykin) Encadrement d'un étudiant de l'ENS Paris en césure (Jonathan Billet)
Jury de concours	Participation à trois comités de suivi de thèse Examinateur de deux thèses (2022 – Jacques Abdul Massih, 2023 – Jules Fillette) Membre de deux jurys de concours de recrutement de maître de conférences Membre de quatre jurys de concours de recrutement d'ATER
Séminaires	Plus d'une vingtaine de présentations orales dans des laboratoires. Les dernières en date : 30/04/2026 – Séminaire au laboratoire Jean Alexandre Dieudonné (Univ. Côte d'Azur) 30/03/2026 – Séminaire *Fluids & Interfaces Seminar* (ENS Paris) 27/05/2025 – Présentation à l'Académie des Sciences 12/05/2025 – Présentation à la 12^{e} *International Conference on Multiphase Flow* 10/12/2024 – Présentation dans un atelier sur la combustion à Sorbonne Université 20/09/2024 – Intervention grand public à la *Nuit de l'ENS, Festival Sciences et Lettres*
Organisation de séminaires	(2023 – présent) Séminaire général de l'IJLRDA (en collaboration avec trois collègues) (2013 – 2019) Séminaires hebdomadaires de physique non linéaire de l'ENS Paris
Organisation de conférences	(2024 – présent) Membre du comité scientifique de la Rencontre du Non Linéaire 2024 – Organisation d'une journée « Acoustique et physique non linéaire »
Autres	(2025 – présent) Membre élu du conseil de laboratoire (2015 – 2016) Responsable de la formation expérimentale à l'ENS Paris des Olympiades Internationales de Physique (2013 – 2014) Secrétaire pédagogique pour le concours d'entrée de l'École Normale Supérieure de Paris

Bibliographie

[1] M. Gregg, E. d'Asaro, J. Riley et E. Kunze, Annu. Rev. Mar. Sci. **10**, 443 (2018).

[2] C. Caulfield, Annu. Rev. Fluid Mech. **53**, 113 (2021).

[3] C. Caulfield, Phys. Rev. Fluids **5**, 110518 (2020).

[4] R. W. Schmitt, Annu. Rev. Fluid Mech. **26**, 255 (1994).

[5] P. A. Bois, Geophys. Astrophys. Fluid Dyn. **58**, 45 (1991).

[6] A. Maffioli, G. Brethouwer et E. Lindborg, J. Fluid. Mech. **794**, R3 (2016).

[7] A. Maffioli, J. Fluid Mech. **870**, 266 (2019).

[8] G. Brethouwer, P. Billant, E. Lindborg et J.-M. Chomaz, J. Fluid Mech. **585**, 343 (2007).

[9] P. Billant et J.-M. Chomaz, Phys. Fluids **13**, 1645 (2001).

[10] E. Lindborg, J. Fluid Mech. **550**, 207 (2006).

[11] P. Augier, P. Billant et J.-M. Chomaz, J. Fluid Mech. **769**, 403 (2015).

[12] A. Maffioli et P.A. Davidson, J. Fluid. Mech. **786**, 210 (2016).

[13] G. D. Portwood, S. M. de Bruyn Kops, J. R. Taylor, H. Salehipour et C. Caulfield, J. Fluid Mech. **807**, R2 (2016).

[14] A. Maffioli, Phys. Rev. Fluids **2**, 104802 (2017).

[15] D. Lucas et C. P. Caulfield, J. Fluid Mech. **832**, R1 (2017).

[16] F. Feraco, R. Marino, A. Pumir, L. Primavera, P. D. Mininni, A. Pouquet et D. Rosenberg, Europhys. Lett. **123**, 44002 (2018).

[17] A. Garanaik et S. K. Venayagamoorthy, Phys. Fluids **30**, 126602 (2018).

[18] S. Khani, J. Fluid Mech. **849**, 373 (2018).

[19] G. D. Portwood, S. M. de Bruyn Kops et C. P. Caulfield, Phys. Rev. Lett. **122**, 194504 (2019).

[20] C. J. Lang et M. L. Waite, Phys. Rev. Fluids **4**, 044801 (2019).

[21] S. P. de Bruyn Kops et J. J. Riley, J. Fluid Mech. **860**, 787 (2019).

[22] C. J. Howland, J. R. Taylor et C. P. Caulfield, J. Fluid Mech **898**, A7 (2020).

[23] P. Garaud, G. P. Chini, L. Cope, K. Shah et C. P. Caulfield, J. Fluid Mech. **991**, R1 (2024).

[24] F. Feraco, R. Marino, L. Primavera, A. Pumir, P. D. Mininni, D. Rosenberg, A. Pouquet, R. Foldes, E. Lévêque, E. Camporeale, S. S. Cerri, H. Charuvil Asokan, J. L. Chau, J. P. Bertoglio, P. Salizzoni et M. Marro, Europhys. Lett. **135**, 14001 (2021).

[25] P. Augier, P. Billant, M. E. Negretti et J.-M. Chomaz, Phys. Fluids **26**, 046603 (2014).

[26] P. Odier, J. Chen et R. E. Ecke, J. Fluid Mech. **746**, 498 (2014).

[27] A. Lefauve, C.R. Phys. (2024).

[28] G. Michel, *Parois et ondes de surface : Dissipation, effet Doppler et interactions non linéaires* (Thèse de doctorat, 2017).

[29] S. Nazarenko, *Wave Turbulence* (Springer, 2001).

[30] P.-P. Cortet et N. Lanchon, C.R. Phys. **25**, 537 (2024).

[31] F. Charru, *Instabilités Hydrodynamiques* (EDP Sciences, 2007).

[32] C.-S. Yih, Quart. Appl. Math. **12**, 434 (1955).

[33] A. Deloncle, J.-M. Chomaz et P. Billant, J. Fluid Mech. **570**, 297 (2007).

[34] G. Lawrence, R. Pieters, L. Zaremba, T. Tedford, L. Gu, S. Greco et P. Hamblin, Deep Sea Res. Part II **51**, 475 (2004).

[35] W. D. Smyth et J. N. Moum, Geophys. Res. Lett. **40**, 6181 (2013).

[36] H. T. Pham, W. D. Smyth, S. Sarkar et J. N. Moum, J. Phys. Oceanogr. **47**, 2189 (2017).

[37] Q. Zhou, J. R. Taylor et C. P. Caulfield, J. Fluid Mech. **820**, 86 (2017).

[38] S. A. Thorpe et Z. Liu, J. Phys. Oceanogr. **39**, 2373 (2009).

[39] H. Salehipour, W. R. Peltier et C. P. Caulfield, J. Fluid Mech. **856**, 228 (2018).

[40] W. D. Smyth, J. D. Nash et J. N. Moum, Sci. Rep. **9**, 3747 (2019).

[41] M. J. Aschwanden, N. B. Crosby, M. Dimitropoulou, M. K. Georgoulis, S. Hergarten, J. McAteer, A. V. Milovanov, S. Mineshige, L. Morales, N. Nishizuka, G. Pruessner, R. Sanchez, S. Sharma, A. Strugarek et V. Uritsky, Space Sci Rev **198**, 47 (2016).

[42] G. Pruessner, *Self-organized criticality : theory, models and characterization* (Cambridge University Press, 2012).

[43] G. Michel et G. P. Chini, Proc. R. Soc. A **475**, 20180630 (2019).

[44] G. P. Chini, G. Michel, K. Julien, C. B. Rocha et C. P. Caulfield, J. Fluid Mech. **933**, A22 (2022).

[45] T. Dauxois, T. Peacock, P. Bauer, C. P. Caulfield, C. Cenedese, C. Gorlé, G. Haller, G. N. Ivey, P. F. Linden, E. Meiburg, N. Pinardi, N. M. Vriend et A. W. Woods, Phys. Rev. Fluids **6**, 020501 (2021).

[46] J. M. Hamilton, J. Kim et F. Waleffe, J. Fluid Mech. **287**, 317 (1995).

[47] G. K. et S. Kida, J. Fluid Mech. **449**, 291 (2001).

[48] M. D. Graham et D. Floryan, Annu. Rev. Fluid Mech. **53**, 227 (2021).

[49] D. Lucas, C. P. Caulfield et R. R. Kerswell, J. Fluid Mech. **832**, 409 (2017).

[50] A. Ferraro, G. P. Chini et T. M. Schneider, Phys. Rev. E **111**, 025105 (2025).

[51] S. Popinet, J. Comp. Phys. **418**, 109609 (2020).

[52] R. A. Plumb, J. Atmos. Sci. **34**, 1847 (1977).

[53] R. A. Plumb et A. D. McEwan, J. Atmos. Sci. **35**, 1827 (1978).

[54] M. P. Baldwin, L. J. Gray, T. J. Dunkerton, K. Hamilton, P. H. Haynes, W. J. Randel, J. R. Holton, M. J. Alexander, I. Hirota, T. Horinouchi, D. B. A. Jones, J. S. Kinnersley, C. Marquardt, K. Sato et M. Takahashi, Rev. Geophys. **39**, 179 (2001).

[55] S. A. Smith, D. C. Fritts et T. E. Vanzandt, J. Atmos. Sci. **44**, 1404 (1987).

[56] R. A. Plumb, in *Dynamics of the Middle Atmosphere* (Terra Sci., 1984), pp. 217–251.

[57] B. Semin et F. Pétrelis, C.R. Phys. **25**, 557 (2024).

[58] J. R. Herring, J. Atmos. Sci. **20**, 325 (1963).

[59] J. Lighthill, J. Sound Vib. **61**, 391 (1978).

[60] M. Bengtsson et T. Laurell, Anal. Bioanal. Chem. **378**, 1716 (2004).

[61] G. G. Yaralioglu, I. O. Wygant, T. C. Marentis et B. T. Khuri-Yakub, Anal. Chem. **76**, 3694 (2004).

[62] B. Verhaagen, C. Boutsioukis, L. W. M. van der Sluis et M. Versluis, J. Acoust. Soc. Am. **135**, 1717 (2014).

[63] N. El Ghani, S. Miralles, V. Botton, D. Henry, H. Ben Hadid, B. Ter-Ovanessian et S. Marcelin, Intl J. Heat Mass Transfer **172**, 121090 (2021).

[64] J. Qu, D. Henry, S. Miralles, V. Botton et F. Raynal, Phys. Rev. Fluids **7**, 064501 (2022).

[65] N. Riley, in *Encyclopedia of Acoustics* (Wiley, 1997), pp. 321–327.

[66] N. Riley, Annu. Rev. Fluid Mech. **33**, 43 (2001).

[67] W. L. Nyborg, in *Nonlinear Acoustics* (Springer Nature Switzerland, 2024), pp. 205–229.

[68] C. Zhang, X. Guo, P. Brunet, M. Costalonga et L. Royon, Microfluid. Nanofluid. **23**, 104 (2019).

[69] C. Zhang, X. Guo, L. Royon et P. Brunet, Phys. Rev. E **102**, 043110 (2020).

[70] B. Moudjed, V. Botton, D. Henry, H. Ben Hadid et J.-P. Garandet, Phys. Fluids **26**, 093602 (2014).

[71] G. Launay, T. Cambonie, D. Henry, A. Pothérat et V. Botton, Phys. Rev. Fluids **4**, 044401 (2019).

[72] B. Vincent, A. Kumar, D. Henri, S. Miralles, V. Botton et A. Pothérat, J. Fluid Mech. **1023**, A25 (2025).

[73] B. Vincent, D. Jenri, A. Kumar, V. Botton, A. Pothérat et M. Sophie, Phys. Rev. Fluids **10**, 114103 (2025).

[74] A. A. Doinikov, Proc. Royal Soc. A **447**, 447 (1994).

[75] T. Baasch, A. Pavlic et J. Dual, Phys. Rev. E **100**, 061102 (2019).

[76] L. Rayleigh, Philos. Trans. R. Soc. London **175**, 1 (1884).

[77] M. Rieutord, *Une introduction à la dynamique des fluides* (De Boeck, 2014).

[78] M. F. Hamilton, Y. A. Ilinskii et E. A. Zabolotskaya, J. Acoust. Soc. Am. **113**, 153 (2003).

[79] M. F. Hamilton, Y. A. Ilinskii et E. A. Zabolotskaya, J. Acoust. Soc. Am. **114**, 3092 (2003).

[80] R. M. Fand et J. Kaye, J. Acoust. Soc. Am. **32**, 579 (1960).

[81] B.-G. Loh, S. Hyun, P. I. Ro et C. Kleinstreuer, J. Acoust. Soc. Am. **111**, 875 (2002).

[82] S. Hyun, D.-R. Lee et B.-G. Loh, Intl J. Heat Mass Transfer **48**, 703 (2005).

[83] Y. Lin et B. Farouk, Intl J. Heat Mass Transfer **51**, 3179 (2008).

[84] M. Nabavi, K. Siddiqui et J. Dargahi, Intl Commun. Heat Mass Transfer **35**, 1061 (2008).

[85] M. K. Aktas et T. Ozgumus, Intl J. Heat Mass Transfer **53**, 5289 (2010).

[86] T. D. Dreeben et G. P. Chini, Phys. Fluids **23**, 056101 (2011).

[87] J. T. Karlsen, W. Qiu, P. Augustsson et H. Bruus, Phys. Rev. Lett. **120**, 054501 (2018).

[88] G. P. Chini, Z. Malecha et T. D. Dreeben, J. Fluid Mech. **744**, 329 (2014).

[89] J. T. Karlsen, P. Augustsson et H. Bruus, Phys. Rev. Lett. **117**, 114504 (2016).

[90] G. Michel et G. P. Chini, J. Fluid Mech. **858**, 536 (2019).

[91] K. J. Burns, G. M. Vasil, J. S. Oishi, D. Lecoanet et B. P. Brown, Phys. Review Res. **2**, 023068 (2020).

[92] J. A. Massih, R. Mushthaq, G. Michel et G. P. Chini, J. Fluid Mech. **997**, A7 (2024).

[93] N. Nama, J. Fluid Mech. **866**, 1–4 (2019).

[94] R. Mushthaq, G. Michel et G. P. Chini, J. Fluid Mech. **1017**, A32 (2025).

[95] V. Botton, J. Fluid Mech. **1024**, F1 (2025).

[96] G. Michel et C. Gissinger, Phys. Rev. Appl. **16**, L051003 (2021).

[97] J. P. Koulakis et S. Putterman, J. Fluid Mech. **915**, A25 (2021).

[98] G. Ahlers, P. C. Hohenberg et M. Lücke, Phys. Rev. A **32**, 3493 (1985).

[99] I. Cisse, G. Bardan et A. Mojtabi, Intl J. Heat Mass Transfer **47**, 4101 (2004).

[100] J.-Z. Wu, B.-F. Wang, K. L. Chong, Y.-H. Dong, C. Sun et Q. Zhou, J. Fluid Mech. **951**, A13 (2022).

[101] A.-K. Liu et S. H. Davis, J. Fluid Mech. **81**, 63 (1977).

[102] S. Popinet, J. Comp. Phys. **302**, 336 (2015).